

AD A088832

DDC FILE COPY

SECURITY CLASSIFICATION OF THIS REPORT

~~Unclassified~~

REPORT DOCUMENTATION PAGE

READ INSTRUCTIONS
BEFORE COMPLETING FORM

1. REPORT NUMBER

AFOSR-TR- 80-0691

2. GOVT ACCESSION NO.

AD-A088832

3. RECIPIENT'S CATALOG NUMBER

4. TITLE (and Subtitle)

Near-Source Phenomena and Their Manifestations
on Signatures of More Distant Radiation of
Seismic Energy

5. TYPE OF REPORT & PERIOD COVERED

FINAL REPORT

6. PERFORMING ORG. REPORT NUMBER

DELTA-R-79-0042 ✓

8. CONTRACT OR GRANT NUMBER(s)

F49620-79-C-0230

7. PERFORMING ORGANIZATION NAME AND ADDRESS

Del Mar Technical Associates ✓
Post Office Box 1083
Del Mar, California 9201410. PROGRAM ELEMENT, PROJECT, TASK
AREA & WORK UNIT NUMBERSARPA Order No. 3368
Program Code 7F10

1. CONTROLLING OFFICE NAME AND ADDRESS

DARPA
1400 Wilson Blvd.
Arlington, VA 22209

12. REPORT DATE

May 1980

13. NUMBER OF PAGES

431

14. MONITORING AGENCY NAME & ADDRESS (if different from Controlling Office)

AFOSR/NP
Bolling AFB
Washington, D.C. 20332

15. SECURITY CLASS. (of this report)

UNCLASSIFIED

15a. DECLASSIFICATION/DOWNGRADING
SCHEDULE N/A

6. DISTRIBUTION STATEMENT (of this Report)

Approved for public release;
distribution unlimited.

17. DISTRIBUTION STATEMENT (of the abstract entered in Block 20, if different from Report)

18. SUPPLEMENTARY NOTES

19. KEY WORDS (Continue on reverse side if necessary and identify by block number)

SEISMIC RADIATION, UNDERGROUND NUCLEAR EXPLOSIONS, THEORETICAL/NUMERICAL
SIMULATIONS, ELASTODYNAMIC REPRESENTATION THEOREM, NEAR-SOURCE EFFECTS,
REGIONAL SEISMOLOGY, SPALL, FINITE ELEMENTS, REVIEW/INTERPRETATION OF
EMPIRICAL DATA

20. ABSTRACT (Continue on reverse side if necessary and identify by block number)

A systematic analysis of buried explosions is performed for the purpose of
determining how near-source effects influence seismic observations. Analytical
Green's function methods are developed and used to efficiently and accurately
extend representations of seismic radiation to the far-field domain of
interest. Representations of nonlinear processes and near-source inhomogeneities
are provided that simplify the complexities of near-source explosion/earth

(continued)

DD FORM 1 JAN 73 1473

EDITION OF 1 NOV 65 IS OBSOLETE

UNCLASSIFIED

DTIC
SEP 4 1980
C

~~Unclassified~~

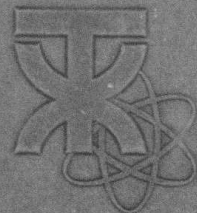
..20. Abstract (continued)

interactions while still allowing for important near-source variations. The theoretical/computational program is conducted in parallel with a review/interpretative program of empirical data from a broad suite of geologic settings.

UNCLASSIFIED

SECURITY CLASSIFICATION OF THIS PAGE (When Data Entered)

AEOSR-TR- 80-0691



TERA CORPORATION

Approved for public release;
distribution unlimited.

80 9 2 217

(18) AFOSR
(14)
Report DELTA-TR-79-0042

(19) TR-80-0697

(6) NEAR-SOURCE PHENOMENA AND THEIR MANIFESTATIONS ON SIGNATURES OF MORE DISTANT RADIATION OF SEISMIC ENERGY.

(10) Randy J. Apse
Glenn Rawson
Gerald A. Frazier
Jeffrey C. Fried
Joel Sweet
Peter Glover

(11) 30 May 80

(12) 438

Del Mar Technical Associates, CA,
1130 Camino Del Mar, Suite H
Post Office Box 1083
Del Mar, California 92014

30 May 1980

(9) Final Report

(15) F 49620-79-C-0330
ARPA Order-3368

Prepared for

AIR FORCE OFFICE OF SCIENTIFIC RESEARCH
Bolling Air Force Base
Washington, D.C. 20332

DEFENSE ADVANCED RESEARCH PROJECTS AGENCY
Washington, D.C. 20301

AIR FORCE OFFICE OF SCIENTIFIC RESEARCH (AFSC)
NOTICE OF TRANSMITTAL TO DDC
This technical report has been reviewed and is
approved for public release IAW AFR 190-12 (7b).
Distribution is unlimited.
A. D. BLOSE
Technical Information Officer

393109

393109 sel

TABLE OF CONTENTS

<u>Chapter</u>	<u>Page</u>
1 INTRODUCTION.	1-1
2 METHODS FOR APPROXIMATING SEISMIC RADIATION FROM COMPLEX EXPLOSION/EARTH INTERACTIONS	2-1
2.1 Empirical Source Functions.	2-2
2.2 Numerical Calculations: ONEDMAR	2-4
2.3 Pseudo Three-Dimensional Simulations.	2-6
3 EMPIRICAL AND THEORETICAL EXAMINATION OF SPALL AND ASSOCIATED NEAR SOURCE GROUND MOTION PHENOMENA	3-1
3.1 Empirical Analysis of Close in Ground Motion Data	3-1
3.2 Finite Element Modeling of Spall	3-41
3.3 Calculation of Surface Waves Generated by Spall Lift-Off and Impact	3-58
4 PROPAGATION OF NEAR-SOURCE EFFECTS TO TELESEISMIC DISTANCES USING REPRESENTATION THEOREM COUPLING	4-1
4.1 Introduction	4-1
4.2 Methodology	4-2
4.3 Validation	4-12
5 SEISMIC SYNTHESIS	5-1
5.1 Wave Propagation Using Prose	5-1
5.2 Regional Synthetic Seismograms	5-13
 REFERENCES	
 APPENDICES	
A ANALYTIC SOLUTION TO THE INVERSION OF MURPHY'S MODEL . .	A-1
B ONEDMAR -- A COMPUTER PROGRAM TO CALCULATE ONE DIMENSIONAL MATERIAL RESPONSE.	B-1
C SPALL FROM CONTAINED EXPLOSIONS RELATED TO YIELDS, DEPTHS OF BURST, AND MATERIAL PROPERTIES	C-1
D AN INTERPRETIVE ANALYSIS OF THOSE NUCLEAR EXPLOSION TESTS WHERE SURFACE WAVE ANALYSES HAVE BEEN PERFORMED	D-1

TABLE OF CONTENTS

(CONT.)

APPENDICES (Cont.)

- E EXPLOSION ENERGY PARTITIONING THAT MAY REFLECT
MATERIALS PROPERTIES VARIATIONS AND VARIATIONS
IN GROUND MOTION DATA E-I
- F FINITE ELEMENT MODELING OF TOP SURFACE SPALL F-I

Accession For	
NTIS GRA&I	<input checked="checked" type="checkbox"/>
DDC TAB	<input type="checkbox"/>
Unannounced	<input type="checkbox"/>
Justification	
By _____	
Distribution/ _____	
Availability Codes	
Dist	Available/or special
A	

CHAPTER I

INTRODUCTION

The work presented in this report has been motivated by the following fundamental goals.

- Develop and refine computational capabilities to efficiently and accurately extend representations of seismic radiation to the far-field domain of interest.
- Provide representations of nonlinear processes and near-source inhomogeneities that simplify the complexities of near-source explosion/earth interactions while still allowing for important near-source variations.

Satisfaction of these goals allows more computational time to be devoted to problem solving and parametric studies of the near-source influences upon the signatures of more distant radiation of seismic energy.

The basic approach has been to conduct a theoretical/computational program in parallel with a review/interpretation of empirical data from a broad suite of geologic settings. Some advantages derived from using empiricism in such an approach include providing a basis for: 1) constructing empirically-based forcing functions; and 2) choosing geologic parameters and configurations to represent near-source responses to explosions. The adequacy of computational short cuts to represent nonlinear and inhomogeneous phenomena (through use of forcing functions and equivalence techniques) is directly tied to empirical experience.

Chapter 2 is devoted to providing methods for approximating seismic radiation from the complex interactions of seismic signals emitted from explosions with the surrounding earth. In Section 2.1 the empirically-based source (forcing) functions are derived for later use in simulating the explosion produced cavity pressure without having to calculate the cavity growth time history. These source functions are designed to accurately predict the elastic fields induced by explosions at distances where material responses are essentially elastic. Section 2.2 introduces the ONEDMAR (ONE-Dimensional MATERIAL Response) method for simulating outgoing shock waves from explosions. The

ONEDMAR code utilizes the previously mentioned source functions and applies them to drive cylindrically symmetric simulations of both linear and non-linear dynamic responses to the induced shock wave.

In Section 2.3, pseudo three-dimensional simulations are considered in which the radiation pattern of the displacement field is known. The SWIS (StrWaves In Solids) finite element code is used to reduce problems involving three-dimensional axisymmetric geometries into the superposition of a small number (typically less than four) of two-dimensional calculations. By using a Fourier series expansion in azimuth, the source may be written as a sum of trigonometric functions; the displacement resulting from a particular Fourier coefficient in the source expansion is the solution to a two-dimensional problem and contains the same azimuthal dependence as the source. The total displacement is then given by superposition in the convergent Fourier series expansion. This methodology is described along with examples validating the capability of the SWIS code to perform calculations involving sources on as well as off the axis of symmetry in axisymmetric geologic configurations. Also presented in this section is an example of how a complex geologic setting (*Granite Test Area of the Nevada Test Site*) may be approximated by an axisymmetric configuration suitable for such pseudo three-dimensional calculations using the SWIS finite element code.

Chapter 3 capsulates results of the review/interpretation of a large body of empirical data. Emphasis is given in Section 3.1.1 to determining the configuration of spall as it varies with yield, depth of burst and geologic setting. Previous investigators studying spall effects upon seismic radiation assumed smaller spalled masses than are indicated by a careful review of the data base. The present ground motion data review also indicates a close link to probable in-situ stress orientations and stress magnitudes -- the greatest motions occurring in the direction of least resistance to the motion. Spall, fracturing and cavity growth asymmetries are all suspected of reflecting the pre-stress field responses to the explosion induced stresses. The interactions are important when trying to understand the relations between explosions and the generation of surface wave anomalies.

New relations between explosion induced Love-wave excitation, spall and geologic settings are presented in Section 3.1.2. Inconsistencies and oversimplifications of previous models (e.g., Fault Trigger Model and Cavity/Fracture Zone Model) are discussed in detail. Emphasis is placed on material properties and site geologic characteristics since the data are thought to reflect how various rocks are able to store stress and undergo deformation. Spall appears to be important in causing the release of stored elastic strain, which in some cases varies azimuthally and appears to contribute to Love-wave excitation.

Limited radial ground motion data have been examined with the goal of determining if near and far-field explosion energy partitioning can be estimated. In Section 3.1.3 the SALMON event is hypothesized to provide evidence that such partitioning can in fact be deduced from certain records. Further analyses may enable development of improved forcing functions for certain environments so as to link cavity growth history directly to ground motion data both within and beyond the elastic radius.

The remainder of Chapter 3 presents the capabilities developed for modeling spall by finite element methods in Section 3.2 and for calculating the surface waves generated by both spall lift-off and impact in Section 3.3. Both computational methods are demonstrated with the megaton explosion, the BENHAM event, conducted in Pahute Mesa at the Nevada Test Site. In both treatments, pre-stress release is not modeled. The finite element method utilizes the SWIS code and enables comparison of the simulated surface ground motion records where spall is allowed and where spall is restrained. The procedure for calculating the surface waves from spall assumes a finite pressure disk acting on a layered half-space with the corresponding synthetic seismograms obtained through use of Harkrider's surface wave code. The surface waves generated by spall depend strongly upon the spalled mass. A comparison is made between the presently interpreted spall configuration and those of previous investigators.

The methodology and computational procedures used to propagate near-source effects to teleseismic distances are presented in Chapter 4. Numerical procedures such as the SWIS finite element technique are useful for simulating the seismic radiation processes only in the immediate vicinity of the source up to the highest frequencies of interest. Assuming that there exists a volume containing the complex source regime outside which the medium is homogeneous or layered and the medium response is linear, analytic Green's function methods may be employed to propagate the near-source processes to the regional or teleseismic distances of interest. Two related methods are discussed in detail in Section 4.2 to couple the output from near-source shock-wave calculations for use as input to the analytical Green's function procedure. An extensive validation of the Representation Theorem Coupling method is presented in Section 4.3 for the case of a simple point source in an axisymmetric geometry. The method is shown to be quite accurate as well as cost efficient in all cases. Applications of this technique to more complex sources will be presented in a supplementary report. In particular, Applied Theory, Inc. (December 1979) has calculated the displacements and tractions on a hemispherical grid enclosing an explosion in NTS granite. A straightforward application of the Representation Theorem Coupling method will then provide the ground motion at any distance of interest beyond the radius defining the hemispherical grid.

Chapter 5 deals with seismic synthesis of buried explosions and elementary earthquake ruptures at regional and teleseismic epicentral distances. The analytical computer program PROSE (PROpagation of Seismic Energy) is discussed in Section 5.1 and is used to generate the results in Section 5.2. The earth structure is modeled by a stack of eight parallel viscoelastic layers extending to a depth of 260 km and overlying a semi-infinite viscoelastic half-space. This earth structure is assumed to represent a generic model of the Eastern United States. Epicentral distances between 100 and 2000 km and source depths between 0.4 and 10.0 km are considered for all source types. All the Green's function displacements are calculated with a frequency content of 0 through 2.0 Hz. Four source types are considered: 1) vertical strike-slip point dislocation; 2) point explosion; 3) vertical dip-slip point dislocation; and 4) 45 degree dip-slip point dislocation. A description of all the synthetic seismograms

appears in Section 5.2.2 including differences and similarities between the various source types considered, with particular emphasis on explosion sources versus elementary earthquake sources.

CHAPTER 2

METHODS FOR APPROXIMATING SEISMIC RADIATION FROM COMPLEX EXPLOSION/EARTH INTERACTIONS

Procedures are presented for characterizing seismic signals emitting from explosions. Of special interest are methods which approximate a buried explosion source in order to account for the highly non-linear responses in the surroundings and to approximate signal transmission through additional geologic heterogeneities. Priority has been given to developing appropriate simplifying methods so that the results of interest become the focus of the computational methods -- the radiated seismic energy rather than the detailed explosion/earth interactions.

Empirically derived forcing functions are used to simulate the explosion produced cavity pressure related to producing the appropriate seismic radiation at the more distant elastic radius. For certain situations it appears that other forcing functions may enable direct calculation of correct responses at the elastic radius using a simple elastic approximation from the cavity to elastic radius. Presently, this region must be simulated with hydrodynamic calculations. Data associated with this strong motion region has been reviewed for a variety of explosions and site characteristics -- discussed in Section 3.1. That section provides a background from which the appropriate forcing functions might be developed. In this chapter the empirically derived source functions of cavity pressure are discussed and applied using the ONEDMAR computer code.

An important simplification, using DELTA's SWIS code, enables 3-D simulations from a small number of 2-D calculations to approximate azimuthal (θ) variations from the source. This is made possible by treating the source as a Fourier series expansion in azimuth, θ . Now the source symmetry axis and the symmetry axis of the geologic setting can be separated -- simulating a non-symmetric or pseudo 3-D condition.

These methods provide substantial efficiencies enabling computerized approximations for a variety of geometric configurations to help better understand source effects upon distant seismic signals. The last section of this chapter illustrates the process used to simplify the geologic setting for the NTS granite site so that it can be adapted to an appropriate pseudo 3-D configuration with detonations offset from the geologic axis of idealized symmetry.

2.1 EMPIRICAL SOURCE FUNCTIONS

Several investigators (Haskell, 1967 and Mueller and Murphy, 1971) have derived methods to obtain reduced displacement potentials for nuclear explosions directly from the free-field ground motion measurements routinely performed during nuclear explosion tests. The intent of this approach is to ignore the details of the non-linear regime and assume that analytic approximations can be used to extrapolate the seismic source function inward from the elastic radius to the cavity wall. Although the stresses and displacements calculated from these source functions are inappropriate in the region between the cavity and the elastic radius, by design they accurately predict the elastic field beyond the elastic radius ($r > r_{el}$). These source representations are considered appropriate for incorporating explosive sources in analytic codes dealing with far-field phenomena. Examples include the Harkrider programs discussed in Section 3.3, and certain 2-D finite element calculations with SWIS (discussed in Section 3.2).

Haskell (1967) derived his source model by fitting functions having the form

$$\frac{\psi(t)}{\psi(\infty)} = 1 - e^{kt} \left[1 + kt + \frac{(kt)^2}{2} + \frac{(kt)^3}{6} - B(kt)^4 \right] \quad (2.1)$$

to reduced displacement potentials calculated from near-field ground motion data recorded from stations just beyond the elastic radius (r_{el}) at several explo-

sion tests. This functional form was chosen so as to make displacement, velocity, and acceleration values constant across the elastic radius. The parameters k and B are material dependent constants; k is assumed to scale inversely as yield to the one-third power, and B defines the amount of overshoot in the reduced displacement potential wave-form. Although Haskell considered explosions in different media, his source function contains no depth scaling. For low frequencies, far-field displacement spectra scale proportionally with yield.

Mueller and Murphy (1971), using the theoretical development of elastic displacements due to a spherical source in a homogeneous medium given by Sharpe (1942), derived the following analytic form for the radial stress (which they term pressure) acting on material at the elastic radius,

$$\sigma_{rr}(r_{el}, t) = (p_o e^{-\gamma t} + p_{oc}) H(t) \quad (2.2)$$

where the peak shock stress $p_{os} = p_o + p_{oc} = 1.5 \rho gh$, p_{oc} is the late time ($t = \infty$) radial stress at the elastic radius, ρgh is the overburden pressure, and $H(t)$ denotes the Heaviside step function. Mueller and Murphy find that for Pahute Mesa volcanics, with compressional and shear wave velocities (α and β) of 3.5 and 2.02 km/sec, and density $\zeta = 2.0 \text{ gm/cm}^3$,

$$r_{el} = 1490 \frac{W^{1/3}}{h^{0.42}} \text{ meters} \quad (2.3)$$

where W is the yield in kilotons and h the depth of burial in meters. The decay constant γ is given by

$$\gamma = 1.5 \frac{r_c}{r_{el}} \quad (2.4)$$

and the cavity radius r_c scales as

$$r_c = 31.4 \frac{W^{0.29}}{h^{0.11}} \text{ meters} . \quad (2.5)$$

The late time radial stress at the elastic radius is

$$p_{oc} = 0.8\nu \left(\frac{r_c}{r_{e1}} \right)^3 . \quad (2.6)$$

This model takes into account the depth of burial of the explosion. A derivation of the reduced displacement potential for the Mueller and Murphy source is given in Appendix A, together with the derivation of the corresponding expression for the radial stress at the cavity wall used in the ONEDMAR sample calculation (Appendix B).

The far-field displacement spectra for Mueller and Murphy's model are also proportional to yield. Synthetic surface waves from both Haskell's and Mueller/Murphy's source models are discussed in Sections 3.2 and 3.3.

2.2 NUMERICAL CALCULATIONS: ONEDMAR

Calculations of the close-in phenomena associated with underground nuclear explosions are usually performed in 1-D spherically symmetric geometry (Rimer, 1975 and Allen, 1975). Such calculations provide pressure functions that are suitable for driving cylindrically symmetric calculations. By applying the 1-D pressure function on or near the final cavity dimension in cylindrically symmetric simulations, an outgoing shock wave can be produced that closely

resembles that obtained in the complex 1-D calculations. Thus many of the computational complexities associated with growing a cavity in an axisymmetric geometry can be avoided, making it possible to concentrate on designing grids for optimal refinement of the particular near source effects being examined.

The program ONEDMAR (ONE-Dimensional Material Response) was developed to provide the above capability. A user's manual describing this code is contained in Appendix B. Both linear and non-linear dynamic behavior can be modeled. Additionally, the code enables modeling both tensile failure of material and plastic flow. A sample problem simulating propagation of a spherical blast wave in an earth-like material is presented in Appendix B. The forcing function representing pressure on the cavity wall due to the explosion was derived from Mueller and Murphy (1971). This derivation is given in Appendix B.

The above mentioned sample problem was designed to demonstrate the capabilities of the ONEDMAR code. It appears that for certain problems the ONEDMAR capability may allow circumvention of direct numerical calculation of the 1-D wave field. This requires a forcing function which, when applied to the cavity, generates the correct response at the elastic radius using elastic, rather than non-elastic or hydrodynamic calculations to propagate the signal through the interior region.

Such a forcing function would further enable much more computing time for non-linear calculations on phenomena of interest, for example, spall. One way to accomplish this is through the use of empirical scaling functions, similar to or modifications of those derived by Haskell (1967) and Mueller and Murphy (1971). In this manner we can avoid the exhaustive studies necessary to establish appropriate constitutive laws required to simulate material behavior in the close-in regime.

2.3 PSEUDO THREE-DIMENSIONAL SIMULATIONS

There are substantial cost and computer time savings when 2-D numerical calculations can be made to simulate 3-D. When using 3-D finite element or finite difference techniques, the number of operations associated with any given problem is proportional to k^4 where k is the largest wavenumber numerically resolvable. For the 2-D calculation, the number of operations is proportional to k^3 . Hence, 2-D methods will be able to resolve much smaller wavelengths (higher frequencies) than the 3-D methods in an equivalent amount of computing time.

Fortunately, many realistic problems possess radiation patterns which are known. An explosion in a layered half-space, for example, produces a radiation which has no azimuthal (θ) dependence. Lamb's problem for a half-space subject to a vertical point force also produces axisymmetric radiation. In fact, as long as the geology and the loading are axisymmetric, the elastic radiation will be also. Once the azimuthal dependence of the displacement field is known, this knowledge can be incorporated into the differential equations to reduce their dimension from three to two; thereby, the equations only depend upon the radial and vertical coordinates.

The case of axisymmetric loading is not the only one in which the radiation pattern of the displacement field is known. A horizontal point load on the geological axis of symmetry produces a radiation pattern $\cos\theta$ or $\sin\theta$ depending upon the component of displacement. A horizontal point dislocation on the axis of symmetry produces a displacement field which depends upon $\cos(2\theta)$ or $\sin(2\theta)$ depending upon the component. In fact, any point source on a symmetry axis which is characterized by a second order moment tensor has a known radiation pattern with azimuth. Just as in the case of axisymmetric radiation, a knowledge of the θ dependence of the displacement field may be substituted into the equations of motion and reduce the problem to a two-dimensional calculation.

Not all 3-D problems can be reduced to a single 2-D problem in this manner. While a point dislocation may be excellent approximation to an earthquake when the observer is many wavelengths from the source, an observer in the near-field will perceive the effects of source dimensions. If we think of the radiation from a finite fault as a Fourier series involving terms like $e^{in\theta}$, then increasing distance from the fault has the effect of a low pass filter on n , the azimuthal order. As distance increases, the larger angular frequencies decrease in amplitude fastest until eventually only the $n=2$ terms remain. This filtering phenomenon is true, not only for earthquakes, but any type of source in an axisymmetric geology, linear or nonlinear. In fact, the earth structure in the vicinity of the source may be quite arbitrary without affecting the decay with distance of the higher angular frequencies: The only requirement is that the geology be axisymmetric at some distance away from the source. The pseudo three-dimensional methodology which utilizes this property of the Fourier coefficients to act as filters, reducing the complicated 3-D problems to a small number of 2-D problems, is presented in the next subsection. This greatly increases the numerical tractability of a large class of quasi 3-D problems.

2.3.1 PSEUDO THREE-DIMENSIONAL METHODOLOGY

The SWIS finite element code has been used extensively to calculate ground motion in an axisymmetric geology. When the θ dependence of the source can be expressed as a trigonometric function, i.e., $e^{in\theta}$, the displacement also has the same θ dependence. Many problems involve an axisymmetric geology such as a circular basin, but with interest in an explosion source that is off axis. In these cases the θ dependence of the source can be quite complicated. By using a Fourier series expansion in θ , a source may be written as a sum of trigonometric functions. The displacement resulting from a particular Fourier coefficient in the source expansion is the solution to a 2-D problem and may be found using SWIS. The total displacement, which is 3-D, is then a superposition, or sum, of these 2-D solutions. This sum often converges very rapidly.

To demonstrate the validity of superposition, the problem of a vertical point load in a homogeneous full space is considered. The analytic solution to

this problem is given first. Two finite element calculations are then performed to determine the solution numerically. The first is performed with the load applied along the vertical coordinate axis (Figure 2-1). The resulting displacement field is known to have no dependence upon θ so that only one 2-D calculation is required. In the second calculation, the load is applied a short distance away from and parallel to the coordinate axis (Figure 2-1). A superposition of 2-D solutions is needed in this case since the load is not sinusoidal in θ . Only four terms in the Fourier series expansion for the load and displacement are needed to obtain satisfactory results.

Although this test problem is the simplest type of axisymmetric geology, it serves to demonstrate the mechanics and advantages of the superposition principle. Any other axisymmetric geology may be handled in the same manner; the only change necessary is in the prescription of different element types in SWIS.

The governing equations and boundary conditions for a point load in homogeneous full space are the following:

$$\mu \nabla^2 \underline{u} + (\lambda + \mu) \nabla (\nabla \cdot \underline{u}) + f_2 H(t) \delta(\underline{x}) e_2 = \rho \ddot{\underline{u}}, \quad (2.7)$$

$$\underline{u}(x_1, x_2, x_3, 0) = \dot{\underline{u}}(x_1, x_2, x_3, 0) = 0 \quad (2.8)$$

$$\lim_{x \rightarrow \infty} \underline{u}(x, t) = 0$$

where $H(t)$ is the Heaviside step function.

The body force, f_2 , has been applied in the direction of the x_2 axis and is centered at the origin of our coordinate system (see Figure 2-1). An analytical solution to this problem is given in Elastodynamics, Vol. 2, p. 394 by Eringen and Suhubi (1975). If the integrations in these equations are carried out, the resulting expression for the i^{th} Cartesian component of displacement is

$$\begin{aligned}
u_i(x, t) = & \frac{f_2}{4\pi\rho} \left\{ \frac{1}{r^2} \left(\frac{3x_i x_2}{r^3} - \frac{\delta_{i2}}{r} \right) * P(t) \right. \\
& + \frac{x_i x_2}{r^3} \left[\frac{1}{a^2} H(t - r/a) - \frac{1}{b^2} H(t - r/b) \right] \\
& \left. + \frac{\delta_{i2}}{r b^2} * H(t - r/b) \right\} \quad (2.9)
\end{aligned}$$

where:

$$P(t) \equiv \begin{cases} 0; & t < r/a \\ t^2/2 - r^2/2a^2; & r/a \leq t \leq r/b \\ r^2/2b^2 - r^2/2a^2; & t > r/b \end{cases}$$

and

$$H(t-\tau) \equiv \begin{cases} 0; & t < \tau \\ 1; & t \geq \tau \end{cases} \quad \text{i.e., the Heaviside Unit Function}$$

$$\delta_{i2} \equiv \begin{cases} 1 & \text{if } i = 2 \\ 0 & \text{if } i \neq 2 \end{cases} \quad \text{i.e., Kroneker Delta}$$

$$r \equiv \sqrt{x_1^2 + x_2^2 + x_3^2}$$

As stated previously, two finite element formulations of this problem will be considered. The first applies to the body force at the origin of a cylindrical coordinate system (the un-primed coordinate system of Figure 2-1). The displacement field then has no dependence upon the azimuthal coordinate. Figure 2-2 shows the finite element grid used in this calculation. The symmetry condition $u_r = u_\theta = 0$ on the plane $z = 0$ is used so the full space may be modeled as a half space. The magnitude of the forcing function, f_2 , has been correspondingly decreased by half in the finite element model because the full space has been eliminated by the symmetry plan. The size of the grid is 19 by 19 elements and the time history of displacement is recorded at the points (r,z) equal to (10,0) and (10,4). These time histories are labeled AXISYMMETRIC in Figures 2-3, 2-4 and 2-5, and can be compared with the analytic solution with the source on axis for a reference standard.

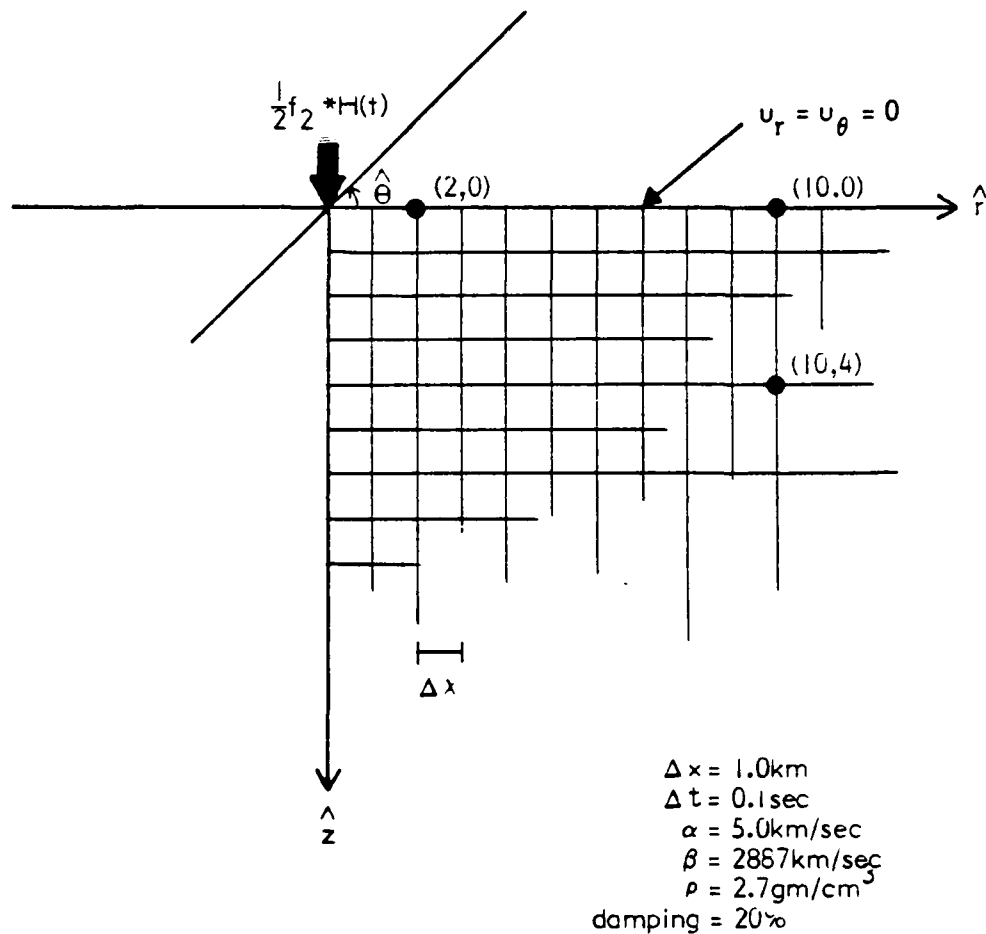


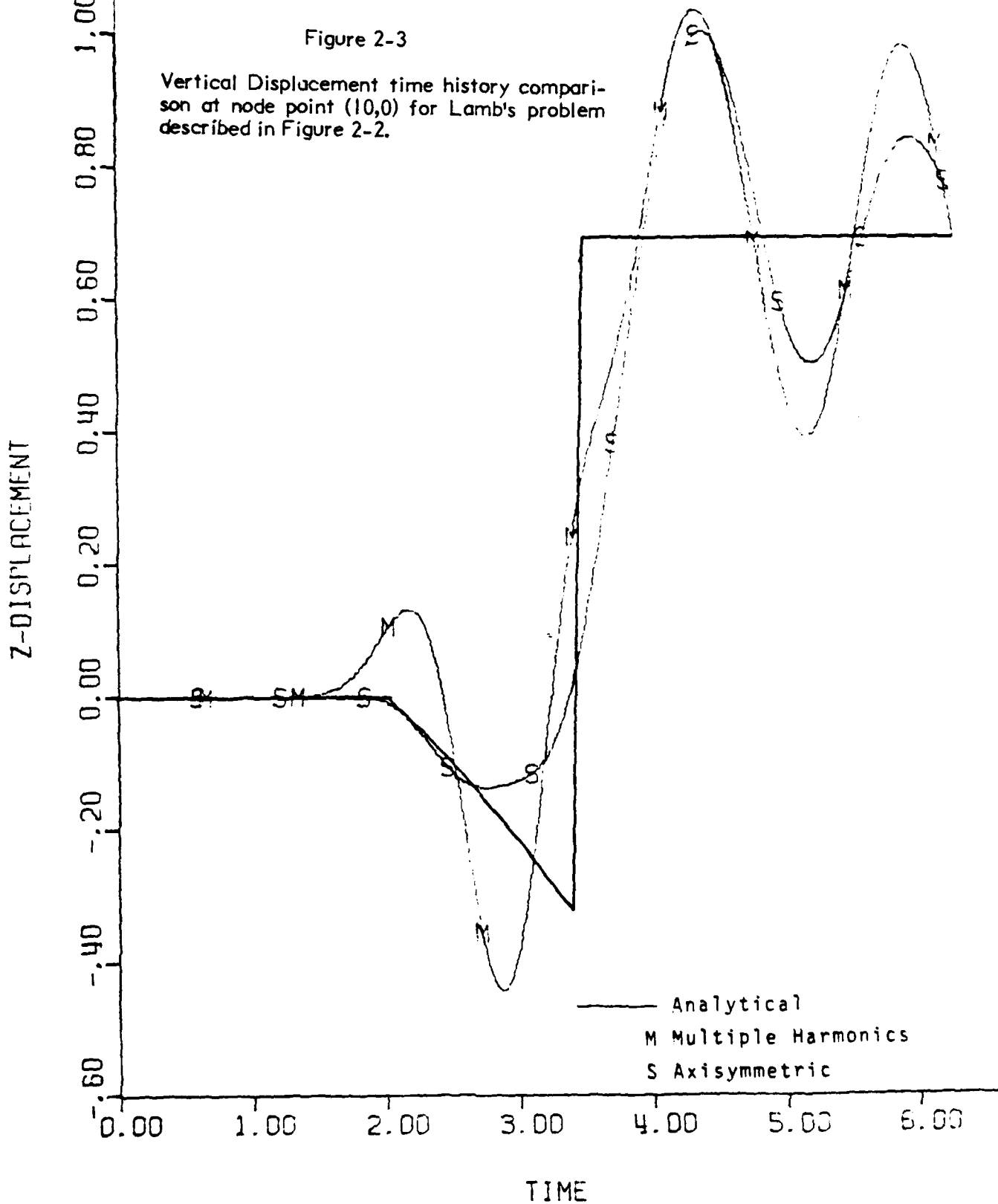
Figure 2-2 Finite element grid used to compare displacement time histories obtained from multiple harmonics and axisymmetric finite element calculations to analytic solution for Lamb's problem.

MULTI-COMPONENT

(10,0)

Figure 2-3

Vertical Displacement time history comparison at node point (10,0) for Lamb's problem described in Figure 2-2.



MULTI-COMPONENT (10,4)

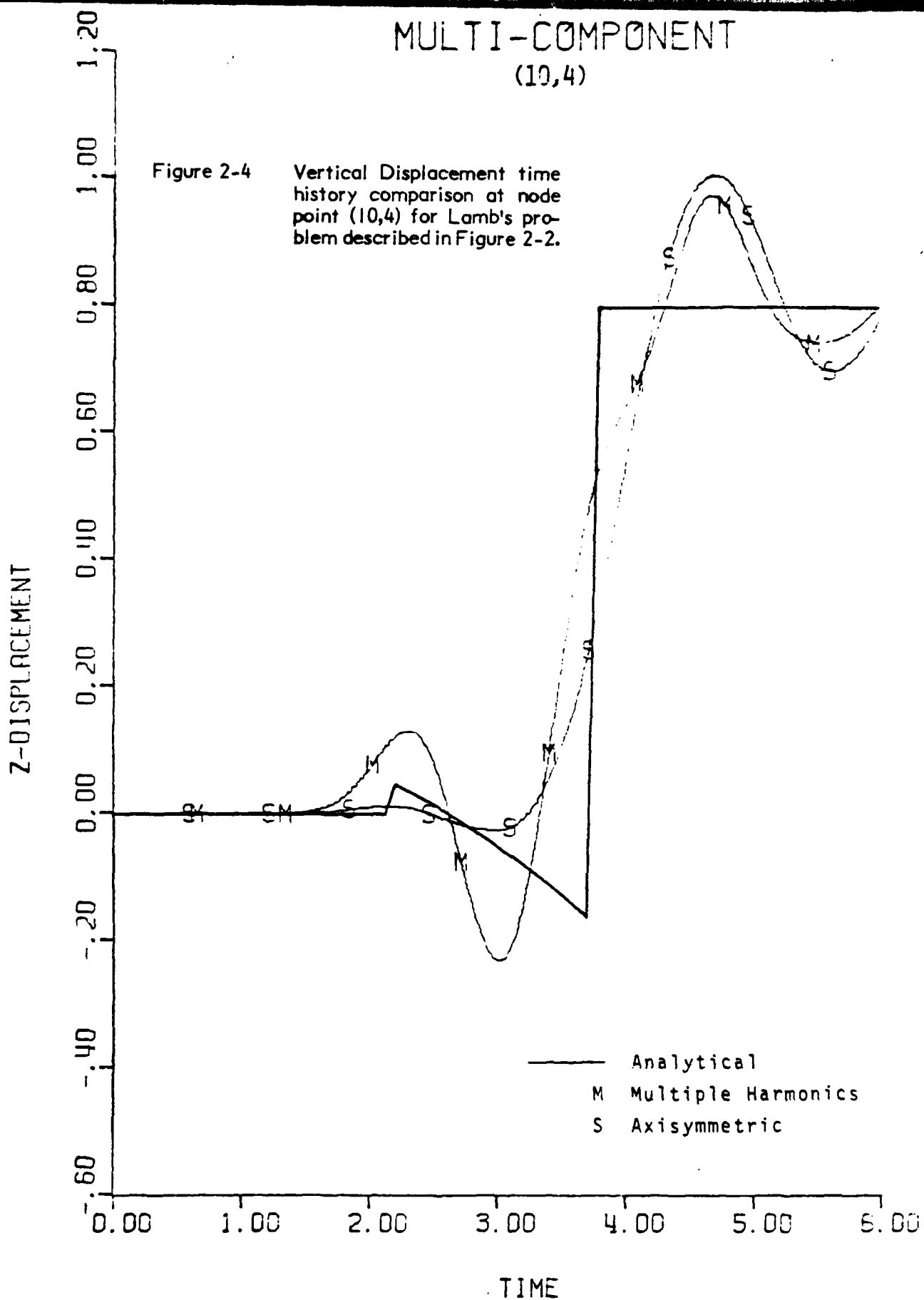


Figure 2-4.

MULTI-COMPONENT (10,4)

Figure 2-5 Radical displacement time history comparison at node point (10,4) for Lamb's Problem described in Figure 2-2.

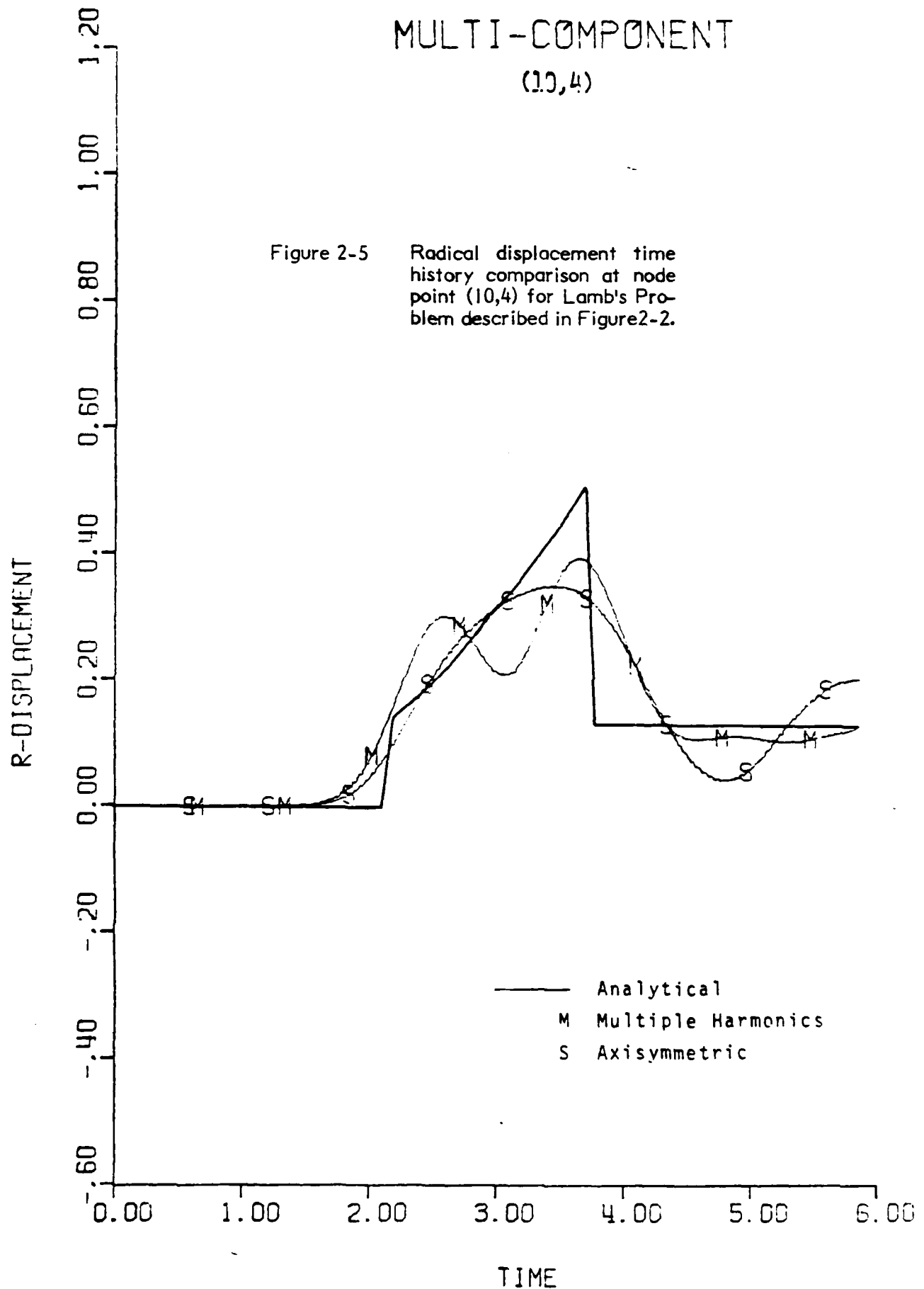


Figure 2-5.

The second finite element calculation differs in only one respect: The force is applied at the point (2,0) in the numerical grid instead of on the axis (Figure 2-2). Since θ dependence of the force is not sinusoidal, more than one 2-D calculation is required to obtain the entire 3-D displacement field. If we approximate the θ dependence of the load f_2 by the first four terms in a Fourier series,

$$f_2(r, z, \theta, t) = \sum_{n=0}^3 F_2^{(n)}(r, z, t) \cos n\theta \quad (2.10)$$

where

$$F_2^{(n)} = \frac{\int_0^{2\pi} f_2(r, z, \theta, t) \cos^2 n\theta \, d\theta}{(\pi + \delta_{0n} \pi)}$$

Then the resulting displacements are given by

$$\begin{aligned} u_R &= \sum_{n=0}^3 R_n(r, z, t) \cos(n\theta) \\ u_z &= \sum_{n=0}^3 Z_n(r, z, t) \cos(n\theta) \\ u_\theta &= \sum_{n=0}^3 \Theta_n(r, z, t) \sin(n\theta) \end{aligned} \quad (2.11)$$

When Equations (2.10) and (2.11) are used in the virtual work relations (Eringen and Suhubi, 1975), four sets of equations result -- one for each harmonic n . For each n , the equations depend only upon r and z relating the body force coefficient $F_2^{(n)}(r, z, t)$ to the displacement coefficients $R_n(r, z, t)$, $Z_n(r, z, t)$ and $\Theta_n(r, z, t)$. For the case of a delta function load, the nodal force at the appropriate finite element grid point is $F_2^{(n)}(t)$ given by

$$\left. \begin{aligned} F_2^{(n)}(t) &= \frac{\int_0^{2\pi} f_2(\theta, t) \cos^2 n\theta \, d\theta}{\pi(1 + \delta_{0n})} = \frac{H(t) \int_0^{2\pi} \frac{\delta(\theta)}{2} \cos^2 n\theta \, d\theta}{\pi(1 + \delta_{0n})} \\ &= \frac{H(t)}{2\pi(1 + \delta_{0n})} \quad n = 0, 1, 2, 3 \end{aligned} \right\} \quad (2.12)$$

The SWIS code is then used to calculate the displacement coefficients one at a time for $n = 0, 1, 2$ and 3 . The sums in Equation (2.11) are then performed to yield the displacements labeled MULTIPLE HARMONIC in Figures 2-3, 2-4 and 2-5.

The two finite element calculations provide a low pass filtered version of the analytic result. The slight differences between the two finite element results are mainly due to using only four terms in the Fourier series of equations (2.10) and (2.11). If a more complicated axisymmetric geology were being considered, e.g., a hemispherical basin, the use of the superposition principle would be much less expensive than conventional 3-D finite element.

2.3.2 AXISYMMETRIC GEOLOGIC SETTING APPROXIMATION FOR THE GRANITE TEST AREA AT THE NEVADA TEST SITE (NTS)

The granite rock for nuclear tests at NTS is known as the Climax Stock. It intrudes the flanking volcanic sedimentary and metamorphic rock strata. This location has been well documented geologically, is crudely axisymmetric in configuration, and has been the site of both the HARDHAT and PILEDRIVER nuclear explosions. Both were detonated a little off center of the apparent and idealized axis of the stock.

We have used the existing geologic descriptive data and interpretations and, through a series of simplifying approximations, reduced a representation of the site to a form suitable for 2-D simulation of 3-D seismic radiation calculations. The explosion would be off-axis from the geology and the core of hard rock would be flanked by less dense bedded strata. Since the original geologic data is itself generalized and simplified from the heterogeneous real situation, the final earth model is obviously a gross simplification. For this reason, any calculation would not be to model HARDHAT or PILEDRIVER, but would better represent a configuration of general interest. The contrasts of material properties with depth surrounding the granite are not large, so it may be more instructive to increase the contrast to study the effects upon radiated signals.

Figure 2-6 is a simplified plan view geologic map of the Climax Stock showing the locations of the north-south and east-west profiles developed primarily from the maps published by the U.S. Geological Survey (see Barnes, 1963; and Houser, 1960). Figures 2-7 and 2-8 are the profiles extrapolating near surface data to considerable depth. The deep data control was provided by the geologic and geophysical interpretation of crustal data across the U.S. along the 37th parallel (see Hamilton, 1965). Also, the inverted cone shape of the Climax Stock is inferred from airborne geomagnetics data shown by Figure 2-9. (Boynton, 1963 and Hazlewood, 1963).

The rock units shown on the geologic profiles are identified by a relative age and a sequence of units code found in the references. Basically the youngest Quaternary (Q) unit is alluvium, the Tertiary age (T) volcanic rocks. The Pennsylvanian-Mississippian age (PMe) quartzites and limestones flank the stock on the west, trapping Ordovician age limestone next to the granite. This rock is metamorphized to a marble where exposed. The older Cambrian rocks (C) are mostly limestone, dolomite shale and quartzite. The granitic mass is considered to merge with the regional granitic/metamorphic basement rocks of pre-Cambrian (pC) age at about 5 kilometers depth.

Figures 2-10 a,b, are simplifications of the north-south and east-west profiles showing generalizations of topography, rock types, as well as geologic structures (bedding and faults eliminated). Figure 2-10 c takes this one step further to make the site axisymmetric.

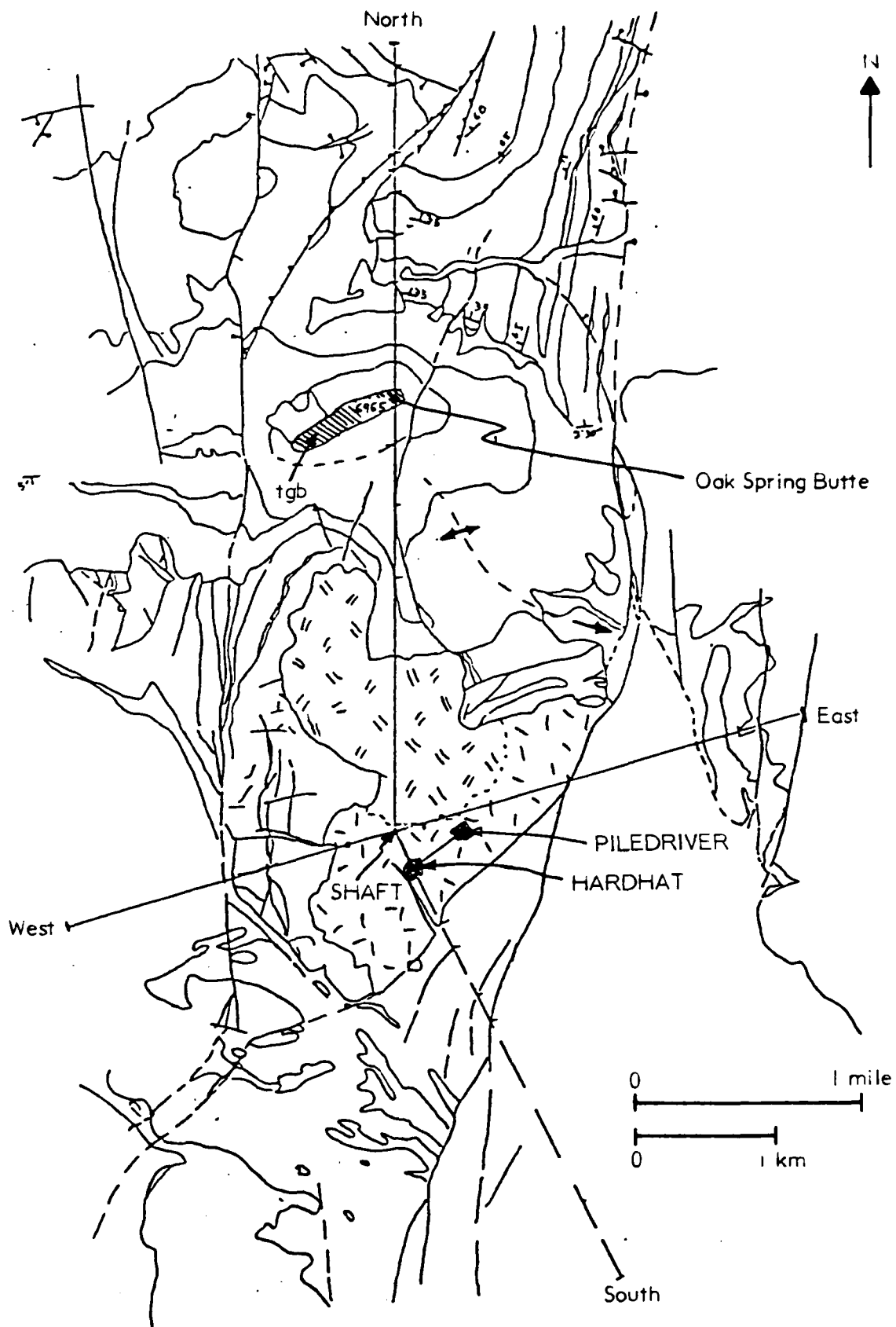


Figure 2-6 Simplified tracing of a portion of the Oak Spring Butte Quadrangle Map showing locations of the North-South and East-West Profiles of Figures 2-7 and 2-8

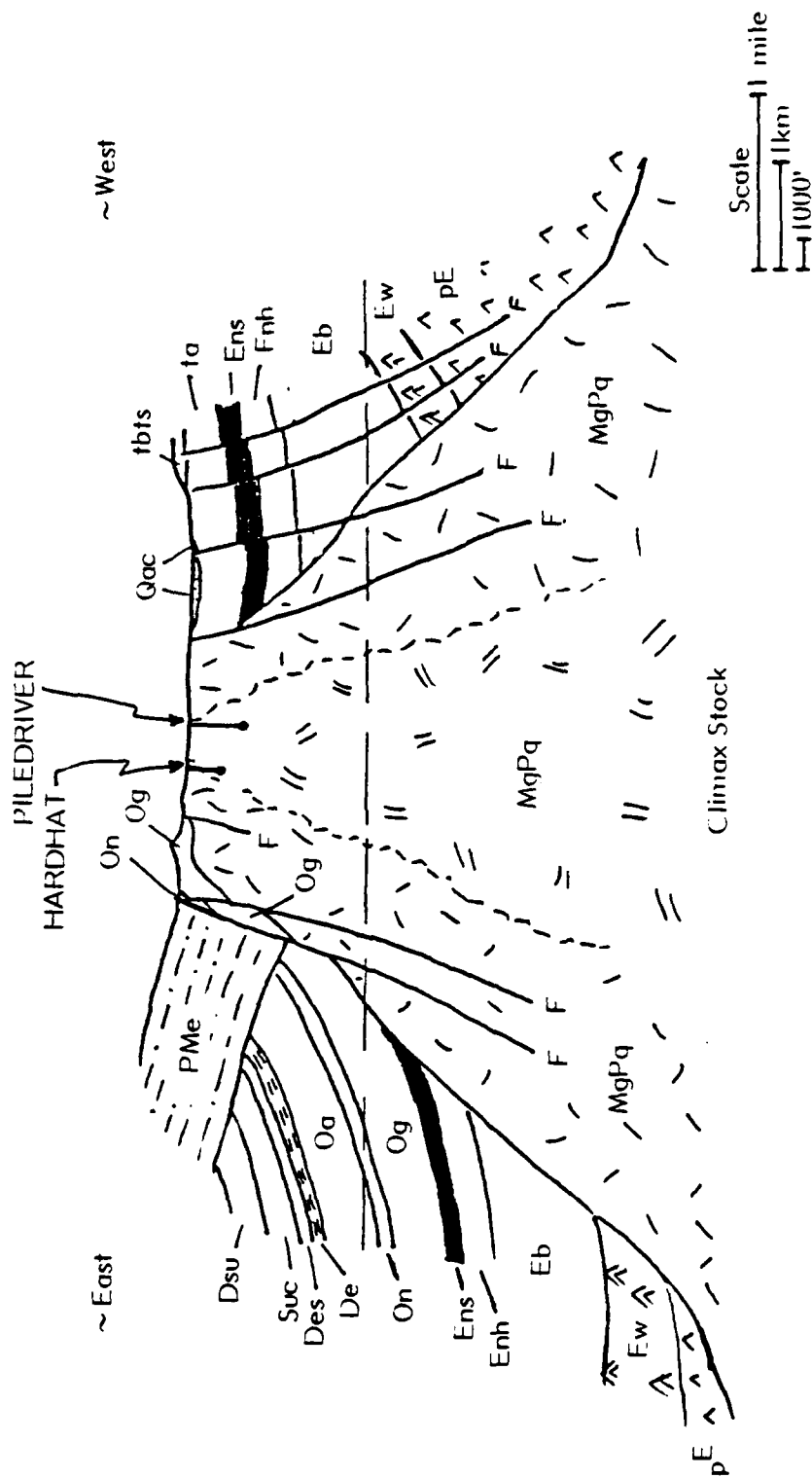


Figure 2-8 East-West Profile Extrapolation of Surface and Shallow Drill Hole geologic Data of the Climax Stock Showing Flanking (F) and Rock Units (PMe, Mg Pg, etc.)

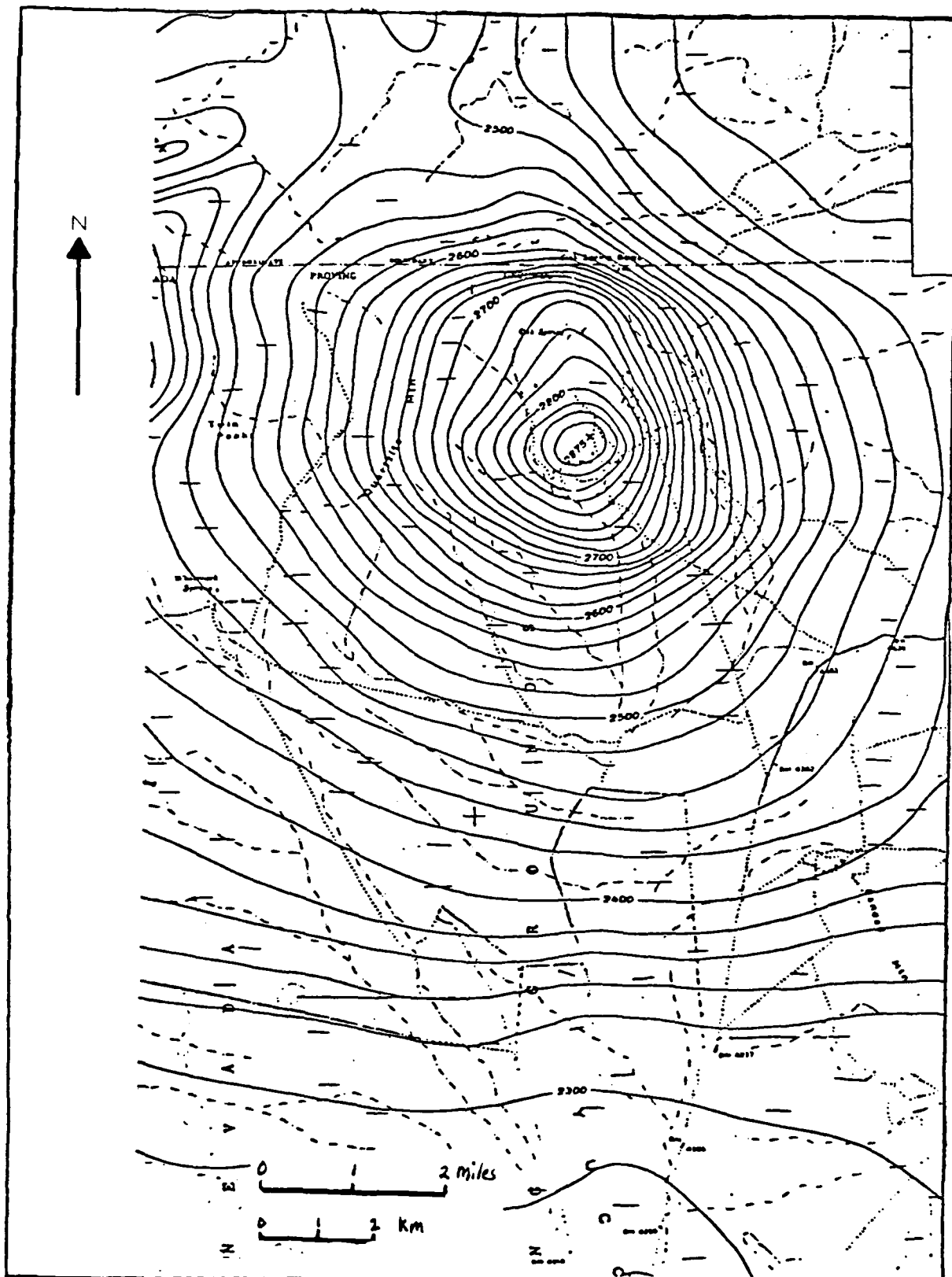


Figure 2-9 A Portion of the Aeromagnetic Map Over the Climax Stock Showing the 20 gamma Countour Spacing on the Magnetic Flux Outlining the Mostly Buried Granite Body.

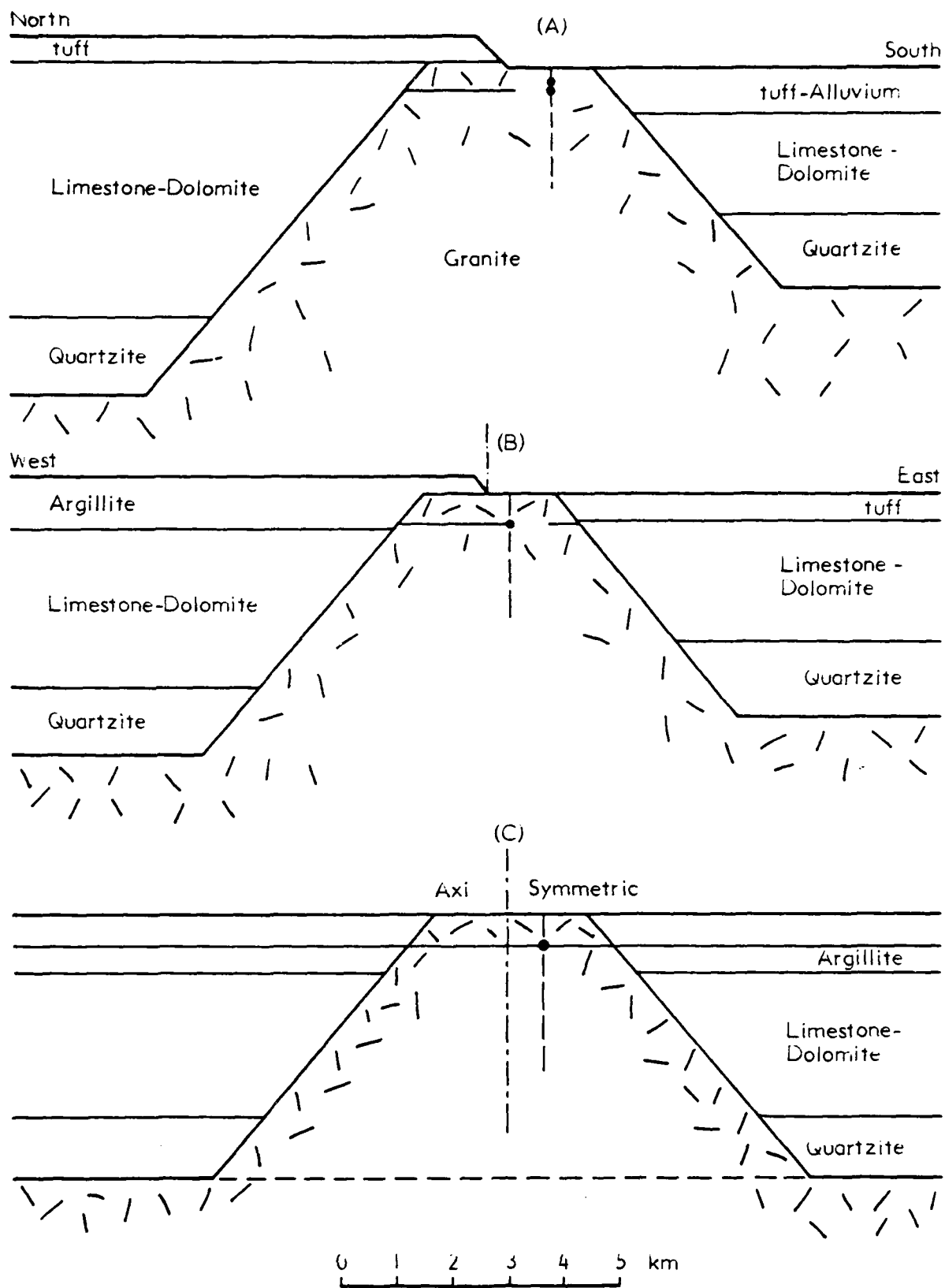


Figure 2-10 Simplifying Profiles of the Climax Stock (A) from Figure 2-7, (B) from Figure 2-8 and (C) Combining A and B.

CHAPTER 3

EMPIRICAL AND THEORETICAL EXAMINATION OF SPALL AND ASSOCIATED NEAR SOURCE GROUND MOTION PHENOMENA

3.1 EMPIRICAL ANALYSIS OF CLOSE IN GROUND MOTION DATA

Review and empirical analyses of the published ground motion data and geologic setting of a number of U.S. underground nuclear explosions have led to preliminary topical draft reports in the categories of: estimated spall configurations from buried explosions; geotechnical interpretation of explosion induced Love-wave excitation; and indications about how explosions energy partitioning may be related to near and far-field ground motion data and how the data scatter may reflect near-field material properties. The three draft reports, provided by consultant Glen Rawson, are appended to this report and are identified as DELTA TR-79-027, IR-79-0038, and PR-79-040, respectively. In what follows is a brief discussion of the findings from these three studies.

3.1.1 Estimated Spall Configuration -- TR-79-027 (Appendix C) For Complete Draft Text and References

The objective of this study was to evaluate spall as it relates to near source geologic environments and explosion yields and to provide guidance for estimating realistic spall configurations and total lofted mass. It was considered that spall might be significant in the generation or modification of seismic waves. To assess these effects, it was important to establish realistic spall configurations. Considerable effort was then given to providing guidance for estimating spall by relating the important parameters of yield and depth of burst related to different geologic and topographic settings. Data in the published literature for nine events in six dissimilar environments were analyzed to locate the depth of the deepest spall layer. Review of 35 events in ten different geologic environments provided the data base for determining the extent of spall and how it varied with material inhomogeneities as well as yield and depth of burst.

- Guide for Estimating Depth to the Deepest Spall Gap

To estimate spall depth from ground motion data, an array of sub-surface gauges is required down to at least the depth of the lowermost spalled zone (layer). In general, the spalled zones can be objectively determined for the uppermost spall gaps where separations between spall lift-off and impact are long in time and where there are a sufficient number of functioning gauges. Frequently the deepest spall gap opening is of a relatively short time duration with more complex wave interactions resulting in a more subjective interpretation. Figure 3-1 illustrates the ray tracing method of estimating the locations of spall gaps (i.e., the point where spall impact signals are generated) sending rays of seismic energy to be detected by gauges above and below the impact point. Figure 3-2 shows the estimated maximum total spall thickness for the nine events in the vicinity of surface ground zero (SGZ) over the explosions as a function of their yields (W in kilotons). Considering the limited data base and recognizing that the depths are only approximate and the geologic settings are greatly different, there is little room for refinements with much certainty. Rawson carries the analysis further, estimating effects for variations in density, topography, depth of burst (DOB) and geology. He proposes an internally consistent guide for estimating spall depth represented by the expression

$$D_{SGZ} \approx \overline{KE} \frac{W^{1/3}}{DOB^{1/2}} \quad (3-1)$$

where D_{SGZ} is the maximum spall depth in meters. The empirical "constant" \overline{KE} is about 1700 for moderately hard rock with a density of about 2.4. The constant is proposed to vary approximately proportionally to the density of the spalled layers. The expression is intended for contained explosions in the yield range of 1 to 5000 kilotons with the scaled depth of burial range of 100 to 300 meters.*

- Guide for Estimating Spall Depth at the Extent of Spall

The depth of the uppermost spall gap can often be estimated from surface ground motion records. There is apparently a subtle increase in this

* Scaled DOB - Actual DOB/ $W^{1/3}$

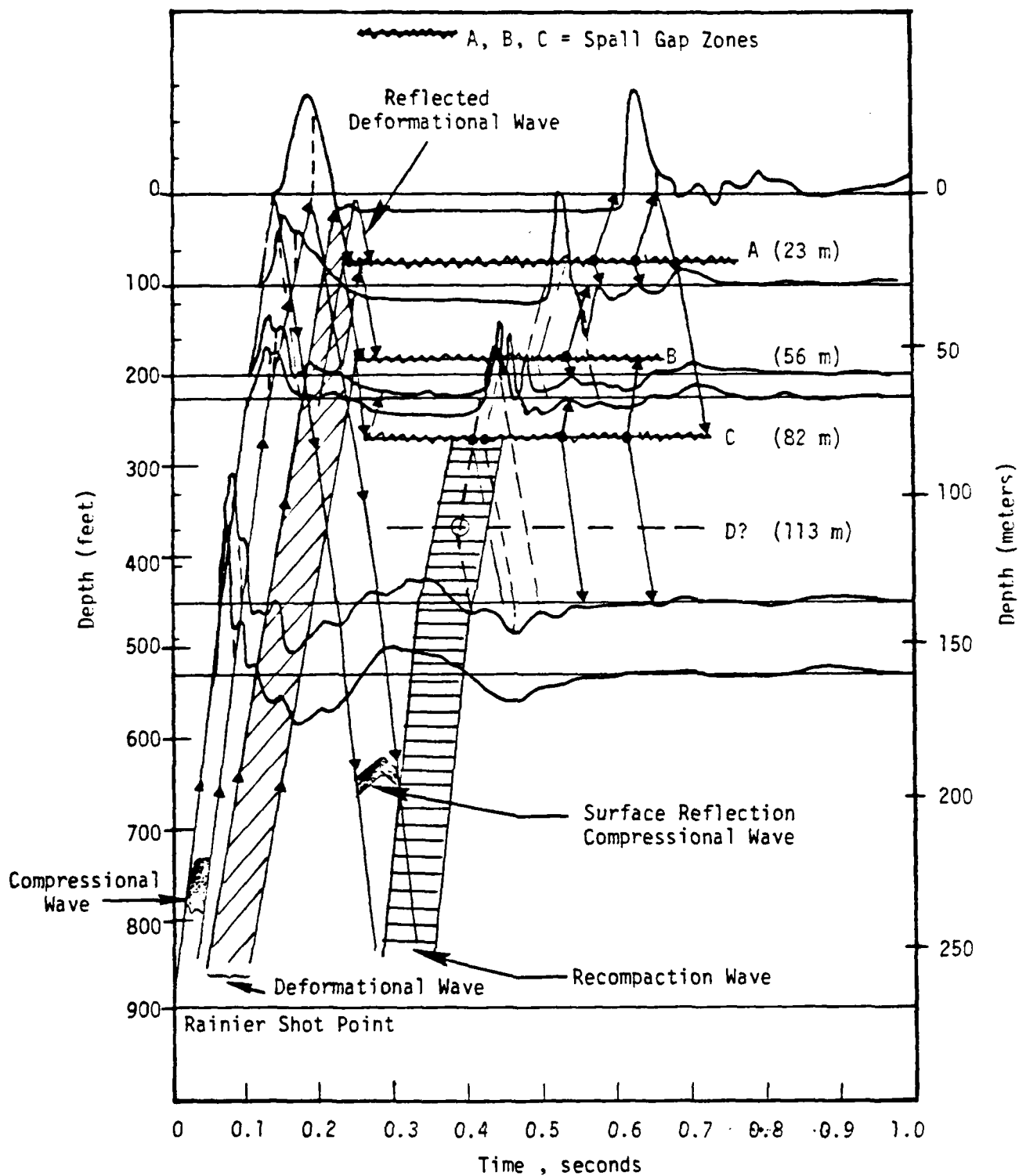


Figure 3-1. Explosion cavity/free surface and impact signal analysis; Rainier event illustrating the ray-tracing method of interpreting spall gaps A, B, C and D.

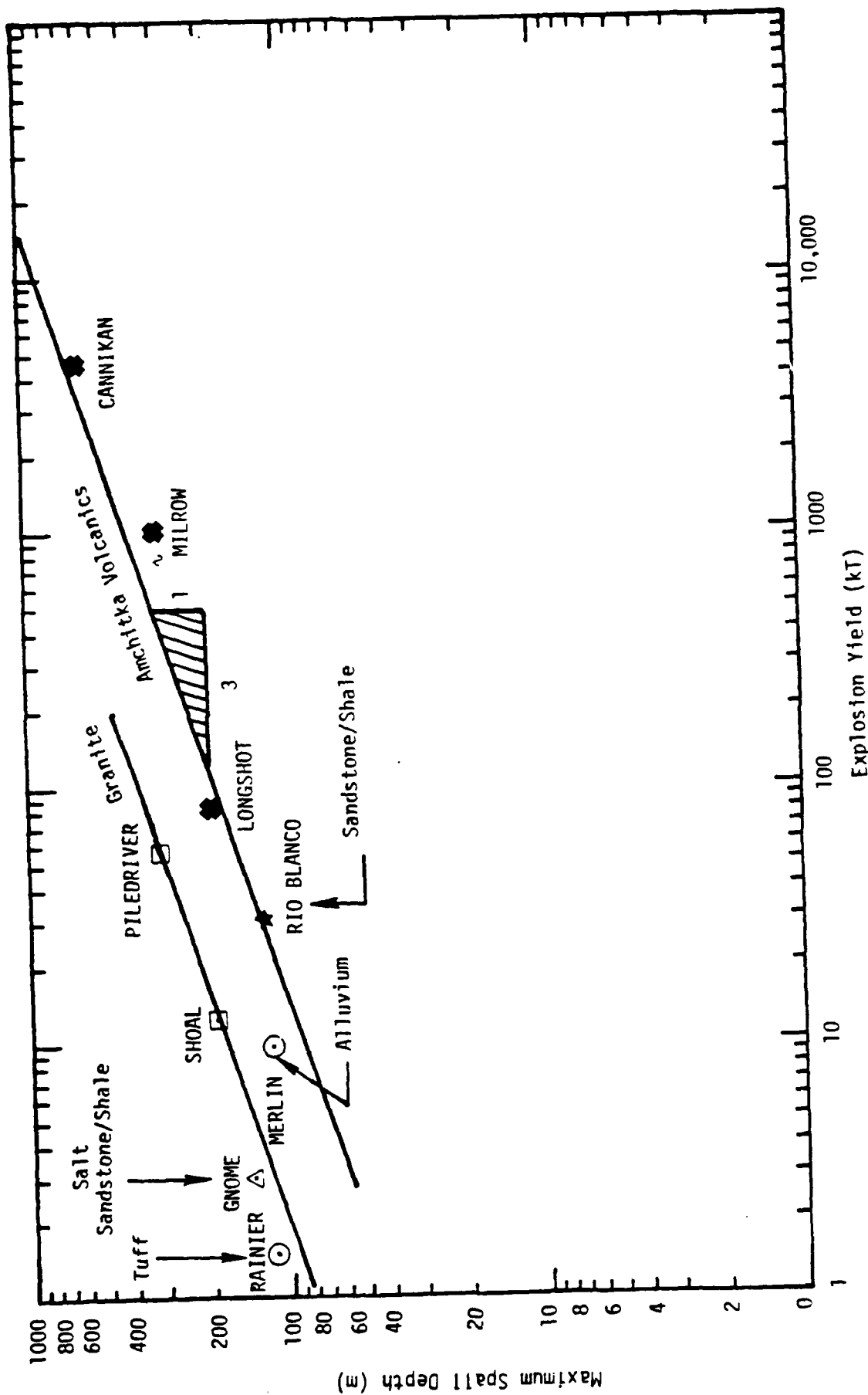


Figure 3-2. Maximum spall thickness versus explosion yield for nine contained nuclear explosion events in six different rock types.

depth with lateral range so that at the lateral limits of spall, the depth often appears roughly twice the depth near SGZ. It is also postulated that this depth is the total spall depth at the extremities, whereas there are commonly multiple spall gaps closer in. Investigators of spall generally agree that Equation (3-2) enables the depth to the upper spall gap (D_{us}) to be estimated from surface motion acceleration records:

$$D_{us} = V_p(t_2 - t_1)/2 . \quad (3-2)$$

The compressional wave velocity (V_p in m/sec) is the average over the thickness D_{us} in meters. Figure 3-3 illustrates the ray tracing method of determining times t_1 and t_2 or t_1 and t_2 using the LONGSHOT acceleration record near SGZ. Not all records are this clear for picking these peak accelerations following the first waves arriving at the surface (t_0 and t_0). The spall impact generates the ray arriving at the surface (t_0) giving rise to the peak acceleration (t_1). The spall depth can be estimated when a second peak (t_2) can be identified. This peak is assumed to be formed from energy re-radiating from the spall gap location as a reflection.

Seventeen events were analyzed where gauges were far enough away to give an indication of spall depth ($D_{S_{ex}}$) near the extremities of spall. These events are described in Table 3-1 and are used to guide estimation of the following relation between $D_{S_{ex}}$ and depth of burst, yield, and geologic setting:

$$D_{S_{ex}} \approx K_e \frac{W^{1/3}}{DOB^{1/3}} . \quad (3-3)$$

The empirically determined constant K_e has a value of about 210 (see Figure 3-4) and varies little with geologic settings in this case. Apparently, this parameter varies little because environmental variations have a more pronounced effect upon the extent of spall. Thus, the depths at Spall Extent (S_{ex}) are associated with a wide variety of ranges (slant distances from the explosion to surface) yet have a strong dependence at those ranges upon depth of burst.

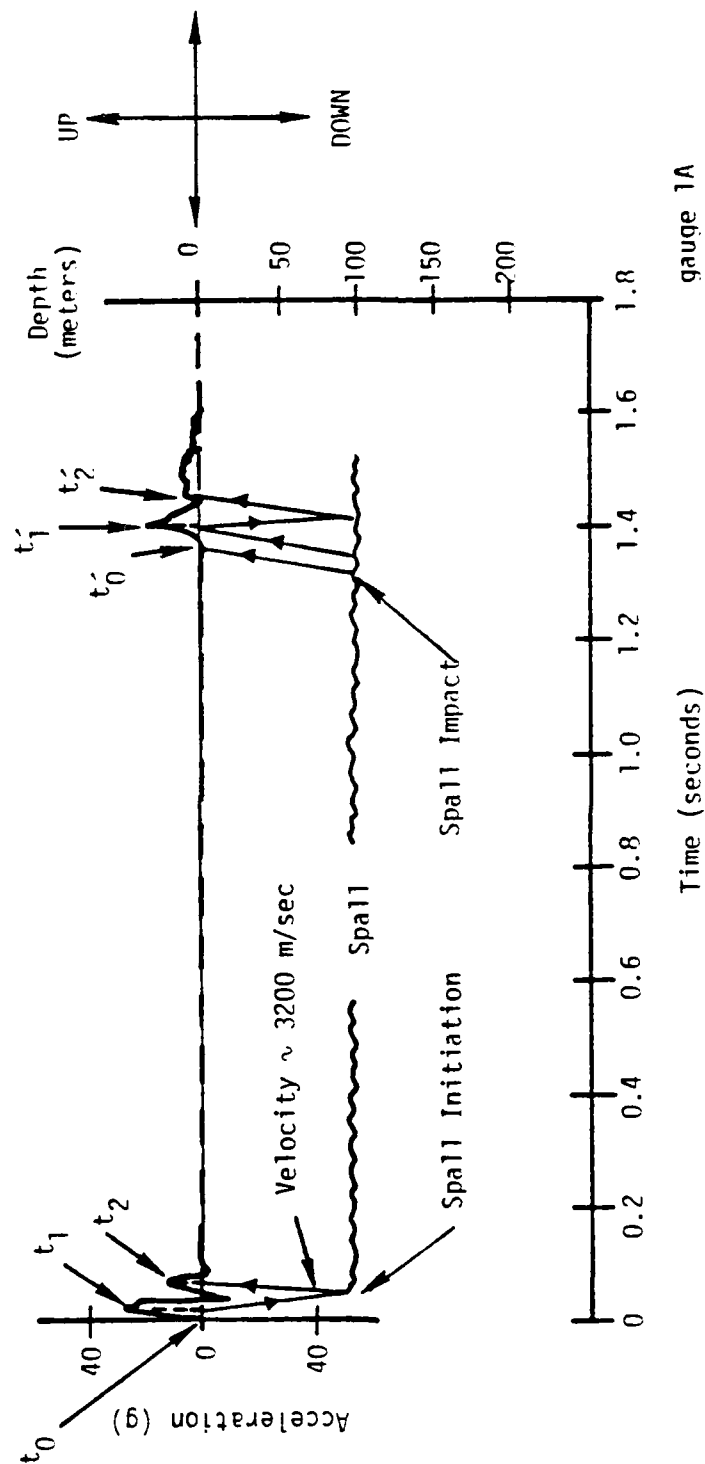


Figure 3-3. LONGSHOT surface ground zero acceleration record illustrating the method of estimating upper spall depth by ray tracing. Zero time is taken as the time of the explosion produced compressional wave first arriving at the surface.

TABLE 3-1

Approximate Spall Extent and Depth of Spall at the
Approximate Edge of Spall for Various Events and Materials

Event	Nominal Spall Extent S_{ex} (m) [1]	Gauge No. Station	Location R_{SL} (m)	Approximate Near Surface Velocity, V_p m/sec	Spall Depth at $\sim S_{ex}$ $D_{S_{ex}}$ (m)
RIO BLANCO	5000	120C	4100	1621	69
GASBUGGY	3300	SB4AV	2874	1600	48+
SALMON	1800	ES-SAV	1110	1800	33+
LONGSHOT	1800	25V	1450	2681	121
MILROW	4300	S17AV	5399	2988	209+
CANNIKAN	7200	SF125AV	3835	2681	201++
PILED RIVER	1640	PD9012AV	1441	3000	113
RAINIER	480	4AP	473	1480	30
BLANCA	1200	0AV	1217	1480	59
DISCUS THROWER	550	5SAV2	354	1060	95+
MUD PACK	220	B4SAV	226	950	48
AARDVARK	900	4AV-4	293	1060	101
MERLIN	380	S5-AV	314	1060	66
DORMOUSE PRIME	340	2-AV	293	1060	64
CHINCHILLA I	225	550AV	236	1000	55
ARMADILLO	325	800AV	344	1000	55
HANDCAR	800	B6-SAV	1003	1000	50
HALFBEAK	2400	55AV	2281	1800	161
SCOTCH	2850	S3AV	4253	1800	270
BOXCAR	4000	S12AV	4000	1800	414

[1] Spall extent is measured as the slant range (SL) from the explosion to the ground surface above where spall seems to terminate

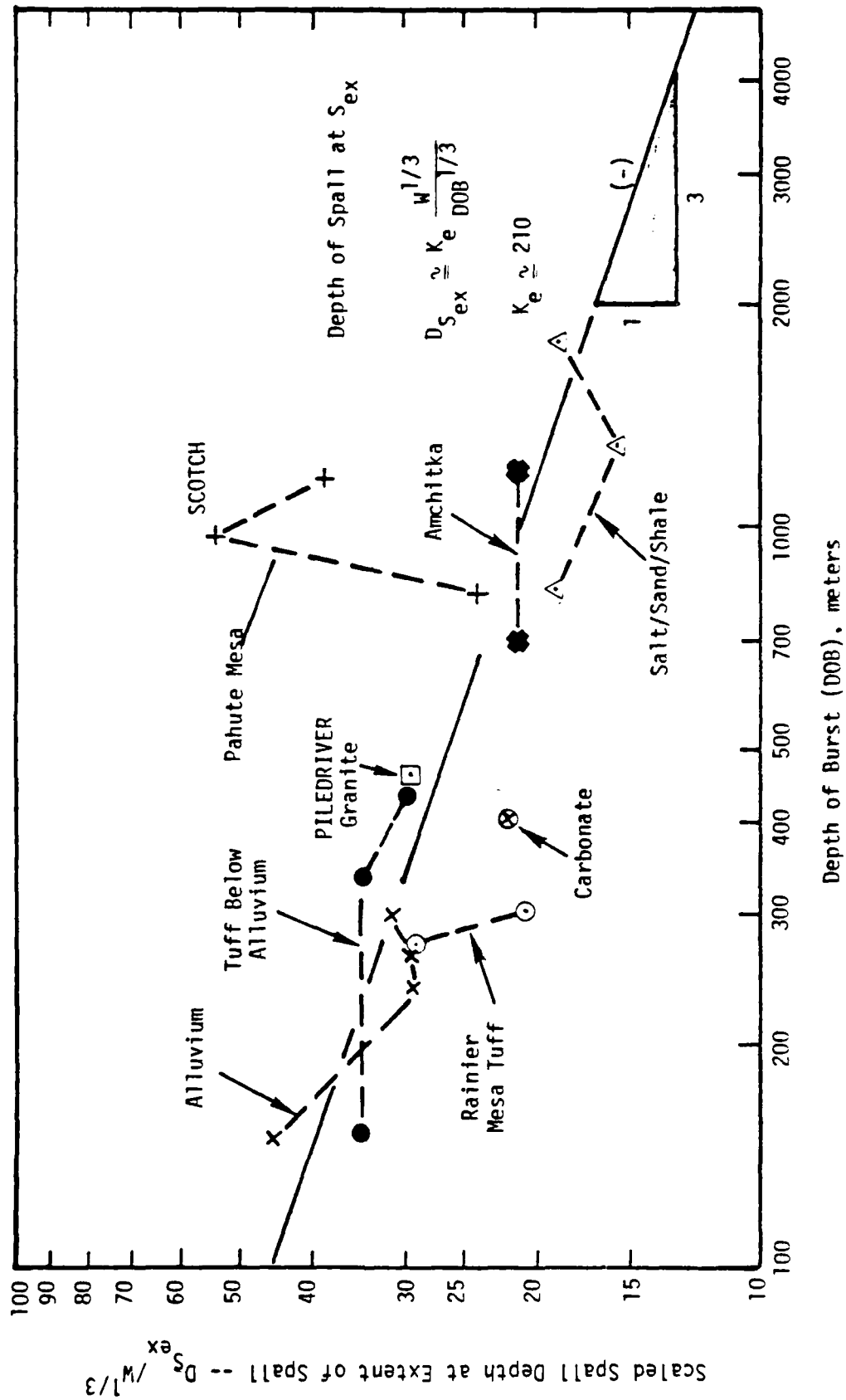


Figure 3-4. Scaled spall thickness at extent of spall versus depth of burst for 17 events in seven different geologic settings.

- Guide for Estimating Extent of Spall

Rawson (report in progress) deduced that there might be a significant depth of burst dependence associated with the extent of spall because rock density and velocity typically increase with depth, especially with sedimentary strata. This is expected to provide some lateral focusing of energy in less attenuating material than would occur at more shallow depths. Sediments are also commonly anisotropic with greater sound speed laterally compared with vertically for flat lying beds. Scattering in the data base does not allow precise definition of the depth dependence, so that estimates are again provided after working with data from 35 events. The relation developed is offered as a working empirical expression formulated to emphasize rock environment dependences that are unseparated in the site dependent "constant" G_p :

$$S_{ex} \approx G_p DOB^{1/2} W^{1/3} \quad (3-4)$$

where S_{ex} is in meters measured as slant range from the explosion. A preliminary effort has been given to evaluate G_p for rational internal consistency from one site environment to another. Rawson has not been able to quantify the dependences in terms of elastic properties, attenuation, wave guide effects, etc. However, such a refinement may be achievable. Figure 3-5 illustrates the apparent relation between the independently derived site dependent "constant" G_p versus \overline{KE} . The data are related by:

$$\overline{KE} \approx 16 G_p \quad (3-5)$$

with those events having especially large spall extents associated with bedded strata and deep scaled depths of burst; whereas more massive rock with multiple weakness orientations characterize the events with G_p values representing the smaller spall extents (other parameters assumed equal).

- Ground Motion and In-Situ Stress

Independent of this DELTA study, Rawson (report in progress) has established a probable causal relation between explosion induced fault motions at the ground surface and spall. The azimuthal variability of the induced fault motions

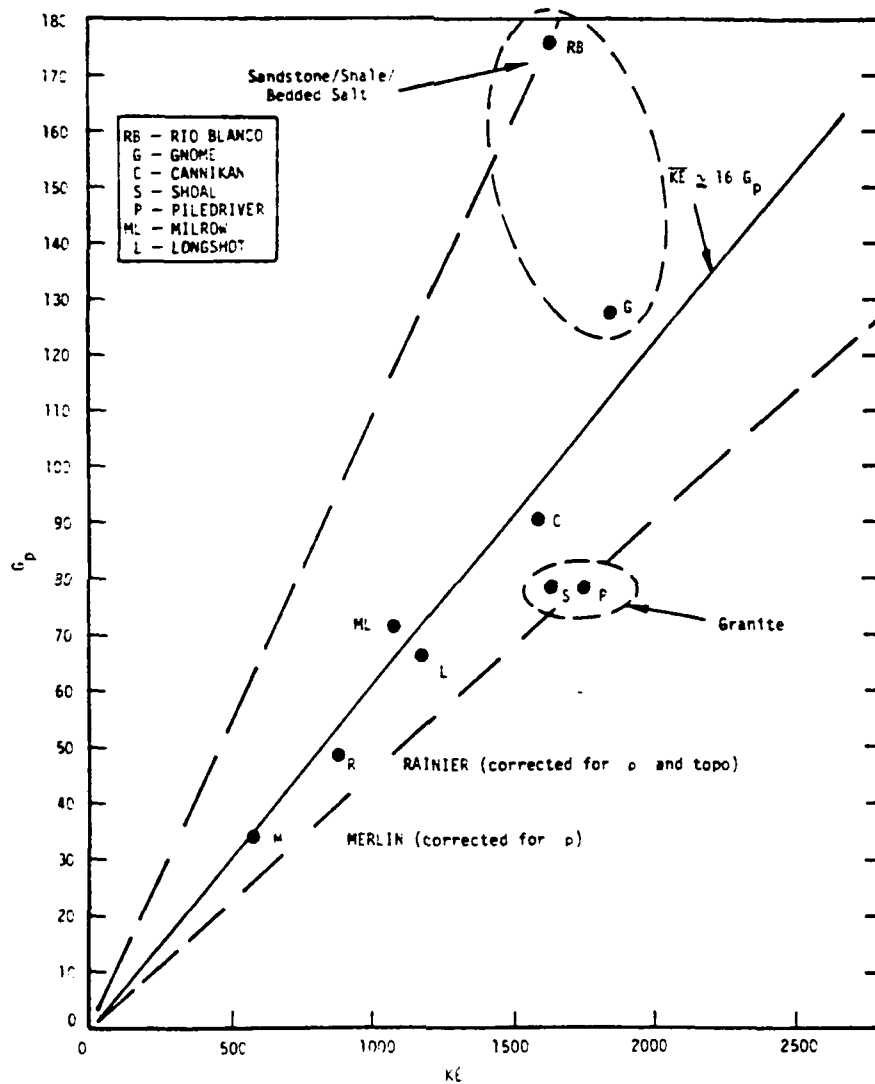


Figure 3-5. Approximate relation between the geologic or environmental parameters G_p and \overline{KE} associated with spall extent and spall depth scaling.

that spall extent may depend significantly upon the orientation of geologic structures such as major faults. These in turn may be relatable to in-situ stresses if the fault orientations reflect present day stress conditions.

The SHOAL event in granite was conducted with azimuthal redundancy of subsurface ground motion gauges near the source. Figure 3-6 illustrates this in plan showing the gauge stations at shot level and the orientation of fault zones mapped in the tunnel. The initial peak radial displacements are listed by each station. Also plotted is Rawson's interpretation of the in-situ horizontal principal stress orientations consistent with published regional stress trends and the fracture orientation. The data are supportive of the expectation that ground motion is minimized by increased confinement and thus it is minimal in the direction of maximum horizontal compression. Similar azimuthal variations were observed at the HANDLEY site in Pahute Mesa at NTS. Here the gauges were measuring surface motion.

- Spall Configuration Summary

Rawson provides empirically based guidance for estimating the configurations and scale of spall relating a considerable range of explosion yields, depths of burst and geologic settings having important differences so as to help refine our understanding of near-sources dependencies. He states that most previous investigators that have reported on the seismic implications of spall have interpreted the lateral extent(s) and depth(s) to be substantially less than found by this study. Therefore, Rawson's results, summarized in a somewhat stylized fashion in Figure 3-7, contribute to any re-assessments of the role of spall in the production of seismic waves, because the cross-sectional area of explosion failed earth material is over twice that of earlier models.

This study also points to probable relationships between spall, observed fault motions and confining stress. In particular, the study indicates that ground motions are minimal in the direction of maximum horizontal compressive stress. If the correlation between extent of explosion induced surface fracturing and extent of spall coincide because spall causes or allows the

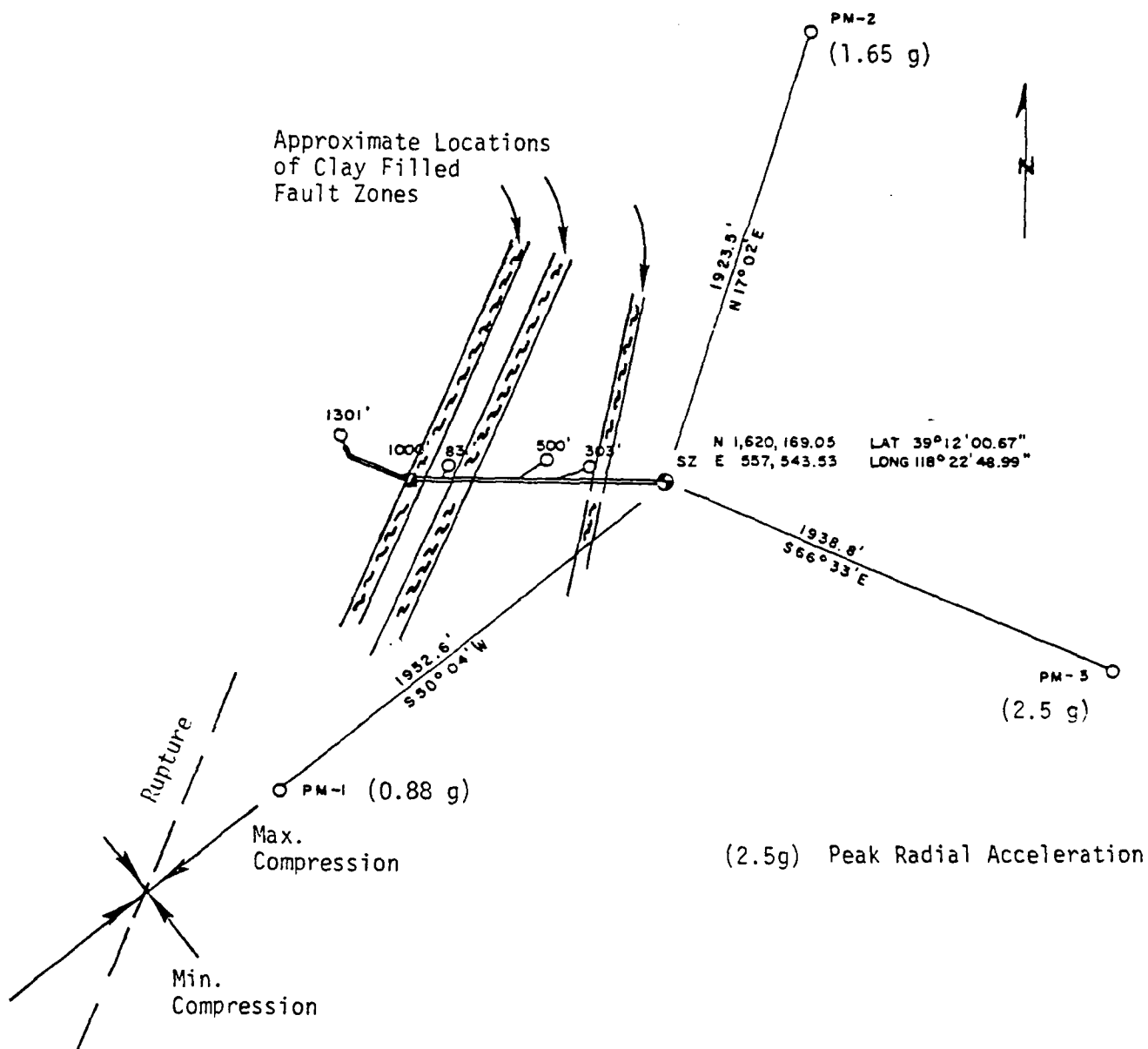


Figure 3-6. Plan view of SHOAL explosion-elevation ground motion station locations. Stations PM-1, -2, and -3 were installed via drill holes. Also shown are fault orientations and inferred in-situ stress orientations.

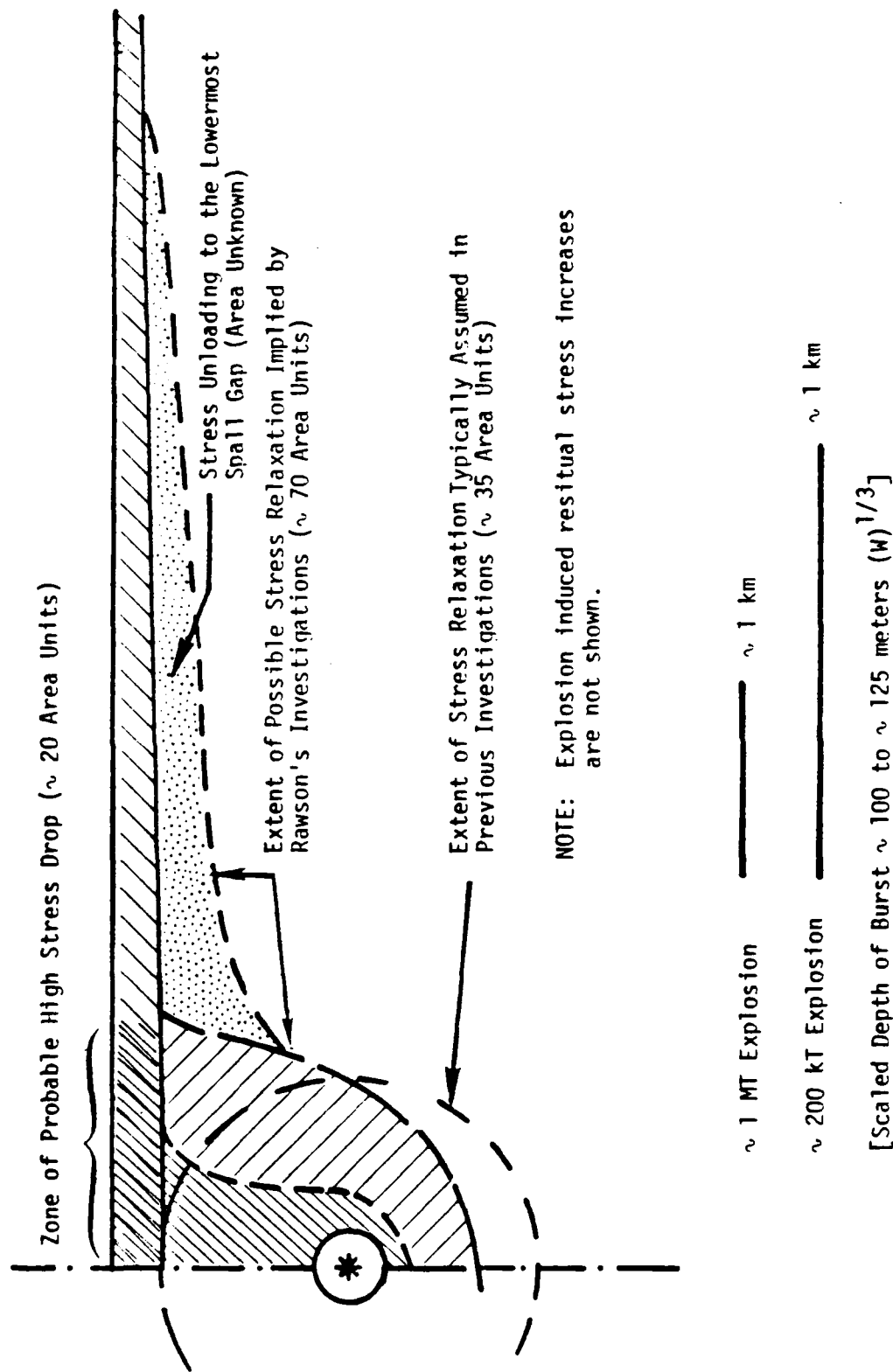


Figure 3-7. Idealized cross section of nuclear explosion induced fracture zones and possible stress relaxation zones.

the shape of the spalled region at its lateral extent would also reflect differences in geologic weakness structures and in-situ stress. It is tempting to speculate therefore that a better understanding of the spalling mechanism at NTS will lead to a clearer understanding of the azimuthal variation in long-period surface wave radiation, and the generation of SH waves being produced by events at NTS. A contribution to such an investigation is the topic of the next summary in Section 3.1.2.

3.1.2 Explosion Induced Love-Wave Excitation -- IR-79-0038, Appendix D For Complete Draft Text and References

Investigators analyzing and interpreting surface waves generated by underground nuclear explosions conclude that for large yield explosions (greater than about 30 KT) the principle mechanism contributing to Love-wave excitation is explosion induced pre-stress release.

Love-wave excitation is qualitatively expressed as the Love- to Rayleigh-wave amplitude ratio. Toksoz (1972) has made this more quantitative by introducing the term F-factor or double couple strength. Table 3-2 lists those events for which F-factors have been determined and subdivides these tests according to location and rock type. For comparison, the Yucca flat events are also listed with relative Love-wave excitations as well as F-factors. Ten additional Yucca Flat tests have relative Love-wave excitations reported and listed in Table 3-3.

- Existing (Conflicting) Models

Presently, the interpretations of surface wave radiation presumed to be generated by explosions in pre-stressed environments are significantly in conflict. There are two competing explanations that probably both represent mechanisms that are operative. Both understandably oversimplify the environmental conditions and present internal inconsistencies when the data base is examined collectively. These models (along with their principle proponents) are:

1. The Fault Trigger Model (Aki, 1972)
2. The Cavity/Fracture Zone Model (Archambeau, 1970)

TABLE 3-2
Comparative Tectonic Strain-Release and Other Site
Related Factors from Underground Nuclear Explosions

Event	Region	Medium	D.C.* Strength Factor	Yield (KT)	Depth of Burst (m)	Depth Water (m)	Date Detonated	Data Reported in LLL Data Bank			
								Density to Surface (gm/cc)	Density at M.P. (gm/cc)	(% Water by Wt.)/ Saturation	Seismic Velocity, Vp at M.P. (m/sec)
PILEDRIER	MTS AREA 15	GRANITE	3.20	56	463	~ 614	6/2/66	2.66	2.67	-- / --	--
HARDHAT	"	"	3.00	5	286	614	2/15/62	--	2.65	-- / --	--
SHOAL	FALLOM, NEVADA	"	0.90	12.2	367	~ 3677	10/26/63	--	--	-- /100	--
GREELEY	MTS PRINITE MESA	TUFF	1.60	825	1215	616	12/20/66	1.94	2.57	(11)/100	3270
BENHAM	"	"	0.85	1100	1402	642	12/19/68	2.01	2.3	(6)/100	3050
CHARTREUSE	"	RHYOLITE	0.90	70	664	662	5/6/66	2.24	2.35	(7)/100	4675
DURYEA	"	"	0.75	65	544	661	4/14/66	--	--	-- / --	--
HALF BEAK	"	"	0.67	300	819	645	6/30/66	2.19	2.49	(3)/100	3540
BOX CAR	"	"	0.59	1200	1166	604	4/26/68	1.93	2.12	(9)/100	4450
CORDURDY	MTS YUCCA FLAT	TUFF	0.72 S	200 - 1000	681	570	12/3/65	--	1.92	(20.2)/100	2164
CUP	"	"	0.72 S	< 20 - 200	537	553	3/26/65	--	--	(13)/100	--
BILBY	"	"	0.47 S	235	715	488	9/13/63	1.78	--	-- /100	--
TAN	"	"	0.39 I	< 20 - 200	561	512	6/3/66	1.71	--	-- / --	--
BRONZE	"	"	0.33 I	< 20 - 200	530	555	7/23/65	1.69	--	-- / --	--
BUFF	"	"	0.31 I	< 20 - 200	500	521	12/16/65	1.68	--	-- / --	--
HAYMAKER	"	ALLUVIUM	0 M	67	408	408	6/27/62	1.70	--	-- / --	--
SEDAN	"	"	0 M	100 crater	194	576	7/6/62	1.78	1.91	-- / --	--
FAULTLESS	CENTRAL, NEVADA	TUFF	0.50	200 - 1000	973	91	1/19/68	--	--	-- / --	--
MILROW	ANCHITKA, ALASKA	ANDESITE	< 0.60	~ 1100	--	~ 3	10/2/69	2.13	--	-- /100	--
CANNIKIN	"	"	0.60	< 5000	1791	~ 3	11/6/71	2.3	2.5	(5)/100	4663
RULISON	GRAND VALLEY, COLORADO	SANDSTONE & SHALE	0.60	40	2568	244	9/10/69	2.35	--	-- / --	--
SALMON	HATTIESBURG	SALT	0	5.3	828	0-2	10/22/64	--	--	(0)/0	--
GNOME	CARLSBAD, N.M.	SALT	0	3.1	361	158	12/10/61	--	--	(3)/100	--

* Double Couple (D.C.) strength or F-factors from Toksoz and Keher (1977); S, I, and M refer to Strong, Intermediate and Weak Love-Wave excitations to compare with F-factors, from Aki and Tsai (1977).

TABLE 3-3

List of Explosion tests in the Yucca Flat (other than listed in Table 3-2)
Giving Relative Love Wave Excitation

Event	Detonated	Medium	Elevation from Sea Level, meters						Seismic Magnitude			Relative Excitation of Love Waves
			Shot Depth	Shot Point	Water Table	Alluvium- Tuff Interface	Tuff Paleozoic Interface	m (LRSM)	m (Canada)	m (Evernden)		
AARDVARK	5/12/62	Tuff	434	804	732	948	351	4.89		4.55	Intermediate	
ALUK	10/2/64	Tuff	452	824	728	1068	610	4.89			Weak	
BOURBON	1/20/67	Tuff	561	770	732	1254	792	5.09	4.93		Intermediate	
CHARCOAL	9/10/65	Tuff	455	814	730	1052	610	516	4.91		Weak	
COMMODORE	5/20/67	Tuff	744	536	732	814	335	5.68	5.77		Strong	
DUMONT	5/19/66	Tuff	671	608	732	840	472	5.48	5.51		Strong	
FORE	1/16/64	Tuff	495	797	728	893	366	5.2		5.85	Intermediate	
MISSISSIPPI	10/5/62	Tuff	494	795	730	853	305	5.06		4.76	Strong	
PIRAHNA	5/13/66	Tuff	549	709	732	994	274		5.37		Weak	
WAGTAIL	3/3/65	Tuff	750	485	732	951	253	5.33	5.32	5.1	Intermediate	

There seems to be general agreement that a number of nuclear explosion tests produced sufficient anomalous surface wave radiation and especially Love-wave excitation so that pre-stress release is required to explain the observations.

- Data Base and Material Dependencies

Table 3-2 presents data associated with those events for which F-factors have been reported. Table 3-4 provides a simple ranking in the order of increasing F-factor by test region and material. Generally, the ordering is as one would expect in relation to the ability of the rock to adjust to applied stress. Both bedded and dome salt behave plastically and deform under low applied stresses, so little stored stress is expected. This is also true of the relatively weak water saturated sediments that surround and overlay the Tatum salt dome containing the SALMON event. Events detonated in alluvium also have near-zero F-factors, being easily deformed, less compacted, and less cohesive than volcanic tuff. The F-factor upper bound for volcanic tuff at NTS exceeds that of the large yield events at Amchitka, Alaska. Also, all of the Pahute Mesa events in volcanic rocks have F-factors that exceed those at Amchitka. The spread of data within the tuff and other volcanic rocks, for tests in Yucca Flat and Pahute Mesa at NTS, and those at Amchitka, can probably best be explained by detailed evaluation of site conditions. Explosions in granite produce the highest F-factors and represent the least deformable, most dense, high strength rocks in Table 3-4. What is not obvious is the explanation of why one granite site is so different from the other.

- Granite Experience

For hard rock like granite it is proposed that the primary differences in Love-wave excitation can often be deduced by examining geologic structural patterns. This method assumes other factors such as the applied stresses are similar from site to site. Fault and fracture orientations and apparent

TABLE 3-4

Explosion Test Materials Ranked in Order of
Increasing Double Couple Strength

F-Factor Double Couple Strength	Shot Material and Location
0	SALT (New Mexico and Mississippi)
0 - ?	ALLUVIUM (Yucca Valley, NTS)
0.31 - 0.72	TUFF Below Alluvium (NTS)
? - 0.60	Amchitka, Alaska VOLCANICS
0.59 - 1.6	Pahute Mesa VOLCANICS (NTS)
0.90 - 3.2	GRANITE (NTS & Fallon, Nevada)

deformation intensity properties reflect the ability of the rock to resist applied stresses. One may then access relative ease of deformation of a certain fracture pattern if something is known or can be deduced about the in-situ stress field.

Figure 3-6 (referred to in Section 3.1.1) illustrated the dominant fracture pattern at SHOAL mapped in subsurface excavations along with the inferred stress pattern. The orientation is consistent with the fracture orientation, regional stress data and elongation of the granitic intrusion. The fact that the faults have well developed fault gouge further indicates that the faults have been subjected to repeated motions. This is presumably because the stress field orientation has migrated very little since the granite was intruded.

SHOAL from Table 3-2 gave a low F-factor of 0.9 compared to 3.0 and 3.2 for HARDHAT and PILEDRIIVER. The explanation offered is that there was less stress to relieve because of frequent natural releases (via earthquakes occurring at a low level of stress build-up). New major faults did not have to be created; the old ones just moved a little.

The Climax Stock at the north end of Yucca Valley at NTS, by contrast, displays much greater structural complexity reflecting various orientations of stress accumulation as a function of time. There are significantly more directions of faulting, much less gouge (rock flour) development, and a higher fracture cleavage frequency at the Climax granite than at the SHOAL site. Regionally, the minimum lateral principal stress is about $N30^{\circ}W$. This is the direction of apparent cavity/chimney elongation and this orientation ($N60^{\circ}E$) is best fit to the teleseismic surface wave data for strike slip motion. The free-field radial particle velocities at PILEDRIIVER at a horizontal range of 610 m in a $N58^{\circ}E$ direction, or about the orientation of maximum compressing stress, was 1.8 m/sec compared to a 2.8 m/sec velocity for the expected intermediate orientation of $N62^{\circ}W$. This tends to confirm lesser ground motion in the direction of maximum confinement.

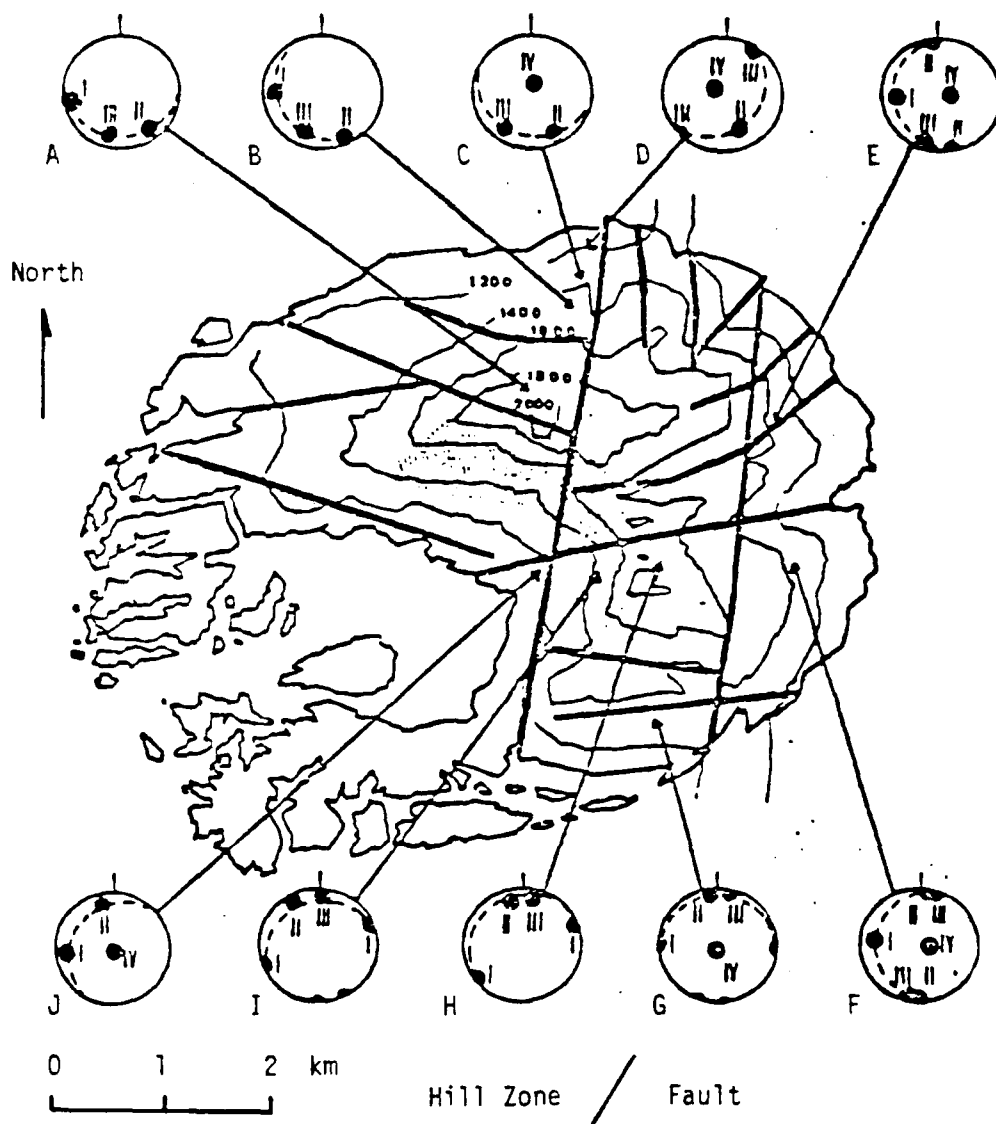
Applying the logic of high F-factors correlating with difficult to deform rock (i.e., few failure planes and few recurrent motions), some speculations can be made about the French tests in the Sahara of North Africa. It is known that

the rock is highly stressed from natural tectonic forces -- about 200 bars above calculated lithostatic stress at a given depth. It has also been observed that the cavity/chimney size and fracture extents are much less than comparable U.S. experience -- consistent with less motion against greater confinement. Figure 3-8 illustrates the faults and fracture cleavage found at the Taourirt Tan Affella Massif where the granite tests occurred.

If it is assumed that cavity asymmetries and the ratio of lateral stress differences are like the U.S. experience, then the major contributors to azimuthally varying surface waves anticipated for the French tests in granite are tectonic stress contributions and differential block motions. Large F-factors are expected because the granite massif is not highly fractured, but is stressed to higher levels than the two U.S. granite test sites. F-factors probably decrease in subsequent tests to the early tests in virgin ground because of spall induced stress relief. The less attenuating Sahara granite is also expected to experience a greater and deeper spall extent from contained explosions than comparable U.S. experience. The stress field is presumed to have migrated gradually since emplacement of the massif to allow for such high stresses to develop. Of course, with a low fracture frequency and a stress field drifting with time, failure criteria for faulting approaches the rock strength, not the pre-existing fracture strength which is what is suspected to be the case at SHOAL. The expected results of surface wave analysis for the early French tests is for F-factors to be greater than 3 with double couples corresponding to an N-S orientation. This orientation is chosen because it was reported that the absorption of the explosive energy varied little within the massif but was greater in a N-S direction parallel to the structural direction in the surrounding rock.

- Pahute Mesa and Amchitka Volcanics Experience

In a separate study, Rawson (report in progress) supported the proposition that observed fault motions at the surface of Pahute Mesa resulted from stress releases to the deepest spall gap caused by each explosion. It was suspected that the conditions that produced natural fault motions were preserved in the shallow



Class I ~ N-S; Class II N80°E; Class III N70°W; Class IV Parallel
Massif
Boundary

Figure 3-8. Fault systems of the Taourirt Tan Afella massif with drill hole data illustrating the classes of fracture cleavage encountered.

volcanic crust as a pre-stress. Spall produced by large nuclear detonations caused a temporary reduction in confining stress. With spall, the underlying material is thought to release some pre-stress to the lower spall gap "free-surface".

From Table 3-2 it can be seen that compared to the other Pahute Mesa events, Greeley is high with an F-factor of 1.6. CHARTREUSE is also somewhat anomalous since only a 70 KT event produced a higher F-factor than the megaton events. Although F-factor is not expected to have a significant yield dependence, it can easily have an apparent yield dependence if there are depth of burst dependences.

Table 3-5 lists the first 19 Pahute Mesa events in detonation sequence. Figure 3-9 illustrates conservative spall radii drawn about these event locations. Inspection of this figure allows for estimating relative pre-stress relief assuming that spall plays a significant part in that process as described in Table 3-5. Because of the rather complete coverage of the Pahute Mesa test region by spall from the first 19 tests, subsequent tests are expected to have lower F-factors than GREELEY at 1.6 and probably lower than 0.85.

GREELEY may have triggered the nearby GREELEY fault adding possibly some stress relief to the relief considered to be spall induced. If so, the double couple would be expected to be about N-S with a dip-slip component of motion to the west.

From Table 3-2 it appears that the F-factor magnitude for the two high yield detonations at Amchitka were in regions of lower pre-stress than the volcanic rock at NTS. The environment shown by Figure 3-10 is water saturated to the surface so energy coupling should be better than at Pahute Mesa. The fault pattern at Amchitka, as at SHOAL, is rather consistent, oriented about $N60^{\circ}$ to 70° E. This is not the orientation of the underlying fault zone forming one of the major global tectonic plate boundaries. Presumably the island overrides the under-thrusting oceanic plate and the shallow stress field is somewhat decoupled from the deeper accumulations of stress. It is proposed that the magnitude of stresses in the vicinity of the three Amchitka detonations is less

TABLE 3-5
Estimated Relative Pre-Stress Release of Pahute Mesa Events
Involving Radius and Detonation Sequence

Detonation Sequence No.	Event	W^+ (KT)	DOB (m)	$\sim R_s$ (m)	F- Factor	E_t/E_e	Relative Pre-Stress Release
1	BUTEO	L	696	1500	--	--	*
2	REX	16	672	1350	--	--	*
3	DUREA	65	544	2100	0.75	0.75	**
4	CHARTREUSE	70	665	2200	0.90	1.05	*
5	HALFBEAK	300	819	3400	0.67	0.60	**
6	GREELEY	825	1214	4700	1.60	3.41	*
7	SCOTCH	150	978	2600	--	--	**
8	KNICKERBOCKER	71	631	2200	--	--	*
9	STINGER	L-I	668	2200	--	--	***
10	BOXCAR	1200	1158	5600	0.59	0.46	***
11	RICKEY	L-I	683	2200	--	--	*
12	CHATEAUGAY	L-I	607	2000	--	--	***
13	SLED	L-I	729	2400	--	--	**
14	BENHAM	1100	1402	5600	0.85	0.95	***
15	PURSE	L-I	599	2100	--	--	***
16	JORUM	L-M	1158	5600	--	--	***
17	PIPKIN	I	617	2200	--	--	***
18	HANDLEY	~ 1000	1206	5600	--	--	**
19	ALMENDRO	I	1064	4000	--	--	***

* Events with little or no likelihood of strain release by earlier detonations.

** Events with probably some strain release by earlier detonations.

*** Events with considerable strain release by earlier detonations.

L is low yield, < 20 KT.

K is intermediate (20 - 200 KT) yield range.

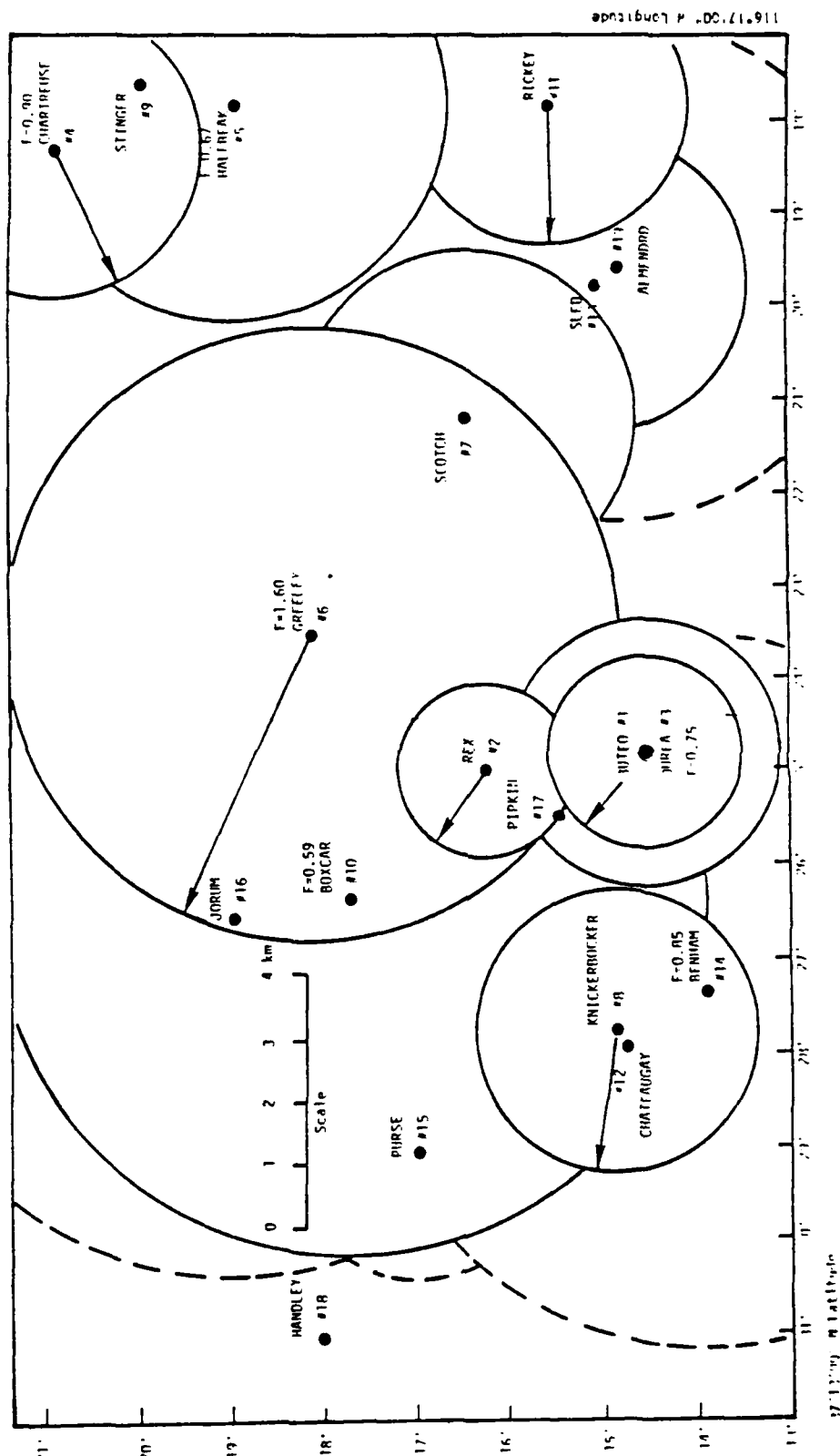


Figure 3-9. Pahute Mesa location and spall extent overlap pattern for the first 19 explosion tests (arrows identify events in near-virgin rock).

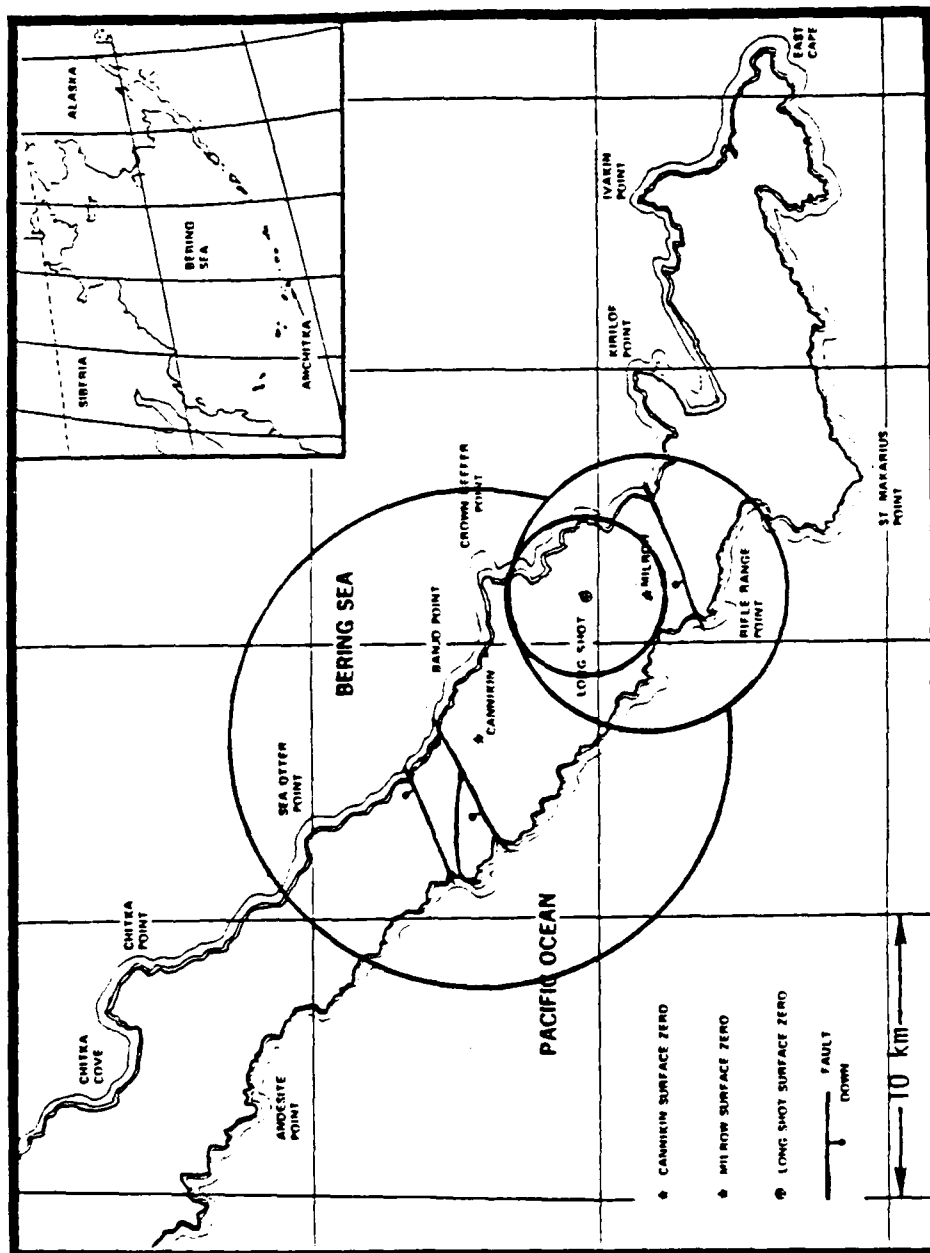


Figure 3-10. Map of Amchitka showing explosions, fault orientations, and approximate extents of spill.

than at Pahute Mesa. Here, like SHOAL, the explanation may be ease of deformation because of the favorable orientation of faults with the present-day stress field at shallow depth. Also, water saturation to very near the surface may prevent storage of significant pre-stress at shallow depths due to more complete stress relief with natural fault motions and earthquakes. Therefore, spall might not play so important a role as is suspected at Pahute Mesa.

- Yucca Valley Experience

Love-wave excitation variations for detonations in Yucca Valley were evaluated by Aki and Tsai (1972) with the relative excitations shown in Tables 3-2 and 3-3. Several of their correlations are not confirmed by this preliminary evaluation of the same data. The reason is that the data were grouped differently. They included some detonations in alluvium that biased the analysis to weak excitation and did not separately analyze events north of 37°06'N latitude from those events to the south. This geologic separation of Love-wave excitation can be seen in Figure 3-11 a and b. There is no pronounced correlation of decreased excitation with time. This indicates minimal explosion interaction effects such as spall lowering the stored stress, as was observed at Pahute Mesa.

Figure 3-12 illustrates circles that are roughly proportioned to the yield and the extent of partial pre-stress relief that may be due to explosion-induced fracturing. The figure shows the locations of the first 24 detonations with yields greater than AARDVARK that followed that early test in the valley. Table 3-6 summarizes data relative to these events. From the overlap of circles it can be seen that MISSISSIPPI might have caused some pre-stress relief of FORE. BILBY probably had little effect on subsequent tests. It would be interesting to see if AGILE lowered the expected F-factor or Love-wave excitation of COMMODORE. Similarly, KICKTITAT affecting CUP; CORDUORY/KANKAKEE and WAGTAIL/TAN. Whether these interactions are confirmed or not, these same couplets might be examined for anomalously high body wave magnitude for the second events in each pair.

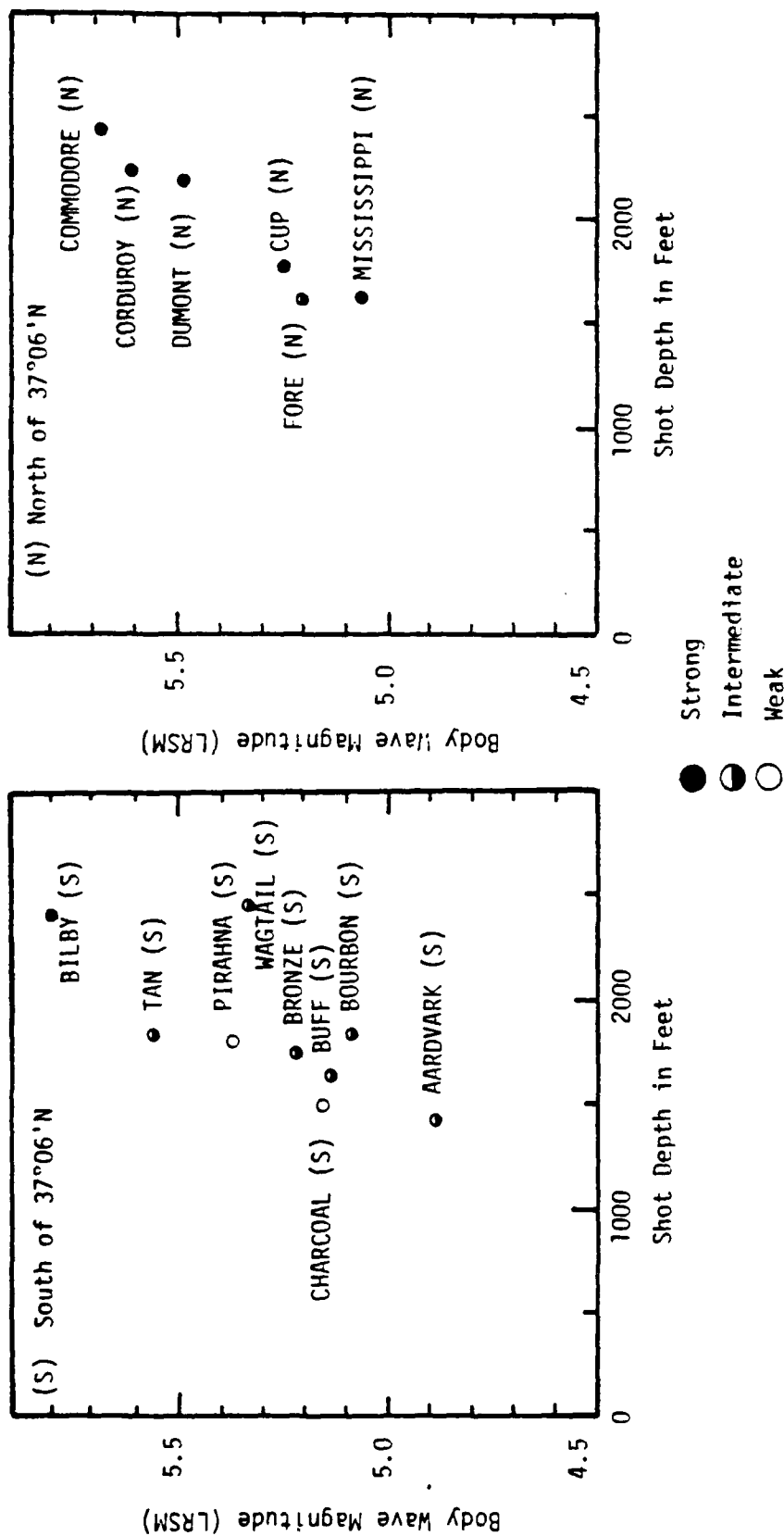


Figure 3-11a. Relative excitation of Love Waves as a function of body-wave magnitude and shot depth for tuff below alluvium and located South of 37°06'N latitude.

Figure 3-11b. Relative excitation of Love Waves as a function of body-wave magnitude and shot depth for tuff below alluvium and located North of 37°06'N latitude.

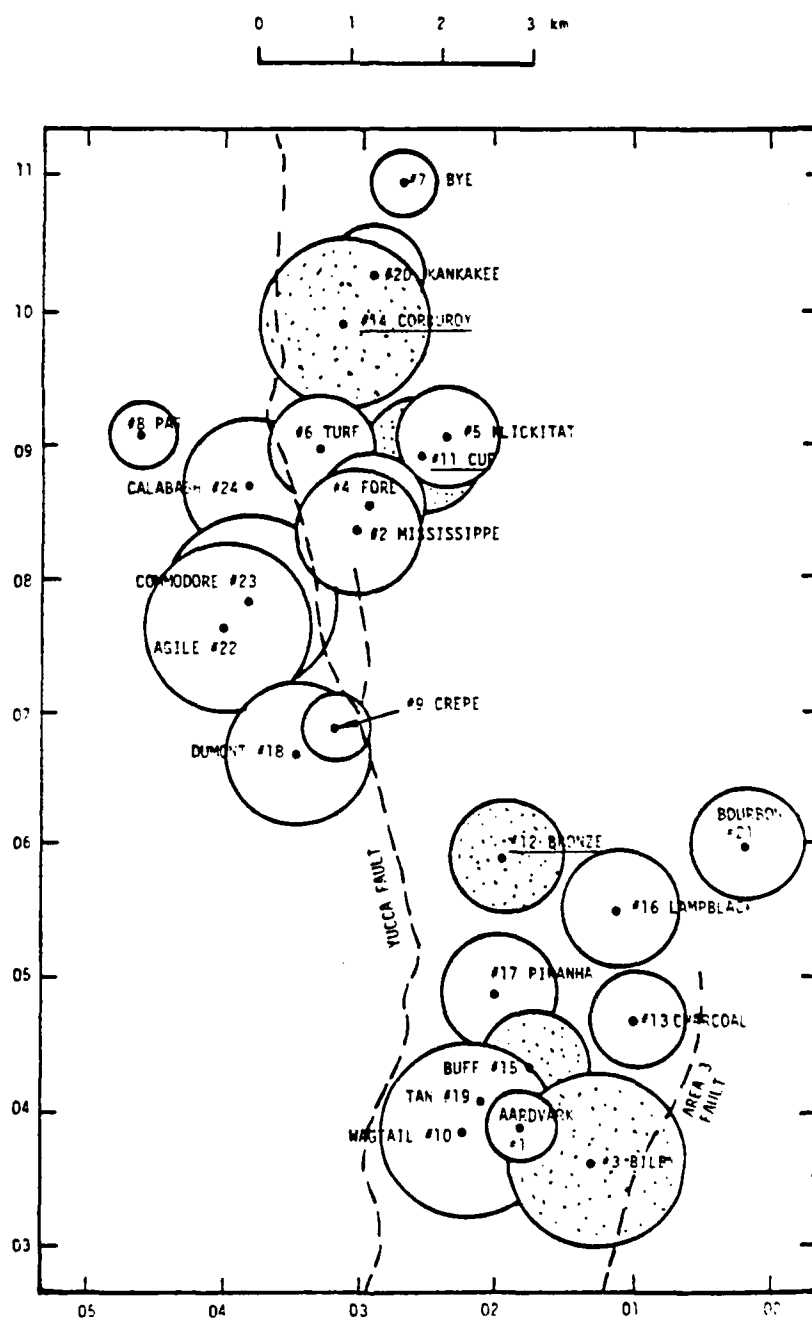


Figure 3-12. Yucca Valley detonation sequence, location, and approximate fracture radii for events greater than 36 KT in tuff or Paleozoic rocks. Dotted circles are tests with F-factors shown on Table 3-2.

TABLE 3-6

Yucca Valley Events and Environmental Data for the
First 24 tests Considered in Figure 3-11 a & b

Detonation Sequence No.	Event	Yield †	DOB (m)	Depth to Water (m)	Date	Approximate Spall Radius Rs (km)	Density		(Water % by Wt.)/ % Saturation	Velocity V _p at M.P. (m/sec)
							ρ to Surface (gm/cc)	ρ at M.P. (gm/cc)		
1	AARDVARK	36	434	509	5/12/62	1.75	--	--	-- / 90+?	--
2	MISSISSIPPI	110	494	561	10/5/62	2.65	--	--	-- / --	--
3	BILBY	235	714	488	9/13/63	3.35	1.78	--	-- / --	--
4	FORE	L-1	492	558	1/16/64	2.15	--	1.64	-- / --	--
5	KLICKHAT	L-1	493	567	2/20/64	2.15	--	1.77	(15.2)/ --	2531
6	TURF	L-1	507	567	4/24/64	2.20	--	1.77	(16)/ --	1909
7	BYE	L-1	389	582	7/16/64	1.70	1.68	1.57	(16)/ --	2850
8	PAR	38	404	594	10/9/64	1.75	1.97	1.48	(13.7)/ --	2322
9	CREPE	L-1	403	549	12/5/64	1.75	--	--	(8.1)/ --	--
10	WAGTAIL	L-1	750	509	3/3/65	3.35	1.79	--	(--)/100	--
11	CUP	L-1	537	554	3/26/63	2.40	--	--	(13)/100	--
12	BRONZE	L-1	531	533	7/23/65	2.40	1.69	--	-- / --	--
13	CHARCOAL	L-1(pz)	455	533	9/10/65	2.00	1.72	--	-- / --	--
14	CORNUROY	1	712	567	12/3/65	3.35	--	1.92	(20.2)/100	2164
15	BUFE	L-1	500	521	12/16/65	2.20	1.68	--	-- / --	--
16	LAMPBLACK	L-1	561	565	1/18/66	2.5	1.73	--	-- / --	--
17	PIRANHA	L-1	549	533	5/13/66	2.4	1.71	--	-- /100	--
18	DUMPHIT	L-1	671	549	5/19/66	3.0	--	--	-- / --	--
19	TAN	L-1	561	512	6/3/66	2.5	1.71	--	-- / --	--
20	KANAKEE	L-1(pz)	455	575	6/15/66	2.00	--	--	-- / --	--
21	BOURBON	L-1(pz)	560	584	1/20/67	2.5	1.70	--	-- / --	--
22	AGILE	L-1	731	564	2/23/67	3.30	--	--	-- / --	--
23	COMMADORE	250	746	567	5/20/67	3.50	--	--	-- / --	--
24	CALABASH	110	625	--	10/29/69	2.65	--	--	-- / --	--

† Materials properties data from ILL data bank
Yield 1 is 20 to 200 KT, L-1 is approximately 0 to 200 KT.

The radii of the circles on the figure are large compared to most reported fracture radii and are estimates that more represent the extent to hydrofracture type failure that is postulated as occurring along pre-existing weaknesses from detonations below or close to the water table.

The best correlation by far for trying to explain F-factor variations and Love-wave excitation in Yucca Valley is geographic location. This may provide a rational approach to explain the low anomalies of both the PIRANHA and CHARCOAL events. Note on Figure 3-12 that at about $37^{\circ}06'N$ latitude, both the Yucca and Area 3 faults change strike (orientation) from NNE to NNW. One intuitively expects stresses to either concentrate or to be somewhat relieved at fault bends. A check in this trend is possible by comparing the F-factors for the closest events north and south of these two events. These are BUFF and BRONZE, having the lowest F-factors listed on Table 3-2. Clearly, more data is needed to evaluate the geographical variability of pre-stress in Yucca Valley. One obvious fact is that the fault scarp along YUCCA fault is visible and has survived erosion in the north near CORDUROY. It is not preserved south of $37^{\circ}05'N$, and the fault motion may not have occurred at the last time of motion causing the scarp to the north. Possibly, the last motion was restricted to the region of highest accumulated stress.

One important indication of this analysis compared to that of Aki and Tsai is that an explosion-triggered fault motion model for the pre-stress relief in Yucca Valley is not supported. This is surprising since the same data was used to refute the volumetric or cavity fracture zone stress relief model proposed by Archambeau (1970). What is indicated is that for the larger yield, tests near or below the water table do apparently release some stored tectonic stress -- possibly as a result of explosion induced fluid pressures along natural weaknesses triggering stress drops at substantial distances from the explosions. Closer in the stress may be largely relieved by microhydrofracturing where many fine scale new fractures are produced.

Fault motions observed at the surface in Yucca Valley are thought to represent pre-stress relief but not associated with differential lateral stresses

giving rise to surface wave double couples. Instead, these are considered the result of spall induced release of stored vertical stress in the partial compaction of voids on the upthrown side of the major faults in the Valley fill -- above the water table.

- Love-Wave Excitation Summary and Tentative "Scaling"

Figure 3-13 is an F-factor/Apparent Yield plot of the NTS tests (plus SHOAL) listed on Table 3-2. A consistent 1/4th power of apparent yield dependence is indicated that is thought to be mostly a result of rock properties changes (better energy coupling) with depth of burst. GREELEY and CHARTREUSE are for the Pahute Mesa tests which are thought to represent virgin ground conditions with the F-factors determined. The same slope passes through the Yucca Valley tests when the north and south tests are considered separately. Further speculation is that if in-situ pre-stress in Pahute Mesa is essentially the same as northern Yucca Valley, then the difference in F-factor may be associated with spall induced pre-stress relief occurring only at Pahute Mesa. If this is the case, then about 50 percent of the total pre-stress relief associated with events at Pahute Mesa is spall induced. When spall and the extent of explosion induced fluid pressure hydrofracturing are considered, then a cross-sectional area or volumetric model substantially larger than that assumed by Archambeau for pre-stress relief, may be the more general mechanism explaining the F-factor data. Explosion triggering of faults is, of course, a credible mechanism that probably contributes to the surface wave double couples -- it just does not appear to dominate at either Pahute Mesa or Yucca Valley.

The basic recommendation of this preliminary review is to obtain additional surface wave analysis results (preferably in terms of F-factors, strike, and motion of apparent double couples). With this larger data base, the analysis can be completed. It may be possible that intermediate and large yield explosions reveal a great deal of information about the state of stress variations in the earth's crust as well as assist in better understanding variations in M_s and m_b .

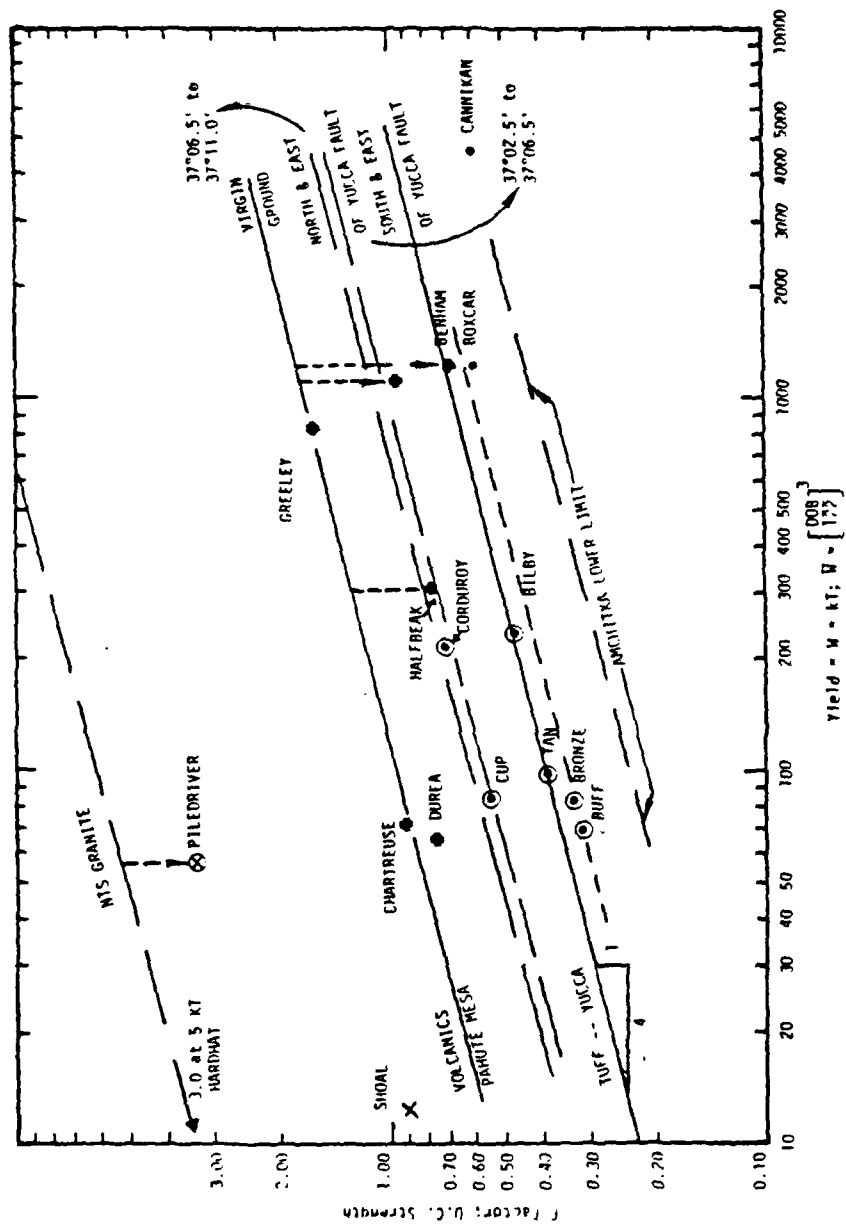


Figure 3-13. Double couple strength (F-factor) versus "apparent" yield dependence for NTS events, SHOAL and CANNIKAN.

3.1.3 Relations of Apparent Explosion Energy Partitioning to Near and Far-Field Motions -- PR-79-040 Appendix E for complete Draft text and references

This progress summary provides evidence for cavity volume history being directly related to ground motion history. There are two primary goals associated with this preliminary investigation:

1. To determine if the complex partitioning in wave mechanics theory, or near-field and far-field terms, can be simply approximated and related to near source ground motion measurements.
 2. To determine if the maximum (dynamic) cavity size can be approximated from the ground motion records so that more accurate empirical relations can be developed to describe cavity dynamics, rock properties, and ground motion history interactions.
- Possible Relation of the SALMON Cavity Volume History to Radial Ground Motion History

Ground motion data from the SALMON event are minimally polluted with indeterminant variables and heterogeneous complexities. Because of the salt's plasticity, the confining stress field was essentially hydrostatic and probably about equal to the overburden weight. Thus, the four important rock properties variables thought to dominate cavity size are well known:

- Compaction -- can be assumed negligible.
- Water Content -- can be assumed negligible.
- Heterogeneities -- can be assumed minimal.
- Confining Stress -- the three principle stresses can be assumed effectively equal and equivalent to the overburden weight.

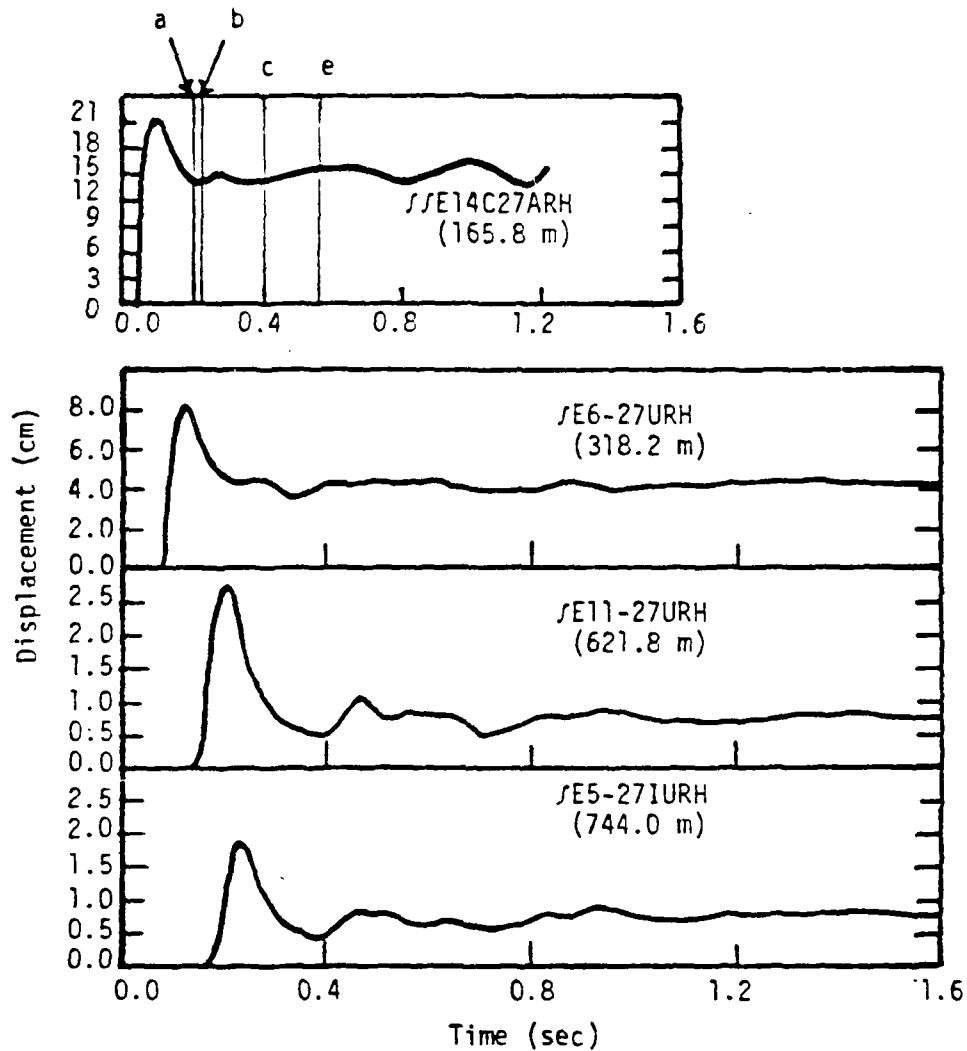
In addition, the salt vapor does not rapidly condense and the plastically responding salt does not allow appreciable early gas leakage. The cavity pressure history, then, can be expected to reflect the induced stress history for at least the first few seconds.

There are three radial velocity gauges and one radial acceleration gauge at four horizontal (shot level) ranges. These gauges are assumed accurate and the displacement integrations are shown in Figure 3-14. Also, the approximate times of expected reflected waves are tabulated and located on the close-in acceleration record. These do not appear to have a large effect so that as a first approximation, the larger displacement oscillations are presumed to be in response to the cavity pressure history (possibly modified by other reflections). Table 3-7 provides the initial peak displacement δ_1 , the second peak δ_2 , the difference between these two peaks δ^* , and the residual displacement at +1.6 seconds, δ_3 . These displacements are also shown on the idealized displacement/time record in Figure 3-15. This shows the first displacement pulse being complex with the remaining wave train essentially showing damped oscillations presumably associated with the explosion produced cavity. The maximum cavity size R_m corresponding to the buried displacement peak δ_2 cannot be directly discerned from the records because of the complex nature of the first pulse. The cavity size R_m is assumed to be accurately reflected, however, in the second displacement peak δ_2 even though this second cavity size peak is probably a little smaller than its initial peak δ_2 hidden within the first pulse.

The cavity size is estimated with the assumption of negligible compaction occurring in the surrounding rock by Equation 3-6:

$$R_x = \left[3 R_{SL}^2 \delta_y \right]^{1/3} \quad (3-6)$$

where R_x is the implied cavity size (m) associated with displacement δ_y (m) at range R_{SL} (m). Thus, R_m or the maximum cavity size under dynamic conditions is equal to or greater than the R_m that is calculated from δ_2 . The residual cavity size R_r is calculated from δ_3 and the final cavity size (traditionally R_c) is the late time apparent size determined by post shot exploration -- a time that may follow considerable induced stress adjustment. Calculated dynamic cavity radii associated with δ_2 and δ_3 are shown in Table 3-4. The indicated R_m is equal to or greater than about 23.8 m or essentially 24 m. This size apparently decreased slightly to about 23 meters by 1.6 seconds after the detonation and then slowly deformed to a final size of 17.4 meters at the time of post shot



Reflectors	Distance	V_p km/sec	Reflection Return
a. Salt Top	~ .450 km	4.67	0.19 sec
b. Salt Near Side	~ 0.4 km	4.67	0.17 sec
c. Salt Far Side	~ 1.0 km	4.67	0.4 sec
d. Salt Base	7.24 km	4.67	3.1 sec
e. Salt Free Surface	.83 km	3	0.55 sec

Figure 3-14. Radial displacement histories at shot level associated with the SALMON event along with estimated arrivals from major reflectors.

TABLE 3-7
SALMON Horizontal (Radial) Displacement Peaks

Record Number	Slant Range Equals Horizontal Range (m)	Displacements (cm)			† Estimated Dynamic Cavity Radii at	
		Initial δ_1	2nd δ_2	δ^* δ_3	+ 0.25 sec After 1st TOA	+ 1.6 sec After Shot
SE14C-27ARH	165.8	21.8	15.4	6.4 --	23.33	--
SE6-27URH	318.2	8.2	4.7	3.5 4.3	24.26	23.55
SE11-27URH	621.8	2.7	1.1	1.6 0.8	23.37	21.01
SE5-27-1UKH	744	1.9	0.85	1.05 0.8	24.17	23.68

$$^{\dagger}r_x = \left[3 R_{SL}^2 \delta_y \right]^{1/3}$$

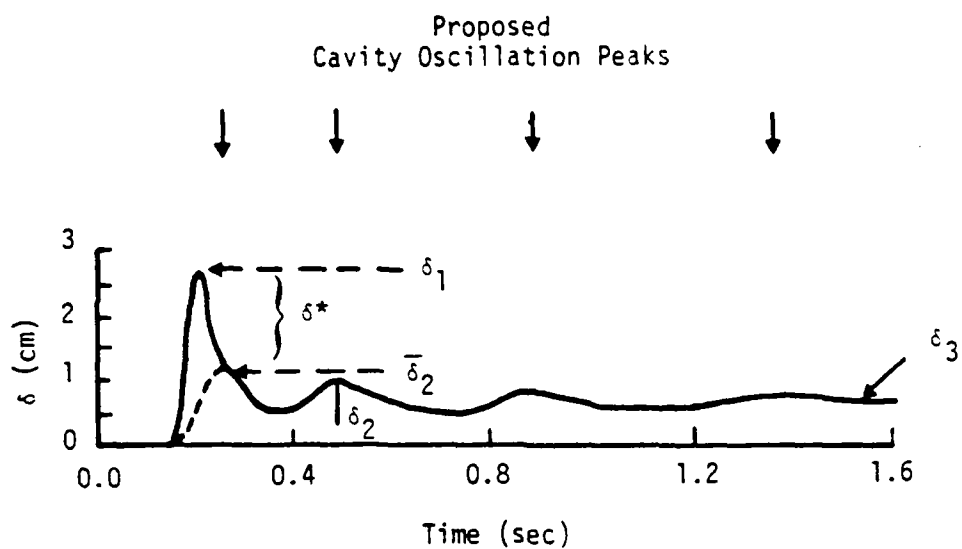


Figure 3-15. Idealized displacement time record modified after gauge record JEl1-27URH.

exploration four months after the detonation. At the time of post shot exploration, the explosion-induced stresses thought to have existed earlier in the rock surrounding the cavity had apparently crept and relaxed -- opening or dilating slightly along explosion induced rock failure surfaces that are well documented by borehole geophysical measurements.

- Tentative Relations Proposed Relating SALMON Displacement Peaks to Near-Field and Far-Field Energy Partitions

Assuming that the displacement peak δ_2 is a reasonable and possibly lower bound approximation of the maximum cavity size -- it is proposed that the initial peak δ_1 shown in Figure 3-15 can be partitioned into roughly two categories of apparent displacement:

1. δ^* representing predominantly the far-field displacement component, which is the difference between δ_1 and δ_2 .
2. δ_2 which is equal to or slightly greater than δ_2 and represents predominantly the near-field displacement component.

The proposition is that the initial displacement peak δ_1 is approximately partitionable as follows:

$$\delta_1(R_{SL}) = \frac{K}{R_{SL}^{1.58}} \approx \frac{K_{NF}}{R_{SL}^2} + \frac{K_{FF}}{R_{SL}} \quad (3-7)$$

and where

$$\delta^* \approx \frac{K_{FF}}{R_{SL}} \approx \text{far-field term}$$

$$\delta_2 \approx \frac{K_{NF}}{R_{SL}^2} \approx \text{near-field term}$$

The attenuation with range of δ_1 for SALMON was determined by Perret (1964) to be

$$\delta_1 = 7.03 \times 10^4 R_{SL}^{-1.58} \quad (3-8)$$

A check on the possible validity of Equation (3-7) is shown in Figure 3-16 -- plotting the attenuation with distance of δ_1 , δ_2 and δ^* versus R_{SL} -- using the values determined in Table 3-7. The displacement component δ_2 attenuates approximately as R_{SL}^{-2} and δ^* attenuates approximately as R_{SL}^{-1} as anticipated by Equation (3-7). Considerably more effort is needed to determine if it is in fact feasible to approximate near and far field motion terms in the near-field ground motion data from a variety of detonations. If this is achievable, it may then be possible to more directly relate the near-field ground motion data to far-field teleseismic data and better assess the source (explosion/earth) interactions as they may relate to teleseismic data.

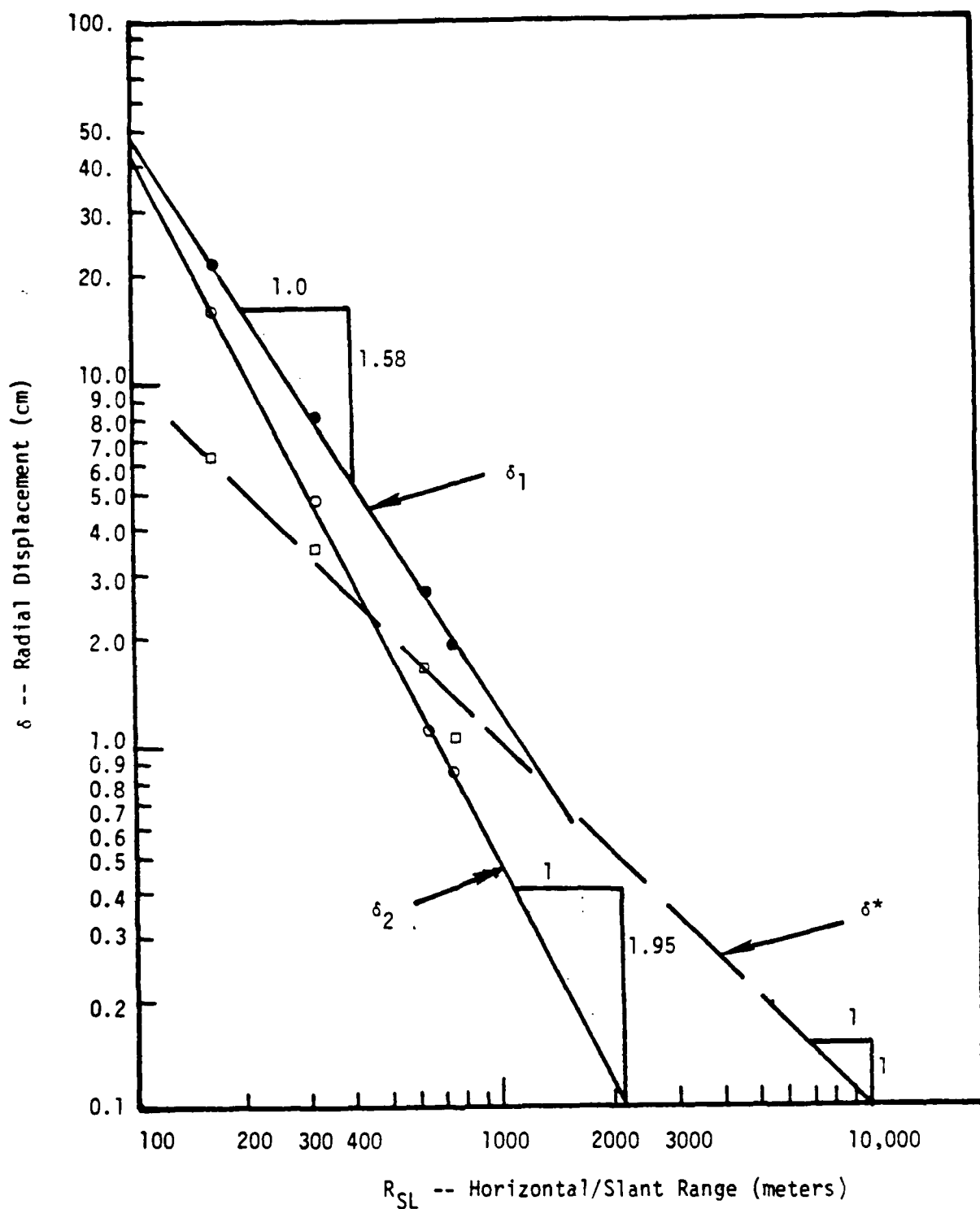


Figure 3-16. SALMON radial displacement peak possibly reflecting near- and far-field energy partitioning.

3.2 FINITE ELEMENT MODELING OF SPALL

The goal of finite element modeling of spall is to provide the theoretical near-source spall related ground motions from buried explosions. The results may be then linked to more conventional wave propagation codes to enable modeling of the far-field ground motion due to events that produce spall.

3.2.1 NUMERICAL SIMULATION OF SPALL — TR-77-012, Appendix F for Complete Text and References

The appended draft report by Sweet (1977) describes DELTA's finite element model for calculating spall related ground motions in response to an underground explosion. The model assumes a pre-selected single plane of weakness along which spall is allowed to develop parallel to the ground surface. Spall is considered to result when the explosion generated stress wave is reflected from the free surface as a tensile wave causing the material to separate along the pre-determined weakness.

The spall modeling technique utilizes the SWIS finite element code developed earlier for fracture modeling. The method adapted to simulate spall is a finite element mesh containing the explosion generated cavity. The dynamic pressure history is applied to the cavity mesh in order to simulate the explosion induced stress history. In addition, a gravitational load is statically applied to the mesh. The fracture model allows the spall layer to rise due to trapped vertical momentum and return to impact the earth. An example test calculation was made to demonstrate the method but at that time systematic study of spall was not accomplished.

3.2.2. A SPALL CALCULATION OF THE BENHAM EVENT

The above summarized method of numerically simulated spall has been applied to the BENHAM event, which was detonated in 1968, in the Pahute Mesa environment of the Nevada Test Site. Table 3-8 presents the epicenter data concerning the explosion as well as the explosion source model parameters using Murphy's model of the cavity pressure history (see Appendix A). The geologic

TABLE 3-8

Epicenter Data* and Murphy[†] Source Model
Parameters for BENHAM

Date:	12/19/68	
From Time:	16:30:00.04	
Location:	37°13' 53.3N 116°38' 24.9W	
Shot Depth:	1402 m	
Shot Medium:	Tuff	
Yield:	1100 kT	
r_c :	107.8 m	Cavity Radius
r_{el} :	733.4 m	Elastic Radius
p_{os}	4.12×10^{-1} kbars	} Murphy Source Pressure Parameters
p_{oc} :	2.08×10^{-1} kbars	
p_o :	2.04×10^{-1} kbars	

* Springer, D. L., and R. L. Kinnaman, Seismic Source Summary for U.S. Underground Nuclear Explosions, 1961-1970, Bull. Seis. Soc. Am., Vol. 61, p. 1073-1098, 1971.

[†] Refer to Appendix A.

layered earth model used for the site is described in Figure 3-17. With these input parameters, the appropriate cavity size was introduced into the finite element mesh and gravity incorporated as a static pre-stress to the mesh (Figure 3-18). The thickness and extent of the layering allowed to spall was conservatively set at a depth of 193 meters and a radius of 1176 meters. Although the spall confirmation is not known for BENHAM, it is probably similar to BOXCAR -- estimated in Appendix B as 4000 meters in extent and possibly as deep as 400 meters.

Figures 3-19a through 3-19i present a series of snap-shots with respect to time of the finite element mesh illustrating deformation about the cavity and the uplift and impact of spall. Spall remains intact until $t = 0.468$ sec. By $t = 0.528$ sec(a) spall has begun, reaching maximum separation at $t = 0.768$ sec(e). Impact is initiated first at the prescribed extent of spall, progressing from its outer limits inwards toward ground zero until spall becomes fully closed by $t = 1.068$ sec. The total spall duration is 0.6 sec.

The calculated ground motion histories for the surface zero location are shown in Figures 3-20a and 3-20b. The upper record (a) showing spall impact (arrow) can be compared to the calculated record (b) where spall was not allowed. An additional comparison with an actual surface zero acceleration record can be made by referring to Figures 3-1 (top) and 3-3. Note that between the initial acceleration peak and the impact peak, the ground reaches a ballistic trajectory that is a constant $-1g$ on a vertical acceleration record. Presumably if vertical failure surfaces were allowed in the simulation, freeing of the spalled layer could occur so that free-fall would be completely achieved. As it is, the spall layer is somewhat constrained; however, a clear impact signal is observed. Also comparing the displacement record between a and b, spall accounts for an additional displacement of about 40 cm associated with the opening of the spall gap.

Figures 3-21a and 3-21b show similar time histories for the surface node #21 of the mesh located 1680 meters from ground zero and 514 meters beyond the selected extent of spall. Here differences between the case allowed to spall (a)

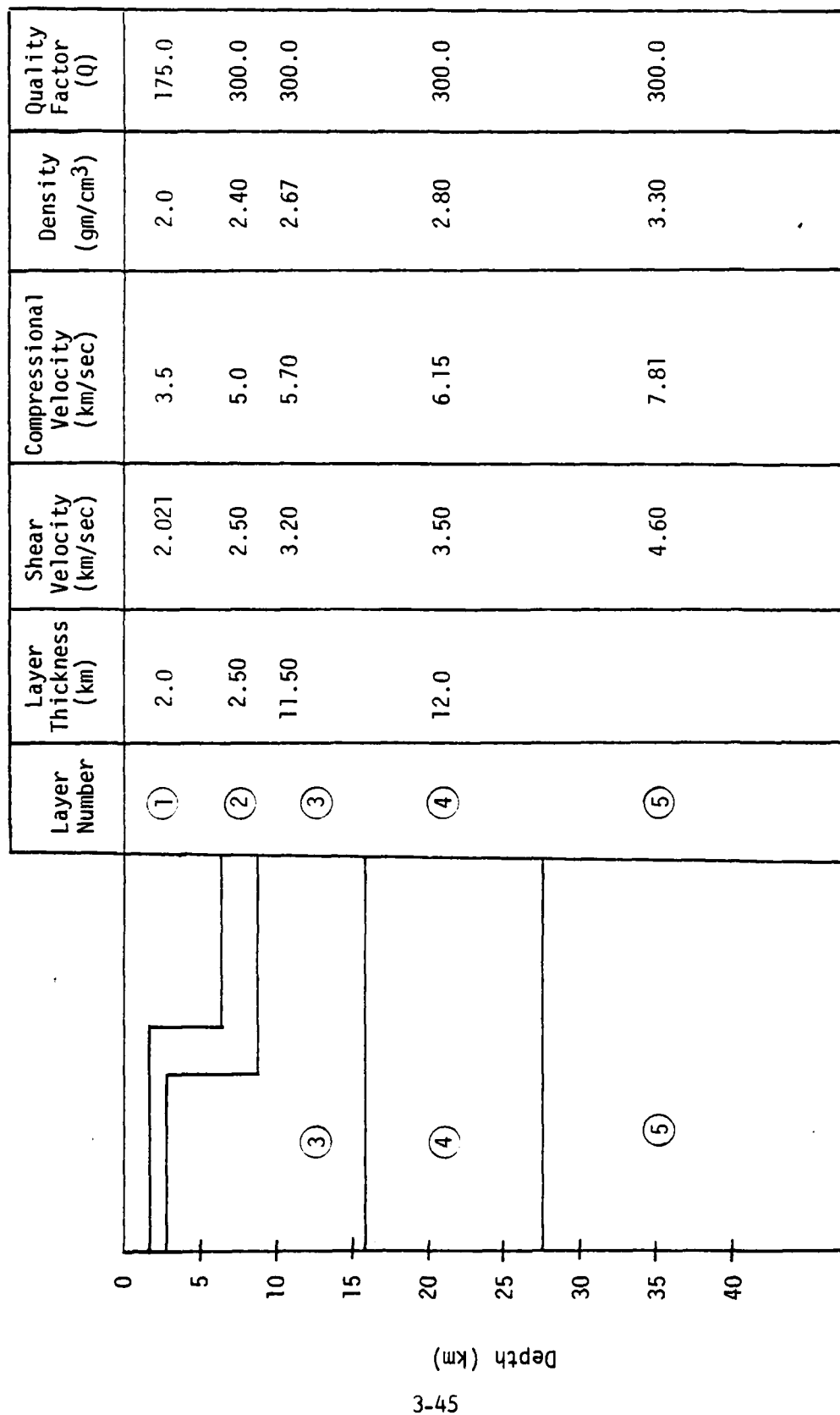


Figure 3-17. Assumed crustal model for Pahute Mesa.

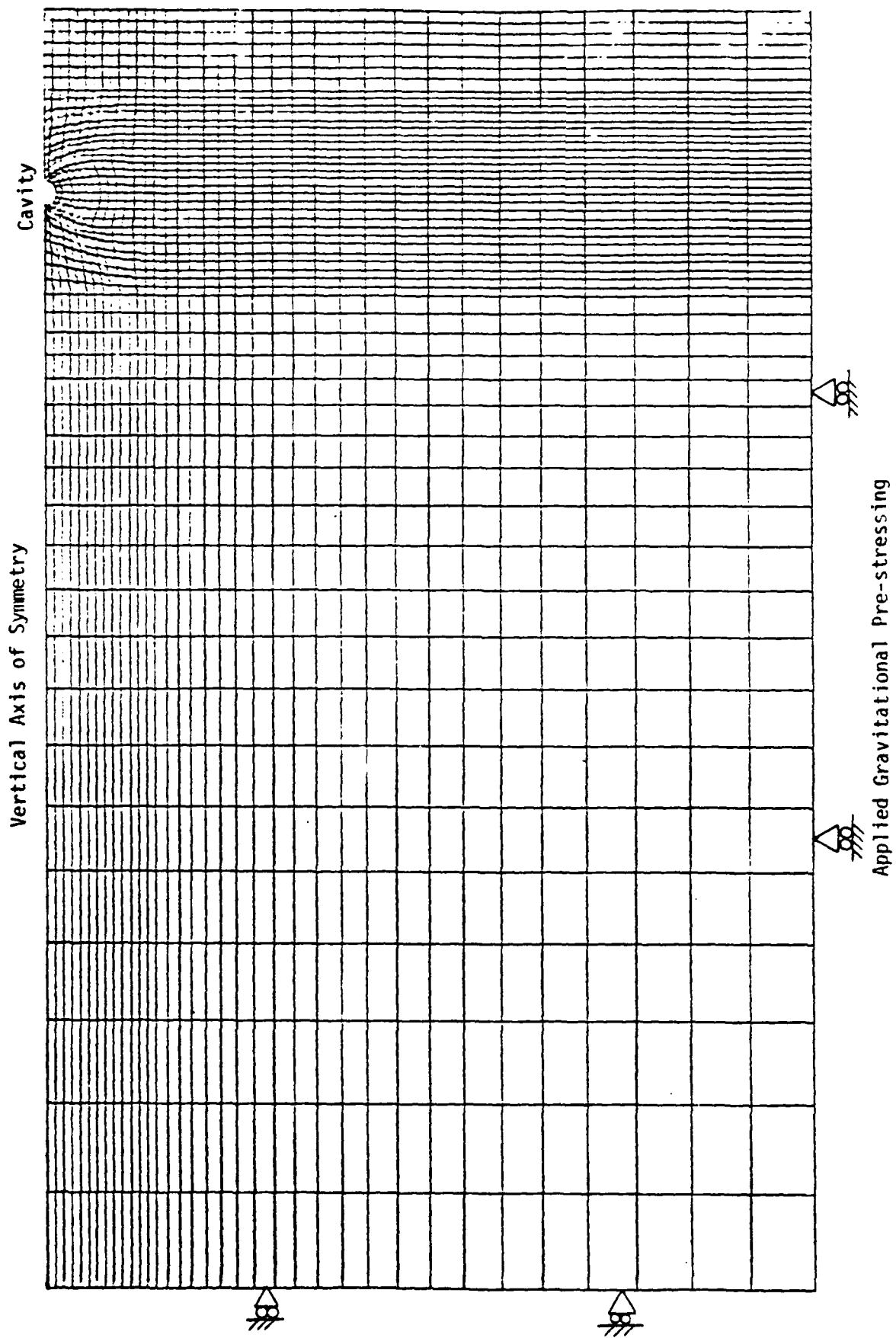
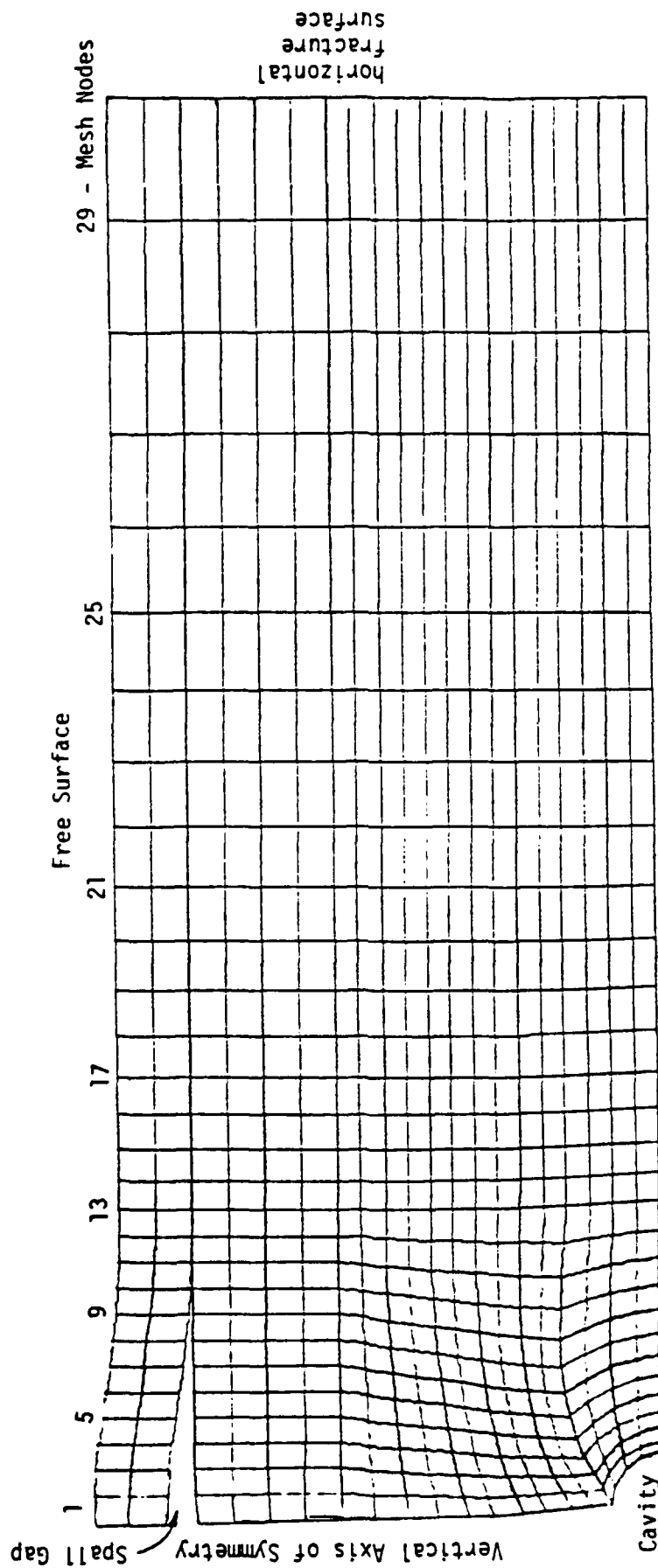
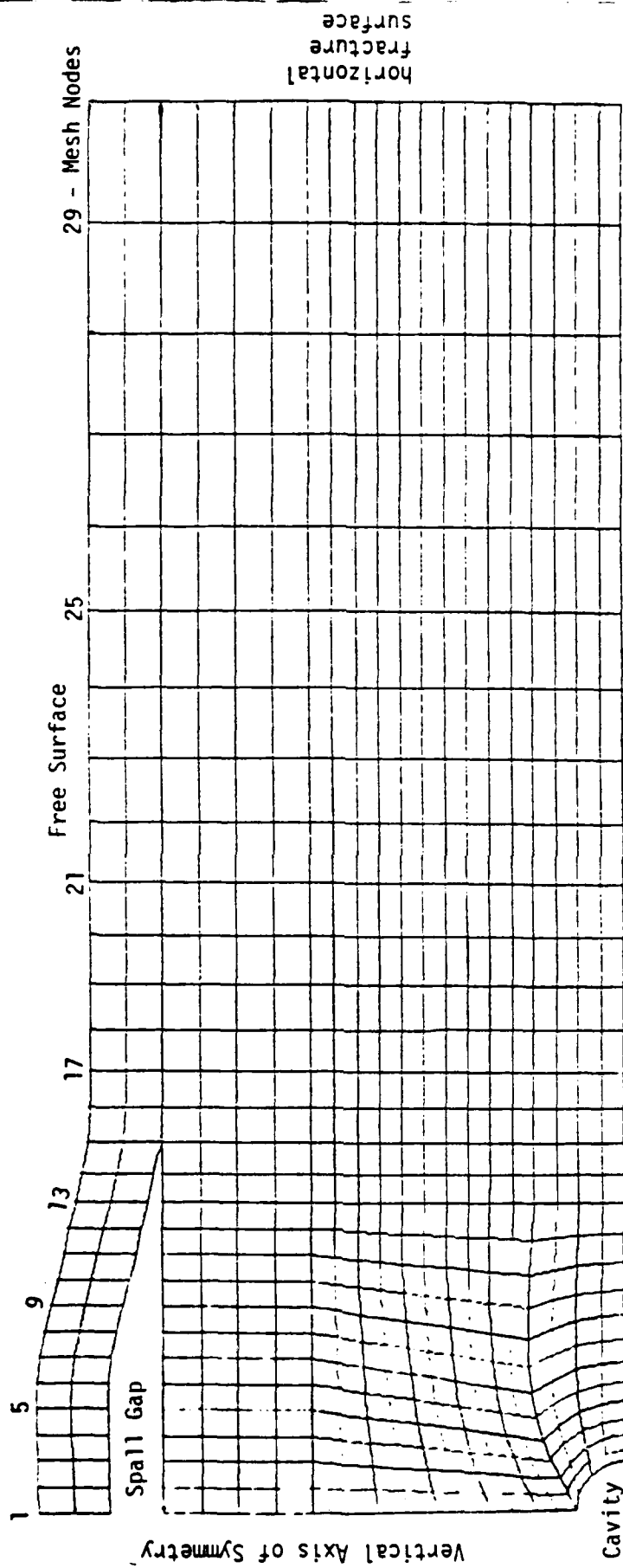


Fig. 3-18 Finite Element Mesh Showing the Introduction of the Benham Cavity & Applied Gravitational Stresses



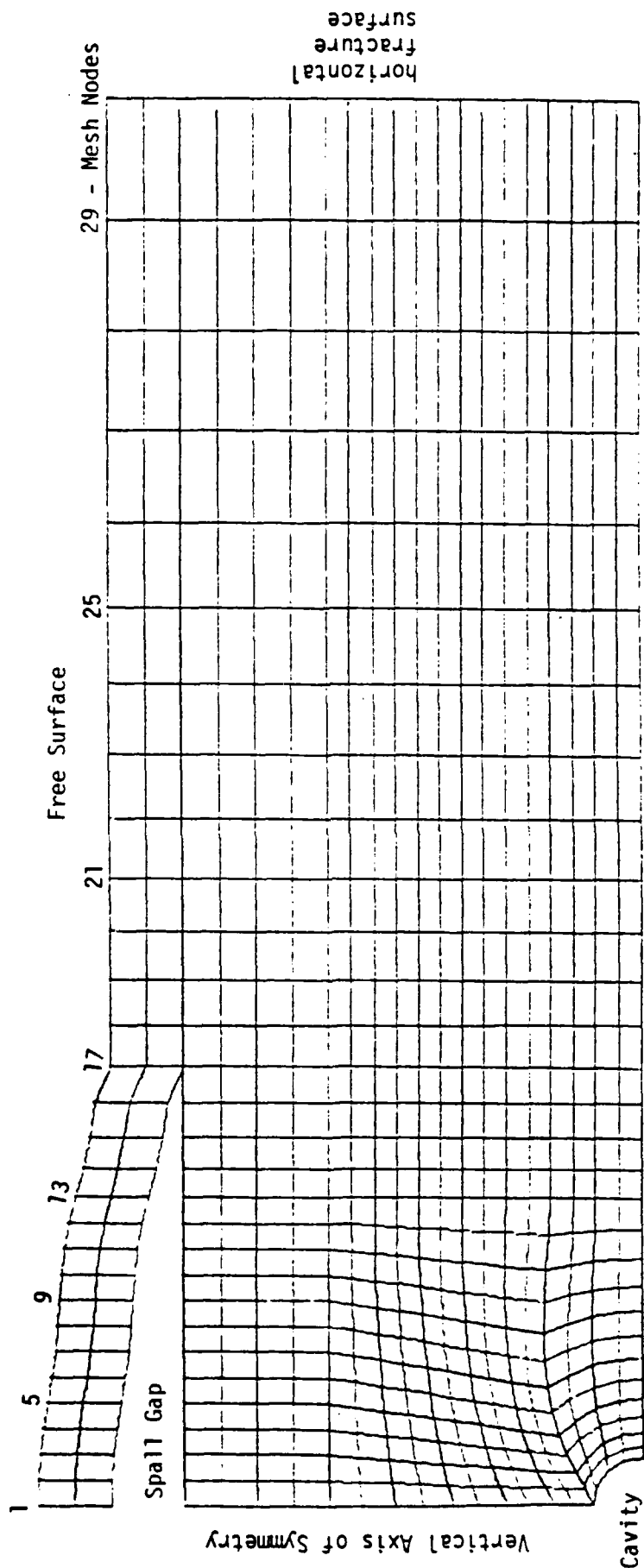
(a) time $t = -.528$ sec

Fig. 3-19a Time Snap Shots of the Benham Mesh Illustrating Uplift and Impact of Spall



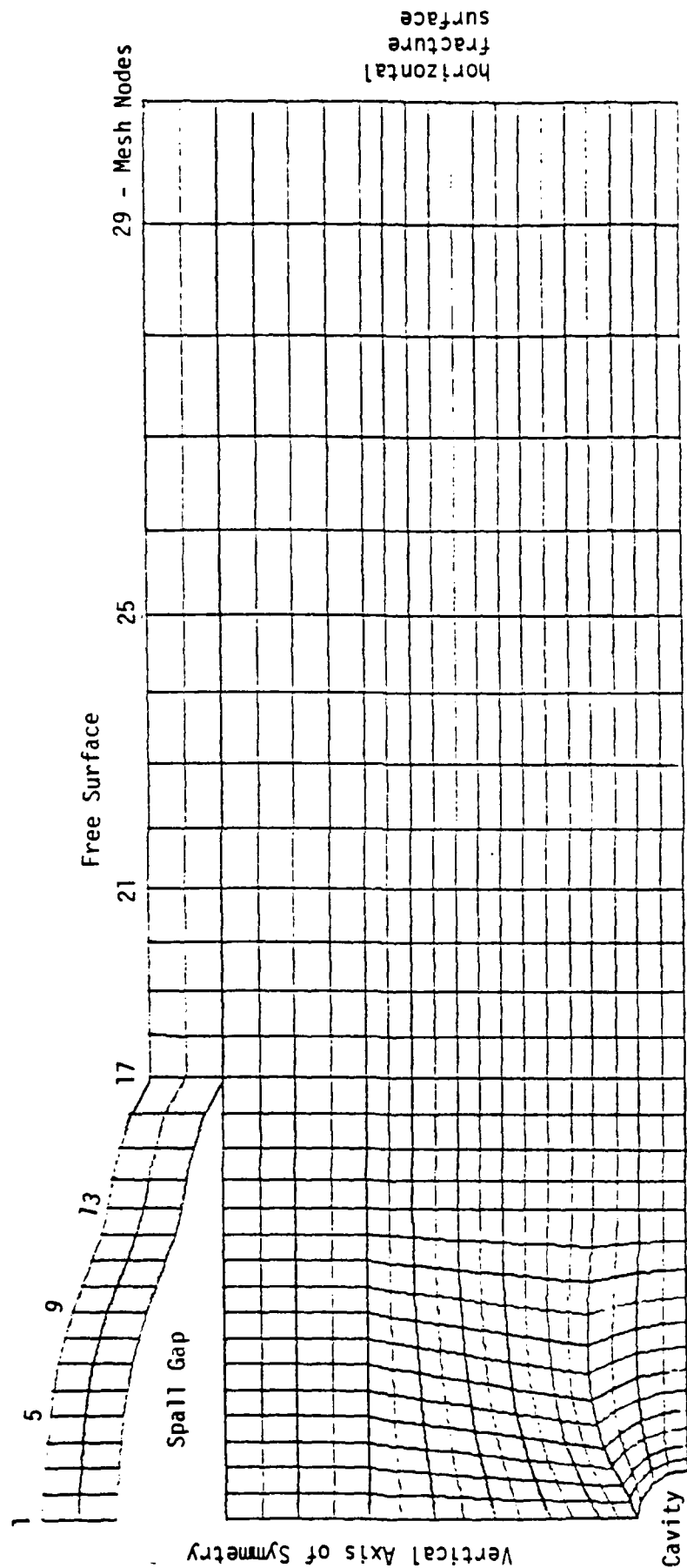
(b) time $t = 0.588$ sec

Fig. 3-19b Time Snap Shots of the Benham Mesh Illustrating Uplift and Impact of Spall



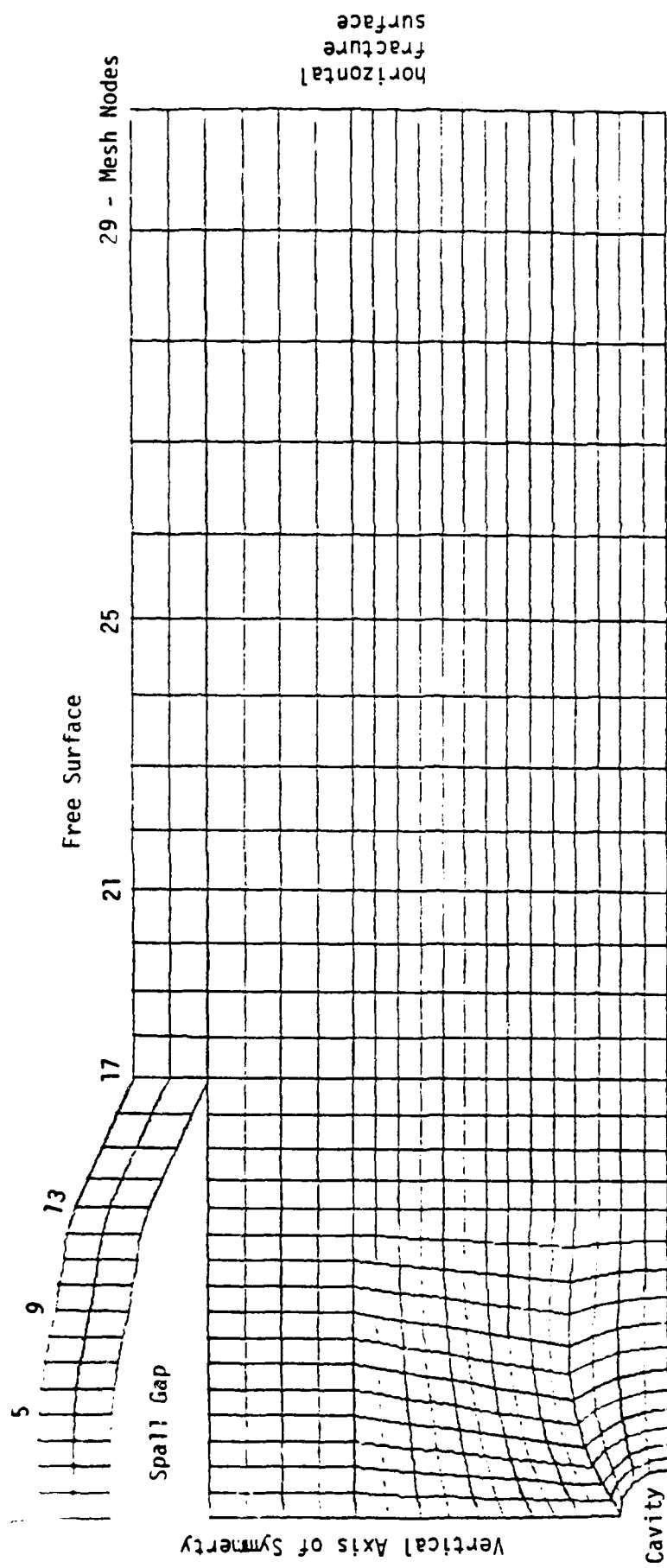
(c) time $t = 0.648$ sec

Fig. 3-19c Time Snap Shots of the Benham Mesh Illustrating Uplift and Impact of Spall



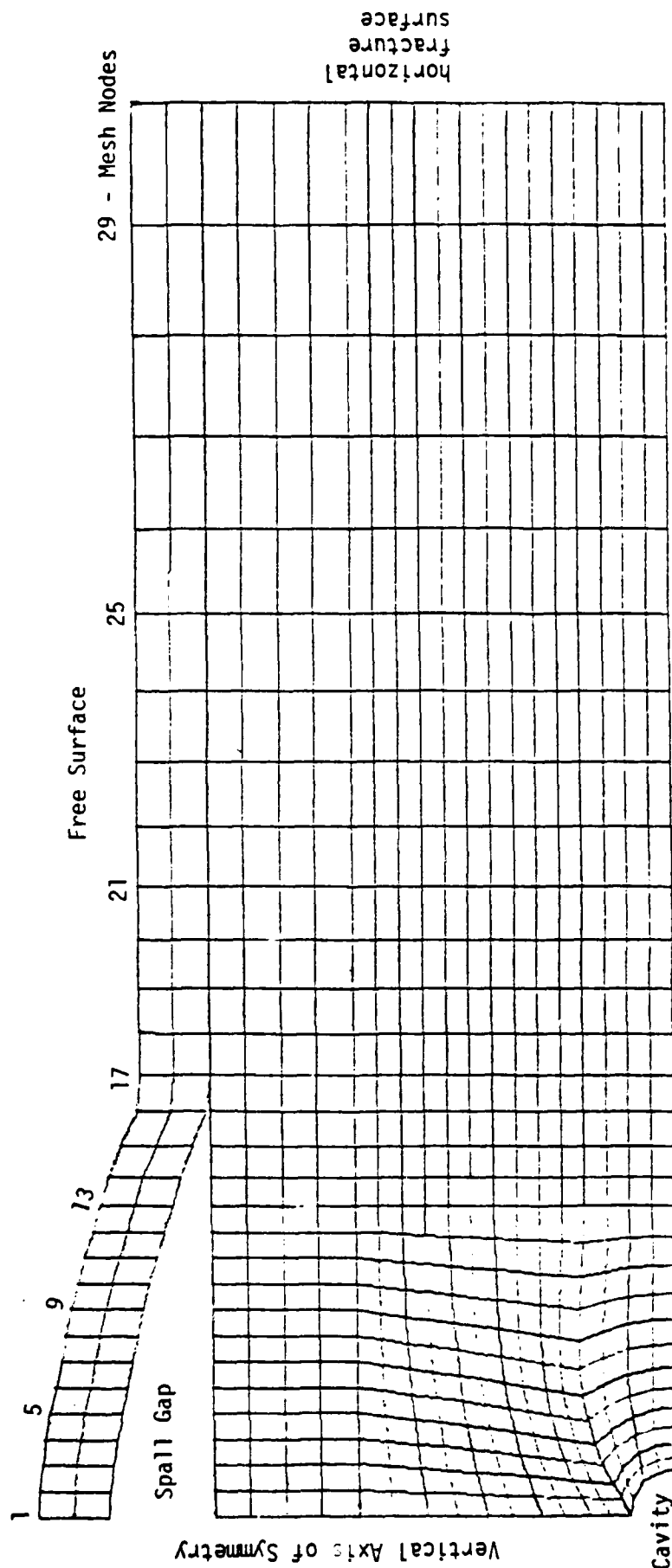
(d) time $t = 0.708$ sec

Fig. 3-19d Time Snap Shots of the Benham Mesh Illustrating Uplift and Impact of Spall



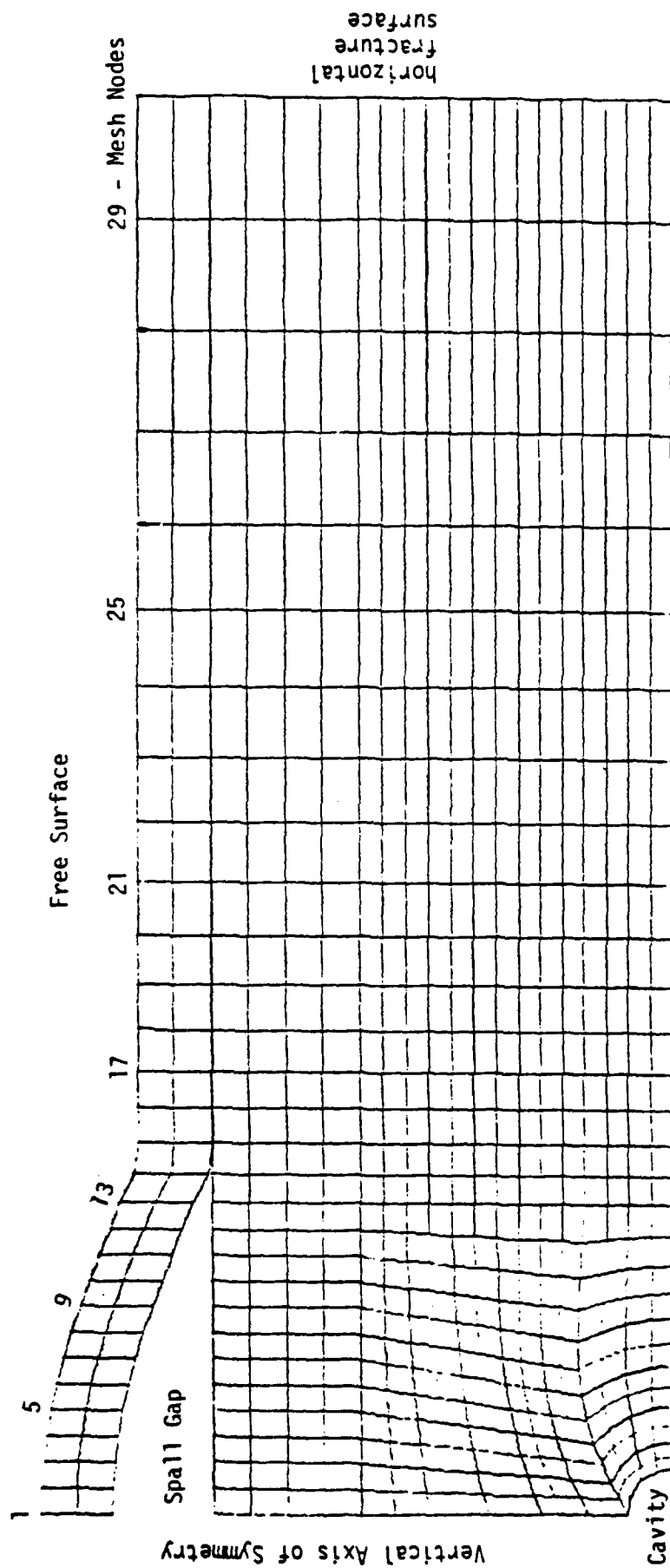
(e) time $t = 0.768$ sec

Fig. 3-19e Time Snap Shots of the Benham Mesh Illustrating Uplift and Impact of Spall



(f) time $t = 0.828$ sec

Fig. 3-19f Time Snap Shots of the Benham Mesh Illustrating Uplift and Impact of Spall



(g) time $t = 0.888$ sec

Fig. 3-19g Time Snap Shots of the Benham Mesh Illustrating Uplift and Impact of Spall

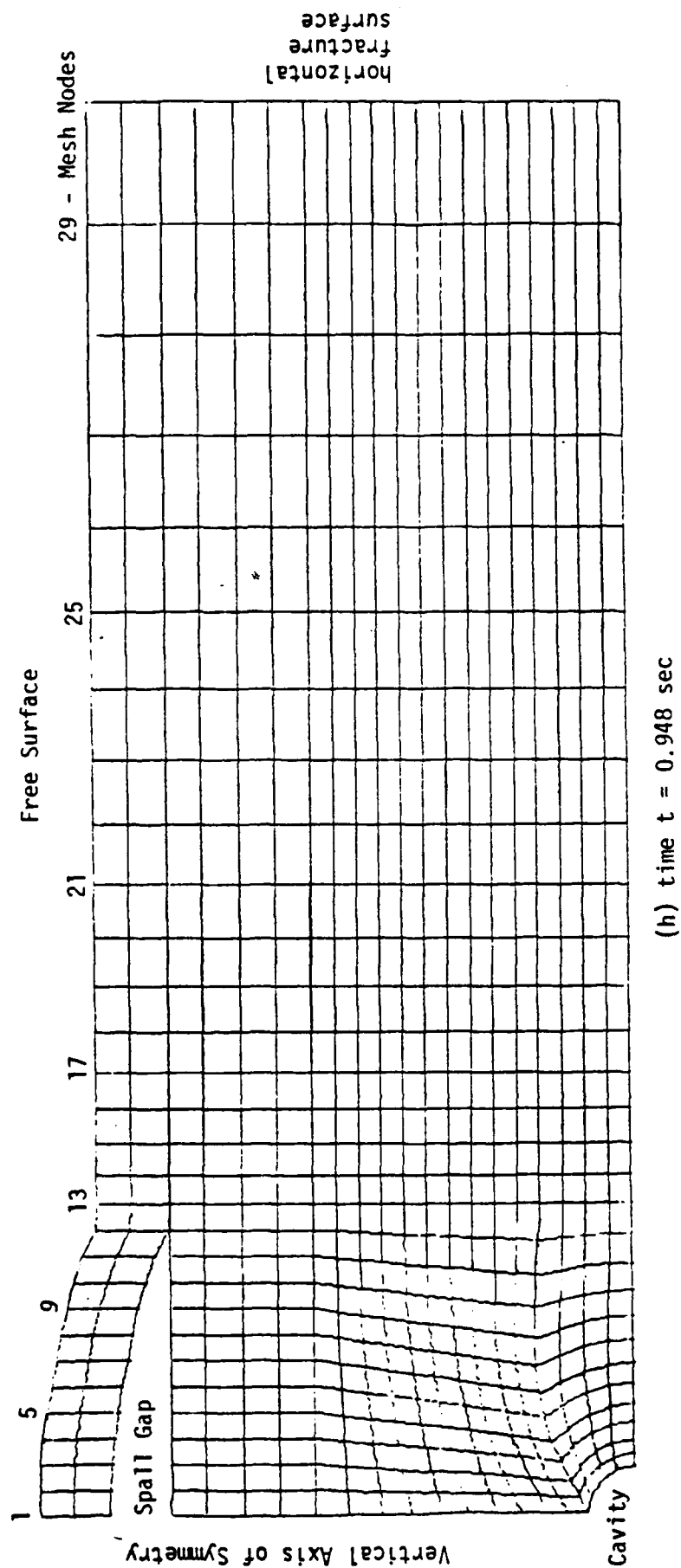
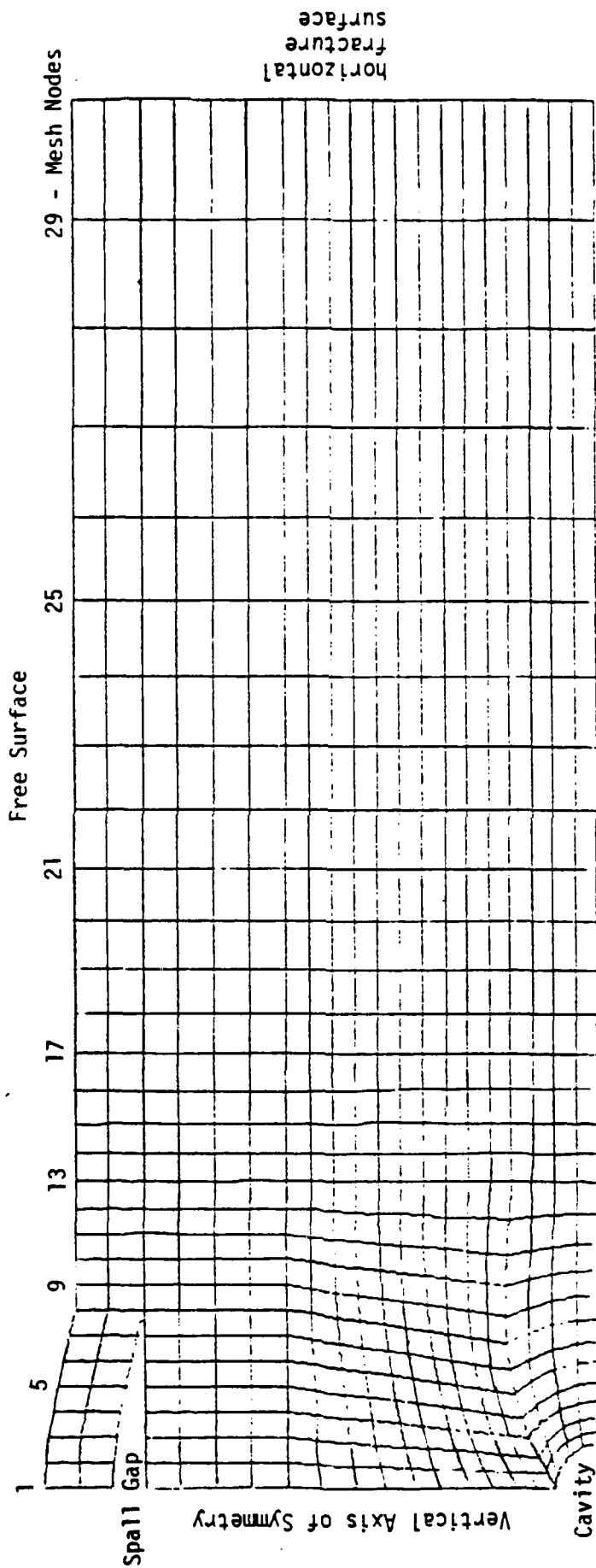


Fig. 3-19h Time Snap Shots of the Benham Mesh Illustrating Uplift and Impact of Spall



(1) time $t = 1.008$ sec

Fig. 3-191 Time Snap Shots of the Benham Mesh Illustrating Uplift and Impact of Spall

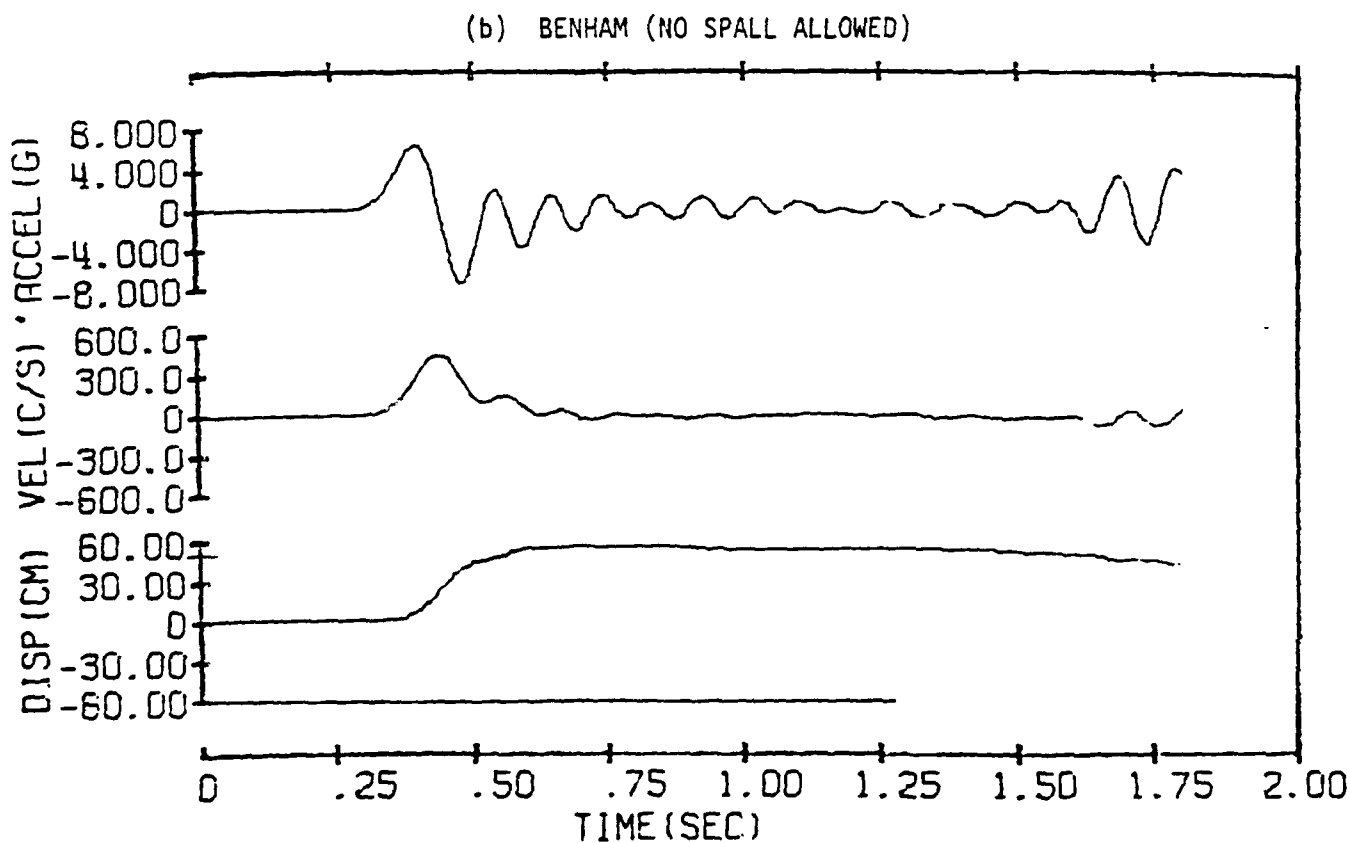
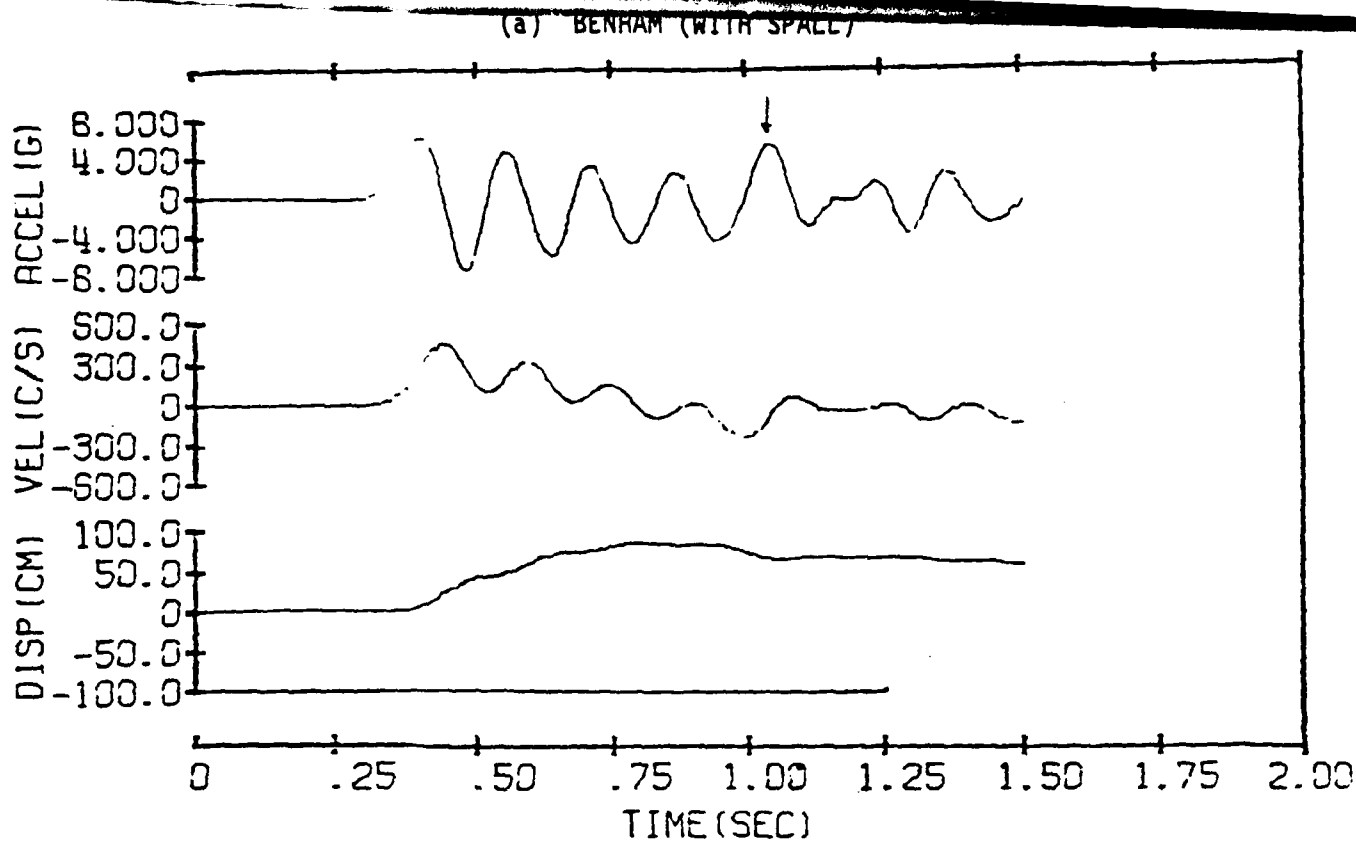


Fig. 3.20 Calculated Vertical Ground Motion at Surface Ground Zero for Benham. Compare spall with the no spall case. Arrow in (a) signifies spall impact.

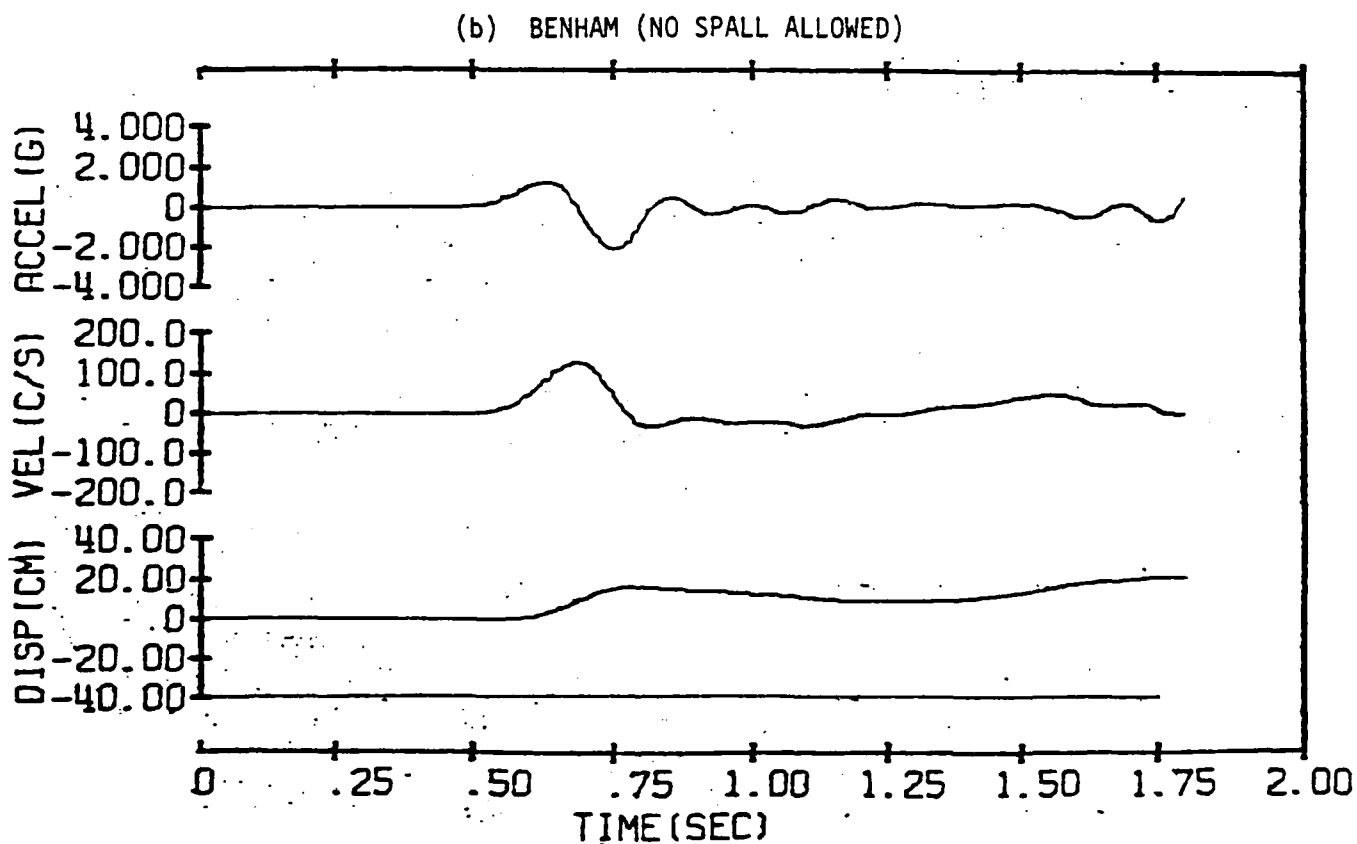
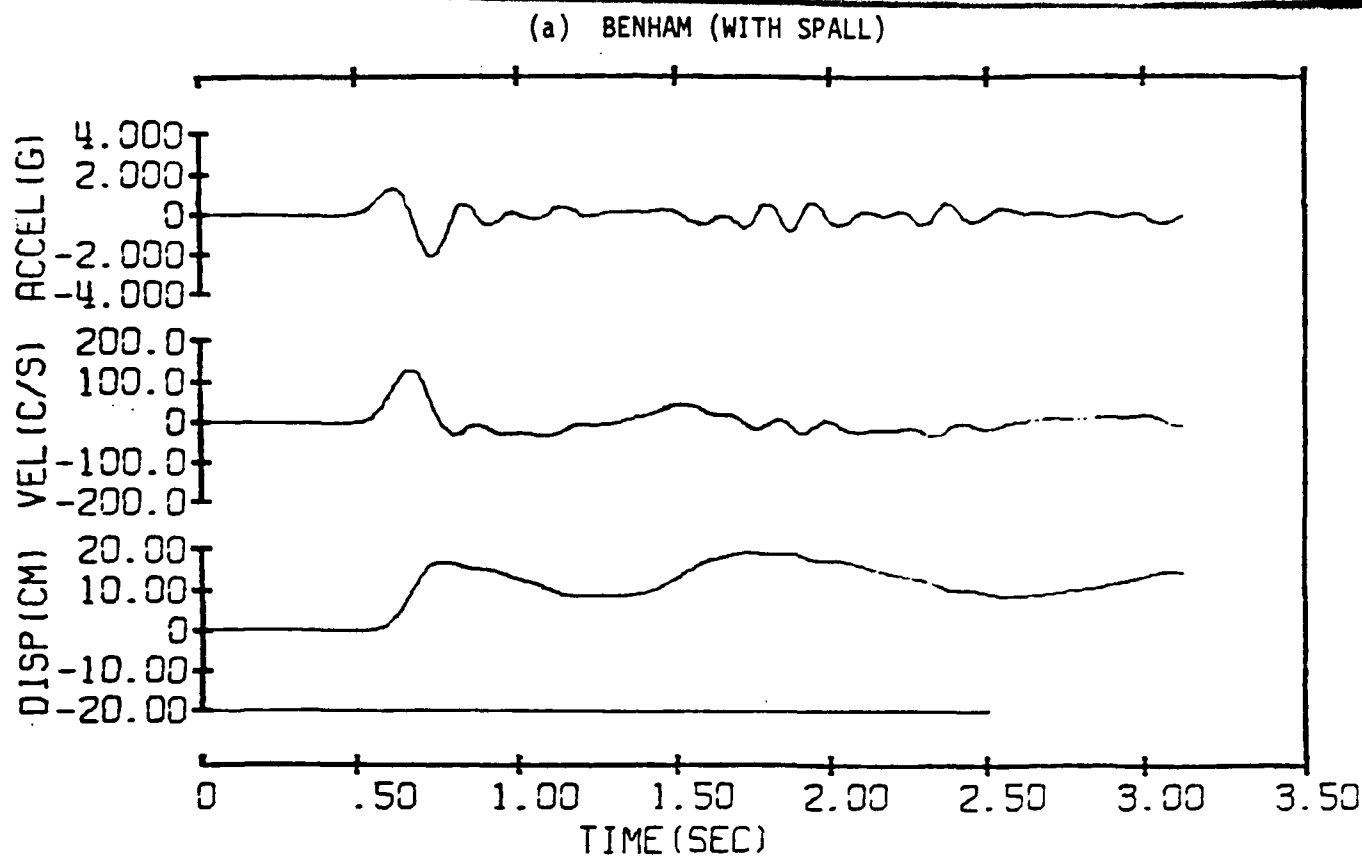


Fig. 3.21 Calculated Vertical Ground Motion for Benham at the Surface Beyond the Allowed Spall Limit at a Range of 1680 m. Compare spall with no spall.

and the case not allowed to spall (b) are negligible. In making the comparison, it is important to note the differences in time scales and the displacement scales.

Assuming the calculation simulates the spall reasonably well, then it follows that there is no appreciable vertical component of motion associated with spall much beyond the extent of spall itself. That extent for a megaton explosion is disk-shaped with a diameter of about 8 kilometers, based upon empirical data.

3.3 CALCULATION OF SURFACE WAVES GENERATED BY SPALL LIFT-OFF AND IMPACT

The configuration of spall (Rawson model) was developed in Section 3.3.1. It calls for a significantly greater spalled mass than that assumed by the previous investigators -- Viecelli (1973) and Sobel (1978).^{*} The maximum effect that each of the above spall models would have on the surface wave generation for the same example explosion (Behnam) is studied in this section.

Viecelli assumed that surface waves resulting from spall associated with a contained explosion can be represented by a single layer impacting the earth at an estimated closure (impacting) velocity. Such a calculation provides an upper bound on the Rayleigh wave amplitudes due to the spall mass assumed. It is not a complete description of the mechanism involved because only impact and not lift-off is considered. It is proposed that, upon completing the spall process, the net resulting forces acting on the earth must be zero, and lift-off is important because it partially cancels the contribution of surface waves due to impact, particularly those having periods of about 20 seconds.

* Viecelli, J.A., "Generation of Rayleigh Waves by Underground Nuclear Explosions: An Examination of Spall Impact and Site Configuration," LLL, UCRL-51417, 1973.

Sobel, P.A., "The Effects of Spall on m_b M_S ," Teledyne Geotech Report SDAC-TR-77-12, April 1978.

Theoretical seismograms for both the unloading and loading (impact) case as well as impact alone for the spall models of the three investigators are presented. These seismograms in turn are compared with the theoretical surface wave signal generated by the explosion itself -- without spall. The calculations do not consider surface waves generated by any mechanism of tectonic stress itself.

3.3.1 COMPUTATIONAL METHOD FOR ESTIMATING RAYLEIGHT WAVES FROM SPALL MODELS

As a first approximation, the Rayleigh waves due to spall can be modeled by considering a finite pressure disk acting on a layered half-space. Following Harkrider (1966, 1970) and Harkrider, *et al.* (1973), the vertical component of the Rayleigh wave at the far-field distance r is given by

$$W_o = \frac{1}{2k} p_s a_s J_1(ka) A_R \left(\frac{2}{kr} \right)^{1/2} \exp \left[-i(kr + \pi/4) \right] \quad (3-9)$$

where a_s is the radius of the spall disc, A_R is the amplitude response of the medium (Harkrider, 1964), and p_s is the Fourier transform of the pressure-time history. For slap-down alone, p_s is given by

$$p_s = \mathcal{F} \{ p_o \delta(t) \} = p_o \quad (3-10)$$

and for lift-off plus slap-down,

$$p_s = \mathcal{F} \{ -p_o \delta^-(t) \} = i\omega p_o, \quad (3-11)$$

where $\mathcal{F} \{ \}$ denotes Fourier transform. The vertical component due to an explosion at depth D , with a cavity radius a_e , is given by Harkrider (1964) as

$$W_o = \frac{k}{2} p_e a_e^3 \frac{\left\{ \frac{1}{2\mu_s} \left[\frac{\sigma^*(D)}{\dot{\omega}_o/c} \right] - \left[\frac{\dot{u}_s(D)}{\dot{\omega}_o} \right] \right\}}{\left[\left(1 - \frac{k_{\beta_s}^2 a_e^2}{4} \right) + k_{\alpha_s}^2 a_e^2 \right]^{1/2}} A_R \left(\frac{2}{kp} \right)^{1/2} \cdot \exp \left\{ i(k_{\alpha_s} a_e + \pi/4 - kr - \theta_e) \right\} \quad (3-12)$$

where

$$\theta_{\epsilon} = \tan^{-1} \left[\frac{k_{\alpha s} a_{\epsilon}}{\left(1 - \frac{k_{\beta s}^2 a_{\epsilon}^2}{4} \right)} \right], \quad (3-13)$$

The subscript s denotes quantities derived from parameters of the layer containing the source, and p_{ϵ} is the Fourier transform of the pressure-time history at the cavity wall. Other quantities are as defined in Harkrider (1964). For the purposes of this comparison, the Mueller and Murphy source-time function derived in Appendix A of this report, as well as the Haskell (1967) source-time function, are considered.

The expressions given in Eqs. (3-9) and (3-10) are evaluated using computer codes adapted from Harkrider, *et al.* (1973) and Harkrider (1964, 1970). The results are presented as synthetic seismograms as seen through an LRSM LPZ seismometer at a distance of 2000 km from the source. The parameters of the source itself are those given in Table 3-8.

3.3.2 COMPARISON OF THE VIECELLI, SOBEL AND RAWSON MODELS

In order to evaluate Eq. (3-9), both the pressure-time history $p_s(t)$ due to the spall mass impacting the earth, and the area of the spall disk must be determined. The pressure is related to the thickness d and the density ρ of the spall layer by

$$p = \rho d \frac{\Delta v}{\Delta t} \quad (3-14)$$

in which Δv is the change in velocity on impact, and Δt is the time over which impact takes place. The term Δv in Eq. (3-14) is equal to the quantity $g \cdot \tau_0 / 2 = \sqrt{2gh}$ in which g is the gravitational acceleration and h is the height reached by the spall layer. Therefore, the impact velocity can be calculated directly from the close-in records, either from the airborne time τ_0 (acceleration records) or the height reached by the spall layer h (displacement records). The dimensions of spall are calculated from empirical relationships given by Viecelli (1973), Sobel (1973), and Rawson (1979) and are compared in Table 3-9.

TABLE 3-9

Spall dimensions for BENHAM, and resultant
Rayleigh-wave amplitudes

	Viecelli	Sobel	Rawson
Radius x 10^5 cm	1.0	2.9	4.0
Thickness x 10^4 cm	2.8	1.6	4.0 + 3.0
Mass x 10^{15} gm	1.8	7.0	29.0
Impulse x 10^{18} dyne/sec	0.5	2.0	5.9
Amplitude, microns			
$\delta(t)$ model	8.9	68.3	105.0
$\delta'(t)$ model	3.1	24.5	36.9

Viecelli gives the spall mass M and the spall impulse I as

$$M = 1.6 \times 10^{12} W \text{ gm} \quad (3-15)$$

and

$$I = 4.6 \times 10^{14} W \text{ dyne-sec} \quad (3-16)$$

in which W is the yield of the explosion in kilotons. The radius of spall, a , estimated from Figure 5 of Viecelli's paper, is 1.0 km.

Sobel also takes into account the depth of burial, DOB. She finds that

$$\begin{aligned} \log d &= 1.35 + 0.35 \log W - 0.07 \log \text{DOB}, \\ \log a &= 2.84 + 0.37 \log W - 0.16 \log \text{DOB}, \end{aligned} \quad (3-17)$$

and

$$\log h_{\max} = 0.57 + 0.52 \log W - 0.50 \log \text{DOB} \quad (3-18)$$

where d , a , h_{\max} and DOB are in meters. Assuming that the thickness of the spall layer is constant, and that the displacements along the surface are "coolie hat" shaped, the impulse due to spall predicted by Sobel is

$$I = \frac{\pi}{3} \rho d a^2 (2gh_{\max})^{1/2} \quad (3-19)$$

The spall mass and impulse for Benham calculated from the above are also shown in Table 3-9.

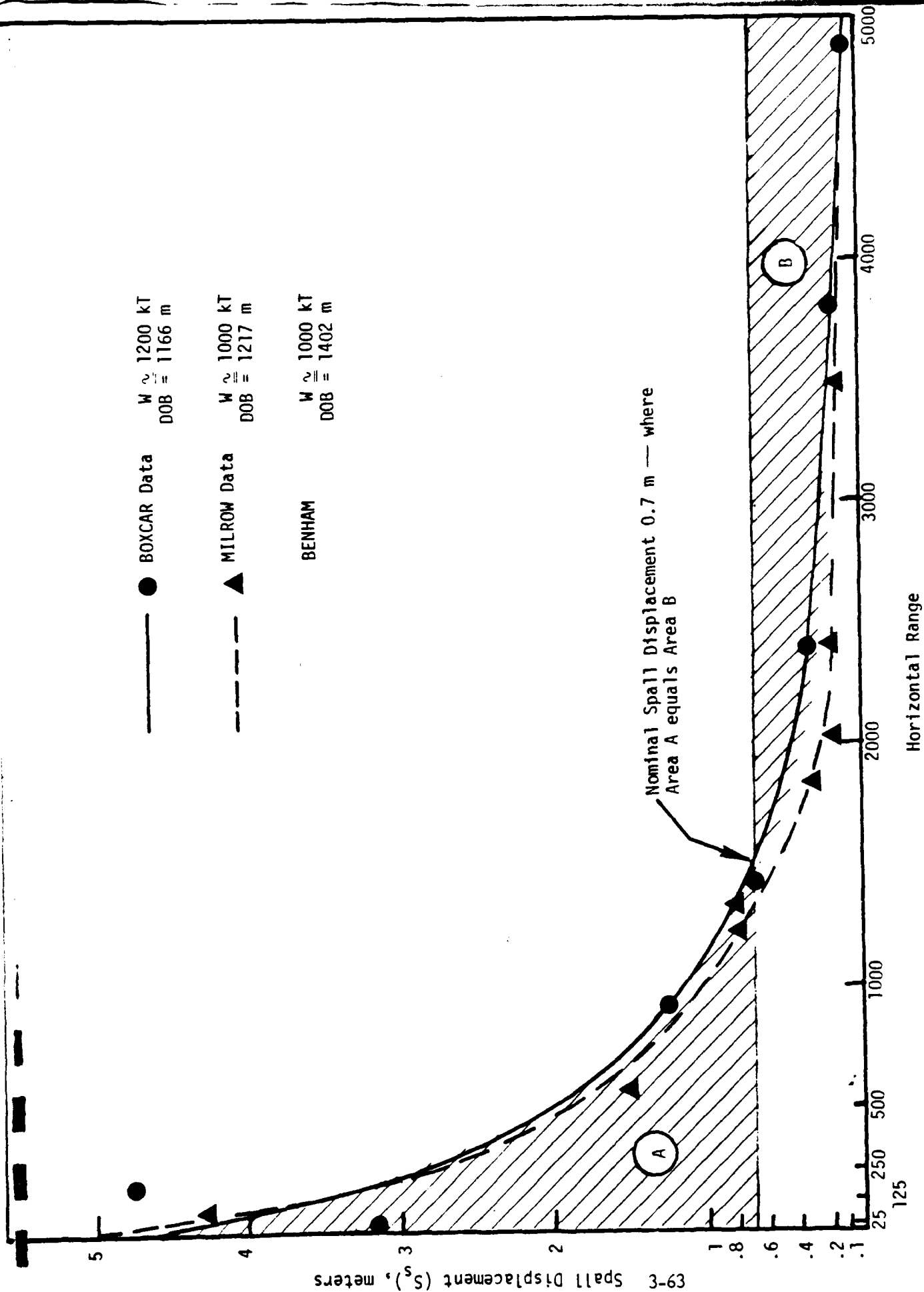


Figure 3-22. Vertical displacement for BENHAM approximated as a function of range from similar explosions.

Rawson recognized that the spall layer need not have a constant thickness. He proposes the three formulae for estimating the spall configuration that were discussed previously in Section 3.1.1. Rawson's formulae have been used to estimate the effective spall mass for the Pahute Mesa explosion, BENHAM. To obtain the impulse, the impact velocity must be estimated from the surface displacement versus distance relation for BOXCAR and MILROW as shown in Figure 3-22. The total impulse computed from Rawson's models is also given in Table 3-9.

3.3.3 SYNTHETIC SEISMOGRAMS FROM THE THREE MODELS

In this section, synthetic Rayleigh wave seismograms are compared for simulations of the actual underground nuclear explosion including the contribution due to spall for the three models discussed in Subsection 3.3.2. To simplify the comparisons, the earth is represented by a model consisting of a 32-km-thick layer with seismic parameters $\alpha = 6.2$ km/sec, $\beta = 3.5$ km/sec, $\rho = 2.7$ gm/cm³ overlaying a half-space with $\alpha = 8.2$ km/sec, $\beta = 6.5$ km/sec, $\rho = 3.4$ gm/cm³. Attenuation coefficients are incorporated in order to simulate both anelastic behavior (Q effects) and scattering. The seismograms are computed for a vertical-component LRSM long-period instrument at a distance of 2000 km. The amplitudes shown in the figures represent actual ground displacement measured in microns.

Figure 3-23 shows three synthetic seismograms for the Pahute Mesa explosion BENHAM. The top trace (a) represents the signal from the 1100 kT event, detonated at a depth of 1.402 km in granite using appropriately scaled versions of the 5 kT values of $\beta = 0.24$, $k = 31.6$ sec⁻¹, $\psi(\infty) = 2500$ m³, given in Table I of Haskell's 1967 paper. The maximum peak-to-peak amplitude is 144.3 microns with an associated period 17 seconds. The second trace (b) represents the signal from the event buried in tuff. For this case, the 5 kT Haskell source parameters are $\beta = 0.05$, $k = 23.5$ sec⁻¹, and $\psi(\infty) = 5120$ m³. However, Haskell indicates that there is considerable uncertainty in both the β and $\psi(\infty)$ values for this medium. The wave form in trace (b) is nearly identical to that for granite except for a factor of approximately two (a result predicted on theoretical grounds by the $\psi(\infty)$ ratio for the top media). The Mueller and Murphy result for BENHAM, detonated in Pahute Mesa tuff (Figure 3-23, trace (c)) shows a waveform identical in shape to Haskell's results. However, the

peak-to-peak amplitude is 148.3 microns. This waveform more closely agrees with Haskell's results for granite than the 369.0 microns for Haskell's tuff medium.

Two tentative conclusions may be drawn from these results: 1) The rise time and overshoot are relatively unimportant parameters in the source-time function when considering the generation of long-period ($t > 4$ seconds) fundamental mode Rayleigh waves; the source-time function being well represented by a step function. (2) Uncertainty in the $\psi(\infty)$ value for Pahute Mesa tuffs from Haskell's data and Mueller and Murphy's model can lead to an uncertainty of 100 percent in the amplitude of 20-second period Rayleigh waves generated by the two models.

Synthetic Rayleigh waves generated by spall phenomena calculated from the Viecelli, Sobel and Rawson models are compared in Figure 3-24. The earth model, the epicentral distance, and the instrument are the same as for the explosion. The spall parameters are listed in Table 3-9. Momentum transfer between the spall waves and the earth was assumed to take place over 0.01 second for all models.

The left-hand (set of) traces in Figure 3-24 show the response due to impact alone. The waveforms for all three spall models are identical, except for a scale factor. They differ from the explosion in that they are relatively enriched in long-period energy with spall amplitudes occurring at a period of about 18 seconds. Rayleigh waves associated with the Viecelli spall model are approximately six percent of the corresponding peak magnitudes generated using the Mueller and Murphy explosion model; the Rayleigh waves associated with Sobel's and Rawson's spall model are 46 and 71 percent, respectively, of the same explosion model. This wide range of values appears to be controlled primarily by the surface area of the spall mass.

The traces in the right-hand column in Figure 3-24 display the surface waves generated by the lift-off plus impact model. Again, the waveforms are identical for the three spall models. However, the signals are relatively deficient in long-period energy compared to impact alone ($\delta(t)$ model) and more

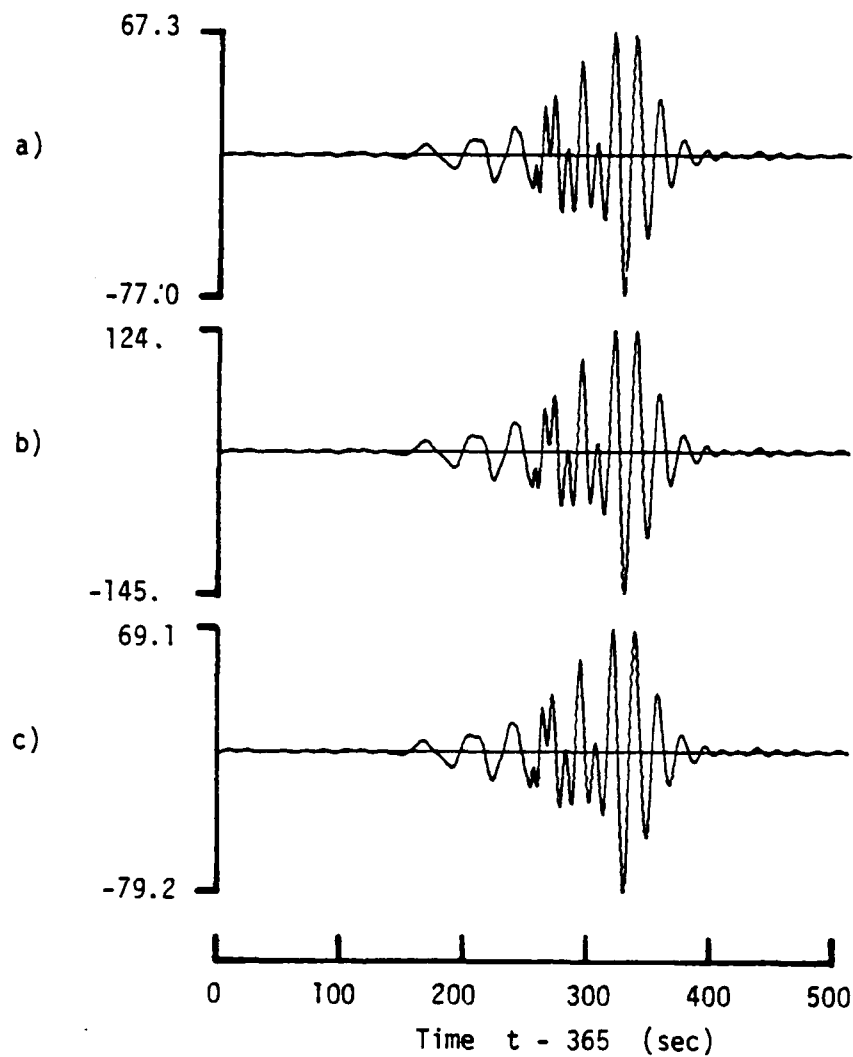


Figure 3-23. Theoretical seismograms calculated from Haskell's model for a) granite and b) tuff; and from Mueller and Murphy's model for c) tuff. Amplitudes represent peak ground displacements in microns as recorded by a long-period CRSM vertical seismometer.

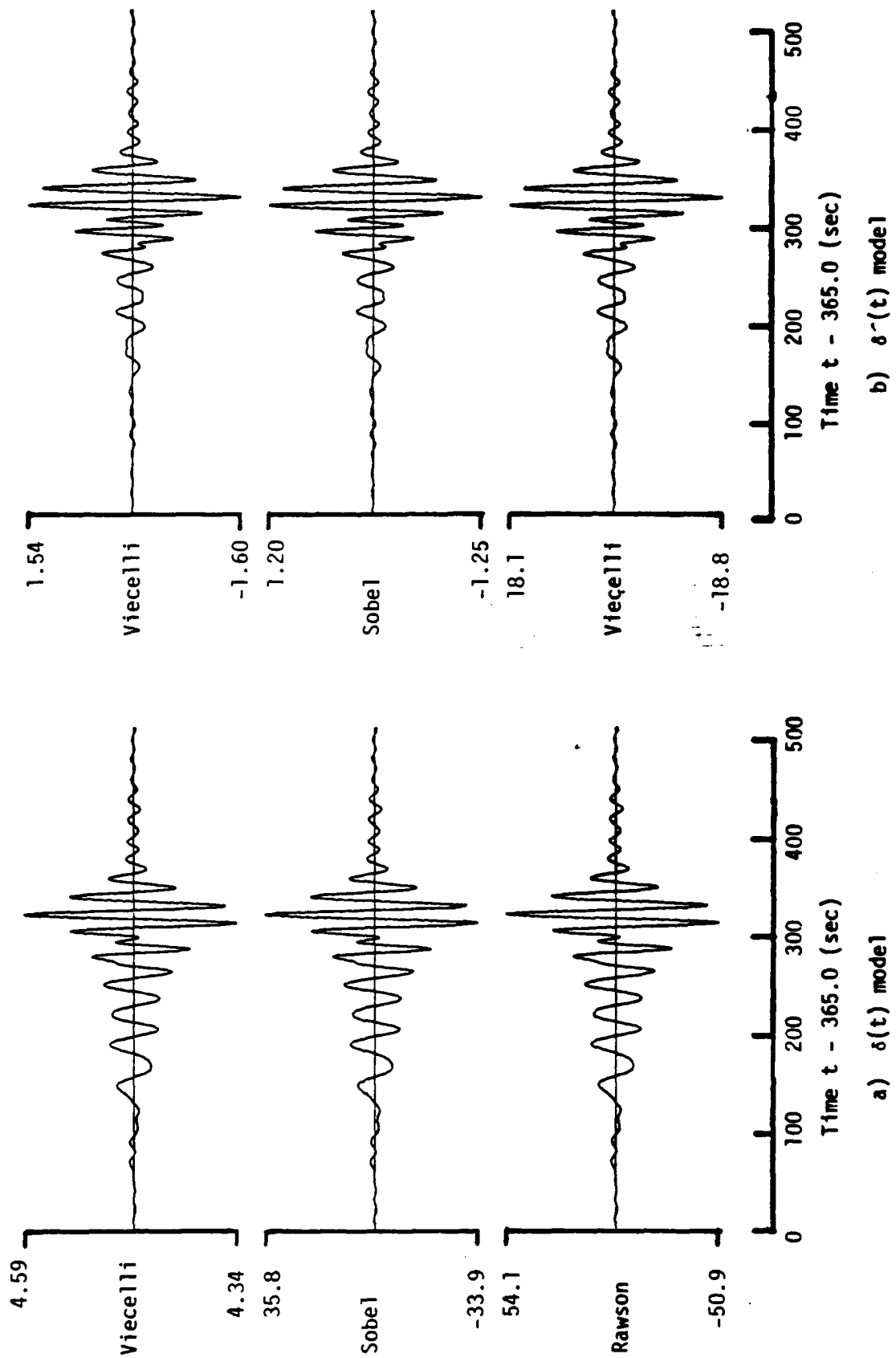


Figure 3-24. Fundamental mode Rayleigh waves generated by explosion induced spall. Amplitudes are shown in microns.

closely resemble the explosion itself. The amplitudes for the lift-off plus slap-down model are only 35 percent of the slap-down model, suggesting that unloading is important when considering Rayleigh waves generated by the spalling process. When compared to the Mueller and Murphy model for BENHAM, the Viecelli, Sobel and Rawson models with lift-off and slap-down give relative amplitudes of 2 percent, 16 percent and 25 percent, respectively. It is important to realize that these numbers and those for slap-down alone tend to maximize the continuation from the spalling process.

CHAPTER 4

PROPAGATION OF NEAR-SOURCE EFFECTS TO TELESEISMIC DISTANCES USING REPRESENTATION THEOREM COUPLING

4.1 INTRODUCTION

A method to propagate seismic energy from sources in regions of complex phenomena out to large distances in more simple regimes is presented and validated in this chapter. Computer codes such as SWIS (Frazier and Petersen, 1974; Sweet, et al., 1976; Sweet, 1976) are available to simulate the complex processes that occur in the immediate vicinity of the source. However, extending the calculations beyond the close proximity of the source using codes such as SWIS and simultaneously retaining any reasonably high frequency content would be too expensive. If it can be assumed that there exists a volume containing the complex source regime outside which the medium is homogeneous or layered and the medium response is linear, then analytical seismic tools may be employed to make the problem tractable. The savings can be considerable depending on the ratio of linear propagation distance to effective nonlinear volume radius.

The source enclosure surface defining the nonlinear source containment volume is denoted S . Waves propagating outward from S are handled using analytical Green's function methods. When a complete outgoing wave-field solution is required for horizontally layered viscoelastic media, the Green's functions are computed using PROSE (refer to Section 5.1). When the surface waves are expected to dominate the solution, the Green's functions may be computed using Harkrider's surface wave technique (1970). The problem is how to utilize these Green's functions to propagate the numerical shock-wave calculations performed within surface S out to the desired teleseismic distances. To couple the output from the numerical codes for use as input to the analytical Green's function procedures, two related methods are available; namely the Representation Theorem method and the Body Force Equivalents method. A detailed discussion of these methods is presented in the next section

and an extensive validation of the Representation Theorem method is presented in the final section of this chapter.

4.2 METHODOLOGY

4.2.1 REPRESENTATION THEOREM APPROACH

In what follows is a mathematical description of the Representation Theorem method used for purposes of seismic coupling. The model geometry is depicted in Figure 4-1. The source is located in the nonlinear containment volume V' with coordinates \vec{x}^* . The source enclosure surface S separates this region of complex phenomena from the linear exterior volume V . The Fourier transform of the i -component of the displacement vector \vec{u} at point $\vec{x} \in V$ can be written in terms of an integral over surface S using the Knopoff-deHoop (1958) representation theorem:

$$u_i(\vec{x};\omega) = \int_S \left[G_{ji}(\vec{y},\vec{x};\omega) \overset{V}{T}_j(\vec{y},\vec{x}^*;\omega) - \overset{V}{H}_{ji}(\vec{y},\vec{x};\omega) u_j(\vec{y},\vec{x}^*;\omega) \right] dS(\vec{y})$$

$$(i,j = 1,2,3) \quad (4-1)$$

in which the summation convention over repeated indices is understood, and the unit normal \vec{n} is defined positive pointing into the volume V' . It is assumed that there are no body forces in volume V and the various terms in Eq. (4-1) are defined as follows:

- $G_{ji}(\vec{y},\vec{x};\omega)$ and $\overset{V}{H}_{ji}(\vec{y},\vec{x};\omega)$ denote the Fourier transforms of the j -component of the Green's function displacement and traction vectors, respectively, at point $\vec{y} \in S$ due to an impulsive point load in the i -direction at point $\vec{x} \in V$; and

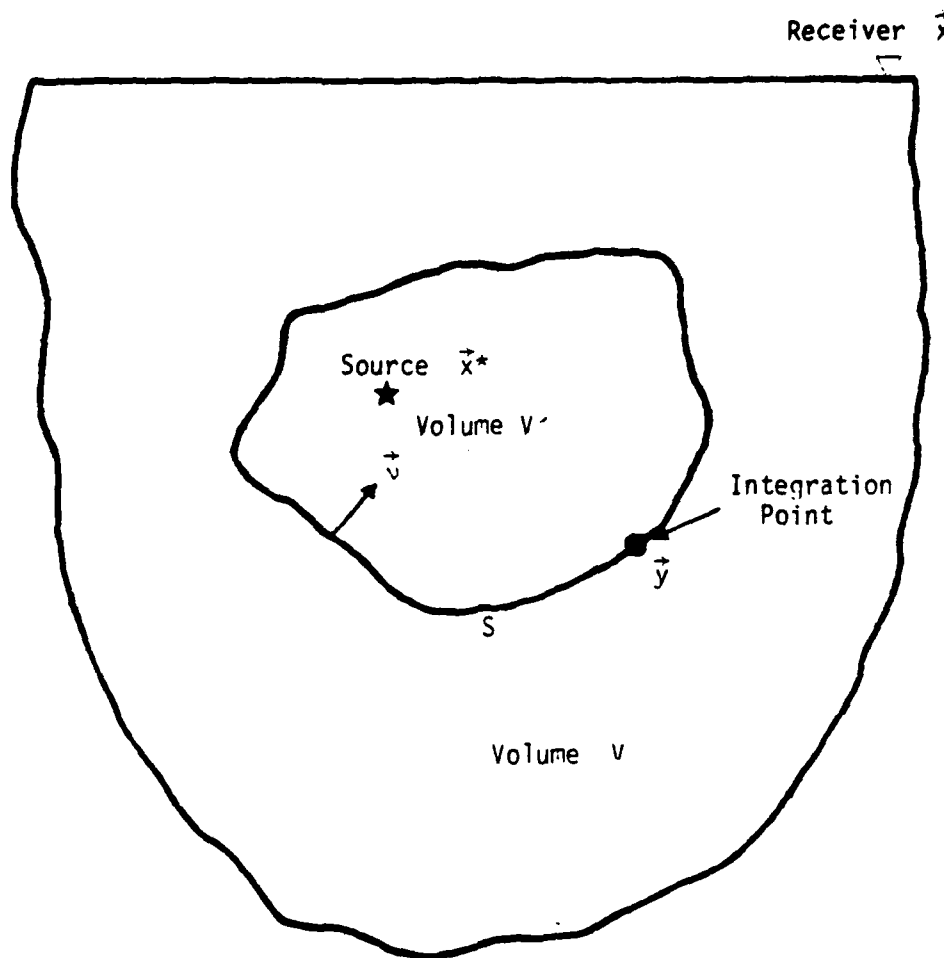


Figure 4-1. Model geometry used to study seismic coupling problems with surface S defining the boundary between volumes V and V'.

- $U_j(\vec{y}, \vec{x}^*; \omega)$ and $\vec{T}_j(\vec{y}, \vec{x}^*; \omega)$ denote the Fourier transforms of the j -component of the displacement and traction "forcing function" vectors, respectively, at point $\vec{y} \in S$ due to the source at $\vec{x}^* \in V'$.

Therewith, the Representation Theorem approach described in Eq. (4-1) provides the capability to obtain the displacements at any point $\vec{x} \in V$ due to an arbitrary source in volume V' . The displacement and traction "forcing function" vectors (U_j and \vec{T}_j) due to the source in volume V' are monitored or numerically calculated at each integration point \vec{y} on S . Then the traction and displacement Green's function vectors (H_{ji} and G_{ji}) are inner-producted with these displacement and traction "forcing function" vectors, respectively, at each integration point on S , so that all the waves radiating from the source in terms of their interactions on S are analytically propagated through the medium in volume V to the receiver of interest. The time domain displacements are then generated through Fourier synthesis by evaluating Eq. (4-1) at a sufficient number of discrete frequency points.

For axisymmetric problems in which the source enclosure surface S is a surface of revolution about a vertical axis (refer to Figure 4-2), the integration over the azimuthal direction in Eq. (4-1) can be handled analytically, leading to a two-dimensional problem in which the representation integrals reduce from surface to line integrals. Defining $L = L(r, z)$ to be a line on surface of revolution, S , it can be shown (see, for instance, Part II of Apsel, 1979) that Eq. (4-1) reduces to

$$u_i(R, Z; \omega) = \int_L \left[G_{ji}^m(r, z, R, Z; \omega) \vec{T}_j(r, z, r^*, z^*; \omega) - H_{ji}^m(r, z, R, Z; \omega) U_j(r, z, r^*, z^*; \omega) \right] \pi \epsilon_m r \, dL(r, z) \quad (4-2)$$

($i, j = 1, 2, 3 = r, \theta, z$)

in which

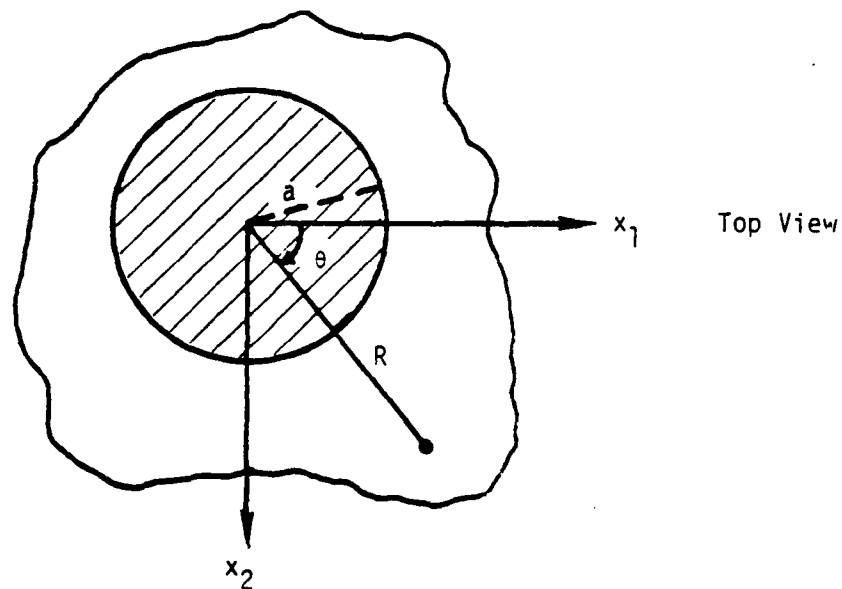
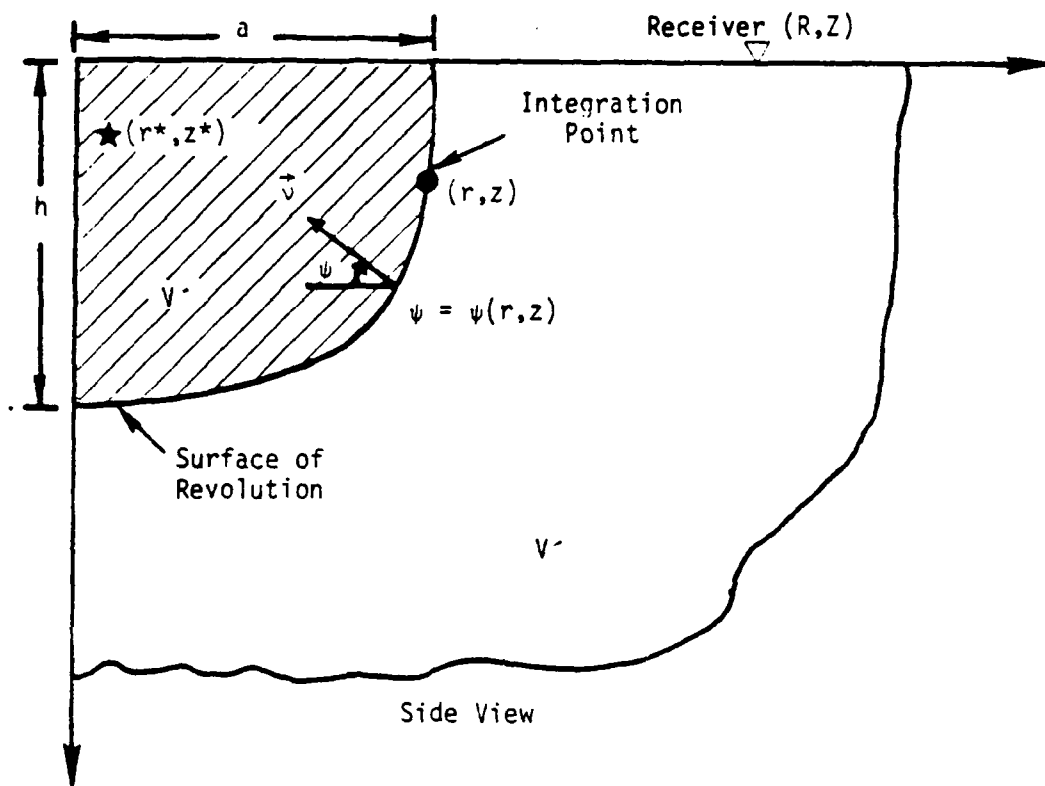


Figure 4-2. Model geometry and coordinate system used to study axially symmetric seismic coupling problems.

- $G_{ji}^m(r,z,R,Z;\omega)$ and $H_{ji}^m(r,z,R,Z;\omega)$ denote the Fourier transforms of the j -component of the Green's function displacement and traction vectors, respectively, at point $(r,z) \in L(r,z) \in S$ due to an impulsive ring load of order m in the i -direction with a ring radius of r at point $(R,Z) \in V$;
- $U_j(r,z,r^*,z^*;\omega)$ and $T_j(r,z,r^*,z^*;\omega)$ denote the Fourier transforms of the j -component of the displacement and traction "forcing function" vectors, respectively, at point $(r,z) \in L(r,z) \in S$ due to a symmetric source of radius r^* at $(r^*,z^*) \in V'$; and

$$e_m = \begin{cases} 2 & \text{for } m = 0 \\ 1 & \text{for } m = 1, 2, \dots \end{cases}$$

Typically, the source is located on the vertical axis (i.e., point source with $r^* = 0$) and the azimuthal ring order m is zero.

Finally, it is useful to express the 3×3 Green's function traction matrix $H_{ji}^m(r,z,R,Z;\omega)$ in terms of the stresses caused by the concentrated ring sources. Referring to Figure 4-2, the unit normal pointing into the volume of revolution V' is given by

$$\vec{v}(r,z) = (v_1, v_2, v_3) = (-\cos\psi(r,z), 0, -\sin\psi(r,z)). \quad (4-3)$$

Utilizing Eq. (4-3) in conjunction with Cauchy's formula (see Fung, 1965, p. 63)

$$H_{ji}^m(r,z,R,Z;\omega) = \sum_{kj}^i (r,z,R,Z;\omega) \cdot v_k(r,z) \quad (4-4)$$

leads to the desired traction-stress relations:

$$\begin{aligned}
 \begin{bmatrix} H_{11}^m \\ H_{21}^m \\ H_{31}^m \end{bmatrix} &= -\cos\psi(r,z) \begin{bmatrix} \sum_{rr}^R & \sum_{rr}^T & \sum_{rr}^V \\ \sum_{r\theta}^R & \sum_{r\theta}^T & \sum_{r\theta}^V \\ \sum_{rz}^R & \sum_{rz}^T & \sum_{rz}^V \end{bmatrix} \\
 &\quad (r,z,R,Z;\omega) \qquad (r,z,R,Z;\omega) \\
 &\quad - \sin\psi(r,z) \begin{bmatrix} \sum_{zr}^R & \sum_{zr}^T & \sum_{zr}^V \\ \sum_{z\theta}^R & \sum_{z\theta}^T & \sum_{z\theta}^V \\ \sum_{zz}^R & \sum_{zz}^T & \sum_{zz}^V \end{bmatrix} \\
 &\qquad (r,z,R,Z;\omega) \qquad (4-5)
 \end{aligned}$$

in which superscripts R,T,V refer to radial, tangential and vertical ring loads of azimuthal order m, respectively.

For illustrative purposes, the indicial notation in Eq. (4-2) is expanded for the special case of the vertical displacement component for an axially symmetric cylindrical source enclosure surface S (arguments omitted for brevity):

$$u_z = \int_L \left[\left(G_{rz}^0 \overset{V}{T}_r + G_{zz}^0 \overset{V}{T}_z \right) - \left(H_{rz}^0 \overset{V}{U}_r + H_{zz}^0 \overset{V}{U}_z \right) \right] 2\pi r dL(r,z) . \quad (4-6)$$

Along the side of the cylinder $\vec{u}(r,z) = (-1, 0, 0)$ so that

$$H_{rz}^0 = \sum_{rr}^V ; \quad H_{zz}^0 = \sum_{rz}^V \quad (\text{Green's function stresses})$$

and $T_r^v = \sigma_{rr} ; \quad T_z^v = \sigma_{rz} \quad (\text{forcing function stresses}) .$

Along the bottom of the cylinder $\vec{u}(r,z) = (0,0,-1)$ so that

$$H_{rz}^0 = \sum_{zr}^V ; \quad H_{zz}^0 = \sum_{zz}^V \quad (\text{Green's function stresses})$$

and $T_r^v = \sigma_{zr} ; \quad T_z^v = \sigma_{zz} \quad (\text{forcing function stresses}) .$

This special case of an axially symmetric cylindrical surface S will serve as the model of the test problems to be discussed in the validation section (4.3).

4.2.2 BODY FORCE EQUIVALENTS APPROACH

The Body Force Equivalents method may be derived directly from the Representation Theorem approach, analogously to the integral equation method formulated by Apsel (Part II, Chapter 2, 1979) to solve embedded foundation-soil interaction problems. Since the derivation is identical for fully 3-D and axisymmetric 3-D geometries, only the 3-D derivation will be presented. Basically, the procedure is to solve a system of symmetric Fredholm integral equations for a set of discrete forces on the interior of or on the surface S that cause the particle motions on S to agree with the original nonlinear prescribed motion (refer to Eq. 4-9).

Then, the total response at the receiver is calculated by inner-producting each body force vector with the appropriate Green's function displacement vector and summing each inner-product (refer to integration required in Eq. 4-11).

Applying the Knopoff-deHoop (1958) representation theorem to Volume V for a point $\vec{x} \in V'$, Eq. (4-1) is written as

$$\int_S G_{ji}(\vec{y}, \vec{x}; \omega) T_j(\vec{y}, \vec{x}^*; \omega) dS(\vec{y}) = \int_S H_{ji}(\vec{y}, \vec{x}; \omega) U_j(\vec{y}, \vec{x}^*; \omega) dS(\vec{y}) . \quad (4-7)$$

With the displacements U_j prescribed on S , the Body Force Equivalents method to solve this integral equation is based on considering a set of forces $\vec{F}(\vec{x}')$ distributed over a surface S' located within volume V' (refer to Figure 4-3) selected in such a way that the unknown tractions at $\vec{y} \in S$ can be represented as

$$\int_{S'} H_{jk}(\vec{y}, \vec{x}'; \omega) F_k(\vec{x}') dS'(\vec{x}') = T_j(\vec{y}, \vec{x}^*; \omega) . \quad (4-8)$$

Substitution from Eq. (4-8) into the left-hand side of Eq. (4-7) and formally interchanging the order of integration leads to the desired system of symmetric Fredholm integral equations of the first kind for the set of forces $\vec{F}(\vec{x}')$ (taking $\vec{x} \in S'$):

$$\int_{S'} \hat{G}_{ij}(\vec{x}, \vec{x}'; \omega) F_j(\vec{x}') dS'(\vec{x}') = \int_S H_{ji}(\vec{y}, \vec{x}^*; \omega) U_j(\vec{y}, \vec{x}^*; \omega) dS(\vec{y})$$

$$x, \vec{x}' \in S' \quad (4-9)$$

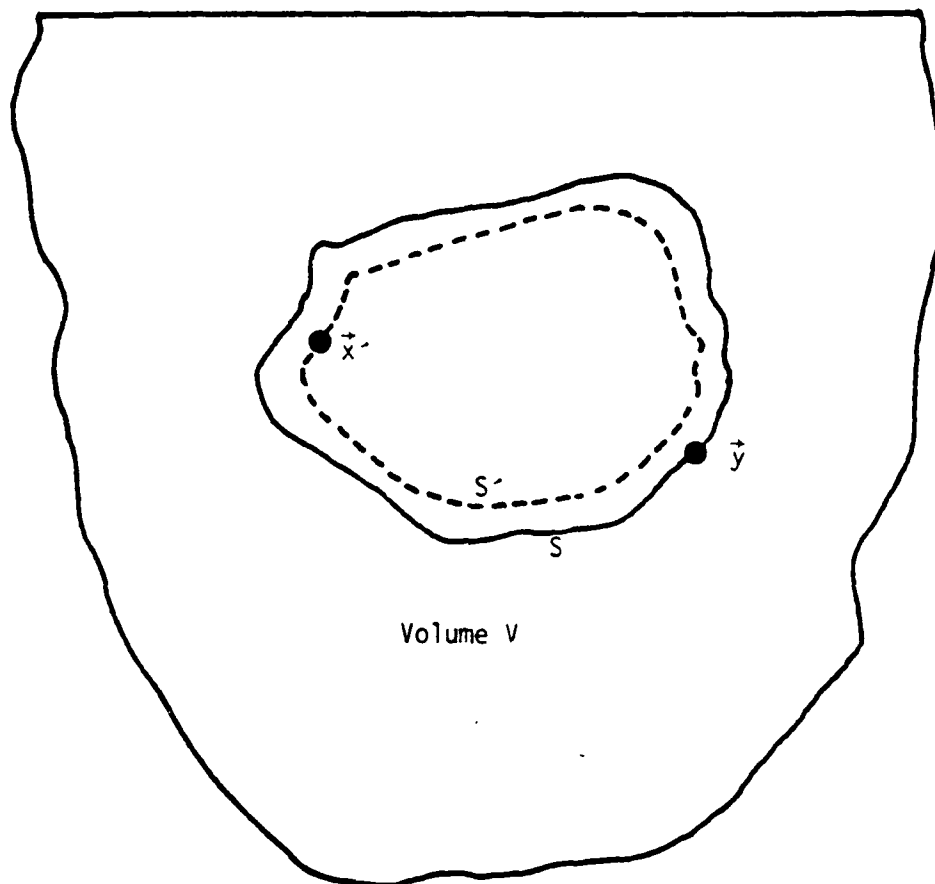


Figure 4-3. Model geometry including internal source surface S' on which the forces \vec{F} are distributed.

in which

$$\hat{G}_{ij}(\vec{x}, \vec{x}') = \hat{G}_{ji}(\vec{x}', \vec{x}) = \int_S G_{ki}(\vec{y}, \vec{x}; \omega) H_{kj}^v(\vec{y}, \vec{x}'; \omega) dS. \quad (4-10)$$

Once Eq. (4-9) is discretized and numerically solved for the set of forces $F(\vec{x}')$, the displacements and tractions are readily obtained at any point $\vec{x} \in V$ or V' by evaluating the following integrals:

$$u_j(\vec{x}; \omega) = \int_{S^-} G_{jk}(\vec{x}, \vec{x}'; \omega) F_k(\vec{x}') dS'(\vec{x}') \quad (4-11)$$

$$T_j(\vec{x}; \omega) = \int_{S^-} H_{jk}^v(\vec{x}, \vec{x}'; \omega) F_k(\vec{x}') dS'(\vec{x}') \quad (4-12)$$

One advantage of using the Body Force Equivalents method over the Representation Theorem method is that the tractions as well as the displacements may be obtained at the receiver points of interest. Also, only the displacement forcing function vectors need to be evaluated at the integration points when solving for the unknown body force amplitudes $\vec{F}(\vec{x}')$ in Eq. (4-9); whereas, the Representation Theorem method additionally requires the traction forcing function vectors (refer to Eq. (4-1)). Otherwise, the two methods can solve the same class of problems. The only advantage of using the Representation Theorem method over the Body Force Equivalents method is that the displacements are directly obtained by evaluating one integral along S in Eq. (4-1); whereas the Body Force Equivalents method first requires the solution of an integral equation before evaluating the displacements in Eq. (4-11). It should be pointed out that if the Body Force Equivalents method is used, it will be

necessary to choose the surface S' , on which the body forces are located, to be everywhere interior to surface S so as to avoid the problem of evaluating single integral equations, since the Green's functions become singular when source and receiver points coincide (see Part II, Chapter 3 of Apsel 1979 for more details).

4.3 VALIDATION

As discussed in the proposal (DELTA-P-79-0026), a rigorous validation of the seismic coupling methodology would be to calculate and compare results for problems in which the analytic solution is known, such as Lamb's problem (see Fung, 1965, Chapter 8). The near-field solutions to Lamb's problem involve significant body wave as well as surface wave contributions, closely coupled in time. The far-field solutions to Lamb's problem are predominantly governed by surface wave contributions. The source enclosure surface S is taken within the near-field regime so that the seismic coupling across S must be highly accurate to cancel out the body wave contributions and leave primarily the fundamental surface wave mode in the far-field.

The axisymmetric problem considered corresponds to the free-surface displacements resulting from an impulsive vertical point force located at a depth of 0.4 km in homogeneous half-space. The model geometry and discretization used to calculate the response with the Representation Theorem method is shown in Figure 4-4. The artificial source enclosure surface S is an axisymmetric circular cylindrical intrusion of radius 2.1 km and embedment depth 2.1 km. The discrete integration points used to evaluate the integrals along line L of surface S in Eq. (4-2) are indicated by dots on surface S in Figure 4-4. The half-space (volumes V and V') is characterized by compressional and shear velocities of 6.2 and 3.5 km/sec, respectively, and a density of 2.7 gm/cc. The results are compared with the analytic response at epicentral distances of 300, 500 and 700 km.

Since the source generates body wave as well as surface wave contributions at each integration point on S , the displacement and traction "forcing function" vectors $\vec{U}(r,z,0.0,0.4;\omega)$ and $\vec{T}(r,z,0.0,0.4;\omega)$, respectively) in Eq. (4-2) are

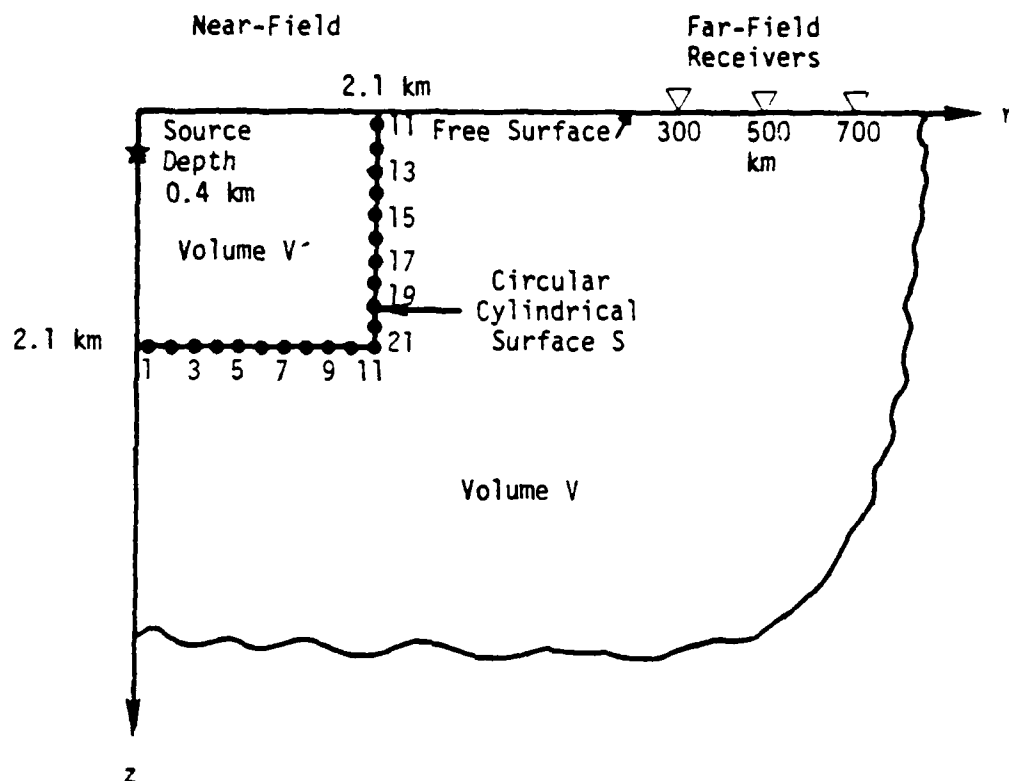


Figure 4-4. Model geometry and discretization used to study Lamb's problem with Representation Theorem method. The artificial source enclosure surface S is an axisymmetric circular cylindrical intrusion of radius 2.1 km embedded 2.1 km into the homogeneous half-space. Volumes V and V' represent the homogeneous half-space with a compressional wave speed of 6.2 km/sec, a shear wave speed of 3.5 km/sec, and a density of 2.7 gm/cc.

calculated using PROSE, which generates the complete response at each frequency. Conversely, the fundamental surface wave mode dominates the propagation from each integration point on S to the receivers of interest. Therefore, the displacement and traction "Green's function" matrices ($\vec{G}^0(r,z,R,Z_0)$ and $\vec{H}^0(r,z,R,Z_0)$, respectively) in Eq. (4-2) are calculated using Harkrider's surface wave code at each frequency. Frequencies between 0 and 2 Hz are included in the calculations and the grid spacing on line L of surface S is taken to be 0.2 km (21 points integration points) as shown in Figure 4-4. The vertical displacement component is shown for all the test calculations in this section and is written out explicitly in Eq. (4-6).

The results in Figures 4-5 and 4-6 represent the running sum of the numerical integration in Eq. (4-6) along the base and side of the cylinder, respectively, for the receiver at 500 km. The time series are displayed only at the odd numbered nodes to simplify the presentation. The top of the cylinder coincides with the free surface so that the integrals are zero there since the free surface cannot sustain any normal stresses. The final result at node 21 is compared to the analytic result obtained using Harkrider's surface wave code FRW (Fundamental Rayleigh Wave). The agreement is superb in both amplitude and phase. The spurious signal around the fundamental Rayleigh wave is associated with band-limiting in the discrete frequency domain, but since both frequency series were processed identically, the results agree wiggle-for-wiggle. This validation lends considerable confidence in the method and the numerical procedure since the individual terms in Eq. (4-6) involved several arrivals that were required to cancel identically leaving these simple wave forms. The comparisons at 500 and 700 km are shown in Figures 4-8 and 4-9, respectively. Once again, the agreement is of near-perfect precision. It is interesting to observe the $1/\sqrt{R}$ decay with distance of the fundamental Rayleigh wave by comparing the results at the three epicentral distances R .

The same test problem has been run for the layered earth structure depicted in Table 5-3 of this report. The nine layers are presumed to be representative of a generic Eastern United States earth model. Once again, the fundamental Rayleigh wave is expected to dominate the signal at the epicentral

Node
Number

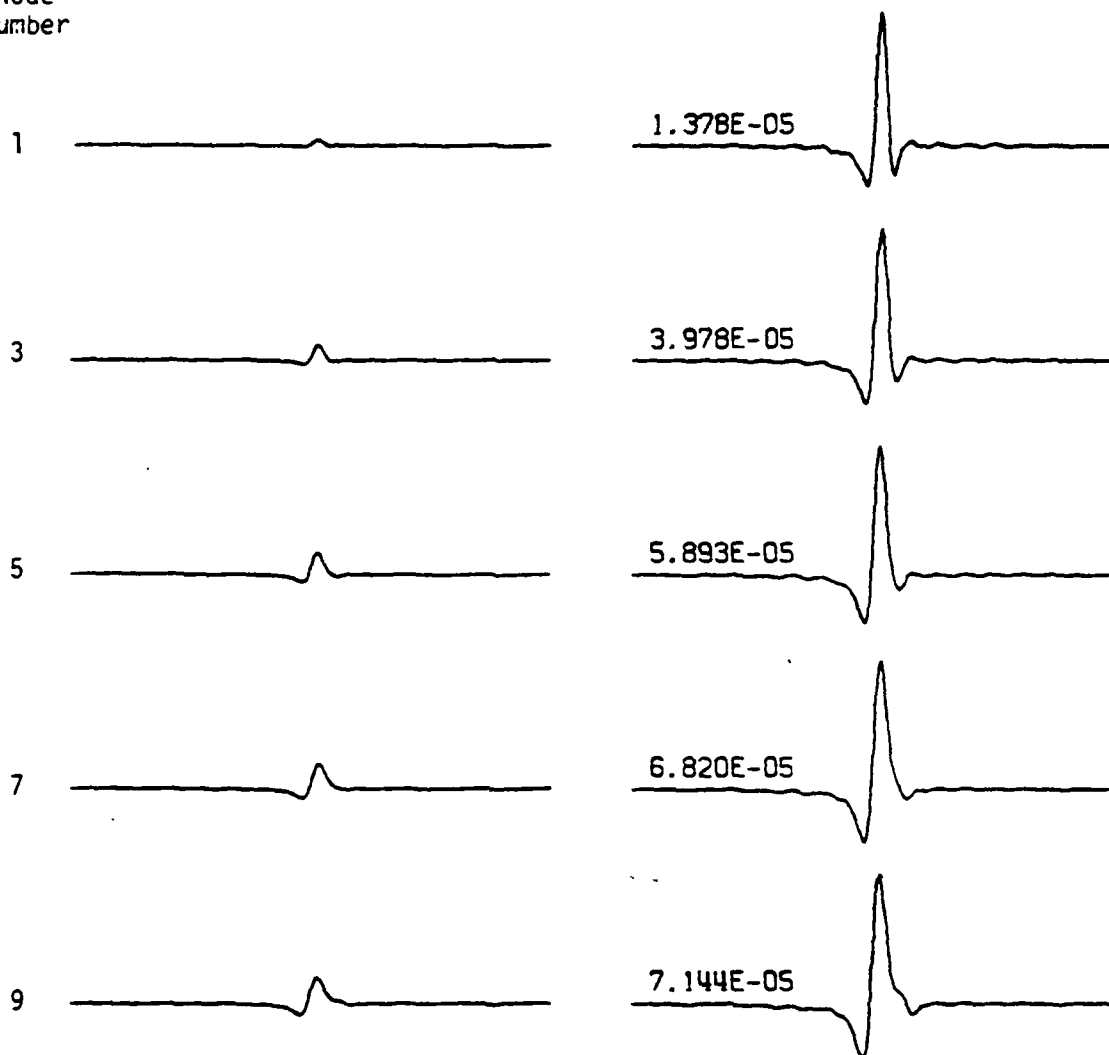


Figure 4-5. Running sum of the integration in Eq. (4-6) along the base of the cylinder depicted in Figure 4-4 for the receiver at 500 km. The time series are shown only at the odd numbered nodes. The results in the two columns are identical except that the time series in the right-hand column are individually scaled while those in the left-hand column are scaled according to the final result (Node 21). The maximum peaks in the running sums (scaling factors in right-hand column) are shown above each time series.

Node
Number

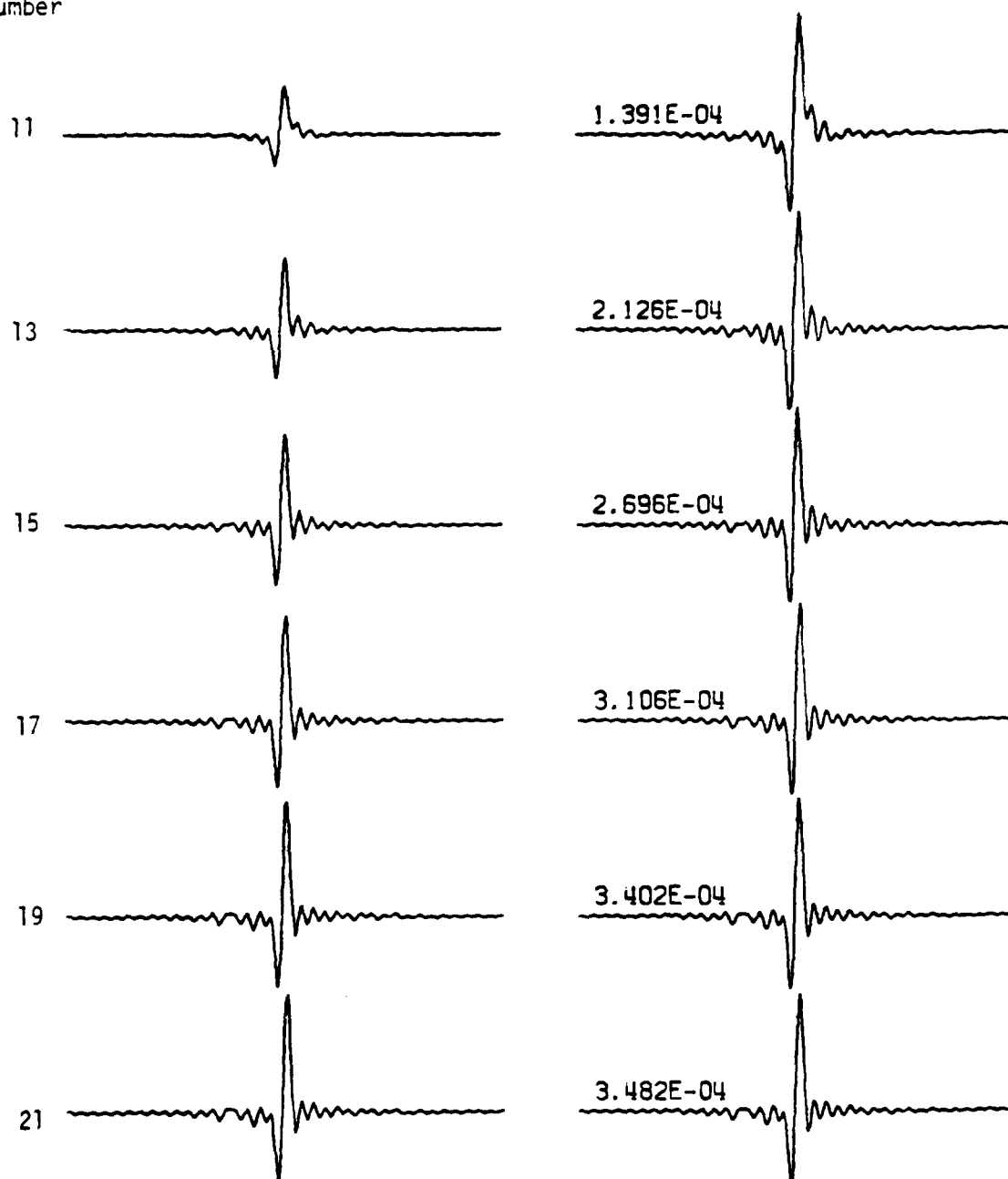


Figure 4-6. Continuation of running sum from Figure 4-5 for the integration along the side of the cylinder depicted in Figure 4-4. The final result at Node 21 for the receiver at 500 km is compared to the analytic result in Figure 4-7.

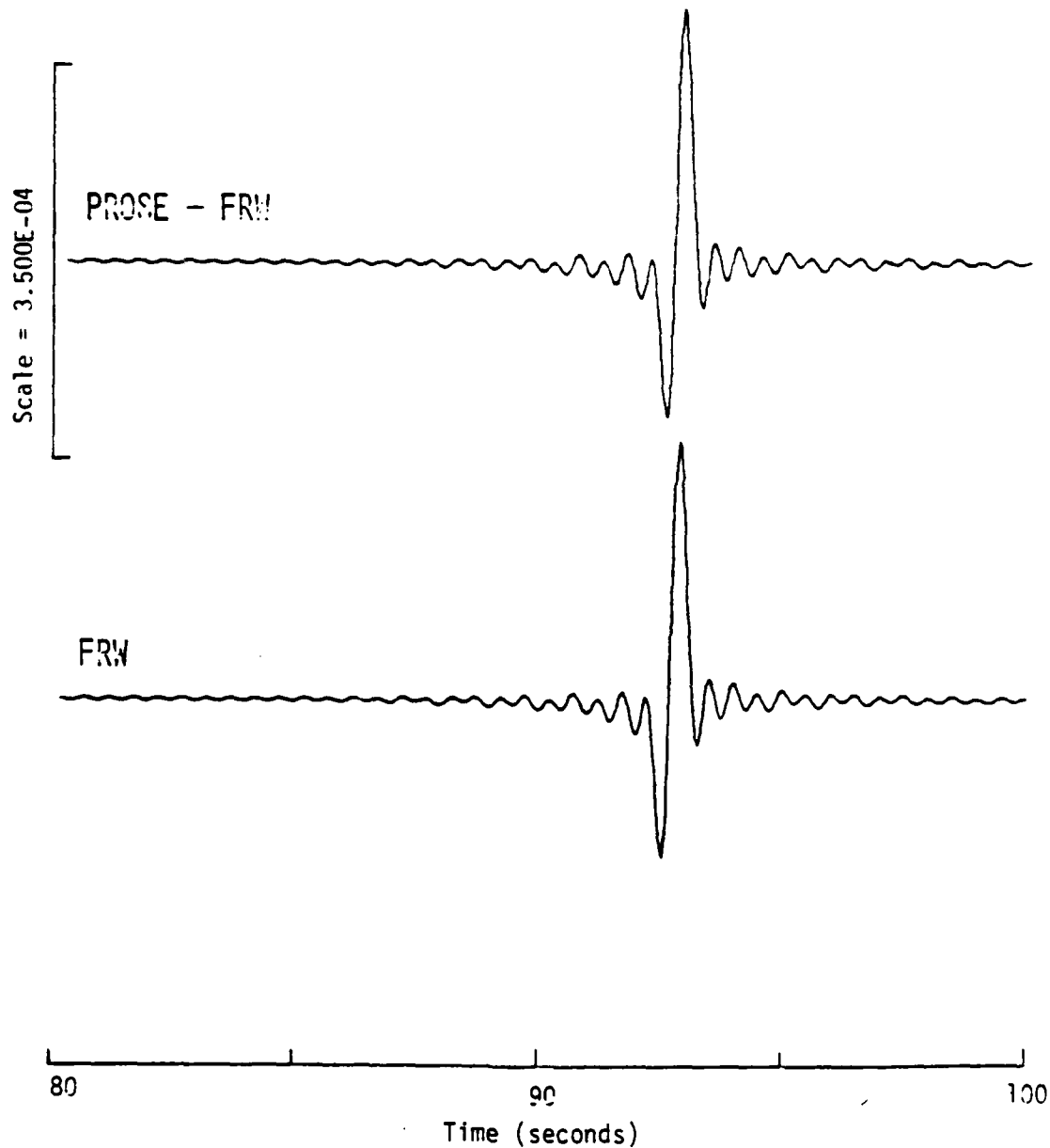


Figure 4-7. Comparison between the Representation Theorem coupling approach (labeled PROSE-FRW) to the analytic solution (labeled FRW) for Lamb's problem depicted in Figure 4-4 with the receiver located at an epicentral distance of 300 km.

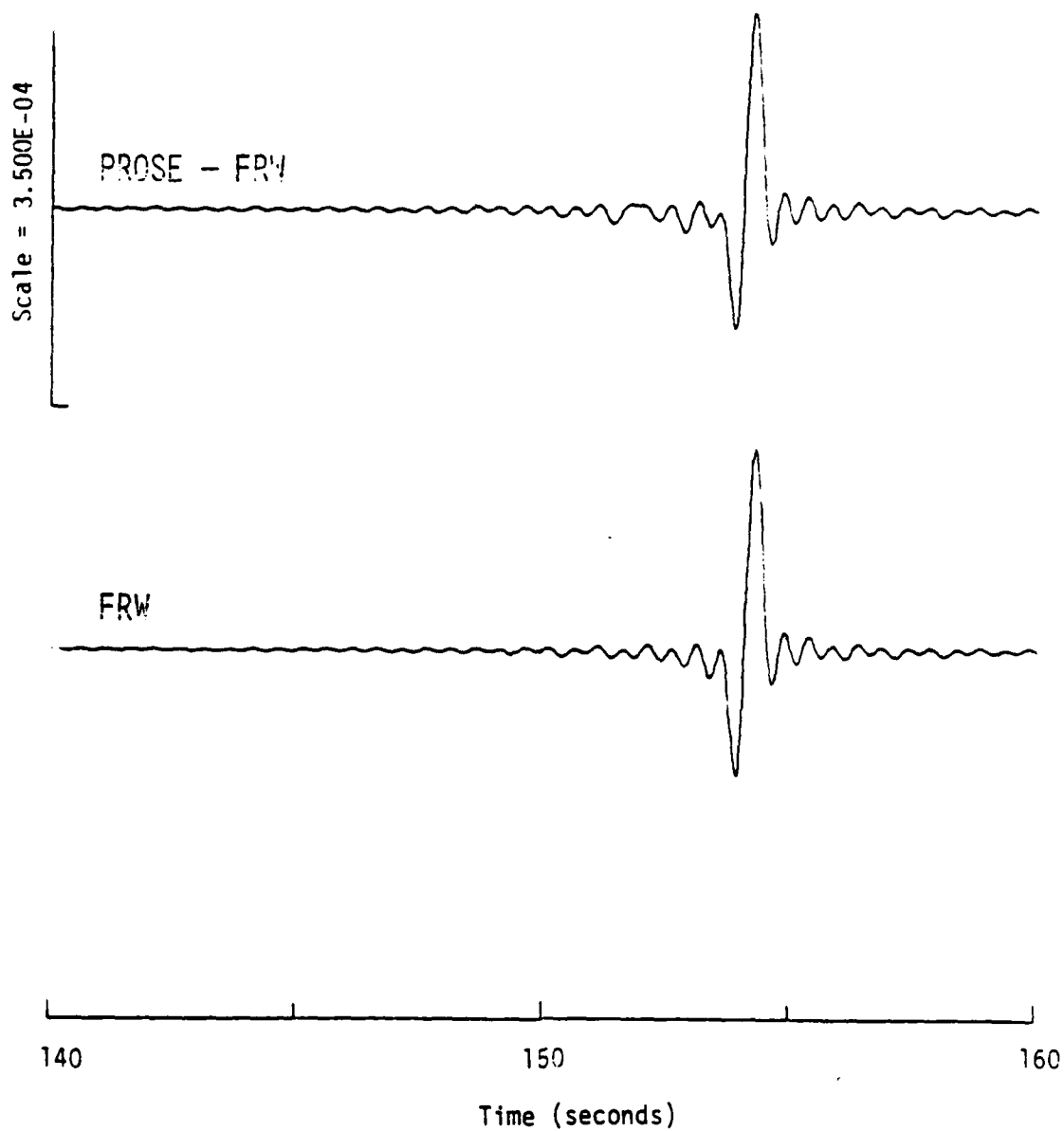


Figure 4-8. Analogous comparison to Figure 4-7 for the receiver located at an epicentral distance of 500 km.

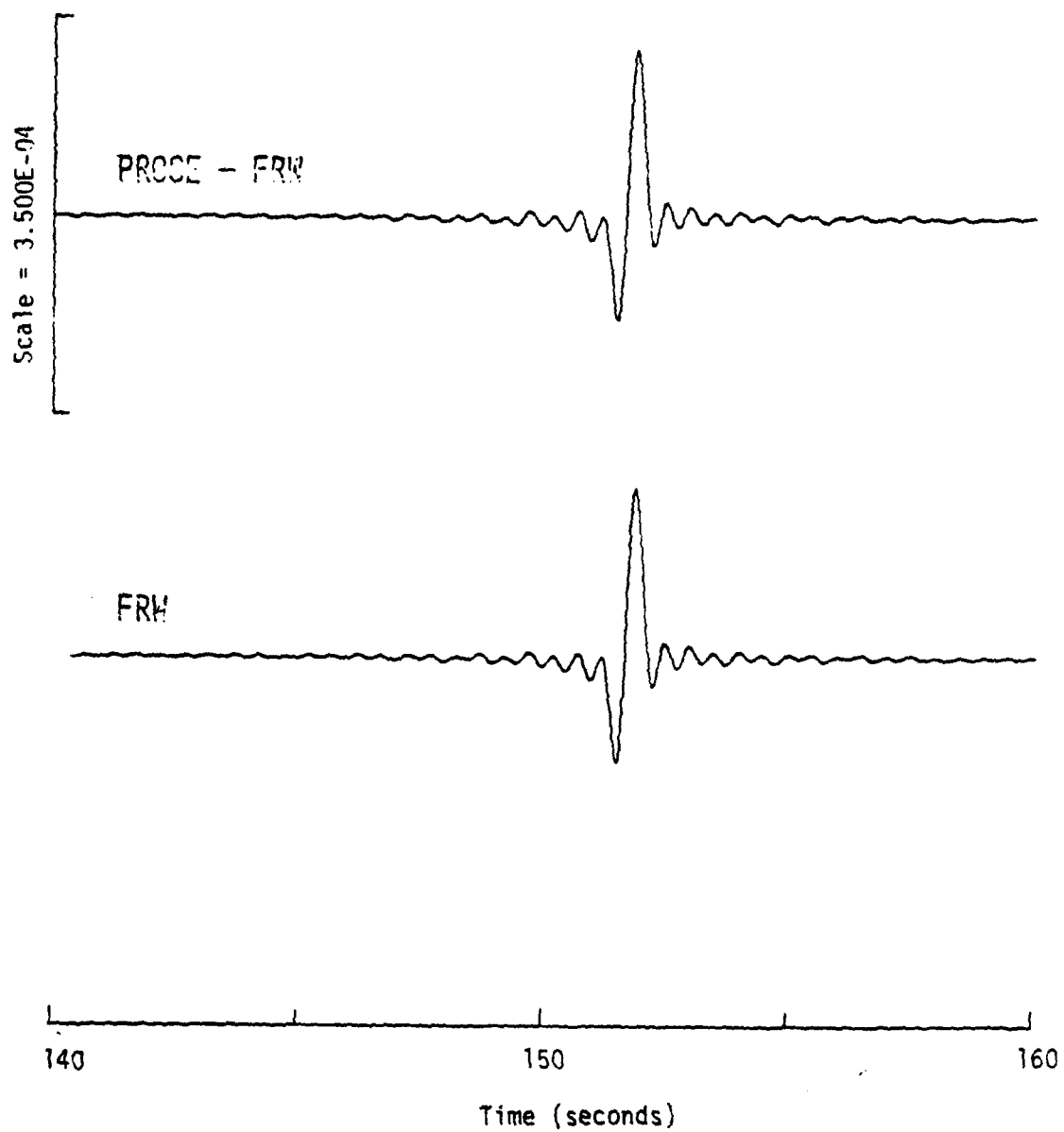


Figure 4-9. Analogous comparison to Figure 4-7 for the receiver located at an epicentral distance of 700 km.

distances of interest, so that PROSE is used only to calculate the "forcing functions" on the surface S of the cylinder in Figure 4-4 resulting from the vertical point force buried at a depth of 0.4 km in the top layer. Since the first layer interface falls within the embedment depth of the cylinder, the impedance mismatch provides an additionally stringent test on the numerical procedure. The comparisons at epicentral distances of 300, 500 and 700 km are shown in Figures 4-10, 4-11 and 4-12, respectively. The agreement is remarkable.

In summary, the methodology and numerical procedure have been validated against known solutions for a homogeneous as well as a layered half-space at several epicentral distances of interest. The seismic coupling technique can therefore be used with considerable confidence to propagate near-field nonlinear simulations out to far-field distances.

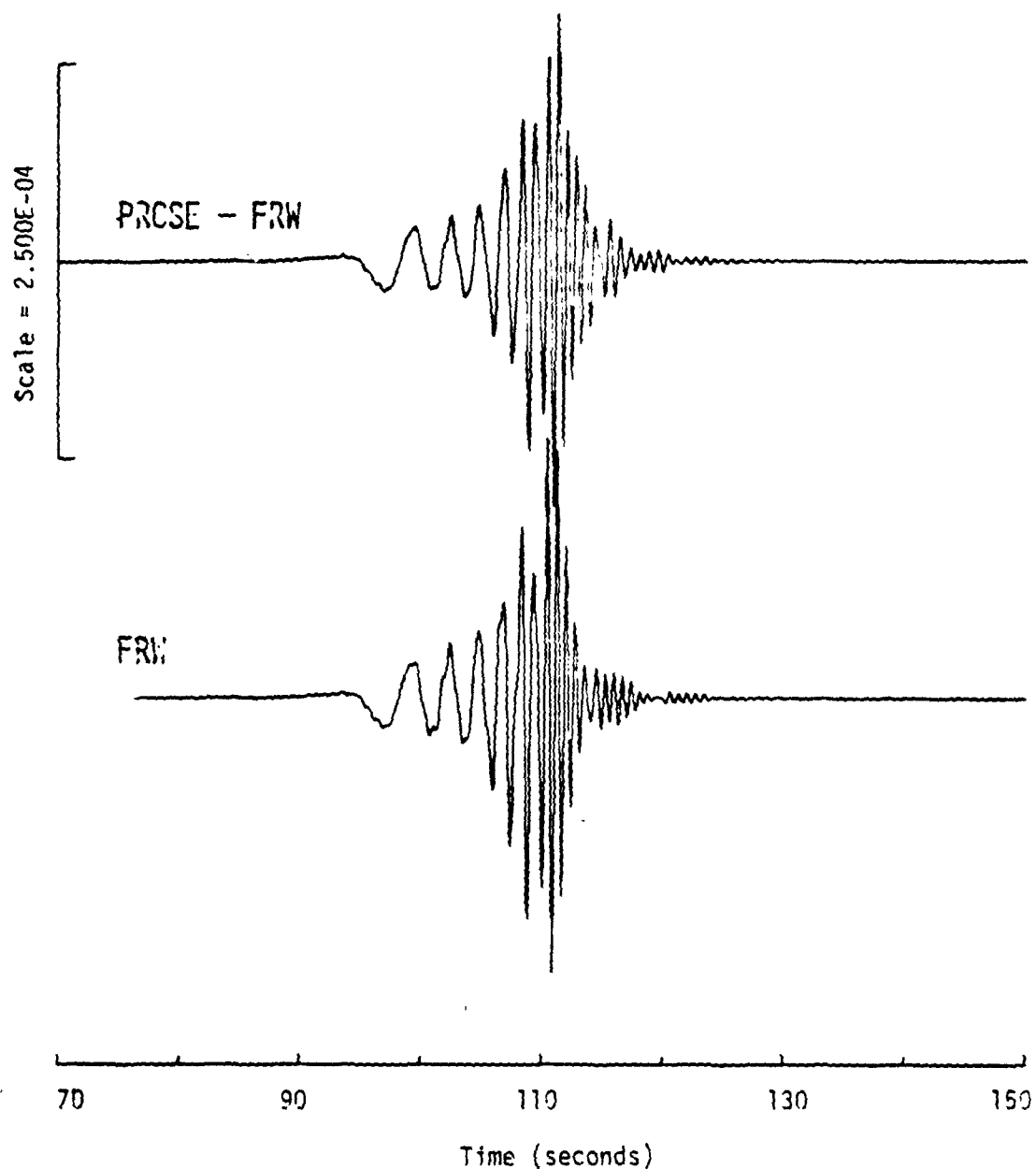


Figure 4-10. Comparison between the Representation Theorem coupling approach (labeled PROSE-FRW) to the analytic solution for the fundamental Rayleigh wave (labeled FRW) for Lamb's problem depicted in Figure 4-4 with the receiver located at an epicentral distance of 300 km. The earth structure has nine layers with the individual material properties characterized in Table 5-3.

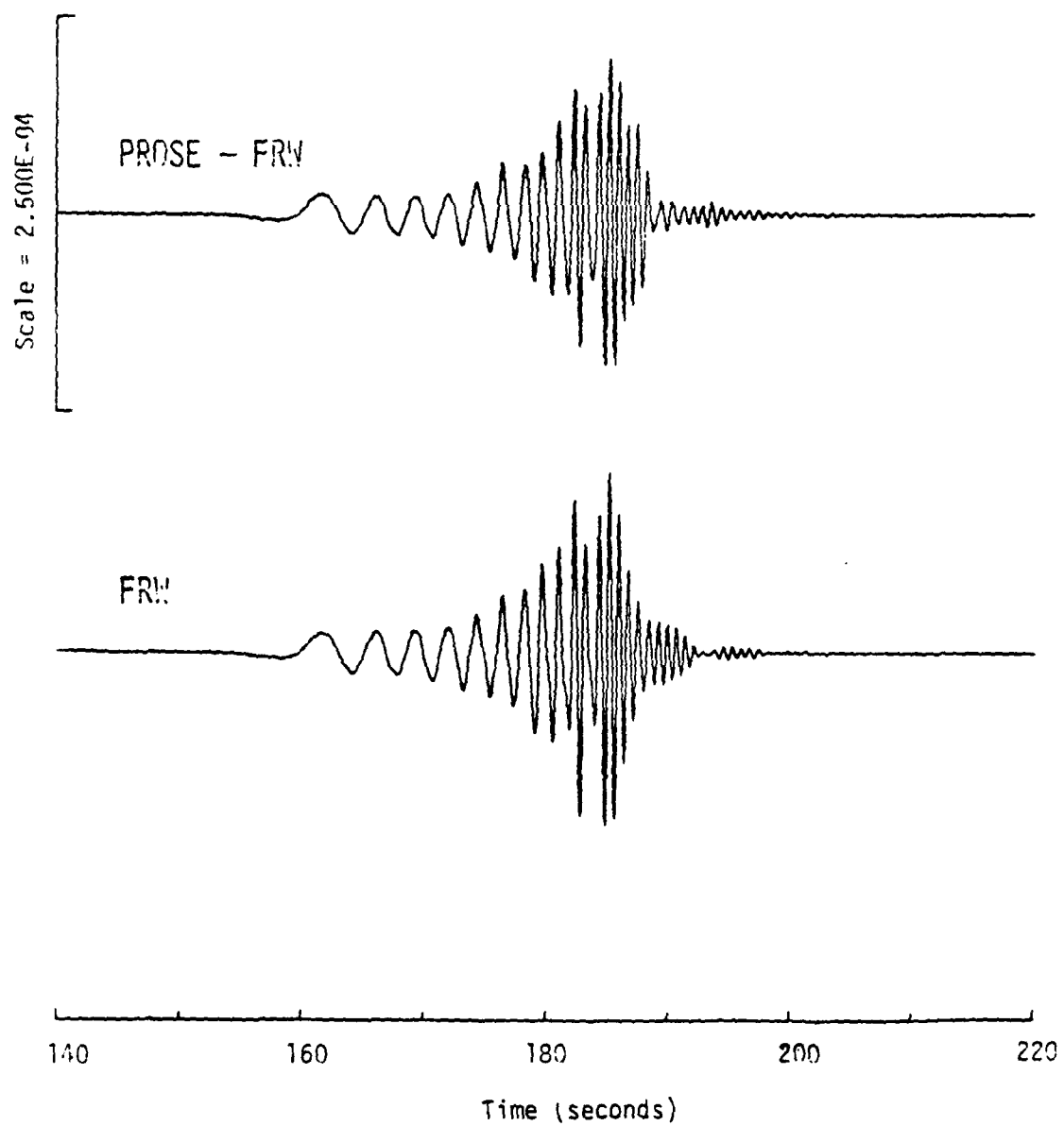


Figure 4-11. Analogous comparison to Figure 4-10 for the receiver located at an epicentral distance of 500 km.

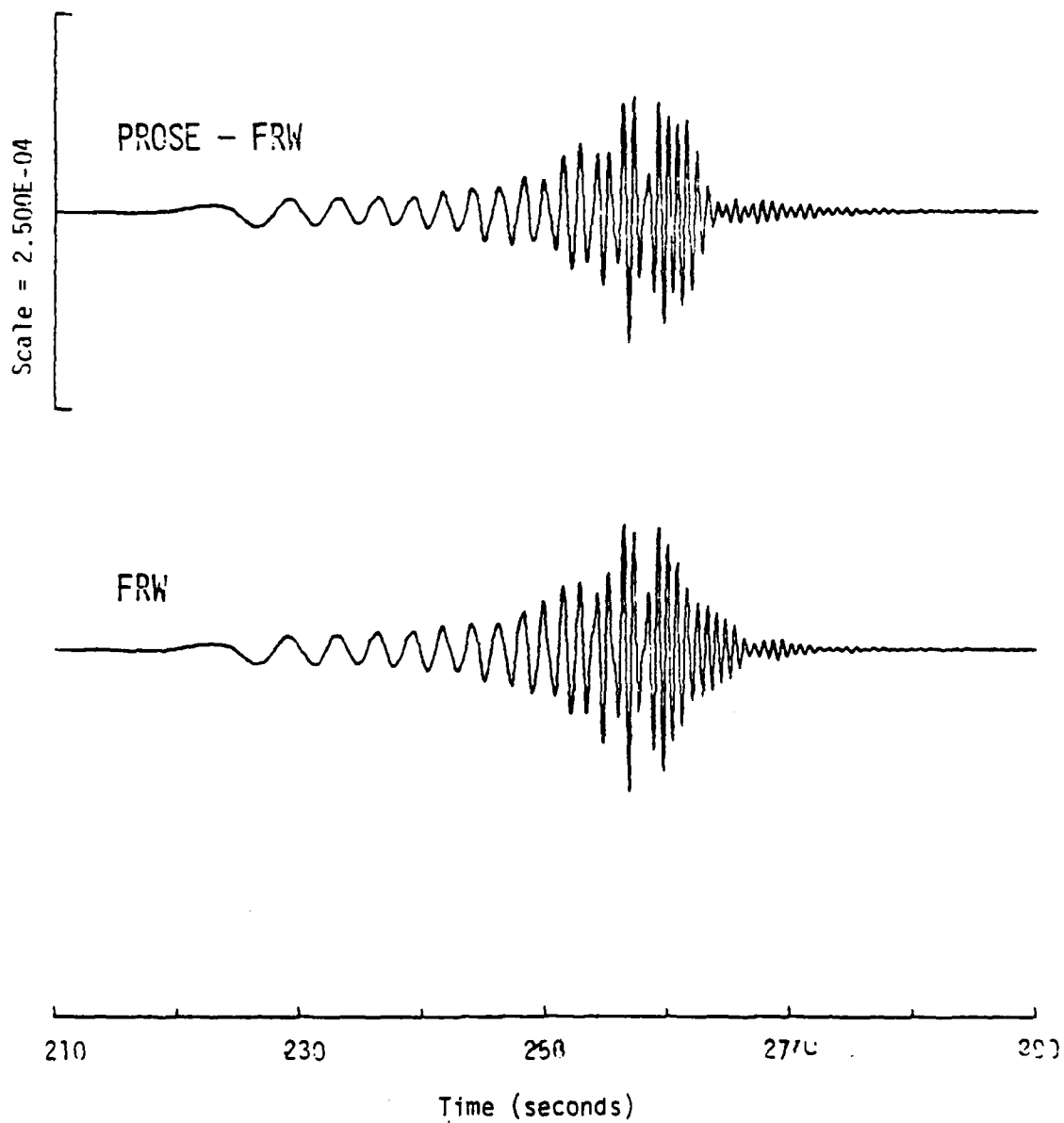


Figure 4-12. Analogous comparison to Figure 4-10 for the receiver located at an epicentral distance of 700 km.

CHAPTER 5

SEISMIC SYNTHESIS

5.1 WAVE PROPAGATION USING PROSE

5.1.1 Methodology

The generic computer program PROSE is used to synthesize the PROpagation of Seismic Energy for buried explosions and elementary earthquake ruptures. Based on an analytical wave propagation method, PROSE generates a discrete mesh of the three-dimensional dynamic Green's functions for a horizontally layered, viscoelastic half-space representation of the earth. Each Green's function corresponds to a particular component of motion observed at a particular distance and azimuth from the source. The source is located at a particular depth in the layered half-space and corresponds to any of the following source types: point explosions; point forces (vertical or horizontal); point dislocations (with arbitrary orientation); or ring forces (vertical, radial or azimuthal). PROSE produces Green's functions at many source/receiver distances for many source depths in one lengthy calculation for a given earth structure.

The Green's functions are calculated in the frequency domain with the azimuthal dependence represented by a Fourier series expansion. The complete response at a particular frequency for any source/receiver geometry is determined by evaluating semi-infinite integrals over wavenumber so as to automatically include all types of waves (both near-field and far-field terms for body waves, head waves, multiple reverberations, leaky modes and surface waves). Time domain results are then generated through use of a discrete Fast Fourier Transform algorithm. The formulation and methodology used to solve the three-dimensional wave propagation problem is discussed in detail by Apsel (1979), and is summarized in Figure 5-1.

The computer program PROSE outputs the displacements and stress components resulting from concentrated point and ring forces. The Green's

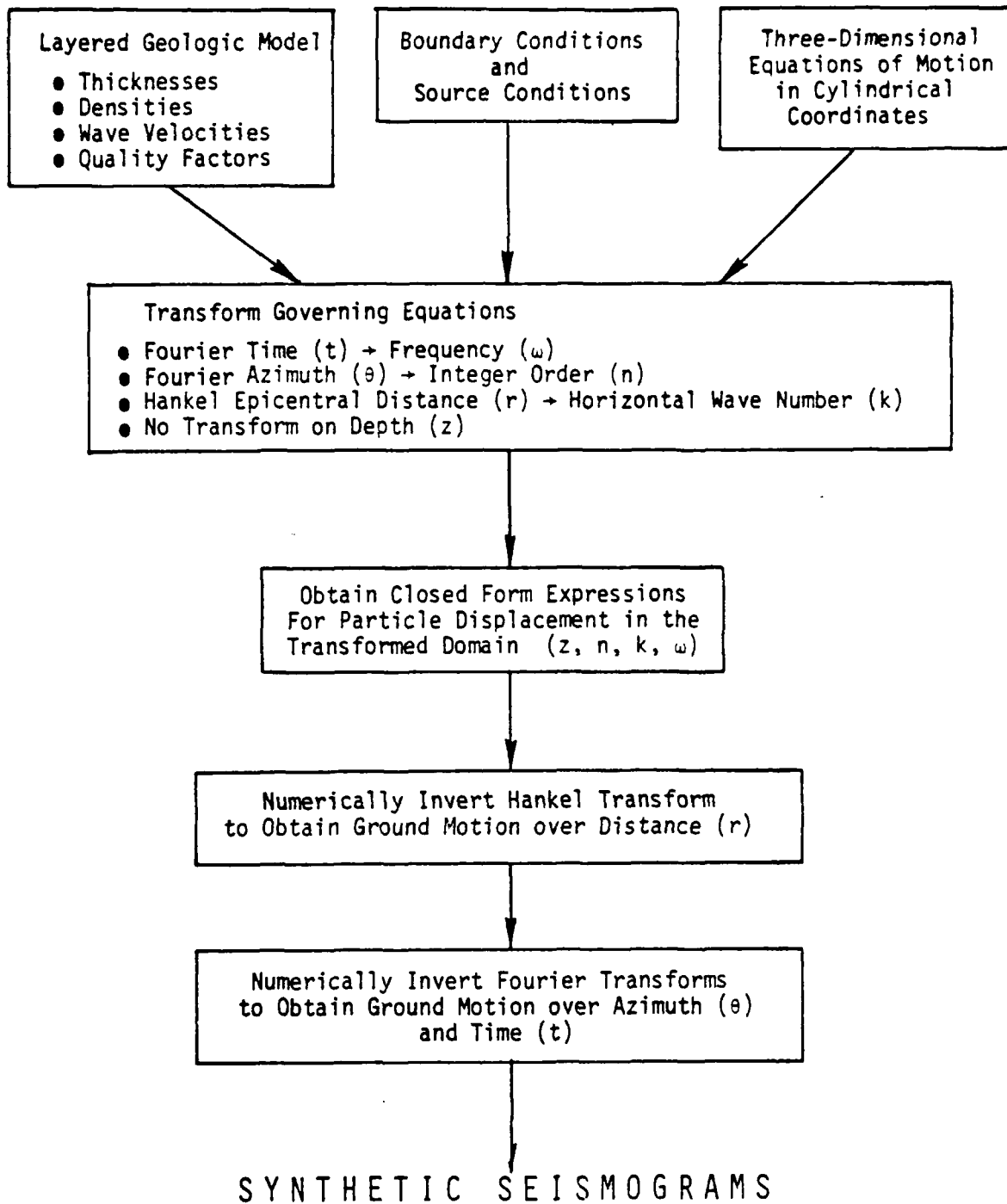


Figure 5-1. Procedure for synthesizing the propagation of seismic energy (PROSE).

function displacements resulting from concentrated point explosions are obtained by directly forming the trace of the stress tensor. In order to obtain the Green's function displacements resulting from concentrated point dislocations, the Knopoff-deHoop (1958) representation theorem is used to reciprocally generate the surface displacements due to a buried dislocation by suitably rotating the stress tensor solution evaluated by PROSE at the depth of the source due to a point force acting at the free surface. The geometry and theory for this reciprocal problem may be found, for instance, in Appendix IV, Part I of Apsel (1979). Utilizing the PROSE output in this manner has the distinct advantage of only having to compute the Green's functions once (at the distances of interest in a given earth structure) for all source/receiver orientations and source types of interest.

5.1.2 Earth Structure

The geologic structure is represented by a stack of viscoelastic horizontal layers overlying a uniform half-space. The material in each layer is characterized by a shear wave velocity, β ; compressional wave velocity, α ; density, ρ ; layer thickness, h ; and specific quality factors, Q_β and Q_α , for both shear and compressional waves, respectively. The layer thickness and wave velocities are extracted from field data such as determined by seismic refraction profiles. The density is estimated from the wave velocities in reference to geologic evidence on rock type.

It is known from seismic and laboratory data that dissipation of energy accompanies transmission of stress waves in solids, even when the waves have small amplitudes. In general, this conversion of elastic energy into heat produces attenuation and dispersion of the stress waves, although the dispersion is typically small for earthquake waves. The specific quality factors are used to include such a phenomenon into the model.

There is considerable evidence from the decay rate of standing wave amplitudes in free vibration laboratory experiments and from the decay rate of waves propagating in the field (including the effects of heterogeneities in the

earth) that the specific quality factors are substantially independent of frequency. The shear wave quality factor Q_β for each layer is empirically related to the shear wave velocity for that layer as shown in Figure 5-2. The attenuation data appearing in the figure are identified in Table 5-1. The empirical attenuation law extracted from the figure is of the form (see DELTA, 1978)

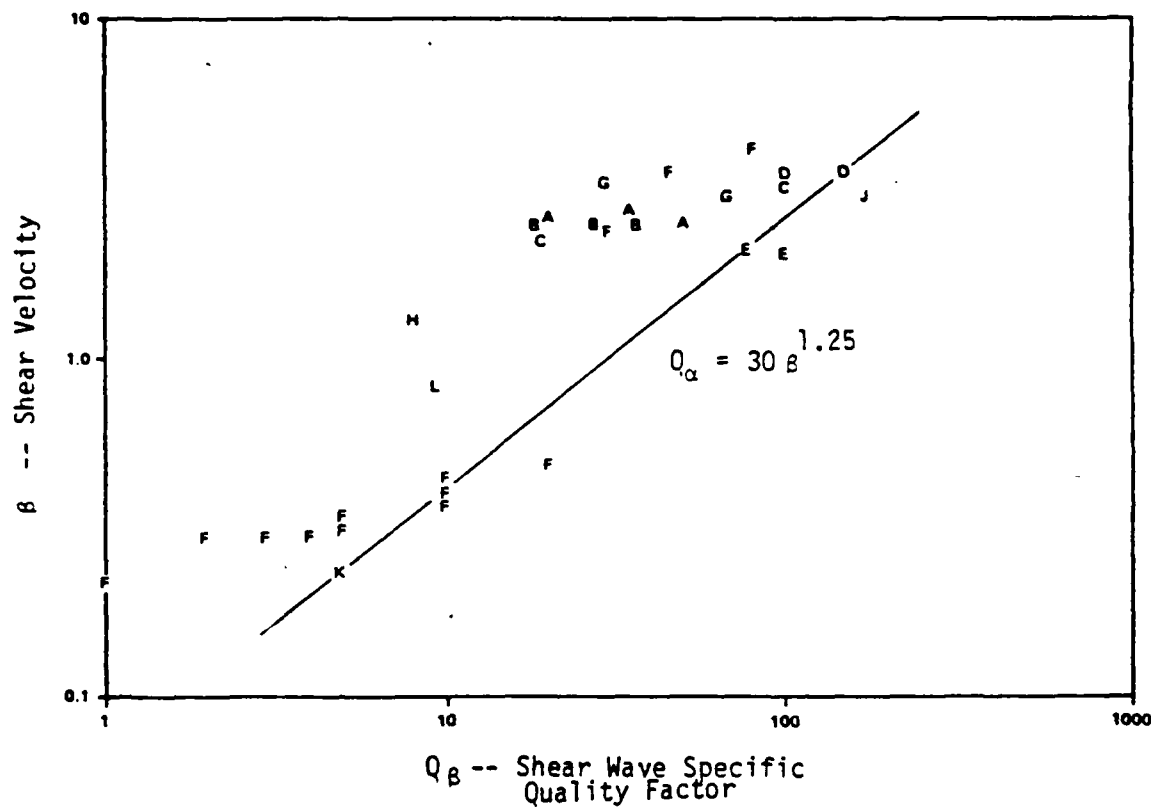
$$Q_\beta = 30\beta^{1.25}$$

where β is expressed in units of km/sec and Q_β is assumed to be independent of frequency. For cases in which conflicting evidence occurs, the quality factors associated with the smallest material attenuation are used (i.e., the largest quality factors). In engineering terminology, a factor of $1/(2Q)$ corresponds approximately to the critical damping ratio in the material so that the larger the specific quality factors, the smaller the amount of material attenuation. If it is assumed that no dissipation occurs in pure compression, then Q_α may be related to Q_β by the expression

$$Q_\alpha = \frac{3}{4} (\alpha/\beta)^2 Q_\beta .$$

5.1.3 Validation

Extensive tests have been performed to document the validity of the results produced by PROSE. One of the most pertinent validation exercises is illustrated in Figures 5-3 through 5-6 where the PROSE results (designated by Wavenumber Integration) are compared to two vastly different solution techniques. The earth structure consists of two layers overlying a uniform half-space with the individual parameters characterizing the layers defined in Table 5-2. The specific quality factors apply only to the PROSE solution since both the finite element solution and the discrete wavenumber/finite element solution



The source of the data is provided in Table 5-1. Some of the data assume that the quality factor for shear-waves (Q_{β}) is half that for compressional waves (Q_{α}).

Figure 5-2. Experimental data for material attenuation factor Q_{β} .

TABLE 5-1
Source of Attenuation Data Presented
in Figure 5-2

Symbol	Description	Reference
A	Earthquake Data, South of Hollister, California	O'Neill and Healy (1973)
B	Earthquake Data at Rangley, Colorado	O'Neill and Healy (1973)
C	Earthquake Data on the San Andreas Fault, Central California	Kurita (1975)
D	Earthquake Data on the San Andreas Fault, Gabilan Range	Bakum et al. (1976)
E	Earthquake Data, Bear Valley, California	Bakum and Bufe (1975)
F	Estimates for Bay Mud and Berkeley Crust	Silva (1976)
G	High-Frequency Laboratory Data in Granite	Silayeva and Shamina (1960) Shamina (1960) White (1965)
H	Field Data in Shale	McDonald (1958)
I	20-sec Rayleigh Waves	Gutenberg (1958)
J	Laboratory Data in Granite	Birch (1938)
K	Soil	Rosset (1970)
L	Laboratory Data in Shale	McDonald et al. (1958)

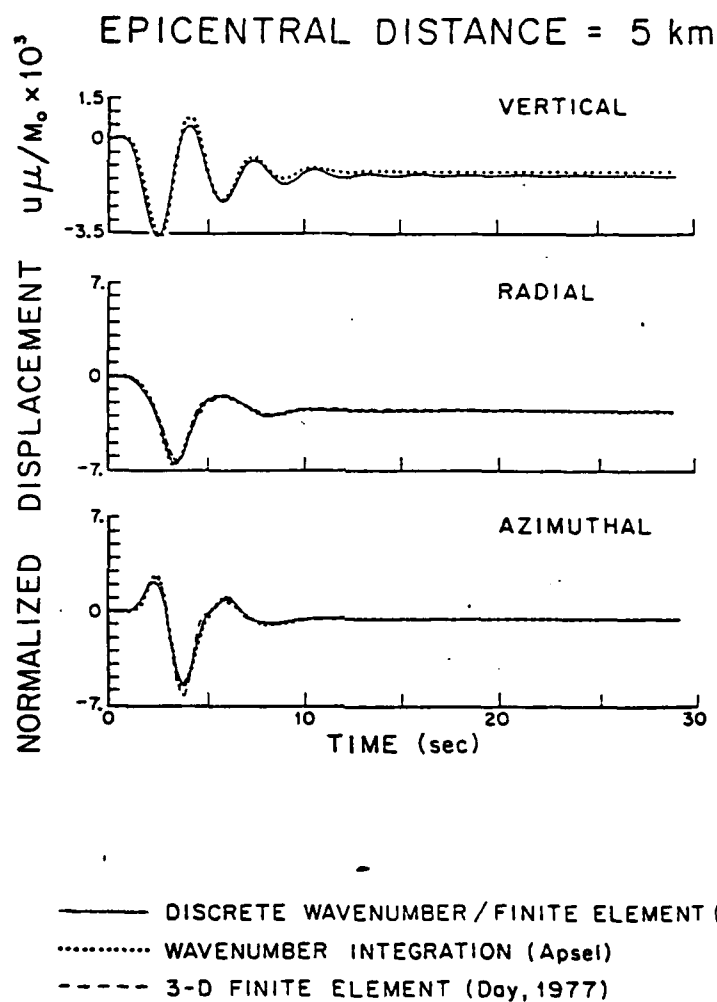
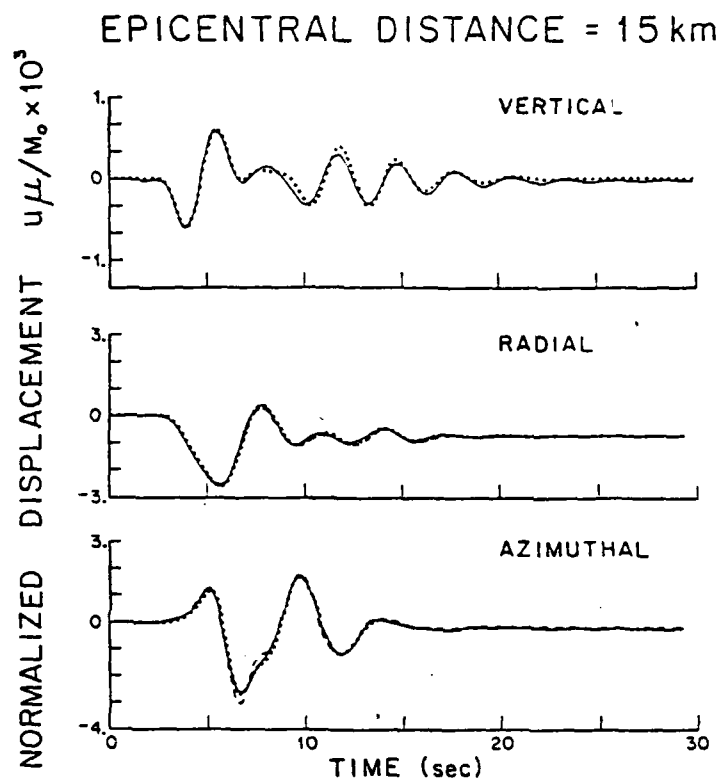


Figure 5-3 PROSE (Wavenumber Integration) Validation by comparison with other solution methods. Also compare with greater epicentral distances (Figure 5-4 to 5-6)



— DISCRETE WAVENUMBER/FINITE ELEMENT (Olson)
 WAVENUMBER INTEGRATION (Apsel)
 ---- 3-D FINITE ELEMENT (Day, 1977)

Figure 5-4

PROSE Validation (Cont.)

EPICENTRAL DISTANCE = 25 km

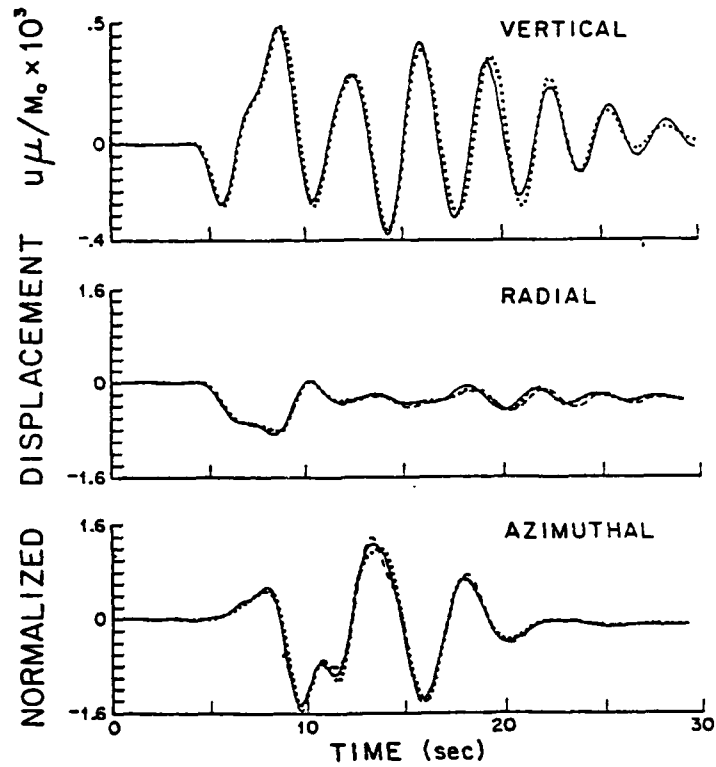


Figure 5-5

PROSE Validation (Cont.)

EPICENTRAL DISTANCE = 35 km

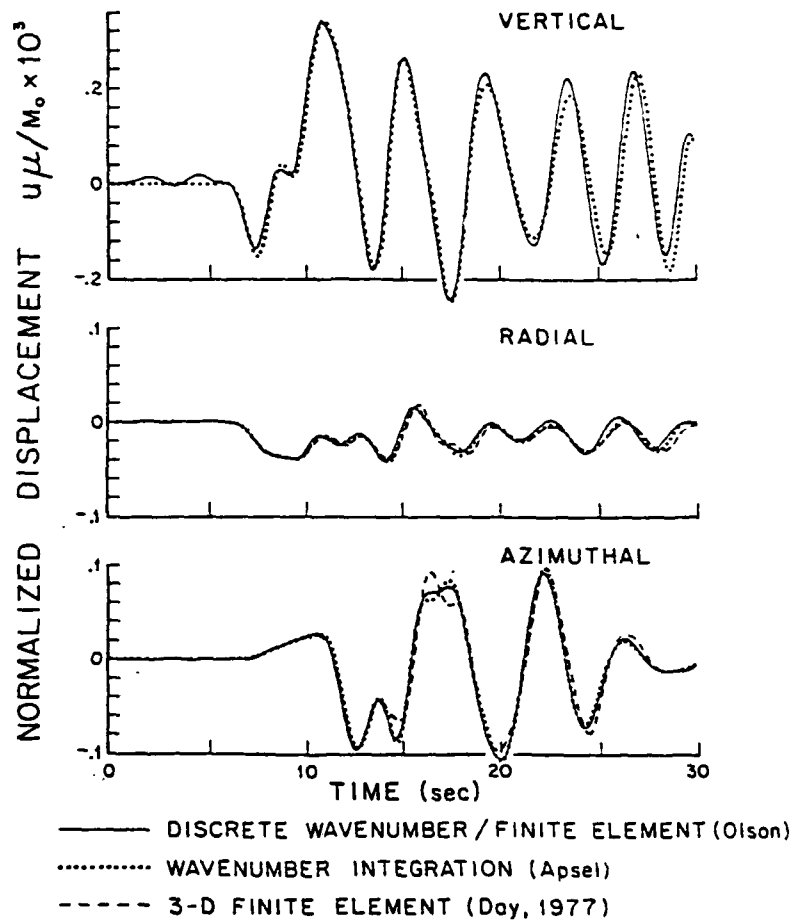


Figure 5-6

PROSE Validation (Cont.)

TABLE 5-2

Viscoelastic Parameters Defining the Geologic
Structure Considered in the Comparisons Shown
in Figures 5-3 through 5-6

Layer	h Layer Thickness km	β S-Wave Velocity km/sec	α P-Wave Velocity km/sec	ρ Density gm/cc	Q_β S-Wave Quality Factor	Q_α P-Wave Quality Factor
1	2.0	1.73	3.0	1.67	198	395
2	2.0	2.887	5.0	2.89	376	748
3	∞	3.46	6.0	3.46	472	939

contain no material attenuation. However, good agreement is expected since the attenuation is virtually inconsequential for the frequency range considered by the alternate solution techniques. The figures are courtesy of Apsel (1979).

The Green's functions are compared at epicentral distances of 5, 15, 25 and 35 km in Figures 5-3 through 5-6, respectively, along an azimuth of 22.5 degrees (in a dilatational quadrant) from the strike of a vertical strike-slip dislocation at a source depth of 5 km. The source time-dependence is represented by a ramp of one second duration and the ground displacements are multiplied by the ratio of the shear modulus in the source layer times 10^3 cm^2 divided by the source moment. The agreement is superb and the slight deviations in phase coherence have periods much lower than the expected resolution of two seconds in the alternate solution techniques.

5.2 REGIONAL SYNTHETIC SEISMOGRAMS

5.2.1 Organization of Results

Regional ground motion due to point explosions and point dislocations has been calculated with the PROSE technique. The earth structure is represented by a stack of eight parallel viscoelastic layers overlying a semi-infinite viscoelastic half-space with the individual layer parameters defined in Table 5-3. The particular velocities, densities, quality factors and layer thicknesses are chosen to provide a reasonable generic model for the Eastern United States geologic environment. Since epicentral distances out to 2000 km are to be considered in this study, the depth of geologic layering is chosen to extend to a depth of 260 km so as to allow the synthesized waves to penetrate as deeply as teleseismic waves in the real Earth at the frequencies of interest. Although an earth-flattening approximation could have been incorporated into the reflection/transmission coefficients for each layer, the effect would only have been second order at the epicentral distances of interest. The source time dependence is represented by the Heaviside unit function and all Green's function displacements have been calculated with frequency content of 0 through 2.0 Hz.

The regional synthetic seismograms are displayed in Figures 5-7 through 5-36. The thirty figures correspond to ten Green's function displacement components for three source depths (i.e., one set of three figures per component). The three source depths are 0.4, 2.0 and 10.0 km. Among the ten components, four source types are represented: 1) vertical strike-slip point dislocation in Figures 5-7 through 5-15 with the first set of three figures (three depths) showing the vertical displacement component and the next two sets of three figures showing the radial and azimuthal displacement components, respectively; 2) point explosion in Figures 5-16 through 5-21 with the two sets showing the vertical and radial displacement components, respectively; 3) vertical dip-slip point dislocation in Figures 5-22 through 5-27 with the two sets showing the vertical and radial displacement components, respectively; and 4) 45 degree dip-slip point dislocation in Figures 5-28 through 5-36 with the three sets showing the vertical, radial and azimuthal displacement components, respectively. From

TABLE 5-3

Viscoelastic Parameters Used by PROSE for the
Eastern United States Earth Structure

Depth to Top of Layer (km)	Layer Thickness (km)	α P-Wave Velocity (km/sec)	β S-Wave Velocity (km/sec)	ρ Density (g/cc)	Q_α Compressional Quality Factor	Q_β Shear Quality Factor
0	1	5.20	3.00	2.60	225	100
1	2	5.70	3.30	2.65	895	400
3	9	6.10	3.58	2.70	1500	689
12	16	6.51	3.76	2.80	1500	667
28	12	6.60	3.80	2.90	1500	663
40	75	8.10	4.62	3.30	1500	679
115	100	8.20	4.54	3.44	1500	613
215	45	8.30	4.51	3.45	1500	591
260	∞	8.44	4.87	3.44	1500	666

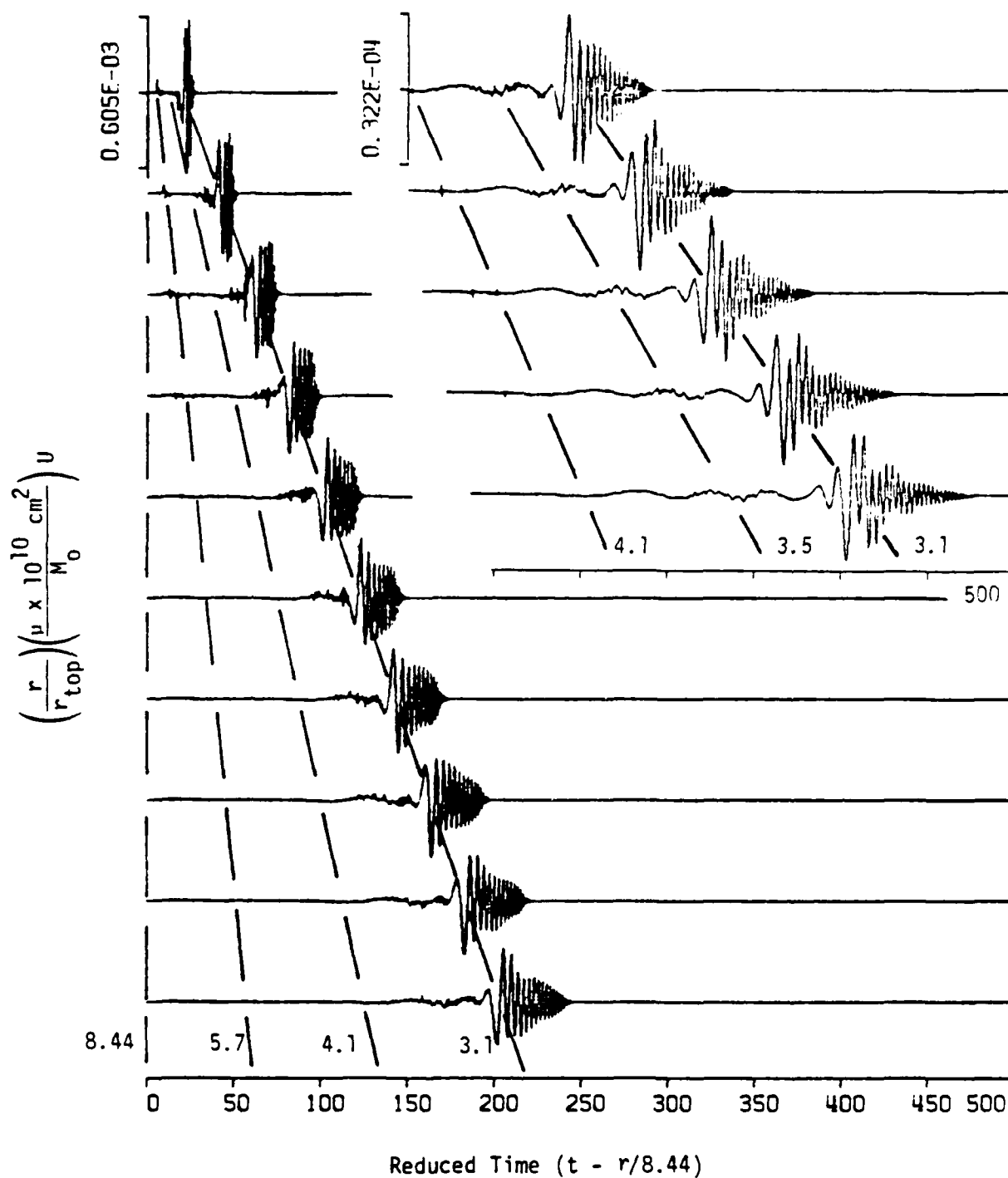


Figure 5-7. Vertical displacement component due to vertical strike-slip dislocation buried at a depth of 0.4 km.

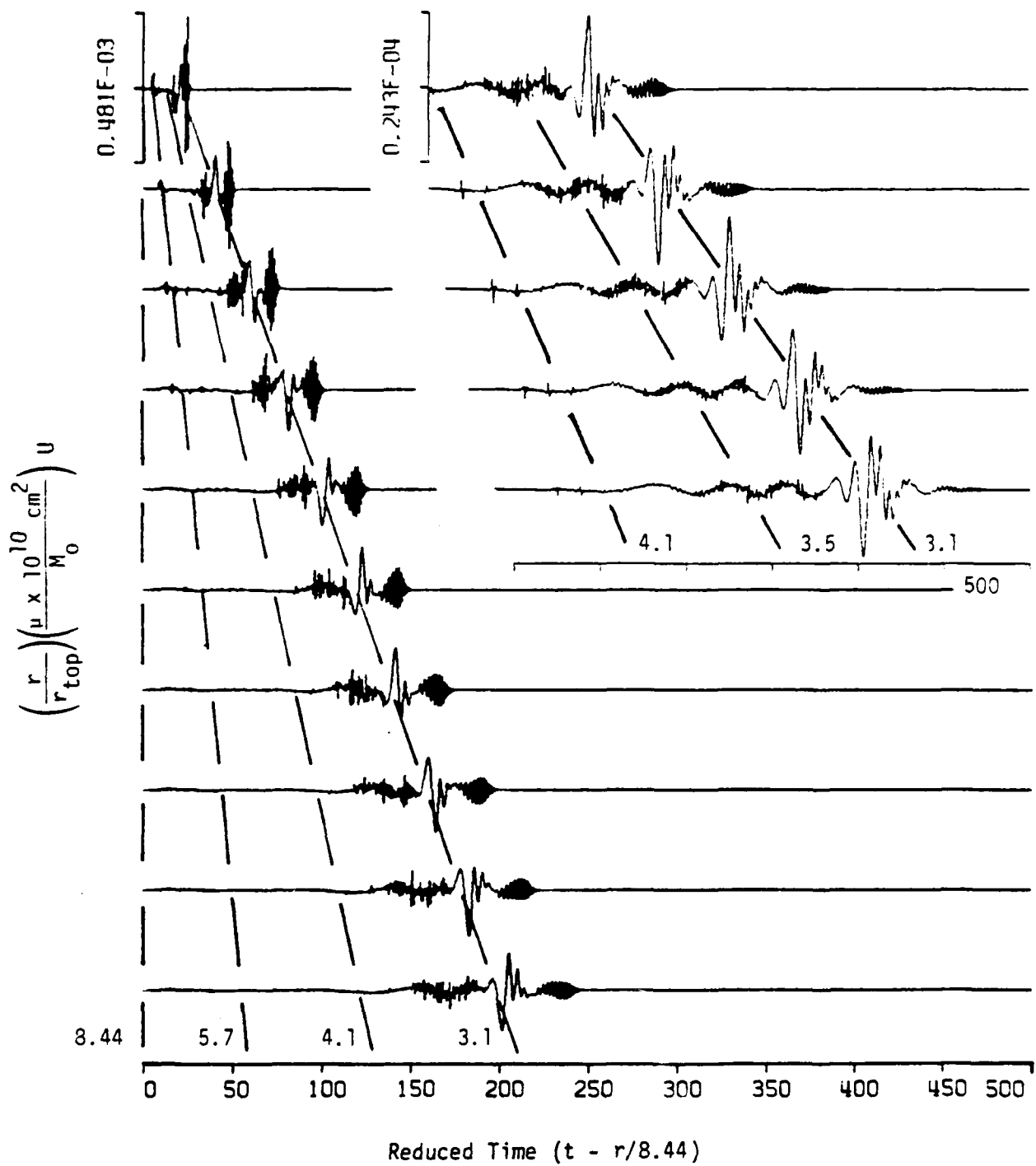


Figure 5-8. Vertical displacement component due to vertical strike-slip dislocation buried at a depth of 2.0 km.

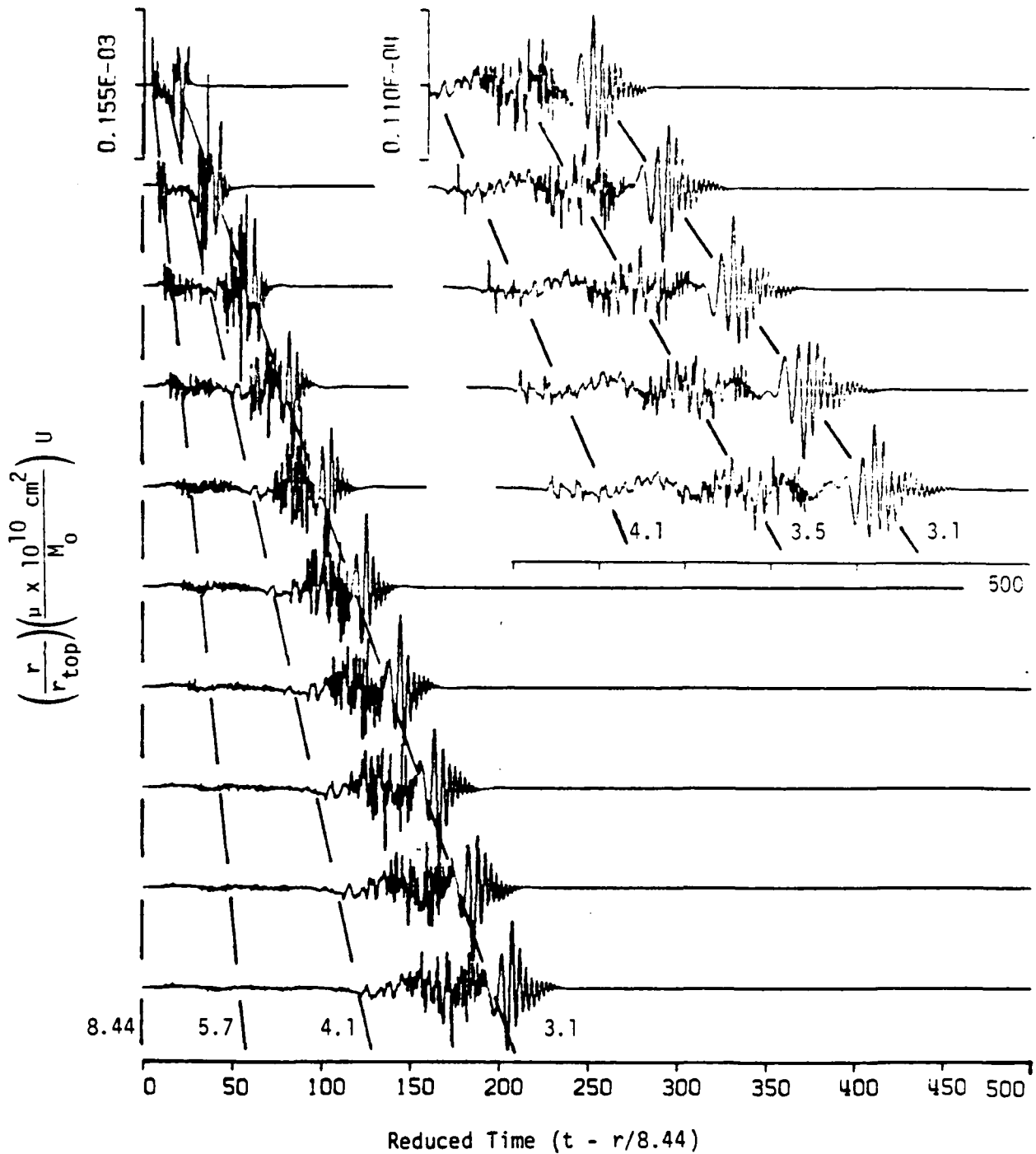


Figure 5-9. Vertical displacement component due to vertical strike-slip dislocation buried at a depth of 10.0 km.

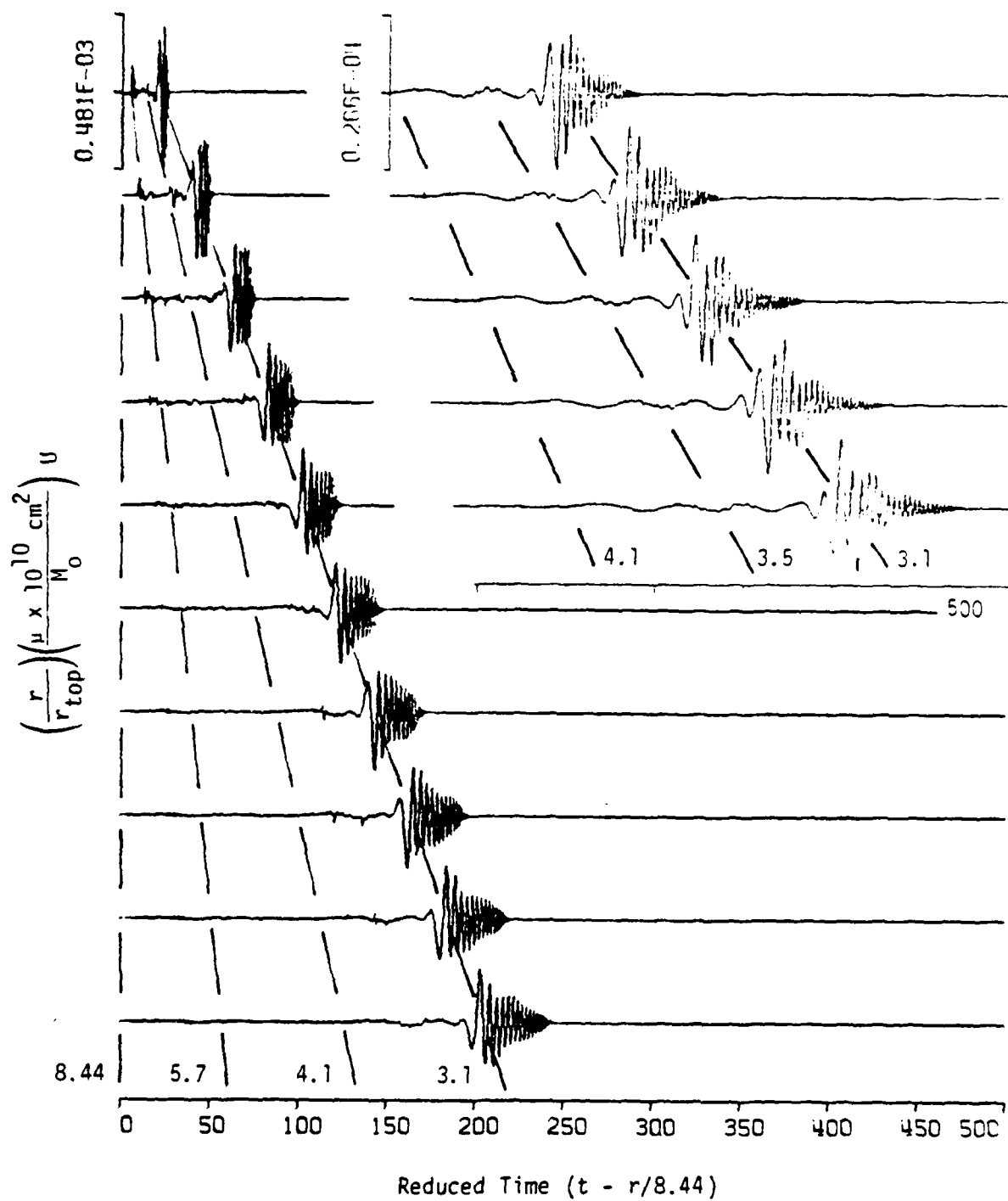


Figure 5-10. Radial displacement component due to vertical strike-slip dislocation buried at a depth of 0.4 km.

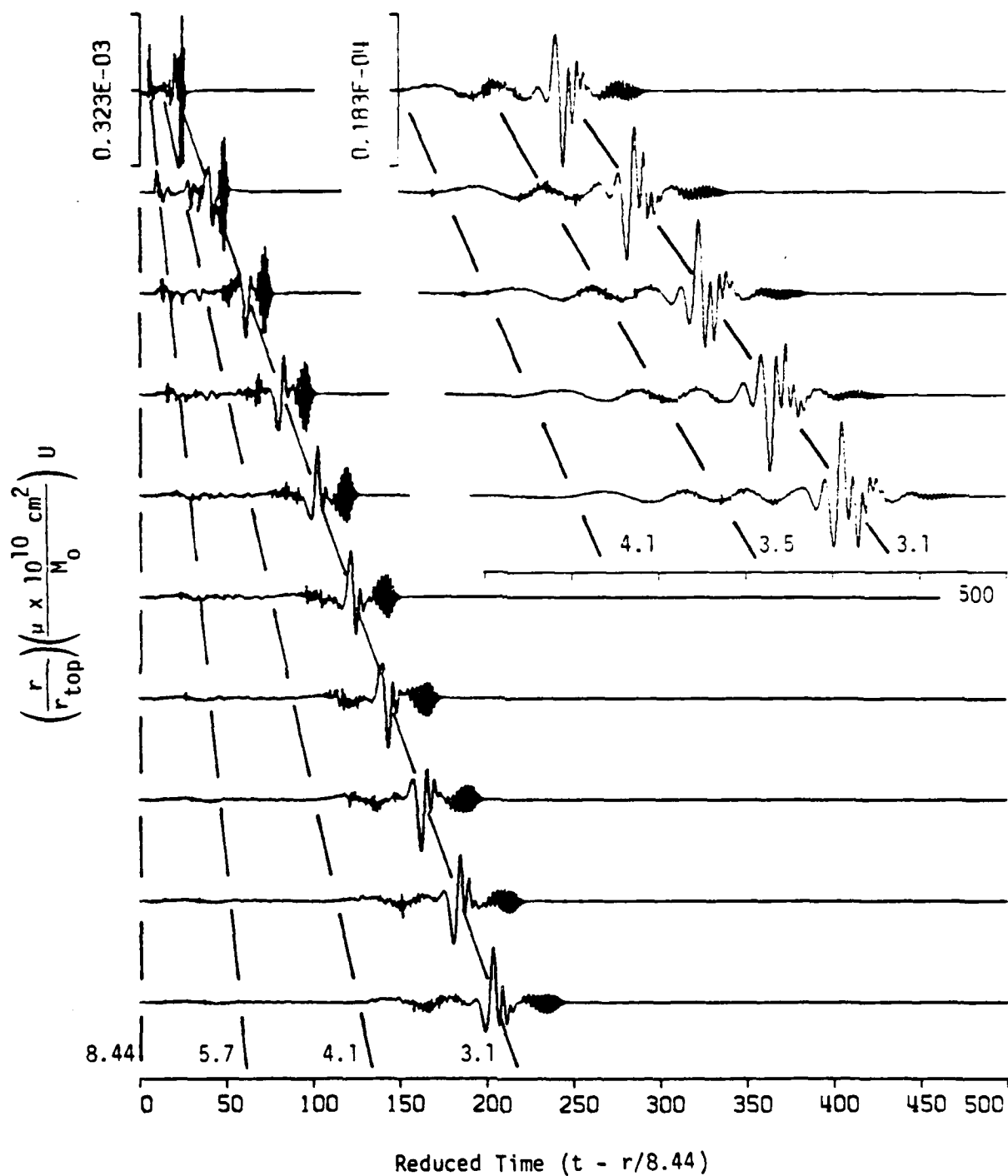


Figure 5-11. Radial displacement component due to vertical strike-slip dislocation buried at a depth of 2.0 km.

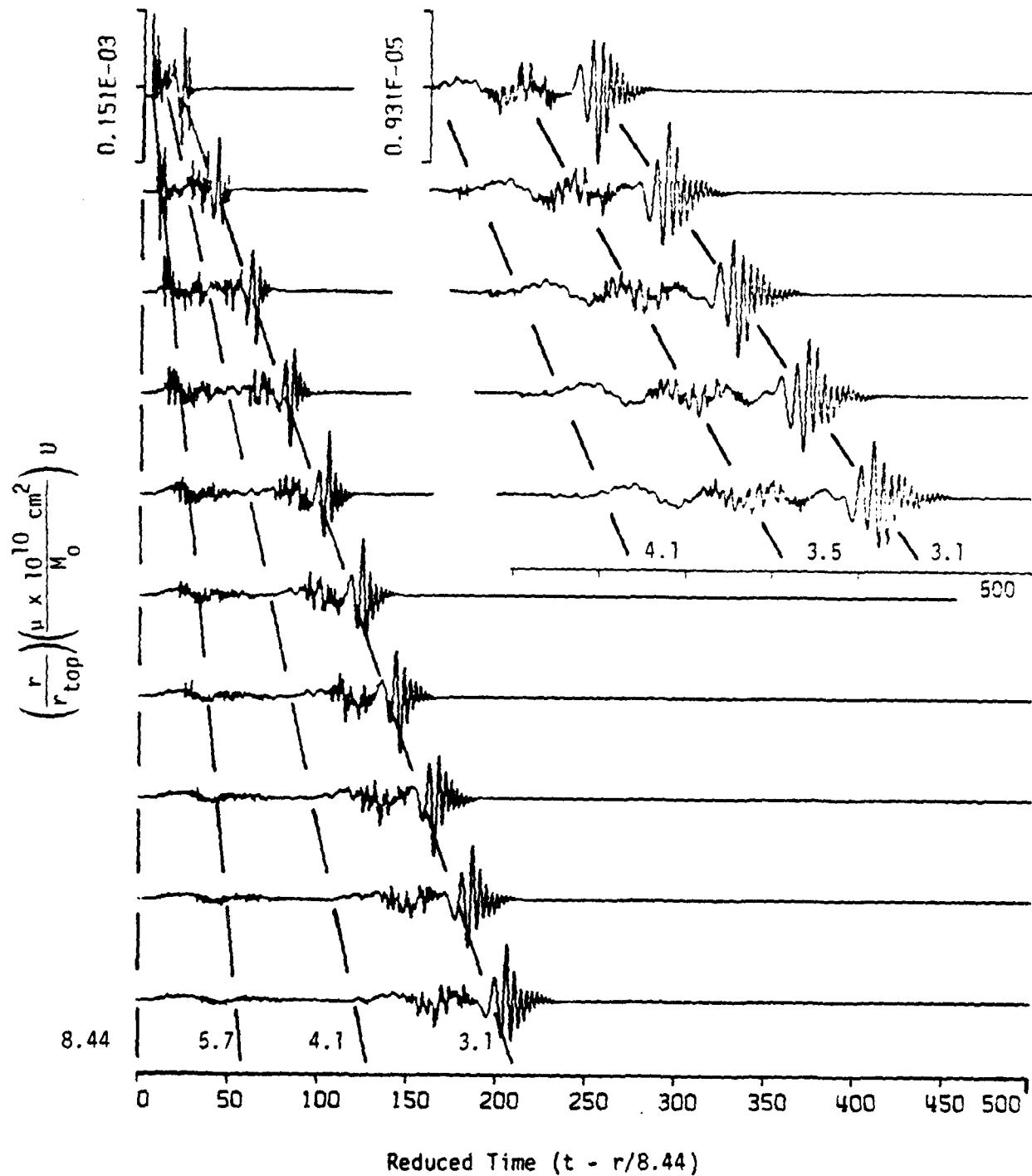


Figure 5-12. Radial displacement component due to vertical strike-slip dislocation buried at a depth of 10.0 km.

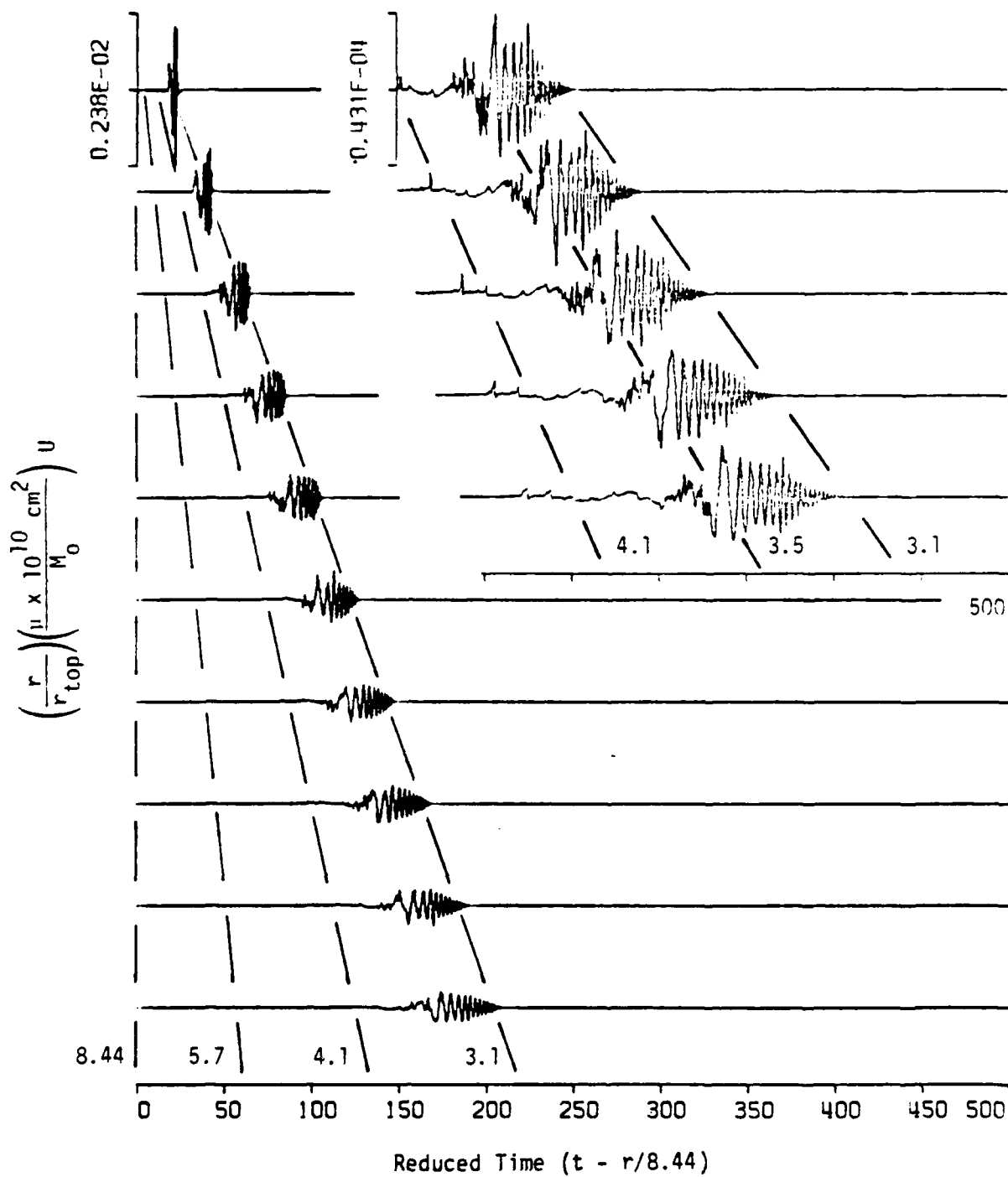


Figure 5-13. Azimuthal displacement component due to vertical strike-slip dislocation buried at a depth of 0.4 km.

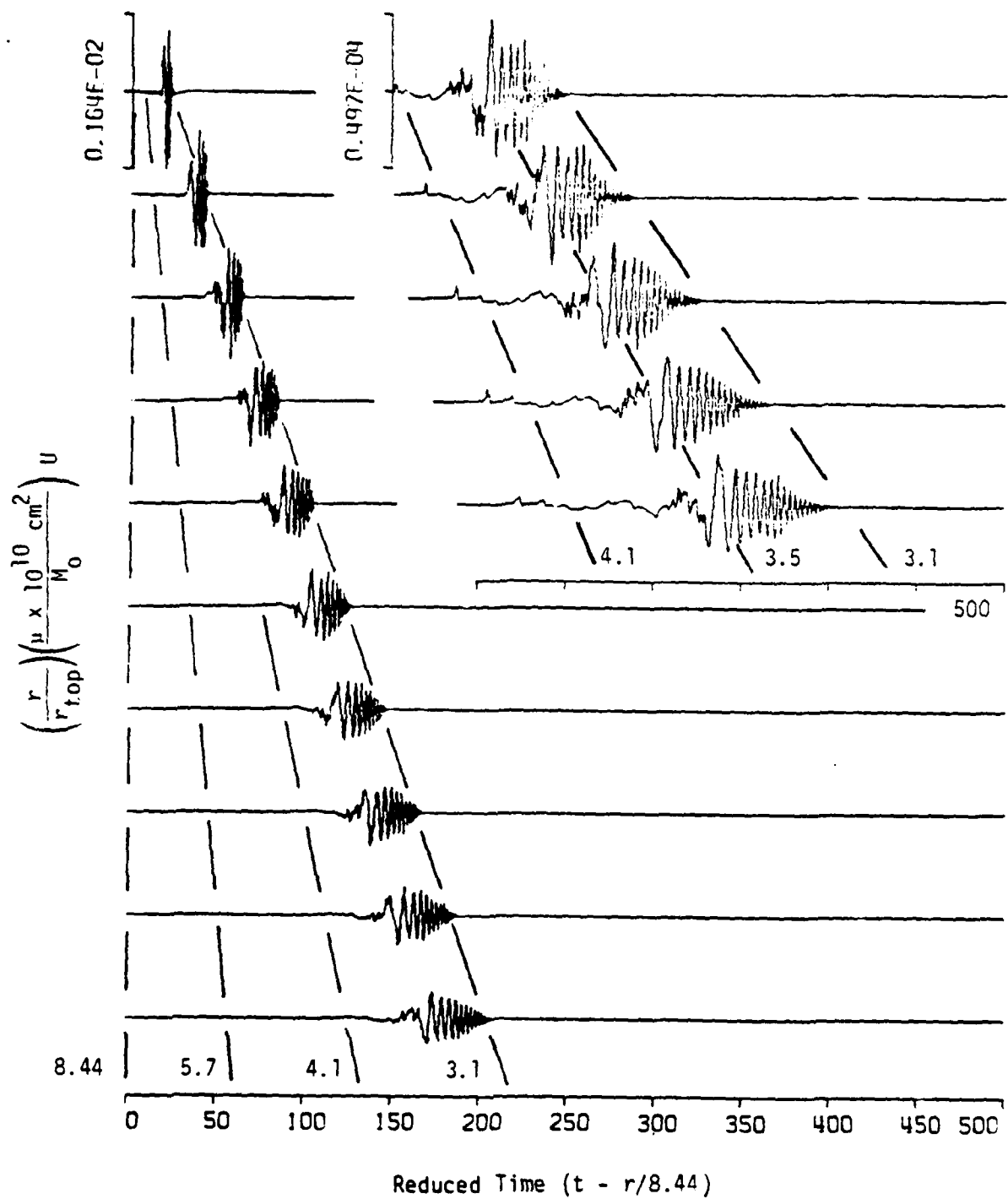


Figure 5-14. Azimuthal displacement component due to vertical strike-slip dislocation buried at a depth of 2.0 km.

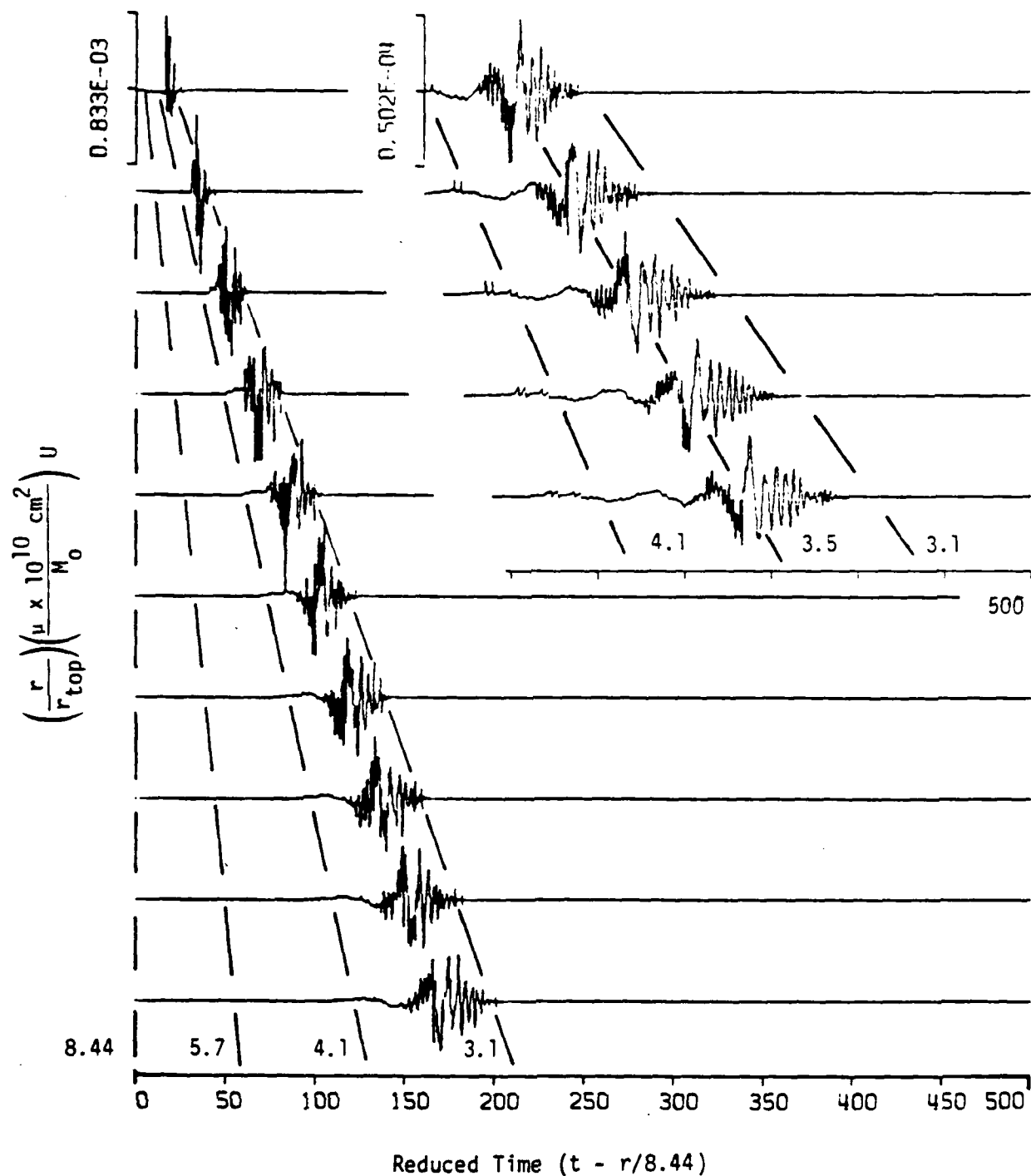


Figure 5-15. Azimuthal displacement component due to vertical strike-slip dislocation buried at a depth of 10.0 km.

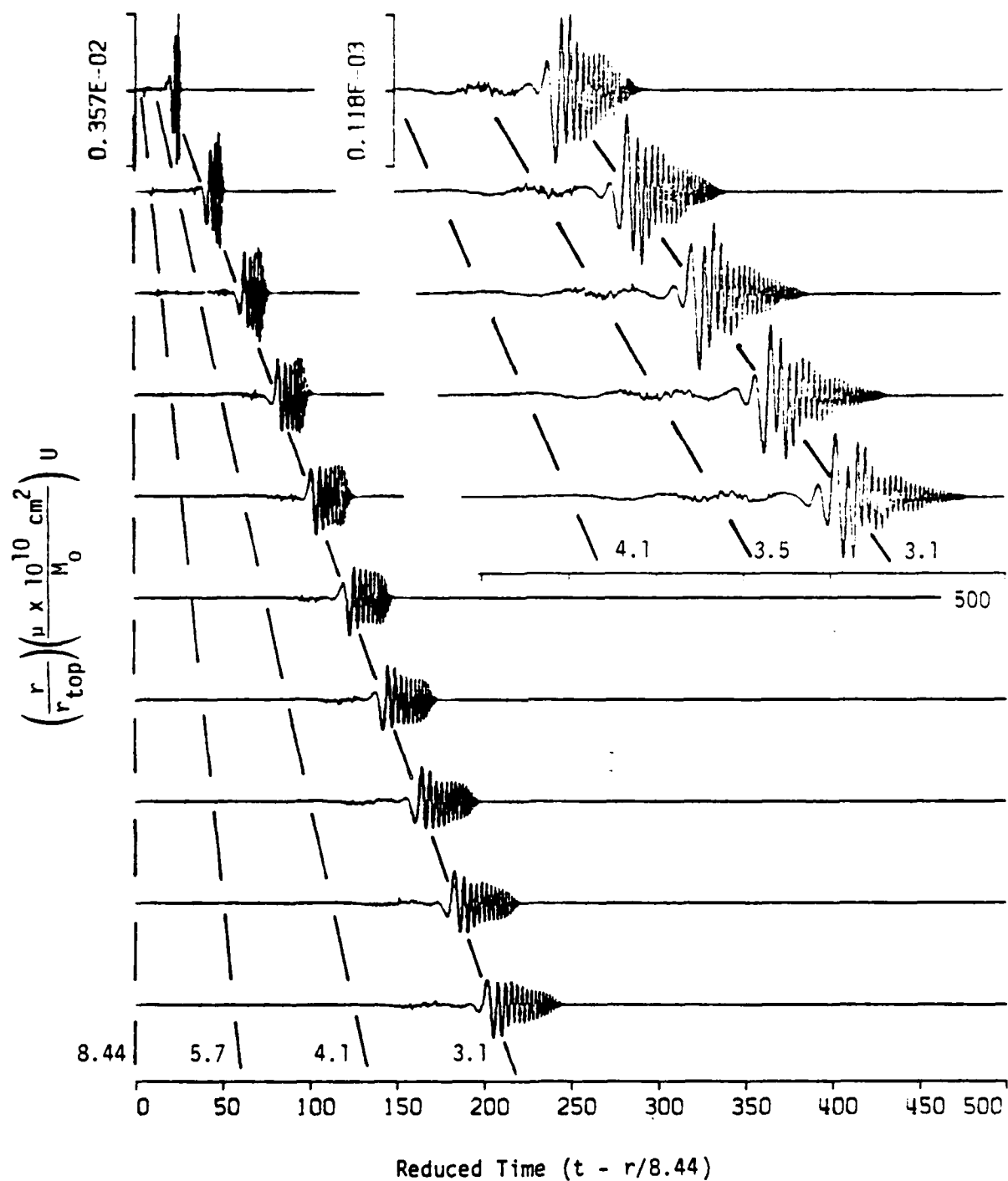


Figure 5-16. Vertical displacement component due to an explosion buried at a depth of 0.4 km.

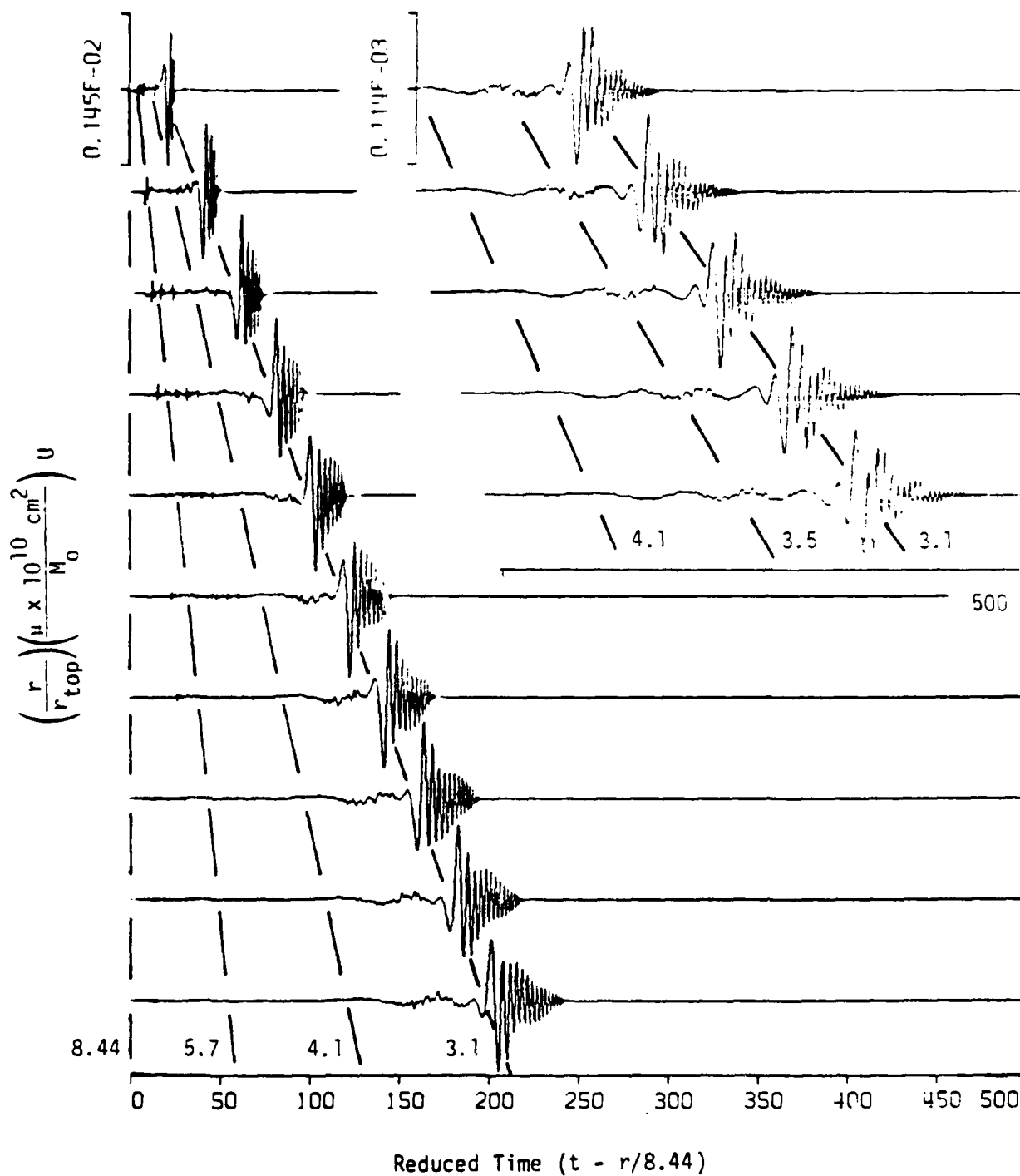


Figure 5-17. Vertical displacement component due to an explosion buried at a depth of 2.0 km.

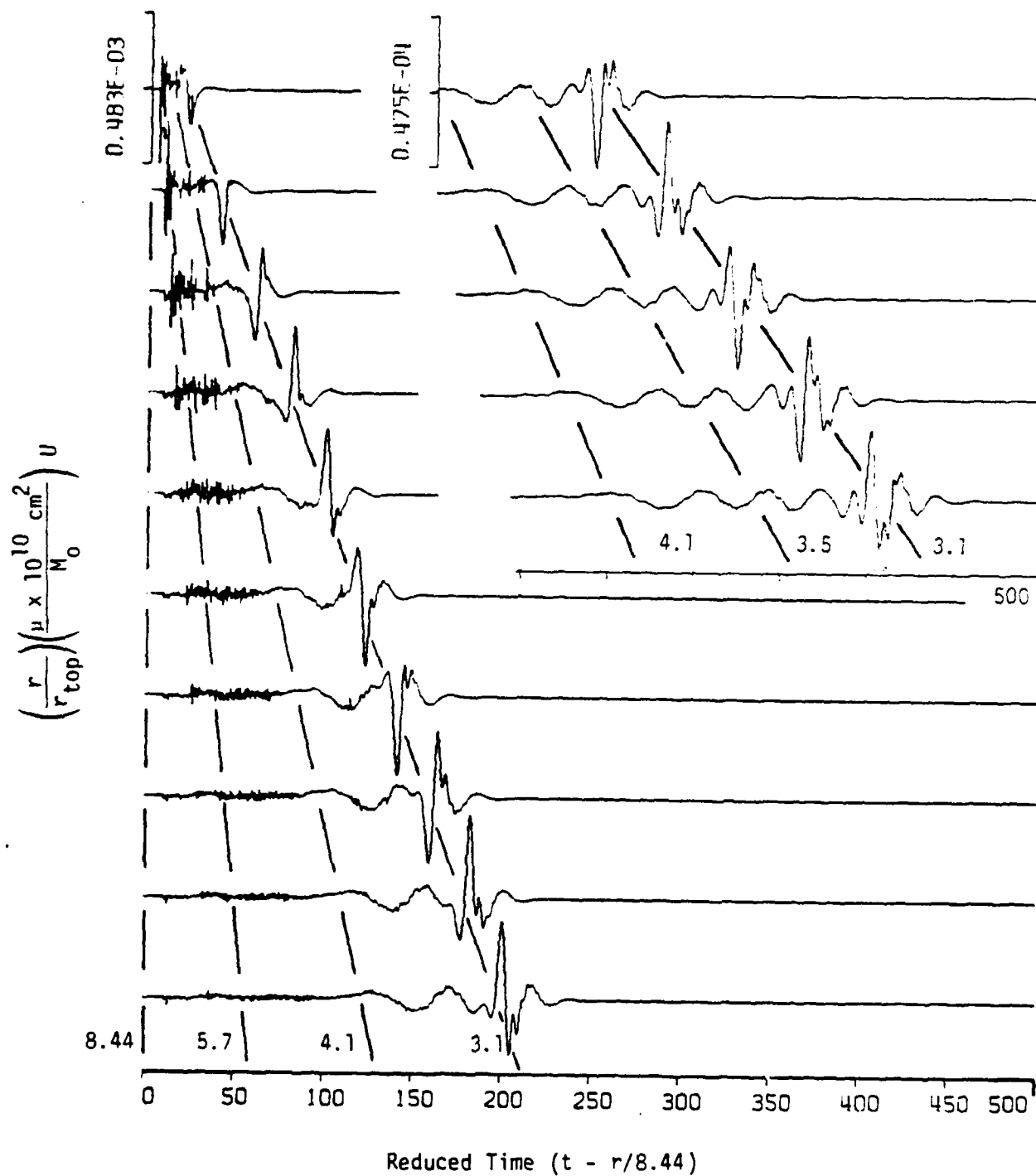


Figure 5-18. Vertical displacement component due to an explosion buried at a depth of 10.0 km.

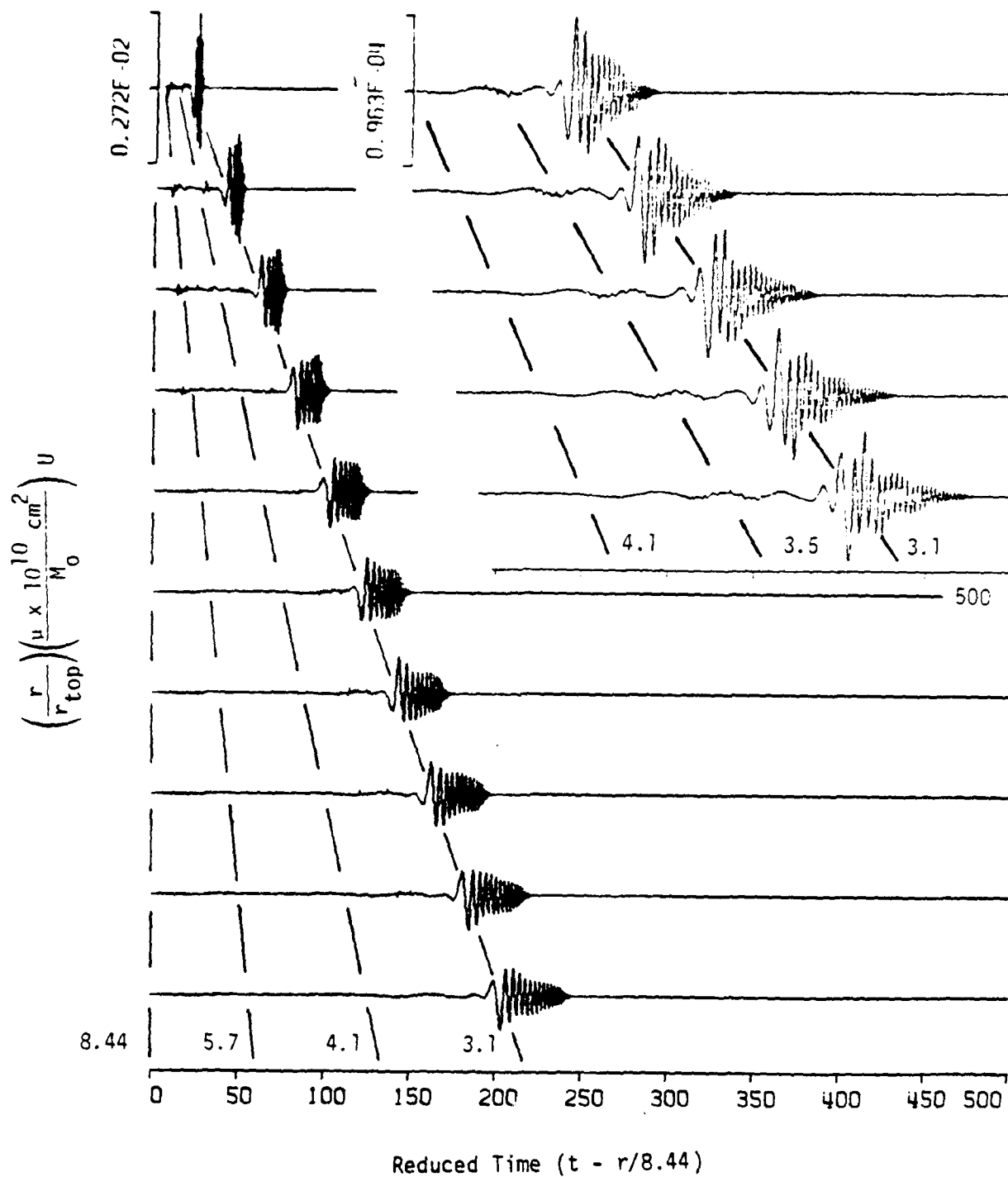


Figure 5-19. Radial displacement component due to an explosion buried at a depth of 0.4 km.

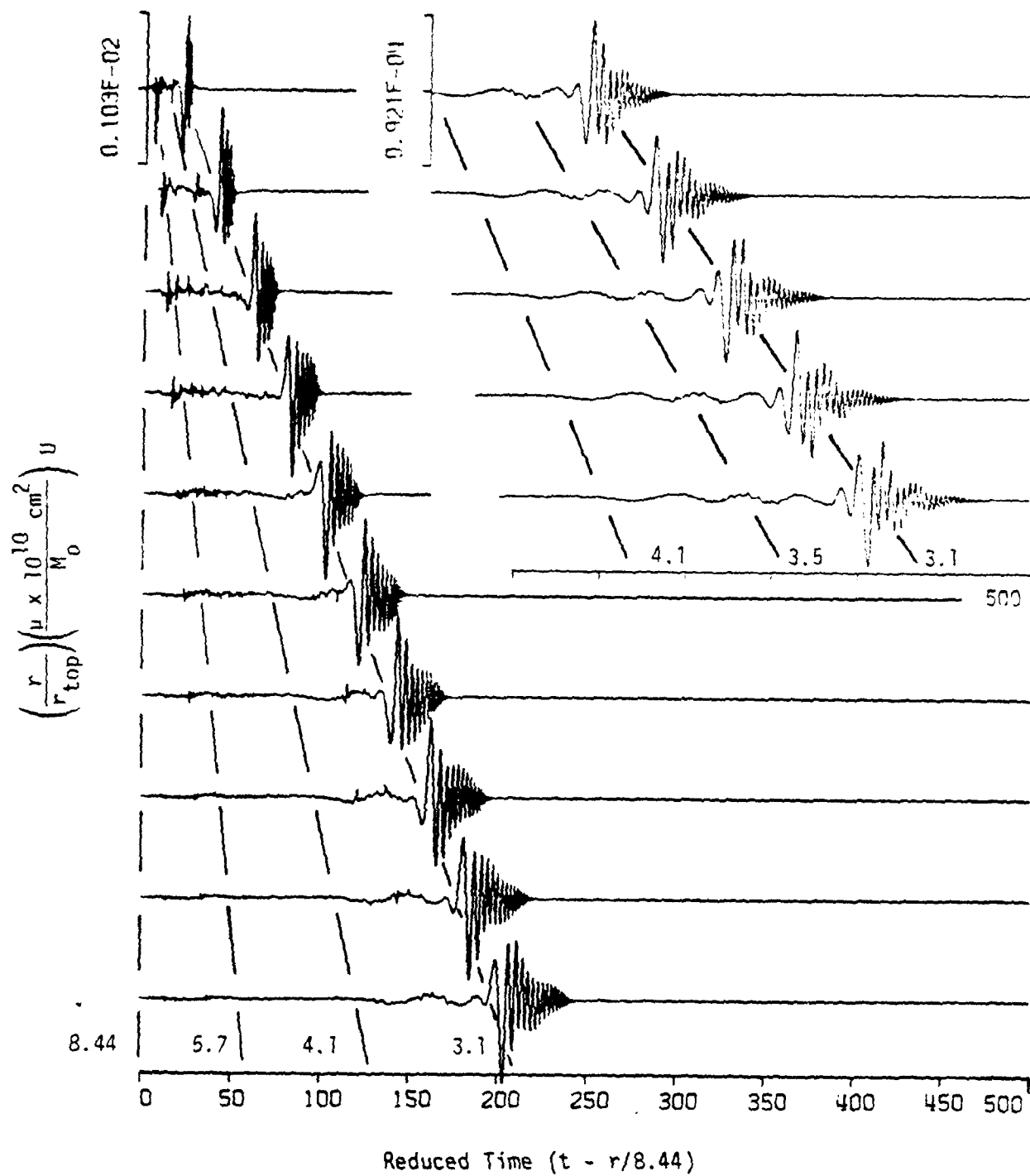


Figure 5-20. Radial displacement component due to an explosion buried at a depth of 2.0 km.

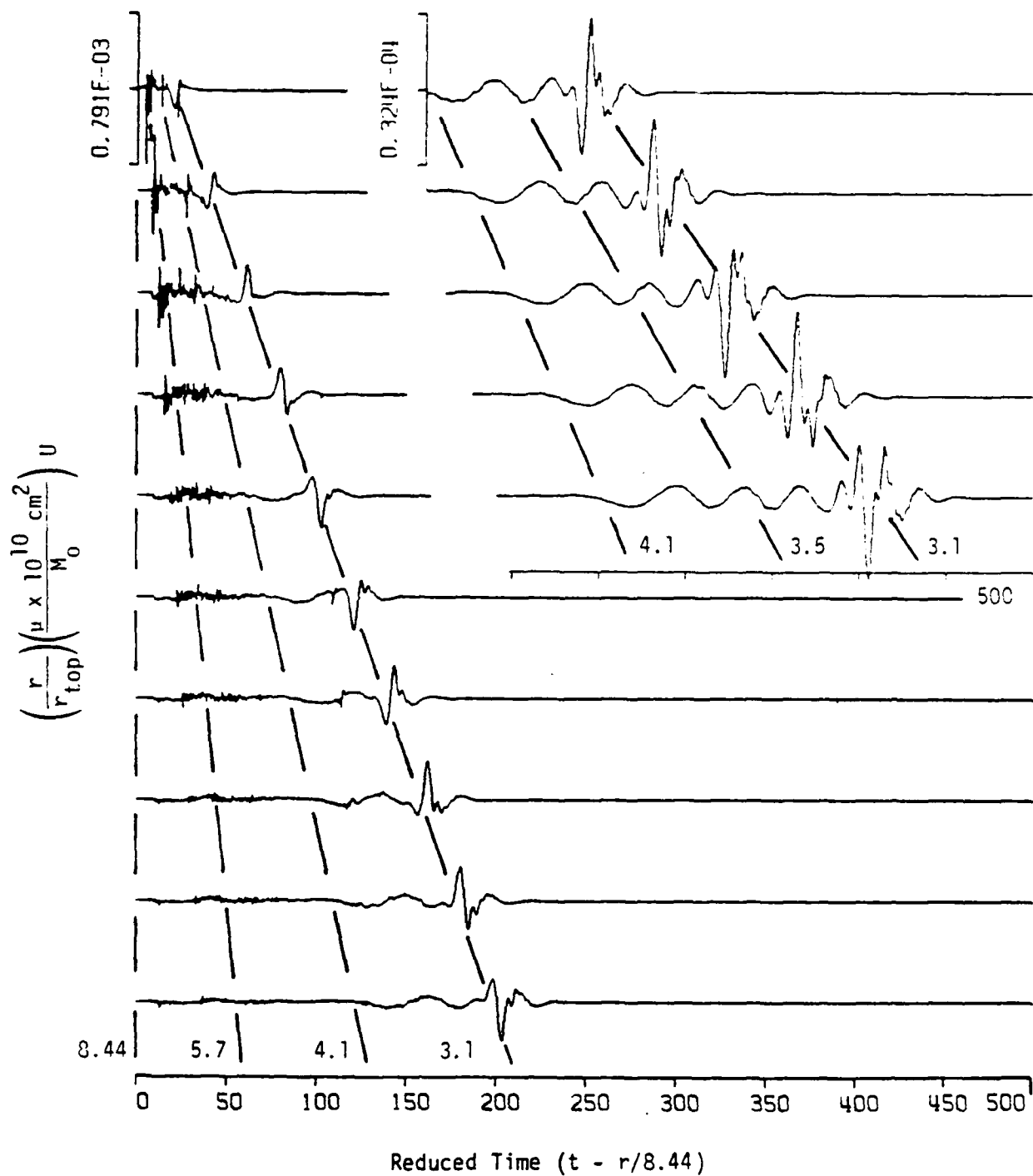


Figure 5-21. Radial displacement component due to an explosion buried at a depth of 10.0 km.

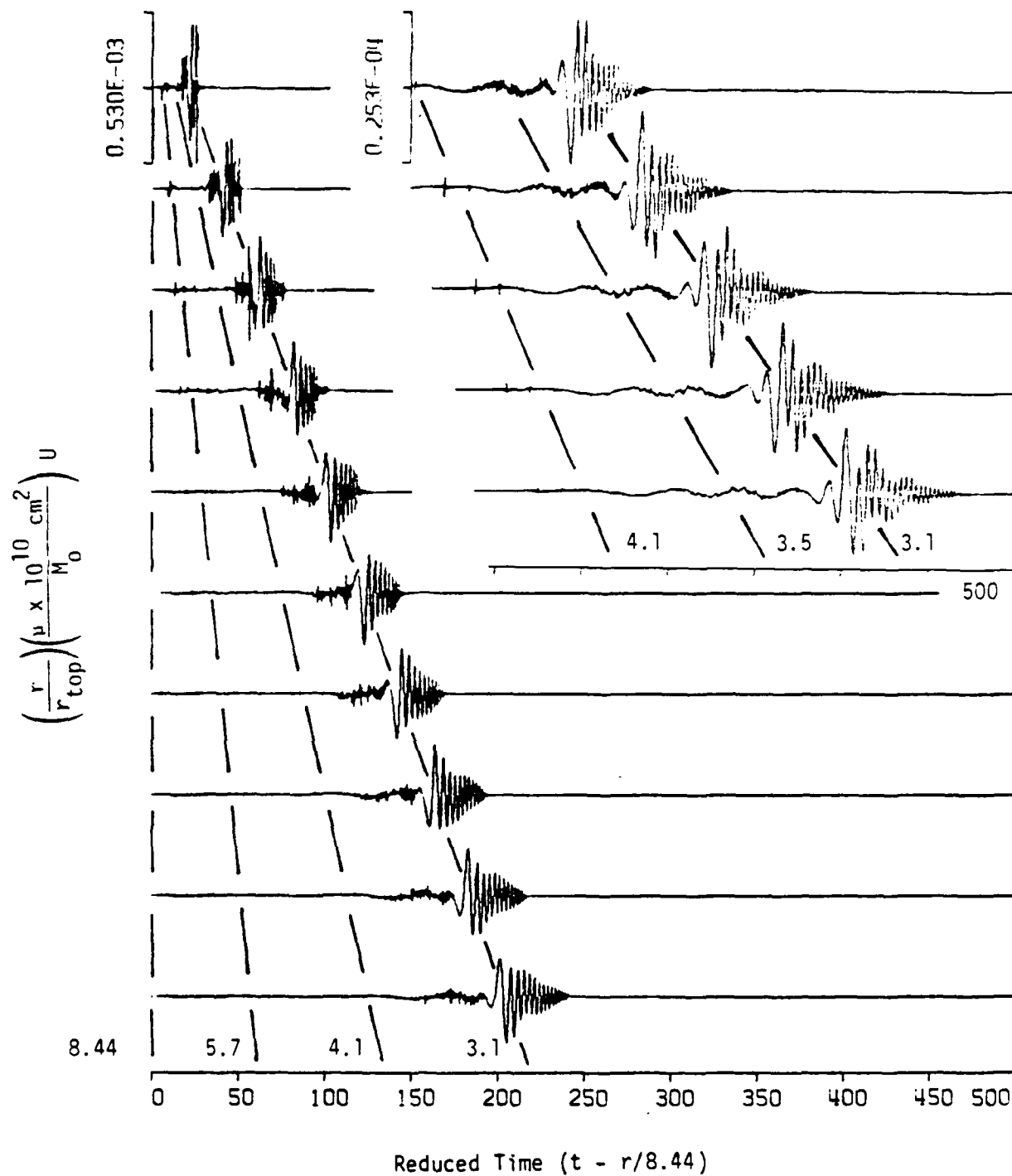


Figure 5-22. Vertical displacement component due to a vertical dip-slip dislocation buried at a depth of 0.4 km.

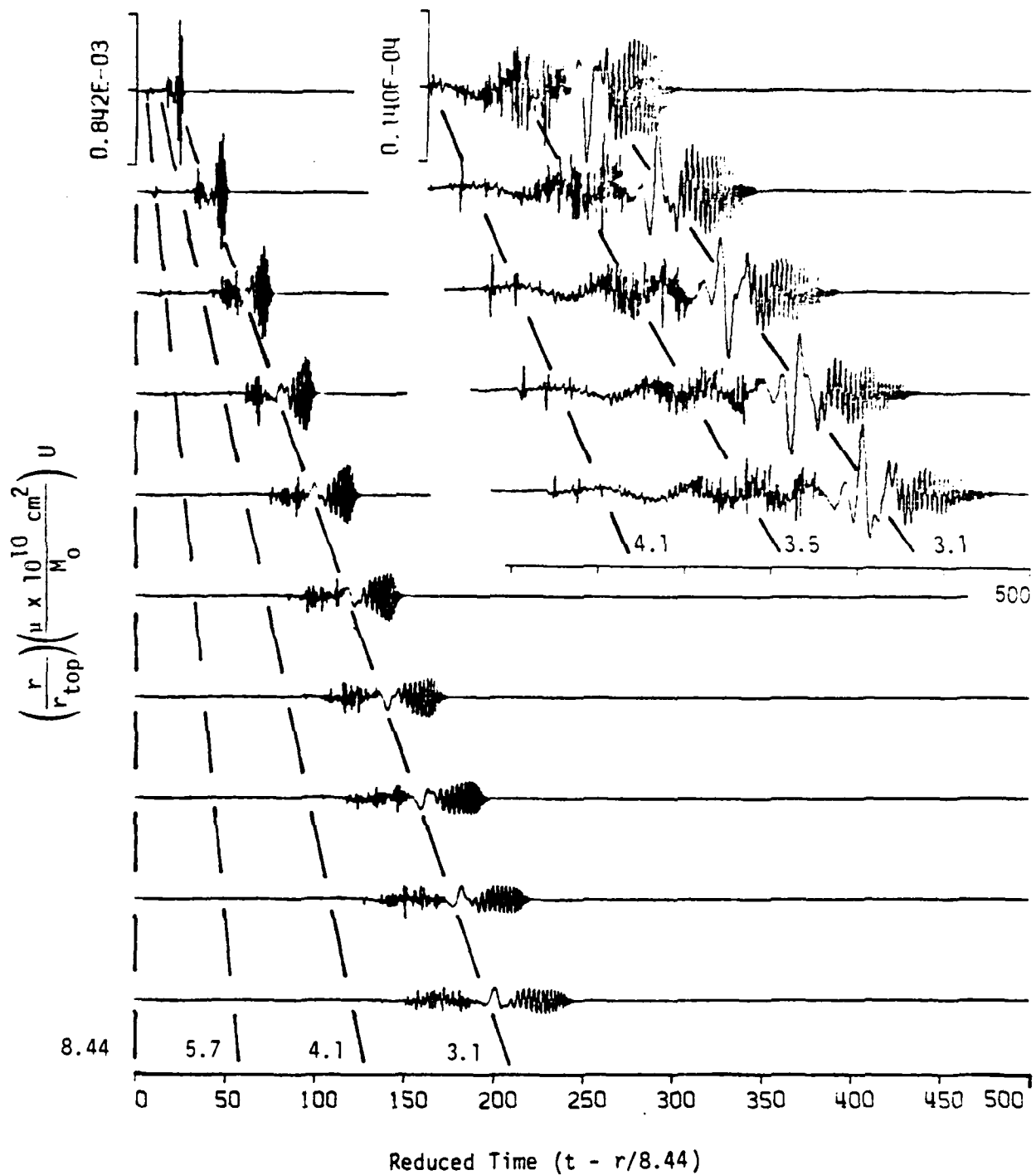


Figure 5-23. Vertical displacement component due to a vertical dip-slip dislocation buried at a depth of 2.0 km.

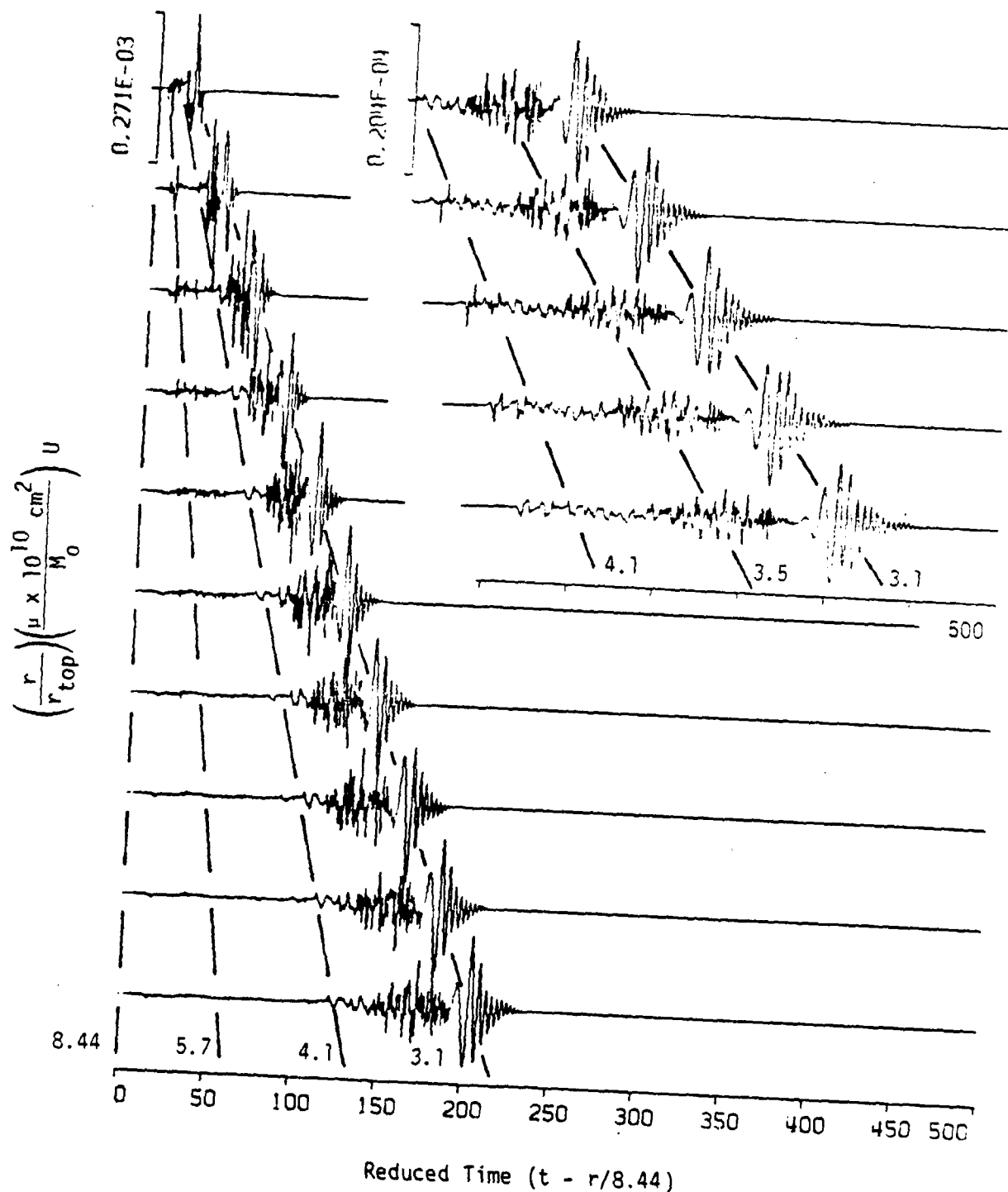


Figure 5-24. Vertical displacement component due to a vertical dip-slip dislocation buried at a depth of 10.0 km.

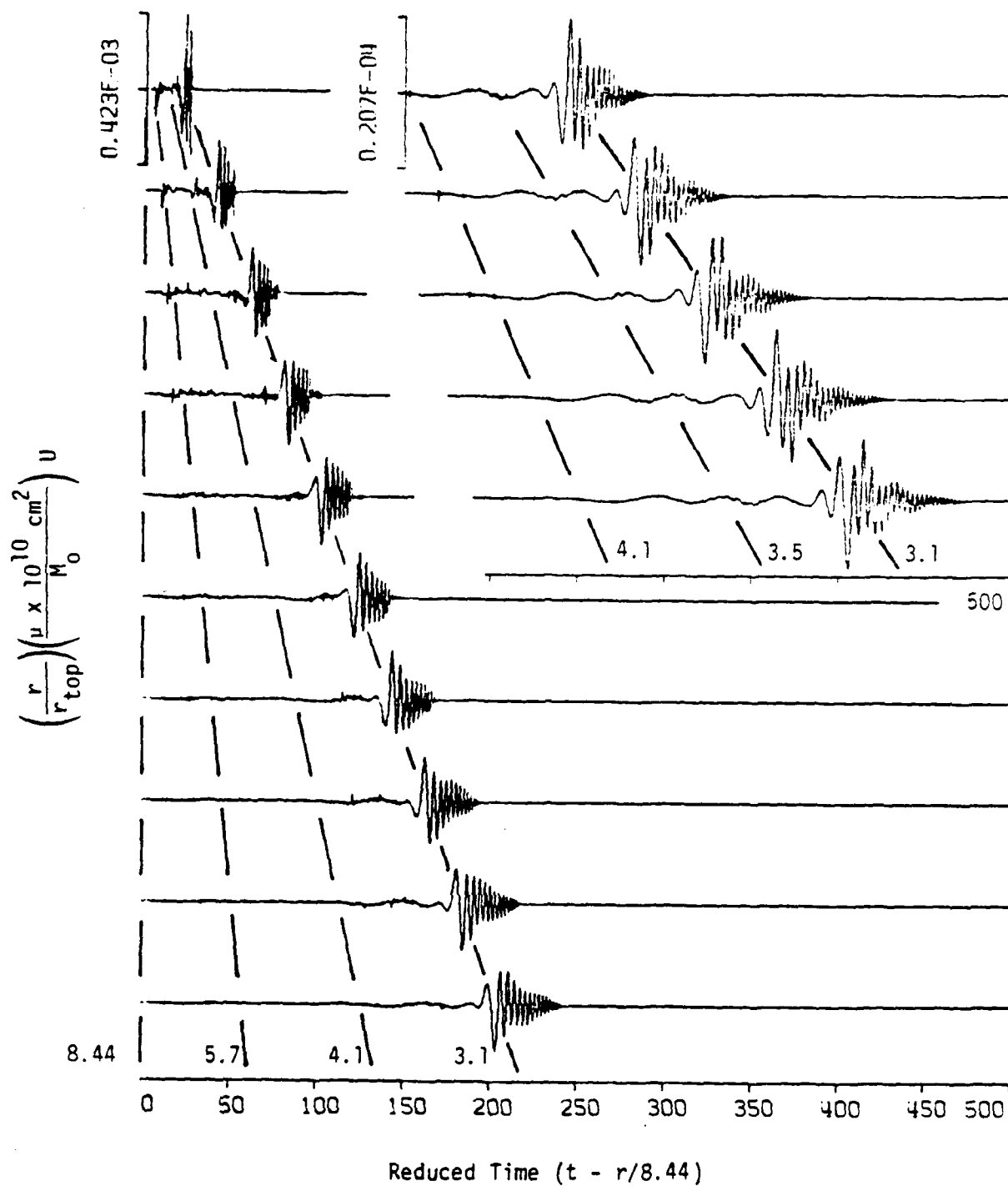


Figure 5-25. Radial displacement component due to a vertical dip-slip dislocation buried at a depth of 0.4 km.

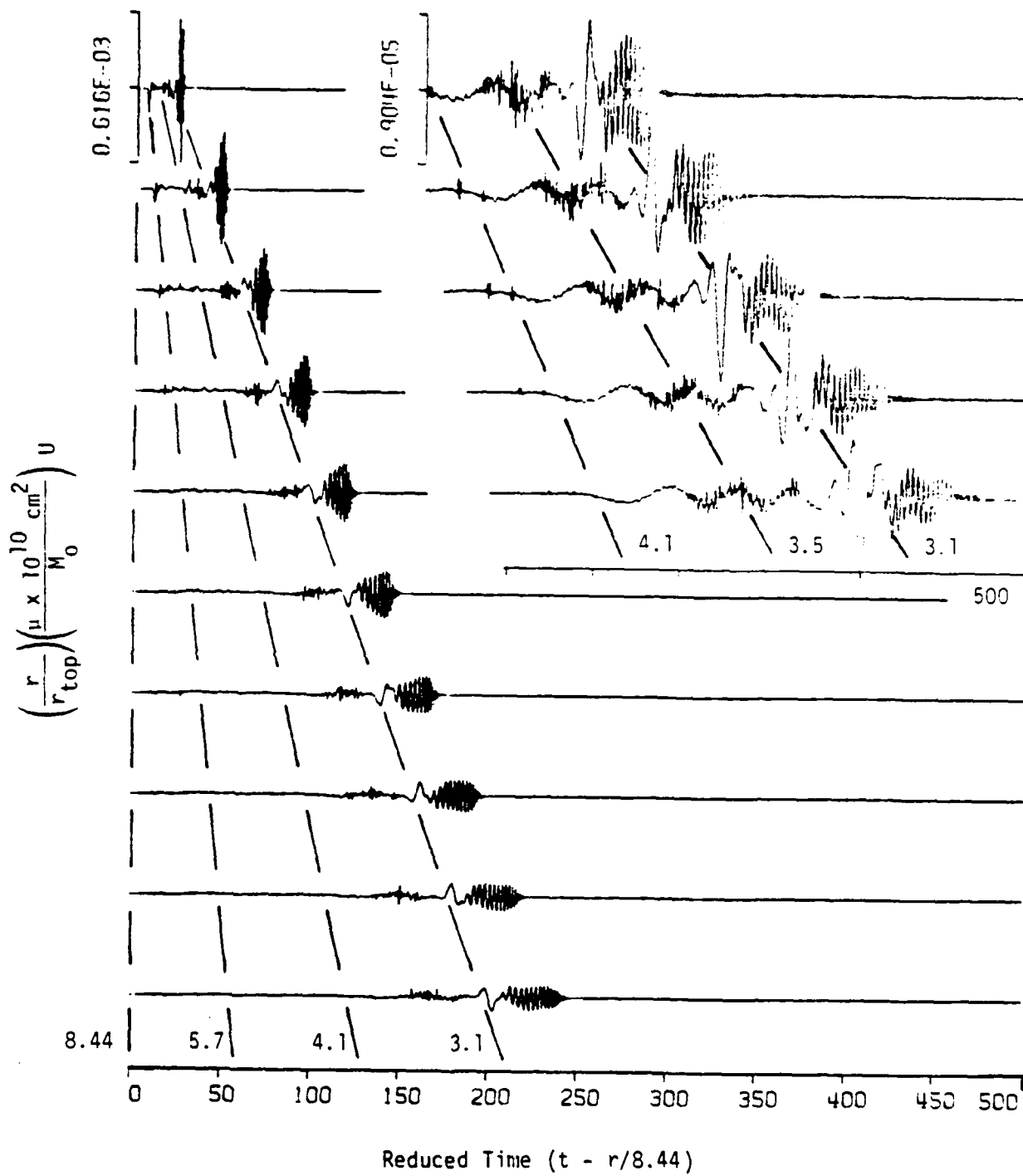


Figure 5-26. Radial displacement component due to a vertical dip-slip dislocation buried at a depth of 2.0 km.

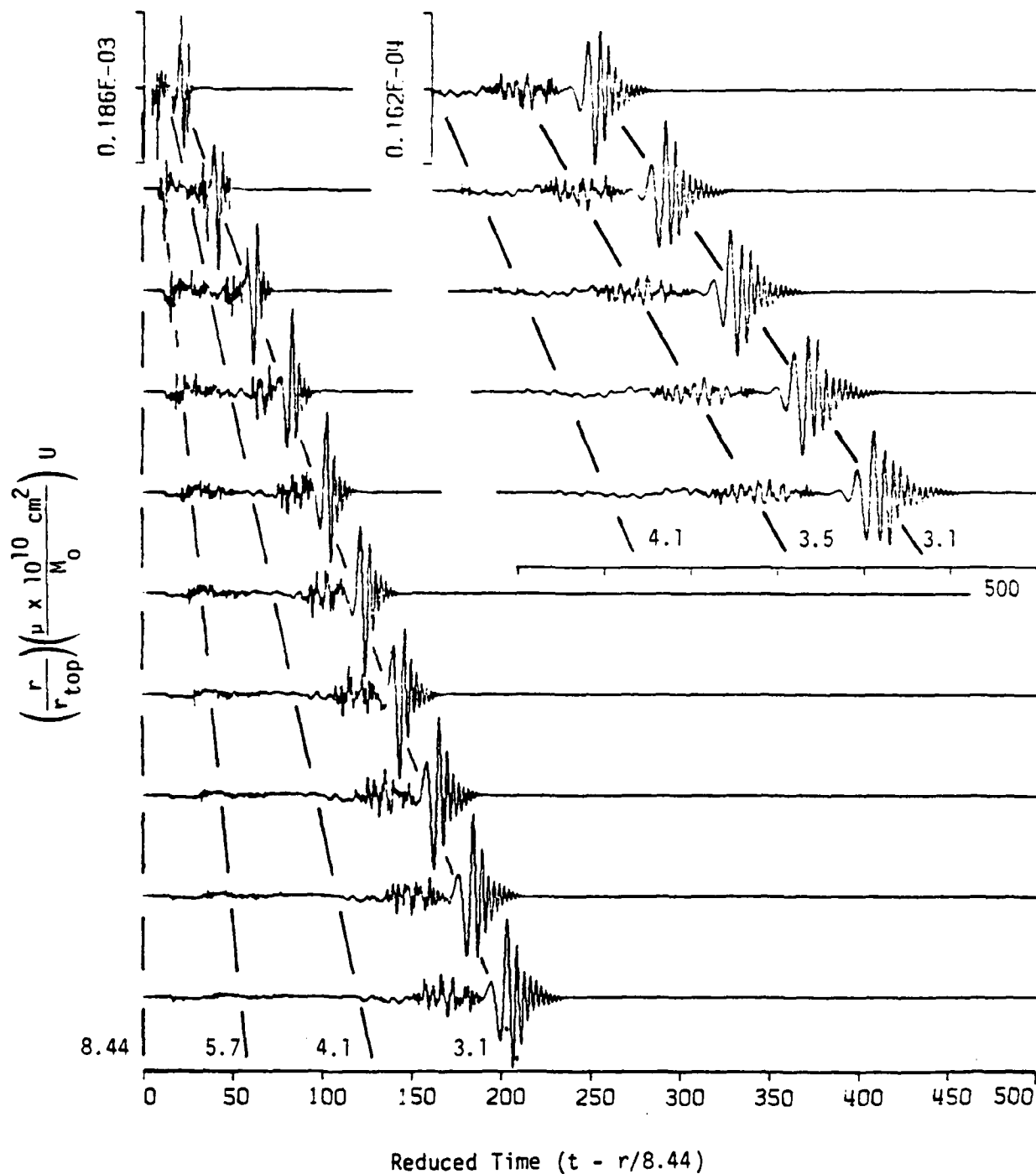


Figure 5-27. Radial displacement component due to a vertical dip-slip dislocation buried at a depth of 10.0 km.

C_g =

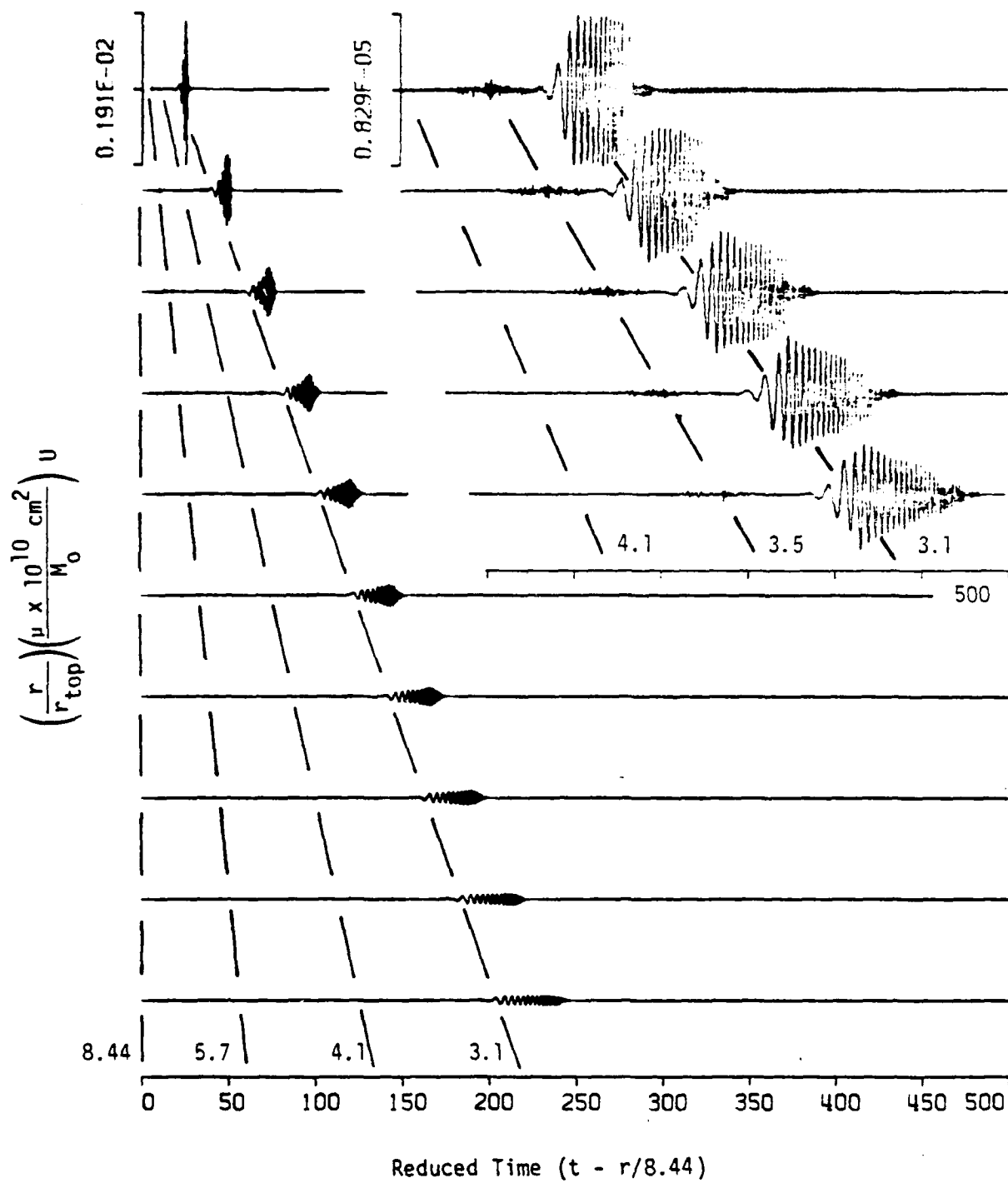


Figure 5-28. Vertical displacement component due to 45 degree dip-slip dislocation buried at a depth of 0.4 km.

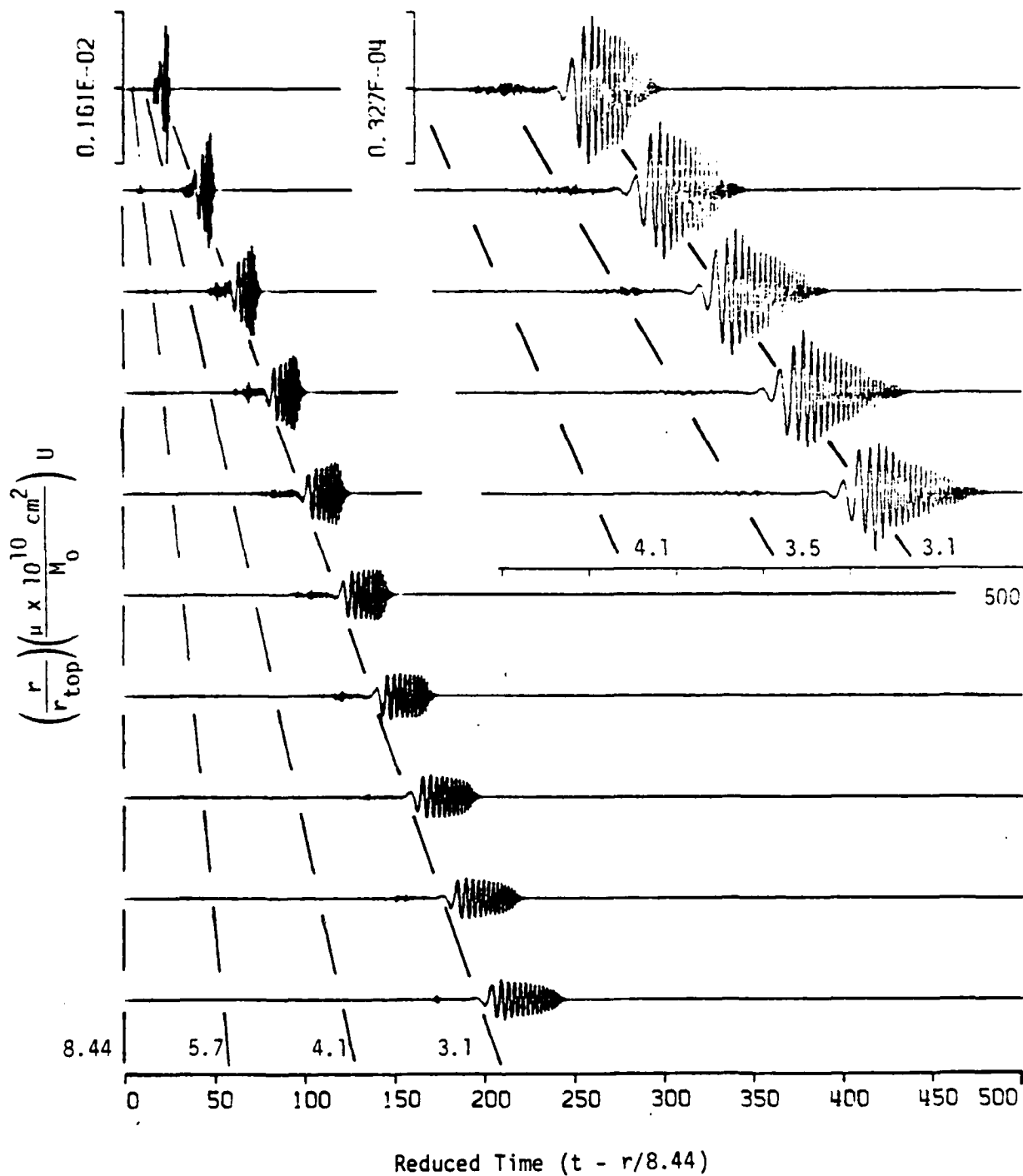


Figure 5-29. Vertical displacement component due to 45 degree dip-slip dislocation buried at a depth of 2.0 km.

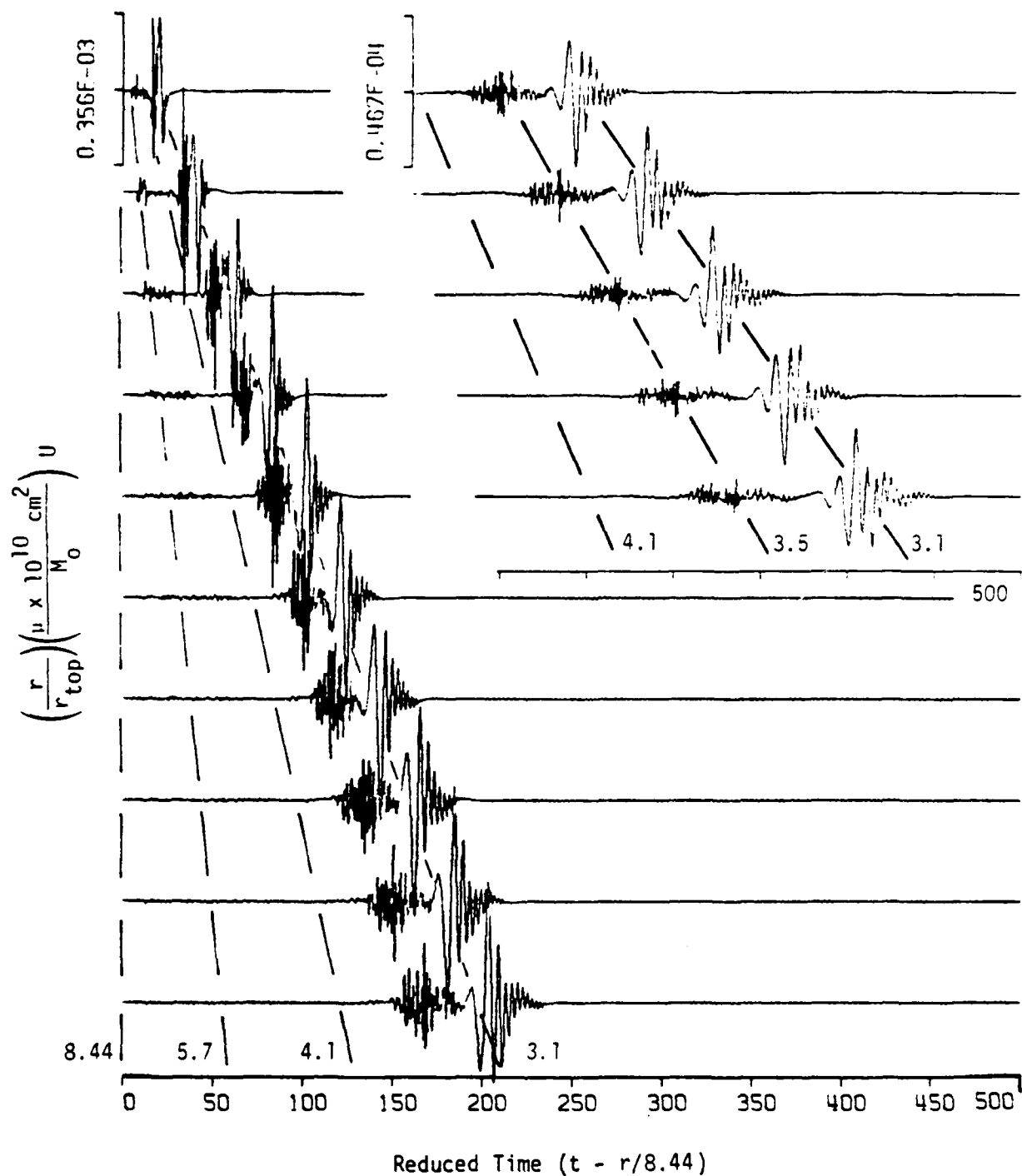


Figure 5-30. Vertical displacement component due to 45 degree dip-slip dislocation buried at a depth of 10.0 km.

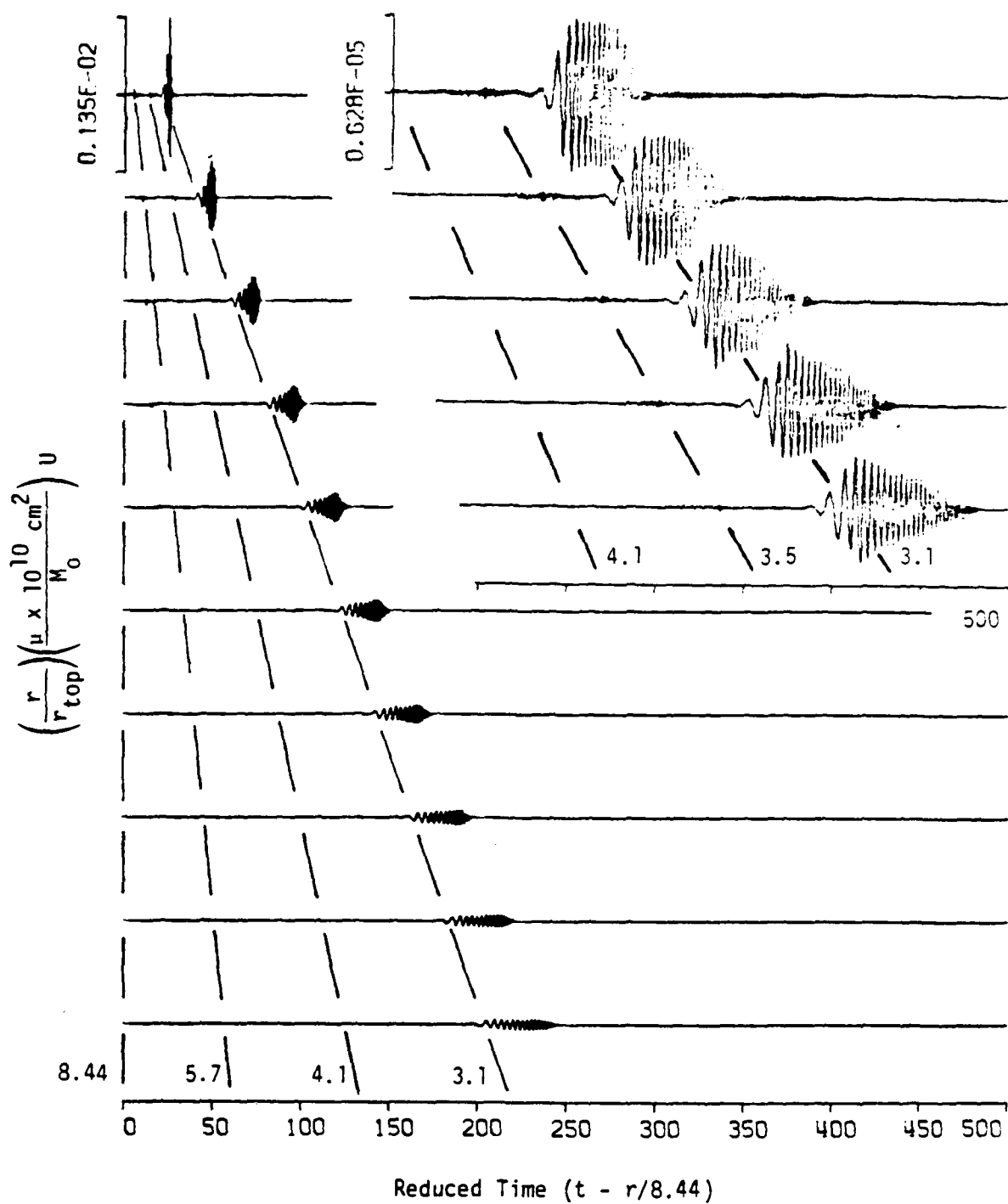


Figure 5-31. Radial displacement component due to 45 degree dip-slip dislocation buried at a depth of 0.4 km.

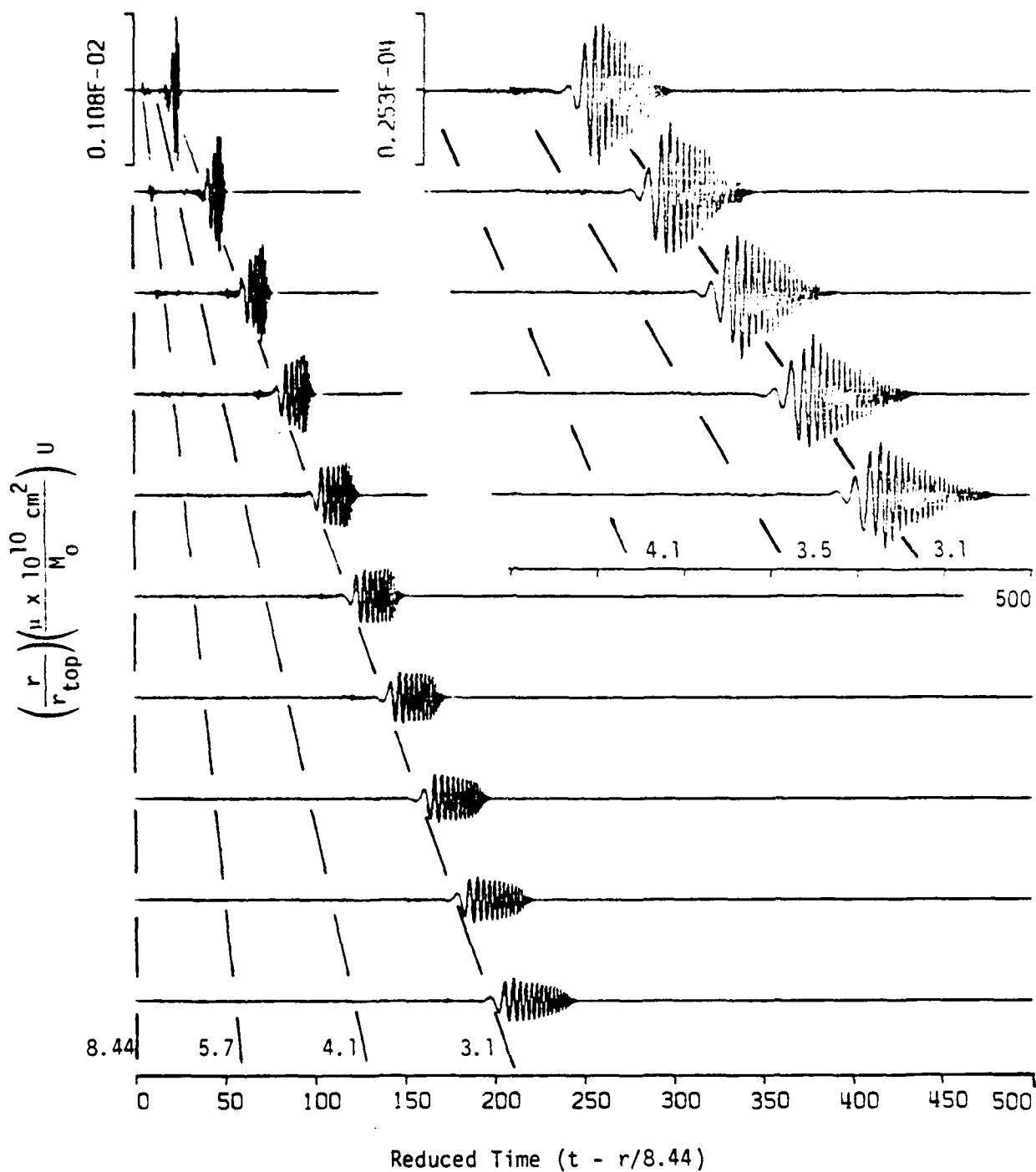


Figure 5-32. Radial displacement component due to 45 degree dip-slip dislocation buried at a depth of 2.0 km.

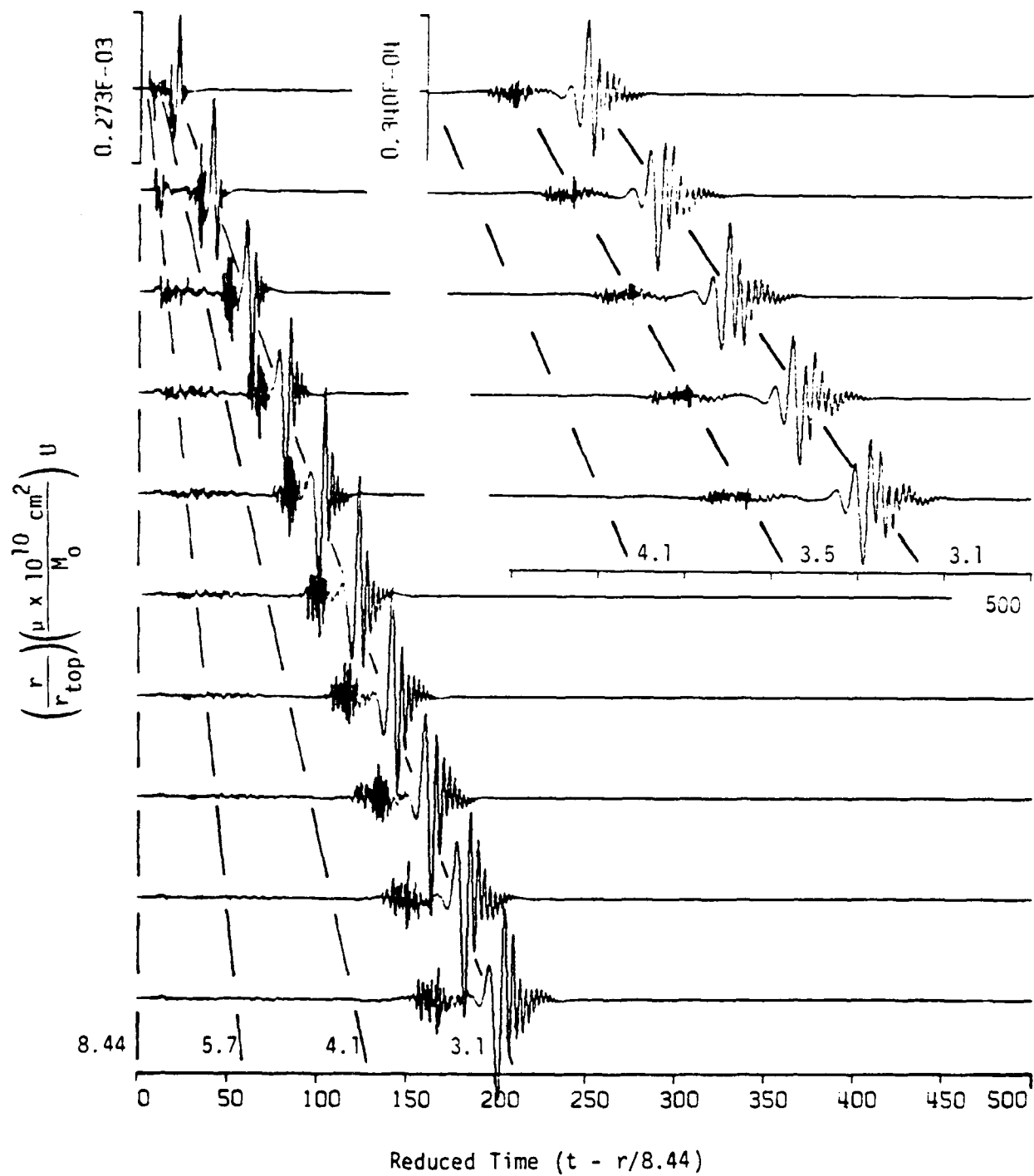


Figure 5-33. Radial displacement component due to 45 degree dip-slip dislocation buried at a depth of 10.0 km.

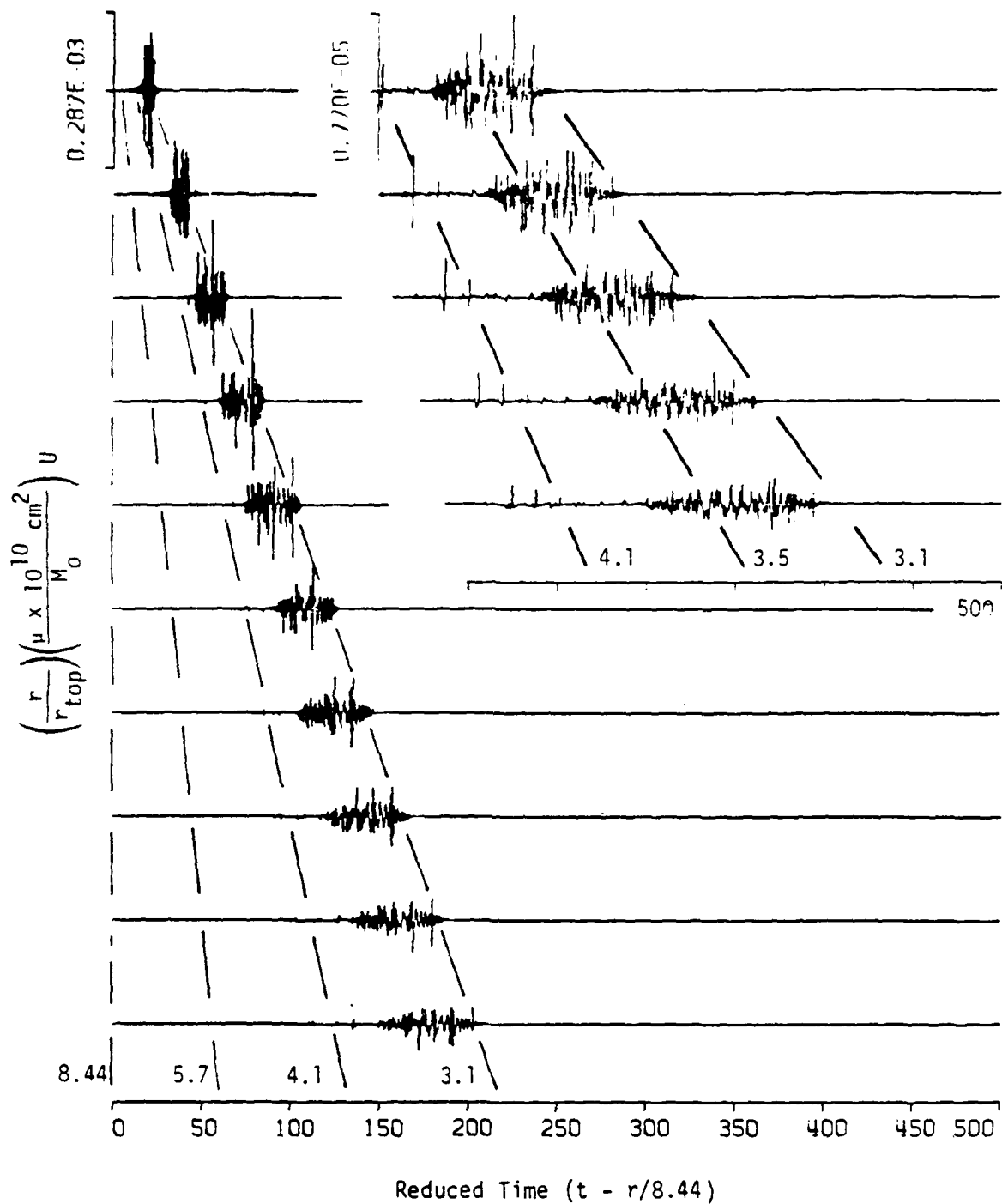


Figure 5-34. Azimuthal displacement component due to 45 degree dip-slip dislocation buried at a depth of 0.4 km.

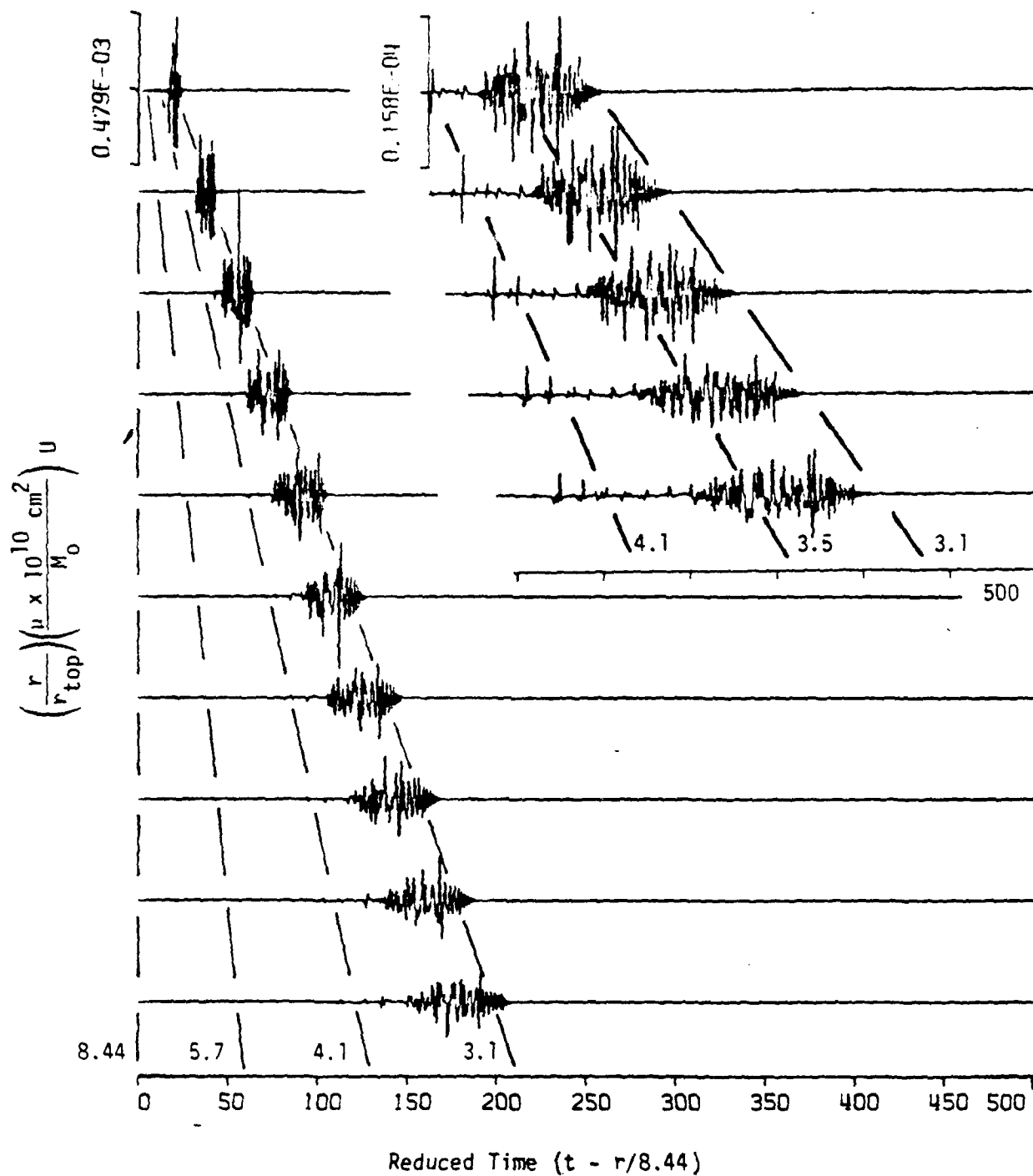


Figure 5-35. Azimuthal displacement component due to 45 degree dip-slip dislocation buried at a depth of 2.0 km.

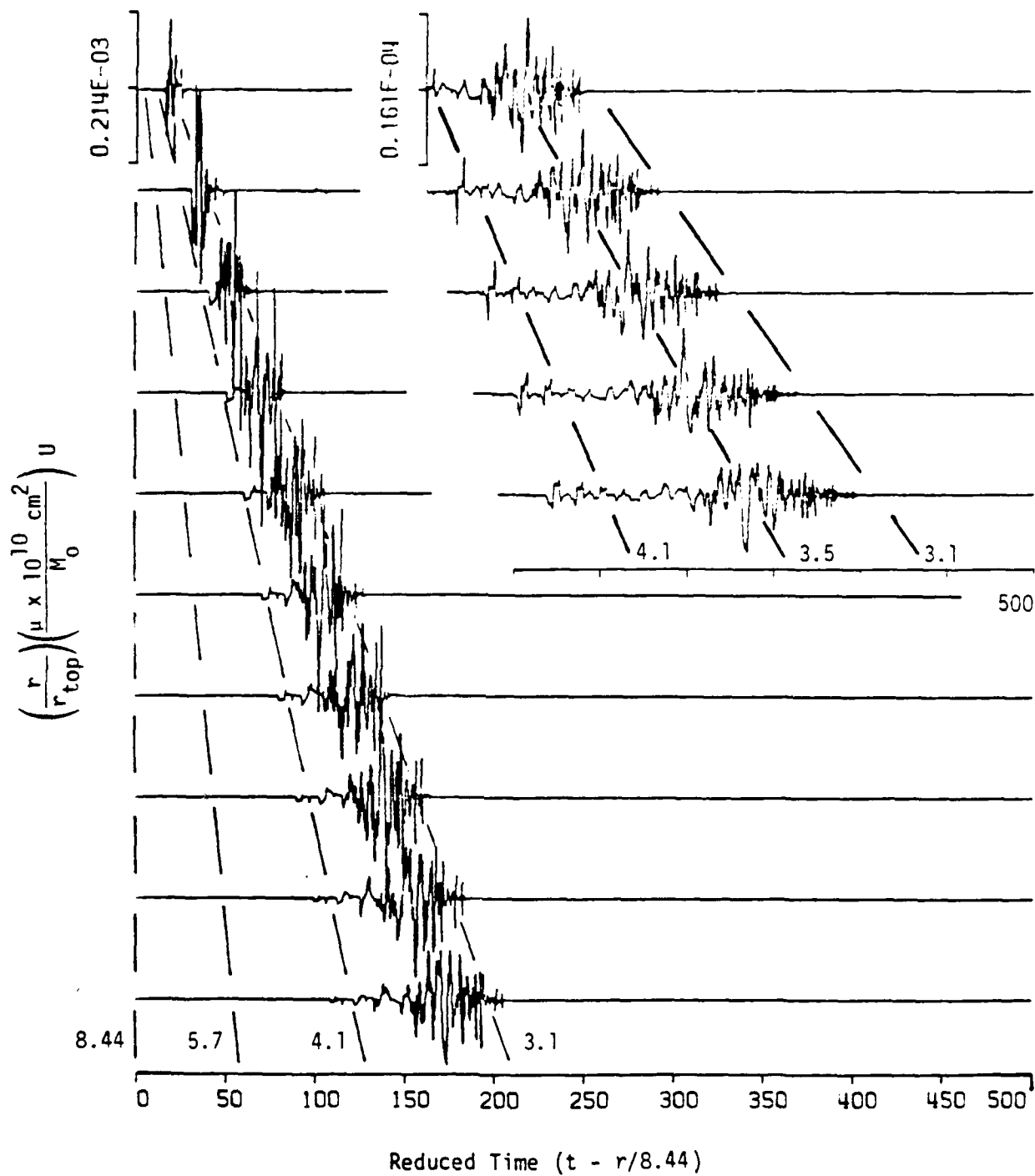


Figure 5-36. Azimuthal displacement component due to 45 degree dip-slip dislocation buried at a depth of 10.0 km.

the ten independent components portrayed, a point dislocation source of any orientation may be formed by superposition, since the reciprocal theorems require the six independent stress tensor components for a horizontal point force plus the four nonzero stress tensor components for a vertical point force (refer to Section 5.1.1).

The synthetic seismograms on each figure correspond to the 15 epicentral distances considered: the left-hand column represents distances between 100 km and 1000 km at an increment of 100 km; the right-hand column represents distances between 1200 km and 2000 km at an increment of 200 km. The displacements are plotted as a function of reduced time from 0 to 500 seconds. Since arrivals are not expected to travel at velocities greater than the highest compressional wave speed, the reduced time shift discards the first $r/8.44$ seconds of each time series (r = epicentral distance). The displacements are normalized by the ratio of the shear modulus (μ) of the first layer times 10^{10} cm^2 divided by the source moment (M_0). The time series in each column are multiplied by a factor of (r/r_{top}) so that each time series could use the scale factor of the first time series. This scaling factor corresponds to the maximum absolute peak of the first time series in each column and is printed next to the vertical axis. The effect of this scaling is such that waves which decay as $1/r$ will appear to be of constant amplitude down a column; waves which decay as $1/r^2$ (such as compressional waves in elastic media) will appear to decay as $1/r$; waves which decay as $1/\sqrt{r}$ (such as surface waves in elastic media) will appear to grow as \sqrt{r} . The effect of material attenuation accentuates these elastic decay rates so that the plots seldom overlap.

5.2.2 Description of Results

To facilitate the discussion of the results, lines of constant phase velocity have been drawn between the seismograms on each figure as a point of reference. The particular phase velocities indicated are 8.44, 5.7, 4.1 and 3.1 km/sec for the left-hand columns (epicentral distances from 100 to 1000 km) and 4.1, 3.5 and 3.1 km/sec for the right-hand columns (epicentral distances from 1200 through 2000 km). It should be pointed out that without the reduced time

shift, arrivals at zero time would have corresponded to waves with infinite phase velocity; whereas, arrivals at zero "reduced" time correspond to waves with phase velocities of the highest compressional wave speed (8.44 km/sec).

The regional ground displacement components are generally dominated by shear waves and normally dispersed surface waves followed by an Airy phase with an exponential tail. For example, in Figure 5-7, the direct shear wave (travelling at a phase velocity of about 3.1 km/sec between source and receiver) dominates the response. As previously mentioned, the apparent constant amplitude of this arrival actually corresponds to a $1/r$ decay rate due to the amplitude normalization of the plots. The compressional waves decay with an additional $1/r$ and hence seem to disappear with increasing epicentral distance (and in fact are not even shown in the right-hand columns). Direct, multiply reflected and critically refracted compressional waves are evidenced at phase velocities between the 8.44 and 5.7 phase velocity lines. Arrivals between the 5.7 and 4.1 phase velocity lines could correspond to converted or multiply converted/reflected shear and compressional waves. The exponential tail of the Airy phase is completely attenuated at a wave speed of 2.7 km/sec (i.e., approximately the fundamental mode Rayleigh wave speed) at all epicentral distances. As the source depth is increased, the body waves become more important than the surface waves as revealed when the results of Figures 5-8 and 5-9 (source depths of 2 and 10 km, respectively) are compared with the results of Figure 5-7 (source depth of 0.4 km). In fact, the body waves are nearly an order of magnitude larger than the fundamental surface wave modes in Figure 5-9 and are clearly identifiable at all epicentral distances.

The radial displacement components due to a vertical strike-slip point dislocation at depths of 0.4, 2.0 and 10.0 km in Figures 5-10, 5-11, and 5-12, respectively, closely resemble the characteristics described for the corresponding vertical displacement components in Figures 5-7, 5-8 and 5-9. The azimuthal displacement components in Figures 5-13, 5-14 and 5-15 also ascribe to similar characteristics except for the absence of all compressional wave arrivals and the presence of Love waves instead of Rayleigh waves, which together account for the less complicated nature of the time series.

The vertical and radial displacement components for the buried point explosions are shown in Figures 5-16 through 5-18 and Figures 5-19 through 5-21, respectively. Except for a scaling factor, the results for the shallow explosion are almost identical to the corresponding results for the shallow strike-slip dislocation (e.g., compare Figure 5-16 to 5-7). As the source depth is increased, it becomes possible to discriminate between the explosion and strike-slip dislocation source types. The most striking difference for the explosion source is the reduced frequency content of the shear and surface waves. As the epicentral distance is increased, the difference could be described as a selective low-pass filtering of all converted and multiply reflected shear waves and surface waves (e.g., compare Figure 5-18 to 5-9).

The vertical and radial displacement components for the buried vertical dip-slip point dislocations in Figures 5-22 through 5-27 are quite similar in amplitude, frequency content and relative importance of body waves versus surface waves to the corresponding results in Figures 5-7 through 5-12 for the buried vertical strike-slip point dislocations at the epicentral distances considered in this study.

The vertical, radial and azimuthal displacement components for the buried 45 degree dip-slip point dislocations in Figures 5-28 through 5-36 are similar in overall frequency content to the corresponding results for the vertical strike-slip and dip-slip dislocation sources. However, there are several outstanding differences. Foremost is the relative dominance of the various arrivals: the surface waves clearly dominate the time series for the 0.4 and 2.0 source depths in the vertical and radial components (e.g., compare Figure 5-29 to 5-23 and 5-8); the increasing relative strength of the direct shear wave as a function of epicentral distance for the deep source (e.g., compare Figure 5-30 to 5-24 and 5-9); and the absence of any significant Love wave arrivals in the azimuthal components (e.g., compare Figure 5-34 to 5-13).

In summary, complete synthetic seismograms have been presented for point explosions and vertical strike-slip, vertical dip-slip and 45 degree dip-slip point dislocations. The results, as generated by the PROSE technique, represent the

complete response for each source type buried in the horizontally layered earth structure depicted in Table 5-3. Epicentral distances from 100 to 2000 km and source depths of 0.4, 0.8, 2.0, 5.0, 10.0 and 20.0 were considered in the calculations (results presented only at source depths of 0.4, 2.0 and 10.0 km). Normally dispersed surface waves and direct and multiply reflected/converted shear waves tend to dominate the response at these epicentral distances. Even at the largest epicentral distances of interest, it is possible to visually discriminate the characteristics of the time series from the different source-types considered in this study.

REFERENCES

- Aki, K., and Y. Tsai, "The Mechanics of Love Wave Excitation by Explosive Sources," J. Geophys. Res., 77, pp. 1452-1475, 1972.
- Applied Theory, Inc. (Dec. 1979). Time Histories of Force on a Closed Surface, Data Tape for Subcontract PSR-79-0191-1 under DNA001-79-6-0191.
- Apsel, R.J. (1979). Dynamic Green's Functions for Layered Media and Applications to Boundary-Value Problems, Ph.D. Thesis, University of California at San Diego, La Jolla, California 380 pp.
- Archambeau, C.B., and C. Sammis, "Seismic Radiation from Explosions in Prestressed Media and the Measurement of Tectonic Stress in the Earth," Rev. of Geophys. and Space Phys., 8, pp. 473-499, 1970.
- Bakun, W.H. and C.G. Bufe (1975). Shear-wave Attenuation Along the San Andreas Fault Zone in Central California, Bull. Seism. Soc. Am., 65, 2, 439-459.
- Bakun, W.H. and C.G. Bufe (1975). Body-Wave Spectra of Central California Earthquakes, Bull. Seism. Soc. Am., 66, 2, 363-384.
- Barnes, H., F.N. Houser and F.G. Poole (1963) Geologic Map of the Oak Spring Quadrangle, Nye Co., Nev.; Dept. of Interior, U.S. Geologic Survey
- Birch, F. and D. Bancroft (1938). Elasticity and Internal Friction in a Long Column of Granite, Bull. Seism. Soc. Am., 28, pp. 243-254.
- Boynton, G.R., J.L. Menschke and J.L. Vargo (1963) Aeromagnetic Map of the Tippipah Spring Quadrangle and Parts of Papoose Lake and Wheelbarrow Peak Quadrangles, NYC Co. Nev; Dept. of Interior, U. S. Geological Survey.
- deHoop, A.T. (1958). Representation Theorems for the Displacement in an Elastic Solid and Their Application to Elastodynamic Diffraction Theory, D.S. Thesis, Technische Hogeschool, Delft.
- Eringen, A.C., and E.S. Suhubi, Elastodynamics, Vol.II, Linear Theory, Academic Press, New York, 1975.
- Frazier, G.A., and C.M. Petersen, "3-D Stress Wave Code for the ILLIAC IV," Systems, Science and Software Report No. SSS-R-74-2103(1974).
- Fung, Y.C. (1965). Foundations of Solid Mechanics, Prentice Hall, Inc., Englewood Cliffs, N.J., 525 pp.
- Gutenberg, B. (1958). Attenuation of Seismic Waves in the Earth's Mantle: Bull. Seism. Soc. Am., 48, pp. 269-282.

- Harkrider, D.G., 1964. Surface waves in multilayered elastic media, Part I. Rayleigh and Love waves from buried sources in a multilayered elastic half-space, Bull. Seism. Soc. Am., 54, 627-680.
- Harkrider, D.G., 1970. Surface waves in multilayered elastic media, Part II. Higher mode spectra and spectral ratios from point sources in plane layered earth models, Bull. Seism. Soc. Am., 60, 1937-1987.
- Haskell, N.A., "Analytic Approximation for the Elastic Radiation from a Contained Underground Explosion," J. Geophy., 72, pp. 2583-2587, 1967.
- Hazlewood, R.M., D.L. Hegley and C.H. Miller (1963) U. S. Geological Survey Investigations of Yucca Flat, NTS--Part B Geophysical Investigation; tech-letter NTS 45, Park B; Dept. of Interior.
- Houser, F.N. and F.G. Poole, "Preliminary Geologic Map of the Climax Stock and Vicinity, Nye Co., Nev.," Map I-328, Misc. Geol. Inv. USGS, 1960.
- Kurita, T. (1975). Attenuation of Shear Waves Along the San Andreas Fault Zone in Central California, Bull. Seism. Soc. Am. 65, pp. 277-292.
- McDonald, F.J., F.A. Angona, R.L. Mills, R.L. Sengbush, R.G. Van Nostrand, and J.E. White (1958). Attenuation of Shear and Compression Waves in Pierre Shale, Geophysics, 23, pp. 421-439.
- Mueller, R.A., and J.R. Murphy, "Seismic Characteristics of Underground Nuclear Detonations, Part I. Seismic Spectrum Scaling, "Bull. Seism Soc. Am., 61, pp. 1675-1692, 1971.
- Olson, A. (1978). Synthesizing Ground Motion Using a Discrete Wave Number/Finite Element Representation, Abstr. in EOS, Trans. Am. Geophys. Union, 59, Dec. pp. 1128.
- O'Neill, M.E. and J.H. Healy (1973). Determination of Source Parameters of Small Earthquakes from P-Wave Rise Time, Bull. seism. Am., 63, 2, pp. 599-614.
- Perret, W. R., "Free-Field Particle Motion from a Nuclear Explosion in Salt, Part I: SALMON Event, VUF-3012, 1964.
- Rawson, Glen (Report in Progress), "Surface Observed Block Motions and Their Relations to Explosion Induced Spall," RDA/DNA Technical Report.
- Rossett, J.M. (1970). Fundamentals of Soil Amplification, In: J.R. Hanson (Editor), Seismic Design for Nuclear Power Plants, MIT Press, Cambridge, Mass., pp. 183-244.
- Silva, W. (1976) Body Waves in a Layered Anelastic Solid, Bull. Seism. Soc. Am., 66, 5, pp. 1539-1554.
- Silayeva, O.I. and O.G. Shamina (1960). Absorption of Ultrasonics in Granites, Bull. Acad. Sci. USSR, Geophys. Ser. (English Translation), pp. 899-903.

Sweet, J., "Dynamic Response of a Buried Cylindrical SWIS Simulation," Systems, Science and Software Report No. SSS-R-76-2948 (1976).

Sweet, J., G.A. Frazier and H.E. Read, "SWIS-SMI, A Nonlinear Finite Element Code with Application for Static or Dynamic Structure-Medium Interaction Problems," Systems, Science and Software Report No. SS-IR-76-2830, 1976.

Sweet, Joel, "SWIS Finite Element Computer Code -- Nonlinear Version," Del Mar Technical Associates Report DELTA-TR-77-005, May 1977.

Toksoz, M.N., and H.H. Kehler, "Tectonic Strain-Release Characteristics of CANNIKIN," Bull. Seism. Soc. A., 62, pp. 1425-1438, 1972.

White, J.E. (1965). Seismic Waves: Radiation, Transmission and Attenuation, McGraw Hill.

APPENDIX A
ANALYTIC SOLUTION TO THE INVERSION OF MURPHY'S MODEL

ANALYTIC SOLUTION TO THE INVERSION OF MURPHY'S MODEL

Parameters

Material

- ρ density
- β shear wave velocity
- α p-wave velocity

Murphy's Prescription

- R Elastic Radius
- p_{oc} Late time radial stress (σ_{rr}) at distance R
- $p = p_{os}/p_{oc} - 1$ Dimensionless change in radial stress where p_{os} is the initial step in radial stress at $r = R$.
- $\omega = \omega_0 = 2\beta/R$ Arbitrary combination of terms which is not consistent with Murphy but all right since γ is multiplied by ω_0 .
- γ Dimensionless parameter which allows for specialization of ω_0 to $2\beta/R$.

Murphy's empirical prescription of the radial stress at $r = R$.

$$\sigma_{rr}(R, t) = p_{oc} H(t) [pe^{-\omega\gamma t} + 1]$$

Convenience

$$x = r/R \quad \omega_d = \omega \sqrt{1 - \xi^2} = 2\beta/R \sqrt{1 - B^2/\alpha^2}$$

$$\xi = \beta/\alpha \quad B = p/[1 - 2\gamma\xi + \gamma^2] \quad \phi_\infty = Rp_{oc}/\rho\omega^2$$

Solution

Φ is the reduced displacement potential such that

$$u_r = \partial/\partial r \left(\frac{\Phi}{r} (t - r/\alpha) \right) = -\Phi/r^2 - 1/\alpha r \dot{\Phi}$$

$$\sigma_{rr} = \rho/r [\ddot{\Phi} + 2\omega\xi/x \dot{\Phi} + \omega^2/x^2 \Phi]$$

where $\dot{\phi}$ and $\ddot{\phi}$ denote total derivatives of the function ϕ with respect to $\tau = t - r/\alpha$.

$$RDP = r\phi \equiv \phi \quad \text{where} \quad u_r = \frac{\partial \phi}{\partial r}$$

Murphy's prescription is uniquely satisfied for

$$\frac{\phi(t)}{\phi_\infty} = 1 + Be^{-\gamma\omega t} - e^{-\xi\omega t} \left\{ [1+B] \cos \omega_d t + \frac{\xi}{\sqrt{1-\xi^2}} \left[1 + B \left(1 - \frac{\gamma}{\xi} \right) \right] \sin \omega_d t \right\}$$

giving

$$\frac{\dot{\phi}(t)}{\phi_\infty} = -B\gamma\omega e^{-\gamma\omega t} + e^{-\xi\omega t} \left\{ \gamma\omega B \cos \omega_d t + \frac{\omega}{\sqrt{1-\xi^2}} [1 + B(1-\xi\gamma)] \sin \omega_d t \right\}$$

and

$$\begin{aligned} \frac{\ddot{\phi}(t)}{\phi_\infty} = & B\gamma^2\omega^2 e^{-\gamma\omega t} + \omega^2 e^{-\xi\omega t} \left\{ [1 + B(1-2\gamma\xi)] \cos \omega_d t - \frac{\xi}{\sqrt{1-\xi^2}} \right. \\ & \left. [1 + B(1 + \frac{\gamma}{\xi} - 2\gamma\xi)] \sin \omega_d t \right\} \end{aligned}$$

which gives

$$\begin{aligned} u_r(r,t) \frac{r^2}{\phi_\infty} = & -1 - B(1 - 2\gamma\xi x) e^{-\gamma\omega(t-r/\alpha)} + e^{-\xi\omega(t-r/\alpha)} \\ & \left\{ [1 + B(1 - 2\gamma\xi x)] \cos \omega_d(t-r/\alpha) + \frac{\xi}{\sqrt{1-\xi^2}} [(1-2x)(1+B) \right. \\ & \left. + \gamma B(2x\xi - 1/\xi)] \sin \omega_d(t-r/\alpha) \right\} \end{aligned}$$

$$\frac{r\sigma_{rr}}{\rho\omega^2\phi_\infty} = \frac{1}{x^2} + B \left(\frac{1}{x^2} - \frac{2\gamma\xi}{x} + \gamma^2 \right) e^{-\gamma\omega(t-r/\alpha)} + e^{-\xi\omega(t-r/\alpha)} \left\{ \left(1 - \frac{1}{x^2} \right) \right.$$

$$\begin{aligned} & \left[1 + B \left(1 - \frac{2\gamma\xi}{(1+1/x)} \right) \right] \cos \omega_d(t-r/\alpha) - \frac{\xi(1-1/x)}{\sqrt{1-\xi^2}} \left[(1-1/x) + B(1-1/x) \right. \\ & \left. - 2\xi\gamma + \frac{\gamma}{\xi} (1 \mp 1/x) \right] \sin \omega_d(t-r/\alpha) \left. \right\} \end{aligned}$$

where ω is in radians/sec

$$\frac{\dot{\phi}(\omega)}{\phi_{\infty}} = \frac{-B\gamma\omega_0}{j\omega + \gamma\omega_0} + \frac{\gamma\omega_0 B(j\omega + \epsilon\omega_0)}{(j\omega + \epsilon\omega_0)^2 + \omega_d^2} + \frac{\omega_d\omega_0[1 + B(1 - \epsilon\gamma)]}{\sqrt{1-\epsilon^2} [(j\omega + \epsilon\omega_0)^2 + \omega_d^2]}$$

$$\frac{\dot{u}_r r^2}{\phi_{\infty}} = \gamma\omega_0 B(1 - 2\gamma\epsilon x) e^{-\gamma\omega(t-r/\alpha)} - e^{-\epsilon\omega_0(t-r/\alpha)} \left\{ (a_1\epsilon\omega_0 - a_2\omega_d) \right.$$

$$\left. \cos \omega_d(t-r/\alpha) + (a_2\epsilon\omega_0 + a_1\omega_d) \sin(\omega_d(t-r/\alpha)) \right\}$$

where

$$a_1 = 1 + B(1 - 2\gamma\epsilon x)$$

$$a_2 = \frac{\epsilon}{\sqrt{1-\epsilon^2}} [(1 + 2x)(1 + B) + \gamma B(2x\epsilon - 1/\epsilon)]$$

APPENDIX B

ONEDMAR -- A COMPUTER PROGRAM TO CALCULATE
ONE DIMENSIONAL MATERIAL RESPONSE

DELTA-R-78-019

ONEDMAR -- A COMPUTER PROGRAM TO CALCULATE
ONE-DIMENSIONAL MATERIAL RESPONSE

USER'S REFERENCE MANUAL

Joel Sweet
Robert A. Cecil

Del Mar Technical Associates
P.O. Box 1083
Del Mar, California 92014

April 1978

TABLE OF CONTENTS

<u>Section</u>	<u>Page</u>
I. INTRODUCTION.	B-1
II. GOVERNING EQUATIONS	B-2
III. CODE ORGANIZATION AND LOGIC FLOW CHART	B-5
3.1 Code Organization	B-5
3.2 Logic Flow Chart	B-5
IV. SUBROUTINE DESCRIPTIONS AND DIFFERENCE EQUATIONS	B-7
4.1 Main Program ONEDMR	B-7
4.2 Subroutine ABSUB	B-7
4.3 Subroutine CAP75.	B-9
4.4 PDP Element CMAIN	B-11
4.5 PDP Element CMAIN2.	B-12
4.6 Subroutine CONSTI	B-12
4.7 Subroutine CRACK	B-19
4.8 Subroutine CYCLES	B-24
4.9 Subroutine DUMP	B-26
4.10 Subroutine DUMPPT.	B-26
4.11 Subroutine EDIT	B-27
4.12 Subroutine GEN.	B-27
4.13 Subroutine INITEL	B-28
4.14 Subroutine MOTION	B-28
4.15 Subroutine PLOTOD	B-31
4.16 Function Subroutine PREL	B-32
4.17 Function Subroutine PRER	B-33
4.18 Function Subroutine PRESS.	B-33
4.19 Subroutine RESTAR	B-35
4.20 Subroutine REZONE	B-35
4.21 Subroutine SCALEO	B-35
4.22 Subroutine SPLOT.	B-36
4.23 Subroutine STATE.	B-36

TABLE OF CONTENTS

(CONT.)

<u>Section</u>	<u>Page</u>
4.24 Subroutine TNSLE.	B-41
4.25 Function Subroutine UDV	B-43
4.26 Subroutine VPLOT	B-43
V. INPUT REQUIREMENTS	B-44
VI. SAMPLE PROBLEM	B-57
VII. REFERENCES.	B-72
APPENDIX A	B-73

SECTION I

INTRODUCTION

Described herein is ONEDMAR — a computer program that calculates one-dimensional material response. Nonlinear (elastic-plastic, large deformation) dynamic behavior can be calculated in planar, cylindrical, or spherical geometry using finite difference analogs of the governing physical equations. The program may also be run in the linear mode. Additional features of the material response model include a tensile failure model for predicting material failure and a cap model for calculating the plastic flow of the material. The tensile failure model is described in Reference 1 and the cap model is described in References 2 through 4.

For the purposes of efficiency and cost reduction, a rezoning model has been included in ONEDMAR. This model, which is described in Reference 5, combines cells in regions of the problem mesh which become inactive as the problem time progresses. Previous documentation describing the adaptation of the rezoning model to ONEDMAR is included herein as Appendix A. Special editing features have also been included which allow on-line printer plots of mesh information at specified problem times and mesh variables as a function of time at specified mesh locations.

The governing equations used in ONEDMAR are described in Section II. Section III presents a brief description of the code organization and the overall flow chart of the program. The subroutines are described in Section IV. Difference equations are included in the subroutine descriptions where appropriate. Input requirements are presented in Section V and a sample problem is described in Section VI.

More detailed discussion of similar one-dimensional material response codes may be found in References 6 through 9.

SECTION II

GOVERNING EQUATIONS

The material deformation is assumed to be characterized by a single displacement component, $u(x,t)$, where x is the spatial coordinate parallel to the deformation and t is the time variable. The present analysis is generally nonlinear. Thus, the coordinates, x , translate in space according to the deformation history (which need not be small) and the stress-strain behavior (i.e., constitutive relationship) is generally nonlinear. The state of strain for planar, cylindrical, and spherical geometries is given by:

$$\text{Planar: } \epsilon_x = \frac{\partial u}{\partial x}, \epsilon_\theta = \epsilon_\phi = 0 \quad (1a)$$

$$\text{Cylindrical: } \epsilon_x = \frac{\partial u}{\partial x}, \epsilon_\theta = \frac{u}{x}, \epsilon_\phi = 0 \quad (1b)$$

$$\text{Spherical: } \epsilon_x = \frac{\partial u}{\partial x}, \epsilon_\theta = \epsilon_\phi = \frac{u}{x} \quad (1c)$$

The subscripts θ and ϕ refer to the directions orthogonal to the x -direction.

The conservation of momentum for the three geometric configurations is given by:

$$\rho \ddot{u} = \rho \frac{\partial^2 u}{\partial t^2} = \frac{\partial \sigma_x}{\partial x} + (c - 1) \frac{(\sigma_x - \sigma_\theta)}{x} \quad (2)$$

where ρ is the density, σ_i is the stress in direction i , and c is defined as:

$$c = \begin{cases} 1, & \text{planar geometry} \\ 2, & \text{cylindrical geometry} \\ 3, & \text{spherical geometry} \end{cases}$$

The conservation of energy is represented by the following equation:

$$\frac{\partial e}{\partial t} = v \left[S_x \frac{\partial \epsilon_x}{\partial t} + (c - 1) S_\theta \frac{\partial \epsilon_\theta}{\partial t} \right] - p \frac{\partial v}{\partial t} \quad (3)$$

The variable $e(x,t)$ is the internal energy per unit volume. The variable v is the relative volume and is related to the initial density, ρ_0 , by

$$v = \frac{\rho_0}{\rho} \quad (4)$$

The conservation of mass may be written as:

$$\frac{\partial v}{\partial t} = \frac{\partial \dot{u}}{\partial x} + (c - 1) \frac{\dot{u}}{x} \quad (5)$$

The pressure, P , and the deviatoric stresses, S_k , are defined as follows:

$$P = - \frac{1}{3} (\sigma_x + \sigma_\theta + \sigma_\phi) \quad (6)$$

and

$$S_k = \sigma_k + P \quad (7)$$

and where the k subscript refers to the x , θ and ϕ coordinates.

Pressures and deviatoric stress components are calculated using one of the following two methods: (1) a cap model which has been developed for plastic flow (References 2 through 4) or (2) a Hugoniot equation of state model coupled with a tensile failure/elastic-perfectly plastic model.

When using the cap model for material response a yield surface for the material is defined in terms of a failure envelope and a hardening cap. The failure envelope is a function of the stress tensors and stress deviators and the hardening cap is a function of the plastic volumetric strain in the material. ²⁻⁴

In the Hugoniot equation of state model the pressure is calculated by:

$$P = (A\lambda + B\lambda^2 + C\lambda^3) \left(1 - \frac{\Gamma\lambda}{2} \right) + \frac{\Gamma e}{v}$$

(8)

where (A, B, C) are material constants, Γ is the Gruneisen ration and λ is defined by

$$\lambda \equiv \frac{1}{V} - 1 \quad (9)$$

Material failure for this model is represented by the plasticity relation:

$$(\sigma_x - \sigma_\theta)^2 + (\sigma_\theta - \sigma_\phi)^2 + (\sigma_x - \sigma_\phi)^2 \leq 2Y^2 \quad (10)$$

where Y is the yield stress which is assumed to be a function of internal energy, e, and pressure, P:

$$Y = Y(e, P) \quad (11)$$

The specific functional form of Y may be found in Equations 30 and 31 of Section IV.

Tensile failure is modeled in ONEDMAR by introducing the tensile strength, σ_t , and using the technique defined in Reference 1 to adjust stresses and strains. Briefly, if any principal stress exceeds the tensile strength (plus an input overburden stress, P_b) it is reduced to the overburden stress through the introduction of a tensile failure porosity.

SECTION III

CODE ORGANIZATION AND LOGIC FLOW CHART

3.1 CODE ORGANIZATION

The ONEDMAR computer program is constructed in the traditional mode that is used for large hydrodynamic and structural analysis programs. A main program controls the flow of the calculation through one of the following two possible paths: (1) problem generation and calculation, or (2) problem restart and calculation. User-supplied input cards define the generation, calculation, and restart parameters.

The calculation sequences are divided into subroutines which control separate tasks such as calculating, editing, storing data or plotting results. Thus the program has a modular appearance and additional physical models or data manipulation tasks may be attached to the program with a minimum amount of interfacing problems.

Name commons are used to transfer mesh variables, constants, and program flags between subroutines. A maximum of 500 cell interfaces and 50 separate material layers may be used to define a problem mesh. These upper limits may be altered by a recompilation of the name commons /VAR/and /MC/ and redefining the size of the mesh and material variable arrays.

The version of ONEDMAR described herein requires approximately 36000 words of storage on the UNIVAC 1108 and is essentially machine independent.

3.2 LOGIC FLOW CHART

Figure 1 contains a logic flow chart which provides the user with an overview of the ONEDMAR computer program. The locations of the subroutines with respect to each other are indicated and brief descriptions of the main tasks accomplished in each of the subroutines are denoted.

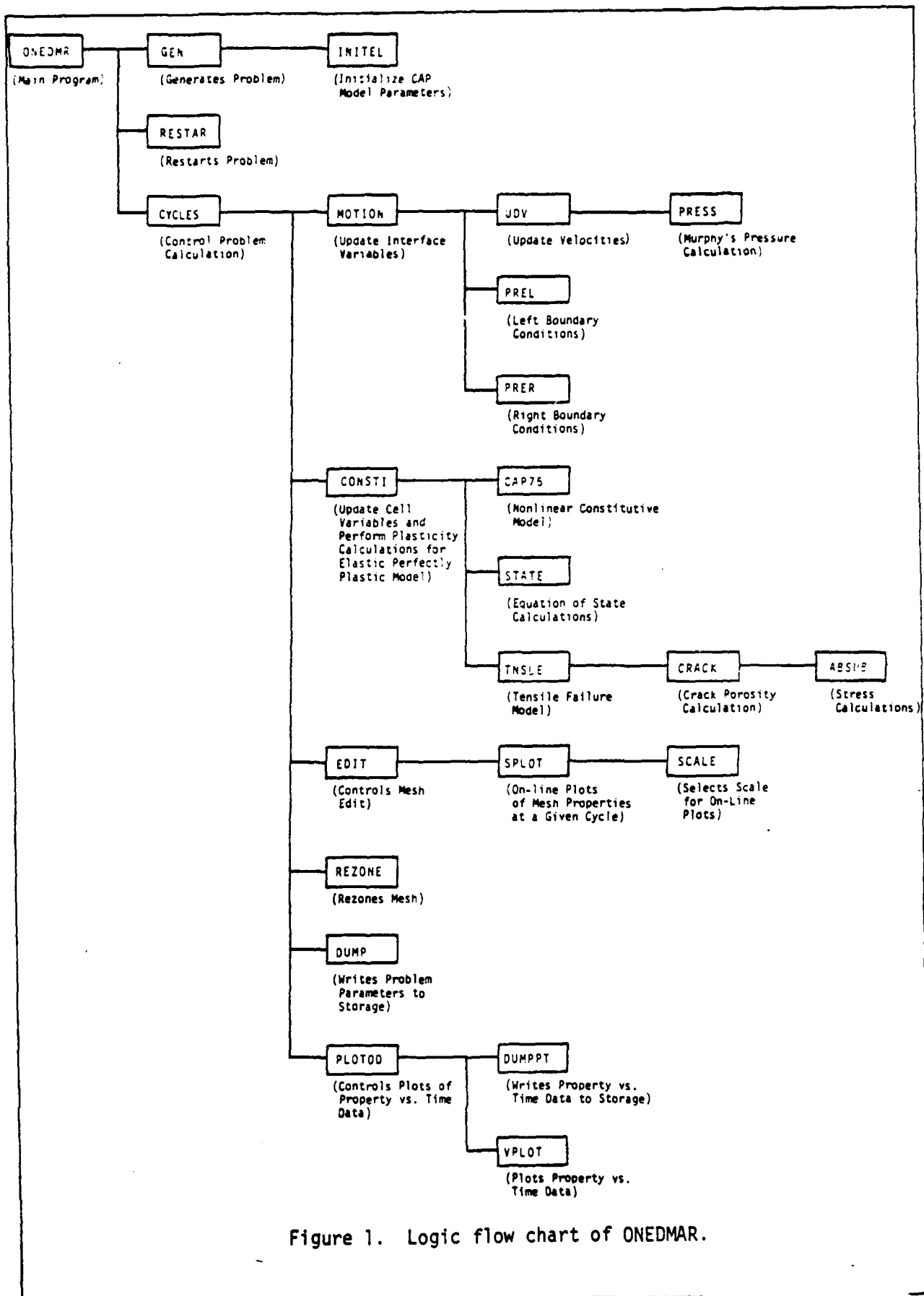


Figure 1. Logic flow chart of ONEDMAR.

SECTION IV

SUBROUTINE DESCRIPTIONS AND DIFFERENCE EQUATIONS

Brief descriptions of the main program and subroutines are presented in this section. The finite difference forms of the governing equations appearing in Section II are provided in the appropriate subroutines.

4.1 MAIN PROGRAM ONEDMR

ONEDMR is the main driver program which guides the code through its calculation sequence. The first step in the main program is to zero the name commons. Then a user-supplied card which contains an identifying description of the calculation is read and printed. The program then reads a user-supplied calculation type card which directs the code through one of the following two sequences: (1) the problem generation and calculation sequences, subroutines GEN and CYCLES, or (2) the problem restarting sequence, subroutines RESTAR and CYCLES. All other subroutines in the code are called from these subroutines. A normal exit from the code is made upon completion of either of the two sequences.

4.2 SUBROUTINE ABSUB

Subroutine ABSUB calculates the stress terms used in the tensile failure model described in subroutine TNSLE. There are two entry points in this subroutine, ACALC (before tensile failure) and BCALC (after tensile failure).

In ACALC, the principal stress terms are calculated as functions of the pressure and the deviatoric stress components as follows:

$$\sigma_x = -P + S_x \quad (12a)$$

$$\sigma_\theta = \sigma_x - (S_x - S_\theta) \quad (12b)$$

$$\sigma_{\phi} = -3P - \sigma_x - \sigma_{\theta} \quad (12c)$$

where

P = pressure at the time of the call to this subroutine

S_x, S_{θ} = deviatoric stresses

$\sigma_x, \sigma_{\theta}, \sigma_{\phi}$ = calculated principal stress.

In BCALC, the pressure and the deviatoric stresses are determined from the principal stresses:

$$P = - \frac{\sigma_x + \sigma_{\theta} + \sigma_{\phi}}{3} \quad (13a)$$

$$S_x = P + \sigma_x \quad (13b)$$

$$(S_x - S_{\theta}) = \sigma_x - \sigma_{\theta} \quad (13c)$$

where

$\sigma_x, \sigma_{\theta}, \sigma_{\phi}$ = principal stresses at the time of the call to this subroutine.

P = calculated pressure.

S_x, S_{θ} = calculated deviatoric stresses.

4.3 SUBROUTINE CAP75

Subroutine CAP75 contains a modified version of the CAP75 subroutine described in pages 17 through 19 of Reference 2. Detailed descriptions of the cap model are contained in References 2 through 4. A brief synopsis of the cap model is included herein for completeness; however, the reader should refer to the previously mentioned references for a detailed analysis of the cap model.

The cap model is a plasticity model for material response to compressive states of stress. The cap model is defined by a convex yield surface and a plastic strain rate vector that is normal to the yield surface in stress space. The yield surface is defined by means of a failure envelope and a hardening cap. The failure envelope is defined by:

$$\sqrt{J_2'} = F_F(J_1) \quad (14)$$

where

J_1 = the first invariant of the stress tensor.

J_2' = the second invariant of the stress deviator.

The hardening cap is defined by

$$\sqrt{J_2'} = F_C(J_1, \kappa) \quad \text{for } L(\kappa) \leq J_1 \leq X(\kappa) \quad (15)$$

where

κ = internal state variable that measures hardening as a function of the history of plastic volumetric strain.

$L(\kappa)$ = lower limit of cap in J_1 space.

$X(\kappa)$ = upper limit of cap in J_1 space.

The functional forms of Equations (14) and (15) included in this version of the cap model are as follows:

$$F_F(J_1) = A - Ce^{BJ_1} \quad (16)$$

$$F_C(J_1, \kappa) = \frac{1}{R} \left\{ [X(\kappa) - L(\kappa)]^2 - [J_1 - L(\kappa)]^2 \right\}^{1/2} \quad (17)$$

where

A, B, C, R = material parameters

and

$$X(\kappa) = \kappa - R \cdot F_F(\kappa) \quad (18a)$$

$$L(\kappa) = \begin{cases} \kappa & \text{for } \kappa < 0 \\ 0 & \text{for } \kappa \geq 0 \end{cases} \quad (18b)$$

The hardening parameter, κ , is a function of the plastic volumetric strain, $\bar{\epsilon}_V^p$, and is determined from the following equation:

$$\bar{\epsilon}_V^p = W \left[e^{DX(\kappa)} - 1 \right] \quad (19)$$

where

W, D = material parameters,

and $X(\kappa)$ is found using Equation (18a)

The plastic volumetric strain, $\bar{\epsilon}_V^p$, is found from the differential equations:

$$\dot{\bar{\epsilon}}_V^p = \begin{cases} \dot{\bar{\epsilon}}_V^p, & \text{for } \dot{\bar{\epsilon}}_V^p \leq 0 \text{ or } \kappa < 0, \\ 0, & \text{for } \dot{\bar{\epsilon}}_V^p > 0 \text{ and } \kappa \geq 0 \end{cases} \quad (20)$$

The quantity $\dot{\bar{\epsilon}}_V^p$ is a function of the state of stress (see Reference 2).

This subroutine is called from subroutine CONST1. Trial values of the stress components in the cell are calculated based upon elastic material behavior. These trial stresses are then tested against three yield criteria: (1) a tension limit, (2) a failure envelope, and (3) a hardening cap. If the trial stresses

do not exceed any of the criteria, the material behavior is elastic and the final stresses are set equal to the trial stresses. If the trial stresses exceed any of the three criteria, the stresses are recalculated using the appropriate failure model.

4.4 PDP ELEMENT CMAIN

CMAIN contains the name commons /VAR/, /CS/ and /MC/ which are used throughout the ONEDMAR code. These name commons are inserted into each subroutine as needed by INCLUDE statements when using the UNIVAC 1108 computer. When using the ONEDMAR code on other computers, the user must adhere to the resident operating system for inserting the name commons where they are needed.

The variables contained in /VAR/, /CS/ and /MC/ are used in the generation and calculation mode. After the calculation is completed and the variables in /VAR/ and /MC/ are written to the restart file, the storage space used by /VAR/ is re-used in the plotting subroutines (see PLOTOD and CMAIN2).

4.5 PDP ELEMENT CMAIN2

CMAIN2 contains the name commons /VAR/, /CS/ and /MC/. In this PDP element the common variables contained in /VAR/ store the data to be plotted after the calculation is completed. The original variables stored in /VAR/ (see CMAIN) are written over and thus destroyed.

The PDP element is only used in the plotting subroutine, PLOTOD, and the data storing subroutine, DUMPPT.

4.6 SUBROUTINE CONST1

Subroutine CONST1 controls the update of the state variables of the materials in the problem mesh. Calculations of all cell-centered properties are based upon the conservation of mass equation, Equation 5. and the user-selected constitutive model. This subroutine is called once for each calculational cycle

after the nodal quantities have been updated using the conservation of momentum equation in subroutine MOTION.

A loop over all active cells in the mesh contains the logic for updating the following cell-centered quantities to the end of the current time step:

- P: pressure.
- e: internal energy per unit volume.
- q: artificial viscous stress
- σ_x : stress in the longitudinal direction.
- σ_θ : stress in the tangential direction; actually
($\sigma_x - \sigma_\theta$) is calculated and saved.
- S_x : deviatoric stress in the longitudinal direction.

A choice of three constitutive models is available for calculating pressure, energy, and stress. An elastic perfectly plastic shear stress model coupled with a Hugoniot equation of state is the default constitutive model. If desired, the user may select to couple the default constitutive model with a tensile failure model which introduces porosity into the material when tensile failure occurs. This model is described in subroutines TENSLE and CRACK. A second alternative to the default constitutive model is a cap plasticity model, which is described in subroutine CAP75.

All of the constitutive models depend upon the updated strain and strain rate parameters resulting from the nodal locations and velocities which have been calculated in subroutine MOTION.

Strain rates are calculated by:

$$\dot{\epsilon}_{j+1/2}^{n+1/2} = \dot{\epsilon}_{x_{j+1/2}}^{n+1/2} + \dot{\epsilon}_{\theta_{j+1/2}}^{n+1/2} + \dot{\epsilon}_{\phi_{j+1/2}}^{n+1/2} \quad (21)$$

$$\dot{\epsilon}_{x_{j+1/2}}^{n+1/2} = \frac{\dot{u}_{j+1}^{n+1/2} - \dot{u}_j^{n+1/2}}{x_{j+1}^n - x_j^n} \quad \text{for } c = 1, 2, 3 \quad (22a)$$

$$\dot{\epsilon}_{\theta_{j+1/2}}^{n+1/2} = \begin{cases} 0 & \text{for } c = 1 \\ \frac{1}{2} \frac{\dot{u}_{j+1}^{n+1/2} + \dot{u}_j^{n+1/2}}{x_{j+1/2}^n} & \text{for } c = 2, 3 \end{cases} \quad (22b)$$

$$\dot{\epsilon}_{\phi_{j+1/2}}^{n+1/2} = \begin{cases} 0 & \text{for } c = 1, 2 \\ \dot{\epsilon}_{\theta_{j+1/2}}^{n+1/2} & \text{for } c = 3 \end{cases} \quad (22c)$$

where

$$c = \begin{cases} 1, \text{ planar geometry} \\ 2, \text{ cylindrical geometry} \\ 3, \text{ spherical geometry} \end{cases}$$

\dot{u} = nodal velocities.

x = spatial coordinates in the longitudinal direction.

and the "j" subscripts refer to the cell indices and the "n" superscripts refer to the time step indices.

Estimates of the deviatoric stresses at the end of the current time step are made assuming linear elastic behavior:

$$s_{x_{j+1/2}}^{n+1} = s_{x_{j+1/2}}^n + 2\mu \left(\dot{\epsilon}_{x_{j+1/2}}^{n+1/2} - \frac{1}{3} \dot{\epsilon}_{j+1/2}^{n+1/2} \right) \Delta t^{n+1/2} \quad (23a)$$

$$s_{\theta_{j+1/2}}^{n+1} = s_{\theta_{j+1/2}}^n + 2\mu \left(\dot{\epsilon}_{\theta_{j+1/2}}^{n+1/2} - \frac{1}{3} \dot{\epsilon}_{j+1/2}^{n+1/2} \right) \Delta t^{n+1/2} \quad (23b)$$

$$s_{\phi_{j+1/2}}^{n+1} = s_{\phi_{j+1/2}}^n + 2\mu \left(\dot{\epsilon}_{\phi_{j+1/2}}^{n+1/2} - \frac{1}{3} \dot{\epsilon}_{j+1/2}^{n+1/2} \right) \Delta t^{n+1/2} \quad (23c)$$

where μ is the shear modulus.

The relative volume, v , is obtained from the finite difference form of the conservation of mass equation, Equation 5:

$$\dot{v}_{j+1/2}^{n+1/2} = \frac{\dot{u}_{j+1}^{n+1/2} - \dot{u}_j^{n+1/2}}{x_{j+1}^n - x_j^n} + (c-1) \left(\frac{\dot{u}_{j+1}^{n+1/2} + \dot{u}_j^{n+1/2}}{2} \right) \frac{1}{x_{j+1/2}^n} \quad (24)$$

and the difference equation

$$v_{j+1/2}^{n+1} = v_{j+1/2}^n + \Delta t^{n+1/2} \dot{v}_{j+1/2}^{n+1/2} \quad (25)$$

When the default constitutive model is used, the equation of state subroutine, STATE, is called and the pressure and energy in the cell are updated to the end of the current time step (see Equations 55 through 62 in subroutine STATE). Upon returning from subroutine STATE, a check of the stress levels in the zone is made against the yield stress. These stress levels are obtained by substituting the estimated deviatoric stresses from Equation 23 and the calculated pressure, p^{n+1} , from the equation of state into Equation 7:

$$\bar{\sigma}_{kj+1/2}^{n+1} = \bar{s}_{kj+1/2}^{n+1} - p_{j+1/2}^{n+1} \quad (26)$$

where k denotes the x , θ and ϕ directions.

Since the deviatoric stresses are only estimates based upon the elastic material assumption, the stresses of Equation 26 must be checked against the yield strength, Y , to determine if the elastic assumption is valid. From Equation 10 a plasticity parameter, α , is defined:

$$2\alpha^2 = \left(\bar{\sigma}_{xj+1/2}^{n+1} - \bar{\sigma}_{\theta j+1/2}^{n+1} \right)^2 + \left(\bar{\sigma}_{\theta j+1/2}^{n+1} - \bar{\sigma}_{\phi j+1/2}^{n+1} \right)^2 + \left(\bar{\sigma}_{xj+1/2}^{n+1} - \bar{\sigma}_{\phi j+1/2}^{n+1} \right)^2 \quad (27)$$

The plasticity parameter is then compared to the yield strength and the state of stress is elastic if

$$\alpha < Y \quad (28)$$

or plastic if

$$\alpha \geq Y \quad (29)$$

A variable yield strength model is available to the user. This model allows the yield strength to vary with pressure and energy as follows:

$$Y = \begin{cases} Y' \left(1 - \frac{e_{j+1/2}^n}{e_m} \right), & \text{for } e_{j+1/2}^n \leq e_m \\ 0 & \text{for } e_{j+1/2}^n > e_m \end{cases} \quad (30)$$

where

$$Y' = \begin{cases} Y_o + Y_{m_o} \left(\frac{P_{j+1/2}^{n+1} + P_b}{P_m + P_b} \right) \left[2 - \left(\frac{P_{j+1/2}^{n+1/2} + P_b}{P_m + P_b} \right) \right], & \text{for } P_{j+1/2}^{n+1/2} < P_m \\ Y_o + Y_{m_o}, & \text{for } P_{j+1/2}^{n+1/2} \geq P_m \end{cases} \quad (31)$$

Y_o = initial value of the yield strength.

Y_{m_o} = final value of the yield strength reached at $P = P_m$.

P_b = overburden pressure.

P_m = value of pressure at which the yield strength reaches its final value.

e_m = melt energy per unit volume.

Figure 2 shows a schematic representation of Equations 30 and 31.

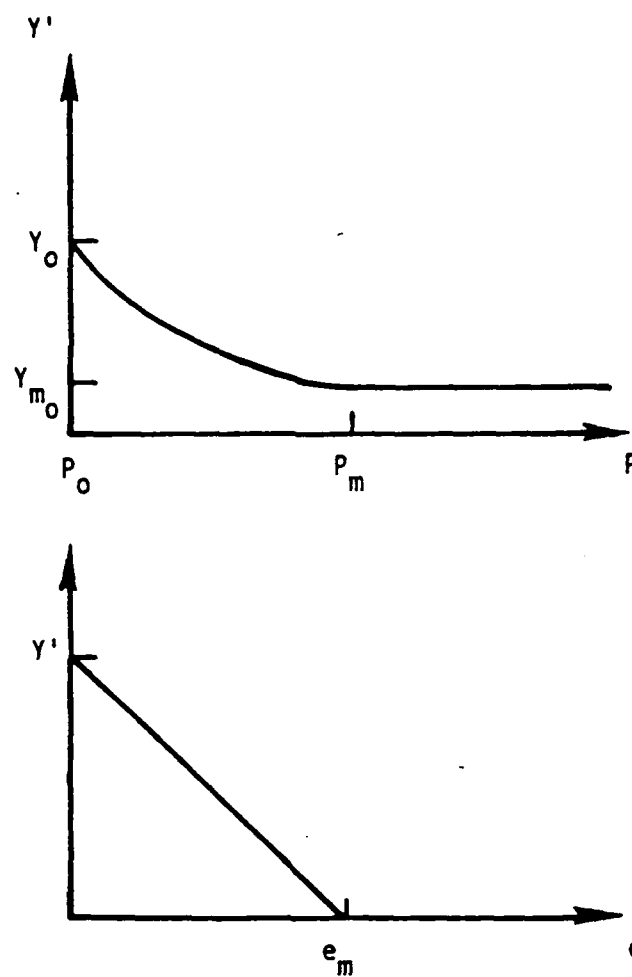


Figure 2. Yield strength model.

The user may negate the effects of Equations 30 and 31 by simply defining e_m to be a very large positive number and Y_{m_0} equal to zero on input.

If the inequality of Equation 29 is satisfied the trial values of the deviatoric stresses are modified by:

$$s_{x_{j+1/2}}^{n+1} = \frac{\bar{s}_{x_{j+1/2}}^{n+1}}{\left(\frac{\alpha}{\bar{Y}}\right)} \quad (32a)$$

$$s_{\theta_{j+1/2}}^{n+1} = \frac{\bar{s}_{\theta_{j+1/2}}^{n+1}}{\left(\frac{\alpha}{\bar{Y}}\right)} \quad (32b)$$

$$s_{\phi_{j+1/2}}^{n+1} = \frac{\bar{s}_{\phi_{j+1/2}}^{n+1}}{\left(\frac{\alpha}{\bar{Y}}\right)} \quad (32c)$$

The equation of state subroutine is then recalled for an additional update of the pressure.

When the tensile failure model is added to the above constitutive model the pressure is calculated in subroutine STATE using the trial values of the deviatoric stresses from Equation 23. Then this value of pressure and the trial values of the deviatoric stresses are supplied to subroutine TNSLE, which in turn recalculates the pressure and stresses according to the tensile failure model (see subroutine TNSLE for details). Upon returning from subroutine TNSLE, control is transferred to the shear stress failure model described above by Equations 27 through 31.

When the cap model of subroutine CAP75 is used all of the state variables are updated within the CAP75 subroutine. The cap plasticity model calculates the updated stress state and pressure in the material independent of the internal energy level in the material. Therefore, the conservation of energy equation is not required for solution and the internal energy in the cells remains at the initial level. The cap model in subroutine CAP75 requires that the trial

values of deviatoric stresses and the change in total strain rate for the current cycle, $\Delta \epsilon$, be supplied. The cap model then calculates the pressure, stress, and deviatoric stresses.

Upon completion of the calculation of the state of the material from any of the three constitutive models, the artificial viscous stress and the sound speed for the given cell are calculated. The viscous stress is composed of linear and quadratic components as follows:

$$q_{j+1/2}^{n+1/2} = \begin{cases} -a_{j+1/2}^{n+1/2} \rho_{o,j+1/2} C_L \left(u_{j+1}^{n+1/2} - u_j^{n+1/2} \right) \frac{\dot{v}_{j+1/2}^{n+1/2}}{v_{j+1/2}^{n+1/2}} ; & \text{for } \dot{v}_{j+1/2}^{n+1/2} > 0 \\ -a_{j+1/2}^{n+1/2} \rho_{o,j+1/2} C_L \left(u_{j+1}^{n+1/2} - u_j^{n+1/2} \right) \frac{\dot{v}_{j+1/2}^{n+1/2}}{v_{j+1/2}^{n+1/2}} \\ + \frac{\rho_{o,j+1/2}}{v_{j+1/2}^{n+1/2}} \left[C_Q \left(u_{j+1}^{n+1/2} - u_j^{n+1/2} \right) \dot{v}_{j+1/2}^{n+1/2} \right]^2 ; & \text{for } \dot{v}_{j+1/2}^{n+1/2} < 0 \end{cases} \quad (33)$$

where

C_L = linear viscosity coefficient.

C_Q = quadratic viscosity coefficient.

a = wave velocity determined in subroutine STATE.

ρ_o = initial density.

The final calculation done in this subroutine is for the minimum allowable time step for the next cycle, Δt_{\min} . The square of this time step is the quotient of the cell size squared divided by the square of the wave velocity. This quantity is used in the calculation of the time step in subroutine CYCLES. The wave velocity from subroutine STATE is modified to account for viscous damping. The minimum time step term is found by:

$$\Delta t_{\min}^2 = \text{Min} \left\{ \frac{(x_{j+1}^{n+1/2} - x_j^{n+1/2})^2}{(a_{j+1/2}^{n+1/2})^2 (1 + 4C_\ell^2) + \frac{64C_q^2 v_{j+1/2}^{n+1/2} q_{j+1/2}^{n+1/2}}{\rho_{o_{j+1/2}}}} \right\} \quad (34)$$

where the $\text{Min}\{ \}$ designation implies that the bracketed term is calculated for each cell in the mesh and the minimum value is saved.

4.7 SUBROUTINE CRACK

Subroutine CRACK controls the update of the inelastic strains which are introduced into cells which experience tensile failure. This subroutine is called from subroutine TNSLE which controls the entire tensile failure model calculation.

This subroutine contains three entry points from which calculations are initiated.

- (1) CRACK — called from subroutine TNSLE when a cell has undergone tensile failure on a previous cycle and non-zero values of the inelastic strains are still present in the cell.
- (2) CR1 — called when a cell undergoes tensile failure on the current cycle in the longitudinal, x , direction and/or in the two tangential directions, θ and ϕ . Prior to the current cycle the cell may never have experienced tensile failure or may have completely "healed" from a tensile failure; i.e., all cracks have closed and the inelastic strains in all directions are zero.
- (3) CR2 — called when a cell undergoes tensile failure on the current cycle in the one or both of the tangential directions, θ or ϕ . The same conditions on the previous cycle as described above in CR1 apply for this call to CR2.

Once tensile failure in a cell is detected in subroutine TNSLE and control transfers to CRACK a testing procedure is initiated which determines

the direction or directions of crack propagation. This testing procedure checks for the existence of previous cracks in each direction and for the stresses exceeding the tensile strength in each direction when cracks do not exist on the previous cycle. Based upon the results of this testing procedure, control transfers to one of the following eight sections for updating the inelastic strains, E , and the principal stresses, σ .

1. Crack in x Direction Only

- Conditions: (1) $E_x^n > 0$ and $E_\theta^n = E_\phi^n = 0$; $\bar{\sigma}_\theta^{n+1} < \sigma_{limit}$ and $\bar{\sigma}_\phi^{n+1} < \sigma_{limit}$: previous crack in x direction.
- (2) $E_x^n = E_\theta^n = E_\phi^n = 0$; $\bar{\sigma}_x^{n+1} > \sigma_{limit}$ and $\bar{\sigma}_\theta^{n+1} < \sigma_{limit}$, and $\bar{\sigma}_\phi^{n+1} < \sigma_{limit}$: new crack or reinitiated crack in the x direction.

The inelastic strain in the x direction is updated by

$$E_x^{n+1} = E_x^n + \Delta E_x^{n+1} \quad (35)$$

where

$$\Delta E_x^{n+1} = \frac{f_r \bar{\sigma}_x^{n+1}}{K + \frac{4}{3} \mu}$$

f_r = relaxation factor defined in subroutine TNSLE.

K = effective bulk modulus calculated in subroutine CONST1.

μ = effective shear modulus calculated in subroutine CONST1.

If the strain calculated by Equation 35 is less than zero, the crack in the x direction has completely closed on the current cycle. The value of the

strain, E_x^{n+1} , is then reset to zero and the strain increment, ΔE_x^{n+1} , is set equal to $-E_x^n$.

The principal stresses are calculated by:

$$\sigma_x^{n+1} = \tilde{\sigma}_x^{n+1} - \left(K + \frac{4}{3}\mu\right)\Delta E_x^{n+1} \quad (36a)$$

$$\sigma_\theta^{n+1} = \tilde{\sigma}_\theta^{n+1} - \left(K - \frac{2}{3}\mu\right)\Delta E_x^{n+1} \quad (36b)$$

$$\sigma_\phi^{n+1} = \tilde{\sigma}_\phi^{n+1} - \left(K - \frac{2}{3}\mu\right)\Delta E_x^{n+1} \quad (36c)$$

where

$\tilde{\sigma}$ = principal stress calculated in subroutine CONST1 assuming elastic behavior.

Based on these updated principal stresses the deviatoric stresses and the pressure are recalculated by a call to subroutine ABSUB (entry BCALC).

2. Crack in the θ Direction Only

The conditions for this case are the same and the update of the strain, principal stresses, deviatoric stresses and pressure are accomplished in the same manner as described in Section 1 if the x and θ subscripts are interchanged throughout.

3. Crack in the ϕ Direction Only

The first condition for this case is the same and the update of the strain, principal stresses, deviatoric stresses and pressure are accomplished in the same manner as described in Section 1 if the x and ϕ subscripts are interchanged throughout. The second condition for this case may not be satisfied physically since $\sigma_\phi < \sigma_\theta$.

4. Crack in the x and θ Directions but not the ϕ Direction

Conditions: $E_x^n > 0$ and $E_\theta^n > 0$ and $E_\phi^n = 0$; $\sigma_\theta^{n+1} < \sigma_{limit}$.

The inelastic strains are updated by:

$$E_x^{n+1} = E_x^n + \Delta E_x^{n+1} \quad (37)$$

and

$$E_\theta^{n+1} = E_\theta^n + \Delta E_\theta^{n+1} \quad (38)$$

where

$$\Delta E_x^{n+1} = \frac{f_r (C_4 \bar{\sigma}_x^{n+1} - C_2 \bar{\sigma}_\theta^{n+1})}{C_1 C_4 - C_2 C_3}$$

$$\Delta E_\theta^{n+1} = \frac{f_r (C_1 \bar{\sigma}_\theta^{n+1} - C_3 \bar{\sigma}_\phi^{n+1})}{C_1 C_4 - C_2 C_3}$$

$$C_1 = C_4 \equiv K + \frac{4}{3} \mu$$

$$C_2 = C_3 \equiv K - \frac{2}{3} \mu$$

The strains calculated by Equations 37 and 38 have a minimum value of zero. The principal stresses are calculated by:

$$\sigma_x^{n+1} = \bar{\sigma}_x^{n+1} - C_1 \Delta E_x^{n+1} - C_2 \Delta E_\theta^{n+1} \quad (39a)$$

$$\sigma_\theta^{n+1} = \bar{\sigma}_\theta^{n+1} - C_3 \Delta E_x^{n+1} - C_4 \Delta E_\theta^{n+1} \quad (39b)$$

$$\sigma_{\phi}^{n+1} = \sigma_{\phi}^{n+1} - C_3 \Delta E_x^{n+1} - C_2 \Delta E_{\theta}^{n+1} \quad (39c)$$

Deviatoric stresses and the pressure are now calculated in subroutine ABSUB using these updated principal stresses.

5. Cracks in the x and ϕ Directions but not the θ Direction

The conditions for this case are the same and the update of the strains, principal stresses, deviatoric stresses and pressure are accomplished in the same manner as described in Section 4 if the θ subscript is interchanged with the ϕ subscript throughout.

6. Cracks in the θ and ϕ Directions but not the x Direction

The conditions for this case are the same and the update of the strains, principal stresses, deviatoric stresses and pressure are accomplished in the same manner as described in Section 4 if the x subscript is replaced by the θ subscript, if the θ subscript is replaced by the ϕ subscript, and if the ϕ subscript is replaced by the x subscript throughout.

7. Cracks in All Three Directions

Conditions: $E_x^n > 0$ and $E_{\theta}^n > 0$ and $E_{\phi}^n > 0$.

In this case the inelastic strains are updated by

$$E_i^{n+1} = E_i^n + \frac{1}{3} \left[(E_x^n + E_{\theta}^n + E_{\phi}^n) - \frac{(p^{n+1} + p_b)}{K} \right] \quad (40)$$

where

i = x, θ , or ϕ directions

p_b = overburden pressure.

The pressure is then reset to equal $-P_b$ and control returns directly to subroutine TNSLE where the deviatoric stresses are set equal to zero.

4.8 SUBROUTINE CYCLES

Subroutine CYCLES contains the main calculation loop in which subsequent subroutines are called for updating all nodal and cell-centered variables in the problem mesh. In addition to controlling the update of the mesh variables through the time steps of the problem, editing and data storing functions are performed.

In the main calculation loop, subroutine MOTION and CONSTI are called every cycle. Subroutine MOTION calculates the displacement and velocity of each node in the active mesh. Subroutine CONSTI controls the update of all cell-centered quantities such as stress, pressure, internal energy and material yield parameters. A test is then made for calling the rezoning subroutine which is used to restructure the mesh to minimize the number of zones in the active mesh. The next step is to calculate the time step for the next cycle, $\Delta t^{n+1/2}$. Time steps used in the problem may be controlled by the user input information or calculated internally using the Courant stability criterion. The equations which control the time steps follow:

$$\Delta t^{n+1/2} = \Delta t_0, \quad \text{for } \Delta t_0 \leq \Delta t_{\min} \quad (41)$$

$$\text{and } N_{\text{CYCLE}} < N_0$$

where

$$\Delta t_0 = \text{initial time step specified by user input (DINT)}$$

$$\Delta t_{\min} = \text{minimum time step allowed during the calculations as specified by user input (DTMIN)}$$

$$N_{\text{CYCLE}} = \text{current cycle number}$$

N_0 = last cycle in which the time step is fixed at Δt_0 (NCYCTO)

Equation 41 is used to insure that a fixed time step is used for a specified number of cycles. This option allows the user to control the time step exactly and is often used during the early stages of a calculation to insure against instabilities. Once the calculation has progressed to a cycle which is greater than N_0 , the time step is updated using the Courant stability criterion. A trial value of the time step, $\Delta t_{COUR}^{n+1/2}$, is calculated by:

$$\Delta t_{COUR}^{n+1/2} = C \cdot \sqrt{\Delta t_{min}^2} \quad (42)$$

where

C = Courant stability factor.

Δt_{min}^2 = minimum value of the cell size squared divided by the wave velocity as calculated in subroutine CONST1.

The trial value of the time step, $\Delta t_{COUR}^{n+1/2}$, is then compared to the time step on the previous cycle, $\Delta t^{n-1/2}$, and the time step for the current cycle, $\Delta t^{n+1/2}$, is determined as follows:

$$\Delta t^{n+1/2} = \Delta t_{COUR}^{n+1/2}, \quad \text{if } \Delta t_{COUR}^{n+1/2} < 1.1 \Delta t^{n-1/2} \quad (43)$$

$$\Delta t^{n+1/2} = 1.1 \Delta t_{COUR}^{n+1/2}, \quad \text{if } \Delta t_{COUR}^{n+1/2} \geq 1.1 \Delta t^{n-1/2} \quad (44)$$

The next step in the main calculation loop is the calculation and storage of any mesh data that will be plotted and/or saved at the completion of the calculation. The mesh variables displacement, velocity, radial and tangential stresses, are saved for nodal or cell indices denoted by the input variable JSEL. These variables are saved at the problem times which are controlled by the user input variable TPEDIT. Storage of the saved information is done on file NTAPE.

The last two steps in the main calculation loop are the calls to subroutines DUMP and EDIT. Subroutine DUMP writes all problem variables (name commons /VAR/ and /MC/) to a storage file for use in the problem restart procedures. The call to DUMP is controlled by the user input variable NRESTR. Subroutine EDIT provides a print of the mesh variables at the current problem time. Calls to EDIT are dependent upon the user input variables NEDIT, NREZ, and DTEDIT.

The main calculation loop is exited when the problem reaches a maximum problem time allowed, TMAX, or a maximum problem cycle allowed, KSTOP. Upon exiting, a final call to DUMP is made if the last cycle was not previously stored during the main calculation loop. Subroutine PLOTOD is then called if data has been saved for plotting.

4.9 SUBROUTINE DUMP

When called, this subroutine writes the contents of the name commons /VAR/ and /MC/ on a storage device (tape or disk). Non-formatted writes are made on the storage unit number determined by MTAPE and a message is printed each time the writing procedure is activated.

4.10 SUBROUTINE DUMPPT

When called, this subroutine writes the plot data contained in the CMAIN2 version of the name commons /VAR/ and /MC/ on a storage device (tape or disk). Non-formatted writes are made on the storage unit number designated as MDTAPE and a message is printed each time the writing procedure is activated. The stored plot data can then be read by a separate computer code and analyzed in accordance with the needs of the user. An example of a computer code which analyzes time histories of displacements and velocities is ANALYZ which is described in Reference 10.

4.11 SUBROUTINE EDIT

Subroutine EDIT provides a print of cell and nodal properties for the mesh at the current problem time. The calling of EDIT is controlled by subroutine CYCLES. Properties are printed for the first node and cell ($J = 1$) and for each NPRINT nodes and cells after the first. The variable NPRINT is controlled by input and has a default value of 1 which causes a print of the entire mesh. The following properties are currently printed in the mesh edit:

J:	node and cell index
u:	node displacement
\dot{u} :	node velocity
σ_x :	cell stress in longitudinal (radial) direction
σ_θ :	cell stress in the tangential direction
P:	cell pressure
q:	cell viscous stress
e:	cell specific internal energy
E_x :	tensile strain in the x direction
E_θ :	tensile strain in the θ direction
E_ϕ :	tensile strain in the ϕ direction
YSS:	number of last cycle at which cell was in plastic state
MPN:	material layer number
JBF:	node and cell index at start of calculation, NCYCLE = 0

An additional feature of this subroutine is to provide on-line plots of stress and/or velocity versus displacement at the problem time at which this subroutine is called. Selection of the desired plots are accomplished by the input variables IOLS and IOLV. (See Section V for the description of the required input.)

4.12 SUBROUTINE GEN

This subroutine controls the initial generation of a problem to be calculated by the ONEDMAR code. The problem is described by the user-supplied input cards. A complete description of the required and optional input

cards is presented in Section V. Where data are omitted by the user on the input cards, appropriate default values are assigned to the program control variables.

The variables defined by the user, the program-defined default variables and the descriptive titles are printed by this subroutine to provide the user with a check against the intended input data.

Mesh generation and material description variables are initialized and the problem is readied for the first calculational cycle. Subroutine INITEL is called by this subroutine to initialize the constitutive cap model parameters.

Upon successful completion of the generation procedures, control returns to the main program, ONEDMAR.

4.13 SUBROUTINE INITEL

Subroutine INITEL initializes two cap model parameters prior to the first call to subroutine CAP75. The parameters are FCUT and ELSTRT. FCUT represents the value of J_1 , for which $F_f(J_1) = 0$ where J_1 is the first invariant of the stress tensor and $F_f(J_1)$ represents the functional form of the failure envelope. ELSTRT is the value of κ which corresponds to the initial value of $X(\kappa)$ (input variable XN(1) on input card 10). The parameter κ is an internal state variable that measures material hardening as a function of the time history of the plastic volumetric strain in the material, and the function $X(\kappa)$ defines the range of the cap.

4.14 SUBROUTINE MOTION

Subroutine MOTION updates the velocity and displacement of all nodes to the current problem time. Displacements, u , are calculated from velocities, \dot{u} , and velocities are calculated from accelerations, \ddot{u} , using the following explicit analogs:

$$u_j^{n+1} = u_j^n + \Delta t^{n+1/2} \dot{u}_j^{n+1/2} \quad (45)$$

$$\dot{u}_j^{n+1/2} = \dot{u}_j^{n-1/2} + \Delta t^n \ddot{u}_j^n \quad (46)$$

where the j subscript refers to the node index and the n superscripts refer to the number of the time integration step or cycle number. The accuracy of this time integration scheme is proportional to the square of the time step, $(\Delta t)^2$. The time steps in Equations 45 and 46 are defined as:

$$\Delta t^{n+1/2} = t^{n+1} - t^n \quad (47)$$

and

$$\Delta t^n = \frac{t^{n+1} - t^{n-1}}{2} \quad (48)$$

These time steps are calculated in subroutine CYCLES using Courant stability analysis and user input parameters.

The acceleration, \ddot{u}_j^n , used in Equation 46 is obtained by rewriting the conservation of momentum equation, Equation 2, as follows:

$$\ddot{u} = \frac{1}{\rho} \left(\frac{\partial \sigma_x}{\partial x} \right) + (c - 1) \left(\frac{\sigma_x - \sigma_\theta}{\rho x} \right) \quad (49)$$

where

ρ = density of material

σ_x = stress in longitudinal direction

σ_θ = stress in radial direction

$$c = \begin{cases} 1, & \text{for plane geometry} \\ 2, & \text{for cylindrical geometry} \\ 3, & \text{for spherical geometry} \end{cases}$$

x = spatial coordinate parallel to the direction of material deformation

Differencing Equation 49 yields:

$$\ddot{u}_j^n = \frac{(\sigma_{x_{j+1/2}}^n + q_{j+1/2}^n) - (\sigma_{x_{j-1/2}}^n + q_{j-1/2}^n)}{\left(\frac{\rho_{j+1/2}^n \Delta x_{j+1/2}^n + \rho_{j-1/2}^n \Delta x_{j-1/2}^n}{2} \right)} + \frac{(c-1)}{2} \left(\frac{\sigma_{x_{j+1/2}}^n - \sigma_{\theta_{j+1/2}}^n}{\rho_{j+1/2}^n x_{j+1/2}^n} + \frac{\sigma_{x_{j-1/2}}^n - \sigma_{\theta_{j-1/2}}^n}{\rho_{j-1/2}^n x_{j-1/2}^n} \right) \quad (50)$$

where

$$\Delta x_{j+1/2}^n = x_{j+1}^n - x_j^n$$

$$x_{j+1/2}^n = \frac{x_{j+1}^n + x_j^n}{2}$$

q = viscous stress (calculated in subroutine CONST1)

Two special cases for calculating the acceleration by Equation 50 are considered. These cases concern the left and right boundaries of the problem mesh. For the left boundary, $j = 1$, Equation 50 becomes

$$\ddot{u}_j^n = \frac{\sigma_{x_{j+1/2}}^n + q_{j+1/2}^n - \sigma_{\text{LEFT}}^n}{\left(\frac{\rho_{j+1/2}^n \Delta x_{j+1/2}^n}{2} \right)} + \frac{(c-1)}{2} \left(\frac{\sigma_{x_{j+1/2}}^n - \sigma_{\theta_{j+1/2}}^n}{\rho_{j+1/2}^n x_{j+1/2}^n} \right) \quad (51)$$

where σ_{LEFT}^n is the externally applied stress which is determined in function subroutine PREL. If a fixed left boundary is specified by input, Equation 51 is bypassed and the velocity and displacement of node 1 remain at the constant values which were initialized during the generation procedures.

For the right boundary, two options are available. The first is a fixed boundary, in which case, $\ddot{u}^n = 0$ and the velocities and displacements remain at their initial values. The second case is a user-specified boundary

stress, σ_{RIGHT}^n , which is calculated in function subroutine PRER. In this case Equation 50 becomes:

$$\ddot{u}_j^n = \frac{\sigma_{\text{RIGHT}}^n - \sigma_{x_{j-1/2}}^n - q_{j-1/2}^n}{\left(\frac{\rho_{j-1/2}^n \Delta x_{j-1/2}^n}{2} \right)} + \frac{(c-1)}{2} \left(\frac{\sigma_{x_{j-1/2}}^n - \sigma_{\theta_{j-1/2}}^n}{\rho_{j-1/2}^n x_{j-1/2}^n} \right) \quad (52)$$

In addition to updating the velocities and displacements of the nodes, the cell sizes and locations of the centers of the cells are updated.

The user also has the option of specifying that the calculation be accomplished in a linear manner, i.e., the displacements are not updated. This is accomplished by bypassing the calculation of Equation 45.

4.15 SUBROUTINE PLOTOD

Subroutine PLOTOD controls the collection, plotting and storing of mesh property versus time data. These data are stored by subroutine CYCLES during the mesh update calculations. The mesh properties for which time histories are saved are nodal displacement and velocity and cell radial and tangential stresses.

Through the use of user-selected input flags, the time histories of interest are collected and stored for on-line plotting and/or data analysis by an independent computer program. The input variables NPLOTS and NP control the number of time histories to be collected and the frequency of data points to be collected for each history.

For each time history requested, an input card (Section V — Card 28) is read which provides the cell or node number, NCPLT, the variable of interest, NTYPE, and a flag which turns on the on-line plot request, IVPLT. Data for more than one variable may be collected for any given cell index.

Subroutine DUMPTT is called to store the collected data and subroutine VPLOT is called for each time history to be plotted.

4.16 FUNCTION SUBROUTINE PREL

This function subroutine calculates the pressure boundary condition on the left end of the problem mesh. The calculated pressure is returned to subroutine MOTION for use in the momentum equations. The current version of PREL contains a generalized linear time-dependent pressure input condition which is controlled by user input through the PRL and TL arrays in the /MC/name common and a call to subroutine PRESS which calculates cavity pressures according to a specialized seismic source function.

A typical pressure-time history input is schematically shown in Figure 3.

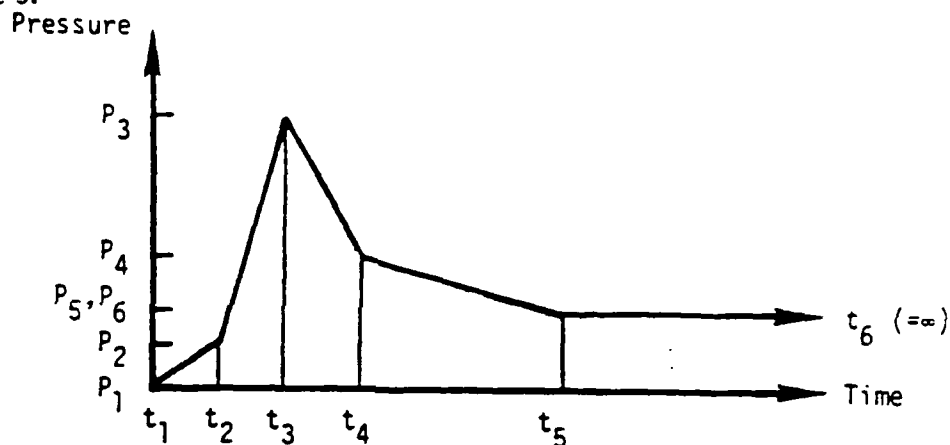


Figure 3. Sample pressure-time history input for subroutine PREL.

The values of t_1 through t_6 and P_1 through P_6 are input into the TL and PRL arrays. (Note: in the example, TL(6) would be input as a very large number.) Pressures are calculated by linear interpolation of the input data at the problem time which is transferred to PREL by a calling argument.

An additional option which may be used in this function subroutine is to multiply the pressures calculated from the above data by the factor, F , which is defined by:

$$F = \begin{cases} \frac{NCYCLE}{NCYCRL} & \text{for } NCYCL < NCYCRL \\ & \text{and } IRAMPL \neq 0 \\ 1. & \text{for } NCYCLE \geq NCYCRL \\ & \text{or } IRAMPL = 0 \end{cases} \quad (53)$$

where NCYCRL is defined by input and NCYCLE is the current cycle number. This option is activated by defining the variable IRAMPL to be a non-zero integer and defining the variable NCYCRL to be equal to the number of cycles required for the pressures to reach their calculated values. This option essentially provides a ramping effect to the calculated pressures.

4.17 FUNCTION SUBROUTINE PRER

This function subroutine calculates the pressure boundary condition on the right end of the problem mesh. The calculated pressure is returned to subroutine MOTION for use in the momentum equations. The current version of PRER contains the same generalized linear time-dependent pressure input condition described in function subroutine PREL. In this function subroutine input variables, PRR, TR, NCYCRR, and IRAMPR are used for the input variable corresponding to PRL, TL, NCYCRL, and IRAMPL in function subroutine PREL.

4.18 FUNCTION SUBROUTINE PRESS

Function subroutine PRESS calculates the pressure applied at the elastic radius from a nuclear explosion based upon the seismic source function for underground detonations developed by Murphy in Reference 11. This special driving pressure is selected by use of the input flag ISPECL which is set by the user (see card 11 - Section V). This function subroutine is called by the function subroutine PREL which controls the left boundary pressure as a function of time calculation.

In Murphy's model the explosion produced cavity pressure, P , is calculated as a function of time, t , by:

$$P = P_{0c} \left(\frac{r_{e1}}{r_c} \right) \left[c_1 + c_2 e^{-\gamma \omega_0 t} + (c_3 \cos \omega_d t + c_4 \sin \omega_d t) e^{-\xi \omega_0 t} \right] \quad (54)$$

where

r_{el} = elastic radius

r_c = cavity radius

P_{oc} = late time pressure at elastic radius

$$\omega_o = \frac{2\beta}{r_{el}}$$

$$\omega_d = \omega_o \left(1 - \frac{\beta^2}{\alpha^2}\right)^{1/2}$$

β = s-wave velocity

α = p-wave velocity

$$\xi = \frac{\beta}{\alpha}$$

γ = material constant chosen such that $\gamma\omega_o = \alpha'$ where α' defines the decay rate of the pressure function.

$$C_1 = \frac{1}{x^2} \text{ where } x = \frac{r_c}{r_{el}}$$

$$C_2 = B \left[C_1 + \gamma^2 - \frac{2\gamma\xi}{x} \right]$$

$$C_3 = (1 - C_1) \left\{ 1 + B \left[1 - \frac{2\gamma\xi}{(1 + \frac{1}{x})} \right] \right\}$$

$$\dot{C}_4 = \frac{-\xi(1 - \frac{1}{x})}{\sqrt{1 - \xi^2}} \left[\left(1 - \frac{1}{x}\right) + B \left\{ \left(1 - \frac{1}{x}\right) - \gamma \left[2\xi - \frac{(1 + \frac{1}{x})}{\xi} \right] \right\} \right]$$

$$B = \frac{\left(\frac{P_{os}}{P_{oc}} - 1 \right)}{(1 + \gamma^2 - 2\gamma\xi)}$$

P_{0_s} = initial pressure at elastic radius.

4.19 SUBROUTINE RESTAR

This subroutine controls the restarting procedure for a previously defined problem whose variables have been saved on a storage unit. User-supplied input cards which are described in detail in Section V are read and the data from these cards are printed as a check for the user.

The storage unit, tape or file, is searched for the restart cycle defined by the user and when found, the data is transferred from the storage unit to the common arrays in the code. Upon successful collection of the restart data, control returns to the main program so that the problem calculation may resume with the subsequent call to subroutine CYCLES.

4.20 SUBROUTINE REZONE

Subroutine REZONE combines mesh cells in order to reduce calculation time and costs. A detailed discussion of the development of the rezoning model for ONEDMAR has been previously documented by memorandum (Reference 12). The text of this memorandum is included herein as Appendix A.

4.21 SUBROUTINE SCALEO

Subroutine SCALEO is called to determine the range, grid intervals, and grid values for an array (X) which is to be plotted by subroutine SPLOT.

A simple search of the array to be plotted yields the minimum and maximum values, X_1 and X_2 respectively. Two integer coefficients, a and b, and an integer exponent, N, are determined such that

$$a \times 10^N \leq X_1 < X_2 \leq b \times 10^N$$

and such that the interval $(b - a) \times 10^N$ can be subdivided into an integral number of intervals (≤ 12) with subinterval size of 1, 2, or 5×10^N .

Subroutine SCALEO was adapted to ONEDMAR from the RIP code (see Reference 8).

4.22 SUBROUTINE SPLOT

Subroutine SPLOT produces a one-page, on-line printer plot of any arbitrary Y array vs any arbitrary X array. The data arrays to be plotted are transferred through calling arguments as are the appropriate titles, cycle numbers, and problem times which appear on the plots.

Maximum and minimum plot values and grid intervals are determined by subroutine SCALEO. The framing is then set up with grid intervals and the locations for the data points to be plotted are calculated using base six arithmetic with positional notation representing characters. The plot is printed, starting at the top of the page and proceeding downward one row at a time. The plot array is unpacked one row at a time and printed with title, framing and/or grid values that are to appear with that row.

Subroutine SPLOT was adapted to ONEDMAR from the RIP code (see Reference 8).

4.23 SUBROUTINE STATE

The hydrostatic pressure, P , the internal energy per unit volume, e , and the sound speed, c , for a given cell are calculated in this equation of state subroutine.

The hydrostatic pressure, P , is determined from the Mie-Gruneisen form of the equation of state, Equation 8. The finite difference form of this equation is

$$p_{j+1/2}^{n+1} = \left[K \lambda_{j+1/2}^{n+1} + B \left(\lambda_{j+1/2}^{n+1} \right)^2 + C \left(\lambda_{j+1/2}^{n+1} \right)^3 \right] \left[1 - \frac{\Gamma \lambda_{j+1/2}^{n+1}}{2} \right] + \frac{\Gamma e_{j+1/2}^{n+1}}{v_{j+1/2}^{n+1}} \quad (55)$$

where

$$v_{j+1/2}^{n+1} = \frac{1}{v_{j+1/2}^{n+1}} - 1$$

K = bulk modulus of material

B, C = coefficients for the fit to the hydrostatic pressure versus λ data

Γ = Gruneisen coefficient

$e_{j+1/2}^{n+1}$ = internal energy per unit volume

$v_{j+1/2}^{n+1}$ = relative volume = $\frac{\rho_0}{\rho} = \frac{\text{initial density}}{\text{current density}}$

In Equation 55, the specific volume and specific internal energy are required at the updated time, t^{n+1} . The specific volume is determined from the conservation of mass equation, Equation 5.

The specific internal energy is determined from the following finite difference equation:

$$e_{j+1/2}^{n+1} = e_{j+1/2}^n + \Delta t^{n+1/2} \dot{e}_{j+1/2}^{n+1/2} \quad (56)$$

The rate of change of internal energy per unit volume, $\dot{e}_{j+1/2}^{n+1/2}$, is determined from the finite difference form of the conservation of energy equation, Equation 3:

$$\begin{aligned} \dot{e}_{j+1/2}^{n+1/2} = & v_{j+1/2}^{n+1/2} \left[s_{x_{j+1/2}}^{n+1/2} \dot{\epsilon}_{x_{j+1/2}}^{n+1/2} + (c-1) s_{\theta_{j+1/2}}^{n+1/2} \dot{\epsilon}_{\theta_{j+1/2}}^{n+1/2} \right] \\ & - \dot{v}_{j+1/2}^{n+1/2} \left(p_{j+1/2}^{n+1/2} + q_{j+1/2}^{n+1/2} \right) \end{aligned} \quad (57)$$

where

$v_{j+1/2}^{n+1/2}$ = relative volume at center of the time step; calculated in subroutine CONSTI,

$\dot{v}_{j+1/2}^{n+1/2}$ = rate of change of relative volume at center of the time step; calculated in subroutine CONSTI,

$$c = \begin{cases} 0, \text{ planar geometry} \\ 1, \text{ cylindrical geometry} \\ 2, \text{ spherical geometry} \end{cases}$$

$\dot{\epsilon}_{xj+1/2}^{n+1/2}, \dot{\epsilon}_{\theta j+1/2}^{n+1/2}$ = strain rates; calculated in subroutine CONSTI,

$q_{j+1/2}^{n+1/2}$ = viscous stress; assumed to equal to $q_{j+1/2}^n$,

$s_{xj+1/2}^{n+1/2}, s_{\theta j+1/2}^{n+1/2}$ = deviatoric stresses.

The pressure term, $p_{j+1/2}^{n+1/2}$, is calculated by:

$$p_{j+1/2}^{n+1/2} = \frac{p_{j+1/2}^n + p_{j+1/2}^{n+1}}{2} \quad (58)$$

The deviatoric stresses are calculated using the following time averaging equations:

$$s_{xj+1/2}^{n+1/2} = \frac{s_{xj+1/2}^n + s_{xj+1/2}^{n+1}}{2} \quad (59)$$

$$s_{\theta j+1/2}^{n+1/2} = \frac{s_{\theta j+1/2}^n + s_{\theta j+1/2}^{n+1}}{2} \quad (60)$$

Estimates of the values of the deviatoric stresses at the end of the current time cycle, t^{n+1} , are calculated in subroutine CONST1 prior to calling subroutine STATE.

Equations 55 through 60 are solved for the pressure at the current time:

$$p_{j+1/2}^{n+1} = \frac{c1 + \frac{r}{v_{j+1/2}^{n+1}} \left[e_{j+1/2}^n + c^2 \Delta t^{n+1/2} v_{j+1/2}^{n+1/2} - t^{n+1/2} \Delta v_{j+1/2}^{n+1/2} \left(q_{j+1/2}^{n+1/2} + \frac{p_{j+1/2}^{n+1/2}}{2} \right) \right]}{1 + \frac{r \Delta t^{n+1/2} v_{j+1/2}^{n+1/2}}{2 v_{j+1/2}^{n+1}}} \quad (61)$$

where

$$c1 \equiv \left[A \lambda_{j+1/2}^{n+1} + B \left(\lambda_{j+1/2}^{n+1} \right)^2 + C \left(\lambda_{j+1/2}^{n+1} \right)^3 \right] \left[1 - \frac{r \lambda_{j+1/2}^{n+1}}{2} \right]$$

$$c2 \equiv s_{x j+1/2}^{n+1/2} \dot{\epsilon}_{x j+1/2}^{n+1/2} + (c-1) s_{\theta j+1/2}^{n+1/2} \dot{\epsilon}_{\theta j+1/2}^{n+1/2}$$

The specific internal energy of the cell is then updated by substituting the pressure from Equation 61 into Equations 56 and 57. The resulting equation from this substitution is:

$$e_{j+1/2}^{n+1} = e_{j+1/2}^n + \Delta t^{n+1/2} \left\{ v_{j+1/2}^{n+1/2} c2 - \dot{v}_{j+1/2}^{n+1/2} \left[q_{j+1/2}^{n+1/2} + \frac{p_{j+1/2}^n + p_{j+1/2}^{n+1}}{2} \right] \right\} \quad (62)$$

The square of the sound speed of the material in the cell, a^2 , is updated by:

$$\left(a_{j+1/2}^{n+1}\right)^2 = \begin{cases} \left[\frac{K + \frac{4}{3} \mu_{j+1/2}^{n+1}}{\rho_{0j+1/2}} \right], & \text{for } \Delta t^{n+1/2} \dot{v}_{j+1/2}^{n+1/2} = 0 \quad (63a) \\ \left[\frac{\frac{4}{3} \mu_{j+1/2}^{n+1} - \left(v_{j+1/2}^{n+1/2}\right)^2 \left[\frac{\partial p}{\partial v} \right]_v - p_{j+1/2}^{n+1} \frac{\partial p}{\partial e} \right]^{n+1/2}}{\rho_{0j+1/2}}, & \text{for } \Delta t^{n+1/2} \dot{v}_{j+1/2}^{n+1/2} \neq 0 \quad (63b) \end{cases}$$

where

$$\left. \frac{\partial p}{\partial v} \right|_e + \frac{\left(p_{j+1/2}^{n+1} - p_{j+1/2}^n \right) - \left(e_{j+1/2}^{n+1} - e_{j+1/2}^n \right) \frac{r}{v_{j+1/2}^{n+1}}}{\Delta t^{n+1/2} \dot{v}_{j+1/2}^{n+1/2}}$$

$$\left. \frac{\partial p}{\partial e} \right|_v = \frac{r}{v_{j+1/2}^{n+1}}$$

$\mu_{j+1/2}^{n+1}$ = shear modulus of material

$\rho_{0j+1/2}$ = initial density of material

If the sound speed calculated by Equation 63b is negative, the value calculated by Equation 63a is used.

4.24 SUBROUTINE TNSLE

This subroutine controls the calculation of the stress state under tensile loading conditions. The tensile failure model used is an extension to the model presented in Reference 1. In this model, inelastic strains, E , are introduced in order to zero those principal stresses which exceed the material tensile strength. The accumulation of these strains defines a tensile failure-induced porosity which is then used in the determination of the pressure from the equation of state.

Subroutine TNSLE is called from subroutine CONST1 after the equation of state subroutine, STATE, is called. In this initial call to STATE, a

preliminary calculation of the pressure in the material is made using deviatoric stresses which are updated by assuming that the material acts in an elastic manner. The three principal stresses, σ_x , σ_θ , and σ_ϕ , are then calculated in TNSLE from the deviatoric stresses and the pressure via a call to subroutine ABSUB (entry point ACALC). These principal stresses are then compared to the limiting tensile strength in the material. The limiting tensile strength has the value that is defined by the user through the TNT array (card 9 -- Section V) until tensile failure is initiated for the given cell. Once tensile failure is detected, the limiting tensile strength is reset to zero for that cell. The zero tensile strength is maintained for the rest of the calculation even if the material "heals" by closing all cracks and reducing the inelastic strains to zero.

The comparison tests of the principal stresses versus the limiting tensile strength, σ_{limit} , determines the path taken through the tensile failure model. These tests are:

- (1) $\sigma_x^{n+1} \leq \sigma_{\text{limit}}$ and $\sigma_\theta^{n+1} \leq \sigma_{\text{limit}}$ and $\sigma_\phi^{n+1} \leq \sigma_{\text{limit}}$ and $E_x^n + E_\theta^n + E_\phi^n \leq 0$: material is elastic and principal stresses do not exceed current tensile limit; control returns to subroutine CONST1 for completion of elastic calculation.
- (2) $E_x^n + E_\theta^n + E_\phi^n > 0$: subroutine CRACK is called to update a cell in which cracks exist in any or all of the three directions. This path is taken regardless of the current signs on the principal stresses; i.e., cracks are updated for cells undergoing compression as well as tension. For the tension cases, cracks are widening and for compression cases cracks are closing.
- (3) $\sigma_x^{n+1} > \sigma_{\text{limit}}$ and $E_x^n + E_\theta^n + E_\phi^n \leq 0$: entry CR1 of subroutine CRACK is called to introduce a crack in the x direction (cracks in the θ and/or ϕ directions may also be introduced at this time in CR1).
- (4) $\sigma_\theta^{n+1} > \sigma_{\text{limit}}$ and $E_x^n + E_\theta^n + E_\phi^n \leq 0$: entry CR2 of subroutine CRACK is called to introduce a crack in the θ direction (a crack in the ϕ direction may also be introduced at this time in CR2).

Prior to calling subroutine CRACK or either of its two entry points CR1 and CR2, a relaxation factor, f_r , is calculated from user input. This relaxation factor allows the user to control the number of time steps required for the principal stresses to be reduced to the overburden stress level. The relaxation factor is calculated by:

$$f_r = \begin{cases} \frac{N_{\text{CYCLE}} - N_I}{N_T}, & \text{for } N_T > N_{\text{CYCLE}} - N_I > 0 \\ 1, & \text{for } N_{\text{CYCLE}} - N_I \geq N_T \end{cases} \quad (64)$$

where

N_{CYCLE} = current cycle number.

N_I = cycle number prior to cycle in which a crack was initiated in the given cell.

N_T = total number of cycles over which stresses are reduced to the overburden stress level.

Subroutine CRACK contains the logic for updating the inelastic strains and for recalculating the principal stresses and pressure. The strains and deviatoric stresses are returned to TNSLE from CRACK and then transferred back to the subroutine CONST1 which is controlling the entire constitutive model calculation.

4.25 FUNCTION SUBROUTINE UDV

This function subroutine determines the node displacement as a function of problem time from user-supplied input at selected nodes. Displacement versus time data is defined in the generation subroutine, GEN, and is stored in the name common /MC/. The displacement time histories for up to 50 nodes may be controlled by the user in the calculation of the node displacement at any given problem time.

4.26 SUBROUTINE VPLOT

This subroutine produces a printer or on-line plot of any two variable arrays. The variable arrays to be plotted, X and F, are transferred through calling arguments. The F array values are plotted on the horizontal. The X array values are plotted on the vertical; one value per printer line. The increment between the X array variables must be constant. The minimum and maximum values of the F array variable, which are included in the calling arguments, are used to determine the appropriate vertical scale.

SECTION V

INPUT REQUIREMENTS

The following input cards are read by the ONEDMAR code. All cards are required except those denoted by an *, which are optional as specified in the description of the card. All variables have a default value of zero unless otherwise denoted.

Card No.	Read In	Description
1	ONEDMR	TITLE(I), I = 1,12: FORMAT (12A6) Heading description or title of calculation.
2	ONEDMR	IC: FORMAT (15) Calculation type <div style="margin-left: 40px;">IC=1: generate problem and call calculation sequence; read card 3 next.</div> <div style="margin-left: 40px;">IC=2: restart problem and call calculation sequence; read card 29 next.</div>
Cards 3-28 are read for IC=1 on Card 3.		
3	GEN	NEDIT, NPRINT, NRESTR, KSTOP, MTAPE, IPLR, NREZ, ILINER, IOLS, IOLV: FORMAT (1615) Problem control variables <div style="margin-left: 40px;">NEDIT: mesh edit every frequency at which the problem solution will be printed, i.e., every NEDITth time step a mesh edit will be produced.</div> <div style="margin-left: 40px;">NPRINT: cell index print increment; solution for every NPTINTth will be printed.</div> <div style="margin-left: 40px;">NRESTR: restart frequency; restart data will be written every NRESTRth time step.</div>

KSTOP: last cycle to be calculated; solution completed after KSTOP time steps.

MTAPE: storage unit on which restart dumps are to be written.

IPLR: geometry flag = 1; planar geometry
2; cylindrical geometry
3; spherical geometry

NREZ: rezone frequency; rezoning procedures are activated every NREZth time step.

ILINER: flag used to remove the non-lineacrities from the material response calculation.

ILINER = $\begin{cases} 0, & \text{nonlinear calculation (Default value = 0)} \\ 1, & \text{linear calculation} \end{cases}$

IOLS: flag which when set to a non-zero integer causes an on-line printer plot of longitudinal stress vs displacement to be produced with the mesh edit.

IOLV: flag which when set to a non-zero integer causes an on-line printer plot of velocity vs displacement to be produced with the mesh edit.

4 GEN

TMAX, DTEDIT, DPTEDT: FORMAT (8E10.3)

Time control variables

TMAX: problem time at which the calculation will stop (Default = 10^{20} time units.)

DTEDIT: problem time increment for editing; problem solution will be printed every DTEDITth time units. (Default = 10^{20} time units.)

5 GEN

DPTEDT: problem time increment for writing data to be plotted to storage file; data will be calculated and saved every DPTEDTth time unit. (Default = 10^{20} time units.)

NL, NPY, XL: FORMAT (215, E10.3)

Layer parameters

NL: number of layers with distinct material description.

NPY: material parameter input format, see Card 6 description.

XL: left-most value of the spatial coordinate x.

A set of the following five cards is required for each layer ($J = 1, NL$) in the problem mesh; i.e., Cards 6-10 for layer 1 ($J = 1$) are followed by Cards 6-10 for layer 2 ($J = 2$), etc.

6 GEN

NI(J), DX, RX, AMM, AKK, ARHO(J): FORMAT (15, 5E10.3)

Layer properties

NI(J): number of cells in layer J.

DX: width of first cell in layer J.

RX: cell size ratio, i.e., $\Delta x_{j+1/2} = \Delta x_{j-1/2} \cdot RX$.
(Default value = 1.0)

AMM: for NPY = $\begin{cases} 1: \mu; \text{shear modulus of material in layer J.} \\ 2: C_p; \text{p-wave velocity of material in layer J.} \\ 3: C_p; \text{p-wave velocity of material in layer J.} \end{cases}$

AKK: for NPY = $\begin{cases} 1: K; \text{linear bulk modulus of material in layer J.} \\ 2: C_s; \text{s-wave velocity of material in layer J.} \\ 3: \nu; \text{Poisson's ratio of material in layer J.} \end{cases}$

7	Gen	<p>ARHO(J): ambient density of material in layer J.</p> <p>YMO(J), PMO(J), EE(J): FORMAT (8E10.3)</p> <p>Material properties</p> <p>YMO(J): limiting yield stress in variable yield stress formulation; Y_{m_0} in Equation 3I of Section IV.</p> <p>PMO(J): limiting pressure in variable yield stress formulation; P_m in Equation 3I of Section IV.</p> <p>EE(J): coefficient C_1 used in variable shear modulus formulation; $\mu = \mu_0 (1 + C_1 \lambda + C_2 \lambda_{\max})$</p> <p>HH(J): coefficient C_2 used in variable shear modulus formulation; $\mu = \mu_0 (1 + C_1 \lambda + C_2 \lambda_{\max})$</p>
8	GEN	<p>CL(J), CQ(J), YIELD(J), GA(J), A2(J), A3(J): FORMAT (8E10.3)</p> <p>Nonlinear properties</p> <p>CL(J): C_L, linear viscosity coefficient of material in layer J.</p> <p>CQ(J): C_Q, quadratic viscosity coefficient of material in layer J.</p> <p>YIELD(J): Y_0, initial yield stress of material in layer J.</p> <p>GA(J): Γ, Gruneisen coefficient of material in layer J.</p> <p>A2(J): A_2, coefficient of squared term in equation of state formulation.</p> <p>A3(J): A_3, coefficient of cubic term in equation of state formulation.</p>
9	GEN	<p>TNT(J), PBT(J), ANTT(J), EMT(J): FORMAT (8E10.3)</p> <p>Tensile failure model parameters</p> <p>TNT(J): σ_t, tensile strength of material in layer J. If TNT(J)<0 on input, the tensile failure model is not activated for layer J.</p>

		PBT(J): P_b , overburden stress.
		ANTT(J): number of time steps over which the stresses are linearly reduced to P_b after tensile failure occurs.
		EMT(J): e_m , melt energy parameter used in tensile failure model. See Equation 30 of Section IV.
10	GEN	CA(J), CB(J), CC(J), CR(J), CD(J), CW(J), POV(J), XN(J): FORMAT (8E10.3) Cap model parameters
		CA(J): coefficient A in the cap model equation for the failure envelope; Equation 16 of Section IV.
		CB(J): coefficient B in the cap model equation for the failure envelope; Equation 16 of Section IV.
		CC(J): coefficient C in the cap model equation for the failure envelope; Equation 16 of Section IV.
		CR(J): coefficient R in the cap model equation for the movable yield cap; Equation 17 of Section IV.
		CD(J): coefficient D in the cap model equation for the volumetric plastic strain; Equation 19 of Section IV.
		CQ(J): coefficient W in the cap model equation for the volumetric plastic strain; Equation 19 of Section IV.
		POV(J): geostatic or baseline hydrostatic pressure used in the cap model.
		XN(J): initial value of $X(\kappa)$ function in the cap model; Equation 18a of Section IV.
11	GEN	BCL, BCR, JVV, NDD, NPL, NPR, ISPECL: FORMAT (2(A6,4X),5I5)

Boundary condition parameters

BCL = { 6HFIXED, left boundary is fixed, $u_1 = 0$.
6HPRESSU, left boundary has an applied pressure (see subroutine PREL and cards 15-17).
6HDISPLM, left boundary has an applied displacement-time history (see cards 12-14).

BCR = { 6HFIXED, right boundary is fixed, $u_{last} = 0$.
6HPRESSU, right boundary has an applied pressure (see subroutine PRER and cards 18-20).
6HDISPLM, right boundary has an applied displacement-time history (see cards 12-14).

JVV: number of nodes with a prescribed displacement time history, $JVV \leq 50$.

NDD: number of data points of input displacement-time history that are read for each node defined by JV on card 12. $NDD \leq 20$.

NPL: number of data points of input pressure-time history on left boundary that are read on cards 15 and 16 when BCL = 6HPRESSU. $NPL \leq 20$.

NPR: number of data points of input pressure-time history on right boundary that are read on cards 18 and 19 when BCR = 6HPRESSU. NPR 20.

ISPECL: flag which when set to a non-zero integer, activates function PRESS.

The following card is not read if JVJ: FORMAT (1615)

12* GEN JV(I) for I = 1, JVJ: FORMAT (1615)

JV(I): node index at which to apply displacement time data prescribed by cards 13 and 14.

A pair of the following two cards is read for each node at which displacement time history is applied; i.e., JVV pairs. If JVV = 0, cards 13 and 14 are not read.

13*	GEN	TD(J,I) for I = 1, NDD: FORMAT (8E10.3) TD(J,I): time used in displacement time history at node J. Twenty data points are allowed at each node.
-----	-----	--

14*	GEN	DD(J,I) for I = 1, NDD: FORMAT (8E10.3) DD(J,I): displacement used in displacement time history at node J. Twenty data points are allowed at each node.
-----	-----	--

The following two cards are read only if BCL = 6HPRESSU and NPL > 0 on card 11.

15*	GEN	PRL(I) for I = 1, NPL: FORMAT (8E10.3) PRL(I): pressure applied on the left boundary. Twenty data points are allowed.
-----	-----	--

16*	GEN	TL(I) for I = 1, NPL: FORMAT (8E10.3) TL(I): time at which pressure from PRL(I) is applied on the left boundary. Twenty data points are allowed.
-----	-----	---

The following card is read only if BCL = 6HPRESSU on card 11.

17*	GEN	IRAMPL, NCYCRL: FORMAT (16I1) Ramping parameters for left boundary pressure. IRAMPL: flag which when set to a non-zero integer, indicates that the applied pressure on the left boundary will be linearly ramped in time. NCYCRL: number of cycles over which ramping of the applied pressure on the left boundary will occur.
-----	-----	---

The following three cards are read only if BRC = 6HPRESSU on card 11.

18*	GEN	PRR(I) for I = 1, NPR: FORMAT (8E10.3) PRR(I): pressure applied on the right boundary.
-----	-----	---

Twenty data points are allowed.		
19*	GEN	TR(I) for I = 1, NPR: FORMAT (8E10.3) TR(I): time at which pressure from PRR(I) is applied on the right boundary. Twenty data points are allowed.
20*	GEN	IRAMPR, NCYCRR: FORMAT (1615) Ramping parameters for right boundary pressure. IRAMPR: flag which when set to a non-zero integer, indicates that the applied pressure on the right boundary will be linearly ramped in time. NCYCRR: number of cycles over which ramping of the applied pressure on the right boundary will occur.
21	GEN	NCELLS, NPLOT, NTAPE: (1615) Control variables for saving data for plotting. Data stored is displacement, u , velocity, \dot{u} , longitudinal stress, σ_x , and tangential stress, σ_y , of the node and cell numbers defined by JSEL on card 22. NCELLS: number of nodes or cells at which data is to be saved for plotting. $NCELLS \leq 50$. NPLOT: cycle frequency at which data will be saved for plotting. NTAPE: storage unit number on which data is stored.
The following card is <u>not</u> read if NCELLS = 0 on card 21.		
22*	GEN	JSEL(I) for I = 1, NCELLS: FORMAT (1615) JSEL(I): node or cell index at which displacement, velocity and stress data will be stored.
23	GEN	NCYCTO, DINT, DTMIN, COUR, VELCUT: FORMAT (15, 4E10.3) Time step and grid activity cutoff parameters. NCYCTO: number of cycles for which the time step is held constant at the value given by DINT. (Default is 0)

DINT: initial value of the time step. If DINT = 0.,
 $.9 \Delta t_{\min}$ will be used where

$$\Delta t_{\min} = \frac{\text{minimum cell size}}{\text{p-wave velocity}}.$$

DTMIN: minimum time step allowed during the calculation. If $\text{DTMIN} \geq \text{DINT}$ on input, the time step will remain constant at the DINT level for the entire problem. If $\text{DTMIN} < \text{DINT}$, the time step will be constant until NCYCTO and then controlled by Courant stability conditions.

COUR: Courant stability factor. Time steps are calculated by $t = \text{COUR} \cdot \Delta t_{\min}$ where Δt_{\min} is determined from the wave speed (see Subroutine CONSTI).

VELCUT: activity level for nodes; node variables are not updated until $|\dot{u}_j| > \text{VELCUT}$.

The following card is not read if NREZ = 0 on card 3.

24* GEN

SIGC, SIGI, CAPF, FRACRZ, DENCOM, UMAXO: FORMAT
 (8E10.3)

Rezone control variables (see Appendix A for details).

SIGC: σ_c , critical stress level in cells below which the cells will not be combined. Used in defining the limiting stress level.

SIGI: σ_l , reference stress level from which the stress in the cell is measured. Used in defining the limiting stress level.

CAPF: C_2 , scaling factor on difference between the stress in a cell and the reference stress. Used in defining the limiting stress level.

FRACRZ: C_1 , scaling factor on limiting stress level.

DENCOM: C_3 , density gradient factor.

		UMAXO: x_{\max_0} , maximum cell size allowed by re-zoning procedure.
25	GEN	JACTB, JACT: FORMAT (I6I5) Activity limits on node indices. If input as zero, subroutine GEN will calculate these parameters. JACTB: index of leftmost node to be updated on cycle 1. Default = $\text{Max} \{1, \text{JV}(1)\}$ where $\text{JV}(1)$ is defined on card 12. JACT: index of rightmost node to be updated on cycle 1. Default = $\text{Max} \{2, \text{JV}(\text{JVV})\}$ where $\text{JV}(\text{JVV})$ is defined on card 12.

The following three cards are read after card 25 when IC=1 on card 2 and after card 32 when IC=2 on card 2.

The following card is read only if Murphy's cavity pressure is applied to the left end of the mesh (see Subroutine PRESS for details) and if ISPECL \neq 0 on card 11.

26*	PRESS	RCAV, RELAST, VP, VS, POS, POC, GAMMA: FORMAT (8E10.4) RCAV: initial cavity radius RELAST: elastic radius VP: p-wave velocity VS: s-wave velocity. POS: initial pressure at the elastic radius. POC: late time pressure at the elastic radius. GAMMA: material constant used in the definition of the decay rate of the pressure function.
27	PLOTOD	NPLOTS, NP, NSAVE, MDTAPE: FORMAT (I6I5) Printer plot control variables NPLOTS: number of printer plots to be made. $\text{NPLOTS} \leq 20$. NP: frequency at which the data points from the saved data files will be plotted and stored, i.e., every NP^{th} point from the data file will be plotted.

NPSAVE: flag which when set to a non-zero integer activates a call to subroutine DUMPPT which stores the selected printer plot data.

MDTAPE: unit number on which the selected printer plot data is stored.

The following card is read for each printer plot to be made or for data to be stored for plotting or analysis; i.e., NPLOTS cards. If NPLOTS = 0 and NPSAVE = 0 on card 27, card 28 will not be read.

28* PLOTOD NCLOT(K), NTYPE(K), IVLOT(K): FORMAT (I6I5)

Printer plot selection variables.

NCLOT(K): cell (or node) number at which data will be plotted and/or stored for plot K.

NTYPE(K): type of data to be plotted and/or stored for plot k.

NTYPE(K) = $\left\{ \begin{array}{l} 1, \text{ displacement vs time} \\ 2, \text{ velocity vs time} \\ 3, \text{ longitudinal stress vs time} \\ 4, \text{ tangential stress vs time} \end{array} \right.$

IVLOT(K): flag which when set to a positive integer causes the K^{th} printer plot to be bypassed. Data for the K^{th} printer plot will be stored for subsequent analysis and/or plotting.

The following four cards are read only for restart calculations, i.e., IC = 2 on card 2. After reading cards 29-32, the cavity pressure parameter card, card 26, is read if required and the plot definition cards 27 and 28 are read.

29* RESTAR MTAP, NRD, NPD, NEWTAP: FORMAT (I6I5)

Parameters used in reading restart information.

MTAP: unit number from which restart information is read.

NRD: cycle number of the restart information dump that will be used to restart the calculation.

		<p>NPD: number of the last cycle for which data to be plotted was stored on unit NTAPE (see card 21).</p> <p>NEWTAP: unit number for storing the new restart dumps that will be made during the current phase of the calculation.</p>
30*	RESTAR	<p>NEDIT, NRESTR, NPLOT, KSTOP, NREZ, NTPNEW, NCELLS: FORMAT (I6I5)</p> <p>Redefined problem control variables. These variables must be redefined for each restart.</p> <p>NEDIT: mesh edit frequency at which the problem solution will be printed during the current restart calculation.</p> <p>NRESTR: restart frequency; restart data will be written every NRESTRth time step.</p> <p>NPLOT: cycle frequency at which data will be saved for plotting.</p> <p>KSTOP: last cycle to be calculated during the current restart calculation.</p> <p>NREZ: rezone frequency; rezoning procedures are activated every NREZth time step.</p> <p>NTPNEW: storage unit on which data will be saved for plotting.</p> <p>NCELLS: number of nodes or cells at which data is to be saved for plotting. NCELLS < 50.</p>
31*	RESTAR	<p>TMAX, DTEDIT, DPTEDT: FORMAT (8E10.3)</p> <p>Redefined time control variables. These variables must be redefined for each restart.</p> <p>TMAX: problem time at which the calculation will stop. (Default = -10^{20} time units.)</p> <p>DTEDIT: problem time increment for editing: problem solution will be printed every DTEDITth time units. (Default = 10^{20} time units.)</p>

		DPTEDT: problem time increment for writing data to be plotted to storage file; data will be calculated and saved every DPTEDT th time unit. Default = 10^{20} time units.)
32*	RESTAR	JSEL(I) for I = 1, NCELLS: FORMAT (1615) JSEL(I): node or cell index at which displacement, velocity, and stress data will be stored.

SECTION VI

SAMPLE PROBLEM

A sample problem has been devised to demonstrate the input and output features of the ONEDMAR code. The sample problem models the propagation of a spherical blast wave in a homogeneous media. The driving force is Murphy's cavity pressure (see subroutine PRESS). Figure 4 presents the input cards that are read by the ONEDMAR code. A card which defines the card column numbers is included as an aid to the reader. This card is not part of the input deck. In addition, the numbers in parentheses in columns 77-80 do not appear on the actual input cards. These numbers correspond to the card numbers in Section V and are included as an aid to the reader.

A brief synopsis of the problem follows. Murphy's cavity pressure model is used to drive a stress wave into an earth-like material. Two layers, one of constant cell size and one of growing cell size, are used to model the earth. The calculation is linear and the Hugoniot equation of state is used. Editing features include stress-displacement plots with each mesh edit (every 50 cycles) and three time history plots to be made at the end of the calculation, which is at 150 cycles.

Figure 5 shows the user the printed output of the input quantities that is provided by subroutine GEN. This output allows the user to check the generated problem variables against the intended problem variables.

Figure 6 shows the output of the calculation. Mesh edits and stress-displacement on-line plots are provided every 50 cycles. At the end of the calculation, the requested stress and velocity time history plots are printed.

```

1234567890123456789012345678901234567890123456789012345678901234567890
SAMPLE PROBLEM 1 - MURPHY'S DRIVING FORCE IN SPHERICAL CAVITY
1
50 3 1000 150 14 3 0 1 1 0
2 0 1000.
200 1 3429.
0. 500. 1.00 0.167E-2 1.361 2.0
-.025 0. 0. 0. 0. 0. 0.
-1.0 0. 0. 1.610 1. 1.620 0. 0.
50 0. 500. 1.03 0.167E-2 1.361 0. 2.0 0.
-.025 0. 0. 1.610 0. 0. 0.
-1.0 0. 0. 1. 1.620 0. 0.
PRESSURE FIXED 0 0 0 0 0 1 0. 0.
0 0
4 1 12
2 43 129 194
0 500. 1.64 1.64 1.64
0 10 24180. .35 .202 1.6E-5 1.016E-4 1.5
3429. 24180.
3 2 0 0
2 3 0
10 2 0
10 3 0

```

CARD NO
(1)
(2)
(3)
(4)
(5)
(6)
(7)
(8)
(9)
(10)
(11)
(12)
(13)
(14)
(15)
(16)
(17)
(18)
(19)
(20)
(21)
(22)
(23)
(24)
(25)
(26)
(27)
(28)
(29)
(30)

Figure 4. Sample problem input cards.

SAMPLE PROBLEM 1 - MURPHY'S DRIVING FORCE IN SPHERICAL CAVITY

INPUT DATA
 EDIT FREQUENCY = 50
 PRINT INCREMENT = 3
 RESTART FREQUENCY = 1000
 LAST CYCLE = 150
 RESTART DUMP UNIT = 14
 GEOMETRY FLAG = 3
 PEZONE FREQUENCY = 0
 LINEAR CALCULATION FLAG = 1
 STRESS-DISPLACEMENT PLOT = 1
 VELOCITY-DISPLACEMENT PLOT = 0

SPHERICAL GEOMETRY

TMAT = 1.00000+20
 DTEDIT = 1.00000+20
 DTIEDT = 1.00000+03
 IPEDIT = 0.00000

LAYERED MATERIAL, X ZONING AND MATERIAL INFORMATION

NUMBER OF LAYERS = 2
 MATERIAL INPUT FORMAT = 1
 XLFFT = .34200+00

MATERIAL	INCREMENTS	DX	RY	SHEAR MOD.	BULK MOD.	DENSITY	VP	VS	MU
1	200	.50000+03	.10000+01	.01670-01	.13610+01	.20000+01	.05720+00	.20200+00	.07050+00
2	50	.50000+03	.10500+01	.01670-01	.13610+01	.20000+01	.05720+00	.20200+00	.07050+00

LAYER	YMD	PMN	FE	MM
1	.00000	.00000	.00000	.00000
2	.00000	.00000	.00000	.00000

NONLINEAR PROPERTIES

L	VIS COEF	N	VIS COEF	VIFIN	GAMMA	A2	A3
.250-01	.000	.10000+11	.00000	.00000	.00000	.00000	.00000
.250-01	.000	.10000+11	.00000	.00000	.00000	.00000	.00000

Figure 5. Sample problem — generated problem description.

INSLT	PRB	ANT	EM	CA	CR	CC	CD	CM	POV	IN
-1.000000E+01	.00000	.100000E+01	.100000E+21	0.00000	0.00000	0.00000	0.00000	0.00000	0.00000	0.00000
-1.000000E+01	.00000	.100000E+01	.100000E+21	0.00000	0.00000	0.00000	0.00000	0.00000	0.00000	0.00000

BOUNDARY CONDITION DATA

```

ACL #PRESSH
BCR #FIXD
JVV = 0
MOD = 0
MPL = 0
MPR = 0
ISPECL = 1

```

IRAMPPL = 0 MEYERL = 0

SAVED VARIABLE INFORMATION

```

NCELLS = 4
NPLOT = 1
NTAPE = 12
NSAVE = 0
CELL LOCATIONS
J
2
41
129
196

```

```

ACVCTN = 0
DIRF = .500000E3
DIRM = .100000E7
CRUR = .600000E0
VELCUR = .100000E4

```

Figure 5 (continued)

SUMMARY OF GRID INFORMATION

J	MPN	X	NY	VZ	DN
1	1	3.42900+03	0.00000	0.00000	0.00000
4	1	4.92000+03	5.00000+02	2.19139+10	2.19139+10
7	1	6.42900+03	5.00000+02	1.91000+10	3.82000+10
10	1	7.92900+03	5.00000+02	2.94930+10	5.40070+10
13	1	9.42900+03	5.00000+02	4.21370+10	6.42700+10
16	1	1.09290+04	5.00000+02	5.70300+10	1.40620+11
19	1	1.24290+04	5.00000+02	7.41700+10	1.40100+11
22	1	1.39290+04	5.00000+02	9.15670+10	1.47130+11
25	1	1.54290+04	5.00000+02	1.15211+11	2.30023+11
28	1	1.69290+04	5.00000+02	1.39105+11	2.78210+11
31	1	1.84290+04	5.00000+02	1.65200+11	3.30097+11
34	1	1.99290+04	5.00000+02	1.91642+11	3.87200+11
37	1	2.14290+04	5.00000+02	2.20205+11	4.40571+11
40	1	2.29290+04	5.00000+02	2.57170+11	5.10150+11
43	1	2.44290+04	5.00000+02	2.92122+11	5.80645+11
46	1	2.59290+04	5.00000+02	3.29714+11	6.59832+11
49	1	2.74290+04	5.00000+02	3.69350+11	7.38719+11
52	1	2.89290+04	5.00000+02	4.11253+11	8.22506+11
55	1	3.04290+04	5.00000+02	4.55390+11	9.10793+11
58	1	3.19290+04	5.00000+02	5.01790+11	1.00350+12
61	1	3.34290+04	5.00000+02	5.50437+11	1.10007+12
64	1	3.49290+04	5.00000+02	6.01327+11	1.20265+12
67	1	3.64290+04	5.00000+02	6.54470+11	1.30800+12
70	1	3.79290+04	5.00000+02	7.09800+11	1.41073+12
73	1	3.94290+04	5.00000+02	7.67507+11	1.53501+12
76	1	4.09290+04	5.00000+02	8.27401+11	1.65000+12
79	1	4.24290+04	5.00000+02	8.89540+11	1.77009+12
82	1	4.39290+04	5.00000+02	9.53010+11	1.90700+12
85	1	4.54290+04	5.00000+02	1.02050+12	2.04116+12
88	1	4.69290+04	5.00000+02	1.04900+12	2.17005+12
91	1	4.84290+04	5.00000+02	1.16062+12	2.32120+12
94	1	4.99290+04	5.00000+02	1.23401+12	2.40002+12
97	1	5.14290+04	5.00000+02	1.30966+12	2.61931+12
100	1	5.29290+04	5.00000+02	1.38755+12	2.77510+12
103	1	5.44290+04	5.00000+02	1.46760+12	2.93539+12
106	1	5.59290+04	5.00000+02	1.55000+12	3.10017+12
109	1	5.74290+04	5.00000+02	1.63473+12	3.26000+12
112	1	5.89290+04	5.00000+02	1.72162+12	3.40125+12
115	1	6.04290+04	5.00000+02	1.81077+12	3.62153+12
118	1	6.19290+04	5.00000+02	1.90210+12	3.80032+12
121	1	6.34290+04	5.00000+02	1.99500+12	4.09161+12
124	1	6.49290+04	5.00000+02	2.09170+12	4.10339+12
127	1	6.64290+04	5.00000+02	2.18900+12	4.37000+12
130	1	6.79290+04	5.00000+02	2.29021+12	4.50007+12
133	1	6.94290+04	5.00000+02	2.39200+12	4.70575+12
136	1	7.09290+04	5.00000+02	2.49777+12	4.90550+12
139	1	7.24290+04	5.00000+02	2.60000+12	5.20000+12
142	1	7.39290+04	5.00000+02	2.71011+12	5.00002+12
145	1	7.54290+04	5.00000+02	2.82505+12	5.65100+12
148	1	7.69290+04	5.00000+02	2.93000+12	5.81000+12

Figure 5 (continued)

151	1	7.98290+04	5.00000+02	1.05590+12	6.11190+12
154	1	7.98290+04	5.00000+02	1.17410+12	6.34870+12
157	1	7.98290+04	5.00000+02	1.29500+12	6.59005+12
160	1	7.98290+04	5.00000+02	1.41790+12	6.83540+12
163	1	7.98290+04	5.00000+02	1.54300+12	7.08610+12
166	1	7.98290+04	5.00000+02	1.67040+12	7.34092+12
169	1	7.98290+04	5.00000+02	1.80010+12	7.60200+12
172	1	7.98290+04	5.00000+02	1.93200+12	7.86990+12
175	1	7.98290+04	5.00000+02	2.06610+12	8.14270+12
178	1	7.98290+04	5.00000+02	2.20250+12	8.42060+12
181	1	7.98290+04	5.00000+02	2.34110+12	8.70380+12
184	1	7.98290+04	5.00000+02	2.48200+12	8.99250+12
187	1	7.98290+04	5.00000+02	2.62520+12	9.28690+12
190	1	7.98290+04	5.00000+02	2.77060+12	9.58720+12
193	1	7.98290+04	5.00000+02	2.91820+12	9.89350+12
196	1	7.98290+04	5.00000+02	3.06810+12	1.01560+13
199	1	7.98290+04	5.00000+02	3.22020+12	1.03840+13
202	2	1.03929+05	5.00000+02	3.37460+12	1.06200+13
205	2	1.05521+05	5.00000+02	3.53130+12	1.08640+13
208	2	1.07260+05	5.00000+02	3.69040+12	1.11160+13
211	2	1.09161+05	5.00000+02	3.85190+12	1.13760+13
214	2	1.11210+05	5.00000+02	4.01590+12	1.16440+13
217	2	1.13407+05	5.00000+02	4.18240+12	1.19190+13
220	2	1.15747+05	5.00000+02	4.35150+12	1.22010+13
223	2	1.18230+05	5.00000+02	4.52320+12	1.24900+13
226	2	1.20859+05	5.00000+02	4.69750+12	1.27860+13
229	2	1.23630+05	5.00000+02	4.87450+12	1.30890+13
232	2	1.26540+05	5.00000+02	5.05420+12	1.33990+13
235	2	1.29590+05	5.00000+02	5.23670+12	1.37160+13
238	2	1.32780+05	5.00000+02	5.42200+12	1.40400+13
241	2	1.36110+05	5.00000+02	5.61020+12	1.43710+13
244	2	1.39590+05	5.00000+02	5.80140+12	1.47090+13
247	2	1.43220+05	5.00000+02	6.00560+12	1.50540+13
250	2	1.46990+05	5.00000+02	6.22290+12	1.54060+13

TAU = .54523+03

INITIAL GRID ACTIVITY LIMITS IACIN = 1 JACT = 10

FUNCTION PRESS DATA
 QCAV = 1.42000+03
 OFLAT = 2.81000+04
 VD = 1.50000+01
 /S = 2.02000+01
 PIG = 1.60000+05
 PDC = 1.81000+04
 GAMMA = 1.50000+00

Figure 5 (continued)

SAMPLE PROBLEM 1 - WIGBOLDY'S DRIVING FORCE IN SPHERICAL CAVITY

NCYCLE#	50	TIME#	.2500+05	SIGX	SIGY	P	D	E	E1	E2	E3	VSS	MPN	J
1	1	1	1	1	1	1	1	1	1	1	1	1	1	1
2	2	2	2	2	2	2	2	2	2	2	2	2	2	2
3	3	3	3	3	3	3	3	3	3	3	3	3	3	3
4	4	4	4	4	4	4	4	4	4	4	4	4	4	4
5	5	5	5	5	5	5	5	5	5	5	5	5	5	5
6	6	6	6	6	6	6	6	6	6	6	6	6	6	6
7	7	7	7	7	7	7	7	7	7	7	7	7	7	7
8	8	8	8	8	8	8	8	8	8	8	8	8	8	8
9	9	9	9	9	9	9	9	9	9	9	9	9	9	9
10	10	10	10	10	10	10	10	10	10	10	10	10	10	10
11	11	11	11	11	11	11	11	11	11	11	11	11	11	11
12	12	12	12	12	12	12	12	12	12	12	12	12	12	12
13	13	13	13	13	13	13	13	13	13	13	13	13	13	13
14	14	14	14	14	14	14	14	14	14	14	14	14	14	14
15	15	15	15	15	15	15	15	15	15	15	15	15	15	15
16	16	16	16	16	16	16	16	16	16	16	16	16	16	16
17	17	17	17	17	17	17	17	17	17	17	17	17	17	17
18	18	18	18	18	18	18	18	18	18	18	18	18	18	18
19	19	19	19	19	19	19	19	19	19	19	19	19	19	19
20	20	20	20	20	20	20	20	20	20	20	20	20	20	20
21	21	21	21	21	21	21	21	21	21	21	21	21	21	21
22	22	22	22	22	22	22	22	22	22	22	22	22	22	22
23	23	23	23	23	23	23	23	23	23	23	23	23	23	23
24	24	24	24	24	24	24	24	24	24	24	24	24	24	24
25	25	25	25	25	25	25	25	25	25	25	25	25	25	25
26	26	26	26	26	26	26	26	26	26	26	26	26	26	26
27	27	27	27	27	27	27	27	27	27	27	27	27	27	27
28	28	28	28	28	28	28	28	28	28	28	28	28	28	28
29	29	29	29	29	29	29	29	29	29	29	29	29	29	29
30	30	30	30	30	30	30	30	30	30	30	30	30	30	30
31	31	31	31	31	31	31	31	31	31	31	31	31	31	31
32	32	32	32	32	32	32	32	32	32	32	32	32	32	32
33	33	33	33	33	33	33	33	33	33	33	33	33	33	33
34	34	34	34	34	34	34	34	34	34	34	34	34	34	34
35	35	35	35	35	35	35	35	35	35	35	35	35	35	35
36	36	36	36	36	36	36	36	36	36	36	36	36	36	36
37	37	37	37	37	37	37	37	37	37	37	37	37	37	37
38	38	38	38	38	38	38	38	38	38	38	38	38	38	38
39	39	39	39	39	39	39	39	39	39	39	39	39	39	39
40	40	40	40	40	40	40	40	40	40	40	40	40	40	40
41	41	41	41	41	41	41	41	41	41	41	41	41	41	41
42	42	42	42	42	42	42	42	42	42	42	42	42	42	42
43	43	43	43	43	43	43	43	43	43	43	43	43	43	43
44	44	44	44	44	44	44	44	44	44	44	44	44	44	44
45	45	45	45	45	45	45	45	45	45	45	45	45	45	45
46	46	46	46	46	46	46	46	46	46	46	46	46	46	46
47	47	47	47	47	47	47	47	47	47	47	47	47	47	47
48	48	48	48	48	48	48	48	48	48	48	48	48	48	48
49	49	49	49	49	49	49	49	49	49	49	49	49	49	49
50	50	50	50	50	50	50	50	50	50	50	50	50	50	50

TIME = 11

Figure 6. Sample problem output.

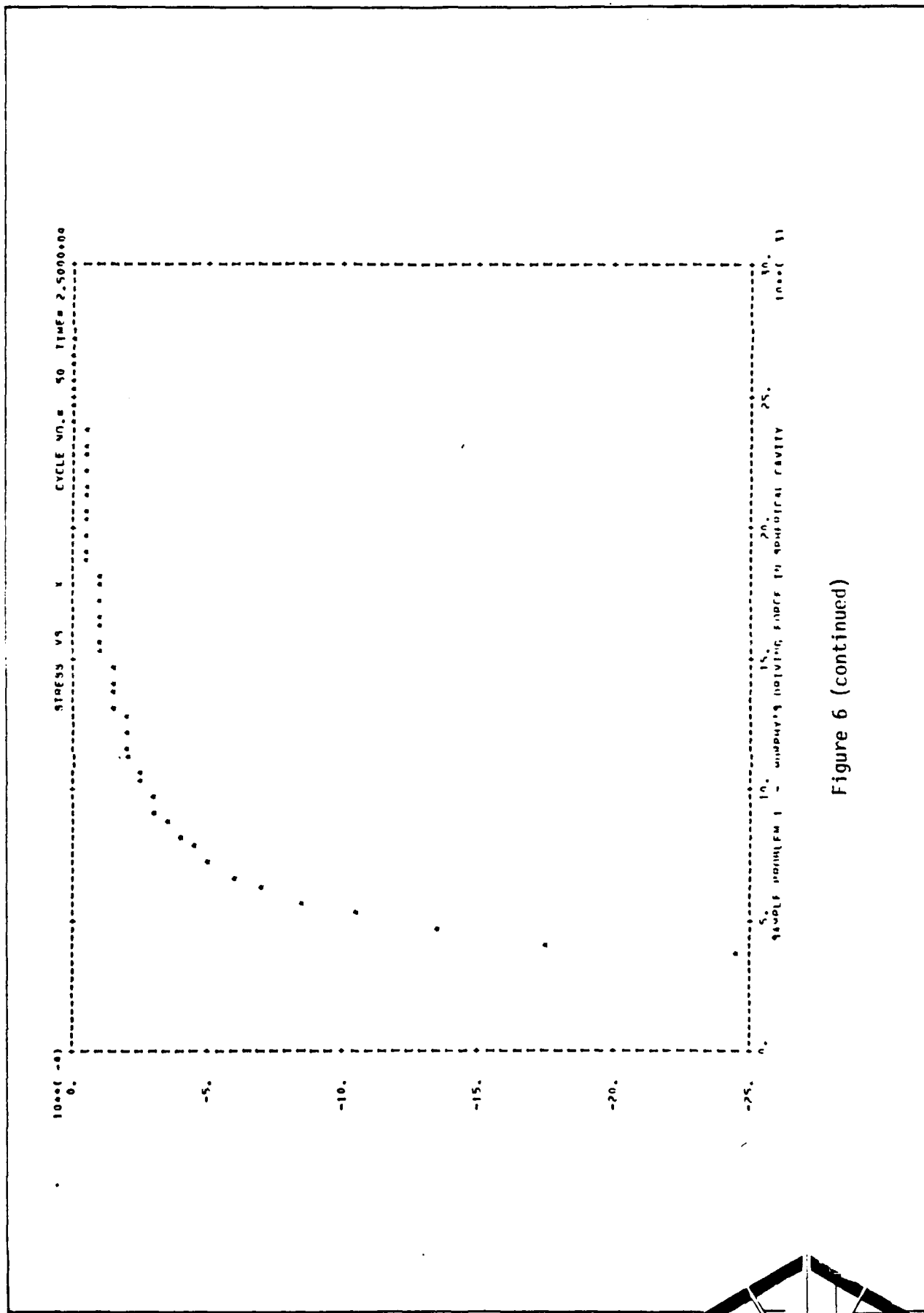


Figure 6 (continued)

SAMPLE PROBLEM 1 - MURPHY'S DRIVING FORCE IN SPHERICAL CAVITY

J	N	MCYCLE=	100	TIME=	.5000E+05	SIGX	SIGY	P	Q	E	E1	E2	E1	VSS	MPN	J
1	3029000					.3607-02	.0000	.0000	.0000	.0000	.0000	.0000	.0000	.0000	0	1
4	4029000					.1700-02	.1555-02	.2755-03	.533A-07	.A301-04	.0000	.0000	.0000	.0000	1	4
7	6029000					.1030-02	.5909-03	.1400-03	.538A-07	.1550-04	.0000	.0000	.0000	.0000	1	7
10	7029000					.4906-03	.2974-03	.1629-03	.5503-07	.4144-05	.0000	.0000	.0000	.0000	1	10
13	8029000					.4804-03	.9474-04	.180A-03	.5039-07	.1029-05	.0000	.0000	.0000	.0000	1	13
16	1003005					.3635-03	.2500-04	.125A-03	.4906-07	.5754-06	.0000	.0000	.0000	.0000	1	16
19	1203005					.2840-03	.1115-04	.1149-03	.471A-07	.2610-06	.0000	.0000	.0000	.0000	1	19
22	1393005					.2249-03	.3582-04	.1070-03	.4282-07	.1312-06	.0000	.0000	.0000	.0000	1	22
25	1583005					.1893-03	.8665-04	.100A-03	.4223-07	.7115-07	.0000	.0000	.0000	.0000	1	25
28	1693005					.1597-03	.5679-04	.0593-04	.370A-07	.4124-07	.0000	.0000	.0000	.0000	1	28
31	1803005					.1370-03	.1171-04	.9100-04	.3315-07	.2542-07	.0000	.0000	.0000	.0000	1	31
34	1903005					.1197-03	.685A-04	.8417-04	.303A-07	.1653-07	.0000	.0000	.0000	.0000	1	34
37	2103005					.1047-03	.1224-03	.8487-04	.234A-07	.1129-07	.0000	.0000	.0000	.0000	1	37
40	2293005					.9203-04	.1120-03	.6162-04	.181A-07	.4053-08	.0000	.0000	.0000	.0000	1	40
43	2483005					.6279-04	.1031-03	.7433-04	.1801-07	.596A-0A	.0000	.0000	.0000	.0000	1	43
46	2593005					.7409-04	.9540-04	.7695-04	.7763-0A	.456A-0A	.0000	.0000	.0000	.0000	1	46
49	2783005					.6639-04	.6471-04	.7116-04	.1160-09	.157A-0A	.0000	.0000	.0000	.0000	1	49
52	2893005					.594A-04	.8165-08	.6707-04	.6193-0A	.2446-0A	.0000	.0000	.0000	.0000	1	52
55	3043005					.5313-04	.7515-04	.533A-04	.1115-07	.2242-0A	.0000	.0000	.0000	.0000	1	55
58	3193005					.4728-04	.6475-04	.432A-04	.1611-07	.1430-0A	.0000	.0000	.0000	.0000	1	58
61	3383005					.4169-04	.6234-04	.500A-04	.216A-07	.1059-0A	.0000	.0000	.0000	.0000	1	61
64	3683005					.3643-04	.5599-04	.4009-04	.2721-07	.1187-0A	.0000	.0000	.0000	.0000	1	64
67	3793005					.3142-04	.495A-04	.430A-04	.3219-07	.4426-09	.0000	.0000	.0000	.0000	1	67
70	3993005					.2665-04	.431A-04	.3452-04	.361A-07	.4594-09	.0000	.0000	.0000	.0000	1	70
73	4043005					.2213-04	.367A-04	.3306-04	.361A-07	.473A-09	.0000	.0000	.0000	.0000	1	73
76	4093005					.176A-04	.3080-04	.2737-04	.3910-07	.3229-09	.0000	.0000	.0000	.0000	1	76
79	4243005					.1391-04	.2410-04	.2210-04	.3643-07	.2040-09	.0000	.0000	.0000	.0000	1	79
82	4393005					.1007-04	.1824-04	.1A67-04	.3A9A-07	.1144-09	.0000	.0000	.0000	.0000	1	82
85	4543005					.6000-05	.1309-04	.1199-04	.7160-07	.5A19-10	.0000	.0000	.0000	.0000	1	85
88	4693005					.1040-05	.3624-05	.3400-05	.440A-07	.4403-11	.0000	.0000	.0000	.0000	1	88
91	4843005					.3720-07	.2103-0A	.1942-06	.4117-0A	.1521-13	.0000	.0000	.0000	.0000	1	91

TIME = 47

Figure 6 (continued)



Figure 6 (continued)

SAMPLE PERMITS 1 - MURPHY'S DRIVING FORCE IN SPHERICAL CAVITY

MCVILE	150	100	7500005	P	D	F	F1	F2	F3	V55	MPN J
1	3420000	4620000	5120000	5120000	5120000	5120000	5120000	5120000	5120000	5120000	1
4	4020000	5220000	5720000	5720000	5720000	5720000	5720000	5720000	5720000	5720000	4
7	4620000	5820000	6320000	6320000	6320000	6320000	6320000	6320000	6320000	6320000	7
10	5220000	6420000	6920000	6920000	6920000	6920000	6920000	6920000	6920000	6920000	10
13	5820000	7020000	7520000	7520000	7520000	7520000	7520000	7520000	7520000	7520000	13
16	6420000	7620000	8120000	8120000	8120000	8120000	8120000	8120000	8120000	8120000	16
19	7020000	8220000	8720000	8720000	8720000	8720000	8720000	8720000	8720000	8720000	19
22	7620000	8820000	9320000	9320000	9320000	9320000	9320000	9320000	9320000	9320000	22
25	8220000	9420000	9920000	9920000	9920000	9920000	9920000	9920000	9920000	9920000	25
28	8820000	10020000	10520000	10520000	10520000	10520000	10520000	10520000	10520000	10520000	28
31	9420000	10620000	11120000	11120000	11120000	11120000	11120000	11120000	11120000	11120000	31
34	10020000	11220000	11620000	11620000	11620000	11620000	11620000	11620000	11620000	11620000	34
37	10620000	11820000	12120000	12120000	12120000	12120000	12120000	12120000	12120000	12120000	37
40	11220000	12420000	12520000	12520000	12520000	12520000	12520000	12520000	12520000	12520000	40
43	11820000	13020000	12820000	12820000	12820000	12820000	12820000	12820000	12820000	12820000	43
46	12420000	13620000	13120000	13120000	13120000	13120000	13120000	13120000	13120000	13120000	46
49	13020000	14220000	13520000	13520000	13520000	13520000	13520000	13520000	13520000	13520000	49
52	13620000	14820000	13920000	13920000	13920000	13920000	13920000	13920000	13920000	13920000	52
55	14220000	15420000	14320000	14320000	14320000	14320000	14320000	14320000	14320000	14320000	55
58	14820000	16020000	14720000	14720000	14720000	14720000	14720000	14720000	14720000	14720000	58
61	15420000	16620000	15120000	15120000	15120000	15120000	15120000	15120000	15120000	15120000	61
64	16020000	17220000	15520000	15520000	15520000	15520000	15520000	15520000	15520000	15520000	64
67	16620000	17820000	15920000	15920000	15920000	15920000	15920000	15920000	15920000	15920000	67
70	17220000	18420000	16320000	16320000	16320000	16320000	16320000	16320000	16320000	16320000	70
73	17820000	19020000	16720000	16720000	16720000	16720000	16720000	16720000	16720000	16720000	73
76	18420000	19620000	17120000	17120000	17120000	17120000	17120000	17120000	17120000	17120000	76
79	19020000	20220000	17520000	17520000	17520000	17520000	17520000	17520000	17520000	17520000	79
82	19620000	20820000	17920000	17920000	17920000	17920000	17920000	17920000	17920000	17920000	82
85	20220000	21420000	18320000	18320000	18320000	18320000	18320000	18320000	18320000	18320000	85
88	20820000	22020000	18720000	18720000	18720000	18720000	18720000	18720000	18720000	18720000	88
91	21420000	22620000	19120000	19120000	19120000	19120000	19120000	19120000	19120000	19120000	91
94	22020000	23220000	19520000	19520000	19520000	19520000	19520000	19520000	19520000	19520000	94
97	22620000	23820000	19920000	19920000	19920000	19920000	19920000	19920000	19920000	19920000	97
100	23220000	24420000	20320000	20320000	20320000	20320000	20320000	20320000	20320000	20320000	100
103	23820000	25020000	20720000	20720000	20720000	20720000	20720000	20720000	20720000	20720000	103
106	24420000	25620000	21120000	21120000	21120000	21120000	21120000	21120000	21120000	21120000	106
109	25020000	26220000	21520000	21520000	21520000	21520000	21520000	21520000	21520000	21520000	109
112	25620000	26820000	21920000	21920000	21920000	21920000	21920000	21920000	21920000	21920000	112
115	26220000	27420000	22320000	22320000	22320000	22320000	22320000	22320000	22320000	22320000	115
118	26820000	28020000	22720000	22720000	22720000	22720000	22720000	22720000	22720000	22720000	118
121	27420000	28620000	23120000	23120000	23120000	23120000	23120000	23120000	23120000	23120000	121
124	28020000	29220000	23520000	23520000	23520000	23520000	23520000	23520000	23520000	23520000	124
127	28620000	29820000	23920000	23920000	23920000	23920000	23920000	23920000	23920000	23920000	127
130	29220000	30420000	24320000	24320000	24320000	24320000	24320000	24320000	24320000	24320000	130
133	29820000	31020000	24720000	24720000	24720000	24720000	24720000	24720000	24720000	24720000	133
136	30420000	31620000	25120000	25120000	25120000	25120000	25120000	25120000	25120000	25120000	136

JTIME = 92

Figure 6 (continued)

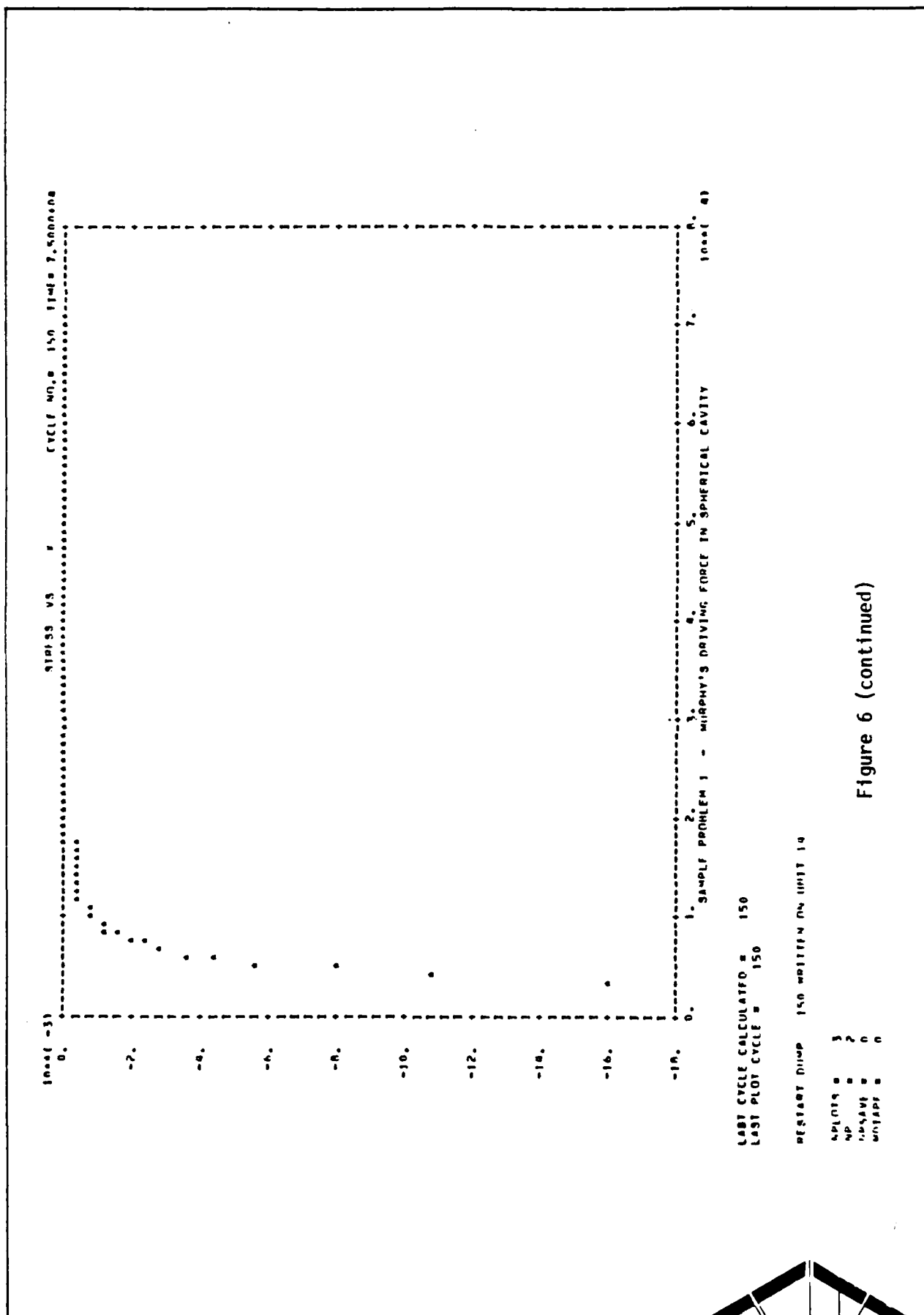


Figure 6 (continued)

PLUT NO. 1 SIGV VS TIME AT CELL NO. 2

EVERY NINETH POINT TO BE PLOTTED

MAX VALUE = -1.38076-04 MIN VALUE = -1.35358-02

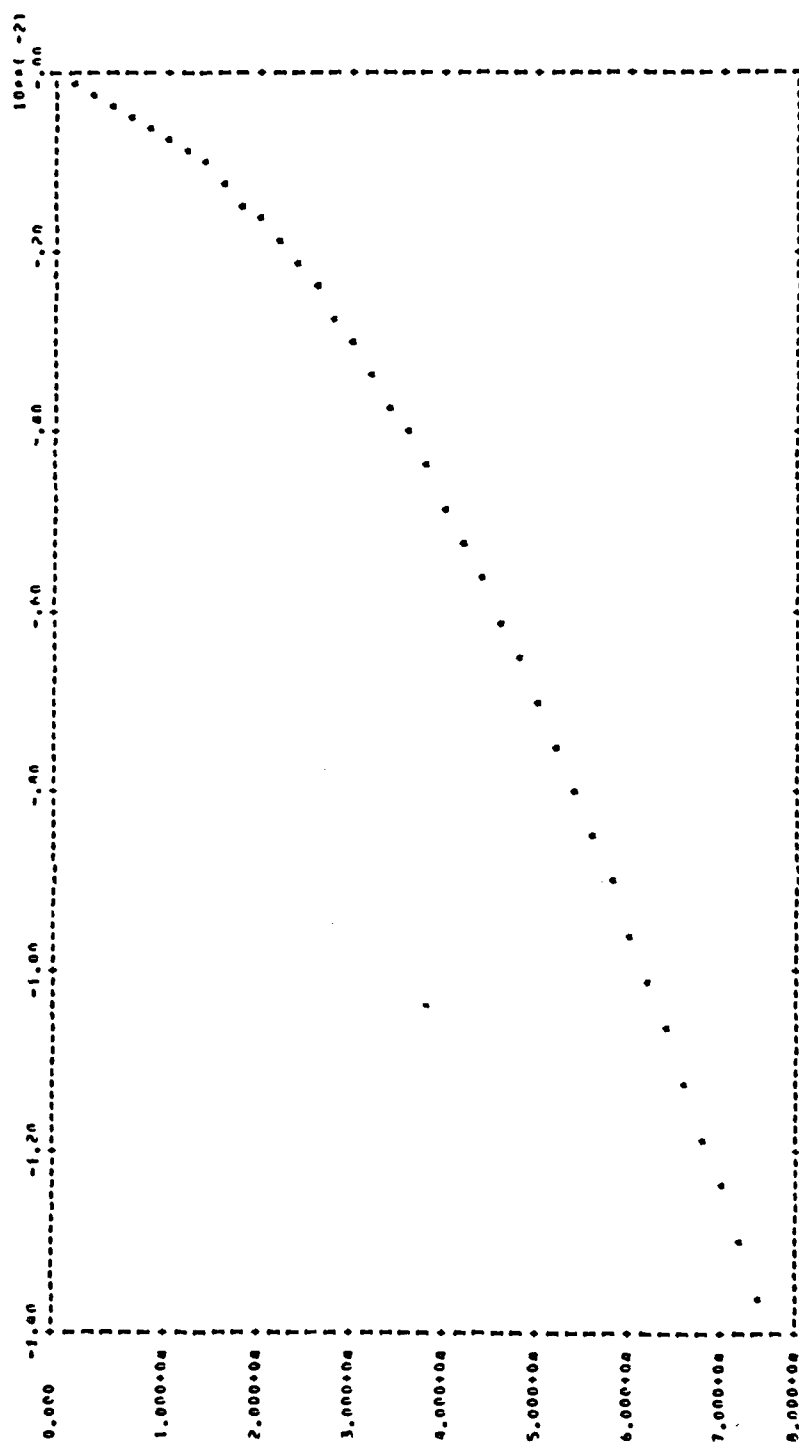


Figure 6 (continued)

PLOT NO. 2 VELOR VS TIME AT CELL NO. 10
 EVERY NINETH POINT IN RE PLOT100
 MAX VALUE = 0.02441-05 MIN VALUE = 0.000000

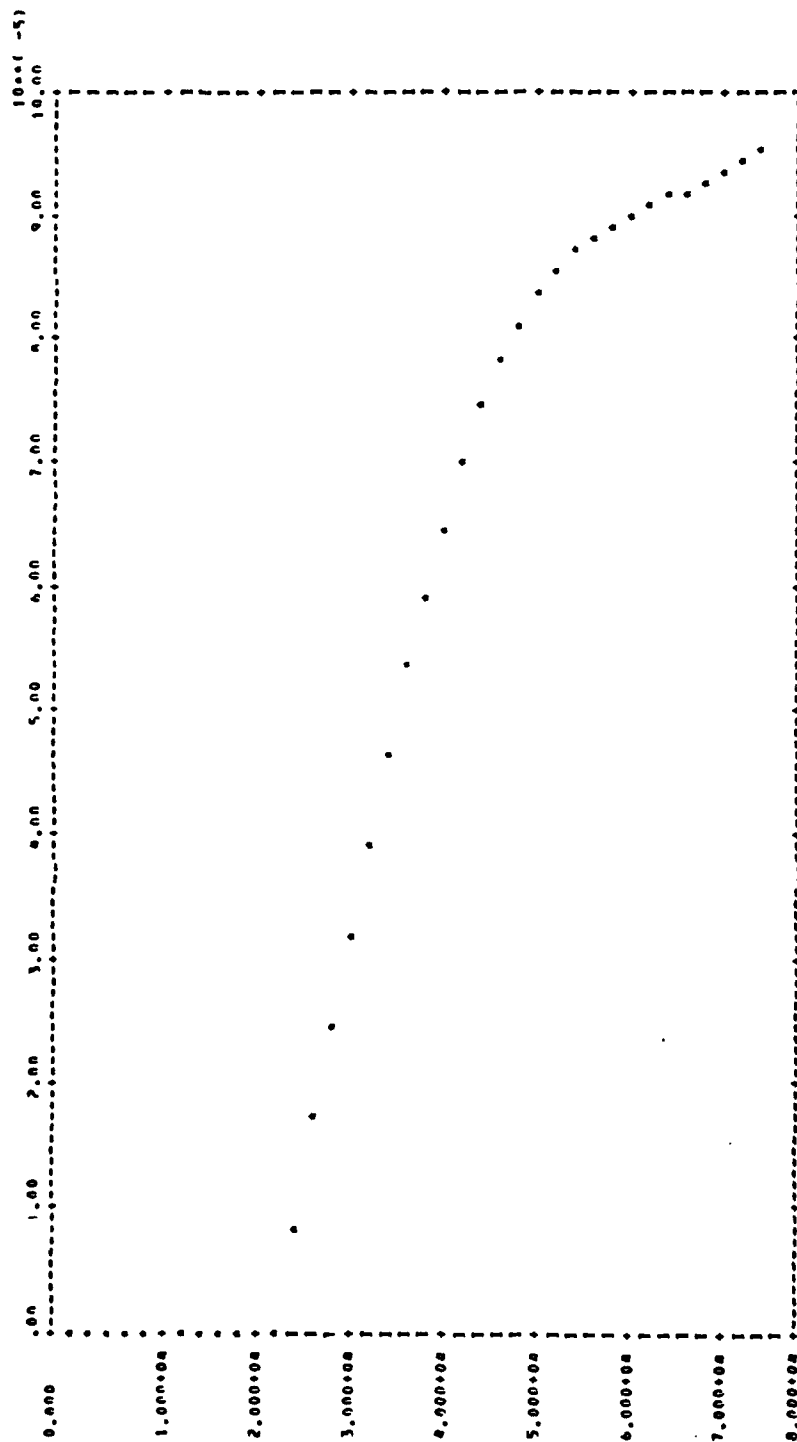


Figure 6 (continued)

PLOT NO. 3 5130 VS TIME AT CELL NO. 10

EVERY OTHER POINT TO BE PLOTTED

MAX VALUE = 3.00000 MIN VALUE = -1.01033-00

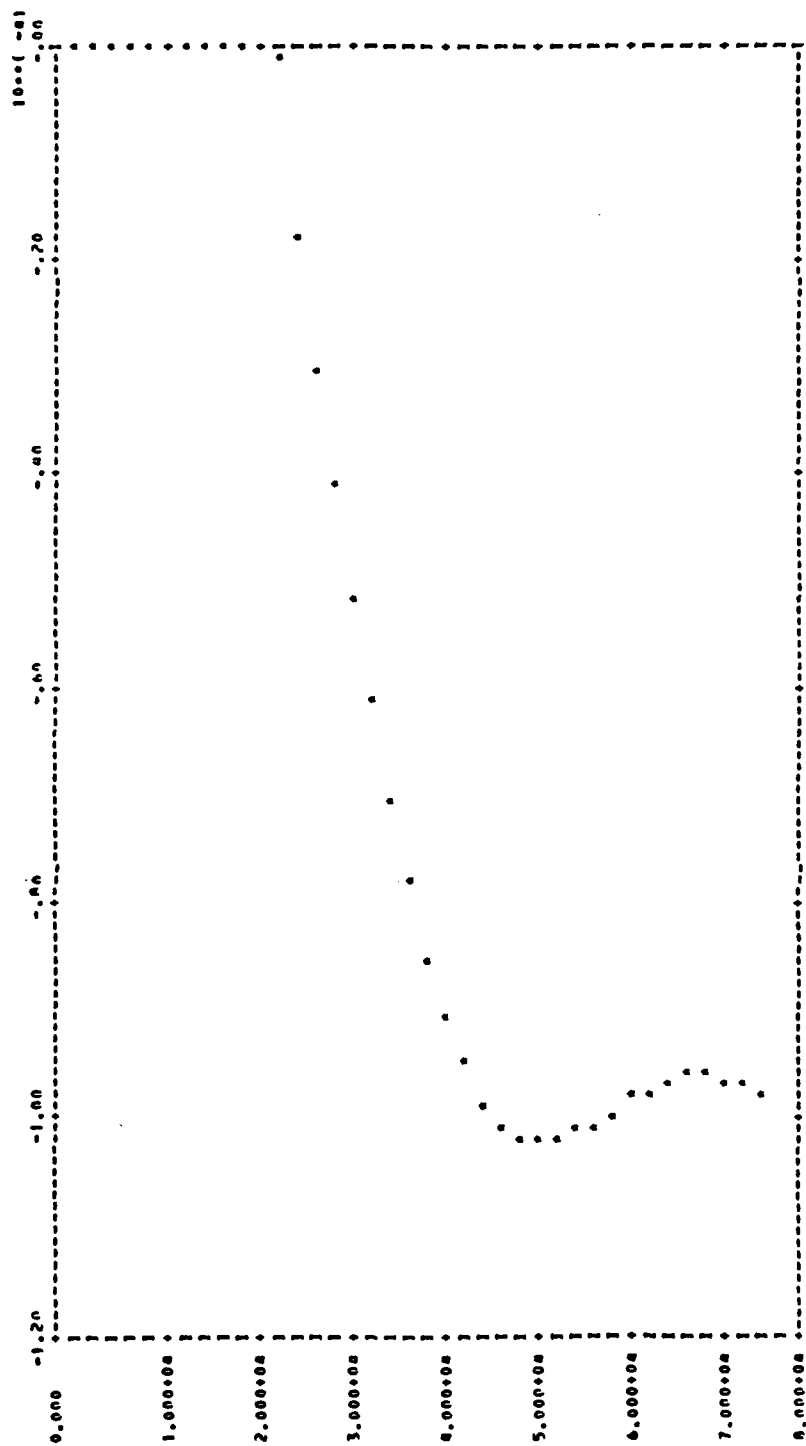


Figure 6 (continued)

SECTION VII

REFERENCES

1. Sweet, J., "Tensile Failure Model," Systems, Science and Software, November 26, 1973.
2. Sandler, I. S. and D. Rubin, "A Modular Subroutine for the Cap Model," DNA 3875F, Weidlinger Associates, Consulting Engineers, January 1966.
3. Sandler, I. S. and F. L. DiMaggio, "Material Model for Rocks," DASA 2525, Paul Weidlinger, Consulting Engineers, October 1970.
4. Sandler, I. S., F. L. DiMaggio and G. Y. Baladi, "A Generalized Cap Model for Geological Materials," DNA 3443T, Weidlinger Associates, Consulting Engineers, November 1974.
5. Mason, D. S. and B. J. Thorne, "A Preliminary Report Describing the Rezoning Features of the WONDY IV Program," SC-DR-70-146, Sandia Laboratories, March 1970.
6. Wilkins, Mark L., "Calculation of Elastic-Plastic Flow," Methods of Computational Physics, Volume 3 ("Fundamental Methods in Hydrodynamics"), edited by Berni Alder, Sidney Fernback and Manuel Rotenberg, Academic Press, New York (1964).
7. Lawrence, R. J., "WONDY IIIA - A Computer Program for One-Dimensional Wave Propagation," Sandia Laboratories Development Report SC-DR-70-315 (1970).
8. Fisher, R. H. and H. E. Read, "RIP, a One-Dimensional Material Response Code," Systems, Science and Software Report SS-R-72-1324 (1972).
9. Dynamic Response of Materials to Intense Impulse Loading, edited by Pei Chi Chou and Alan K. Hopkins, Air Force Materials laboratory, Wright-Patterson Air Force Base, Ohio, Library of Congress #73-600247.
10. Fried, J. C. and R. A. Cecil, "ANALYZ, A Computer Code for Analyzing Time History Data from One-Dimensional Material Response Codes," Del Mar Technical Associates (to be published).
11. Murphy, J. R., "Seismic Source Functions and Magnitude Determinations for Underground Nuclear Detonations," Bulletin of the Seismological Society of America, Vol. 67, no. 1, February 1977.
12. Cecil, Robert A., "Rezone Model for ONDEMAR," Del Mar Technical Associates, Memo to Joel Sweet, July 1977.

APPENDIX A

This appendix describes the rezoning model that has been incorporated into the ONDEMAR code. Also included is a description of a study that was undertaken to determine the optimum values of the parameters that the user must supply when using the rezoning capabilities of the ONDEMAR code.

BACKGROUND

The capability to combine zones in a mesh has been added to the ONDEMAR code. The rezoning procedures used in Sandia's WONDY code (Ref. 1) have been modified and adapted to ONDEMAR.

Rezoning capabilities are included in "hydro" codes to provide optimum calculational efficiency, i.e., low cost. Of course, this efficiency must be obtained without degrading the results of the calculations. To achieve this optimum efficiency, the calculational mesh used in ONDEMAR should contain the minimum number of zones that would be required to accurately simulate the problem of interest. This minimum number of zones will vary as a function of time for each problem.

The rezoning procedures added to ONDEMAR at this time have been "tailored" to the following class of problems. A driving force (blast wave, energy deposition, etc.) is supplied to one end of the mesh over a finite time. The resulting stress wave propagates through the mesh and decays with distance. Following the stress wave the material unloads to a relatively constant value. Since the main interest in this type of problem is focused on the loading and unloading effects of the main stress wave, the constant stress level zones on the unloading side are of secondary importance to the calculation. In many instances, these zones are the smallest zones in the mesh and are controlling the time step. Combining these zones allows the time step to grow and decreases the number of active zones in the mesh. Calculation time and costs decrease accordingly. The rezone model added to ONDEMAR allows these zones to be combined.

REZONE MODEL

The rezone model for combining zones is coded in subroutine REZONE. When the subroutine is called the mesh is scanned from the zone which contains the maximum stress level ($-\sigma_x$) back to the first zone. During this scan, zones are defined as "combinable" if they satisfy all of the following three criteria (see Figure 1a for index nomenclature):

$$1. \quad \left| \sigma_{x_j} - \sigma_{x_{j-1}} \right| < \sigma_{\ell_j} \quad \text{and} \quad \left| \sigma_{x_{j+1}} - \sigma_{x_j} \right| < \sigma_{\ell_j}$$

where σ_x = stress in direction of wave propagation

$$\sigma_{\ell_j} \equiv C_1 |\sigma_c + C_2 |\sigma_{x_j} - \sigma_1||$$

and $C_1, C_2, \sigma_c, \sigma_1$ are user-defined input parameters. (Default values are $C_1 = 1., C_2 = 0.2, \sigma_c = \sigma_1 = 0.$)

$$2. \quad X_j - X_{j-1} < \Delta X_{\max}$$

where X = interface location

$$\Delta X_{\max} \equiv \text{Min} \left\{ \Delta X_{\max_0}, \frac{\pi X_1}{20} \right\}$$

and ΔX_{\max_0} is a user-defined input parameter.

(Default value is $\Delta X_{\max_0} = 1 \times 10^{10}$ cm.)

$$3. \quad \left| \rho_j - \rho_{j+1} \right| < C_3 \left| \frac{\rho_j + \rho_{j+1}}{2} \right|$$

where ρ = density

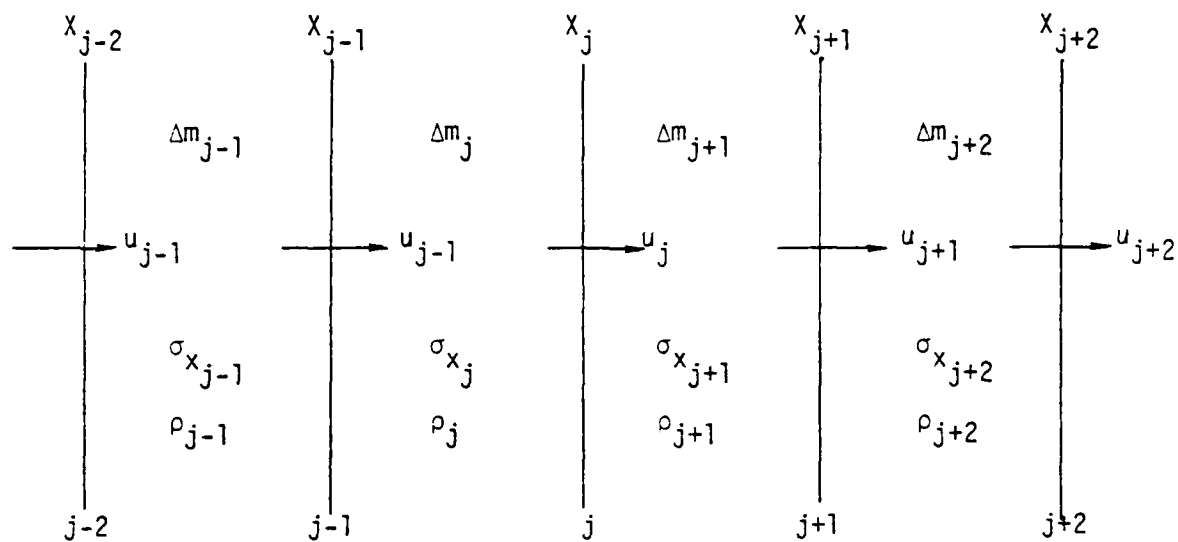


Figure 1a. Zoning Nomenclature

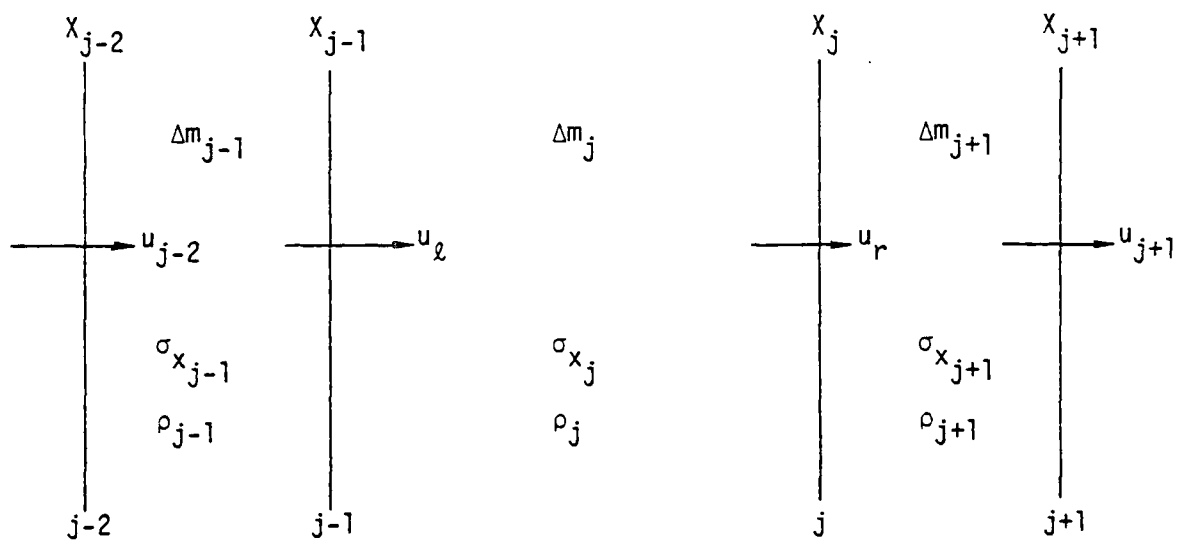


Figure 1b. Schematic diagram of zoning after combining zones "j" and "j+1" in Figure 1a.

and C_3 is a user-defined input parameter.

(Default value is $C_3 = .02$)

Criterion 1 assures that the stress variation between a zone and its two adjacent zones does not exceed a user-controlled limiting value. This limiting stress is calculated for each zone in the mesh. With the current default values, the limiting stress is simply a small percent of the current stress level. Additional parameters (C_1 , σ_c and σ_l) are provided to allow a more flexible limiting stress level to be calculated.

Criterion 2 prevents zones from becoming too large. This control is accomplished through a comparison of the zone size with a user-supplied value for maximum zone size or a calculated value which is currently related to the cavity radius for a spherical blast wave problem.

Criterion 3 assures that the density variation across zones does not exceed a user-defined limiting value. This limiting value is simply a percentage of the average density of the zone and its adjacent zone.

When a zone satisfies all three of these criteria, it is flagged as combinable. When two adjacent zones are determined to be combinable, the coincident interface is removed and the two zones are merged. This rezone model will not allow two successive interfaces to be removed on the same call to the subroutine. However, a zone may be combined more than once on successive calls to the subroutine.

When an interface is removed and two zones are combined as shown in Figure 1b, the properties of the interface velocities are recalculated using the conservation of momentum law, and the assumption that the two interfaces adjacent to the removed interface undergo velocity changes of the same percentage. Thus, the two equations used to solve for the two new velocities, u_l and u_r , are:

$$u_l M_1 + u_r M_2 = I_0 \quad (1)$$

where $M_1 = \Delta m_{j-1} + \Delta m_j + \Delta m_{j+1}$

$$M_2 = \Delta m_j + \Delta m_{j+1} + \Delta m_{j+2}$$

$$I_0 = (\Delta m_{j-1} + \Delta m_j) u_j + (\Delta m_j + \Delta m_{j+1}) u_{j+1} + (\Delta m_{j+1} + \Delta m_{j+2}) u_{j+2}$$

$$\frac{u_l - u_j}{u_j} = \frac{u_r - u_{j+2}}{u_{j+2}} \quad (2)$$

Solving Equations (1) and (2) yields

$$u_r = \frac{I_0}{\left(M_2 + \frac{M_1 u_j}{u_{j+2}} \right)} \quad (3)$$

$$u_l = \frac{I_0 - u_r M_2}{M_1} \quad (4)$$

All zone centered quantities, such as the stresses, energies, and pressures use the following volume weighting equation to obtain the combined zone values:

$$\phi_{j_{NEW}} = \frac{\phi_j V_j + \phi_{j+1} V_{j+1}}{V_j + V_{j+1}} \quad (5)$$

where

V = volume of zone,

and ϕ represents any zone centered quantity.

PARAMETER STUDY

Three rezoning parameters were investigated in this study: (1) calling frequency, (2) C_2 in the stress criterion for allowing zone combining and (3) C_3 in the density change criterion for allowing zone combining. A matrix of seven calculations was designed to determine reasonable default values for these parameters. It should be noted that all seven calculations had the same initial mesh configuration and starting conditions. The values of the three parameters determined during this study may change somewhat for problems which vary significantly from the test problem, chosen for this study. The results of the parameter study should be used as a guide and not as gospel.

The test problem modeled a spherical blast wave propagation (pressure-time history applied to left boundary). The initial mesh was 51.83 meters long. The size of the first zone was 3.182 cm and a zoning ratio of 1.03 was used. Each problem was run to a problem time of 3000 μ sec.

Table I shows the results of this study. Runs 1 through 4 tested the calling frequency, NREZ. Based upon the CPU costs on the S³ UNIVAC 1108, a calling frequency of 200 cycles was determined to be the most efficient. (Run 1 contained some additional plotter calls that were not included in the other six runs and therefore the costs are slightly on the high side). The calculated results, cavity radius, stress at the cavity radius, peak stress and location of the peak stress were essentially identical for these four calculations. These results are also shown in Table I.

Runs 2, 5 and 6 were made to compare values of C_2 . Although run 6 was the least expensive, the relatively loose stress change criteria (.05) was causing the problem results to degrade slightly. For this reason a value of .02 was selected for C_2 .

Runs 2 and 7 were made to compare the density gradient criteria. The results were identical and the lower value of .02 was chosen for C_3 .

TABLE 1

Run	MREZ	C ₂	C ₃	Cycles	Zones Combined/Total	Total/ Cost	CPU	X(1) meter	$\sigma_x(1)$ mbar	X(σ_{max}) meters	σ_{max} mbar	$\sigma_{x=4}$ mbar	$\sigma_{x=5}$ mbar
1	100	.02	.05	1542	24 / 51	\$24.09 / 12.54	161	2.217	$.7254 \times 10^{-3}$	6.822	$.4398 \times 10^{-2}$	$.1015 \times 10^{-2}$	$.1472 \times 10^{-2}$
2	200	.02	.05	1657	25 / 50	16.25 / 8.55	126	2.216	$.7238 \times 10^{-3}$	6.822	$.4388 \times 10^{-2}$	$.1008 \times 10^{-2}$	$.1472 \times 10^{-2}$
3	300	.02	.05	1831	23 / 52	16.09 / 8.99	133	2.216	$.7263 \times 10^{-3}$	6.822	$.4388 \times 10^{-2}$	$.1019 \times 10^{-2}$	$.1471 \times 10^{-2}$
4	500	.02	.05	2711	20 / 55	18.25 / 11.35	169	2.216	$.7245 \times 10^{-3}$	6.822	$.4386 \times 10^{-2}$	$.1020 \times 10^{-2}$	$.1471 \times 10^{-2}$
5	200	.01	.05	2422	14 / 61	21.28 / 12.13	182	2.216	$.7217 \times 10^{-3}$	6.822	$.4390 \times 10^{-2}$	$.1020 \times 10^{-2}$	$.1469 \times 10^{-2}$
6	200	.05	.05	1231	37 / 39	13.19 / 6.79	98	2.216	$.7414 \times 10^{-3}$	6.822	$.4395 \times 10^{-2}$	$.1026 \times 10^{-2}$	$.1479 \times 10^{-2}$
7	200	.02	.02	1657	25 / 50	16.86 / 9.16	135	2.216	$.7238 \times 10^{-3}$	6.822	$.4388 \times 10^{-2}$	$.1008 \times 10^{-2}$	$.1472 \times 10^{-2}$

TABLE 2

Run	Rezone	Maximum Time	Cycles	Zones Combined/Total	Total/ Cost
1	Off	3000 μ sec	6681	0 / 125	\$63.58 / 52.78
2	On	3000 μ sec	1427	51 / 74	28.82 / 15.87

A final set of two calculations was made to compare the overall savings provided by the rezone capability. The two calculations simply compare costs between a calculation in which the rezone is activated and a calculation in which the rezone is turned off. Table 2 shows the results of this comparison.

CONCLUSIONS

For the types of problems studied, spherical blast waves, the recommended rezone parameters are:

Calling frequency, NREZ: 200 cycles

Stress criterion parameter, C_2 : .02

Density criterion parameter, C_3 : .02

Maximum allowable zone size:

$$\Delta X = \frac{\pi X_1}{20}$$

- Ref. 1. Mason, D, S, and B. J. Thorne, "A Preliminary Report Describing the Rezoning Features of the WONDY IV Program," SC-DR-70-146, Sandia Laboratories, March 1970.

APPENDIX C

SPALL FROM CONTAINED EXPLOSIONS RELATED TO
YIELDS, DEPTHS OF BURST, AND MATERIAL PROPERTIES

DELTA-TR-79-027

SPALL FROM CONTAINED EXPLOSIONS RELATED TO
YIELDS, DEPTHS OF BURST, AND MATERIAL PROPERTIES

TECHNICAL REPORT

by

Glen Rawson

Consultant to

Del Mar Technical Associates
P.O. Box 1083, Del Mar, California 92014

ARPA Order No. 3368

Program Code: 7F10

Effective Date of Contract: 15 March 1977

Contract Expiration Date: 31 January 1979

Amount of Contract: \$338,956

Contract Number: F49620-77-C-0079

Principal Investigator and Phone Number: Gerald A. Frazier (714) 481-9292

Program Manager: Gerald A. Frazier (714) 481-9292

Title of Work: Near Source Effects and Their Manifestations in Seismic Observations

Sponsored by

Advanced Research Projects Agency (DOD)

ARPA Order No. 3368

Monitored by AFOSR Under Contract # F49620-77-C-0079

March 1979

TABLE OF CONTENTS

<u>Section</u>	<u>Page</u>
1. INTRODUCTION.	C-1
2. PREVIOUS SPALL RELATED GROUND MOTIONS STUDIES	C-3
3. SPALL DEPTH METHODS OF INTERPRETATION	C-10
4. GENERAL CONFIGURATION OF NEAR SURFACE SPALL	C-16
5. DEPTH OF SPALL ANALYSIS SUMMARY AND APPARENT SCALING RELATIONS	C-29
6. EXTENT OF SPALL ANALYSIS SUMMARY	C-40
7. DEPTH OF SPALL AT THE EXTENT OF SPALL ANALYSIS SUMMARY .	C-48
8. SPALL RELATED TO GEOLOGIC PARAMETERS	C-53
9. FREE SURFACE/CAVITY GROWTH HISTORY INTERACTIONS — THE MERLIN EVENT.	C-58
10. CONCLUSIONS AND RECOMMENDATIONS	C-68
11. REFERENCES.	C-72
APPENDIX: DEPTH OF MAXIMUM SPALL ANALYSES	C-76

I. INTRODUCTION

There has not, to this author's knowledge, been a comprehensive evaluation of spall related surface and subsurface ground motion data from nuclear explosions. Examination of existing literature reveals several assumptions of what spall is, and the estimates of spall depth and/or extent vary considerably — even when all estimates are based upon the same data.

Spall is of interest to the Department of Defense in order to:

- Better understand explosion-generated seismic waves and the role spall may play in generating the waves.
- Determine if the rock failure and associated strain release associated with spall is significant in producing surface wave double couples related to near source and near surface in-situ stress inhomogeneities.
- Better characterize and predict spall related ground motions and block motions.
- Assure containment of *nuclear explosions* as well as survival of measurement equipment subjected to severe ground motions.

The focus of this study is to evaluate spall as it relates to near source inhomogeneities and the generation or modification of seismic waves. The investigation under this contract involved examination and interpretation of subsurface and near surface ground motion records in the published (open) literature. Thus, evidence to estimate spall and subsurface wave interactions between the explosion, free-surface, and the expanded cavity are sought. In addition, this study incorporates the tentative results of a parallel ground motion (spall) investigation of the published free-surface ground motion records being conducted also by the author*. That study is focused upon obtaining evidence to characterize the extent of spall and allow for exploring possible empirical scaling relations as a function of yield (W), depth of burst (DOB), material properties, etc.⁽¹⁾

* Rawson, Glen; Consultant to R & D Associates, Marina del Rey, CA for DNA; report in progress.

The integration of these two spall related ground motion studies provides an initial contribution toward a comprehensive interpretation of the configuration of spall and how it might be extended to various environmental conditions. Most events are buried at about a scaled depth of burst of $122 \text{ m/kT}^{1/3}$, that which is typically assumed for adequate containment. The data are biased with most tests occurring at scaled depths of burst between 100 and $160 \text{ m/kT}^{1/3}$. The cratering scaled depths of burst are generally less than $50 \text{ m/kT}^{1/3}$. In the other direction, there are few tests with scaled depths of burst greater than $160 \text{ m/kT}^{1/3}$ **..

Examination of the published literature that would enable estimation of spall depth near the explosion (surface ground zero -- SGZ) revealed only about ten events in six grossly different geologic environments. Thus, the statistics are poor for developing rigorous empirical scaling relations for the maximum depth of spall. The surface motion data relating to the extent of spall is more complete (about 35 events in about ten grossly different geologic environments). This enables a more complete description of spall extent to help determine scaling relations and prediction methods.

An additional outcome of this investigation is that several of the nuclear explosion tests at scaled depths of burst between 100 and 160 m/kT showed considerable interaction between the detonation produced cavity and the free-surface. This provides an opportunity to evaluate the hypothesis that the explosion produced chimney (resulting from upward propagation of the cavity through failed material) is controlled by fracture surfaces resulting from the early explosion dynamics. The data help resolve between two distinctly different models to explain chimney and subsidence crater development resulting from detonations in or below deep alluvium.

** Scaled depth of burst (SDOB) is assumed to be a function of the cube root of the explosion yield.

2. PREVIOUS SPALL RELATED GROUND MOTION STUDIES

The early work in delineating spall from nuclear explosions was accomplished principally by the following investigators during the 1960's: J.D. Eisler, F. Chilton, W. R. Perret, J. S. Rinehard, and L. M. Swift.⁽²⁻⁷⁾ Many of these reports will be specifically referred to in the following sections. Most of the spall studies involved limited interpretations associated with each ground motion data report. Some reports incorporate analyses of a few events. The most comprehensive investigation of spall may have been the MERLIN event, involving 17 ground motion gauges in two subsurface drill holes at different ranges to establish the depth of spall near the explosion. The extent of spall and character of surface motion along one azimuth was documented by 21 surface gauges. In addition, there was a shot level array of eight gauges at the bottom of five additional drill holes.⁽³⁾ Although this study contributed greatly to delineating spall configuration, spall in compactable alluvium may differ significantly from more competent rock. When large yield tests at Pahute Mesa, Amchitka, and Central Nevada were conducted, spall had not been sufficiently documented in the relevant materials and yields to predict depths and extents of spall. Furthermore, there was not a significant priority given to attract much attention to understanding details of spall.

The Round Robin program did exist, which rather routinely obtained limited surface motion data. Typically, gauges were installed near SGZ, 1/2 DOB, 1 DOB and 2 DOB ranges (ground level from SGZ.* Rarely were subsurface spall related data obtained, were there more than four to six surface gauge stations, or were there gauges located in more than one azimuth. Often in the more competent materials, all of the gauges were located well within the extent of spall.⁽⁸⁾

Especially with the large yield tests (200 to 5000 kT), surface effects (movements for several kilometers) along pre-existing faults and subsurface

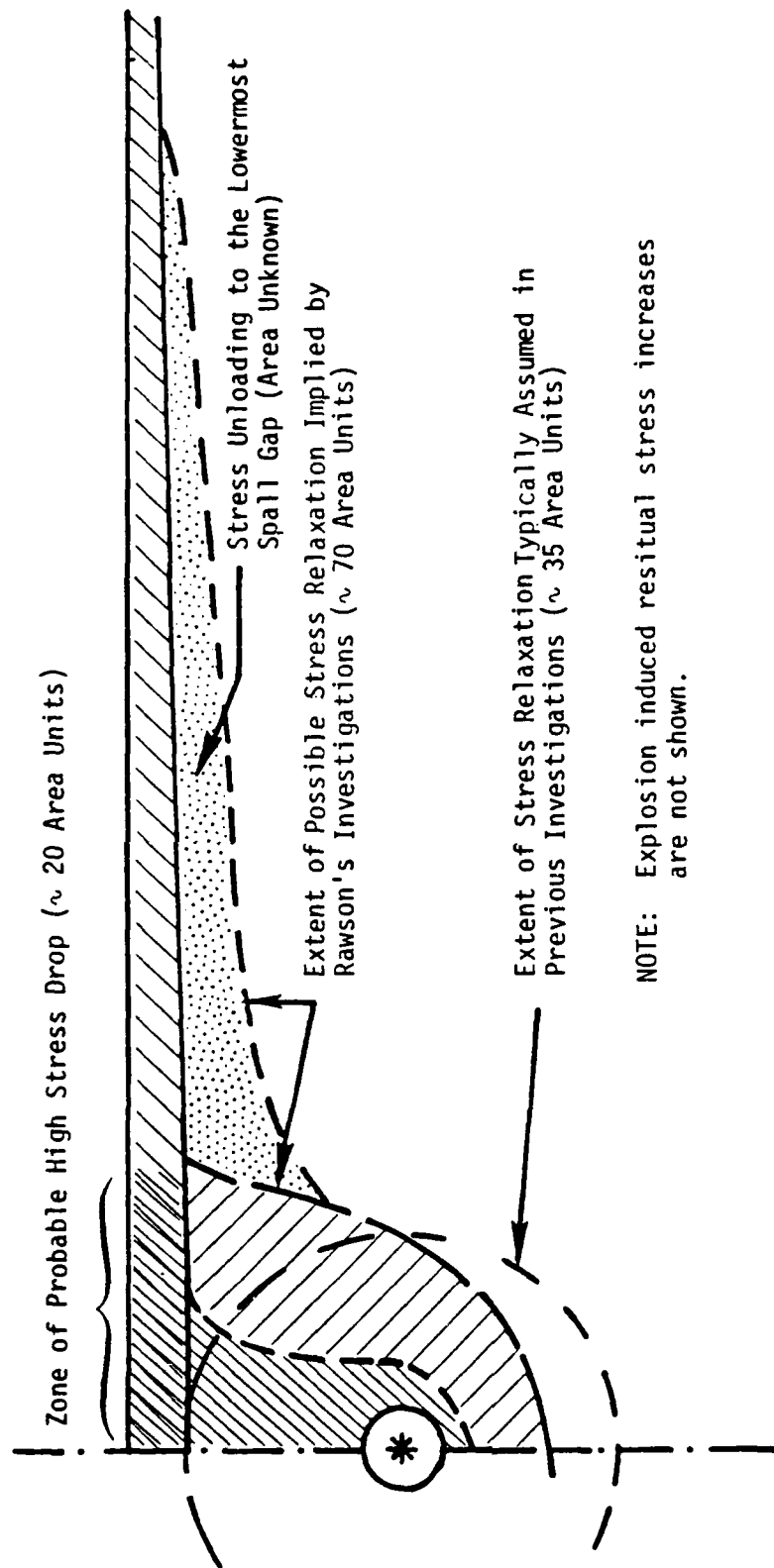
* SGZ (surface ground zero); DOB (Depth of Burst).

effects (seismic aftershocks) were observed. These effects pointed to the likelihood of explosions triggering earthquakes and releasing of in-situ tectonic stresses.^(9,10) Earlier with such events as BILBY, HARDHAT, SHOAL, etc., it had been noted that surface wave double couples had been produced.⁽¹¹⁻¹⁴⁾ These were interpreted as both triggering of specific faults and as general partial release of strain from the fractured regions around the detonations. The models did not include the contributions that might be made by either stress drop due to spall or to a chimney region failure zone between the shot and the deeper positions of spall. Such a difference is a factor of two or more in cross-sectional area as illustrated by Figure 1 — generalizing results of this study.

The early 1970's data reports from MILROW and RIO BLANCO enabled those reading the reports to learn something of the large extent of spall for those events. The 1-MT MILROW event was in water saturated volcanic rock and the 90-kT (three 30 kT explosions) deeply buried RIO BLANCO event have extents and depths of spall reported as follows:^(15,16)

	<u>Spall Depth</u>	<u>Spall Extent</u>
MILROW	Probably Greater Than 152 m	Out to 5180 m
RIO BLANCO	Probably Less Than 107 m	Less than 7300 m Greater Than 3650 m

The depth comparisons between measurements and calculations for the RIO BLANCO events were in reasonably good agreement. No prediction of spall extent was made but the extent must have been surprising, considering the effective yield as it affects spall, must be equal to or greater than only 30 kT and certainly less than 90 kT, since the explosions were significantly separated in both space and time. From the above, it is seen that spall radii of several kilometers were documented for shots in competent material. These two events, however, imply relatively shallow spall depths. The fact that 30 to 90 kT could do what a megaton did in terms of spall extent, even though it was buried at almost five times the scaled depth of burst, seems indicative of the lack of in-depth understanding of the spall process.



~ 1 MT Explosion ~ 1 km

~ 200 kT Explosion ~ 1 km

[Scaled Depth of Burst ~ 100 to ~ 125 meters ($W^{1/3}$)]

Figure 1. Idealized cross section of nuclear explosion induced fracture zones and possible stress relaxation zones.

During this same time period, J. A. Viecelli reported on a doctoral dissertation relating spallation to the generation of surface waves by underground explosions.^(17,18) Part of this investigation was the characterization of spall from field data to be used in computing or modeling the generation of Rayleigh waves by the spall process. Data from five events in volcanic rocks at Rainier and Pahute Mesas were utilized to guide the modeling of the spall mass and momentum. The spall extent was not the total spall extent, but only went out to the limits of severe spallation where displacements are still ~ 0.3 meters. The depths of spall cited appear to be in error because the spall depths appear to be estimated from surface gauges only. This occasionally enables unambiguous estimation of the uppermost spall gaps close to SGZ or possibly the thickness of spall near the limits of spall. Thus the spall thickness errors are large. For RAINIER, spall depth is reported as 17 meters instead of the 82 meters reported by Perret, 1972, or the 113 meters reported by Eisler, et al., 1966, and indicated by the reanalysis in this study.^(3,7)

The Viecelli analysis determined the following scaling relations:

- Effective spall thickness scales as the one-third power of yield assuming a constant shot medium and scaled depth of burst.
- Cube root scaling of spall thickness versus scaled depth of burst indicates an inverse power law where thickness varies inversely with the yield.
- The radius of severe spallation (measured along the ground) scales as the one-third power of yield.
- The radius of severe spallation has little or no dependence on scaled depth of burst. It appears that increased spallation with decreased depth of burst (expected) is balanced by decreased spallation with increasing angle of incidence of the shock wave.

A goal of the present study is to expand upon the limited data base (analyzed, interpreted, and integrated), so that implied scaling relations can be tested and alternative scaling proposed if indicated.

The Viecelli study concludes that:

- Inelastic spallation processes are important in generating surface waves, even though the explosion is completely contained.
- It is not yet clear that spall related surface waves are detectable at teleseismic ranges.
- A combination of multiple explosion configuration and topography (mountain/valley as opposed to plain) can significantly alter peak Rayleigh-wave amplitudes.

The above conclusions are made even though the thickness and areal extent of spall by Viecelli are considerably less than indicated by this study.

Recently, P. A. Sobel conducted an independent evaluation of the importance of spall to the generation of both body waves and surface waves.⁽¹⁹⁾ This report adds some complications to the relations of spall to the generation of both body waves and surface waves. In the characterization of spall extent and spall depth, more events are analyzed but they are not evaluated as to materials properties differences. Considering the spectrum of geologic environments from alluvium to highly competent rock, this introduces a large uncertainty factor in establishing empirical scaling relations.

The thicknesses of spall as determined by (and/or reported by) Sobel are similar to that of Viecelli -- that is, possibly representing the upper-most spall or spall thickness near the extent of spall, rather than some average value. Her estimates of the extent of spall are generally greater than Viecelli's, but the analysis was neither rigorous nor internally consistent. In one case, the extent of spall is at a ground motion station where the initial peak acceleration is 9.6 g. In another, it is as low as 0.03 to 0.15 g. The lack of a criteria consistently applied to estimating the extent of spall places considerable uncertainty upon the conclusions of the study.

The extent of spall for a number of events (both classified and unclassified) that were detonated in Pahute Mesa and Yucca Valley at NTS were informally reported by Vortman of Sandia Corporation.⁽²⁰⁾ These determinations of the extent of spall are internally consistent and generally are greater than the estimates of Sobel and certainly much greater than the estimates of Viecelli.

Viecelli and Sobel reportedly used the extent of spall determination method described by Eisler and Chilton.⁽²⁾ This is done by plotting the "flight" time (the time between initial and spall impact acceleration signals) versus range from surface ground zero. When the times become constant or slowly varying, the extent of spall is assumed to have been determined. This is not a precise way of defining spall, because the "flight" time changes slowly with distance, making the range choice very subjective. As a result, the three different investigators have all reported different extents of spall for RAINIER: Sobel, 458 m; Viecelli, 120 m; Eisler and Chilton, 340 m.^(19,17,2) These are all radii measured as horizontal ranges. Interestingly enough, the estimate by Rawson⁽¹⁾ for the nominal extent of spall for RAINIER is 400 m, between the estimates by Sobel and that of Eisler and Chilton. This result is from a totally different criterion enabling the estimation of extent of spall from limited data. The method used is based upon the initial peak acceleration being extrapolated or interpolated to a value of +1 g. The extent of spall is defined by this method as the radial distance from the detonation where the initial vertical acceleration pulse equals +1 g. The log-log plot is a function of slant range (from the shot) instead of horizontal ground range. The data set defines a range and a nominal spall extent associated with the data scatter (see Figure 2).

Vortman used a somewhat different criterion that is a more accurate description of spall if there is sufficient gauge coverage (it tends to define the maximal extent of spall). This criterion is that a recognizable -1 g vertical acceleration persists for a time period long enough to reflect ballistic motion. There is also some additional confirming evidence of spall, such as an impact acceleration reversal. The data base contains numerous examples of initial accelerations being less than the impact acceleration for the same measurement stations. The reverse is not very commonly observed.^(21,22) The impact accelerations scatter greatly so they are not as useful for interpolation or extrapolation as the initial vertical accelerations. Vortman used a go- no-go approach; each station either spalled, did not spall, or had a short -1 g duration and was thus considered at the edge of the spall.

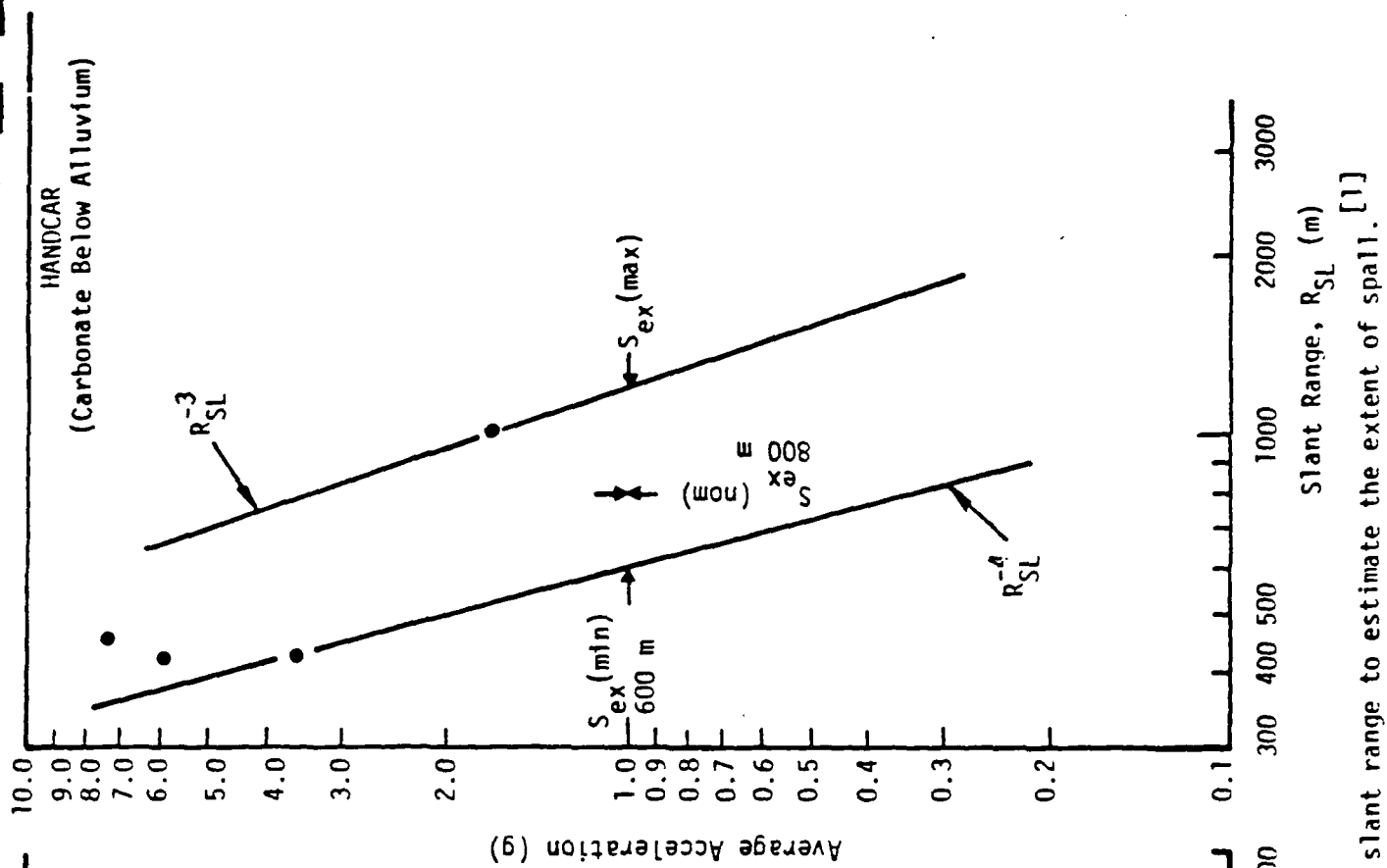
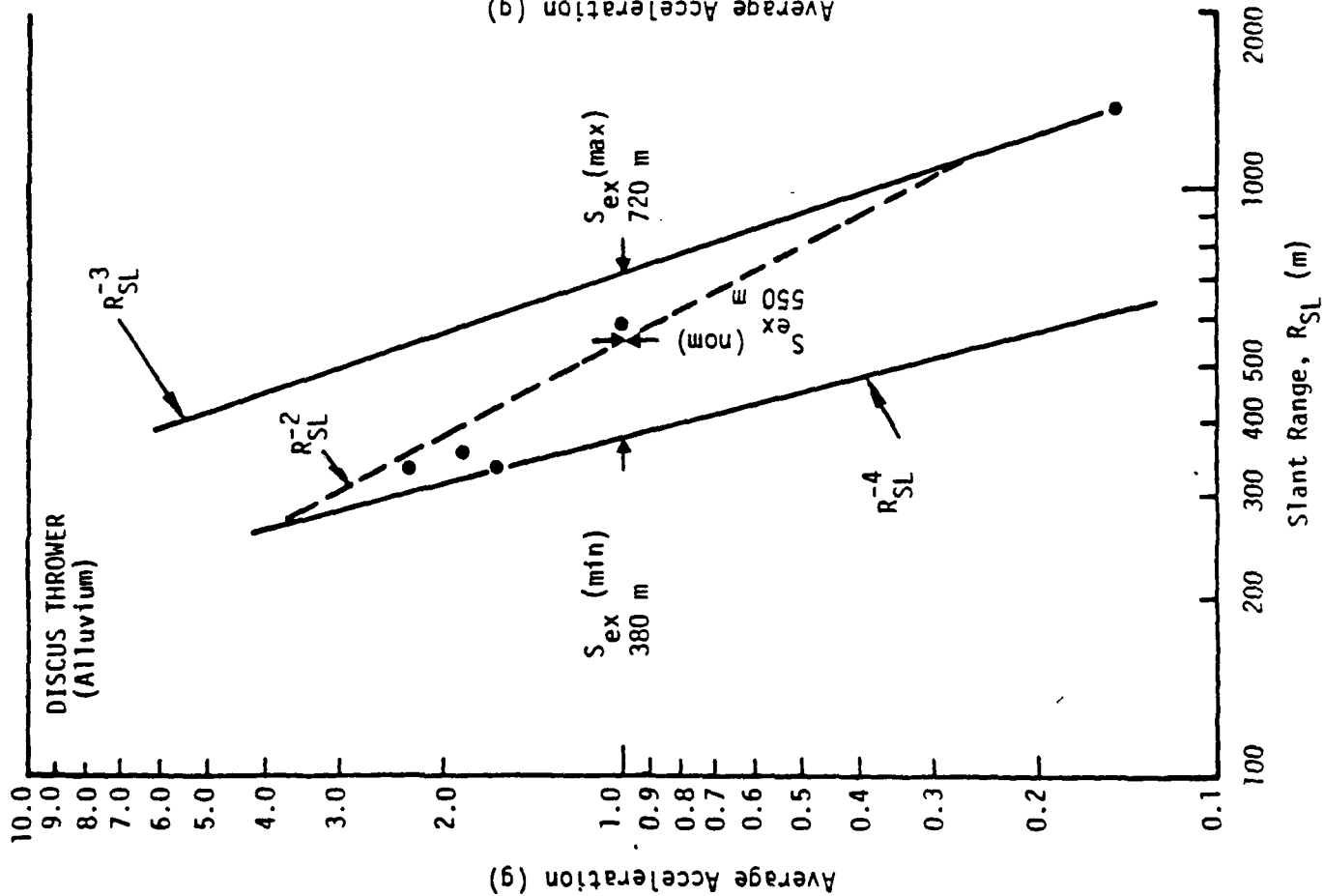


Figure 2. Example plots of vertical acceleration vs slant range to estimate the extent of spill. [1]

3. SPALL DEPTH METHODS OF INTERPRETATION

Because of multiple spalls, especially in the close-in regions to the detonation where the seismic energy is greatest, one cannot determine maximum spall depth from surface stations. At best, surface gauges only record signals from the upper spall gap. Subsurface gauges are required to accurately determine the third dimension of spall.⁽³⁾

Figure 3 illustrates a rather subjective method for estimating the depth of spall from subsurface stations. It was accomplished by qualitative ray tracing of incident and reflected ground motions waves making use of correlating signatures of ground motion traces. Upon spall gap impact, compressional waves are generated that radiate both upward and downward, typically resulting in + acceleration above and - acceleration below the point of impact. This method is, of course, subjective because it depends upon the assumptions of wave phenomena of each investigator. Perret interpreted the same RAINIER data (Figure 4) somewhat differently, with the maximum spall depth at 82 meters. A re-analysis of the same data, as part of this study (Figure 5) independently estimated the possible maximum spall depth as about 113 meters. This depth is essentially coincidental with location C', the maximal spall depth, in Figure 3.

The depth of spall of the uppermost spall gap (at least formed initially) can sometimes be determined from the initial spall acceleration signature. The upper spall gap at the time of spall impact can possibly be inferred through the impact acceleration signature. The method is illustrated with the data from LONGSHOT, Figure 6.⁽²³⁾ The initial arrival of the compressional wave at the surface gauge is t_0 at 0 time (the time scale has been shifted to subtract the time from shot time to the first arrival). Following t_0 are two positive acceleration spikes. The initial peak (t_1) follows the first wave arrival and represents the approximate time of major reflection of the compressional wave. At the point labeled spall initiation a compressional wave is generated by the opening of spall gap opening. This reacceleration produces the second peak, t_2 . Following this, the record is constant -1 g characteristic of free-fall, or the ballistic period, before spall impact. The arrival time of the impact

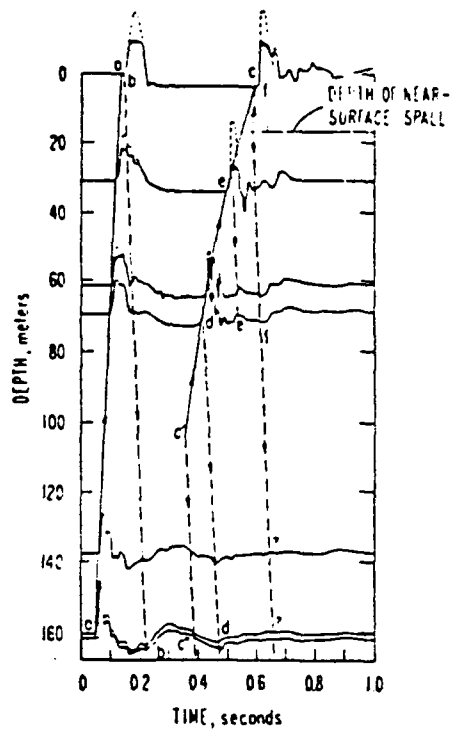


Figure 3. Acceleration traces illustrating multiple subsurface spalling for a shot in tuff [7]. The quiescent trace positions correspond to the depths of the gauges. The directions of the arrowheads indicate the direction of flow of seismic energy.

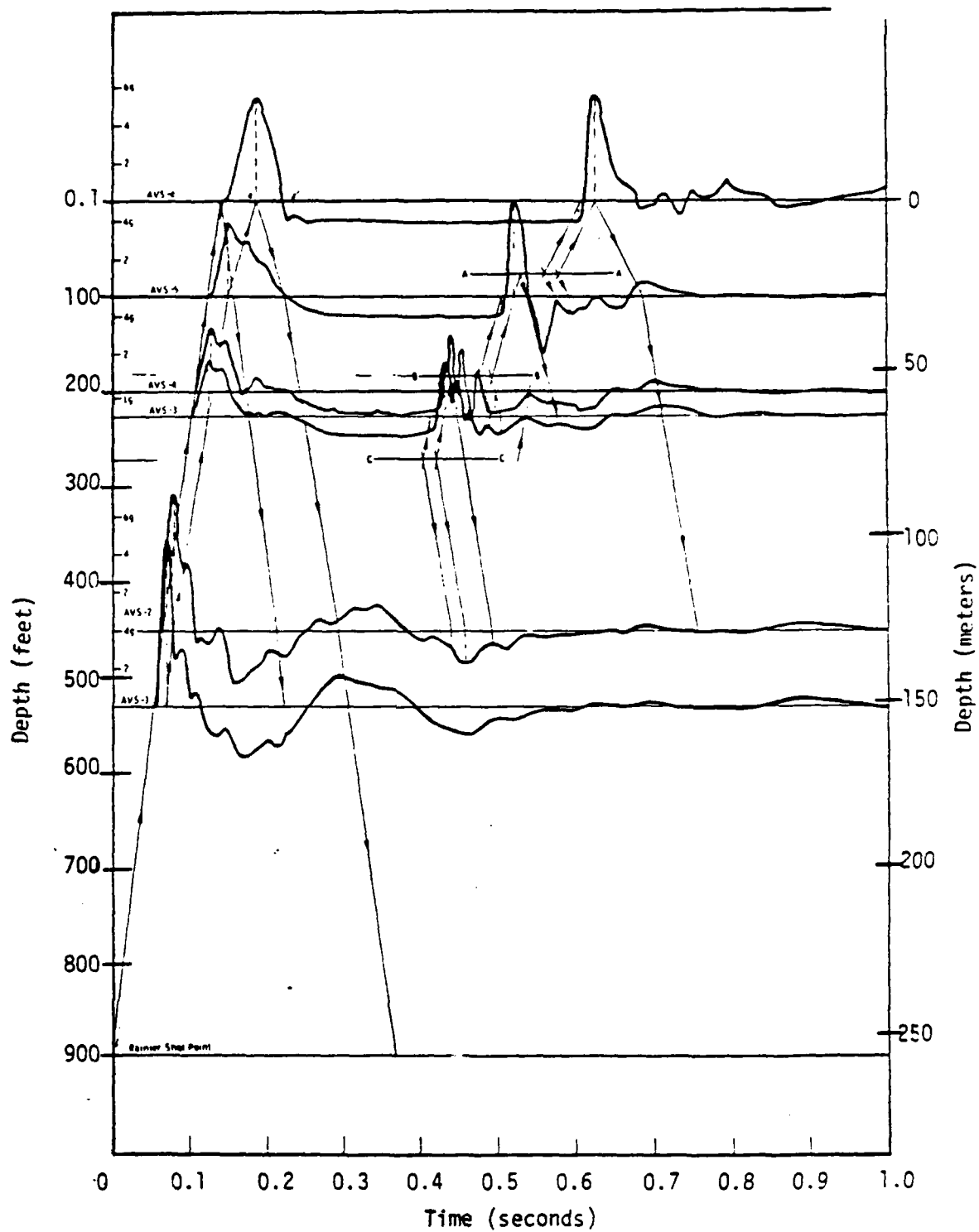


Figure 4. Impact signal analysis, RAINIER event. [3]

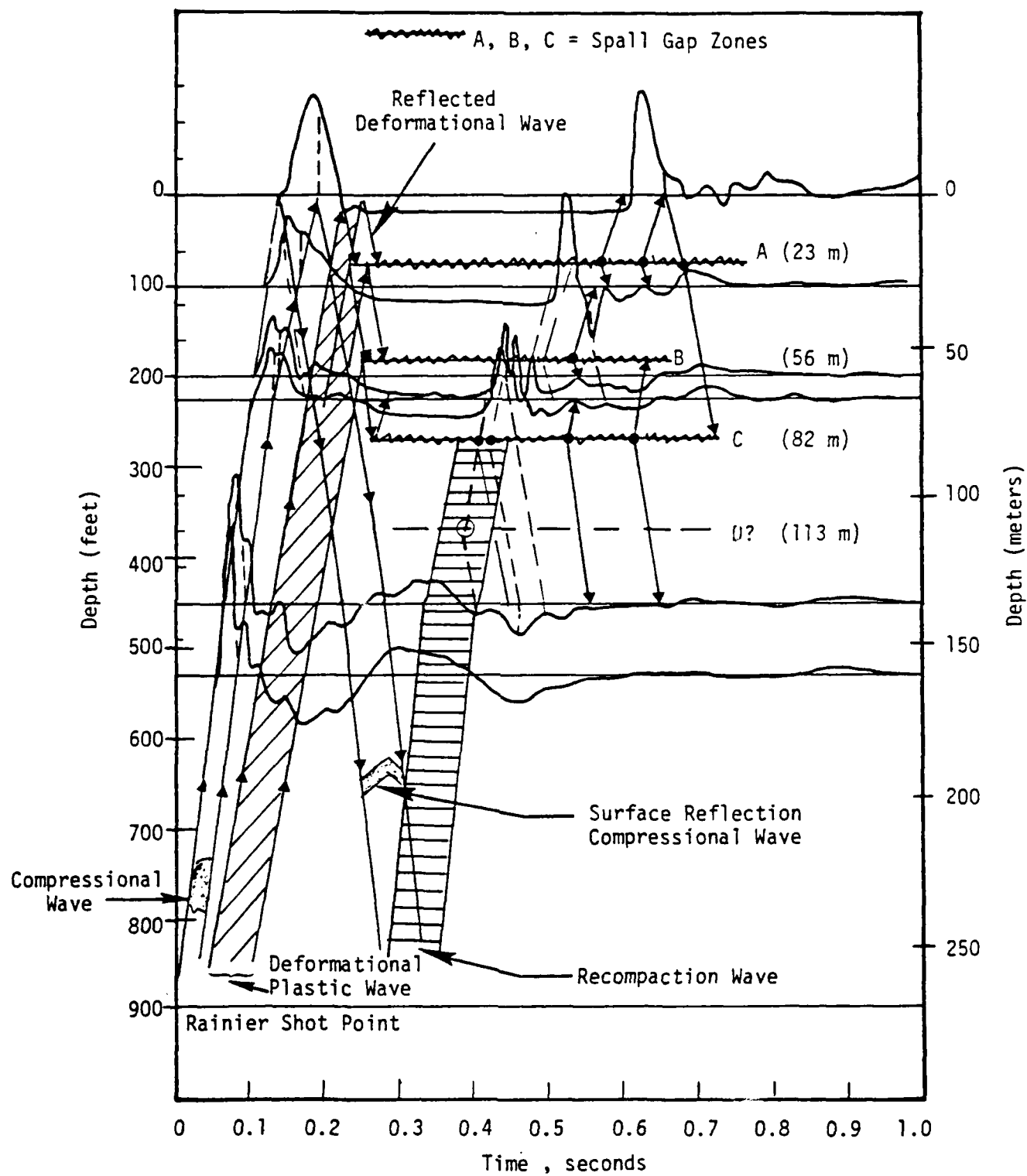


Figure 5. Explosion cavity/free surface and impact signal analysis; Rainier event.

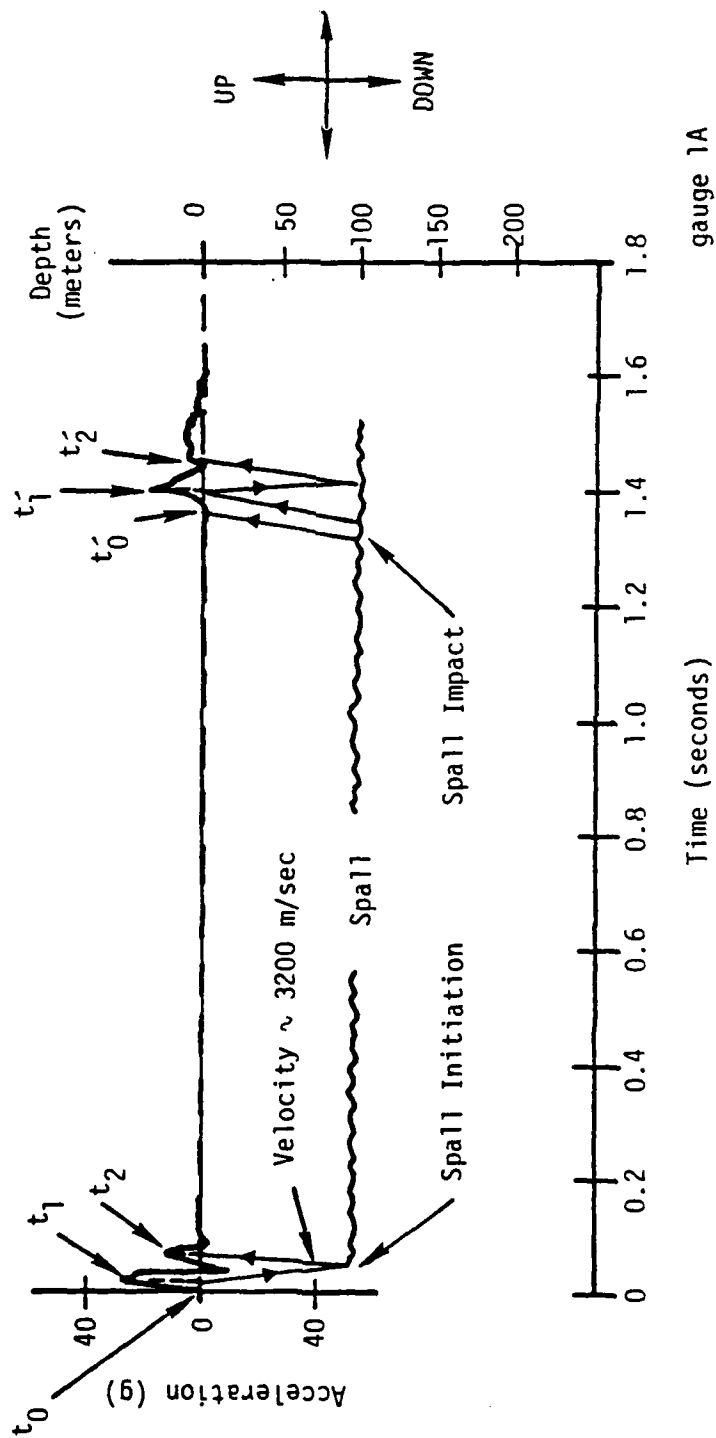


Figure 6. LONGSHOT surface ground zero acceleration record illustrating the method of estimating upper spall depth. [23]

acceleration peak, t_1 , minus that of the spall initiation acceleration, t_2 , is the free fall period at that ground motion station. This time decreases with depth below SGZ and with lateral distance (increasing horizontal ground range or slant range). The spall impact signature also has a second and sometimes a series of re-accelerations. The major re-acceleration peaks in Figure 6 are labeled t_1 and t_2 . For LONGSHOT the time differences $t_2 - t_1$ and $t_2 - t_1$ are essentially equal possibly indicating that spall initiation and spall impact occurred on the same gap. The depth of this spall gap is estimated by:

$$D_{sg} \approx \frac{t_2 - t_1}{2} \cdot V_p \quad (1)$$

The spall gap depth is D_{sg} , t_1 is the arrival of spall initiation or impact, t_2 is the arrival of the spall gap initiation compressional wave causing a positive re-acceleration. The compressional or sonic velocity (V_p) is that of the near surface spalled material (~ 2681 m/sec for LONGSHOT). It appears from the literature on spall that most investigators agree with Eq. (1). Some use times of arrival, some use peak values, and some assume that spall depth is actually determined without recognizing that the deeper spalls are hidden. Wave transmission does not jump the deeper spall gaps if they are open. The waves may close portions of the gaps, air may transmit some of the compression, but the waves are so attenuated that detection is generally not possible for the deeper spall gaps.

4. GENERAL CONFIGURATION OF NEAR SURFACE SPALL

Figure 7 illustrates the results of an early computational model of nuclear-explosion-induced spall based upon the RAINIER event. This investigation was by Chilton, et al., on the Dynamics of Spalling.⁽⁶⁾ The upper and lower bounds agree with data at zero horizontal distance (near SGZ). The horizontal extent of spall, however, is indicated as probably being between 183 and 200 meters instead of the 310 to 450 meters indicated earlier in this report as most probable. The calculation assumes a tensile strength of 3.8 m.* The figure is of interest in that, with the assumptions they used, the upper spall gap surface is expected to be concave downward while the lower spall surface is concave upward. These combined as shown indicate that "the spalled region can be considered a solid of revolution about a vertical axis passing through the working point and SGZ."⁽⁶⁾ Close-in (near the explosion) data tend to support this model. The extent of spall is more complex than this model dictates. Actual spall surfaces are greatly controlled by the orientation and distribution of natural weaknesses and associated in-situ "tensile strength".

The field evidence used to help indicate the possible character of spall near the edge of spall region is poor data from the BLANCA event. Here an indication of spall depth is possible by both surface gauges and subsurface gauges near the extent of spall range.⁽²⁴⁾ This unique experiment resulted from the re-use of subsurface gauges originally installed for close-in measurements of the EVANS event. EVANS went low yield and left the gauges intact so they could be used on BLANCA. It was not feasible to change the set ranges on the gauges but recorder sensitivities were altered.⁽²⁵⁾ Figure 8 and 9 display the data and the ray path interpretations from the depth of spall. Note that these acceleration records are inverted from what is common practice (up is down). The surface gauges (O-AV and AX-O) are located horizontally 1019 m from SGZ and 1097 m slant range. The estimated extent of spall for BLANCA was 1200 ± 200 meters

* A 3.8 m tensile strength means that a rock column 3.8 m in length can be suspended vertically without breaking, but a longer column would break.

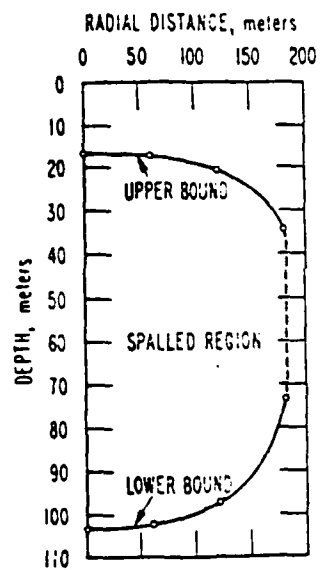


Figure 7. Upper and lower bounds of a spalled region. [6]

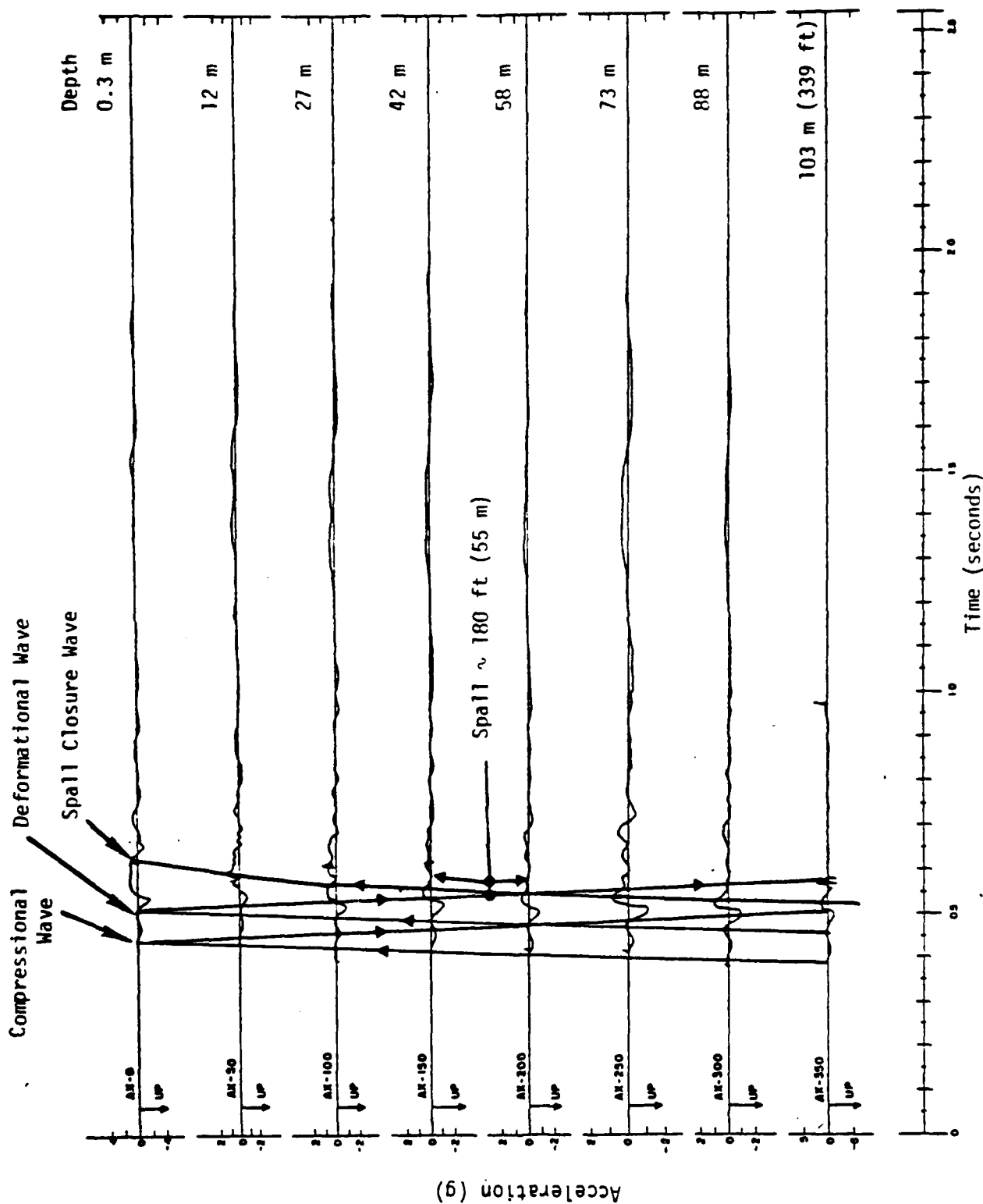


Figure 8. Vertical acceleration-time data, BLANCA event
Shallow boring instrument

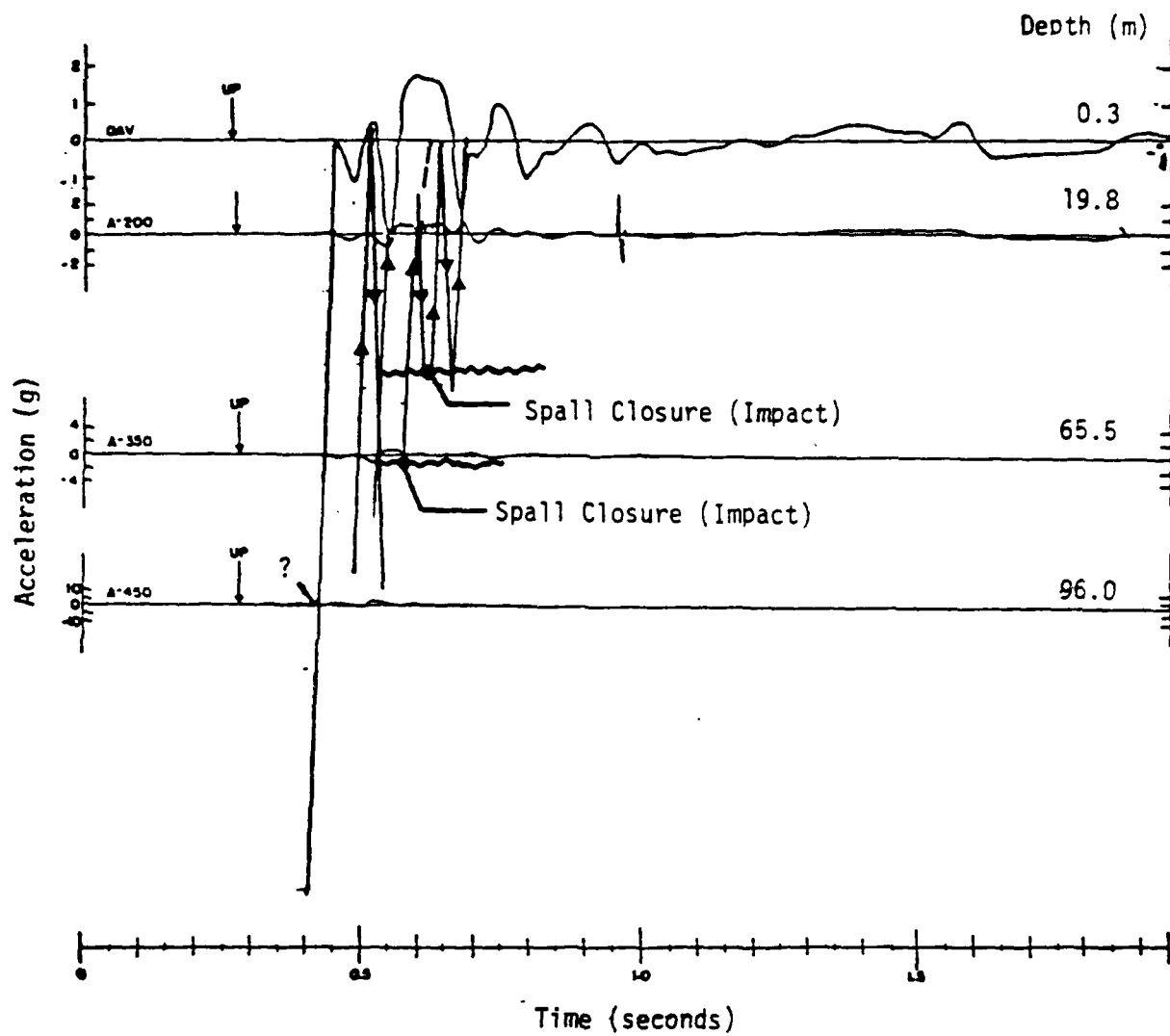


Figure 9. Vertical acceleration-time data, BLANCA event. Deep boring instruments.

slant range.⁽¹⁾ The estimated depth of spall from the surface gauge 1-AV (located at a slant range of 1217 meters) is 59 m -- where the near surface velocity is assumed to be 1480 m/sec using Eq. (1).⁽²⁵⁾ This is very close to the upper depth determined in Figure 8 of 55 m. Figure 9 indicates that an upper and lower spall may not have quite come together but are interpreted as two spalls closer together at ~48 m and ~68 m. Unfortunately, the records are reproduced at a scale making accurate determinations impossible. Perhaps more confidence in the spall depth estimates would be possible using the original (not published) data. It is postulated that toward the limits or lateral edge of spall that a single spall probably exists and can be reasonably well estimated from surface gauge records.

The inferred spall configuration for the RAINIER Event is illustrated in Figure 10, drawing upon the spall gap locations determined in Figure 5 plus analysis of surface motion data using Eq. (1). Figure 10 is to be compared with Figure 7, contrasting interpreted ground motion data with the RAINIER spall model that assumes a homogeneous medium. Other important spall related factors for RAINIER and BLANCA are that the topography and geologic layering may have had an effect on spall depth. Spall thicknesses for these events are probably greater than if the ground were flat and not a mesa (see Figure 11). The figure illustrates the mesa topography and the bedding boundaries of major volcanic rock units. Also shown is the estimated spall configuration related to the topography. One would suspect that this would at least increase spall depth in the vicinity of the reflected wave convergence axis near the shot region. BLANCA was located nearby in E tunnel and the shot point was closer to the mesa edge. Also, the high contrast paleozoic carbonate rocks were located not far below the tunnel portal entrance. Thus for BLANCA, the topographic and geologic factors coupled with the shallow depth or burial would likely lead to an especially deep spall. This is further discussed in Section 5 on spall depth.

Another aspect of the configuration of spall is the variability of spall extent and depth with direction or spatial orientation. Few detonations have more than a single direction or line of surface motion gauges -- to say nothing of the lack of multiplicity of lines of subsurface gauges. Those that do have gauges

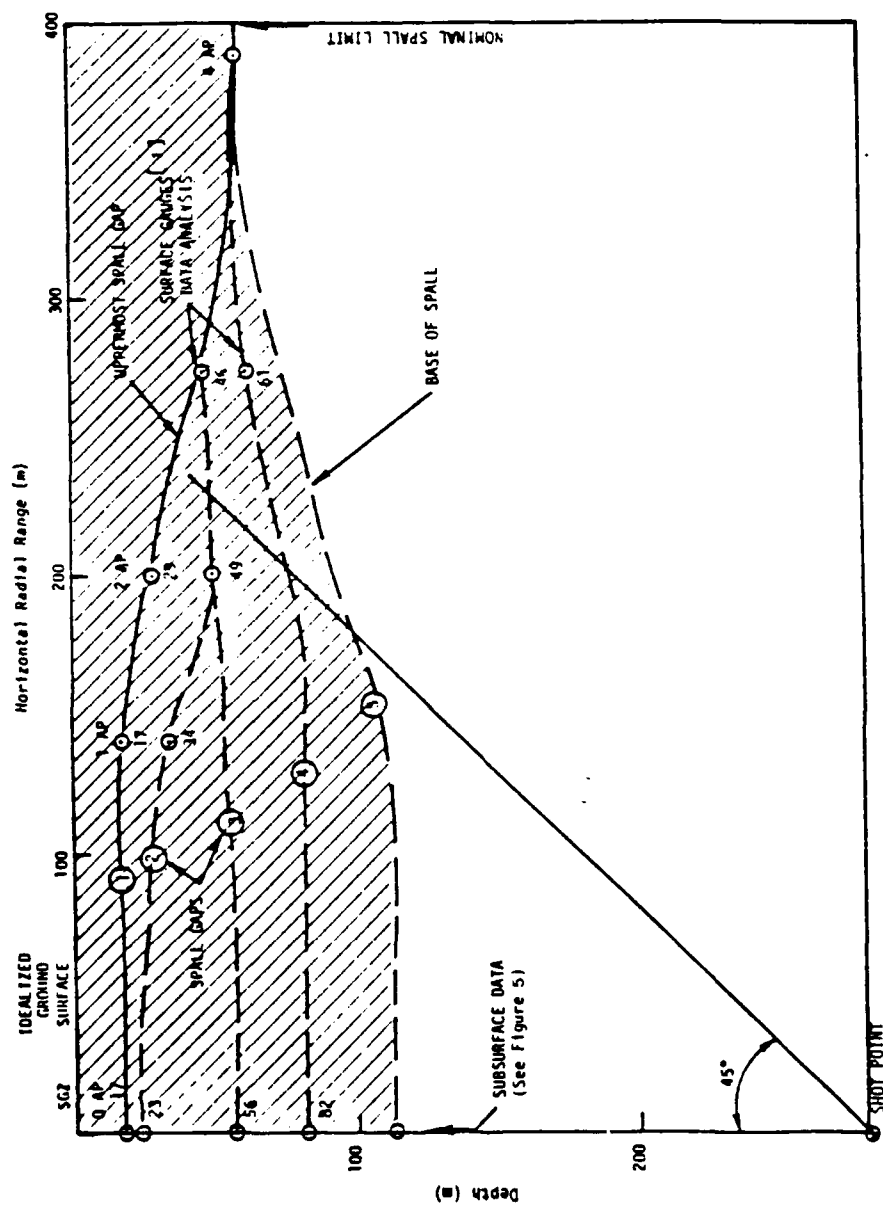


Figure 10. Rainier spill cross section.

Depth of Spall, 113 m

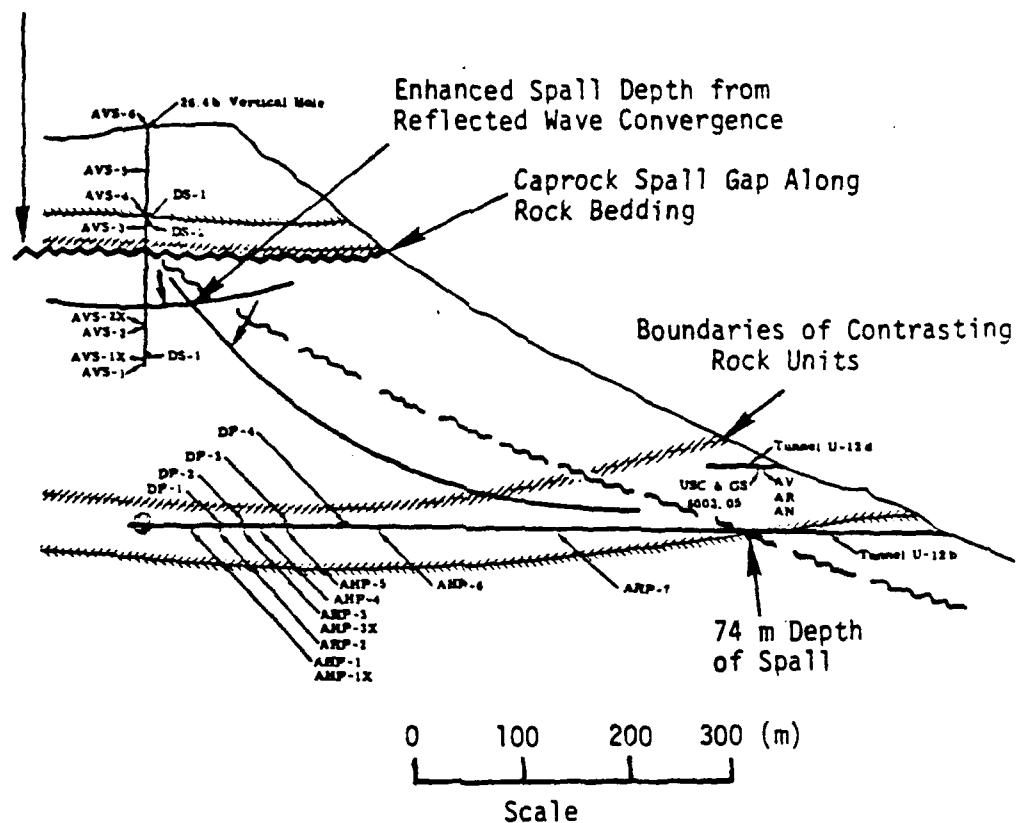


Figure 11. Cross section of RAINIER Event showing spall configuration and reflected wave convergence.

in several different directions have very few stations. The two events that help demonstrate directional variability are SHOAL and HANDLEY. Figure 12, showing the plan view of subsurface gauges for SHOAL, also has the orientation of the major fault and joint (weakness) trends. This direction is parallel to the path PM-2 and about perpendicular to PM-3. All three stations are essentially at the same distance. The initial vertical accelerations of PM-1, 2, and 3 are respectively 0.88 g, 1.65 g, and 2.5 g. Also shown in the figure is an interpretation of the in-situ stress orientation relative to the shot, the fracture pattern, and the ground motion gauges. The orientation of the maximum principal compressive stress is inferred to coincide with the minimum ground motion, consistent with regional stress patterns and with the expectation that ground motion is reduced by increased explosion confinement. If this is true of the initial accelerations typically associated with the compressional wave, it should certainly be true of the following deformational waves associated with explosion cavity expansion against the confining stress field. Thus, if these interpretations are correct, in-situ stress variations are probably reflected in the ground motion data, cavity growth history asymmetries, spall asymmetries, and associated surface wave asymmetries. Much of the ground motion data scatter is expected to be a reflection of in-situ stress variations with path directions from the source to the receiver stations.⁽²⁶⁾

Figure 13 illustrates the gross orientation and location of the maximum horizontal compressional in-situ principal stresses in the contiguous United States. The SHOAL location near Fallon, Nevada and Pahute Mesa at NTS are also shown.

The HANDLEY event was located at Pahute Mesa at NTS. The ground motion stations at the surface are located as follows for three general different directions; NE, SE, and W as listed in Table 1, with the initial vertical spall velocities for the stations located approximately on Figure 14 and related to geologic structure.⁽²⁷⁾ The ground motion variations with range and direction indicate maximal and minimal lateral compressional stress axes orientated as shown on Figure 14. The orientations assume that maximum lateral stress goes with minimal ground motion and that the axes are near horizontal and at right angles.

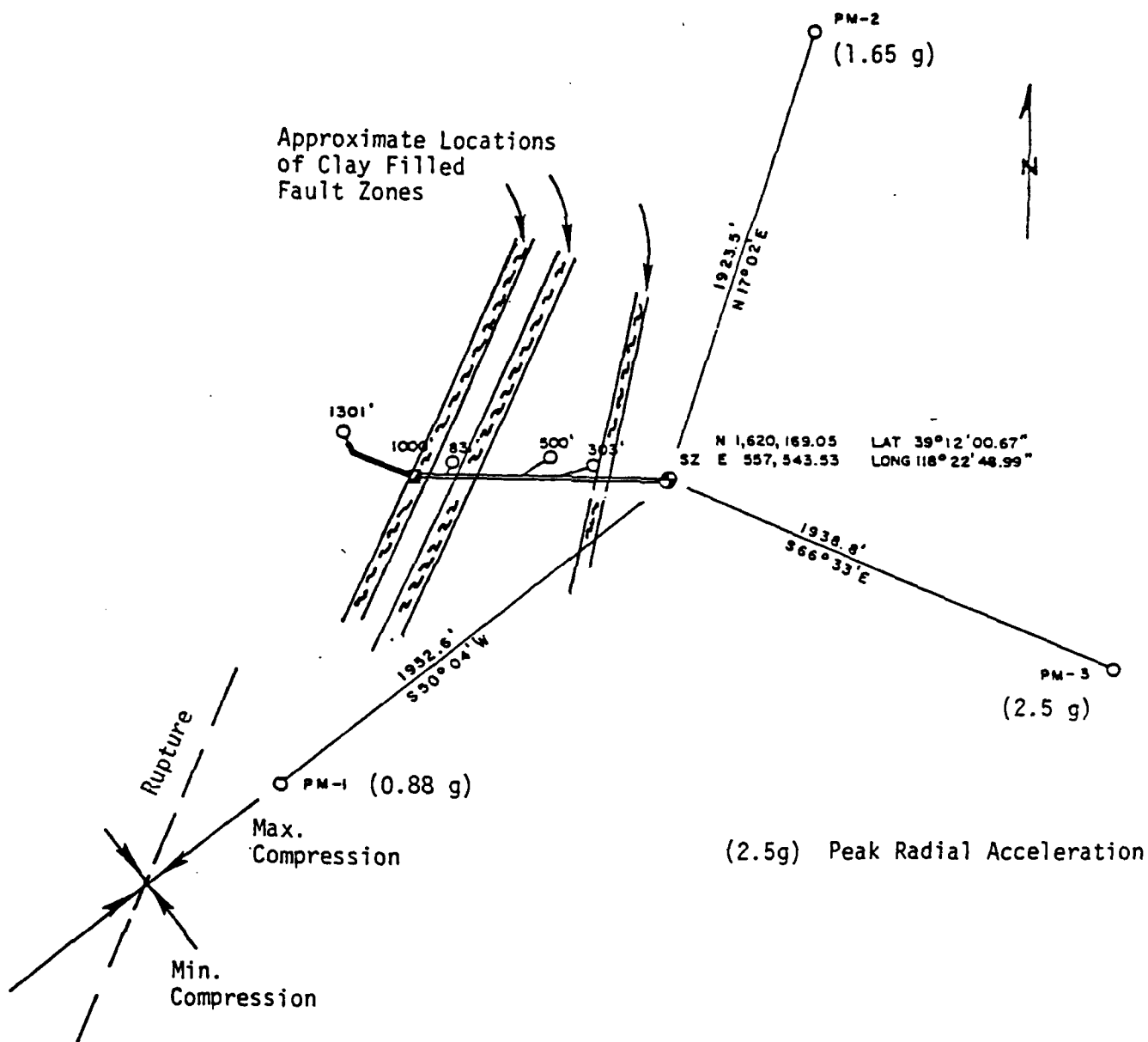


Figure 12. Plan view of SHOAL explosion-elevation ground motion station locations. Stations PM-1, -2, and -3 were installed via drill holes. Also shown are fault orientations and inferred in-situ stress orientations.

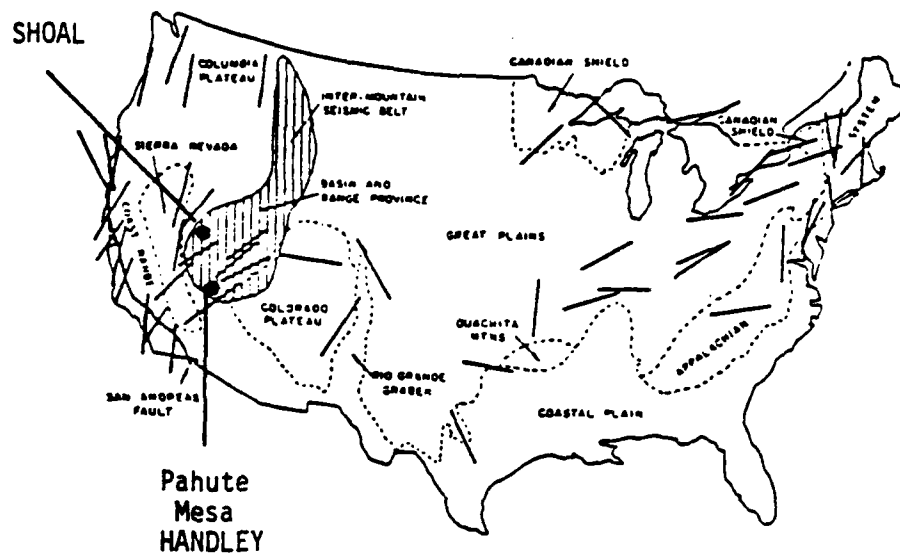
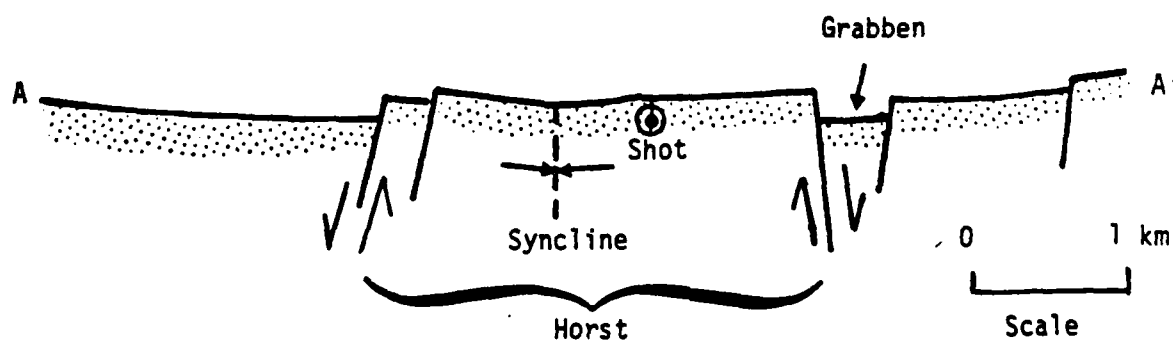
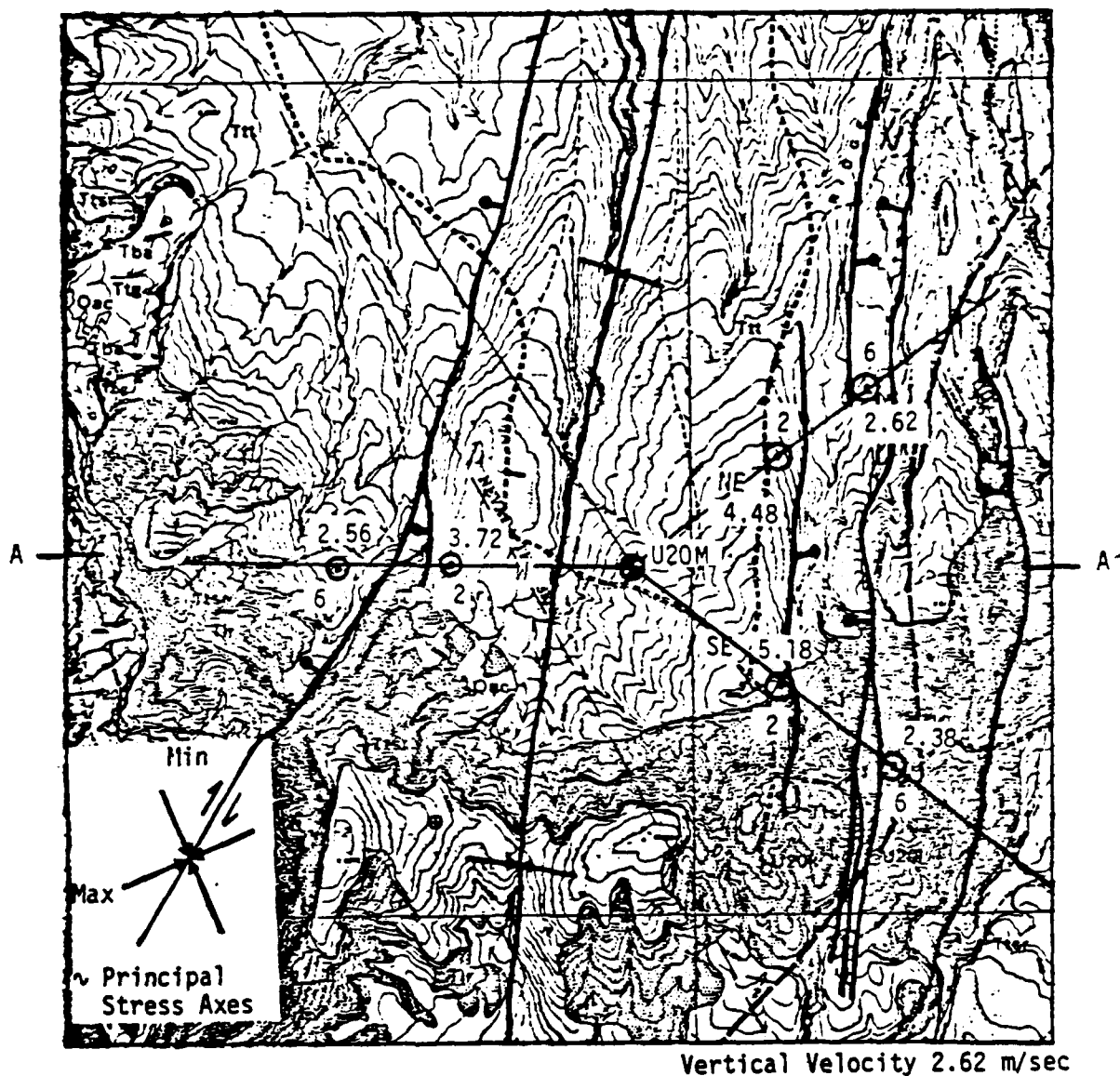


Figure 13. The location and orientation of principal in-situ compressional stress in the United States (exclusive of Alaska and Hawaii).[28]

Table 1. HANDLEY surface ground motion summary. [27]

Slant Range (meters)	Gauge Number and Direction from SGZ	Vertical Velocity m/sec	Radial Velocity m/sec	Azimuthal Sum
1357	NE#2	4.48	1.04	9.18
2182	NE#6	2.62	1.04	
1378	SE#2	5.18	1.83	11.01
2241	SE#6	2.38	1.62	
1328	W#2	3.72	1.37	8.38
2166	W#6	2.56	0.73	



Exaggerated Structural Cross Section

Figure 14. Plan view of HANDLEY and local geology.

Pahute Mesa is located within a large collapse caldera. Subsidence was initiated by removing large quantities of material by volcanic eruption. Regional tectonic stress accumulation with time is superposed upon the grain of this earlier deformation. Possibly, this causes a shift from the maximum horizontal stress (both regionally and locally) that is generally about N45 to 50°E. The shift implied is to approximately a N75°E orientation. This orientation is consistent with the orientation of the principal strain axes determined for the region by geodetic strain history measurements about the HANDLEY Event.⁽⁴⁷⁾ The orientation is also consistent with fault plane solutions of HANDLEY aftershocks and post HANDLEY strain "relaxation" observations. The anomaly is that the greatest strain is about coincident with the maximum lateral stress orientation. This observation is not so inconsistent if the explanation is that there was at shot time a greater strain parallel with the minimum lateral stress direction that more rapidly relaxes within two weeks, so the whole history was not recorded. The greatest residual stress (strain) can be expected in the direction of maximum pre-stress or said differently -- the direction of minimal deformation.

5. DEPTH OF SPALL ANALYSIS SUMMARY AND APPARENT SCALING RELATIONS

Table 2 is a preliminary summary of the data and spall depth related estimates associated with the nine unclassified detonations found useful for estimating depths to spall gaps. Subsurface ground motion data was successfully obtained at several depths for these events so that ray tracing of acceleration and/or velocity pulses could be made. Both initial and impact pulses were utilized. The accuracy of the method is uncertain, since limited published data were used and the approach taken is subjective. A Gerber variable scale and a magnifying lens were used to minimize errors associated with determining time and peak values. Figures of the individual ray tracings are in the Appendix along with notations interpreting specific signatures and comparing results with those of other investigators, where other interpretations exist.

Figure 15 is a log-log plot of explosion yields versus maximum spall thickness or spall depth. The RAINIER event, R, might be discounted because topography may have caused an anomalously large spall depth as discussed previously. Since there are explosion tests in several grossly different geologic environments, the two granite events, SHOAL and PILEDRIIVER, are assumed most useful to guide determination of the slope determining the yield dependence of spall thickness. A one-third power law as expected seems confirmed. The three Amchitka volcanic rock events, LONGSHOT, MILROW, and CANNIKAN, support this apparent yield dependence. The other three events, MERLIN, GNOME and RIO BLANCO, do not seem to fit in very well, and explanations other than the depth estimates being in large error were sought. One might expect RIO BLANCO to be with GNOME and the Granite Shots, because of their similar relatively high density, and for MERLIN to be considerably below the line of the Amchitka volcanics. Such a logical ordering might emerge by examining scaled depth of burial effects.

A log-log plot of depth of burst versus scaled maximum spall thickness is shown in Figure 16. Now RAINIER remains anomalous as expected. SHOAL and

Table 2. Preliminary Summary of Nuclear Explosion Event Parameters Associated with Maximum Spall Depth Estimates

Event (Environment)	Yield ^[29,30] W (kT)	Depth of Burst, DOB (m)	Max. Spall Depth, D _{SGZ} (m)	Scaled Depth D _{SGZ} /W ^{1/3} (m/kT)	KE	Refs.
RAINIER (Mesa Tuff)	1.08 ^[31] 1.70 ^[32]	274	113	110	30,140	32, 7, 3
MERLIN (Alluvium)	10	298 ^[3] 296	114	52.9	15,711	3
MILROW (Amchitka Volcanics)	~ 1000 ^[15]	1219	310	31	37,790	15
CANNIKAN (Amchitka Volcanics)	< 5000 Assume 4500	1791	618	37.4	66,980	33
LONG SHOT (Amchitka Volcanics)	85 ^[31] 80+ ^[23]	701	195	44.4	31,124	23
PILEDRIIVER (Granite)	56	463	310+	81+	37,503	37
SHOAL (Granite)	12.2 ^[31] 12 ^[29]	367	195	84.7	31,085	34
GNOME (Bedded Salt)	3.1 ^[29] 3.0 ^[31]	361	~ 140	97	35,017	35, 7
RIO BLANCO	90, 3 each 30 Explosives	1738 1899 2039	122	39.3 for 30 kT	68,300	16, 36

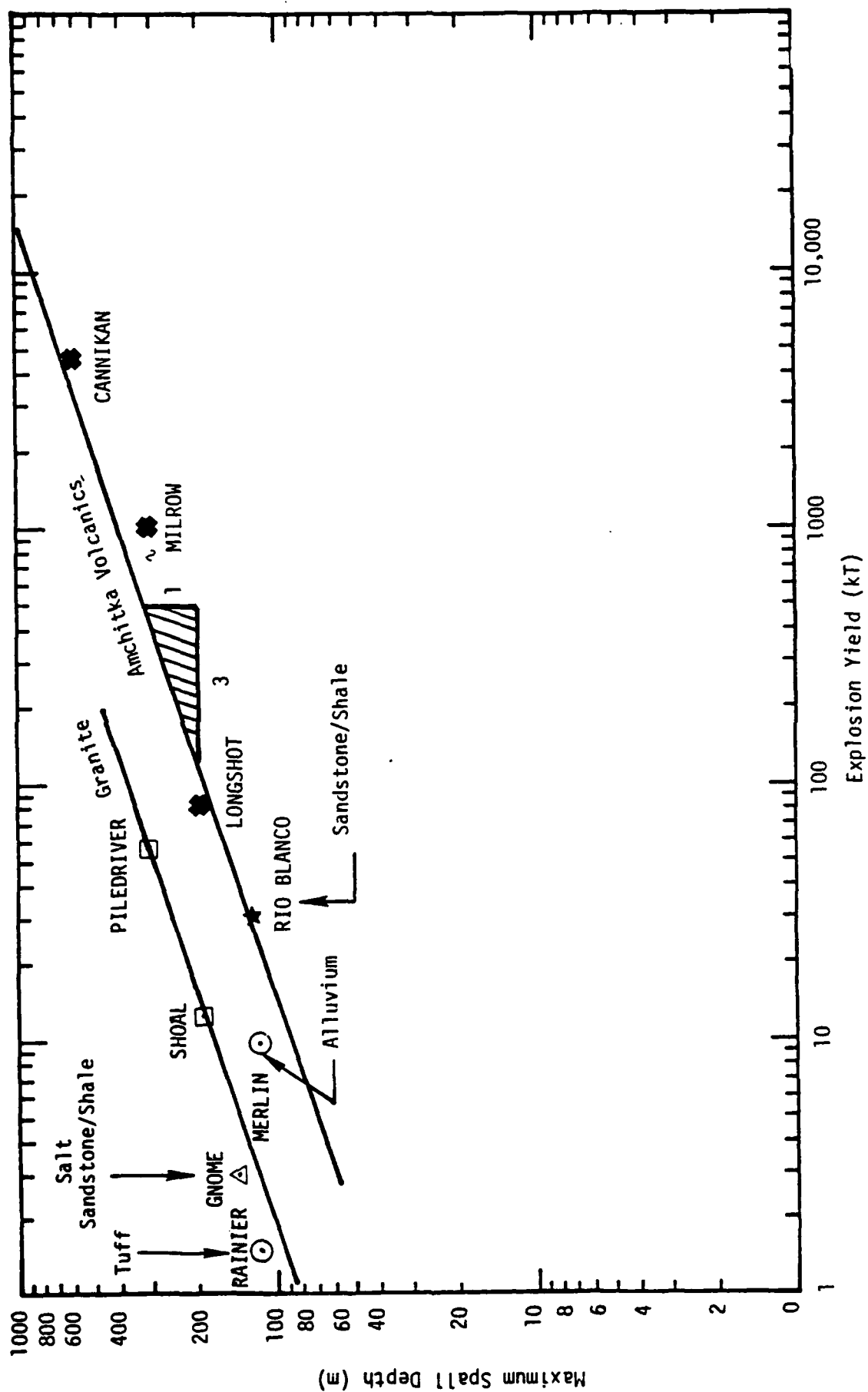


Figure 15. Maximum spall thickness versus explosion yield.

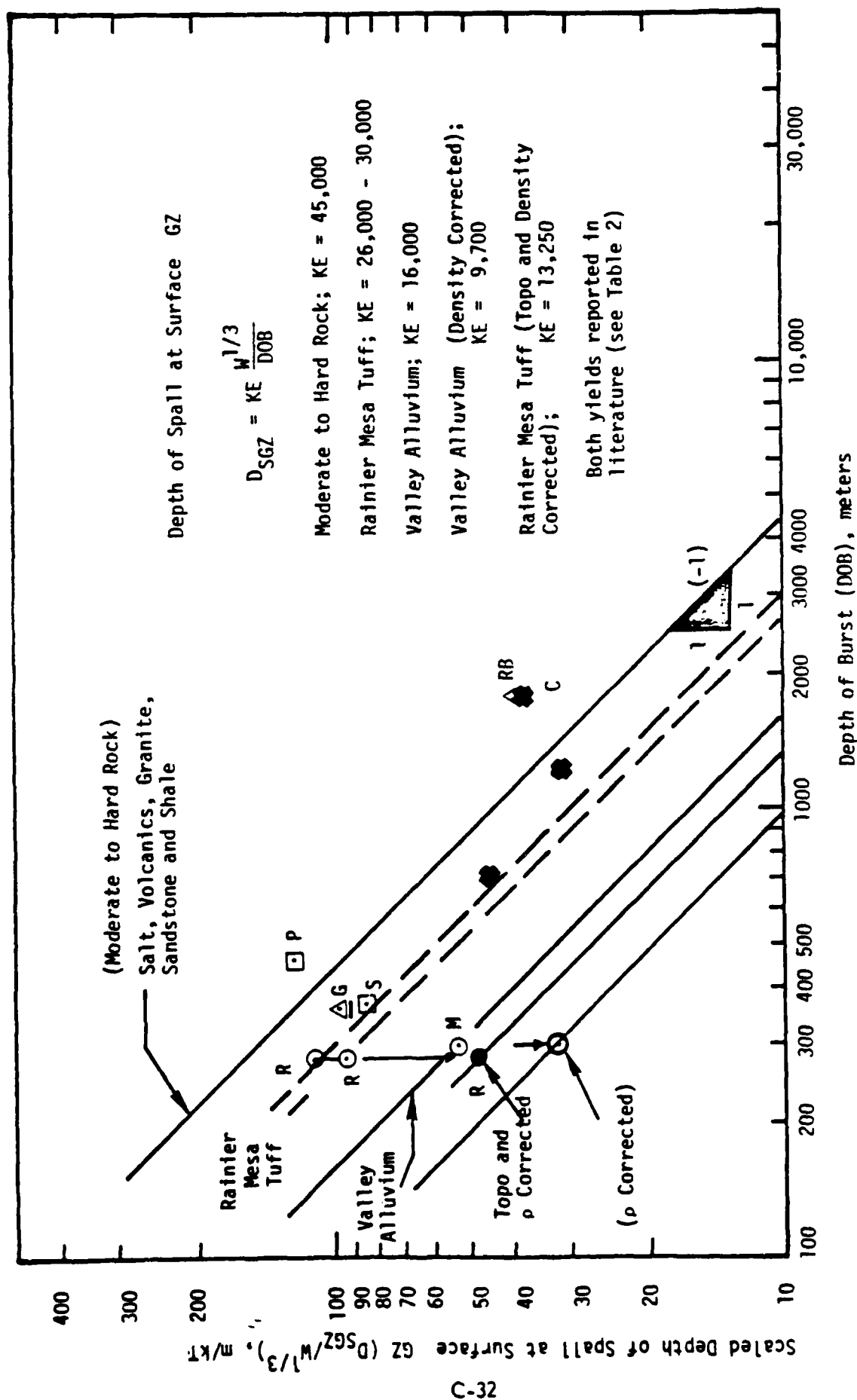


Figure 16. Maximum spall thickness (scaled) versus depth of burst.

PILED RIVER no longer correlate so well. Material differences and spall depth uncertainties may be the culprit if the depth of burst scaling is correct. MERLIN is now separated significantly from the moderate-to-hard rocks and GNOME and RIO BLANCO are now in reasonable agreement. The additional corrections shown on Figure 16 for RAINIER and MERLIN are discussed in Section 8.

Spall from detonations in granite does not appear to simply slab off as horizontal planes. The interlocking blocks and high strength between joints provides an effective interblock friction that is interpreted as resulting in the spall gaps being very irregular surfaces. This difference shows up especially with the spall impact signals, because the diffuse arrivals come from many surfaces. The dilated and interconnected weaknesses apparently recompact slowly due to the multiplicity of orientations that must adjust to the volumetric strain history. Compare the PILED RIVER and SHOAL surface zero record (Figure 17) with any other in the report. It was found that for granite shots, velocity rather than acceleration records were more useful. Also notice that the impact accelerations are more for SHOAL. This is consistent with the observation that the granite is characterized by fewer and more regular failure plains for a given volume than the NTS granite. Also, at SHOAL near-surface horizontal (unloading) fractures are documented. (34, 37, 38)

Figure 16 provides the basis for a tentative spall depth empirical relationship:

$$D_{SGZ} \approx KE \frac{W^{1/3}}{DOB} \quad (2)$$

where D_{SGZ} is the spall depth in the vicinity of the surface ground zero area; W is the explosion yield in kilotons and DOB is the depth of burst in meters. The "constant" KE is dependent upon environmental and geologic factors. The KE of 30,000 for the RAINIER event is probably high because of the earlier discussed topographic influence. Applying Eq. (2) to estimate the depth of spall for BLANCA is of interest in light of the earlier discussion anticipating deep spall. BLANCA was a 22 kT event buried at a depth of 301 meters. From Eq. (2) the

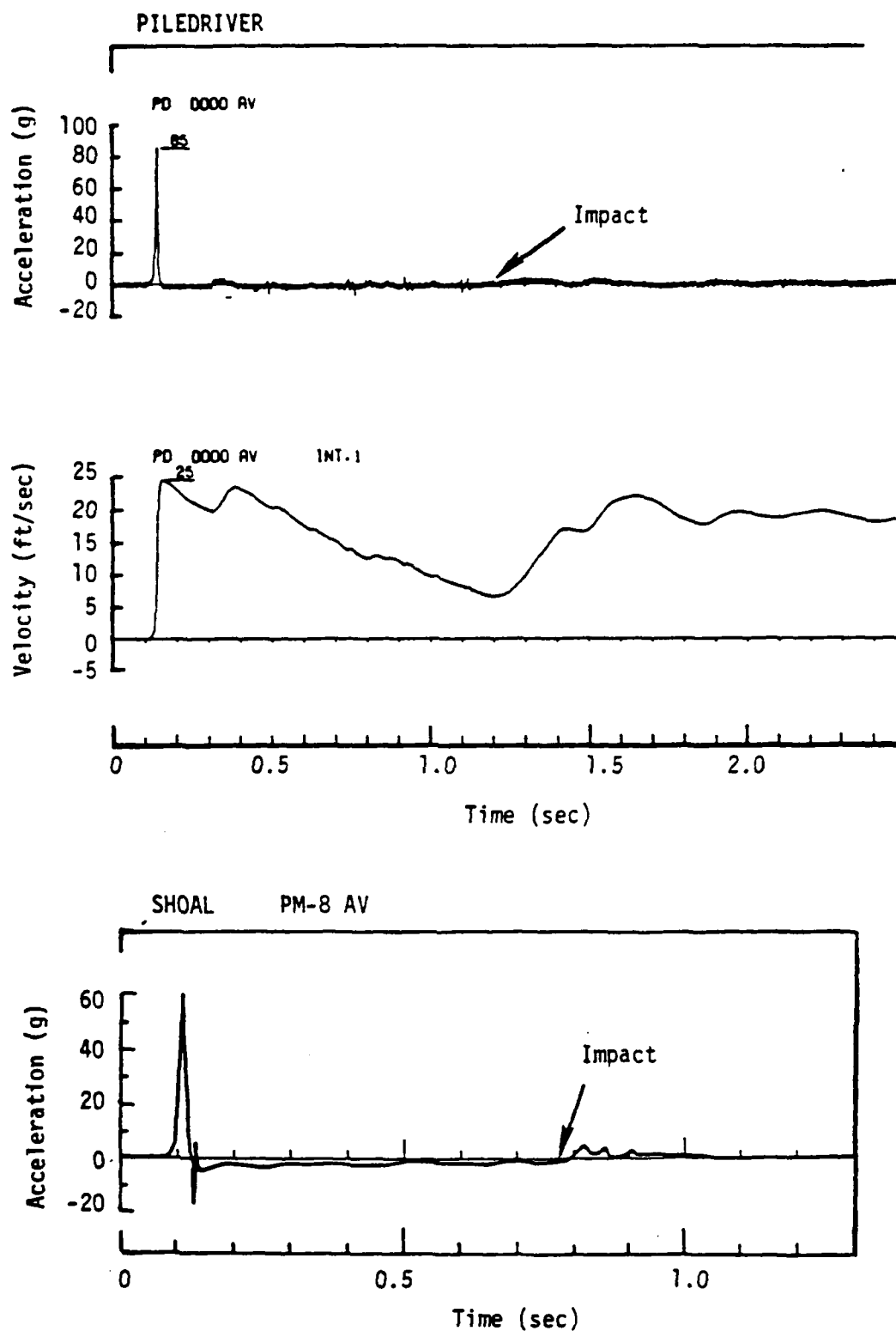


Figure 17. Surface Ground Zero ground motions for granitic events PILED RIVER and SHOAL.

depth of spall (D_{SGZ}) is 242 to 279 m. Thus the spall depth is almost as deep as the depth of burst. Post shot investigations of BLANCA did reveal bedding plane thrust faulting along a surface that projects to below the BLANCA shot point (Figure 18). Molten rock was injected in bedding planes a considerable lateral distance from the explosion. The chimney, following cavity collapse, also cratered to the surface (slope of the mesa).^(39, 40) (Also see Appendix discussion for BLANCA.)

Equation (2) was derived from the limited data shown plotted on Figure 16 and with the foreknowledge that Viecelli determined that spall thickness varied inversely with depth of burst. This equation was used to compare spall thickness with that predicted for a 0.5 kT granite detonation at 200 meters.⁽⁵²⁾ This prediction, using LLL's SOC code, gives a total spall depth of 40.5 meters versus a 179 meter depth predicted from Eq. (2). The difference is too large to be explained by the high tensile strength assumed (2 MPa) in the prediction.

A re-examination of Figure 16 indicates that the lower limit for spall depth is:

$$D_{SGZ} \approx KE \cdot W^{1/3} \quad (2a)$$

This gives a spall depth of 65 m compared to 40.5 m for the hypothetical 0.5 kT event. Equation (2a) is not considered reasonable because alluvium, sandstone/shale, and Amchitka volcanics would all spall to the same depth for the same explosion-yield independent of depth of burst. A compromise that is supported both by the limited data and by reasonable variations with geologic setting is:

$$D_{SGZ} \approx \overline{KE} \frac{W^{1/3}}{DOB^{1/2}} \quad (2b)$$

Figure 16(A) and Table 2(A) illustrate the same data as Figure 16 and Table 2 with the DOB slope of $-1/2$ instead of -1 and \overline{KE} values replacing the KE's.

Using Eq. (2b), the estimated depth of spall for the 0.5 kT granite event becomes about 95 m and for BLANCA it remains about 280 m if left uncorrected for density and topography.

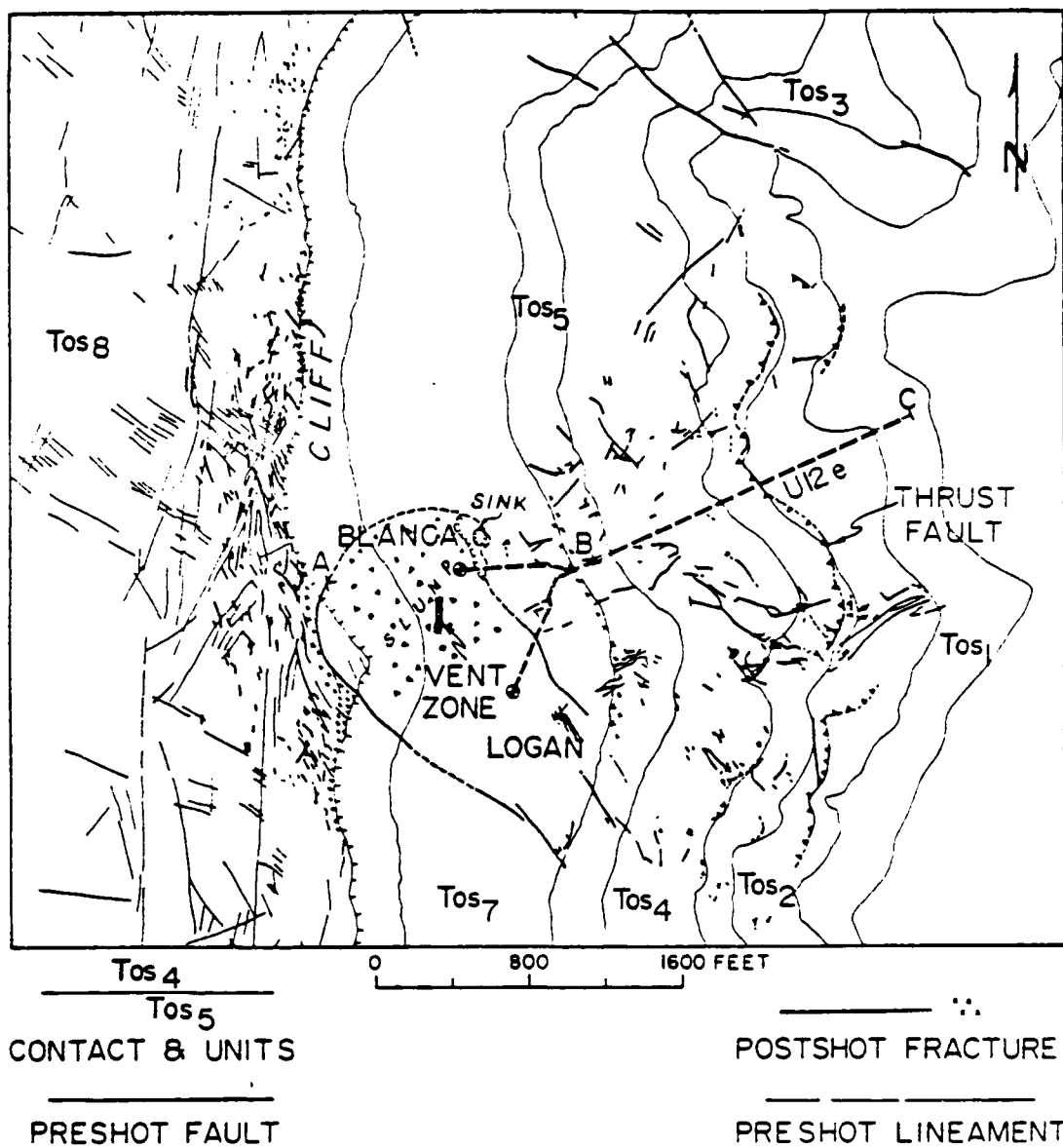
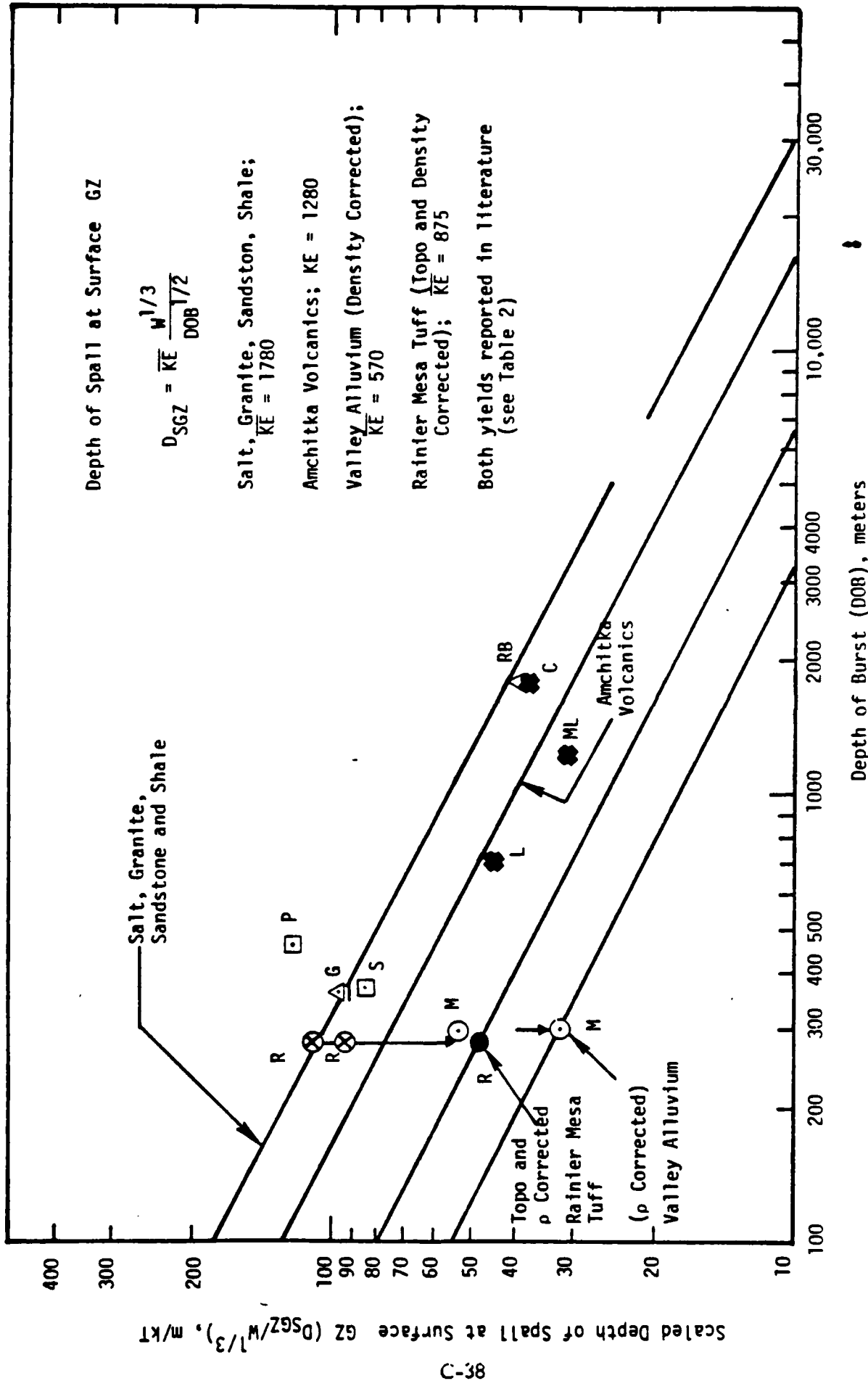


Figure 18. Fractures produced by BLANCA Event. [39]

Table 2A. Summary of Corrected Nuclear Explosion Event Parameters Associated with Maximum Spall Depth Estimates

Event (Environment)	Yield ^[29,30] W (kT)	Depth of Burst, DOB ^{1/2} (m)	Max. Spall Depth, D _{SGZ} (m)	Scaled Depth D _{SGZ} /W ^{1/3} (m/kT)	\overline{KE}
RAINIER R* (Mesa Tuff)	1.08 ^[31] 1.70 ^[32]	16.553	113	~ 53 Corrected	~ 875
MERLIN M (Alluvium)	10	17.234	114	~ 33	~ 570
MILROW ML (Amchitka Volcanics)	~ 1000 ^[15]	34.914	310	31	1082
CANNIKAN C (Amchitka Volcanics)	< 5000 Assume 4500	42.320	618	37.4	1583
LONGSHOT L (Amchitka Volcanics)	85 ^[31] 80+ ^[23]	26.476	195	44.4	1176
PILEDRIIVER P (Granite)	56	21.517	310+	81+	1743
SHOAL S (Granite)	12.2 ^[31] 12 ^[29]	19.157	195	84.7	1622
GNOME G (Bedded Salt)	3.1 ^[29] 3.0 ^[31]	19.000	~ 140	97	1843
RIO BLANCO RB	90, 3 each 30 explosives	41.690	122	39.3 for 30 kT	1638

* Abbreviations R, M, etc. shown on Figures 16, 16A and 24A.



Although the depth of spall data are limited, it is my opinion that Eq. (2b) is preferred over Eq. (2) and \overline{KE} values preferred over KE values. To test this \overline{KE} vs G_p values were plotted on Figure 24A and can be compared with Figure 24. The internal consistency of geologic parameter dependences was improved (assuming an improved linear relationship is the appropriate test criterion -- see text discussion in Section 8).

6. EXTENT OF SPALL ANALYSIS SUMMARY

This chapter draws mostly from the companion spall study being currently prepared for RDA/DNA.⁽¹⁾ Surface motion records of over 30 events were analyzed for detonations in about nine different geologic settings. Table 3 is a summary table of those events where the depth of spall could be estimated from surface motion gauges near the extent of spall by Eq. (1). Listed are the slant range gauge locations (R_{SL}) to be compared with the nominal extent of spall (S_{ex}) also measured by slant distance. Also tabulated are estimates of near surface compressional velocity (V_p) taken usually from the same references that reported the original ground motion data for each event.

Figure 2 illustrates the +1 g criteria for determining the extent of spall for contained nuclear explosions. This method was developed to enable interpolation and extrapolation from limited data to estimate the extent of spall. If anything, this method underpredicts the maximum extent of spall. Comparison with recent (but unpublished) data on spall extent by Vortman of Sandia Corp. show conservative estimates.⁽²⁰⁾ The two example plots of initial vertical acceleration versus range are for DISCUS THROWER and HANDCAR. The upper and lower bounds of the data are estimated by applying bounding lines as shown. The nominal extent of spall is either the midpoint of the limits or determined by inspection of the data.

Spall extent was found to vary roughly as the 1/3 to 1/4 power of the explosion yield when all other parameters were ignored. Upon closer inspection a 1/4 power law seemed to provide a better fit to the data if similar geologic environments are considered separately.⁽¹⁾ Using this scaling relation, the effect of geologic environment and depth of burst are estimated from Figure 19 by plotting the radial distance extent of spall S_{ex} , scaled by dividing by $W^{1/4}$, against depth of burst (DOB) in meters. The data groups into three general classes of material. The extremes are deeply buried events in dense sandstone, shale, and salt (the most spall extent per kT) and weak unsaturated soft rock (the least spall per kT). The scaling relation derived from the data is:

$$S_{ex} \approx G_p DOB^{1/3} W^{1/4} \quad (3)$$

where G_p is a geologic dependent parameter.

Table 4 illustrates the results of a trial and error approach to estimate G_p from geologic information of specific explosion environments. What is assumed is that density, porosity, compressional velocity, and velocity contrasts associated with bedding of layered strata are the geologic parameters most responsible for affecting the extent of spall. These parameters are all inter-related but this author does not yet know how to treat them quantitatively. The approach used is merely a means of illustrating that Eq. (3) gives a consistent and rational gradation of required G_p values for the different geologic settings.

$$G_p \approx \rho^2 V_p (R_p + R_b) \quad (4)$$

where ρ is the average bulk density in gm/cc, V_p is the average compressional velocity in m/sec, R_p and R_b are relative porosity and bedding coefficients both graduated on a scale of 1 to 10. The values are the author's best estimates based upon personal experience. All values are average estimates between the shot point and the surface. The least reliable parameter is R_b , the relative bedding coefficient. The rational ordering of this parameter provides the main justification that Eqs. (3) and (4) are useful relationships for predicting spall extent. Equations (3) and (4) are for events with scaled depths of burst greater than 100 m (depths greater than $100 W^{1/3}$ m/kT).

The geologic parameter G_p varies rather systematically between about 30 and 180 going from weak porous poorly layered alluvium (30) to dense water-saturated interbedded sandstone and shales (180). The empirical values for G_p come from the effort to develop an empirical scaling relation that was as consistent as possible with the various parameters that influence the extent of spall. There are the obvious factors of yield, depth of burst, density/porosity/velocity; but there are also geometric considerations, reflection and refraction considerations, and a variety of possible anisotropic effects. These combine to somewhat suppress the importance of the explosion yield in

Table 3. Approximate Depth of Spall at the
Approximate Edge of Spall for Various
Events and Materials

Event	Nominal Spall Extent S_{ex} (m) [1]	Gauge No. Station	Location R_{SL} (m)	Approximate Near Surface velocity, V_p m/sec	Spall Depth at S_{ex} $D_{S_{ex}}$ (m)	Refs.
RIO BLANCO	5000	1200	4100	1621	69	16
GASBUGGY	3300	S84AV	2874	1600	48+	41
SALMO	1800	ES-SAV	1110	1800	33+	42
LONGSHOT	1800	25V	1450	2681	121	23
MILROW	4300	S17AV	5399	2988	209+	15
CANNIAN	7200	SF125AV	3835	2681	201	33
PILEDRIVER	1640	PD9012AV	1441	3000	113	37
RAINIER	480	4AP	473	1480	30	5
BLANCA	1200	OAV	1217	1480	59	25
DISCUS THROWER	550	SSAV2	354	1060	95+	43
MUD PACK	220	B4SAV	226	950	48	44
AARDVARK	900	4AV-4	293	1060	101	22
MERLIN	380	S5-AV	314	1060	66	22
DORMOUSE PRIME	340	2-AV	293	1060	64	22
CHINCHILLA I	225	S50AV	236	1000	55	22
ARMADILLO	325	B00AV	344	1000	55	22
HANDCAR	800	B6-SAV	1003	1000	50	22
HALFBEAK	2400	S5AV	2281	1800	161	21
SCOTCH	2850	S3AV	4253	1800	270	21
BOXCAR	4000	S12AV	4000	1800	414	21

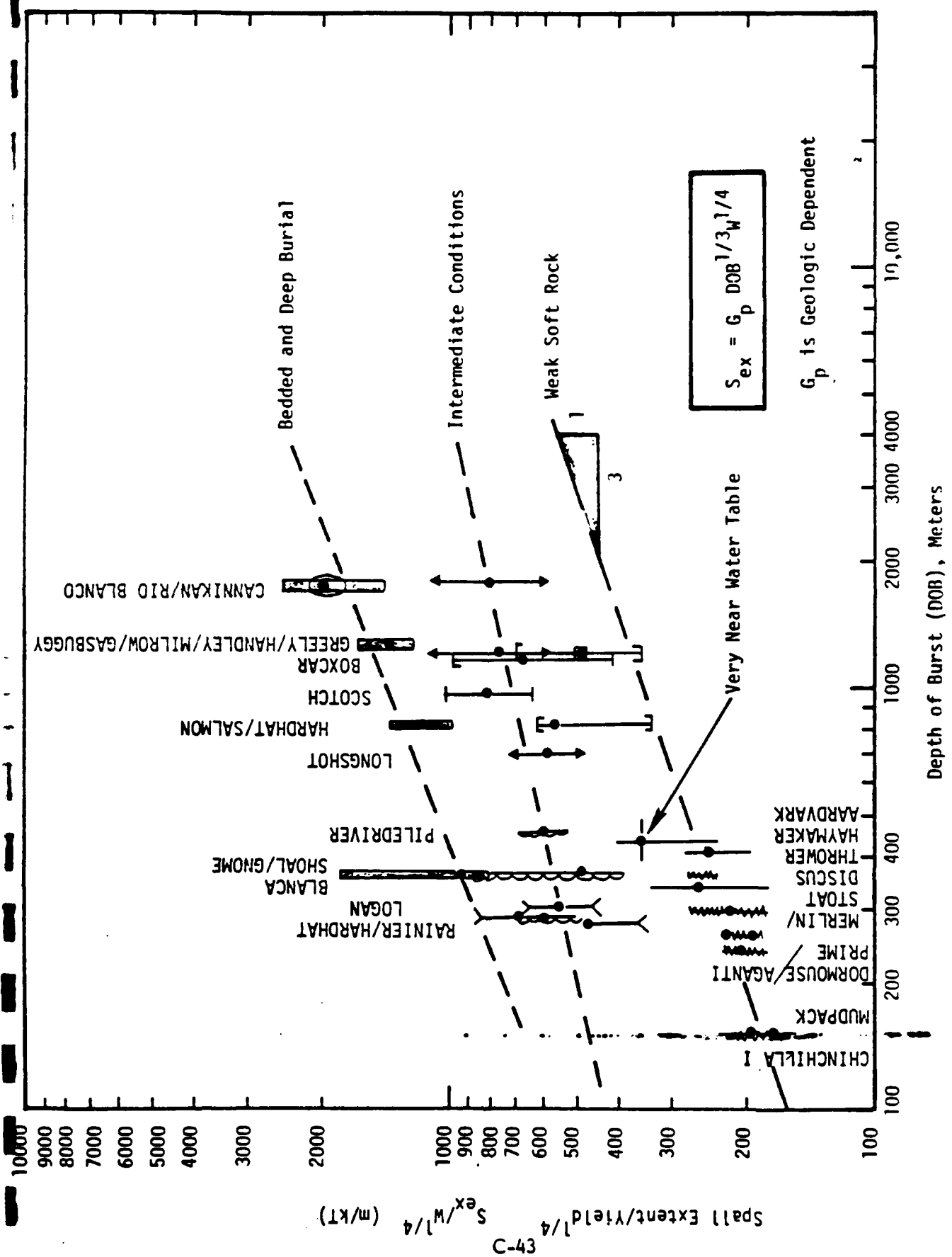


Figure 19. Scaled spall extent (1/4 power of yield) versus depth of burst.

Table 4. Estimated Variables Comprising the Geologic Parameter (G_p)

Event	(Shot Media)	Density gm/cc Shot to Surface (S to G)	Compression Velocity (km/sec) (S to S)	Relative Porosity 1 to 10 (S to S)	Relative Bedding 1 to 10 (S to S)	G_p
GASBUGGY	(Sandstone & Shale)	2.35	3.32	1.05	5.7	131
RIO BLANCO	(Sandstone & Shale)	2.40	3.50	1.2	7.5	176
MILROW	(Amchitka Vol- canics Shallow)	2.39	3.66	1.00	3.7	71.6
LONGSHOT	(Amchitka Vol- canics Shallow)	2.39	3.2	1.00	3.7	66.7
CANNIKAN	(Amchitka Vol- canics Shallow)	2.41	3.80	1.00	3.7	90.5
GNOME	(Bedded Salt)	2.20	2.80	1.8	7.7	128
SALMON	(Dome Salt)*	2.20	3.00	1.00	7.7	126
LOGAN	(Deep Rainier Mesa Tuff)	2.0	2.50	2.5	6.2	91.1
BLANCA	(Deep Rainier Mesa Tuff)	2.0	2.50	2.15	6.2	82.7
5	(Pahute Mesa Volcanics)	2.30	2.62	1.8	3.0	66.2
3	(Granite)	2.60	4.40	1.6	1.00	78.3
HANDCAR	(Carbonate Below Alluvium)	2.10	2.36	4.6	1.6	58.2
RAINIER	(Shallow Mesa Tuff)	1.80	1.98	5.6	2.0	49.6
4	(Tuff Below Alluvium)	1.70	1.60	6.5	1.6	37.5
7	(Alluvium Below Alluvium)	1.50	1.32	10.0	1.4	34.2

*Although dome salt is a massive piercement structure, it penetrates highly bedded sedimentary strata.

determining the extent of spall because as depths of bursts increase the energy coupling generally increases. It is not so readily attenuated laterally as at more shallow depths.

Figure 20 helps to illustrate the importance of general increased material velocity with depth and lateral energy channeling by alternating sand/shale layers. Such a model helps explain why RIO BLANCO at no more than 90 kT was able to spall further than MILROW at ~1000 kT. An effort has been made to illustrate the bedding differences for alternating sandstone and shale (RIO BLANCO) and the andesite and breccia layering of MILROW. The velocity increases with depth are greater for MILROW. The shot depth velocities are about the same. There are more velocity contrasts between individual sandstone and shale beds so more energy is trapped into lateral flow for RIO BLANCO.

Referring back to Table 4, it is noted that RIO BLANCO and MILROW both have a relative porosity coefficient of near 1.0. This corresponds to deep burial with a shallow water table. The MILROW site is characterized by water saturation almost to the ground surface, hence the R_p of 1.0; the RIO BLANCO site is saturated to within 150 meters of the surface. Figure 21 provides correlation charts relating approximate average unsaturated porosity between the shot point and the surface with relative porosity coefficient. For RIO BLANCO, only about 12 percent of the overburden is unsaturated and that portion has about 12 percent porosity, giving an average unsaturated porosity of one percent and from Figure 20 a R_p of 1.2.

The other extreme shown in Figure 20 is for alluvium with an R_p of 10, corresponding to an unsaturated porosity average value of about 36 percent. The intermediate values for R_p listed in Table 4 for the various geologic settings are reasonably close estimates guided by field data where possible.

Since the values of density, compressional velocity, and unsaturated porosity are reasonably quantitative and presumed representative of the different geologic setting; and since G_p is obtained from Eq. (3), the values for R_b (relative bedding coefficient) are obtained from Eq. (4). This equation is not

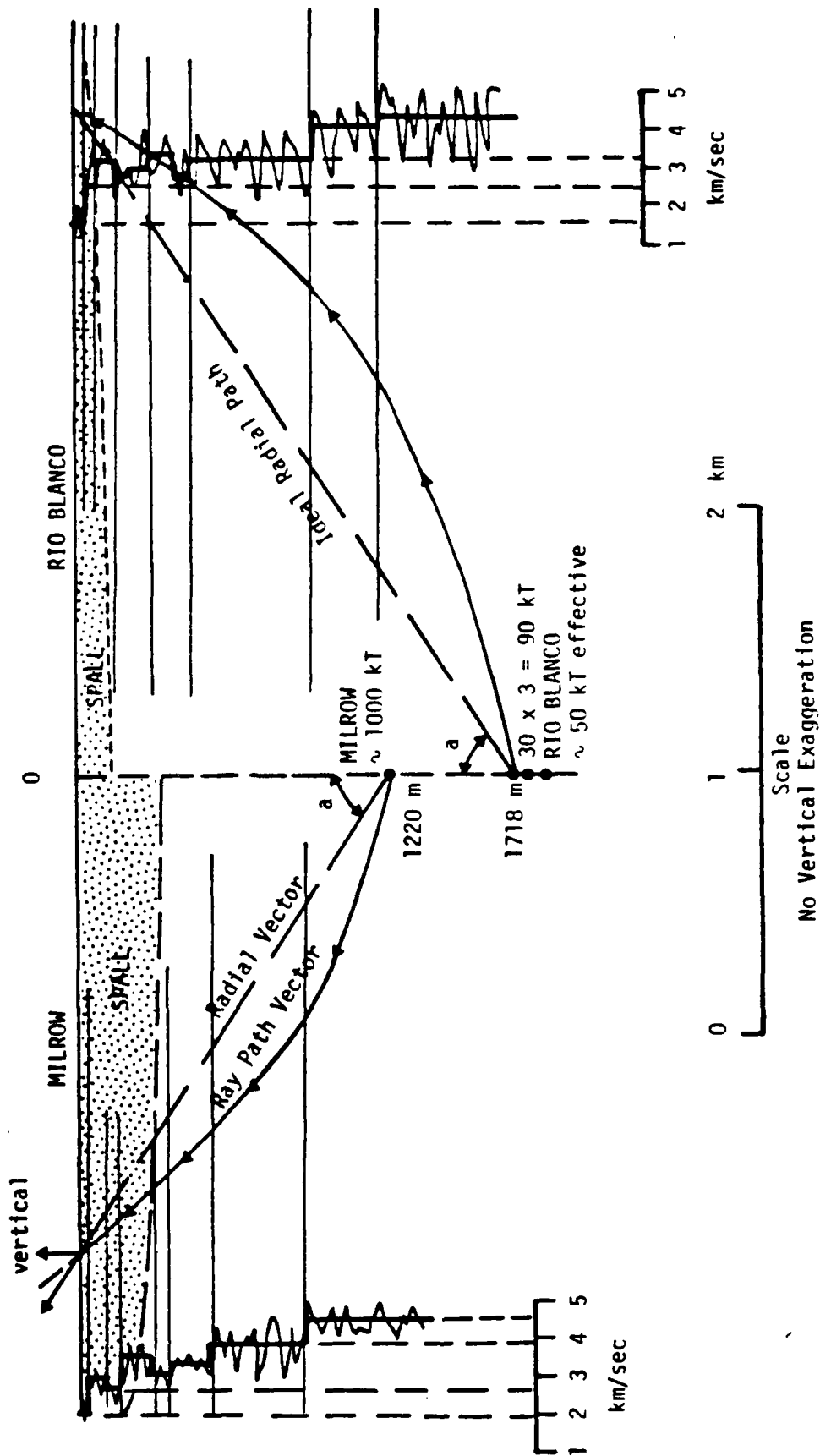


Figure 20. Comparison of MILROW and RIO BLANCO spalls illustrating differences of yield, depth of burst, and compressional velocity profile.

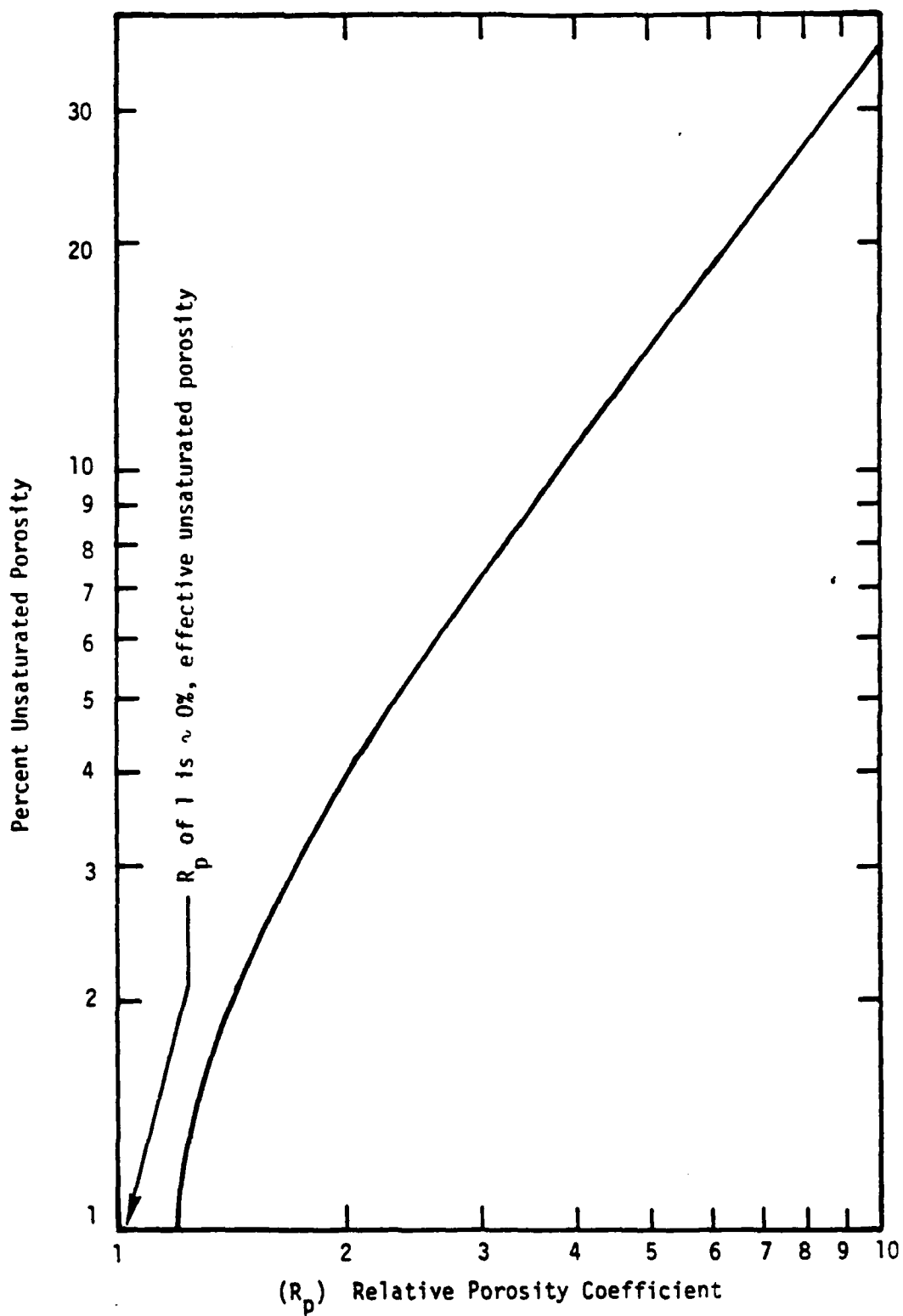


Figure 21. Approximate conversion chart from percent unsaturated porosity to relative porosity coefficient.

really a mathematical relationship but an attempt to find a way of validating the G_p values. The ranking of R_b thus is critical to assessing the usefulness of Eq. (3). Following is a brief discussion of that ranking.

The most massive environments or the environments with the most structural homogeneity are dome salt, then granite and then alluvium. Dome salt, however, is a small diameter vertical structure surrounded by highly bedded sand, shale, and limestone sediments. These are more porous and provide less of a contrast than the dense sandstone and shales of the GASBUGGY and RIO BLANCO sites. They are probably similar to the bedding at the GNOME site. From Table 4, the least bedded is in fact granite, then alluvium with all other environments intermediate to the highly bedded materials of RIO BLANCO, GASBUGGY, GNOME and SALMON. The deep Rainier Mesa tuff events BLANCA and LOGAN follow in decreasing order of R_p (less bedded than sandstone and shale associated with salt). These two events in tuff are just above the high velocity paleozoic limestones that help laterally refract energy for spall. Next are the Amchitka Volcanics with the alternating andecite and breccia that give the velocity contrasts shown in Figure 19. Note that the amplitude of the velocity contrasts are about half that of RIO BLANCO also shown in the figure. From Table 3, the Pahute Mesa Volcanics are a little less bedded than those at Amchitka; the shallow depth events in Rainier Mesa follow, and then the tuff and carbonate events detonated below alluvium. The ordering appears to be very consistent. It appears that velocity log profiles of the different sites could be analyzed for refraction, attenuation, and energy channeling effects to provide a more quantitative basis for assigning relating bedding coefficients.

7. DEPTH OF SPALL AT THE EXTENT OF SPALL ANALYSIS SUMMARY

The method described in Chapter 4, Figure 6, and Eq. (1) was used to estimate the depth of spall near the extent of spall from surface ground motion gauges. Table 3 provides a summary of the data necessary to estimate depth of spall at the extent of spall ($D_{S_{ex}}$) as contrasted with D_{SGZ} covered in Chapter 5. Where possible, records were analyzed from gauges near the extent of spall. Where the gauges were well within the extent of spall, the estimates may be minimal as the uppermost spall gap probably increases in depth with range (Figure 7). The near surface velocity values used in applying Eq. (1) were estimated from either velocity logs or gauge time-of-arrival data for each event. For some events, the values were assumed the same as that determined for a similar near surface geology.

Figure 22 illustrates that generally the depth of spall at the extent of spall scales as the cube root of the explosion yield as evidenced by the $1/3$ slope. The events are named and different geologic environments are symbolized separately, but the line fit ignores geologic or depth of burst effects. Yield scaling appears to follow the form determined for the depth of spall near surface ground zero (Figure 15).

By assuming cube root depth scaling with yield, Figure 23 showing scaled depth at S_{ex} versus depth of burst (DOB) indicates the dependence upon DOB and geologic setting. All events seem to fit on a $DOB^{-1/3}$ slope with little data scatter obviously related to geologic differences. SCOTCH is anomalously deep but the data were taken from the extreme extent of spall. If geologic effects were significant, the alluvium or the sandstone shale events would most likely be anomalous, as they were in the extent of spall analysis and to a lesser degree on analysis of spall thickness near SGZ. Thus, from Figure 23, the depth of spall at the extent of spall can be estimated by the empirical relationship:

$$D_{S_{ex}} \approx K_e \frac{W^{1/3}}{DOB^{1/3}} \quad (5)$$

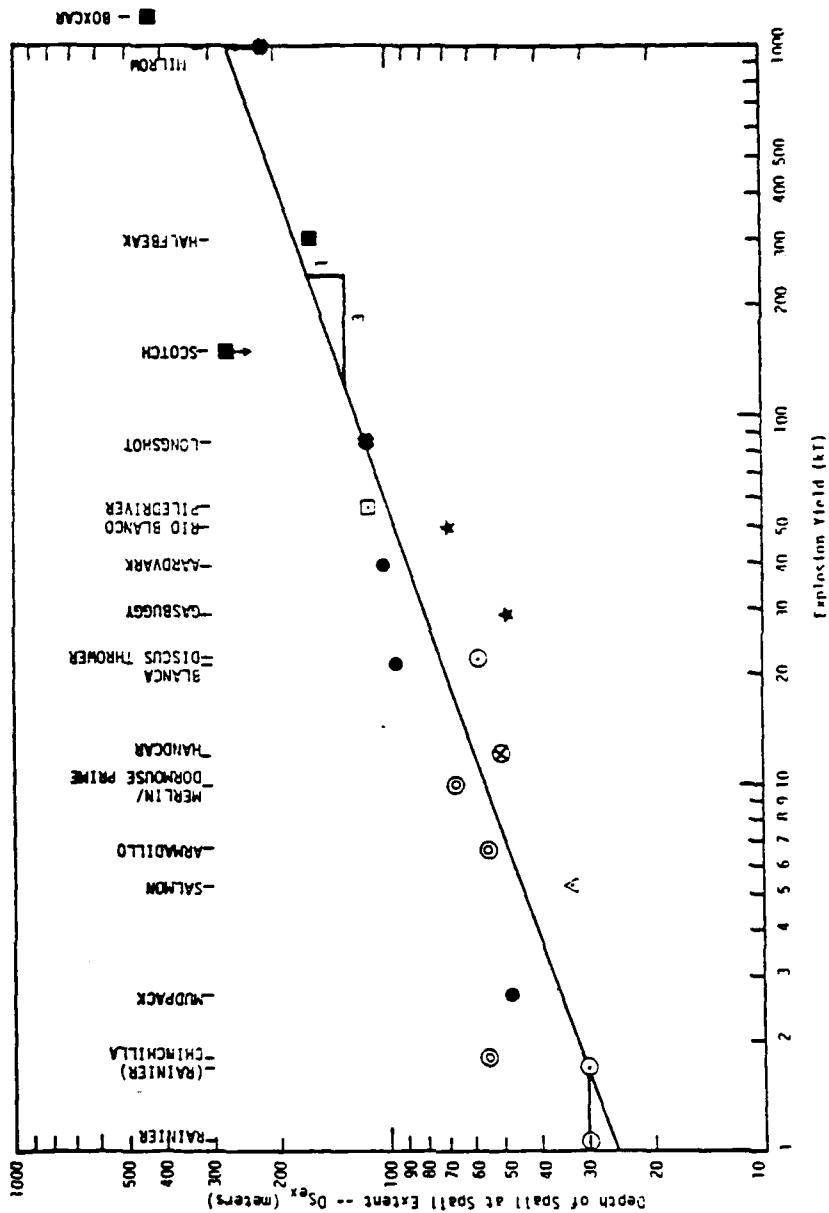


Figure 22. Depth of spall at the extent of spall versus explosion yield.

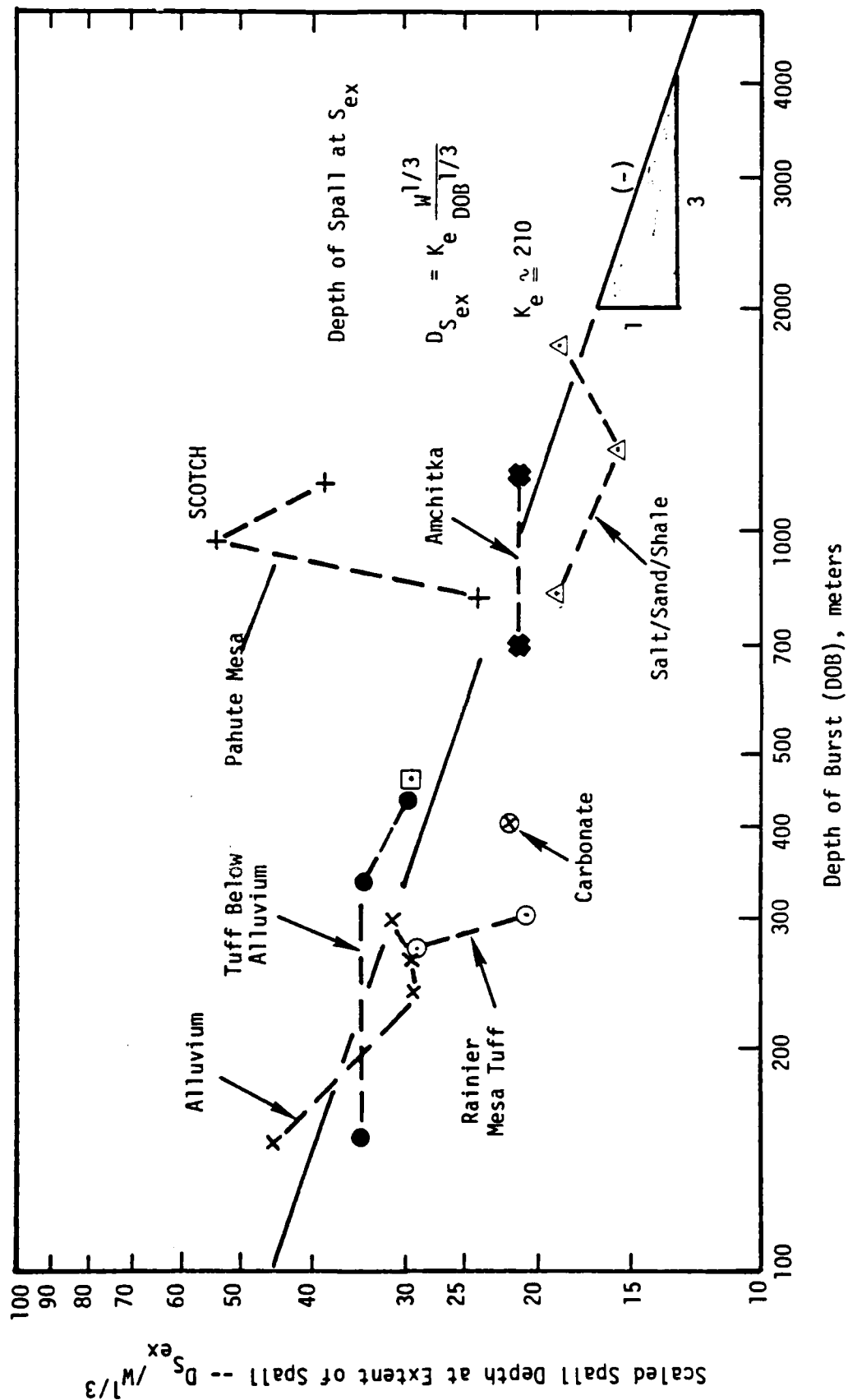


Figure 23. Scaled spall thickness at extent of spall versus depth of burst.

where K_e is an environmental constant of ~ 210 , the depth of burst effect has changed from a $-1/2$ to a $-1/3$ power function (see Eqs. (3) and (5)), and there is much less dependence upon the geologic parameters (K_e vs $\bar{K}\bar{E}$).

8. SPALL RELATED TO GEOLOGIC PARAMETERS

Equations (2), (2a), (3) and (5) have resulted in four geologic or environmentally related empirical constants G_p , KE , \overline{KE} , and K_e . They are associated respectively with spall extent, maximal spall thickness (uncorrected and corrected), and spall thickness near the extent of spall. For G_p an approximation was found that relates density, velocity, and porosity that also required a qualitative correction for geometry and rock stratification (bedding) effects. Apparently the geologic setting has a considerable effect upon spall extent. From Eq. (5) and Figure 23, it is apparent that depth of spall at the extent of spall does not depend greatly upon geologic differences. These have already had their effect in determining the extent where the spall depth estimates are made.

The dependence upon geologic parameters is again important when estimating maximal spall depth (near SGZ). Here the depth of burst dependence is also more important -- about $DOB^{-1/2}$ instead of $DOB^{1/3}$ and $DOB^{-1/3}$ in Eqs. (3) and (5). Spall depth close-in must in part be related to tensile strength and/or density of the spalled mass. Inspection of Figures 15 and 16 show that for alluvium (MERLIN) the spall thickness is larger compared to the Amchitka Volcanics events. This can be corrected for by adjusting the thickness to a constant density (that of 2.4 for the Amchitka Volcanics). By assuming that the near surface density ratio is the same as that of the average overburden values listed in Table 4, then the alluvium to volcanic correction ratio is $1.50/2.40$ or 0.62 . Thus, if the alluvium were a density of 2.4 rather than 1.5, then the depth of spall would be $114 \text{ m} \times 0.62$ or 70.7 m . This plots a little below the Amchitka Volcanics projection line on Figure 15, as would be expected, if mass is more accurate than thickness for comparison. Now, using the corrected depth of 70.7 m and cube root yield scaling for the spall thickness, the MERLIN alluvium point on Figure 16 is 33 rather than $53 \text{ m/kT}^{1/3}$ shown on Figure 16. This gives an environment constant KE of 9,700 instead of 16,000 and a \overline{KE} of 570 shown on Figure 16A.

Similarly, RAINIER is anomalous in Figure 15, having a low density and being on the slope above granite. First, let us assume that a yield uncertainty

1.08 to 1.7 exists. This is an uncertainty associated with published yield changes and possible misprints.⁽³¹⁾ Secondly, the previously mentioned topographic effect would likely decrease spall thickness if a proper correction were known. As a first approximation, let us assume that the spall thickness after a topographic correction is 70 m. This is a rational value being above a projection from alluvium and about half-way between the projected granite and Amchitka Volcanic slopes. The RAINIER tuff to volcanic rock density ratio from Table 4 is 1.80/2.40 or 0.75. Applying this correction to the 70 m revised depth gives an estimated corrected spall thickness of $53 \text{ m/kT}^{1/3}$. This revised depth gives a KE of 13,250 and a $\overline{\text{KE}}$ of 875 (Figures 16 and 16A).

No corrections have been applied to the other events that are in moderate to hard rock. The KE of 45,000 first appeared to be a good average value. It bisects the two granite shots, the two sandstone/shale and salt shots and two of the three events in Amchitka Volcanics. The mean density of the overburden of these events from Table 4 is 2.42. When it was determined that $\overline{\text{KE}}$ values may be improved over KE values (the result of choosing a different DOB dependence to fit the depth values) the volcanics became separated from the other moderate to hard rocks. This resulted in $\overline{\text{KE}}$ values of 1280 for the volcanics and 1780 for granite and the dense bedded sediments.

Having applied corrections for topography and density differences of the spalled material, the revised KE and $\overline{\text{KE}}$ values can be compared with the corresponding G_p values. Alluvium has a G_p of about 34, the RAINIER event about 49, and the average of the two sandstone/shale and salt events is 152. These were chosen instead of granite or the volcanics because the near surface material is alluvium and highly bedded (weak in tension) materials. The other G_p value of comparison interest is in the average of the moderate to hard rock events in Figure 16. This G_p value is 102. Figure 24 illustrates the possible relationship between G_p and KE. It appears that the density and topography corrections are reasonable in light of the very limited data. The depth related environmental "constant" KE is about equal to ± 345 times the spall extent related geologic "constant" G_p ; Figure 24A was prepared after values of $\overline{\text{KE}}$ were thought to provide better fit to the data than KE's (Eqs. (2) versus (2b)). This

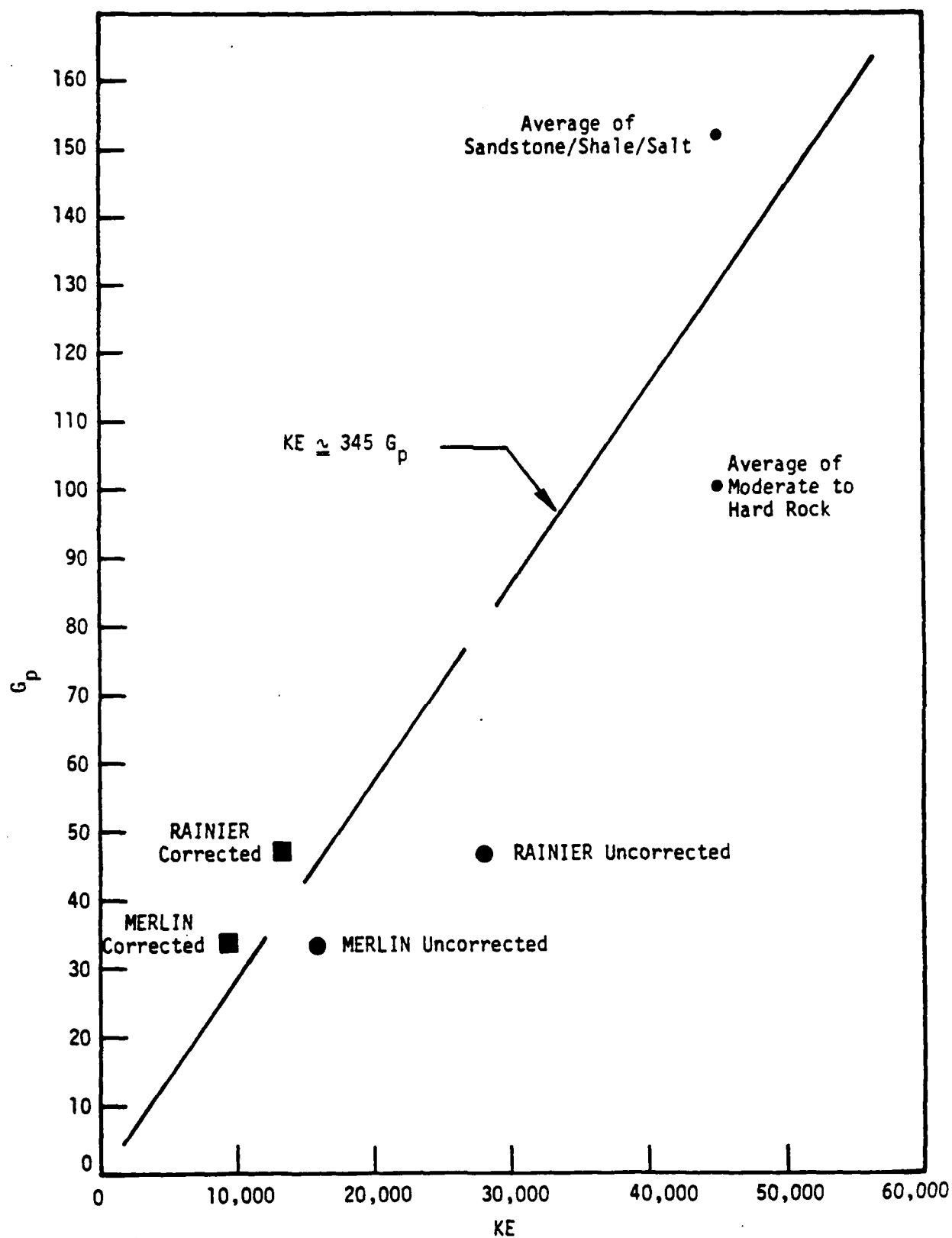


Figure 24. Approximate relation between the geologic or environmental parameters G_p and KE associated with spall extent and spall depth scaling.

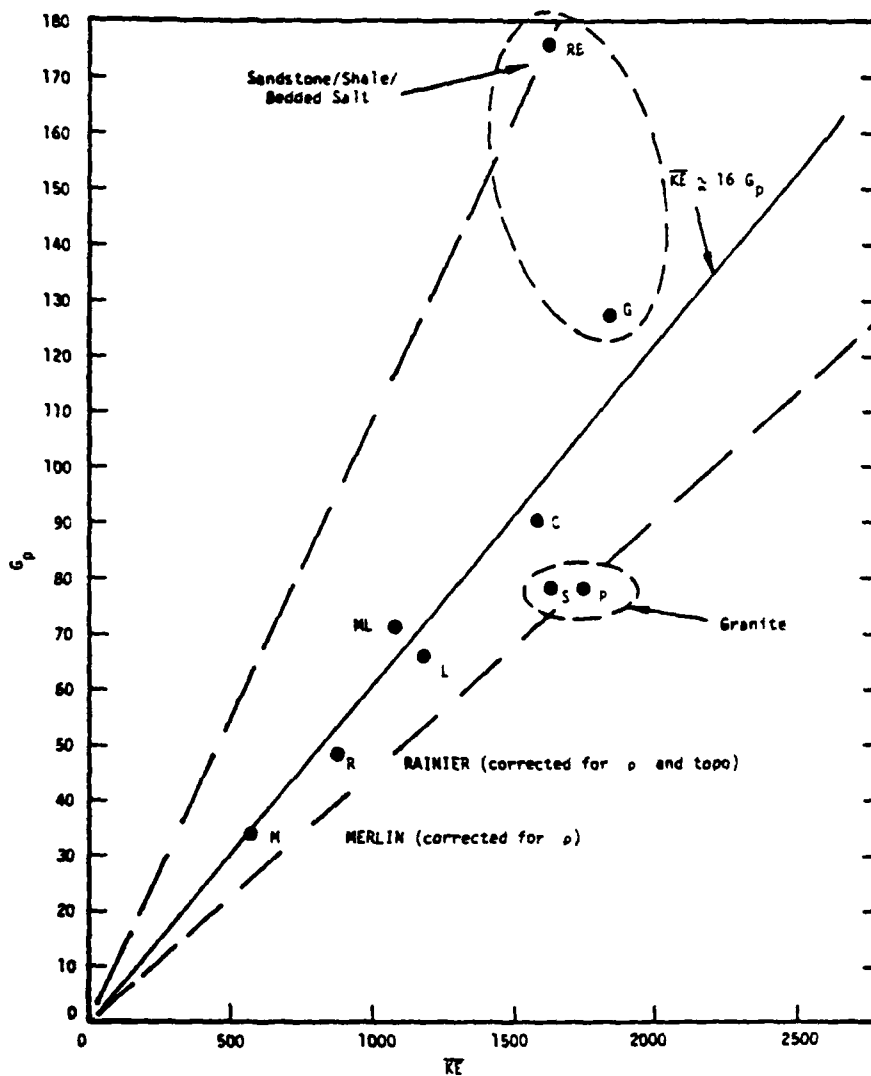


Figure 24A. Approximate relation between the geologic or environmental parameters G_p and \overline{KE} associated with spall extent and spall depth scaling.

figure compared to Figure 24 illustrates a somewhat better correlation between G_p and \overline{KE} . It shows a linear relation of:

$$KE \approx 16 G_p$$

for the Amchitka Volcanics as well as the corrected values for RAINIER and MERLIN (Rainier Mesa tuff and alluvium). The events that scatter from this are those with extremes of bedding that show up as a spread of G_p . These are the moderate to hard rock events in massive granite (unbedded) and highly bedded salt and sandstone and shale.

The relations between \overline{KE} and G_p are approximately linear and are suggestive that after a density correction is made, attenuation of the shock wave most affects depth of spall. It is further suggestive that on the scale of spall, the effective tensile strengths of all of the materials are low and about equal -- i.e., pre-existing weaknesses are numerous and control spall failure.

9. FREE SURFACE/CAVITY GROWTH HISTORY INTERACTIONS -- THE MERLIN EVENT

The MERLIN Event in NTS Alluvium was a 10-kT detonation at a depth of 296 m. The subsurface ground motion data from Boring 1, 15 meters from SGZ and Boring 2, 46 meters from SGZ, were analyzed by Perret, 1971.⁽³⁾ This current study is in basic agreement with his ray path and spall impact signal analysis. The major difference is possibly a deeper maximum depth of spall in Boring 1. Figure 25 illustrates the analysis of acceleration data by this study for Boring 1. The spall gap at E was not identified by Perret and its existence is questionable. The analysis of Boring 2 by Perret is confirmed by this study and is shown in Figure 26.

Figure 25 illustrates an interpretation of wave interactions with the cavity and the free surface as well as locating suspected spall gaps. The figure draws upon cavity dynamics relations to ground motion data that are being prepared as a separate report from this study (Rawson, 1979 progress report in preparation⁽⁴⁶⁾). Notice that the initial acceleration pulses are associated with what is generally referred to as the initial compressional wave. The bulk of the cavity growth history is thought to be related to a deformational wave that trails behind the compressional wave.⁽⁴⁶⁾ Both reflect from the free surface and again from their return to the expanded cavity. The reflection from the cavity is termed a recompaction wave. For this event the recompaction wave appears to hit the gauges at the same time the initial impacts or closure of the spall gaps occur. Additionally, there is a rather diffuse wave recognized at 0.8 to 1 sec that is interpreted as a compaction unloading wave where the compacted and stressed overburden materials unload primarily toward the free surface following spall impacts.

The following table is a comparison of the MERLIN depth of spall estimates of this study with that of Perret:

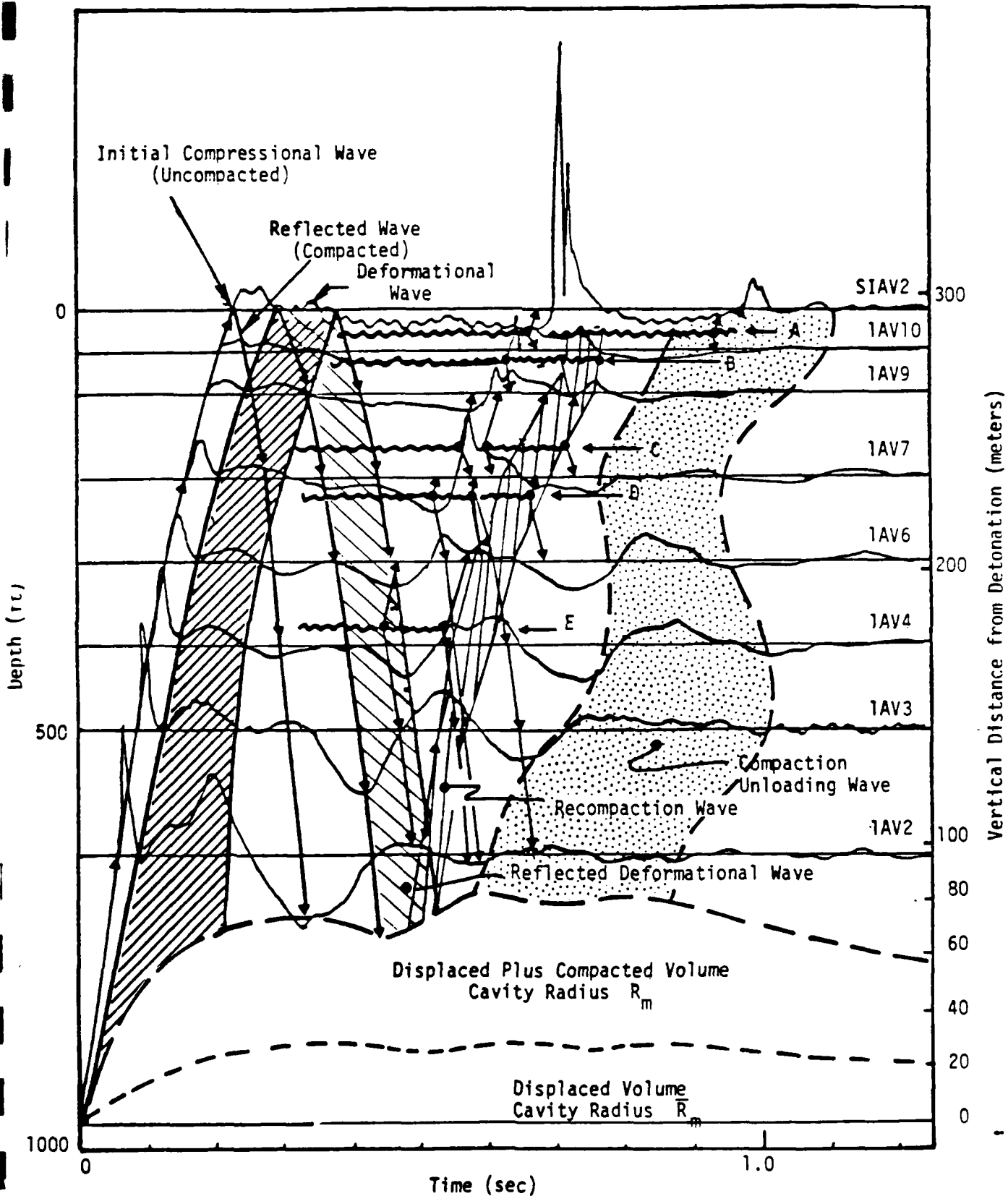


Figure 25. Signal analysis of near surface ground zero accelerometer records from Boring #1 -- MERLIN.

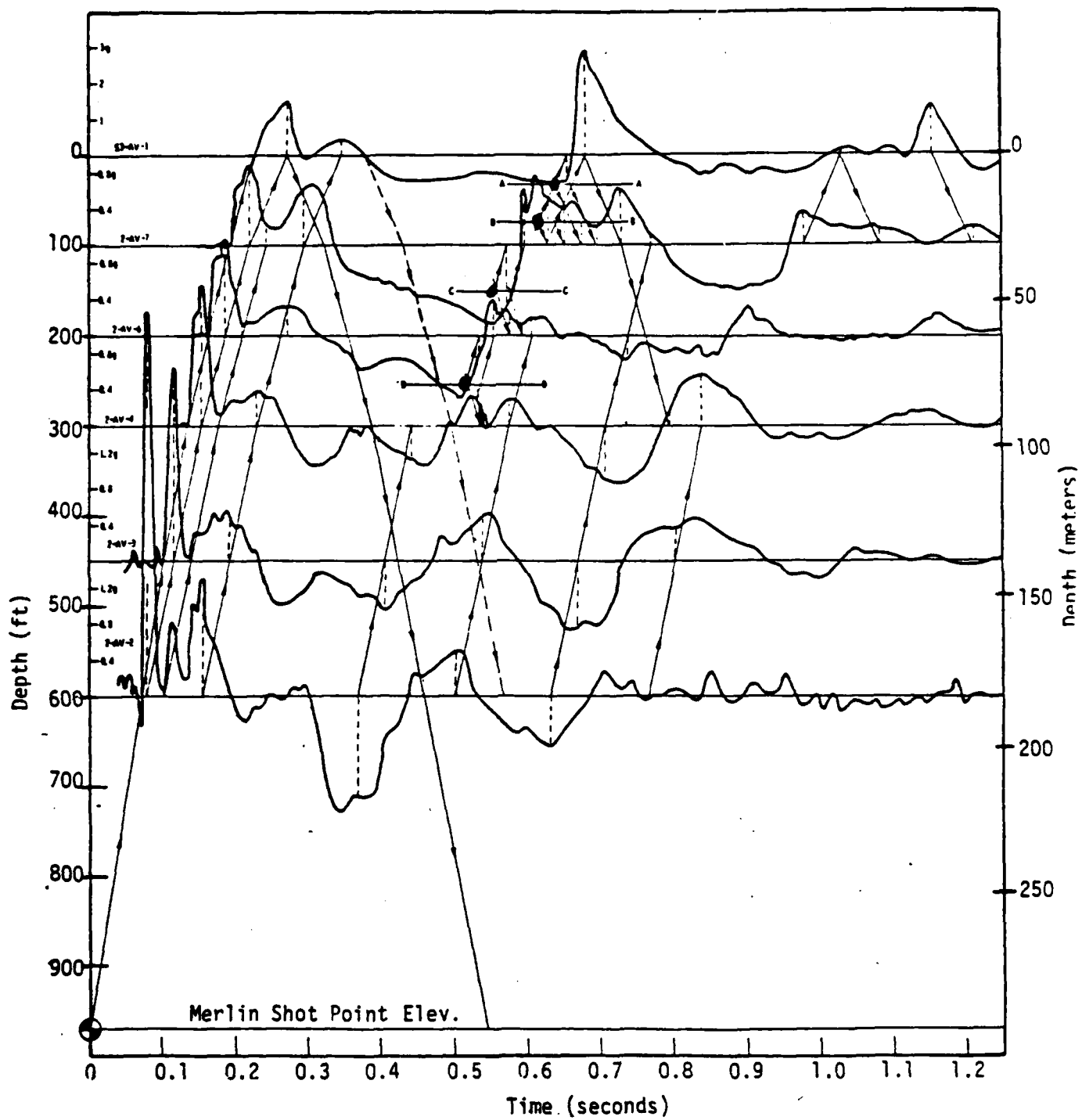


Figure 26. Impact signal analysis, Boring 2.^[3]

Range Horizontal Range (m)	Depth of Spall (meters)	
	Perret ^[3]	This Study
Boring 1, 15 m	7, 21, 47, 78	10, 20, 50, 70 and 116
Boring 2, 46 m	10, 23, 46, 78	10, 23, 46, 78

Figure 27 is a profile summarizing the spall configuration for MERLIN. It is instructive to compare this event in alluvium and at a relatively shallow depth of burial with the profiles of the large yield MILROW Event and the deep RIO BLANCO Event. Both were in competent rock (Figure 20).

Figures 25 and 27 imply a close interaction between the cavity and the free surface. One manifestation of this interaction is development of the failure surfaces that apparently control the geometry of chimney collapse and subsidence crater formation in alluvium. Note that the diameter of the major subsidence sink is about equal to the estimated maximum lateral extent of the cavity radius of ~ 75 m (Figure 25 and Rawson/DELTA report, 1979 in progress⁽⁴⁶⁾). This failure interaction between the cavity and the free surface is thought to occur with shallow scaled depth of burial events and with detonations with weak overburden. It did not occur at RIO BLANCO, Figure 20. The mechanism of cavity dynamics interaction with the free surface -- forming first an uplifted "plug" followed by subsidence within the failed zone -- was first recognized in study of the VULCAN Event.⁽⁴⁸⁾ It was suspected as a result of surface and subsurface deformation caused by GNOME.⁽⁴⁹⁾

Consistent with the implication that cavity dynamics are reflected in the dimensions and character of the subsidence craters of alluvium events are the observations of at least three other events with vertically elongate rather than point source energy deposition. These events all possess right cylindrical subsidence craters rather than the typical dish-shaped sinks. The nonspherical

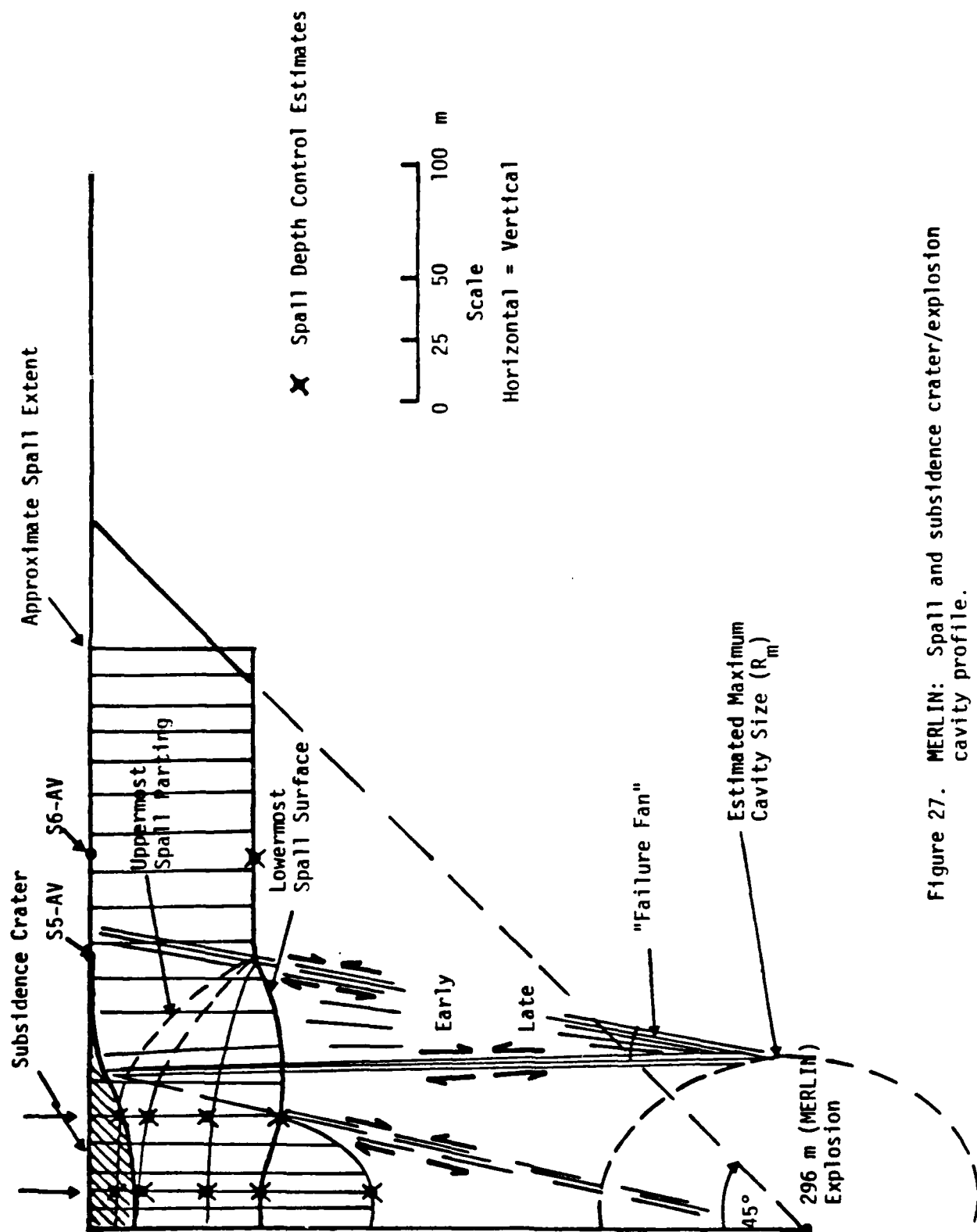


Figure 27. MERLIN: Spall and subsidence crater/explosion cavity profile.

energy deposition is thought to reduce the maximum lateral cavity radius and greatly increases the vertical cavity radius. It is postulated that this simulates a shaped explosive charge, and decreases the lateral extent of spall while increasing the near SGZ depth of spall. Also, the "failure fan" shown in Figure 27 is reduced to a cylindrical "plug" for the "shaped charge" case (Figure 28). Cursory unpublished analysis of the right cylindrical subsidence crater accomplished at the Lawrence Livermore Laboratory in the late 1960's concluded that these anomalies were geologic and not related to explosion physics. Also, U.S.G.S. analyses of subsidence craters have not recognized a link between explosion-induced overburden "failure fan" and subsidence crater shape.⁽⁵⁰⁾ They favor the tulip-shaped configuration of Figure 29 to the cone-shaped geometry for point source events implied by this study and the earlier VULCAN study.

For cratering events a gas acceleration phase is initiated when the confined bubble of expanding gases responds to free surface interactions and the overburden confinement drops. Soon after the bubble breaks and a crater is formed.⁽⁵¹⁾ Similarly, with contained events, the reduction of confinement by placing a significant fraction of the overburden in spall, is thought to initiate a subdued "gas acceleration" phase. This differential motion causes failure between the cavity and the free surface or to the lower spall gaps. Evidence that appears to relate to this phenomena has been found for all of the events in this study, where subsurface data has been analyzed (Table 2), except for RIO BLANCO and possibly MILROW. These events are discussed in the Appendix. There, the discussion for PILEDRIVER includes evidence for an overburden plug development also for the HARDHAT event.

The subsurface indications are that the subdued "gas acceleration" phase of recompaction of the overburden and associated cavity expansion and uplift commonly initiate closure of the lowermost spall gaps. The broad reacceleration at about 0.5 seconds for MERLIN (Figures 23 and 24) illustrate how this motion flows right into the spall closure accelerations of the gauges above the spall gaps. It is postulated that where this occurs, the gap closure is both the spalled overburden falling and the lower material uplifting. Such a ground motion record is considered good evidence for suspecting a recompaction phase and likely failure of the overburden. The RAINIER and MINK data clearly illustrate this

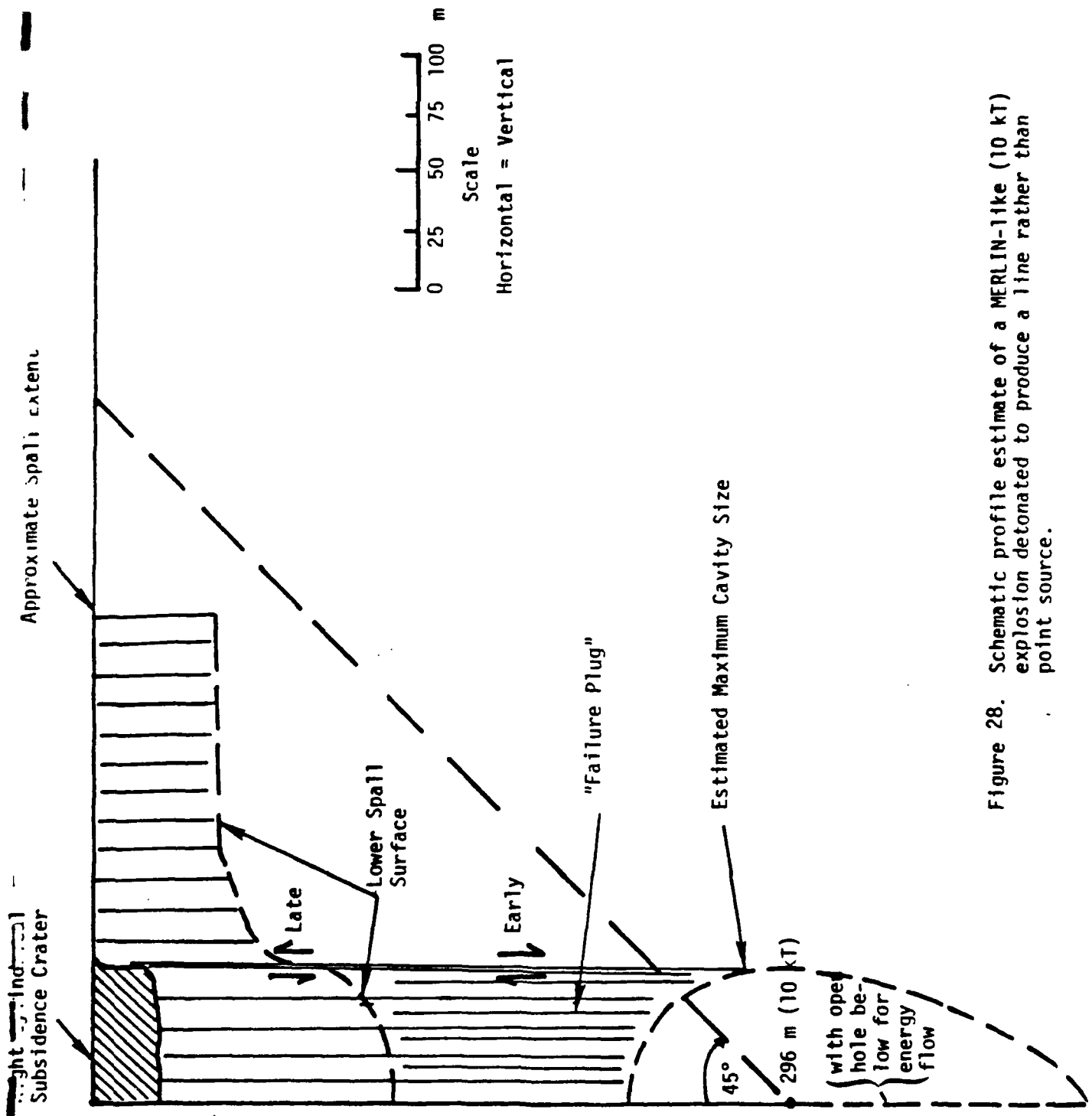


Figure 28. Schematic profile estimate of a MERLIN-like (10 kT) explosion detonated to produce a line rather than point source.

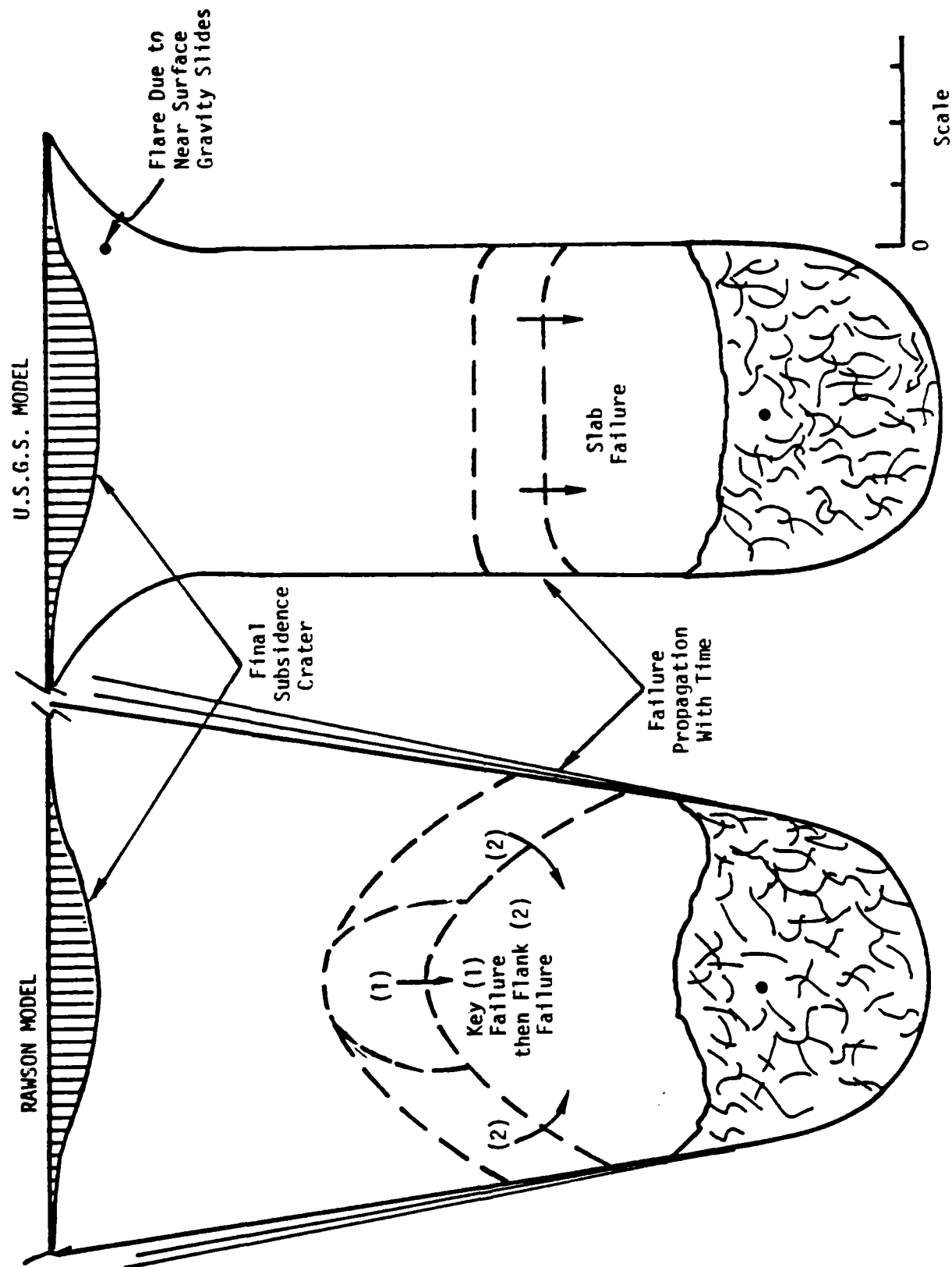


Figure 29. Contrasting models of subsidence crater/chimney development for point source alluvium events.

of the overburden. The RAINIER and MINK data clearly illustrate this phenomenon (see Appendix). Most of the gauges of other events have suffered cable failure of the deeper gauges, so the evidence is circumstantial associated with timing of the electrical losses. Even the RIO BLANCO Event demonstrates a re-acceleration that emanates from the cavity region and flows into the ray path of the spall closures (see Appendix). The timing of this recompaction pulse is too early for a surface reflection to have reflected again from the cavity(s). It is interpreted as a late stage cavity growth phenomenon where the separate cavities of the three explosions coalesce to form a single elongated cavity. When this occurred, there may have been repressurization of the uppermost cavity region re-compacting the overburden somewhat.

The interpretation of the explosion induces stress field being directionally focused by either detonating at one end of an open tunnel or drill hole or by sequential detonation of spaced explosion charges in a confined (tamped) tunnel or drill hole, leads to some possibilities of seismic wave modification. How such man-made non-spherical deposition of energy affects m_b and M_s and their detailed wave patterns -- when optimally designed for deception -- has yet to be evaluated in light of the near source evidence presented in this study.

The late-time interaction between the free surface and the detonation region is interpreted as explosion induced stress unloading. When the detonation occurs, it is now thought to expand a cavity that grows in a shape that reflects the magnitude and variations of the confining stress field. The maximum dynamic cavity size is postulated as often substantially larger than the late time size observed by post shot exploration.⁽⁴⁶⁾ Rebound is thought to occur as a result of stored overstress in the rock. This stored stress can unload to the free surface, to the cavity, and diffuse laterally and any other down-gradient direction. Since, at early times of 0.5 to 3 seconds following the explosion, the cavity pressures are still rather high, only so much rebound is allowed compared to the energy stored. What may happen is partial unloading to the free surface, resulting in a broad uplift. This may be subdued because of the large volume of compacted rock so the net surface displacements may be down even though they are up laterally from shot level. The lateral uplift has been reported for the MIGHTY EPIC Event along with an interpretation of the fluid pressure (ground water)

response to the stored induced stress. Further examination of this phenomena is expected to lead to a better understanding of aftershock development from large yield explosion events.⁽²⁶⁾

The phenomena of induced stress unloading, cavity volume history, compaction distribution evidence and in-situ stress perturbations are being developed in the companion study.⁽⁴⁶⁾

10. CONCLUSIONS AND RECOMMENDATIONS

This study is one of several being concurrently accomplished by the author that involve the analysis and interpretation of near field ground motion data from contained nuclear explosions. These studies involve relating ground motions to observed block motions and contributing toward an evolving predictive capability so that near surface detonations can be evaluated as to block motion threats to strategic facilities. One study relates spall to observed surface fracturing.⁽¹⁾ Another effort is to assist Engineering Decisions Analysis Corp. (EDAC) in the analysis and interpretation of block motion related data from the MIGHTY EPIC and DIABLO HAWK Events.⁽²⁶⁾ The combination of these studies provides a rather extensive re-analysis and re-evaluation of ground motion data and site related data for a substantial range of explosion yields, depths of burst, environmental settings, and goals associated with a wide range of Defense Department needs. They contribute to improving the predictive capability of ground motions and related effects as well as helping to reduce uncertainties and increase detailed understanding of the ground motion records. *These records contain the imprint of what happened from the explosions to the measurement stations as a function of time.* There is a real need to refine the tentative interpretations of this and the other work in progress so that results are more quantitative and conclusions more definitely established.

The configurations and scale of spall from nuclear explosions are documented by this study so as to provide an empirical basis that relates the geologic setting to yield and depth of burst. Most previous investigators that have reported on the seismic implications of spall have interpreted the lateral extent(s) and depth(s) to be substantially less than found by this study. Therefore, any recognized importance of spall can be increased relative to these differences. The importance of spall in modifying the interpretations of surface and body wave magnitudes has received considerable attention and does not yet appear to be resolved. This study is a contribution to any re-assessments of those issues. Additionally, this study points out the importance of both the spalled region and the commonly failed overburden, between spall and the explosion produced cavity, in contributing to tectonic stress adjustments and the

development of surface wave double couples. It is indicated that the cross-sectional area of explosion failed earth material is over twice that of models proposed by previous investigators.

Another observation of both free-field and surface ground motion data is that variations with direction are large and probably related to lateral (or horizontal) pre-stress differences. There may be a direct link between data scatter, in-situ stress differences, and surface wave double couples. In-situ stress data are sadly lacking and the ground motion data are generally limited to one line of gauges. Correcting these deficiencies for future events will contribute greatly to refinement of a predictive capability and improving our understanding explosion earth interactions. The DIABLO HAWK Event serves as a good example and analysis of results will be important in helping to refine, confirm or deny many of the proposed interpretations presented in this study.

An analysis of surface waves should be accomplished with a knowledge of at least the principal horizontal stress orientation. To date, these data only exist (to the author's knowledge) for Rainier Mesa and possibly the Climax Stock at NTS. If the correlation between the documented limits of surface fracturing (by the U.S.G.S.) and the estimated limits of spall coincide because of causal relations, as postulated by the author, then the shape of spall extent reflects in-situ stress orientations.⁽¹⁾ This study indicates that ground motions are minimal in the direction of the principal (maximum) horizontal stress. Similarly, cavity size reflects differences in confinement with direction. The period of spall typically lasts from about 0.5 to 3 seconds, depending upon details of the governing variables. During this period, overburden confinement is reduced and the expanded cavity commonly undergoes a preferential upward push associated with a subdued "gas acceleration", analogous to the cratering process except that differential motions of the overburden are much less and venting is usually avoided. The cavity growth history also is typified by late stage rebound from explosion-induced stress stored in the surrounding rock. This region also unloads to the free-surface, resulting in broad uplifting of the regions lateral from the detonation. The postulated stored stress becomes very important for detonations at or below the water table. Here, little permanent compaction can occur and

the fluid pressure history and associated pressurized volume may be important to the generation of aftershocks and late stage stress adjustments.

This study, in combination with the spall study being prepared by the author for RDA/DNA, provide the following tentative scaling relations for spall from contained detonations. These relations allow for application to a range of geologic environments and have:

- Confirmed Viecelli's determination that close-in spall thickness scales as the one-third power of the explosion yield (with constant material and scaled depth of burst, etc.)
- Determined that scaled spall thickness close-in ($D_{SGZ}/W^{1/3}$) varies approximately as:

$$D_{SGZ} \approx \overline{KE} \frac{W^{1/3}}{DOB^{1/2}}$$

where \overline{KE} is a material dependent "constant".

- Determined that the depth of spall near lateral limits of spall ($D_{S_{ex}}$) scales approximately as a material independent constant (K_e) times the yield to the one-third power ($W^{1/3}$) divided by the depth of burst to the one-third power ($DOB^{1/3}$):

$$D_{S_{ex}} \approx K_e \frac{W^{1/3}}{DOB^{1/3}}$$

where K_e is about 210, independent of material.

- Determined that the extent of spall measured radially from the detonation (S_{ex}) scales approximately as a material dependent constant (G_p) times $DOB^{1/3}W^{1/4}$:

$$S_{ex} \approx G_p DOB^{1/3}W^{1/4}$$

- Determined that the two material dependent constants \overline{KE} and G_p are approximately related by:

$$\overline{KE} \approx 16 G_p$$

- Determined that the material dependent "constant" G_p is relatable to the competency and structural character of the overburden by the trial and error approximation:

$$G_p \approx \rho^2 V_p (R_p + R_m)$$

where ρ is the overburden bulk density, V_p is the compressional velocity, R_p and R_b are relative porosity and bedding coefficients. These coefficients vary between the relative values of 1 to 10, and can be approximated from site geologic data and descriptions.

The above relationships must be viewed as tentative as well as preliminary since the data are generally sparse, there is substantial data scatter, and the accuracy of the analyses are limited by published ground motion records -- some of which are at scales where timing and amplitudes are very uncertain. The links to materials properties also suffer from lack of precise or representative measurements so considerable judgement was involved in developing the empirical relationships. Sufficient background material has been assembled, reviewed, analyzed, etc. that a number of hypotheses have been proposed. More quantitative analyses and testing of concepts are a needed refinement.

II. REFERENCES

1. Rawson, Glen (Report in Progress), "Surface Observed Block Motions and Their Relations to Explosion Induced Spall," RDA/DNA Technical Report.
2. Eisler, J. D. and F. Chilton (1964), "Spalling of the Earth's Surface by Underground Nuclear Explosions," J. Geophys. Res., 69, no. 24.
3. Perret, W. R. (1971), "Free-Field and Surface Motion from a Nuclear Explosion in Alluvium: MERLIN Event," Sandia Laboratories, SC-RR-69-334.
4. Rinehart, J. S. (1960), "How to Predict the Effect of Spalling when Caused by Large Blasts," Engineering & Mining Journal, 161, no. 8.
5. Swift, L. M. and D. C. Sachs (1959), "Surface Motion from an Underground Detonation, Project 26.4a, Operation Plumbbob, RAINIER Event," SRI, WT-1528.
6. Chilton, F., et al. (1966), "Dynamics of Spalling of the Earth's Surface Caused by Underground Explosions," J. Geophys. Res., 71, no. 24.
7. Eisler, J. D., et al. (1966), "Multiple Subsurface Spalling by Underground Nuclear Explosions," J. Geophys. Res., 71, no. 16.
8. Perret, W. R., Personal Communication.
9. Boucher, G. A., et al. (1972), "Earthquakes Associated with Underground Nuclear Explosions," J. Geophys. Res., 74.
10. Hamilton, R. M., et al. (1972), "Earthquakes Caused by Underground Nuclear Explosions on Pahute Mesa, Nevada Test Site," Bull. Seism. Soc. Am., 62, no. 5.
11. Brune, J. N. and P. Q. Pomeroy (1963), "Surface Wave Radiation Pattern for Underground Nuclear Explosions and Small Magnitude Earthquakes."
12. Press, F. and C. B. Archambeau (1962), "Release of Tectonic Strain by Underground Nuclear Explosions," J. Geophys. Res., 67.
13. Aki, K. (1964), "A Note on Surface Explosions," J. Geophys. Res., 69, no. 6.
14. Archambeau, C. B. and C. Sammis (1970), "Seismic Radiation from Explosions in Prestressed Media and the Measurement of Tectonic Stress in the Earth," Review of Geophysics and Space, 8, no. 3.
15. Perret, W. R. and D. R. Breiding (1972), "Ground Motion in the Vicinity of an Underground Nuclear Explosion in the Aleutian Islands: MILROW Event," Sandia Laboratories, SC-RR-71-0668.

16. Toman, J., et al. (1973), "The RIO BLANCO Experiment: Subsurface and Surface Effects and Measurements," Lawrence Livermore Lab., UCRL-51504.
17. Vieceili, J. A. (1973), "Spallation and the Generation of Surface Waves by an Underground Explosion," J. Geophys. Res., 78, 2475-2487.
18. Vieceili, J. A. (1973), "Generation of Rayleigh Waves by Underground Nuclear Explosions: An Examination of the Effect of Spall Impact and Site Configuration," Lawrence Livermore Laboratory, UCRL-51417.
19. Sobel, P. A. (1973), "The Effects of Spall on m_b and M_s ," Unpublished Teledyne Geotech Report.
20. Vortman, L. (1978), Written communication to Robert Port of R & D Associates from Sandia Laboratories and transmitted to G. Rawson.
21. Perret, W. R. (1976), "Surface Motion Induced by Nuclear Explosions Beneath Pahute Mesa," Sandia Laboratories, SLA-74-0348, Part I.
22. Perret, W. R. (1978), "Surface Motion near Underground Nuclear Explosions in Desert Alluvium -- Operation Nougat I, Area 3, NTS," Sandia Laboratories, SAND-77-1435.
23. Day, J. D. and D. W. Murrell (1967), "Ground and Water Shock Measurements: VELA UNIFORM Project LONGSHOT," U. S. Army Engineers, VUF-2701.
24. Adams, W. M., et al. (1960), "Summary Report of Strong Motion Measurements, Underground Nuclear Detonations; Operation HARDTACK, Phase II, ITR-1711.
25. Perret, W. R. (1959), "Surface and Subsurface Strong Motion Measurements; Operation HARDTACK, Projs. 26.2 and 26.1, ITR-1703.
26. Short, S. A., et al., and G. Rawson (1978), "MIGHTY EPIC/DIABLO HAWK Block Motion Program, Prediction of DIABLO HAWK Block Motion," Engineering Decision Analysis Co./RDA/DNA, EDAC-177-020.3.
27. Perret, W. R. (1977), Written communication of data copies of the HANDLEY surface ground motions -- not yet published.
28. Raleigh, C. B., et al. (1974), "Crustal Stress and Global Tectonics," Proc. Third International Society of Rock Mechanics, Vol. I.
29. Springer, D. L. and R. L. Kinnaman (1971), "Seismic Source Summary for U. S. Underground Nuclear Explosions, 1961-1970," Bull. Seism. Soc. Am., 61, 1073-1098.
30. Springer, D. L. and R. L. Kinnamon (1975), "Seismic Source Summary for U. S. Underground Nuclear Explosions, 1971-1973," Bull. Seism. Soc. Am., 65, 343-351.

31. Higgins, G. H. (1970), "Nuclear Explosion Data for Underground Engineering Applications," Lawrence Radiation Lab/International Atomic Energy Agency, IAEA-PL-388/14.
32. Perret, W. R. (1961), "Subsurface Motion from a Confined Underground Detonation -- Part I, Operation Plumbbob -- Project 26.4b," Sandia Corp. WT-1529.
33. Perret, W. R. (1973), "Ground Motion in the Vicinity of the CANNIKAN Nuclear Explosion," Sandia Laboratories, SLA-73-0043.
34. Weart, W. D. (1965), "Free-Field Earth Motion and Spalling Measurements in Granite: Proj. SHOAL, VELA UNIFORM," Sandia Corp., VUF-2001.
35. Weart, W. D. (1963), "Particle Motion Near a Nuclear Detonation in Halite, Project GNOME," Sandia Corp., PNE 108F.
36. Terhune, R. W. (1973), "Prediction of Nuclear Explosion Effects for RIO BLANCO," Lawrence Livermore Laboratory, UCRL-51377.
37. Hoffman, H. V. and F. M. Sauer (1969), "Free-Field and Surface Motions: Operation Flintlock, Shot PILEDRIIVER, SRI, POR-4000.
38. _____ (1962), "Geological, Geophysical and Hydrological Investigations of the Sand Springs Range, Fairview Valley and Fourmile Flat, Churchill Co., Nev.," Univ. of Nev., Reno, Nev.
39. McKeown, F. A. (1971), "Summary of Geologic Structural Information Relative to Noncontained and Contained Nuclear Explosions," U. S. Dept. of Interior -- For Official Use Only.
40. Rawson, Glen, personal observations.
41. Perret, W. R. (1970), "Gasbuggy Seismic Source and Surface Motion," PNE-1002.
42. Perret, W. R. (1964), "Free-Field Particle Motion from a Nuclear Explosion in Salt, Part I, SALMON Event," VUF-3012.
43. Perret, W. R. And K. B. Kimball (1971), "Ground Motion Induced in a Multilayered Earth by a Contained Nuclear Explosion -- DISCUS THROWER Event," POR-6400.
44. Perret, W. R. (1970), "Ground Motion in a Multilayered Earth, Part II: Nuclear Explosion in Tuff -- MUD PACK Event," POR-2900.
45. Perret, W. R. (1970), "Ground Motion in a Multilayered Earth, Part I: Nuclear Explosion in Hard Rock -- HANDCAR/PAINTED PONY Event," POR-2800.

46. Rawson, Glen (1979), "Explosion Energy Partitioning That May Reflect Materials Properties Variations and Variations in Ground Motion Data," DELTA Report in Progress.
47. Savage, J. C., et al. (1974), "Geodetic Determination of Strain at the Nevada Test Site Following the HANDLEY Event," Bull. Seism. Soc. Am., 64, no. 1.
48. Rawson, D. E. (now Glen) and R. Rohrer (1968), "Surface Motion and Subsidence Study of the DUMONT, VULCAN, and GREELEY Events," Lawrence Livermore Laboratory, UCRL-50432 (Title Unclassified, Report Confidential).
49. Rawson, D. E. (now Glen), et al. (1961), "The Environment Created by a Nuclear Explosion in Salt: Project GNOME," PNE-107F.
50. Houser, F. N. (1969), "Subsidence Related to Underground Nuclear Explosions, Nevada Test Site," Bull. Seism. Soc. Am., 59, no. 6.
51. Cherry, J. T. (1967), "Computer Calculations of Explosion Produced Craters," Int. J. Rock Mech. Min. Sci., 4, no. 1.
52. Glenn, H. D. (1976), "Spall Study in One Dimension," Lawrence Livermore Laboratory, UGID 17144.

APPENDIX
DEPTH OF MAXIMUM SPALL ANALYSES*
(Listed by Explosion Event)

RAINIER

Figure 5 of the text is an analysis of the subsurface acceleration records from gauges in hole 26.4b near surface ground zero. Identification of the deepest spall gap D is uncertain because of possible wave form modification due to the up-flowing recompaction wave. The depth of 82 m at gap C is thought to be shallow because of instrument cable failures at a depth of 98 m in the nearby shallow instrument hole, hole 26.4a.⁽⁵⁾ The deeper location of 113 m is in agreement with the interpretation of Eisler, et al., and was picked independently.⁽⁷⁾

RAINIER IMPLICATIONS ABOUT BLANCA

The yield for RAINIER has been reported as 1.08 and 1.7 kT.^(31,32) This places the scaled depth of burst ($DOB/W^{1/3}$) as $267 \text{ m/kT}^{1/3}$ or $230 \text{ m/kT}^{1/3}$. This is considerably deeper than BLANCA with a yield of 22 kT and a scaled DOB of $107 \text{ m/kT}^{1/3}$. This, coupled with the possibility that the Mesa topography increases the maximum depth of spall from that of a flat surface, raises suspicions about the possible causes of BLANCA venting. That detonation was the first nuclear explosion to fail rock to the ground surface and vent (see Figure 18 in text). From Eq. (2) using the apparent KE of 30,000, the estimated spall depth for BLANCA is 279 m compared to a vertical depth of burst of 301 m and a slant depth of burial to the nearest free-surface of 254 m. In other words, the depth of spall virtually reached the detonation point. The event was originally planned to be deeper into the tunnel but damage from LOGAN resulted in abandoning some of the emplacement drift.⁽³⁹⁾ Figure 18 illustrates the failed slumped zone surrounding the vent zone that is interpreted here as the region pre-failed by the cavity-free-surface shearing discussed in Section 9. Chimney

*See Table 2 Summary in text.

propagation and subsidence resulted in the slump zone and sink also shown on the figure. The thrust fault shown is on a bedding plane natural weakness between units T_{os_2} and T_{os_3} . The detonation was in T_{os_3} with the contact slightly below the shot point. It is postulated that cavity growth caused failure and differential motion along this bedding surface and that spall resulted in propagating this motion as a thrust fault to the surface. This lack of confinement in the overburden allowed for failure along both pre-existing weaknesses and caused new ones. The vent location is not on a known fault or weakness surface.⁽³⁹⁾ According to Dr. G. Morey observing BLANCA, it vented at twenty seconds after the detonation, ejecting a spout of dust about 100 m above the Mesa rim. Collapse of the chimney occurred at 4.5 minutes following the detonation and apparently sealed the venting.⁽³⁹⁾

MERLIN

Figures 25 and 26 in the text represent the ray tracing analysis of spall from MERLIN. The analysis was in basic agreement with that of Perret.⁽³⁾ The deeper spall gap (E in Boring #1, Figures 25 and 27) differs from Perret's interpretation.

MILROW

The MILROW acceleration records (Figure A-1) are at a poor scale for spall analysis, so both acceleration and velocity were used.⁽¹⁵⁾ Clearly, spall occurs to a maximum depth greater than 152 m (500 ft) or below Gauge 1-1-35-UV. The estimated depths of the spall gaps identified by ray path analysis of impact signals are 82, 146, 190 and 310 meters. The velocity record (Figure A-2) for Gauge 1-1-35UV does not display the clear -lg slope of the upper two gauges. This is interpreted as resulting from spall impacts above and below the gauge producing the complex record.

CANNIKAN

CANNIKAN was originally planned to be buried a little deeper (1829 m) instead of the 1791 meters depth of burial. The yield was announced to be less

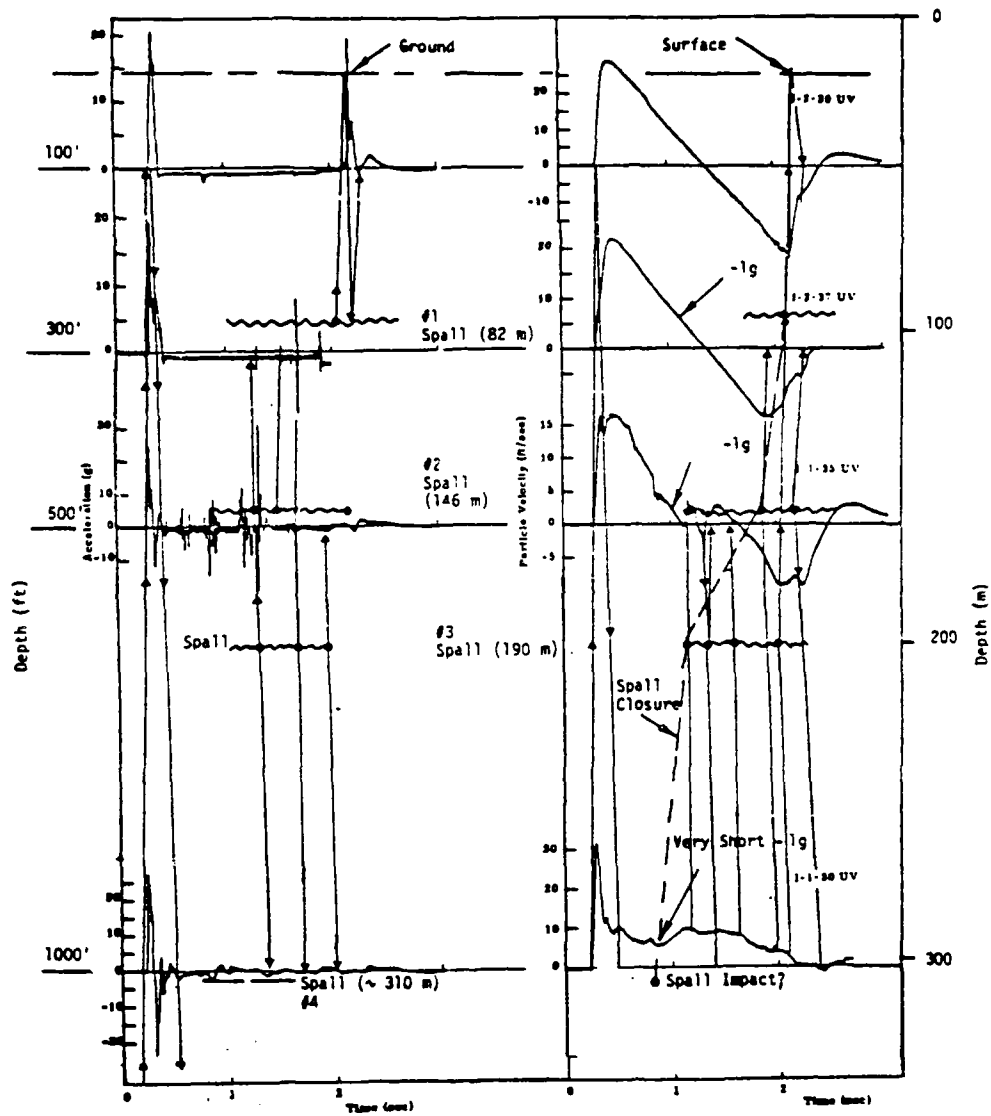


Figure A-1. MILROW: Signal analysis-subsurface ground motion.

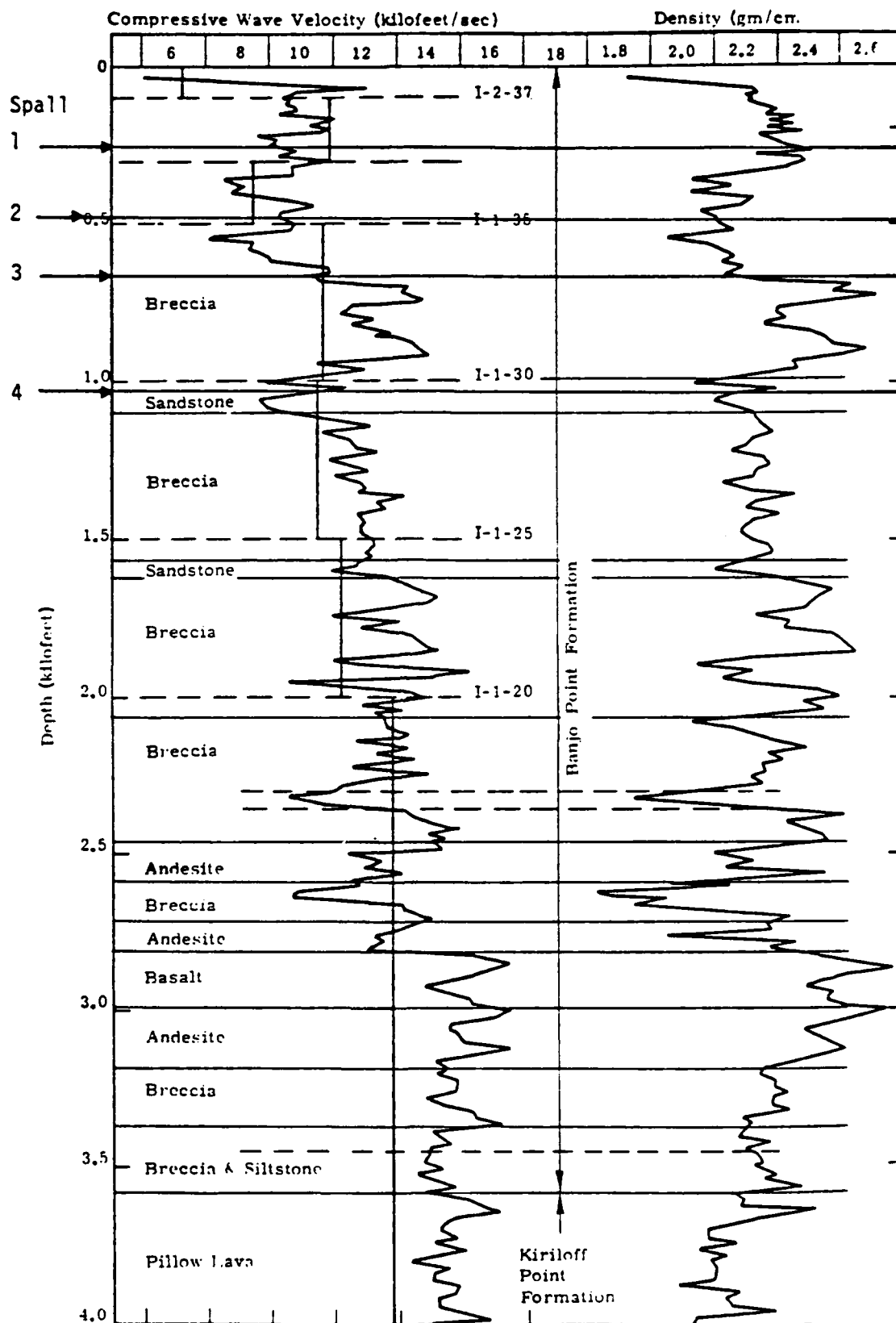


Figure A-2. Velocity and density logs and spall gap locations for MILROW.

than 5 Megatons. By assuming the yield as 4.5 MT, the scaled depth of burst is $108 \text{ m/kT}^{1/3}$. This is substantially more shallow than the conventional scaled DOB of about $122 \text{ m/kT}^{1/3}$ and similar to BLANCA. The ground motion gauges failed either during the early expansion of the deformational wave, in spall following the arrival of the tensile waves, or at 1.81 seconds when there was recording trailer power failure. The subsurface gauges are located within a cased drill hole about 150 meters laterally from SGZ that was completely grout filled. It may be assumed that cable failures occurred under stresses capable of failing the cased drill hole having strengths exceeding that of the rock. If cable failure implies rock failure (prior to the power failure at the trailer park) then the detonation failed all of the overburden -- either by the outgoing stress wave or the spall-inducing reflected (tensile) waves. This is consistent with BLANCA and the lack of venting may well be due to water saturation and the flat topography.

Since there were no subsurface records that survived until spall impact, depth of spall must be inferred from the earlier part of the vertical velocity records. The three uppermost gauges installed in the near SGZ drill hole are shown in Figure A-3. Clearly, spall extends below these gauges as all developed a -1g slope (free fall) after the compressional and deformational reflected waves initiate spall. From ray tracing analysis, two upper spall gaps are identified -- one at about 44 m and a second at about 117 m.

The next two gauges in descending order down the hole are shown in Figure A-4. Gauge I-57UV apparently suffered a cable failure at about the time the reflected deformational wave arrived. The lower gauge at 158 m depth appears to have suffered cable damage following arrival of the reflected (compressional) waves, but cable failure occurred somewhat later. A clear -1g slope was not developed, possibly due to cable damage.

Figure A-5 displays records for all of the gauges below those shown in Figures A-3 and A-4 (the gauge at 158 meters depth is repeated). Clear

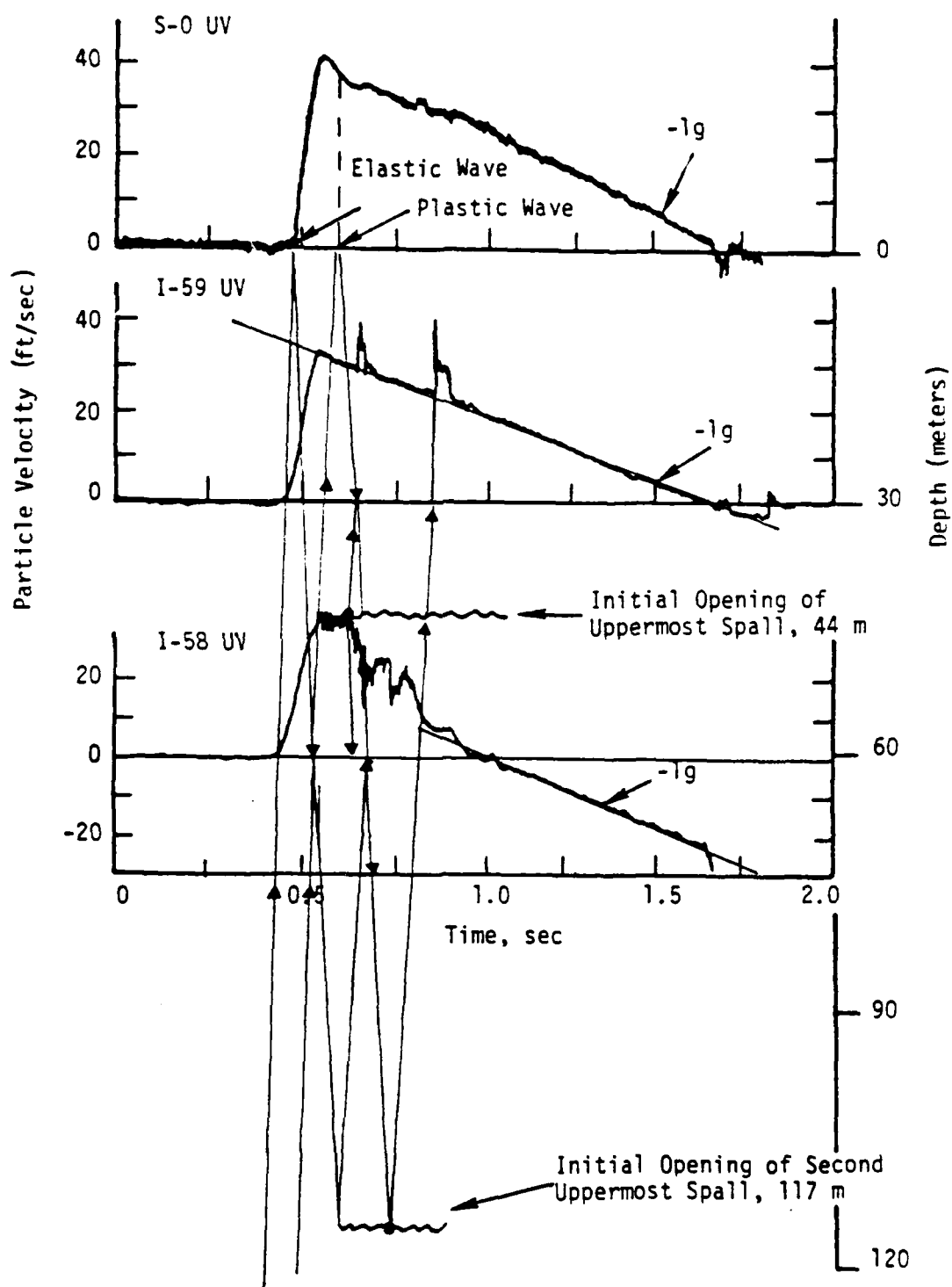


Figure A-3. CANNIKAN signal analysis of subsurface ground motion -- upper gauges.

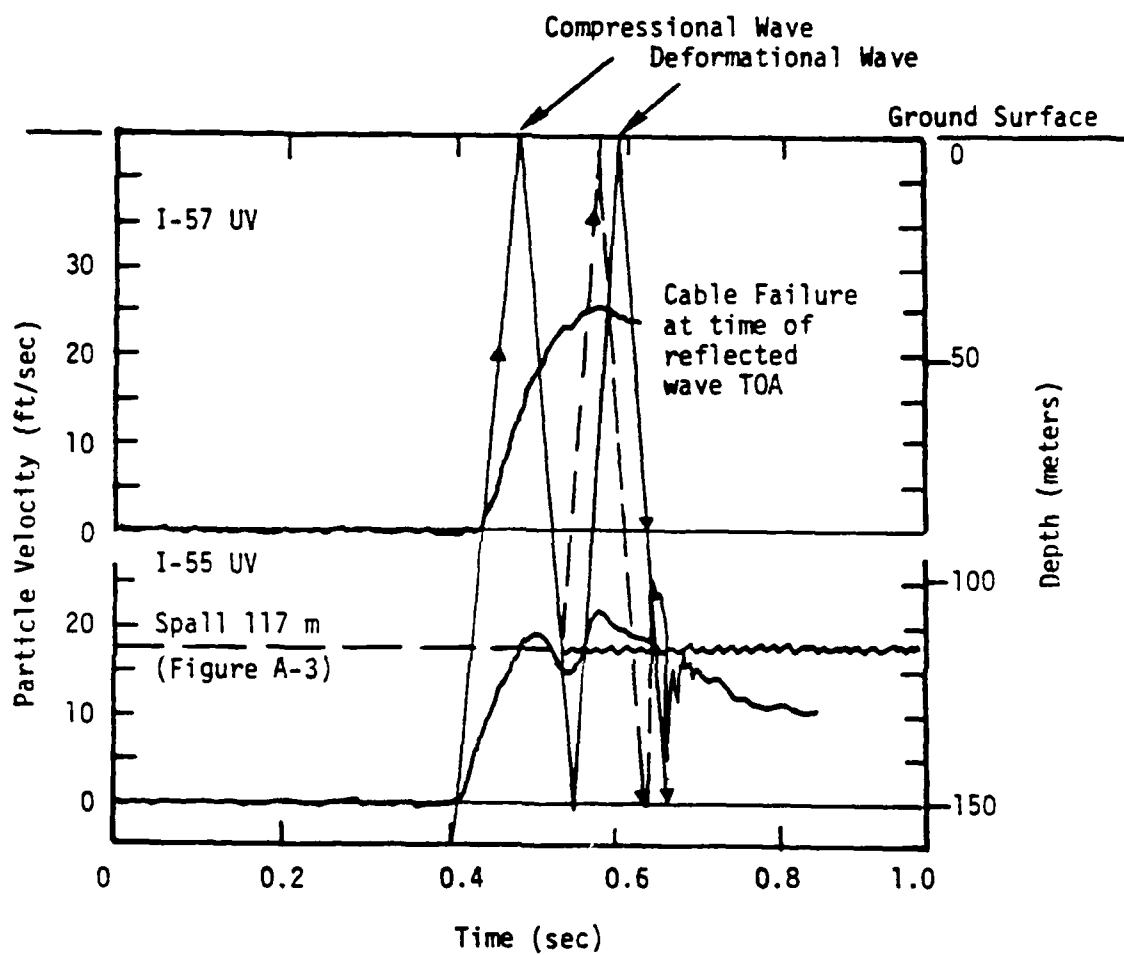


Figure A-4. CANNIKAN (Figure A-3 continued).

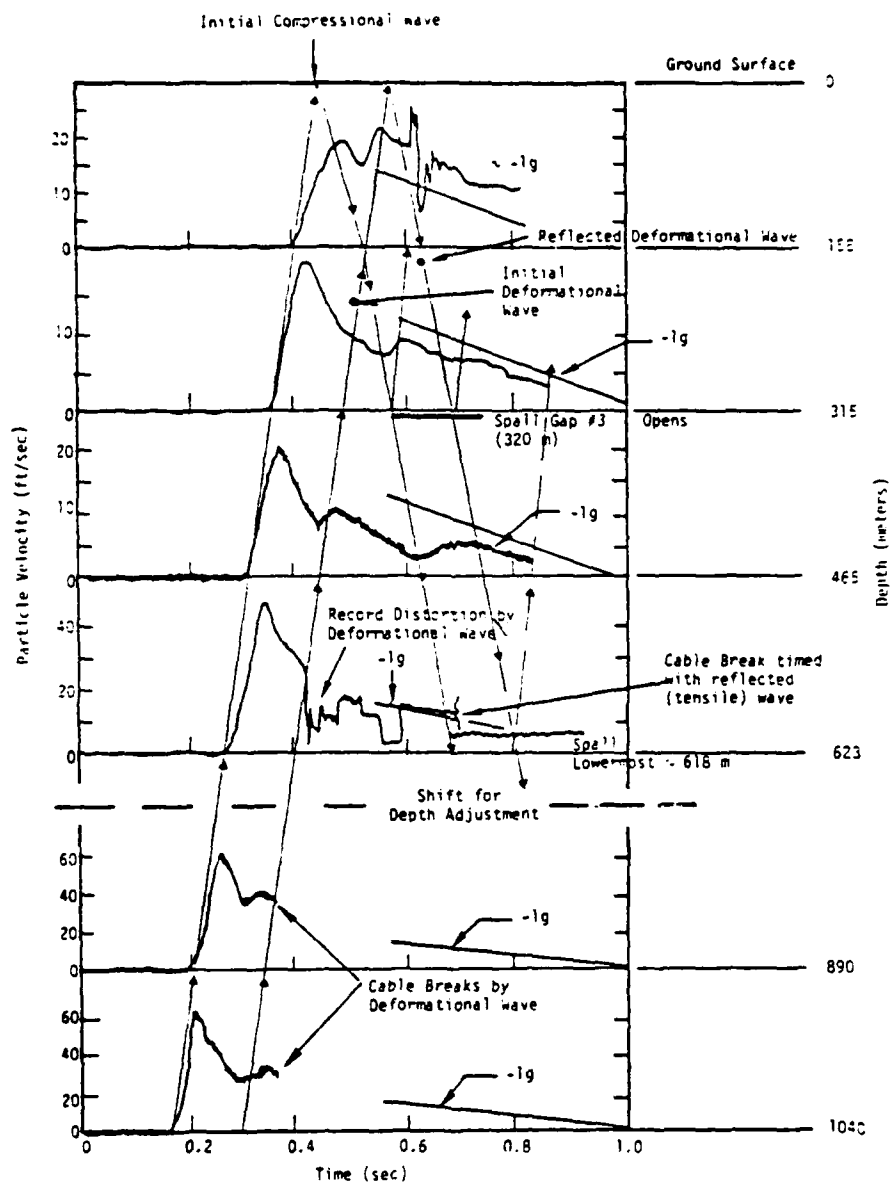


Figure A-5. CANNIKAN (Figure A-3 continued).

development of the -lg slope characteristic of material in ballistic trajectory is shown for gauges to a depth of 465 m. The next gauge at 623 m illustrates a distorted record following passage of the outgoing deformation wave with failure occurring at the arrival of the reflected compressional wave. The cable failure at 623 probably reflects a spall development near that gauge. This is postulated as occurring at about 618 meters and the reflected wave from this spall gap causing the failure of the two gauges directly above. Another spall gap at 320 m is postulated to explain the upward departure from the -lg slope of gauge I-50UV. Reflection from the gap may have contributed to the early cable failure of gauge I-55UV. The two lower most gauges are shown shifted in time to compensate for foreshortening the depth scale. These gauges failed shortly after the arrival of the deformation wave or the compressional stress wave. This early shock loading failure precludes analysis of spall. The short segments of record just before termination appear not to have -lg slopes.

LONGSHOT

LONGSHOT, like CANNIKAN, indicates from cable failure that the overburden material is failed all of the way to the free surface.⁽²³⁾ Figure A-6 illustrates the gauge layout and Table A-1 gives the time of cable failure following arrival of the compressional wave (TOA). Also shown are spall related comments to aid in estimating the depth of spall.

Interpretation of Table A-1 in terms of where possible spall gaps are located is shown in Figure A-6. The uppermost spall is estimated using Eq. (1) and Figure 6 of the text. This gives a depth for the uppermost spall as about 100 m. A similar analysis was possible for gauge 11 located at a depth of 30 meters in hole EH-1. Here the initial spall is indicated 121 m.

Deeper spall certainly could have developed as well as more shallow ones. The estimated depth of spall at the maximum extent of spall (about 1800 m (slant range)) is 101 m. This depth is consistent with the above estimates representing the deepest spall, since uppermost spall surfaces are theoretically concave downward and lowermost spall surfaces are theoretically concave upward.

Table A-1. LONGSHOT — Time of cable failures.

Hole	Gauge	Spall Comments	Time of Cable Failure (sec) Following 1st to A	Depth (m)
EH-5	1	Complete record to spall impact	--	0
EH-5	2	Reflected wave failure (spall)	0.125	30
EH-5	3	Reflected wave failure (spall)	0.148	152
EH-5	4	Incident stress wave (SW) failure	0.038	213
EH-5	5	Incident stress wave (SW) failure	0.08	274
EH-5	6	Incident stress wave (SW) failure	0.023	335
EH-3	7	Spall (- lg developed)	0.893	0
EH-3	8	Spall (- lg developed)	0.895	30
EH-3	9	Incident SW failure	0.07	152
EH-1	10	Failed on impact	0.85	0
EH-1	11	Complete record to spall impact	--	30
EH-1	12	Incident SW failure	0.055	52

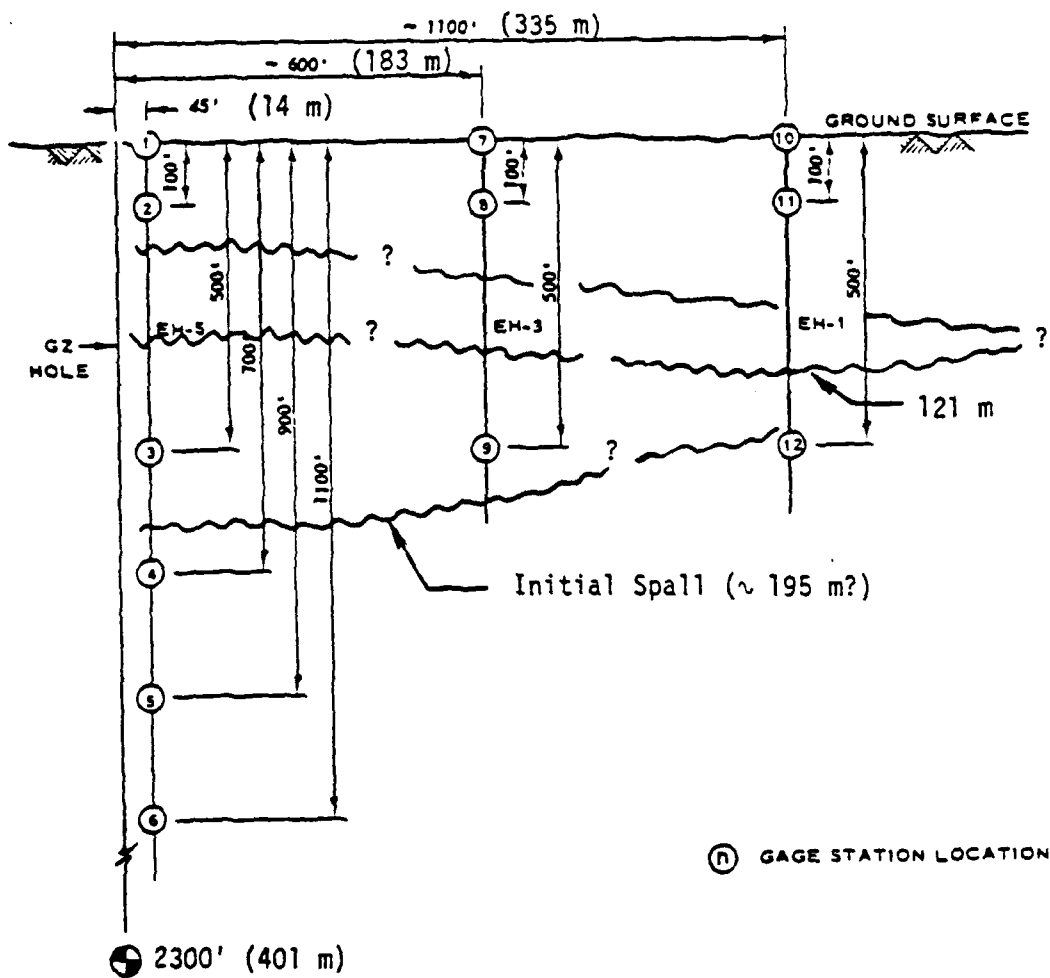


Figure A-6. Downhole gauge layout — LONGSHOT.

The data do not allow for a good estimate of the maximum depth of spall near SGZ. From Table A-1 it appears that it could be between gauges EH-5 #3 and #4, or between 152 and 213 meters. A depth of 195 m is rather arbitrarily selected to plot on Figures 15 and 16 of the text. By comparison with MILROW and CANNIKAN, it is likely that the actual spall thickness is greater.

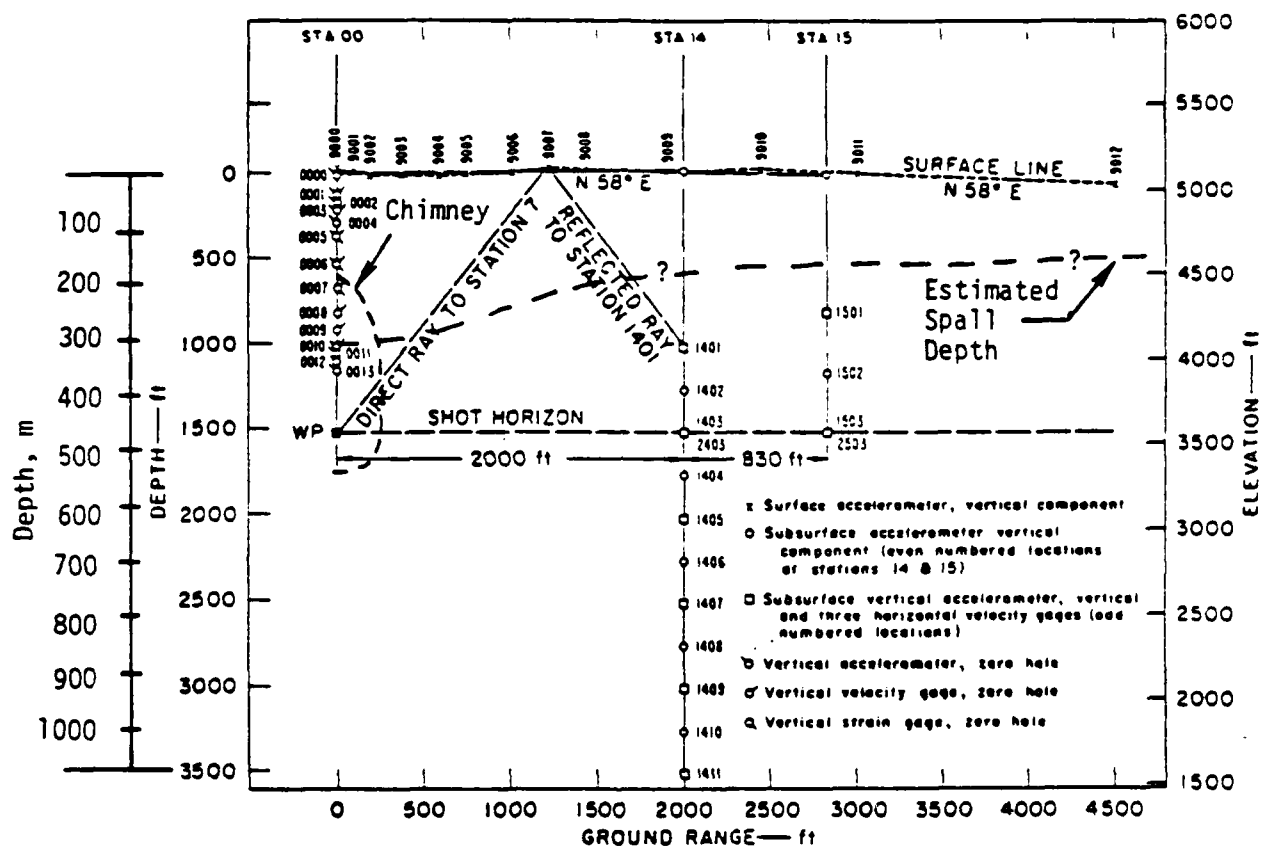
PILED RIVER

PILED RIVER subsurface ground motion gauges of relevance to spall are primarily in the vertical drill holes -- STA 00, STA 14, STA 13 -- shown in Figure A-7.⁽³⁷⁾ The gauges in the latter two holes indicate that spall was considerably more shallow than the depth to those gauges as a - 1g acceleration did not develop.

The string of gauges close to SGZ in hole STA 00 have ground motions shown in Figures A -8 and A -9. Hoffman and Sauer (1969) recognized spall down to below gauges 0005 (below 112 m) by the characteristic - 1g slope. Gauge failures, DC shifts, and other complicating factors made spall interpretation difficult for the lower gauges. The analysis this study presents takes these uncertainties into consideration. Records from gauges 0006, 0007 and 0009 display well developed - 1g slopes. The curious thing is that at gauges 0009, 0008 and 0007, the - 1g slopes start before the reflections and tensile failure occurred. It appears that there is a strong subsurface reflection from a depth of about 200 meters putting the material into spall before that from the ground surface. The deepest spall is thus interpreted to occur close to that gauge at a depth of 310 m with dynamic rock failure (block motions) occurring between there and the explosion produced cavity. Such a failure model would connect the chimney well into the spalled zone (the chimney height is 227 m).⁽³¹⁾

PILED RIVER IMPLICATIONS ABOUT HARDHART

The above interpretation implies strong shear failure between the cavity and the ground surface. It is interesting to examine HARDHART with a deeper



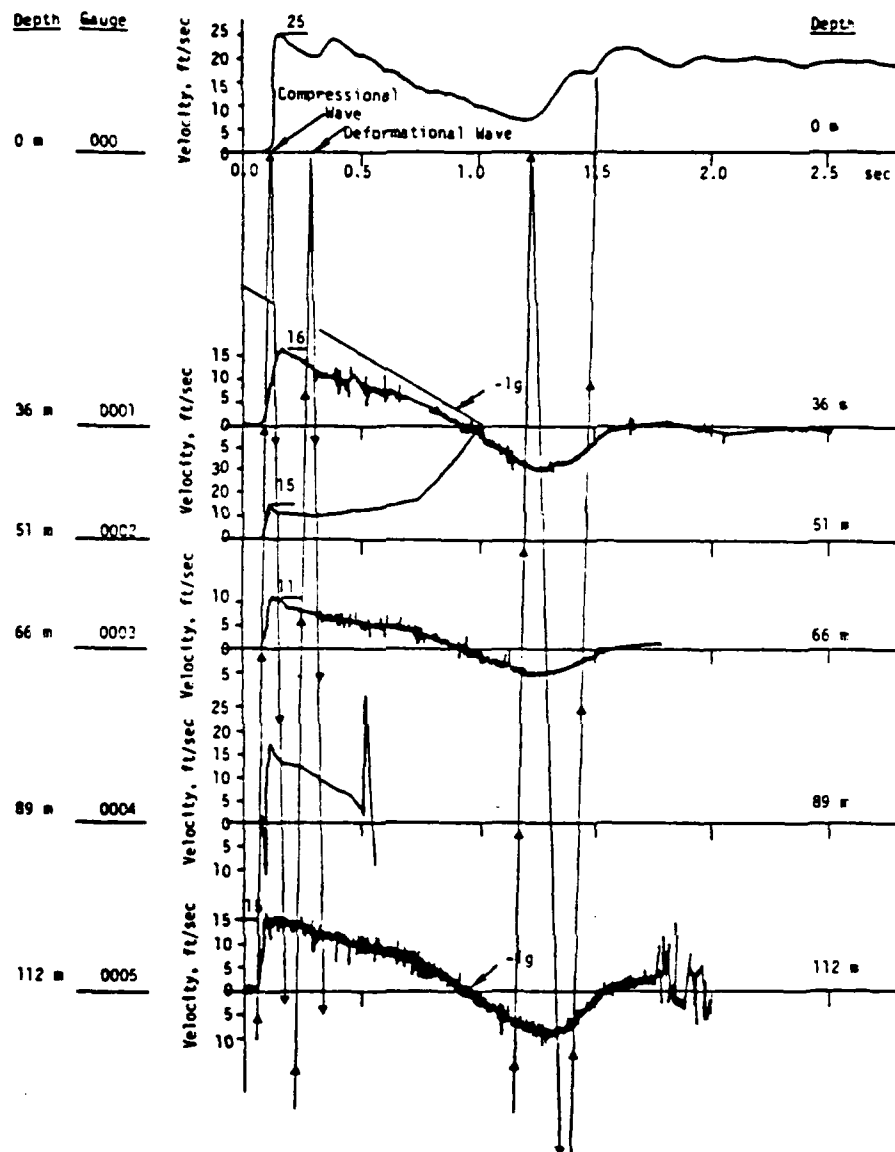


Figure A-8. PILEDRIVER upper spall region.

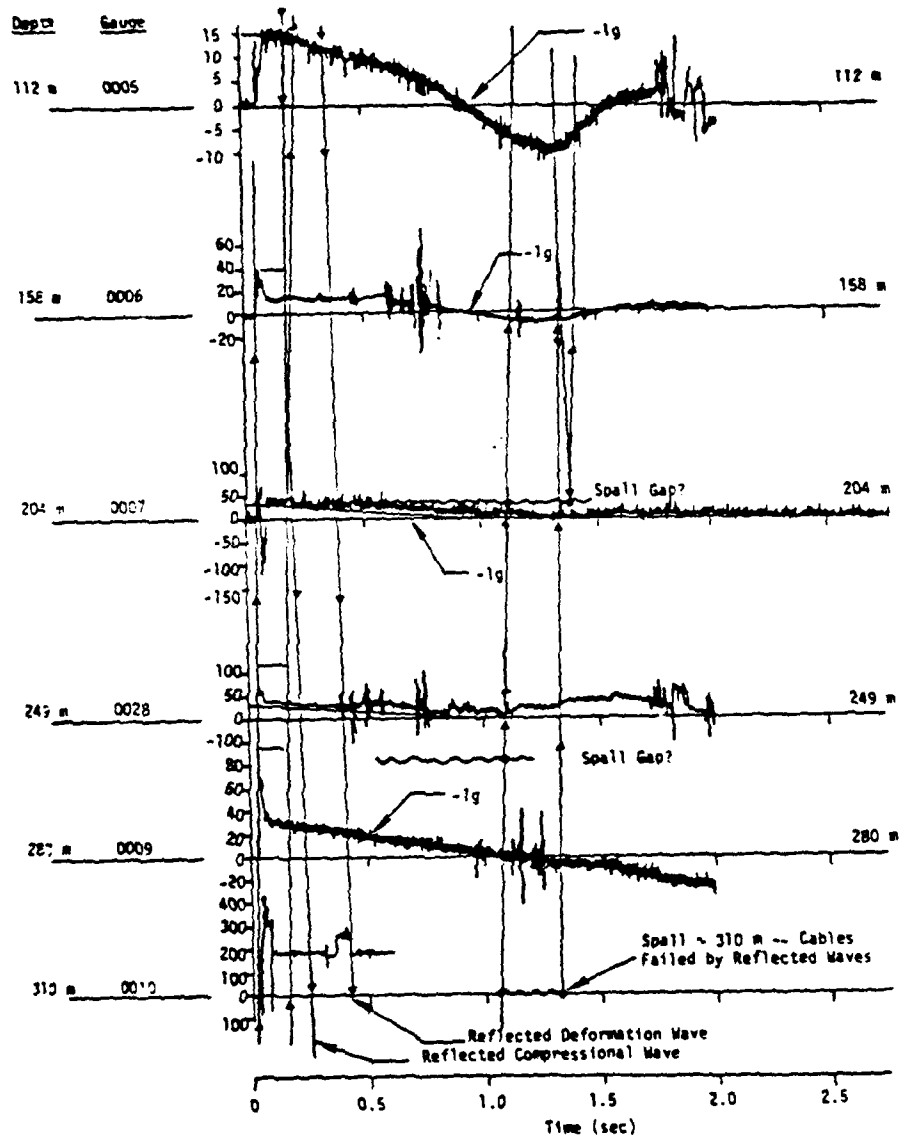


Figure A-9. PILEDRIER lower spall zone.

scaled depth of burial ($170 \text{ m/kT}^{1/3}$) compared to PILED RIVER ($121 \text{ m/kT}^{1/3}$) for indications of cavity-free-surface interactions. Sub-surface exploration of the "barber pole" experiment allowed for documentation of pre- and post-test locations of a measurement tape grouted into the drill hole illustrated in Figure A-10. Also shown are documented fault and relative motions in the region bounding the chimney. Indicated are upward step-like shear failure as one approaches the chimney until abrupt reversals occur that are clearly related to collapse and chimney development. It is probable that if collapse had not occurred, the stair steps would have continued upward from point 7 to directly over the shot. The "barber pole" deformation is interpreted as dynamic shear motion between the cavity and the free surface. This is thought to result from spall temporarily reducing confinement of the pressurized cavity, causing an upward push, failing the overburden.

SHOAL

The spall analysis of SHOAL indicates the maximum depth of spall at 195 meters. It is clearly below the deepest gauge at about 120 m as shown by the -1g slope in Figure A-11. Figure A-12 illustrates the ray paths (dashed) that are the Weart interpretation to explain the early re-acceleration following the initial acceleration spike. It was postulated that this resulted from a subsurface reflection at 88 m depth (a low impedance zone) causing an early tensile wave initiating a spall break — accounting for the second acceleration. The ray path analyses (solid lines) show a different interpretation. A spall gap is recognized at a depth of 42 m, and another one is postulated at 195 m on the basis of ray tracing to subtle re-accelerations not resulting from surface reflected waves (see points A, B and C in Figure A-12). Points D, E and F are re-accelerations believed to be caused by the reflected deformational wave. The re-accelerations in the Weart interpretation are considered as expressions of the deformational wave emanating from the expanding cavity.

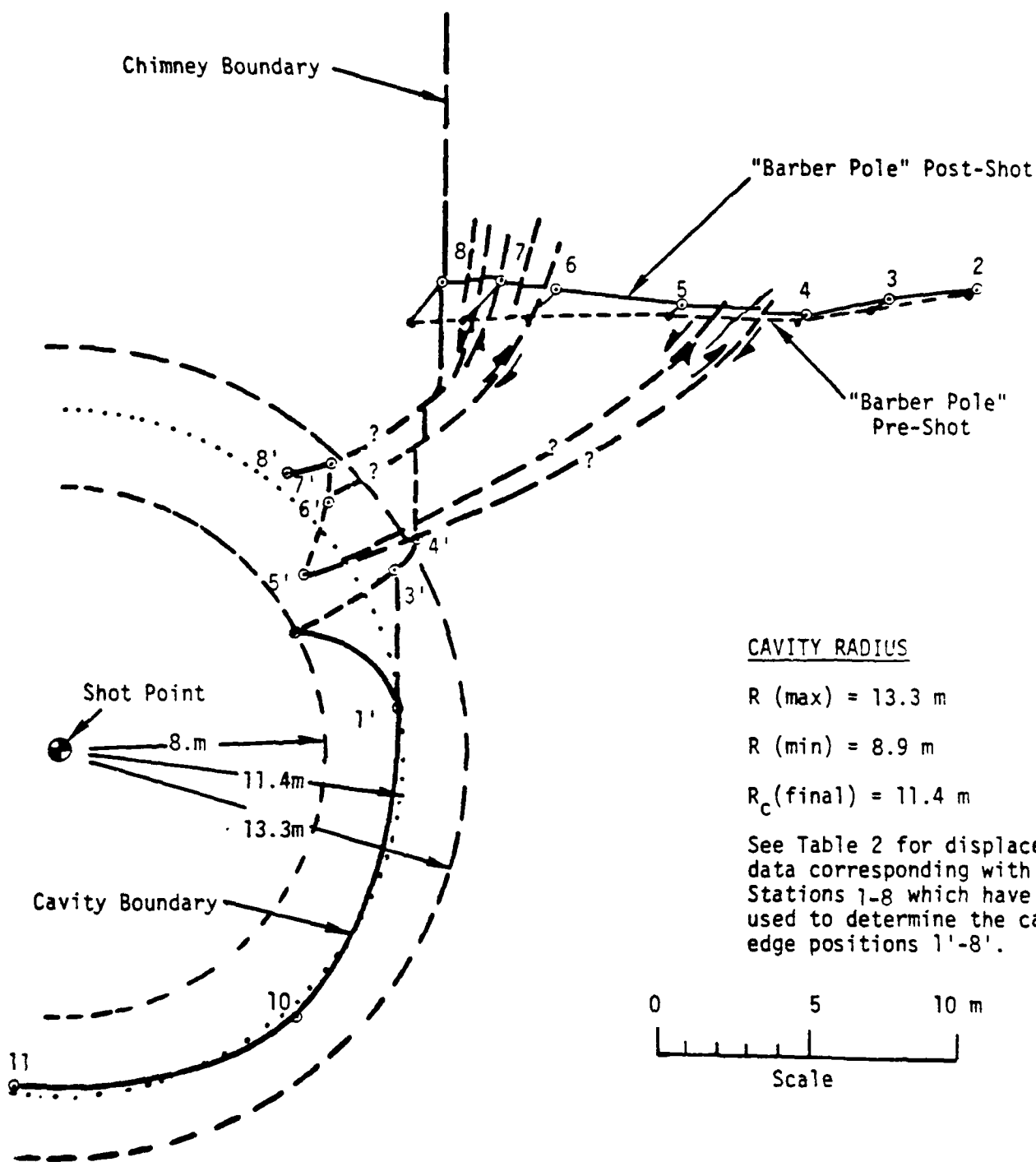


Figure A-10. HARDHAT cavity displacement profile (scaled to 1 kT).

Table A-2. HARDHAT Cavity Radius Data (scaled to 1-kT)
(See Figure A-10)

"Barber Pole" Post Shot Survey Data

Station	Slant Range $r(m)$	Residual Displacement $\delta_r (m)$	Apparent Cavity Radius $R_c - (3r^2 \delta_r)^{1/3}$	Scaled $R_c/w^{1/3}$
2-2'	57.91	0.335	14.99	2' 8.89
3-3'	52.18	1.25	21.69	3' 12.86
4-4'	48.55	1.77	23.21	4' 13.76
5-5'	42.46	0.88	16.85	5' 9.99
6-6'	36.36	2.26	20.76	6' 12.31
7-7'	33.53	3.29	22.31	7' 13.23
8-8'	31.51	2.90	20.53	8' 12.17

Radial Displacement from Velocity Gauge:

Stations	$r(m)$	$\delta_r(m)$	R_c	Scaled R_c
1-1'	457 (1)	0.0119	19.5	11.6 (1')

Station 10 — Cavity Radius from Drill Data: $R_c = 20.1$
Scaled $R_c = 11.9$

Station 11 — Cavity Radius from Drill Data: $R_c = 18.8$
Scaled $R_c = 11.2$

Cavity Radius from Pressurization Test
— Considered Nominal — $R_c = 19.2$
Scaled $R_c = 11.4$

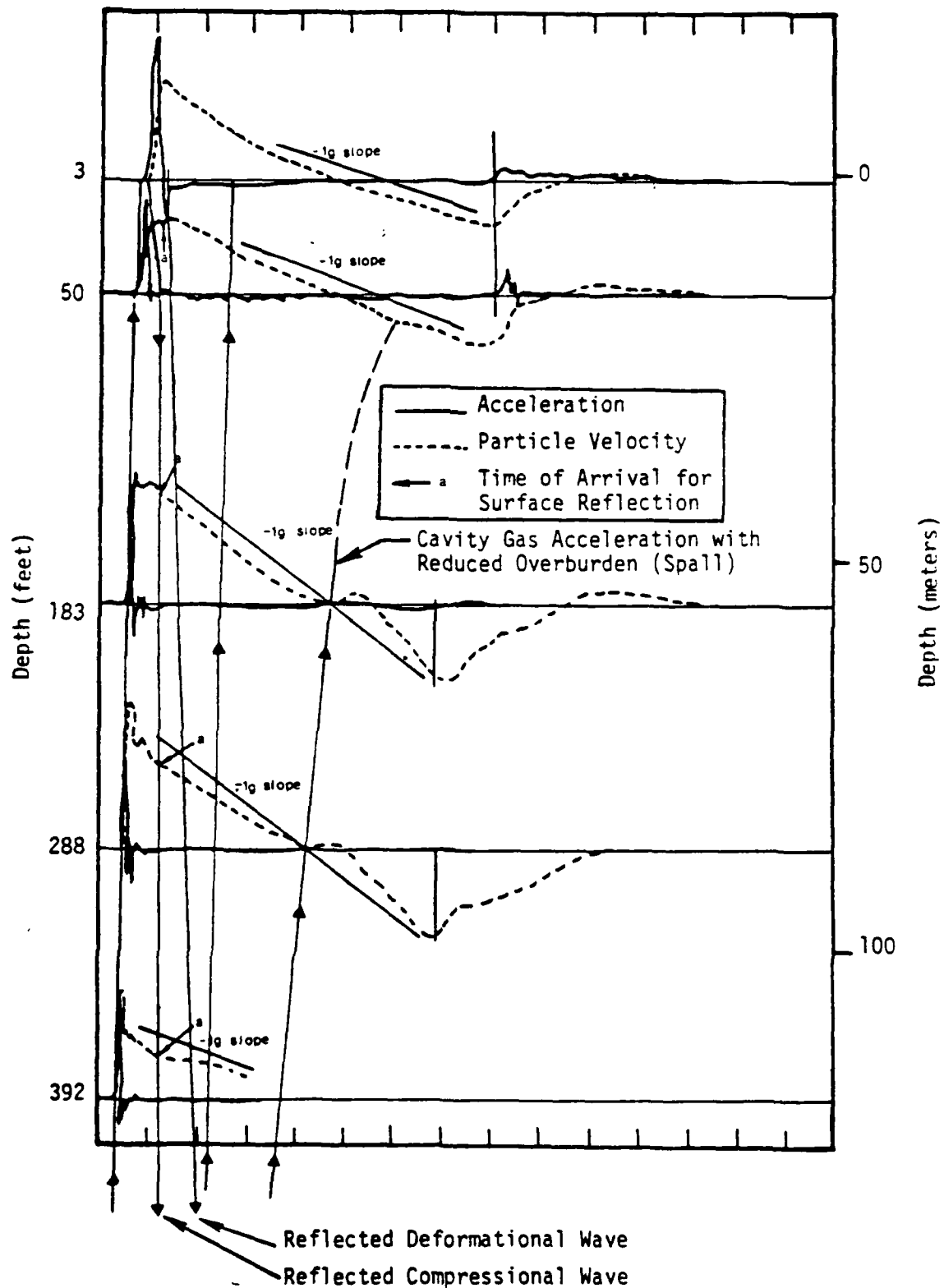


Figure A-11. SHOAL — Subsurface velocity and acceleration gauge record analysis relative to spall.

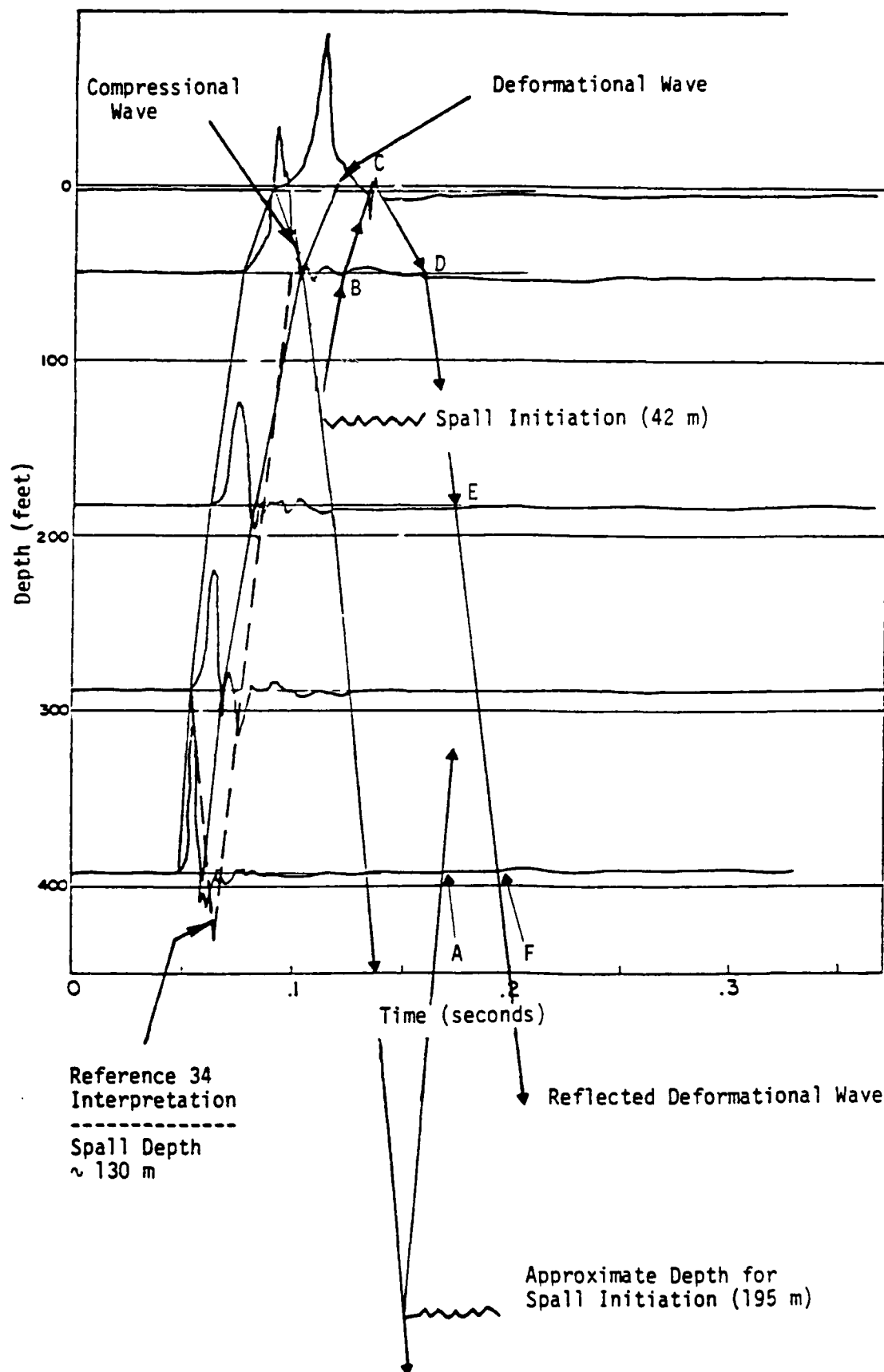


Figure A-12. SHOAL — Subsurface acceleration record analysis relative to spall.

Figure A-11 provides good evidence for a strong pulse of outward flowing energy at 0.35 to 0.6 seconds that coincides in time with a re-reflection of the deformational wave from the cavity back toward the free surface. This late time cavity growth pulse is postulated as due to the reduced overburden confinement resulting from spall.

GNOME

Figure A-13 shows the accelerograms from the borehole at ground zero for GNOME. Two of the gauges failed at the time of arrival of the reflected compressional wave. This probably indicates spall to at least the lowermost gauge of 140 meters. Projection of the spall closure ray path back to where the time between this and the reflected wave is small would place a maximum depth of spall at about 200 meters. Such a depth, if plotted on Figure 16 of the text, would give much better agreement with the RIO BLANCO data point which is a somewhat similar geologic environment. Thus, the 140 m depth is considered minimal.

RIO BLANCO

RIO BLANCO consisted of three separate 30-KT explosions at deep depths of burial (1780 m, 1899 m and 2039 m). The detonations were not simultaneous but slightly time delayed. Near surface ground zero, the separation between initial acceleration peaks is about 0.04 sec, well separating the shock pulses (see Figure A-14, A, B and C). Each detonation appears to be sufficiently separated to show both a well developed compressional wave and a partially developed deformational wave. Following the three initial acceleration pulses is a fourth upward acceleration phase that is thought to represent the final stages of cavity growth and coalescence of the separate events. Because of the great depth, the spall process is essentially completed before surface reflected waves return to the depths of the explosions.

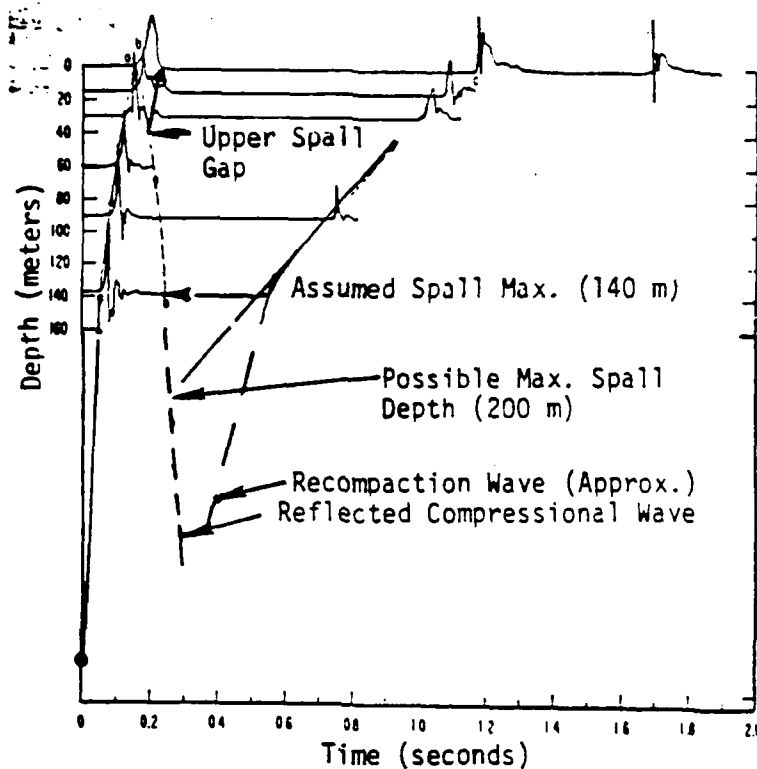


Figure A-13. GNOME — Subsurface acceleration data interpreted relative to spall — modified after Eisler. [7]

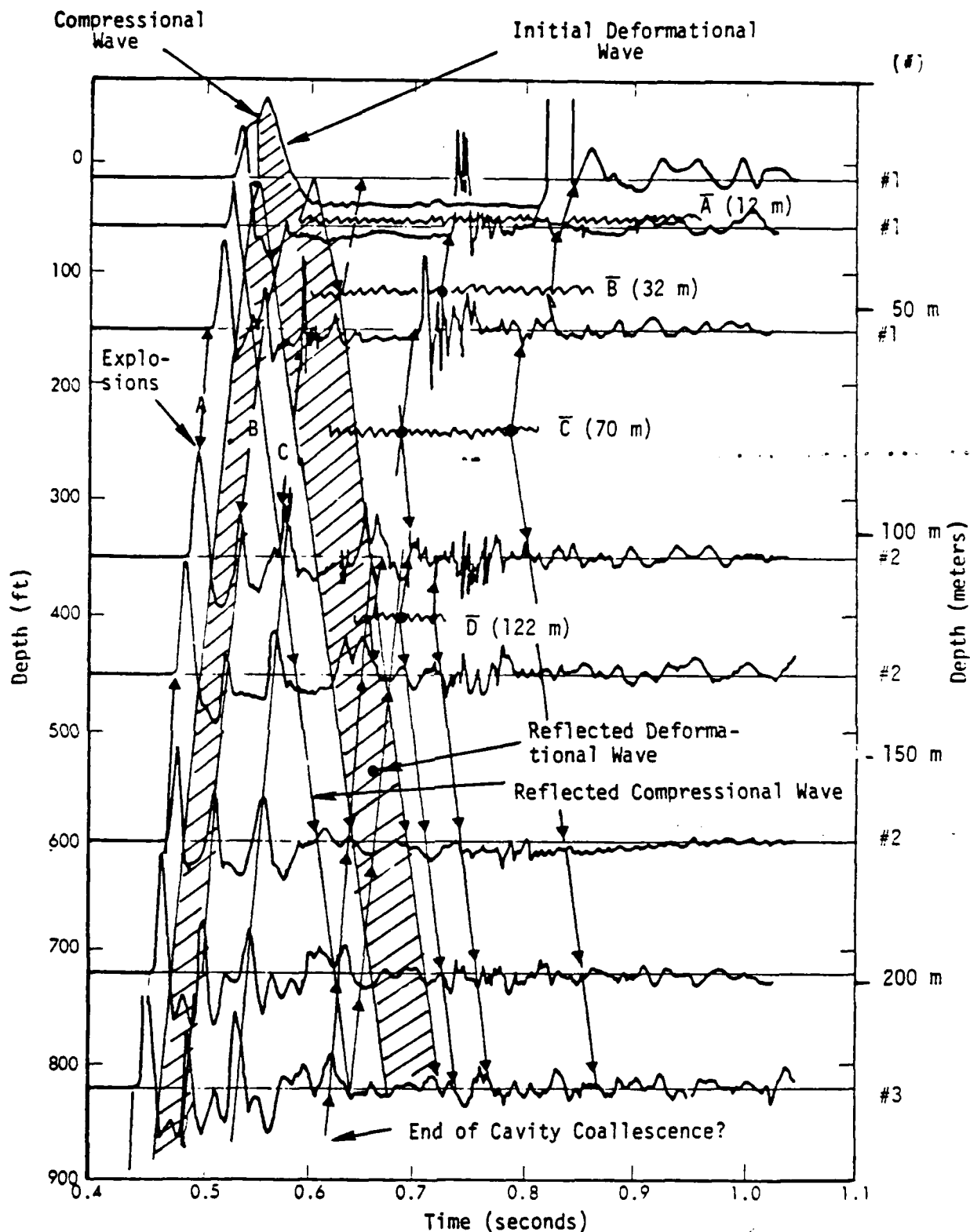


Figure A-14. Accelerometer records from various depths in holes numbers 1, 2 and 3 near surface ground zero — Signal Analysis — RIO BLANCO.

In the vicinity of surface ground zero (SGZ) there are four spall gaps identified by ray tracing analyses. These are \bar{A} , \bar{B} , \bar{C} , \bar{D} at depths of 12, 32, 70 and 122 meters respectively (Figure A-14). The figure combines three vertical holes, all located within 220 meters horizontally from SGZ. Holes 4 and 5 are located at about 750 m horizontally from SGZ. Depth of spall is clearly greater than 87 meters and probably very close to 122 m. The impact signal of the lower gauge is apparently truncated by the negative acceleration ray from the impact signal from above (205 m depth) (see Figure A-15).

The vertical gauge array in hole #6 is located about 2225 meters from SGZ. The two spall gaps at this range, identified by ray path analysis, are at 73 and 109 meters depth (see Figure A-16).

The horizontal extent of spall is bracketed by gauges at 3660 and 7010 m laterally from SGZ. The extent of spall is nominally about 5000 meters slant range or 4670 m horizontal range.⁽¹⁾ At the 3660 station the depth of spall from impact signal analysis is about 69 meters deep.

The previous analysis⁽¹⁶⁾ of the RIO BLANCO spall data is compared with this analysis in Table A-3. Their analysis apparently is a rigorous requirement for a -1g slope on the velocity record and a sharp impact acceleration spike. They did not do the more subjective ray path analyses. The predicted maximum possible depth of spall by the same authors was 163 meters in the vicinity of holes #1 through #3 and 130 meters at hole #6. Their predictions are in closer agreement with the interpretations of observed data by this analysis than with their own analysis.

Because of the three separated explosions, the depth close to SGZ is probably related to an effective yield of about 30 kT event. Near the extent of spall the three events are not so well separated so both distant depth and extent are related to an effective yield between 30 kT and 90 kT; probably about 50 kT.

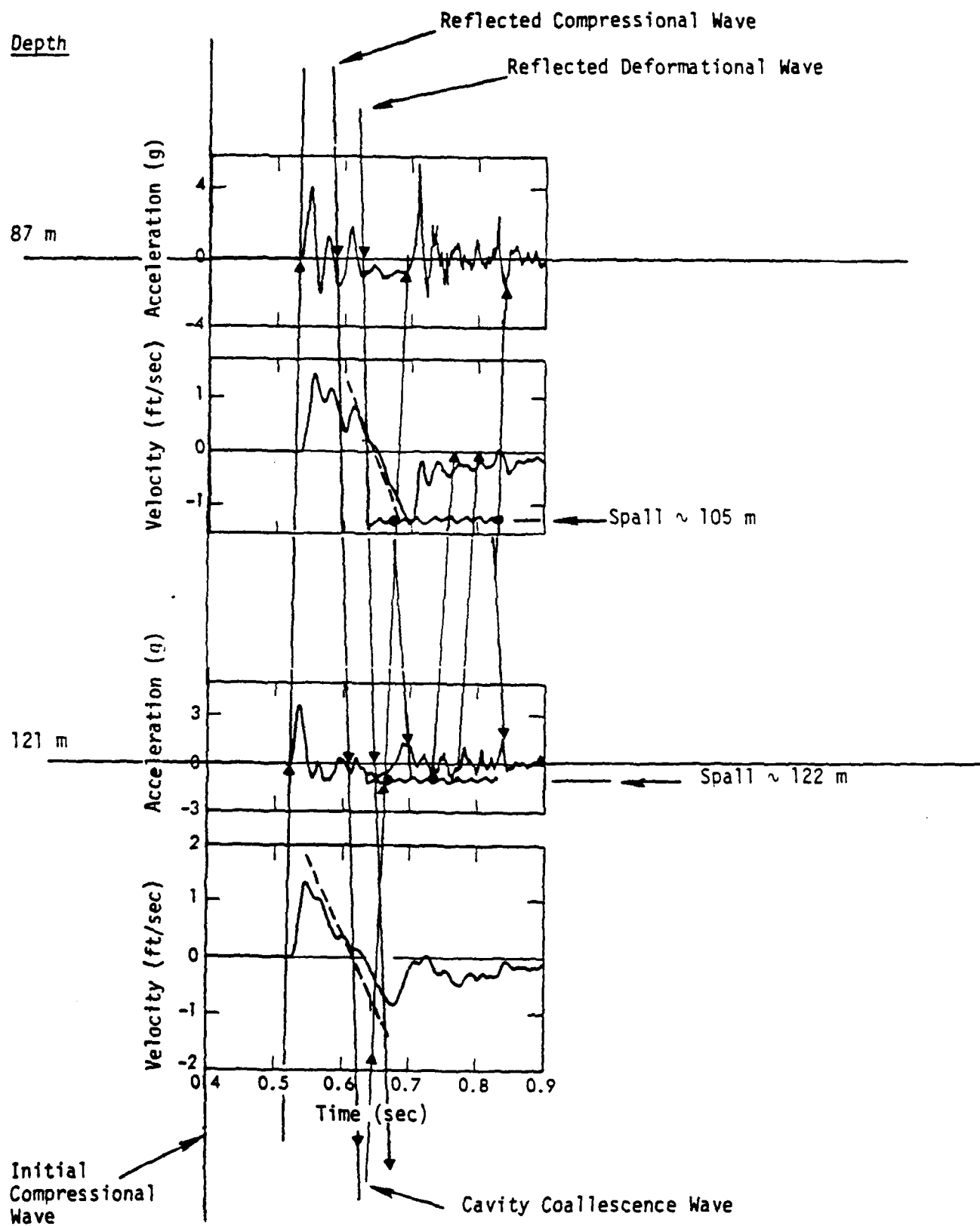


Figure A-15. Accelerometer and velocity records from Hole #5
—Signal Analysis—RIO BLANCO.

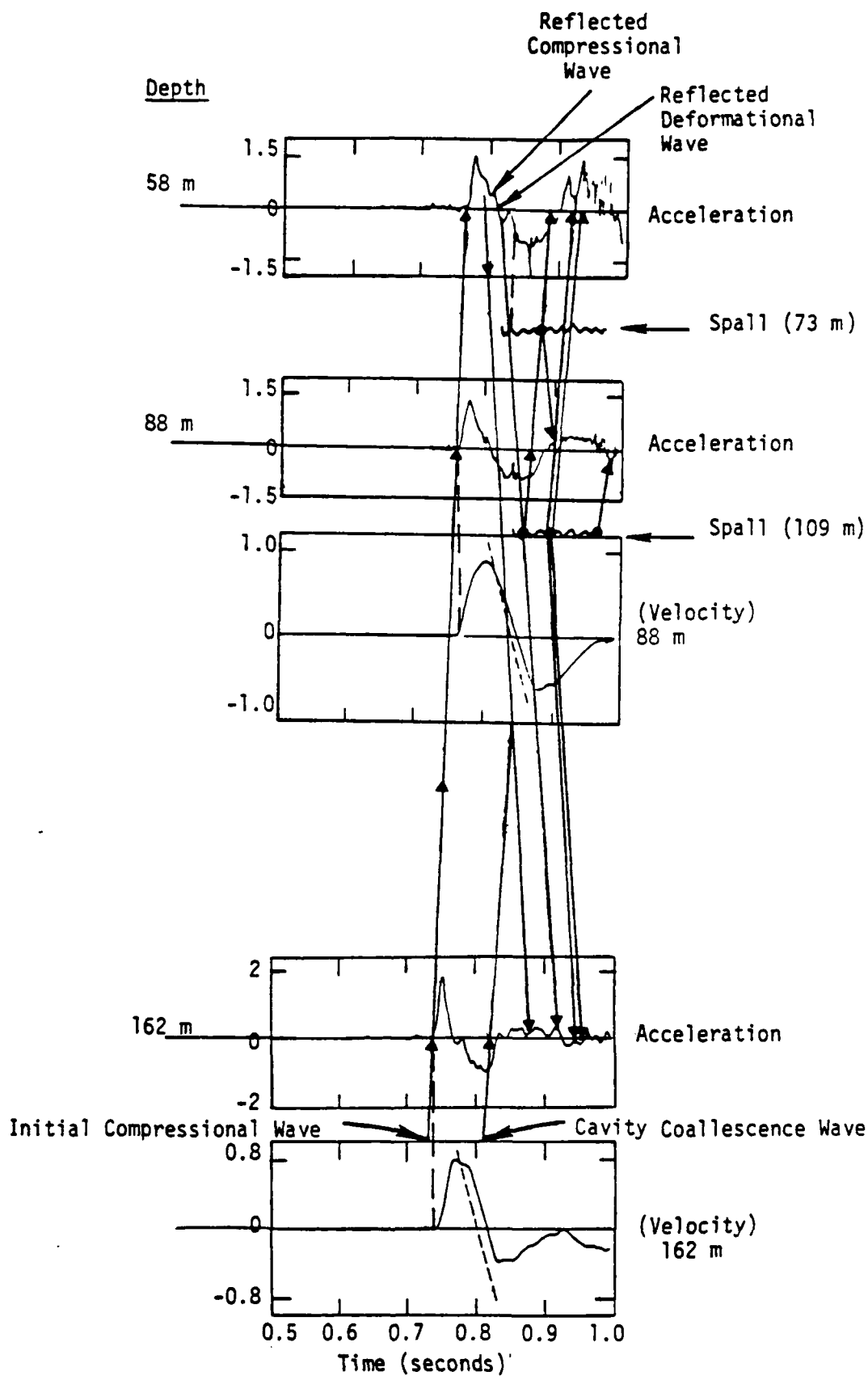


Figure A-16. Accelerometer records (and velocity) from Hole #6
—Signal Analysis—RIO BLANCO.

Table A-3. Depth and Extent of Spall Analysis Comparison

Horizontal Range (m)	Drill Holes With Gauges	Toman, et al. (1973)		This Study
		Data Analysis	Max. Prediction	
0-220 m	#1, 2, 3	40-107 m	163 m	122
~ 750 m	#4, 5	85-116 m	111 m	122
2225 m	#6	58-88 m	130 m	109

		Horizontal Range		Horizontal Range
Spall Extent	--	3660-7010 m	--	4700 m ⁺
Depth at 3660 m	--	--	--	69 m

⁺ Nominal Value

APPENDIX D

AN INTERPRETIVE ANALYSIS OF THOSE NUCLEAR
EXPLOSION TESTS WHERE SURFACE WAVE ANALYSES
HAVE BEEN PERFORMED

APPENDIX D

1.0 BACKGROUND

Investigators analyzing and interpreting surface waves generated by underground nuclear explosions conclude that for large yield explosions (greater than about 30 KT) the principle mechanism contributing to Love-wave excitation is explosion induced pre-stress release.^(1,2,3,4) These investigators differ substantially, however, on the models explaining that release.

Love-wave excitation is qualitatively expressed as the Love- to Rayleigh-wave amplitude ratio. Toksoz has made this more quantitative by introducing the term F-factor or double couple strength. Table 1 (modified after Toksoz) lists those events for which F-factors have been determined.⁽³⁾ These tests are subdivided by location and rock type in which the tests were conducted. For comparison, the Yucca flat events are also listed with relative Love-wave excitations as well as F-factors. Ten additional Yucca Flat tests have relative Love-wave excitations reported by Aki and Tasi (1972) and are listed in Table 2.⁽¹⁾

Thus, the data base is small, but perhaps these data can be sufficiently well interpreted to predict relative values for other tests and better understand Love-wave excitation. Presumably there are more F-factor and/or relative Love-wave excitation values available than covered in this review. A goal of this preliminary investigation is to work with this limited data base to develop hypotheses and propose models to explain the differences in F-factors or Love-excitation from different events. Qualitative predictions are then made for a number of events -- some of which may have or presumably could have Love-wave excitation or F-factor determinations made.

Presently the interpretations of surface wave radiation presumed to be generated by explosions in pre-stressed environments are significantly in conflict. There are two competing explanations and both probably represent mechanisms that are operative. These models (along with their principle

TABLE 1
Comparative Tectonic Strain-Release and Other Site
Related Factors from Underground Nuclear Explosions

Event	Region	Medium	D.C.* Strength Factor	Yield (kt)	Depth of Burst (m)	Depth Water (m)	Date Detonated	Data Reported in ILL Data Bank			
								Density to Surface (gm/cc)	Density at M.P. (gm/cc)	(7 Water by M.P.) Saturation	Seismic Velocity, V _p at M.P. (m/sec)
PILEDRIVER	NTS AREA 15	GRANITE	3.20	56	463	~ 614	6/2/66	2.66	2.67	-- / --	--
HARDHAT	"	"	3.00	5	286	614	2/15/62	--	2.65	-- / --	--
SHOAL	FALLON, NEVADA	"	0.90	12.2	367	~ 1677	10/26/63	--	--	-- /100	--
GREELEY	NTS PARUTE MESA	TUFF	1.60	825	1215	616	12/20/66	1.94	2.57	(11)/100	3270
BENHAM	"	"	0.85	1100	1402	647	12/19/68	2.01	2.3	(6)/100	3050
CHARTREUSE	"	RYHOLITE	0.90	70	664	662	5/6/66	2.24	2.35	(7)/100	4675
DURIEA	"	"	0.75	65	544	661	4/14/66	--	--	-- / --	--
HALF BEAK	"	"	0.67	300	819	645	6/10/66	2.19	2.49	(3)/100	3540
ROX CAR	"	"	0.59	1200	1166	604	4/26/68	1.93	2.12	(4)/100	4450
COROURDY	NTS YUCLA FLAT	TUFF	0.72 S	200 - 1000	681	570	12/3/65	--	1.92	(20, 2)/100	2164
CUP	"	"	0.72 S	< 20 - 200	537	553	3/26/65	--	--	(13)/100	--
BILBY	"	"	0.47 S	235	715	488	9/13/63	1.78	--	-- /100	--
TAN	"	"	0.39 I	< 20 - 200	563	512	6/3/66	1.71	--	-- / --	--
BRONZE	"	"	0.33 I	< 20 - 200	510	555	7/23/65	1.69	--	-- / --	--
BUFF	"	"	0.31 I	< 20 - 200	500	521	12/16/65	1.68	--	-- / --	--
HAYMAKER	"	ALLUVIUM	0 M	67	408	488	6/21/62	1.70	--	-- / --	--
SEDAN	"	"	0 M	100 crater	194	576	7/6/62	1.78	1.91	-- / --	--
FAULTLESS	CENTRAL, NEVADA	TUFF	0.50	200 - 1000	973	91	1/19/68	--	--	-- / --	--
MILROW	ANCHITKA, ALASKA	AMOEJITE	< 0.60	~ 1100	--	~ 3	10/2/69	2.13	--	-- /100	--
CANNIKIN	"	"	0.60	< 5000	1791	~ 3	11/6/71	2.3	2.5	(5)/100	4663
MILITON	GRAND VALLEY, COLORADO	SANDSTONE & SHALE	0.60	40	2568	244	9/10/69	2.35	--	-- / --	--
SALMON	HATTIESBURG	SALT	0	5.3	R/R	0.2	10/22/64	--	--	(0)/0	--
GNOME	CARLSBAD, N.M.	SALT	0	3.1	361	158	12/10/61	--	--	(3)/100	--

* Double Couple (D.C.) strength or F-factors from Toksoz and Kehler (1972); S, I, and M refer to Strong, Intermediate and Weak Love-Wave excitations to compare with f-factors, from Aki and Tsai (1972).

TABLE 2
List of Shots in the Yucca Flat (other than listed in Table 1)
Giving Relative Love Wave Excitation*

Event	Detonated	Medium	Elevation from Sea Level, meters					Seismic Magnitude			Relative Excitation of Love Waves
			Shot Depth	Shot Point	Water Table	Alluvium- Tuff Interface	Tuff Paleozoic Interface	m (LRM)	m (Canada)	m (Evernden)	
ARRIVARK	5/12/62	Tuff	434	804	732	948	351	4.89		4.55	Intermediate
AUX	10/2/64	Tuff	452	824	728	1068	610	4.89			Weak
BOHARRON	1/20/67	Tuff	561	770	732	1254	792	5.09	4.93		Intermediate
CHARCOAL	9/10/65	Tuff	455	814	730	1052	610	5.16	4.91		Weak
COMMODORE	5/20/67	Tuff	744	536	732	814	335	5.68	5.77		Strong
DUMONT	5/19/66	Tuff	671	608	732	840	472	5.48	5.51		Strong
ROPE	1/16/64	Tuff	495	797	728	893	176	5.2		5.85	Intermediate
MISSISSIPPI	10/5/62	Tuff	494	795	730	853	306	5.06		4.76	Strong
PIPAHNA	5/11/66	Tuff	549	709	732	904	274		5.37		Weak
WAGTAIL	3/3/65	Tuff	750	485	732	951	253	5.33	5.32	5.1	Intermediate

* From Aki and Tsai (1972).

proponents) are:^(1,2)

- The Fault Trigger Model (Aki)
- The Cavity/Fracture Zone Model (Archambeau)

There seems to be general agreement that a number of nuclear explosion tests produced sufficient anomalous surface wave radiation and especially Love-wave excitation so that pre-stress release is required to explain the observations. Mode conversion at interfaces and media heterogeneities alone cannot reasonably produce the strong azimuthal variations in surface wave radiation.⁽¹⁾

This investigation draws significantly from two draft status reviews of ground motion data concerning contained nuclear events. Several hypotheses were offered in those studies that bear upon relationships between surface wave radiation, fracture zone(s) development, explosion yield dependences, geologic environments, and in-situ stress history.^(5,6) There are two other studies in progress, but not yet in draft report form, that also contribute to the hypotheses about specific variations of explosion-induced surface radiation.^(7,8)

1.1 OVERVIEW OF APPARENT EXPLOSION INDUCED TECTONIC ENERGY RELEASE AS SURFACE WAVE RADIATION

Table 1 presents data associated with those events for which F-factors have been reported. Table 3 provides a simple ranking in the order of increasing F-factor by test region and material. Generally, the ordering is as one would expect in relation to the ability of the rock to creep and adjust to applied stress. Both bedded and dome salt behave plastically and deform under low applied stresses, so little stored stress is expected. This is also true of the relatively weak water saturated sediments that surround and overlay the Tatum salt dome containing the SALMON event. Events detonated in alluvium also have near-zero F-factors, being easily deformed, less compacted, and less cohesive than volcanic tuff.*

It is a little surprising that the F-factor upper bound for volcanic tuff at NTS exceeds that of the large yield events at Amchitka, Alaska. Also, all of the Pahute Mesa events in volcanic rocks have F-factors that exceed those at Amchitka. The spread of data within the tuff and other volcanic rocks, for shots in Yucca Flat and Pahute Mesa at NTS, and those at Amchitka can probably best be explained by detailed evaluation of site conditions. Before going into specific sites and attempting to explain F-factor differences, it may be instructive to examine basic assumptions and propositions so mechanisms and processes considered important are identified.

* Note, however, that the tabulated data in Table 2 show little difference in density and seismic velocity -- a greater contrast is apparent with the raw geophysical logs.

TABLE 3

Explosion Test Materials Ranked in Order of
Increasing Double Couple Strength [3]

F-Factor Double Couple Strength	Shot Material and Location
0	SALT (New Mexico and Mississippi)
0 - ?	ALLUVIUM (Yucca Valley, NTS)
0.31 - 0.72	TUFF Below Alluvium (NTS)
? - 0.60	Amchitka, Alaska VOLCANICS
0.59 - 1.6	Pahute Mesa VOLCANICS (NTS)
0.90 - 3.2	GRANITE (NTS & Fallon, Nevada)

1.2 ASSUMPTIONS AND PROPOSITIONS GUIDING THE INTERPRETA-
TION OF SITE DIFFERENCES THAT MAY RELATE TO F-FACTOR
DIFFERENCES

1.2.1 Assumptions

- Mode conversion and local environmental heterogeneities contribute little to quadrupole or azimuthal variations of surface wave radiation — compared to explosion induced pre-stress relief and differential ground motions with azimuth.
- Crustal and subcrustal geologic variations beyond the first few kilometers from the explosions (laterally) do not significantly alter the basic azimuthal variations initiated within the surface wave source region.
- Differential slip or "block motions" induced by explosions and modified by geologic structure and in-situ stress account for most of the azimuthal varying patterns of surface-wave radiation; i.e., F-factors increase with increased surface area and magnitude of differential slip.
- Earth properties related to explosion energy coupling and the attenuation of seismic waves are important in controlling the magnitude and distance of differential slip. These same properties are generally related to the ability of the material to store stress or deform, i.e., F-factors will increase with increased explosion energy coupling in an environment where fracture orientation, frequency, stress field, etc. are held equal.
- Some combination of depth of burst, explosion yield, receiver station effects, and other unidentified variables interrelate to provide an effective F-factor dependence upon "yield". Thus, there may be an apparent yield scaling factor.

1.2.2 Propositions

1. Four important factors that contribute to explosion energy coupling are rock density, percent water saturation, confining stress, rock strength or resistance to deformation.
 - (a) Spall and cavity dynamics/free surface interactions can be expected to significantly affect F-factor values because confining stress fields and resistance to deformation are dynamically altered.
 - (b) Fracture frequency, orientation, and frictional properties affect the storage of accumulating tectonic stress and/or the magnitude of natural or explosion induced residual stress.
 - (c) Other things being equal, the more porous and weaker the surrounding rock, the lower the F-factor.
2. Ease of deformation rather than magnitude of in-situ stress may be a useful concept since there are little in-situ stress data, but there is good documentation of pre-shot fracturing and other rock weakness structures (joints, bedding planes, etc.).
 - (a) Deformation commonly is a continuum with differential motion decreasing with distance from the cavity. Variations in ground motion with range may be reflected as asymmetries in cavity radii -- as might variations of orientation of confining stresses.
 - (b) The complexity of fracture orientations reflects the complexity of varying tectonic stress history. Thus, parallel fracturing with considerable fault gouge reflects a near constant tectonic stress orientation over time and offers easy deformation compared to a complexly intersecting fracture pattern with little gouge development -- other things being equal.
 - (c) Water saturation greatly affects ease of explosion induced deformation, initiating hydrofracturing-like processes and in-situ stress alteration similar to fluid injection experience that also produces earthquakes and fault slippages.

(d) The ease of deformation concept also applies to stress relief at interfaces such as the ground surface, the explosion induced cavity, and associated fracture regions. Such phenomena as stress stored at shallow depth and induced stress unloading (rebound) need to be considered in F-factor interpretation.

3. Empirical evidence does not support the proposition that differential slips along one or a few faults extending for long distances from explosions are the principle causes of Love-wave excitation or large F-factors. The evidence reviewed supports the hypotheses that numerous slips occur and that they are mostly within the regions of direct explosion induced fracturing (including spall induced fracturing and explosion induced hydrofracturing).
4. With internally consistent relationships developed between site environmental data, ground motion data and F-factors; a qualitative prediction capability can be constructed and tested against data not covered by this review. Such tests would also allow improvement in determining dominant mechanisms relative to F-factors associated with site differences.

2.0 NUCLEAR EXPLOSION TEST SITE COMPARISONS THAT MAY
RELATE TO F-FACTOR DIFFERENCES

Table 3 lists categories of test sites that will be further evaluated to determine if explanations can be related to non-zero F-factor differences. The categories examined are:

- Granite at two U.S. test sites compared to the French test site in the Sahara -- with qualitative predictions.
- Tuff (and upper Paleozoic carbonate rock) below alluvium in Yucca Valley -- with qualitative predictions.
- Pahute Mesa Volcanics at NTS -- with qualitative predictions.
- Amchitka Alaska tests in volcanic rock contrasted with Pahute Mesa.

2.1 COMPARISON OF NUCLEAR TESTS AT THREE GRANITE TEST SITES -- WITH QUALITATIVE PREDICTIONS FOR EARLY FRENCH TESTS IN THE SAHARA

It is suspected that the primary differences in the three test locations are structural (as the faults and fractures relate to the ability for applied stresses to accumulate and the relative ease of deformation) -- Proposition 2 (a), (b) and (c).

There are differences in topography that may amplify the F-factor differences. Detonations below domes or mesa edge locations may result in enhanced reflected stress waves. This could increase the spall depth and the release of near surface tectonic stresses.

Figure 1 illustrates the dominant fracture pattern at SHOAL as mapped in subsurface excavations. Also shown are the subsurface radial accelerations associated with the different directions at about the same range. Inferred is a stress field that is consistent with recurrent faulting required to develop thick gouge.⁽⁶⁾

Figure 2 tends to confirm the predominant N30°E orientation of major faulting with gouge development.* This is also the orientation of the mountain range exposing the granite. The cross cutting N50°W fracturing appears subsidiary to the NE set. Both orientations appear to have been persistent and intermittently activated ever since shortly after the intrusion of the granite.⁽⁹⁾

SHOAL from Table 1 produced an F-factor of 0.9 compared to 3.0 and 3.2 for HARDHAT and PILEDRIIVER. The explanation offered is that there was less stress to relieve because of more frequent natural releases -- earthquakes occurring at a low level of stress build-up. New major faults no longer have to be created; the old ones just moved a little, so long as the stress orientation remains nearly constant.

The Climax Stock at the north end of Yucca Valley at NTS, by contrast, displays much greater structural complexity reflecting various orienta-

* Gouge is rock flour thought to be produced by repeated fault motion.

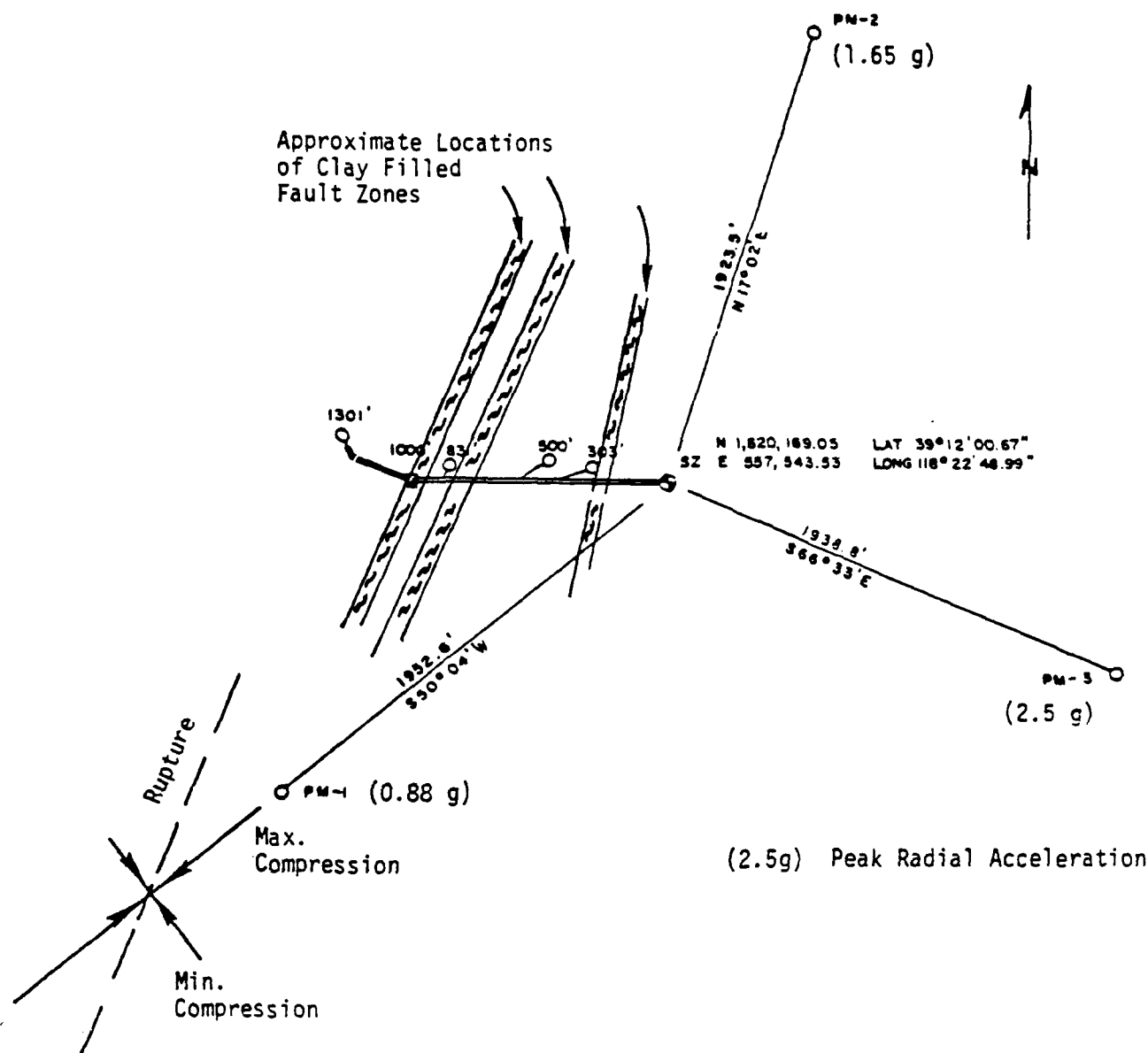


Figure 1. Plan view of SHOAL explosion-elevation ground motion station locations. Stations PM-1, -2, and -3 were installed via drill holes. Also shown are fault orientations and inferred in-situ stress orientations.

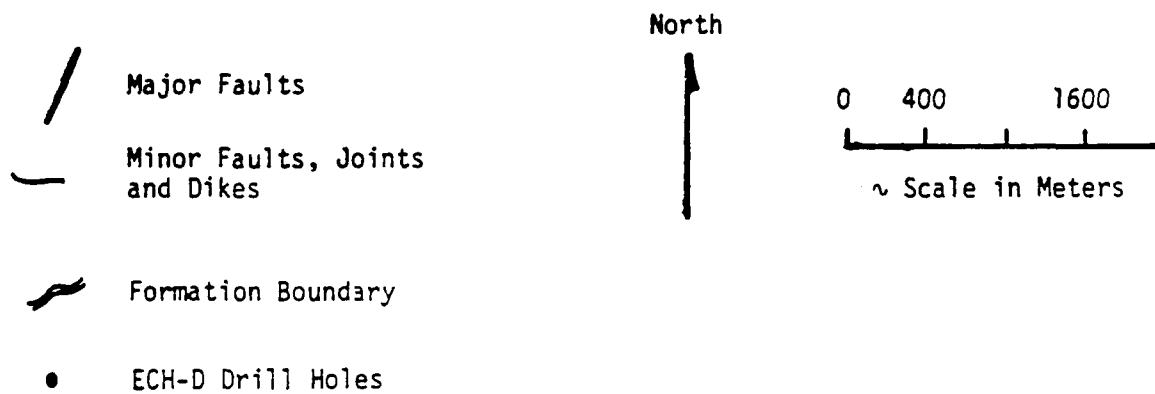


Figure 2. Structural geologic map of the SHOAL site. Churchill County, Nevada. [9]

tions of stress accumulation as a function of time. Fault orientation and in-situ stress data support this conclusion.^(10,11) The Yucca Fault in the northern Yucca Valley (oriented nearly N-S) displays a fault scarp of recent (few thousand years old) movement. Also, the closely associated and possibly older Boundary Fault (oriented about N45°E) displays a scarp that may be part of that same movement -- even though it might be more strike-slip where the Yucca Fault is more dip-slip. These faults apparently intersect to form a 45-degree turn that occurs just south of the granite. Bends in faults or active fault intersections might logically be regions of anomalous stress concentration. The bend occurs at the granite intrusion where the competent rock is capable of storing high stress because stress relieving weaknesses are interlocking to resist slip. The predominant fracture sets mapped pre-shot (to HARDHAT) are N55°W, 85°NE Dip; N40°E, 85°SE Dip; and N36°W, 22°NE Dip.⁽¹²⁾ The most persistent fracture within the granite activated by the PILEDRIVER explosion was mapped at the surface as a N25° - 30°W fracture zone just west of the explosion. No dip-slip motion was observed and strike-slip motion is difficult to determine without fixed station monitoring. This zone developed an expression 335 m long. Figure 3 illustrates the patterns of major pre-shot and some post-shot fractures for PILEDRIVER at the Climax Stock.⁽¹³⁾

Qualitatively there are more directions of faulting, less fault gouge development, and a higher joint and fracture cleavage frequency at Climax than at the SHOAL site. Interestingly enough, surface wave analyses of HARDHAT are consistent with the double couple corresponding to either a N30°W or N60°E vertical strike-slip fault.⁽¹⁴⁾ If it is assumed that HARDHAT and PILEDRIVER data can be lumped together to help interpret the tectonic character of the Climax Stock, then an interesting story develops. A N30°W vertical strike-slip orientation coincides with the above-mentioned 335 M long fault zone that became apparent as a result of the PILEDRIVER event. During post-shot excavations at HARDHAT some cavity/chimney asymmetry was dictated but there was not sufficient exploration to determine minimum and maximum lateral variation directions. Unpublished PILEDRIVER data may be available through LLL concerning these cavity asymmetries. David Rabb recalls that there was apparent flattening in the direction ~ N40°E to N60°E or about parallel to the

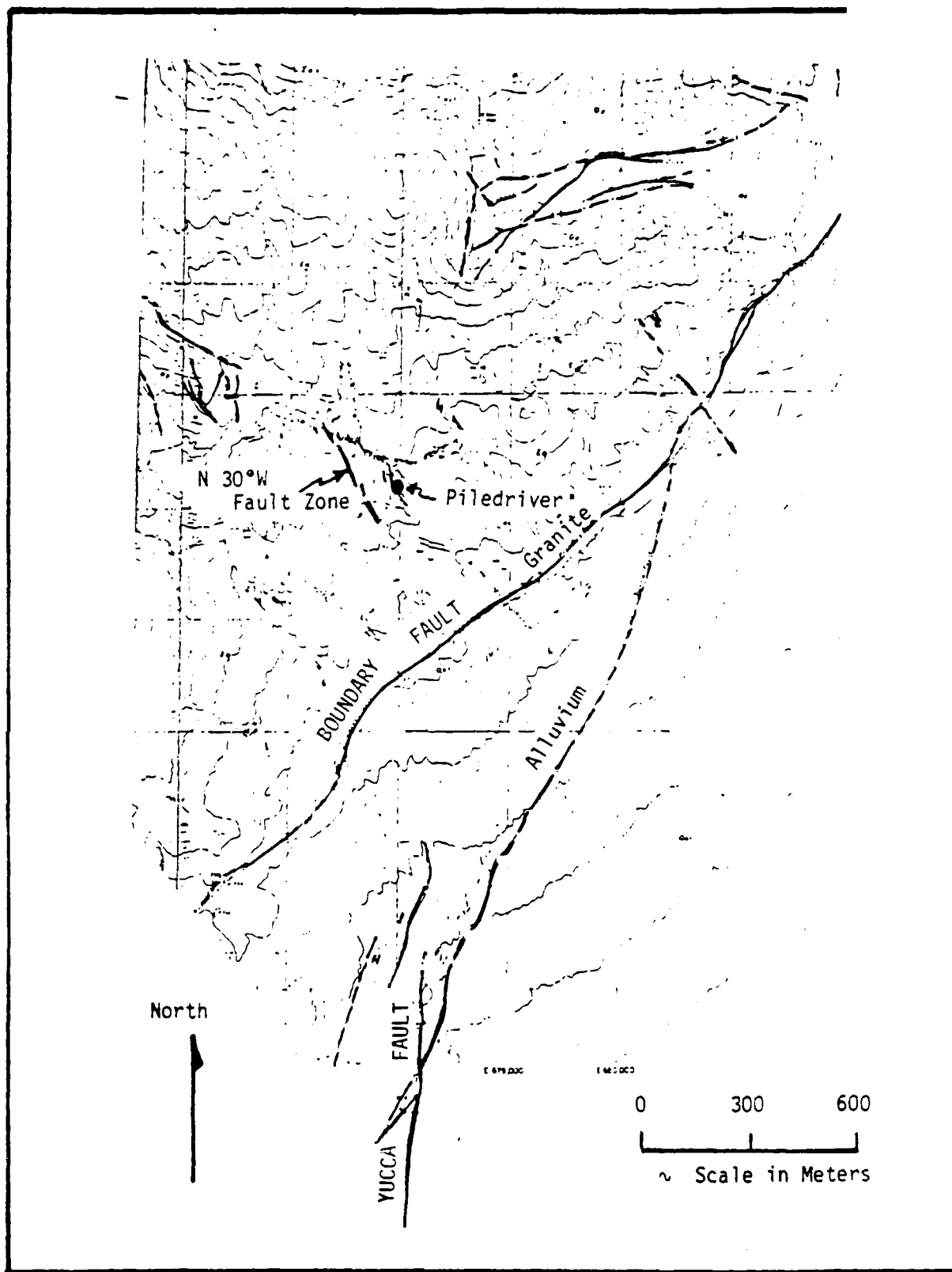


Figure 3. Fault pattern near PILEDRIVER, Climax Stoc, NTS.

Boundary Fault.⁽¹⁵⁾ Regionally, this is the orientation of maximum lateral confining stress.⁽¹⁶⁾ Accepting this, an approximate N30°W orientation would be about that of the minimum lateral confining stress. It is proposed then that strike-slip motion along the N30°W fault zone plus cavity elongation in that direction sufficiently biased other slip motions so that it was the best fit to the teleseismic surface wave data.

Free field radial particle velocity at PILED RIVER at a horizontal range of 610 m in a N58°E direction, or about the orientation of maximum confining stress, was 1.8 m/sec compared to a 2.8 m/sec velocity for the expected intermediate orientation of N62°W. This tends to indicate lesser ground motion in the direction of maximum confinement.⁽¹⁷⁾ The peak acceleration data from SHOAL (Figure 1) also indicates that possibility.

It is postulated that the regional lateral stress orientations at the SHOAL and NTS granite sites are about the same but the magnitude of differential stress at the NTS site is larger. This is because stress accumulation is considered less easily relieved because of fault orientations. Thus, azimuthally varying surface waves produced by cavity asymmetry resulting from asymmetric variations in confining stress and associated differential block motions would be greater for the NTS granite shots. Also, a little increase in F-factor may be due to possible close-in triggering of a N30°W fault zone at the Climax Stock.

The expected F-factors for nuclear explosions by the French in the Sahara are probably at least as large as those at NTS (F-factors of three or greater for events in near virgin rock). The basic reasoning is that the tectonic stresses are so high —about $\rho gh + 200$ bars.^{(18)*} If it is assumed that the yields, cavity asymmetries, and the ratio of lateral stress differences are the same for the NTS and Sahara sites, then the major contributor to differences in the magnitude of azimuthally varying surface waves is the magnitude of total

* ρgh is the calculated overburden stress based upon the rock density () and the depth of burst (h) times the acceleration of gravity (g).

tectonic stress. One factor that is expected to cause a large F-factor for the first Sahara shots is stress relief caused by overburden confinement reduction due to spall. The less attenuating Sahara granite is expected to cause a greater radial extent for spall and deeper spall than the U.S. experience -- even if there is no topographic enhancement as postulated in Figure 4. For hard rock events with high pre-stress, spall is expected to be a large contributor to azimuthally varying surface waves. Explosion triggering of earthquake faults at the Sahara site is not expected since the faults have several orientations that could result in an interlocking tendency. Figure 5 illustrates structural orientations of fractures and major faults at the Sahara site -- the Taourirt Tan Afella Massif.⁽¹⁸⁾ At the time of intrusion of the massif, the minimum stress orientation was probably the direction of elongation (N80°E). Possibly the more recent stress field produced the major N15°E fault orientation. It is anticipated that a fault plane solution to the Sahara teleseismic surface wave data would give a N-S \pm about 30° orientation to the double couple. The stress field is presumed to have migrated gradually since emplacement of the massif to allow for such high stresses to develop. Of course, with a low fracture frequency and a stress field drifting with time, then the failure criteria for faulting approaches the matrix rock strength, not the pre-existing fracture strength. The N-S orientation is really based upon very little evidence for prediction -- just an intuitive preference. It was chosen because it was reported that the absorption of the explosive energy varied little within the massif but was greater in an N-S direction parallel to structural direction in the surrounding rock.⁽¹⁸⁾

The state of stress is apparently near that of the tensile strength of the massif rock. Core from drilling near the flanks of the massif spontaneously fracture into disks upon unloading the stress by the core drilling process. This phenomena was not reported at the shot locations pre-shot, but severe diking occurred in a region just beyond crushing as a result of the detonations. Even with post-shot relaxation and stress readjustment with time, a significant amount of residual stress is in the rock beyond the cavities at levels higher than the high pre-stress conditions.

Following are some observed radii scaled to 1 KT compared with U.S. data:

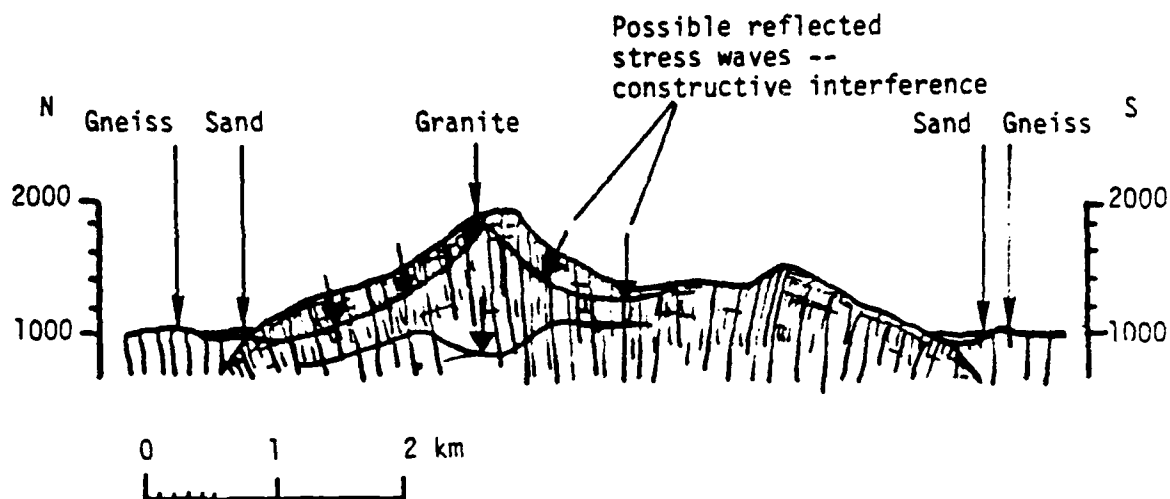
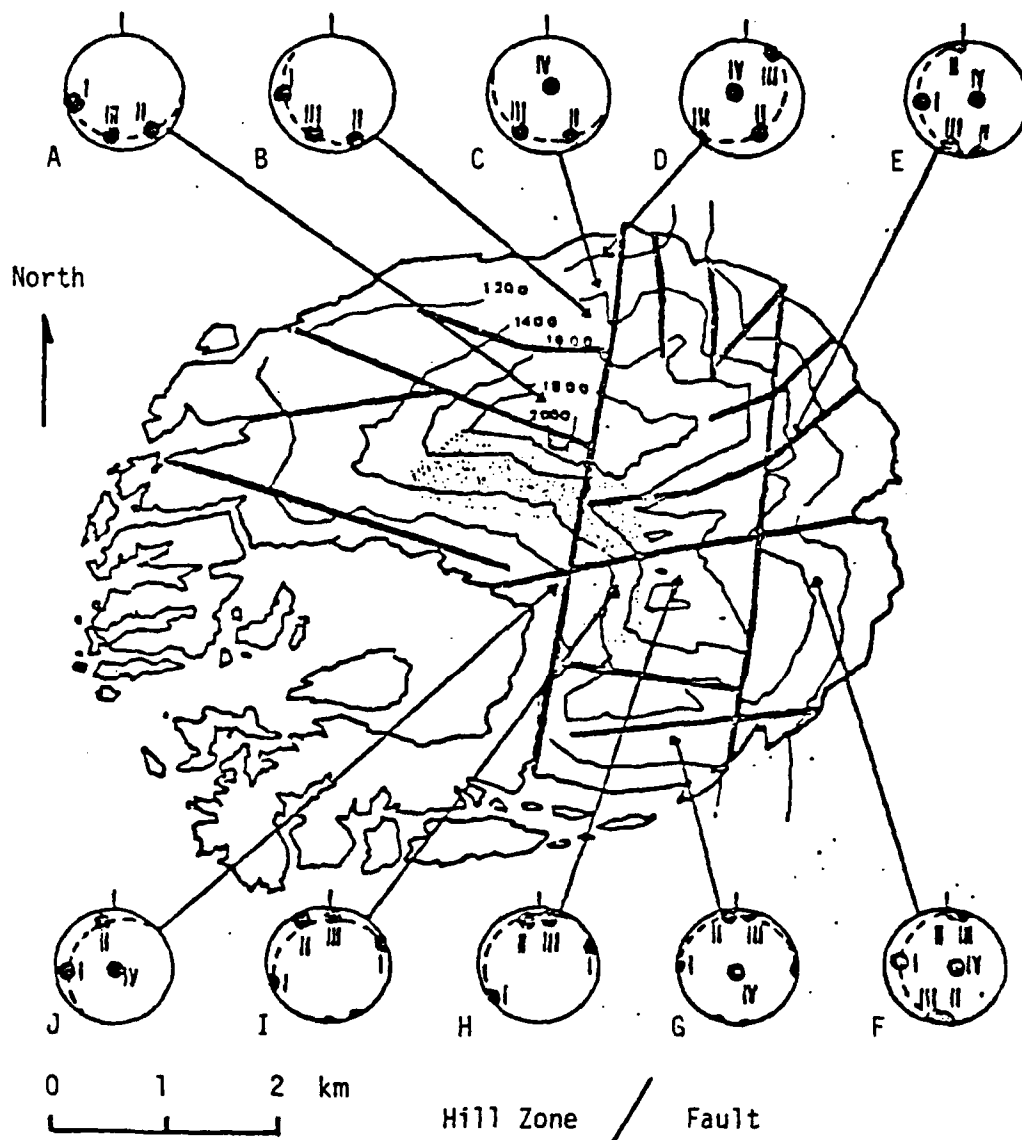


Figure 4. Geomorphological section across the Taourirt Tan Afella massif.



Class I ~ N-S; Class II N80°E; Class III N70°W; Class IV Parallel
Massif
Boundary

Figure 5. Fault systems of the Taourirt Tan Afella massif with drill hole data illustrating the classes of fracture cleavage encountered.

	<u>Sahara Site</u>	<u>NTS Site</u>
External Limit of Cavity Radius (lower hemisphere)	k = 7.3 m	k = 11.4 m
External Limit of Crushing	k = 10 m	Not Documented
External Limit of Shock Fracturing	k = 26 m	Not Documented
External Limit of Induced Residual Stress (Disking)	k = 35 m	Not Observed
External Limit of Altered Seismic Velocity	k = 71 m	Not Measured (Fracture Limit k = 51 m)

These radii (k) scaled to 1 KT are reported as follows where $R = KW^{1/3}$ and R is the radius in meters for events different than 1 KT and k is that radius for a 1 KT event.

Additionally, the tensile and compressive strengths of intact (unfractured) granite are reported at 50 and 2000 bars respectively.⁽¹⁹⁾ Cavity and chimney radii varying by about ± 10 percent are suggestive that the ratio of azimuthal variations in stress are not appreciably greater than the U.S. experience, possibly even less if ground motion data scatter indicates confining stress variations.

COMPARISON OF SOME PAHUTE MESA NUCLEAR TESTS AT NTS
--WITH QUALITATIVE PREDICTIONS FOR OTHER EVENTS NOT
ANALYZED

A preliminary analysis of F-factors has been accomplished for early Pahute Mesa events and reported in draft form.⁽⁵⁾ This was done to help evaluate whether the correspondence between the extent of the surface observed fractures and the extent of spall might be related by spall causing the fault motions. It was suspected that the stress conditions which produced natural fault motions were somewhat preserved in the shallow volcanic crust as a residual pre-stress. Spall produced by large nuclear detonations caused a temporary reduction in confining stress. With spall, the underlying material is thought to release some pre-stress to the lower spall gap "free-surface". Since spall is quite extensive and represents a considerable confining mass, this mechanism may be an important contributor to double-couple type surface wave generation.

From Table 1 it can be seen that, compared to the other Pahute Mesa events, Greeley is high with an F-factor of 1.6. CHARTREUSE is also somewhat anomalous since only a 70 KT event produced a higher F-factor than the megaton events. Although F-factor is not expected to have a significant yield dependence, it can easily have an apparent yield dependence if there are depth of burst dependences. At Pahute Mesa both density and velocity material properties increase with depth, increasing energy coupling of explosives. The study of spall configuration indicates that there is a depth of burst dependence that seems to be controlled by energy attenuation and layering produced wave guide effects. The deeper the explosion the less ground shock attenuation with range and the larger the extent of spall.

Table 4 lists the first 19 Pahute Mesa events in detonation sequence. Figure 6 illustrates conservative spall radii drawn about these event locations. Inspection of this figure allows for estimating relative prestress relief assuming that spall plays a significant part in that process. These are listed in Table 4. Only low to intermediate yield events in this early sequence appear to be in relatively virgin ground. If the stress relief by spall hypothesis is correct and

TABLE 4.
Estimated Relative Pre-Stress Release of Pahute Mesa Events
Involving Radius and Detonation Sequence

Detonation Sequence No.	Event	W^{\dagger} (KT)	DOB (m)	$\sim R_s$ (m)	F- Factor	E_t/E_e	Relative Pre-Stress Release
1	BUTEO	L	696	1500	--	--	*
2	REX	16	672	1350	--	--	*
3	DUREA	65	544	2100	0.75	0.75	**
4	CHARTREUSE	70	665	2200	0.90	1.05	*
5	HALFBEAK	300	819	3400	0.67	0.60	**
6	GREELEY	825	1214	4700	1.60	3.41	*
7	SCOTCH	150	978	2600	--	--	**
8	KNICKERBOCKER	71	631	2200	--	--	*
9	STINGER	L-I	668	2200	--	--	***
10	BOXCAR	1200	1158	5600	0.59	0.46	***
11	RICKEY	L-I	683	2200	--	--	*
12	CHATEAUGAY	L-I	607	2000	--	--	***
13	SLED	L-I	729	2400	--	--	**
14	BENHAM	1100	1402	5600	0.85	0.95	***
15	PURSE	L-I	599	2100	--	--	***
16	JORUM	L-M	1158	5600	--	--	***
17	PIPKIN	I	617	2200	--	--	***
18	HANDLEY	~ 1000	1206	5600	--	--	**
19	ALMENDRO	I	1064	4000	--	--	***

* Events with little or no likelihood of strain release by earlier detonations.

** Events with probably some strain release by earlier detonations.

*** Events with considerable strain release by earlier detonations.

† L is low yield, < 20 KT.

K is intermediate (20 - 200 KT) yield range.

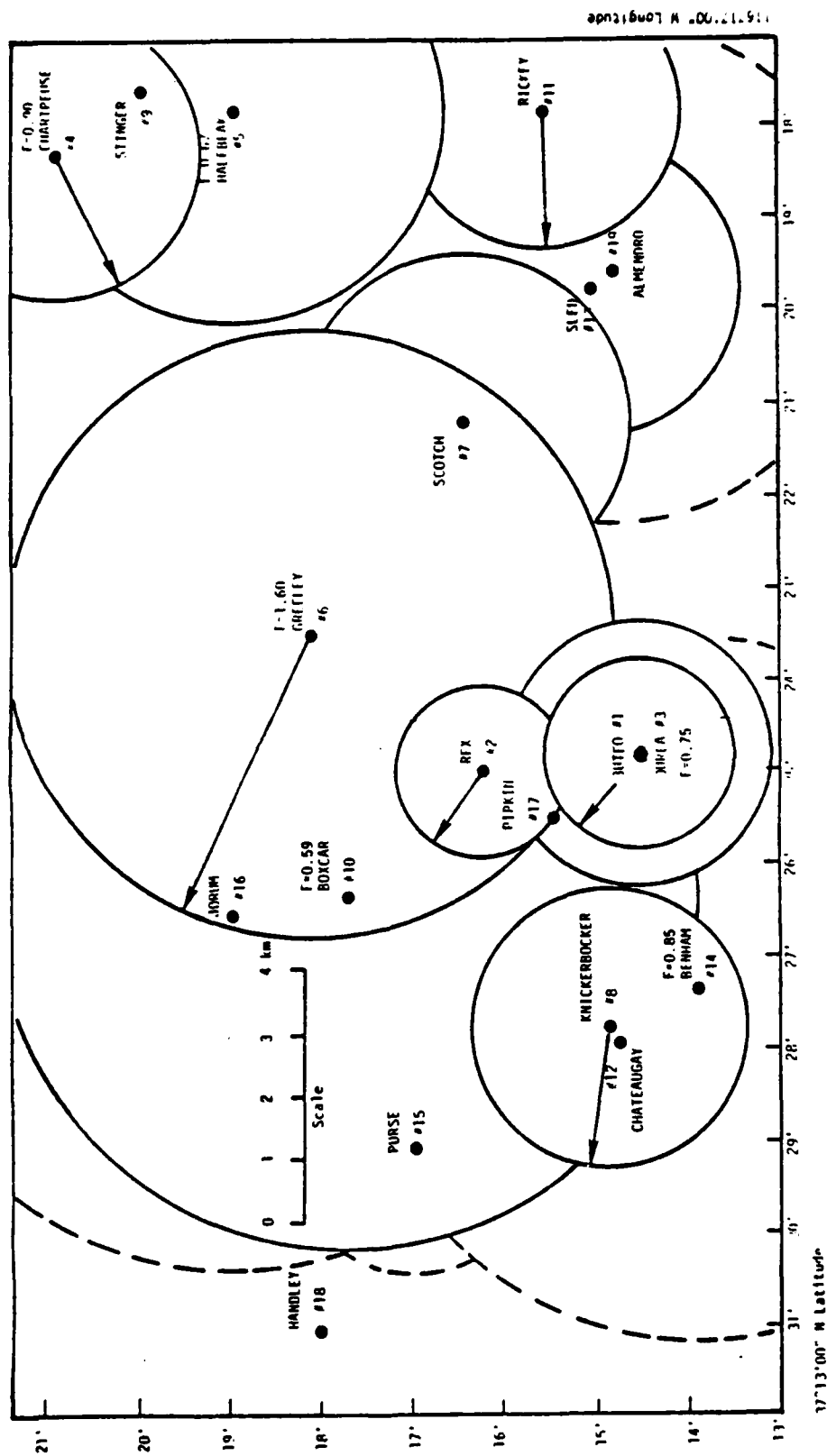


Figure 6. Pahute Mesa location and spall extent overlap pattern for the first 19 explosion tests (arrows identify events in near-virgin rock).

detonations below the water table couple better than those at more shallow depths, then no subsequent events are expected to have F-factors greater than 0.85. The only unanalyzed event at Pahute Mesa prior to ALMENDRO listed in Table 4 expected to have produced an F-factor equal to or greater than 0.85 is HANDLEY. HANDLEY is expected to have been subjected to pre-stress relief due to earlier detonations to a degree less than BENHAM because it is further from spall by earlier events than BENHAM and it is located on the other side of the cauldron boundary containing the other events.⁽²⁰⁾ No other detonation at Pahute Mesa is expected to have an F-factor as high as GREELEY.

GREELEY may have triggered the nearby GREELEY fault adding to the suspected spall induced and fluid pressure induced mechanisms for pre-stressed relief. If so, the double couple would be expected to be about N-S with a dip-slip component of motion to the west. By the time these 19 events were detonated, the near surface and deeper subsurface region shown in Figure 6 may have undergone significant pre-stress relief. Spall had occurred virtually everywhere within the area of Figure 6 and aftershocks had migrated as far as 42 km from HANDLEY during the post HANDLEY decay of the hypothesized fluid pressure mound produced by the earlier detonations.⁽⁸⁾

COMPARISON OF YUCCA VALLEY NUCLEAR TESTS AT NTS --
WITH QUALITATIVE "PREDICTIONS" FOR OTHER YUCCA VALLEY
EVENTS NOT ANALYZED

Love-wave excitation variations for detonations in Yucca Valley were evaluated by Aki and Tsai.⁽¹⁾ Several of their correlations are not confirmed by this preliminary evaluation of the same data. The reason is that the data were grouped differently. They included some detonations in alluvium that may have biased the analysis to more events with weak excitation and did not separately analyze events North of 37°06'N latitude from those events to the south. They did, however, recognize this geographic distribution correlation in the data but concluded "this may be due to the nearly complete stress release by the biggest shot, BILBY, detonated early in the area south of 37°06'n". There appears to be very little data to support that statement. By removing the events with a lower yield than AARDVARK and detonations in alluvium -- as well as separating the events north and south; the same data are reinterpreted:

- Figures 7(a) and (b) illustrate a sharp difference in Love-wave excitation between north and south with a weak correlation with increased yield (body wave magnitude) and increased depth of burst.
- Figures 8(a) and (b) illustrate no correlation between Love-wave excitation, relative yield and distance to the Paleozoic harder rock -- expected of being able to carry the higher pre-stress.
- Figures 9(a) and (b) illustrate no correlation as a function of time with decreased Love-wave excitation resulting from previous tests.

In all of the above plots, the tests that were anomalous were CHARCOAL, PIRANHA (low Love-wave excitation); and FORE. The latter event is only anomalous because it did not have a strong Love-wave excitation as did the other northern tests.

- Figure 10 shows the location of the events analyzed by Aki and Tsai included with the first 24 tests in that area of Yucca Valley having yields greater than AARDVARK (36 KT). Pertinent data for the tests are listed in Table 5. Interaction circles about each test are approximately the

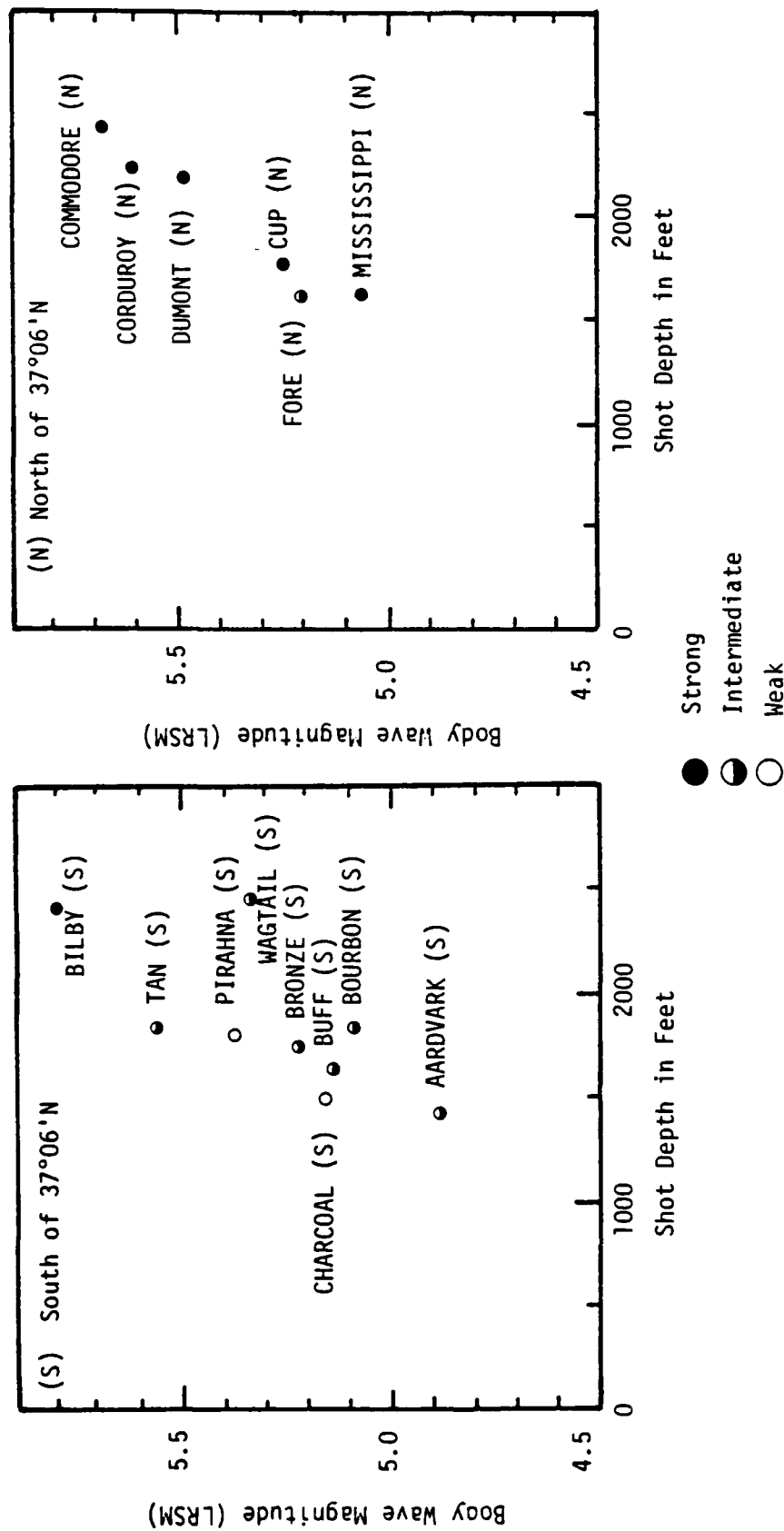


Figure 7a. Relative excitation of Love waves as a function of body-wave magnitude and shot depth for tuff below alluvium and located South of 37°06'N latitude.

Figure 7b. Relative excitation of Love waves as a function of body-wave magnitude and shot depth for tuff below alluvium and located North of 37°06'N latitude.

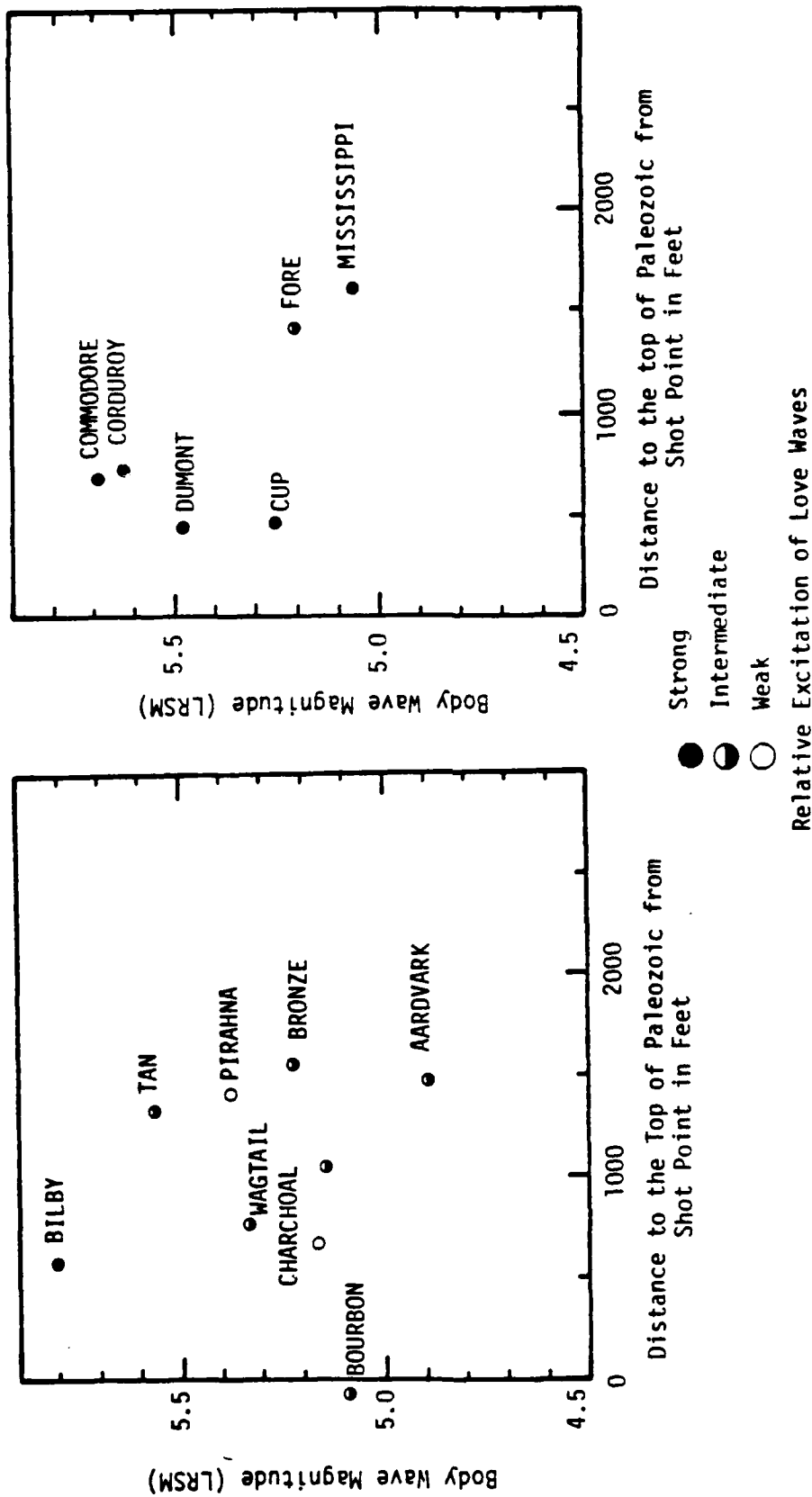


Figure 8a. Relative excitation of Love waves as a function of body-wave magnitude and distance to the top of Paleozoic layer from the shot point -- tuff (Paleozoic) below alluvium located South of 37°06'N latitude.

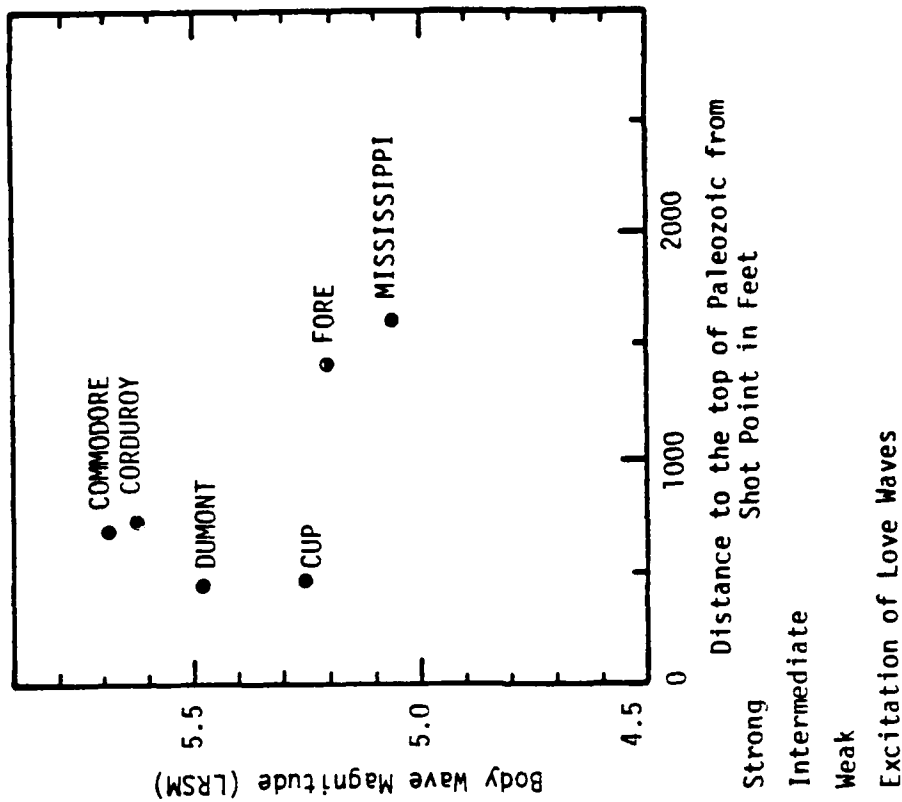


Figure 8b. Relative excitation of Love waves as a function of body-wave magnitude and distance to the top of Paleozoic layer from the shot point -- tuff (Paleozoic) below alluvium located North of 37°06'N latitude.

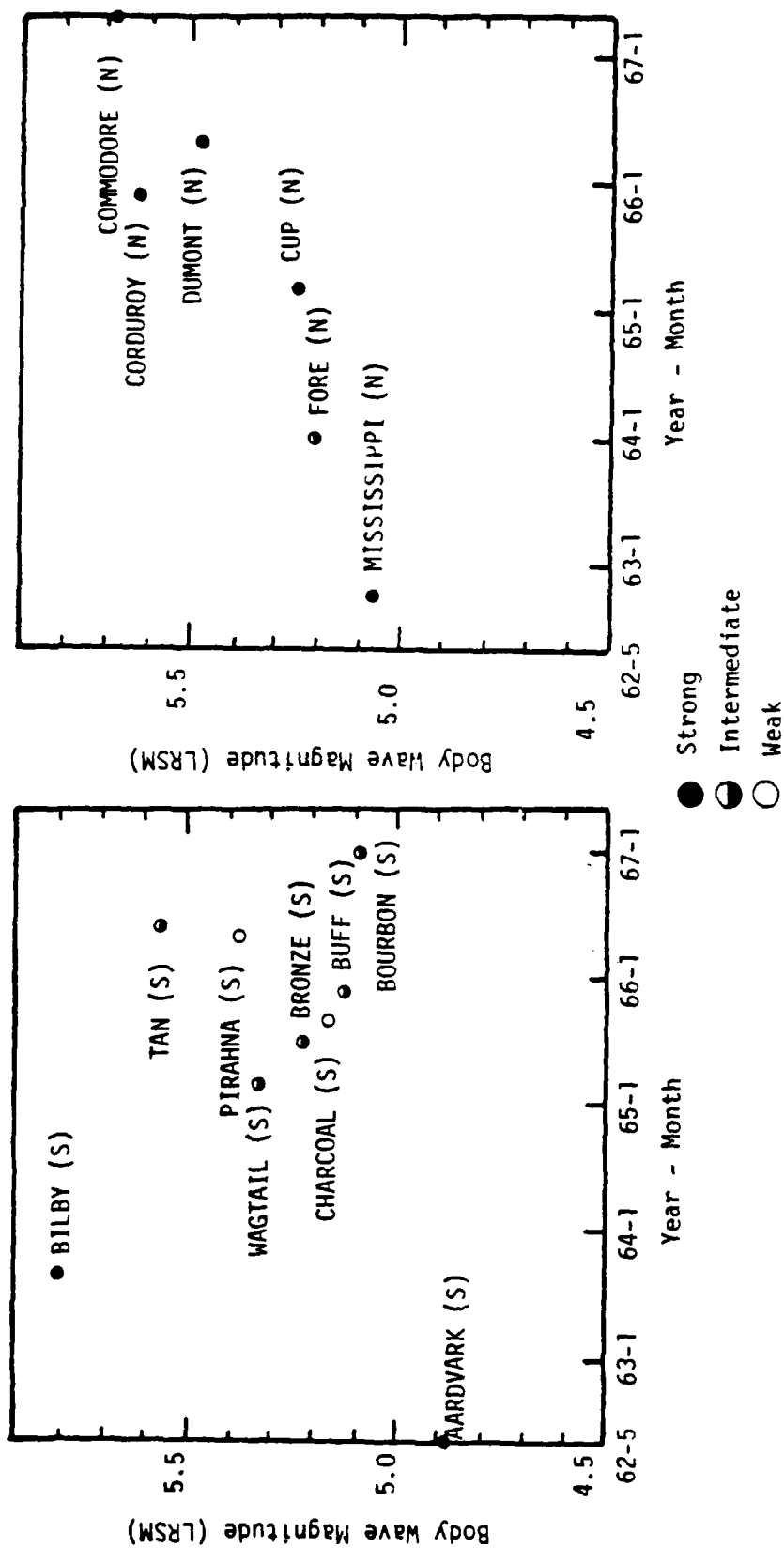


Figure 9a. Relative excitation of Love waves as a function of body-wave magnitude and time for tuff below alluvium and located South of 37°06'N latitude.

Figure 9b. Relative excitation of Love waves as a function of body-wave magnitude and time for tuff below alluvium and located North of 37°06'N latitude.

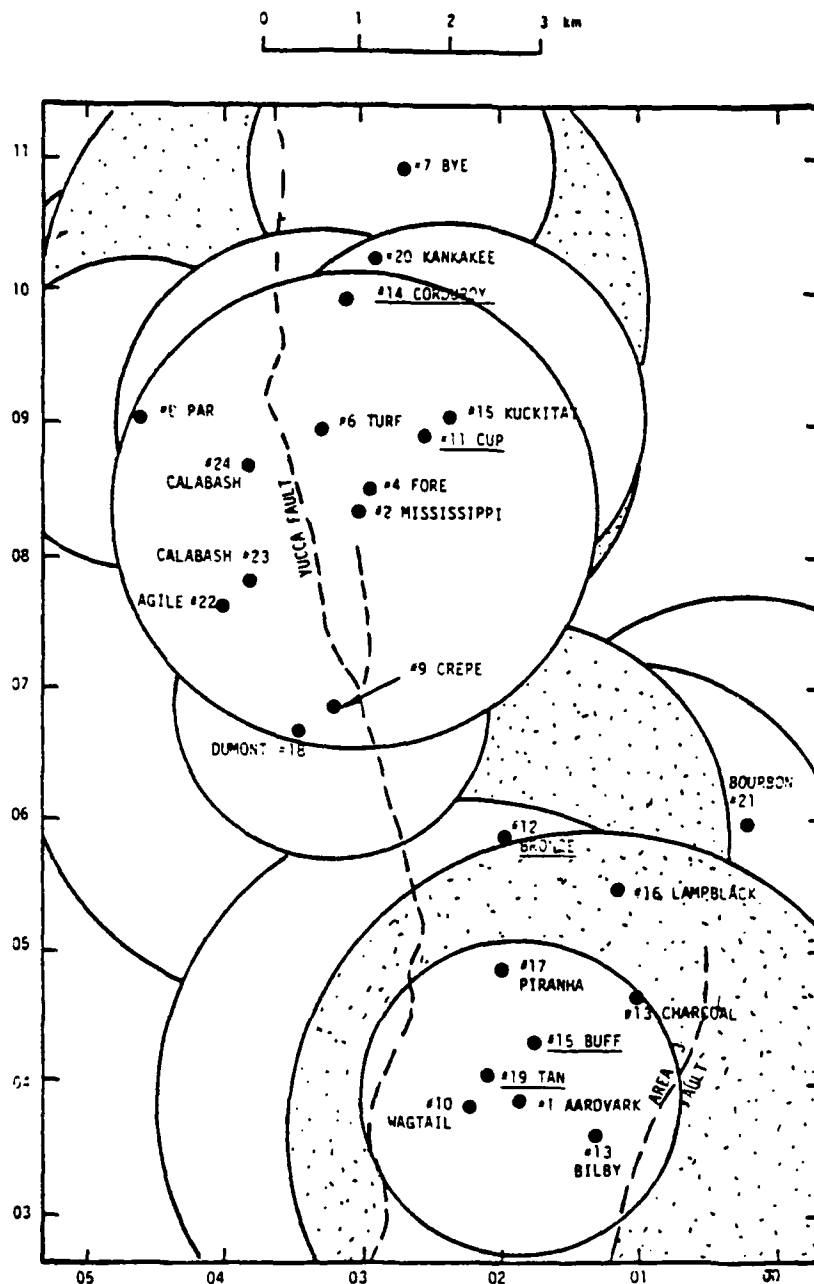


Figure 10. Yucca Valley detonation sequence, location, and approximate spall radius for detonations in tuff and Paleozoic rocks greater than 36 KT.

TABLE 5
Yucca Valley Events and Environmental Data for the
First 24 Considered in Figures 10 and 11

Detonation Sequence No.	Event	Yield †	DOB (m)	Depth to Water (m)	Date	Approximate Spall Radius Rs (km)	Density		(Water % by Wt.)/ % Saturation	Velocity V _p at M.P. (m/sec)
							ρ to Surface (gm/cc)	ρ at M.P. (gm/cc)		
1	AARDVARK	36	434	509	5/12/62	1.75	--	--	-- /90+?	--
2	MISSISSIPPI	110	494	561	10/5/62	2.65	--	--	-- / --	--
3	BILBY	235	714	488	9/13/63	3.35	1.78	--	-- / --	--
4	FORE	L-1	492	558	1/16/64	2.15	--	1.64	-- / --	--
5	KLICUNAT	L-1	493	567	2/20/64	2.15	--	1.77	(15.2)/ --	2531
6	TURF	L-1	507	567	4/24/64	2.20	--	1.77	(16)/ --	1909
7	BYE	L-1	389	582	7/16/64	1.70	1.68	1.57	(16)/ --	2850
8	PAR	38	404	594	10/9/64	1.75	1.97	1.48	(13.7)/ --	2322
9	CREPE	L-1	403	549	12/5/64	1.75	--	--	(8.1)/ --	--
10	MAGTAIL	L-1	750	509	3/3/65	3.35	1.79	--	(--)/100	--
11	CUP	L-1	537	554	3/26/63	2.40	--	--	(13)/100	--
12	BROWNIE	L-1	531	533	7/23/65	2.40	1.69	--	-- / --	--
13	CHARCOAL	L-1(pz)	455	533	9/10/65	2.00	1.72	--	-- / --	--
14	CONDOR	I	712	567	12/3/65	3.35	--	1.92	(20.2)/100	2164
15	BUFF	L-1	500	521	12/16/65	2.20	1.68	--	-- / --	--
16	LAMPBLACK	L-1	561	565	1/18/66	2.5	1.73	--	-- / --	--
17	PIRANHA	L-1	549	533	5/13/66	2.4	1.71	--	-- /100	--
18	DUPONT	L-1	671	549	5/19/66	3.0	--	--	-- / --	--
19	TAN	L-1	561	512	6/3/66	2.5	1.71	--	-- / --	--
20	KANKAKEE	L-1(pz)	455	575	6/15/66	2.00	--	--	-- / --	--
21	BOURBON	L-1(pz)	560	584	1/20/67	2.5	1.70	--	-- / --	--
22	AGILE	L-1	731	564	2/23/67	3.30	--	--	-- / --	--
23	COMMAORE	250	746	567	5/20/67	3.50	--	--	-- / --	--
24	CALABASH	110	625	--	10/29/69	2.65	--	--	-- / --	--

† Materials properties data from LLL data bank
Yield I is 20 to 200 KT, L-1 is approximately 0 to 200 KI.

extent of the spall. Note that if stress-relief interactions were this extensive, AARDVARK would have caused stress relief for BILBY and it in turn would have affected most of the southern tests. If this were true (as it could be if only the southern tests were considered), then why did not MISSISSIPPI do the same up north. The only northern test without strong Love-wave excitation is FORE detonated close to MISSISSIPPI. FORE might register a large body-wave magnitude for its yield because of this close proximity with some compaction and increased coupling caused by MISSISSIPPI. Also, some pre-stress relief may have occurred as a result of MISSISSIPPI. Clearly in Yucca Valley, spall does not appear to play a role in pre-stress relief that generates Love-wave excitation (or high F-factors). This is consistent with the model for spall induced fault motions in Yucca Valley proposed recently.⁽⁵⁾ The alluvium is considered too weak to support substantial lateral stress inhomogeneities but it is sufficiently cohesive to store partial compaction resulting from earlier natural deformations between the water table and the surface on the upthrown side of the faults. This postulated compaction from recent geologic fault motions is thought to be relieved by spall, temporarily lowering the confinement and allowing hysteretic expansion. The motions (explosion induced) are expected to die out at the water table and not reflect deep-seated tectonic energy release.

- Figure 11 illustrates smaller circles that are roughly proportioned to the yield and the extent of partial pre-stress relief that may be due to explosion-induced hydrofracturing. From this it can be seen that MISSISSIPPI might have caused some pre-stress relief of FORE. BILBY probably had little effect on subsequent tests. It would be interesting to see if AGILE lowered the expected F-factor or Love-wave excitation of COMMODORE. Similarly, KLIKTITAT affecting CUP; CORDUROY/KANKAKEE and WAGAIL/TAN. Whether these interactions are confirmed or not, these same couplets might be examined for anomalously high body wave magnitude for the second events in each pair.

The best correlation found to explain F-factor variations and Love-wave excitation in Yucca Valley is geographic location. This may also provide a rational approach to explain the low anomalies of PIRANHA and CHARCOAL. Note on Figure 11 that at about 27°06'N latitude, both the Yucca and Area 3

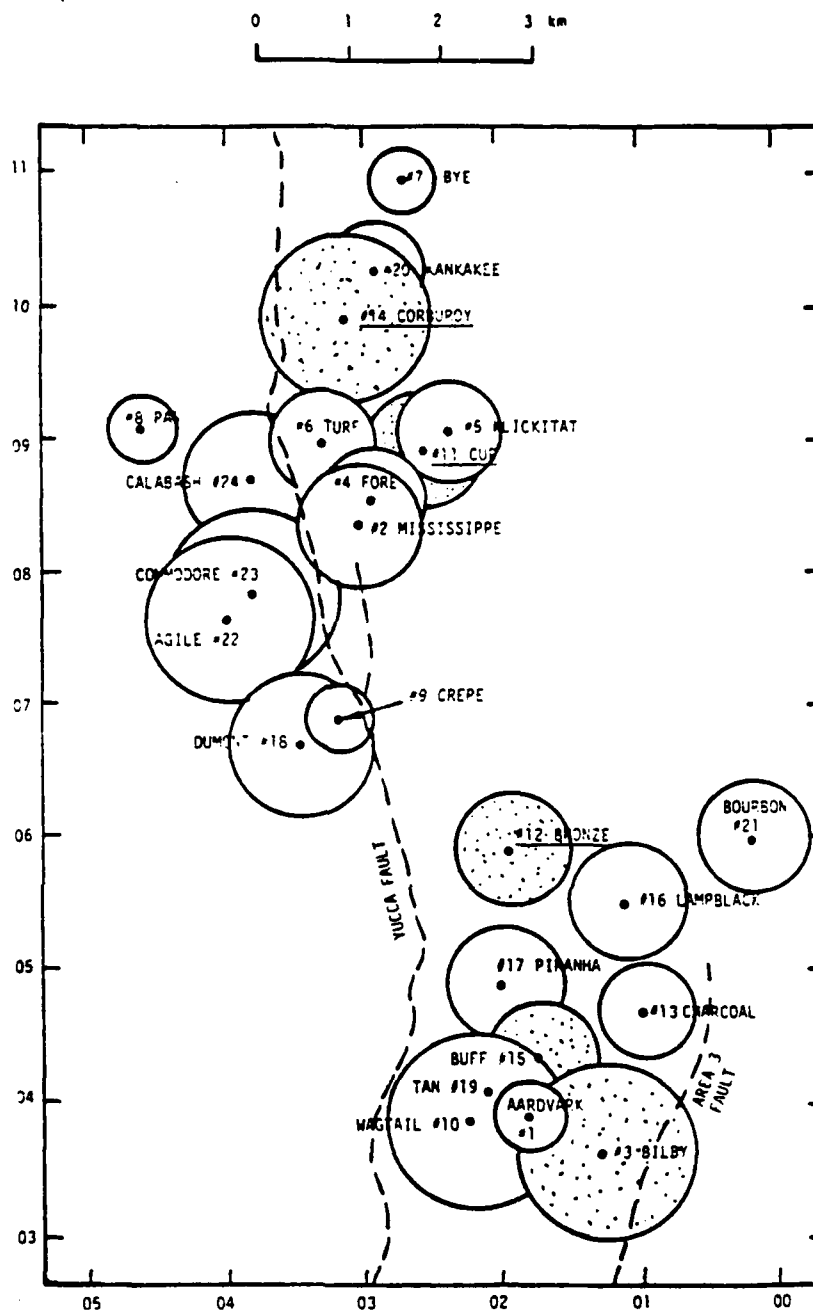


Figure 11. Yucca Valley detonation sequence, location, and approximate hydrofracture radii for events greater than 36 KT in tuff or Paleozoic rocks.

faults change strike (orientation) from NNE to NNW. One intuitively expects stresses to either concentrate or be somewhat relieved at fault bends. A check on this trend is possible by comparing the F-factors for the closest events north and south of these two events. These are BUFF and BRONZE, having the lowest F-factors listed on Table 1. Possibly, BUFF was subject to a little pre-stress relief from AARDVARK and BILBY. Clearly, more data is needed to evaluate the geographical variability of pre-stress in Yucca Valley. The fault scarp along YUCCA fault is visible and has survived erosion in the north near CORDUROY. It is not preserved south of $37^{\circ}05'N$ to my knowledge. The last major movement then was probably in the north a few thousand years ago. If fault-motion-related residual stresses (compaction) can be stored in the alluvium — residual stresses from earlier deformations are likely stored in the underlying tuff and paleozoic rocks.

One important indication of this analysis is that an explosion-triggered fault motion model for the pre-stress relief (other than discussed above) in Yucca Valley is not supported. This is surprising since the same data were used to refute the volumetric or cavity fracture zone stress relief model proposed by Archambeau.⁽²⁾ If the fault motion stress relief model were appropriate, then Figure 10 showing the interactions of spall would be expected to show a sequential stress relief pattern. Also, there is no obvious relationship associated with Love-wave excitation and distance from the two major faults shown in Figures 10 and 11. The mechanisms that appear appropriate for producing Love-wave excitation are stress relief caused by explosion induced ground water pressurization and associated hydrofracturing that aids on the relief of pre-stress. Asymmetric cavity growth and differential motions along weaknesses likely contribute to developing surface wave double couples. Spall does not appear to be a significant factor in Yucca Valley except to temporarily reduce confinement of stresses.

Qualitative prediction for other F-factors associated with Yucca Valley events is made possible by the indicated Depth of Burst/Apparent Yield dependence for the north and south regions. It would be interesting also to see if the latitude $37^{\circ}04.5'$ to $37^{\circ}05.5'N$ is in fact a consistent location dividing weak and strong Love-wave excitation associated with nuclear tests to the south and north. Figure 12 is an F-factor/Apparent Yield plot of the NTS tests (plus SHOAL) listed on Table 1. A consistent $1/4$ th power of apparent yield

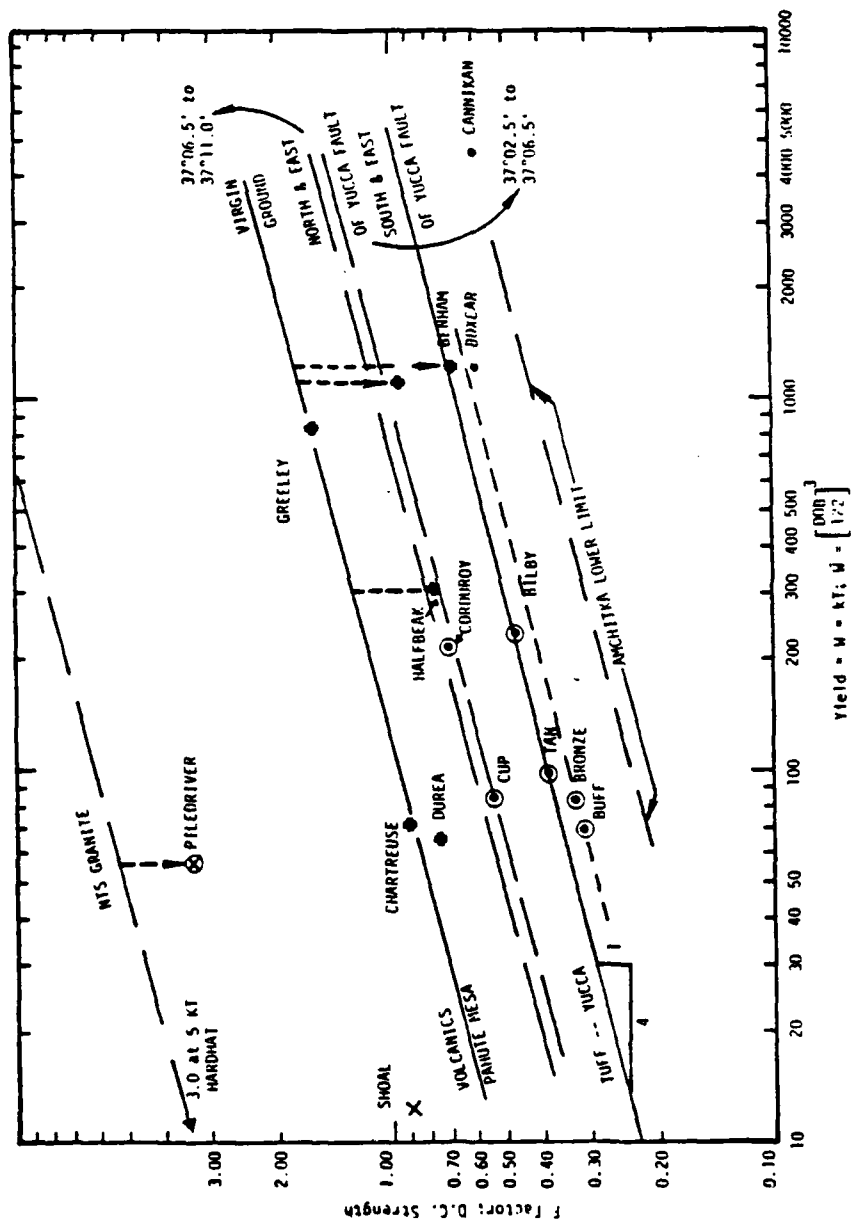


Figure 12. Double couple strength (F-factor) versus "apparent" yield dependence for NTS events, SHOAL and CANNIKAN.

dependence is indicated that is probably mostly a result of rock properties changes (better energy coupling) with depth of burst. Again, the interaction effects for the Pahute Mesa tests are apparently absent with only GREELEY and CHARTREUSE. These events are thought to represent virgin ground conditions with the F-factors determined. The same slope passes through the Yucca Valley tests when the north and south tests are considered separately. Further, we can speculate that if in-situ pre-stress in Pahute Mesa is essentially the same as northern Yucca Valley, then the difference in F-factor may be associated with spall induced pre-stress relief. If this is the case then about 50 percent of the total pre-stress relief associated with events at Pahute Mesa is spall induced. When spall and the extent of explosion induced fluid pressure hydrofracturing are considered, then a cross-sectional area or volumetric model for pre-stress relief may be the more general mechanism explaining the F-factor data. Explosion triggering of faults is, of course, a credible mechanism that probably contributes to the surface wave double couples — it just does not appear to dominate at either Pahute Mesa or Yucca Valley.

2.4 COMPARISON OF AMCHITKA ALASKA TESTS WITH THOSE IN
VOLCANIC ROCKS AT NTS -- WITH A QUALITATIVE
"PREDICTION" FOR LONGSHOT

From Table I and Figure 13, it appears that the F-factor magnitude for the two high yield detonations at Amchitka were in regions of lower pre-stress than the volcanic rock at NTS. The environment is water saturated to the surface so energy coupling should be better than at Pahute Mesa. The fault pattern at Amchitka like at SHOAL is a rather consistent pattern about N60° to 70° E, which is not the orientation of the underlying fault zone forming the tectonic plate boundary. Presumably the island overrides the under-thrusting oceanic plate and the associated stress field is somewhat decoupled from the deeper accumulations of stress. An F-factor determination for the 85 KT LONGSHOT event in virgin ground at Amchitka would be instructive in assisting in evaluating the range of hypothesized explosion-induced hydrofracture stress relief. An F-factor of anything between 0.25 and 0.6 is credible. If it is closer to 0.25 then the in-situ stress level is lower than at NTS. If, however, the F-factor is 0.6 or more, then the 1/4-power of apparent yield dependence is not confirmed.

Another question comes to mind with regard to the low F-factors at Amchitka. Possibly water saturation to very near the surface prevents storage of significant pre-stress at shallow depths due to more complete stress relief with natural fault motions and earthquakes. Therefore, spall might not play so important a role as is suspected at Pahute Mesa.

It is interesting to note that static magnetic field changes (increases) permanently occurred within at least a 3 km radius of CANNIKAN and that at least part of the magnetic changes were fault controlled. It was concluded that the magnetic field changes were produced by stress changes in the rock.⁽²²⁾ The explanation is uncertain, but may be related to the quasi-permanent explosion induced stress increases that were fault block controlled.⁽²³⁾ Increased in-situ stress conditions that remain long after explosions have been documented by the French tests in granite and by post-shot measurements in Rainier Mesa

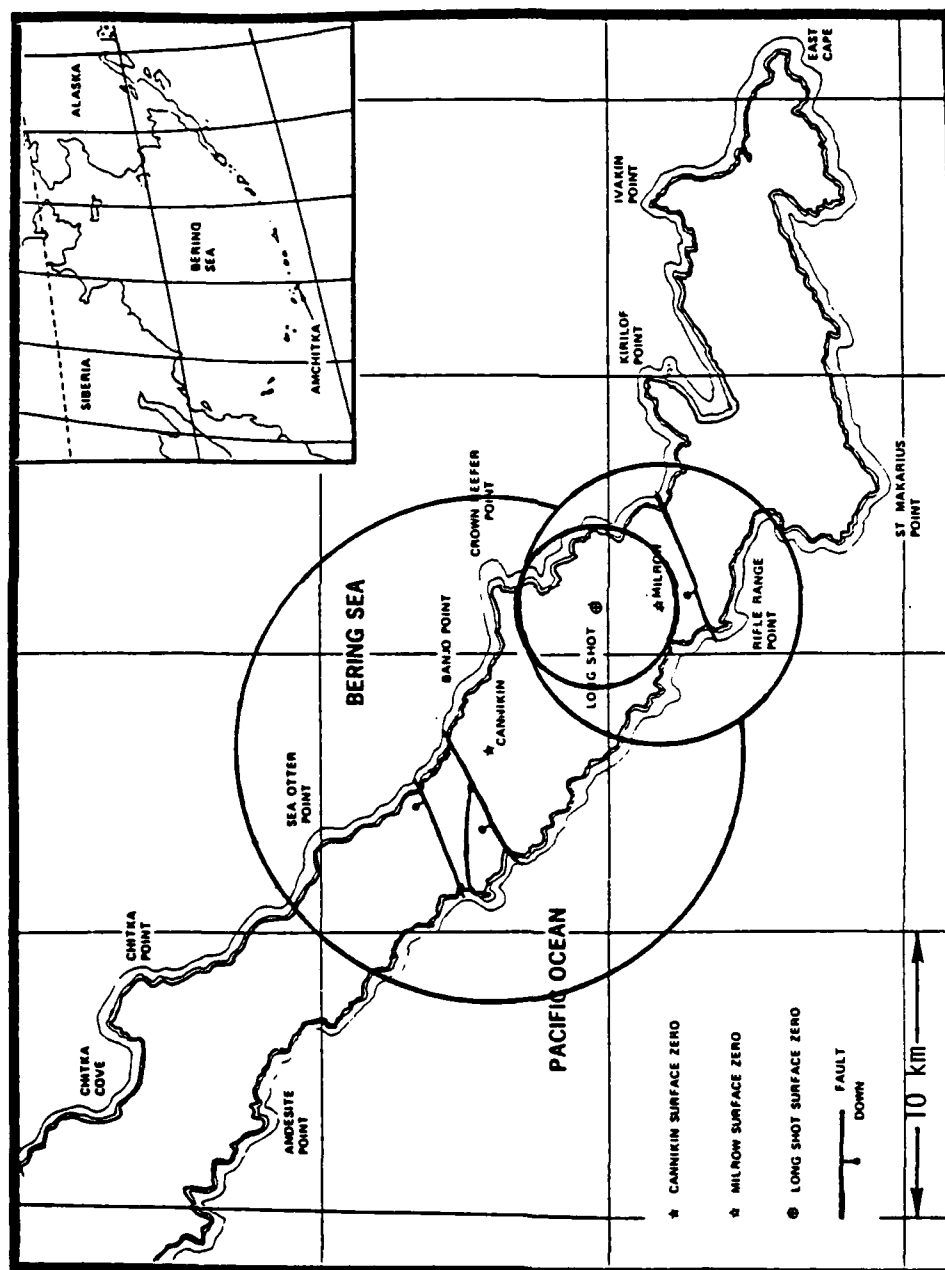


Figure 13. Map of Amchitka showing explosions, fault orientations, and approximate extents of spill. [23]

tuff.^(18,21) It seems possible that azimuthally varying surface waves may be generated by anisotropic stress increases as well as stress drops. Tectonic stress relief may not necessarily be required for Love-wave excitation.

3.0 SUMMARY AND RECOMMENDATIONS

Preliminary evaluation of F-factors and Love-wave excitation values for contained nuclear explosion tests in a variety of environments tends generally to support volumetric pre-stress relief models rather than the triggering of one or two major faults. The extent of the pre-stress relief zone is substantially larger than three or four cavity radii and may include material seeing initial explosion induced stresses of only a few tens of bars.

The basic recommendation is to obtain additional surface wave analysis results (preferably in terms of F-factors, strike, and motion of apparent double couples). With a larger data base, the analysis started in this preliminary draft can be completed. It may well turn out that intermediate and large yield explosions reveal a great deal of information about that state of stress variations in the earth's crust as well as enabling improved understanding of variations in M_s and m_b .

REFERENCES

1. Aki, K. and Y. Tsai, "Mechanism of Love-Wave Excitation by Explosive Sources," J. Geophys. Res., 77, no. 8, pp. 1452-1475, 1972.
2. Archambeau, C. B. and C. Sammis, "Seismic Radiation from Explosions in Prestressed Media and the Measurement of Tectonic Stress in the Earth," Rev. Geophys. Space Phys., 8, pp. 473-500, 1970.
3. Toksoz, M. N. and H. H. Kehler, "Tectonic Strain-Release Characteristics of CANNIKAN," BSSA, 62, no. 6, pp. 1425-1438, 1972.
4. Toksoz, M. N., et al., "Determination of Source Parameters by Amplitude Equalization of Seismic Surface Waves, 2, Release of Tectonic Strain by Underground Nuclear Explosions and Mechanisms of Earthquakes," J. Geophys. Res., 70, pp. 907-922, 1965.
5. Rawson, G., "Surface Observed Block Motions and Their Relations to Explosion Induced Spall," R & D Associates Report RDA-TR-110006-004, Draft Report to DNA.
6. Rawson, G., "Spall from Contained Explosions Related to Yields, Depths of Burst, and Material Properties," DELTA-TR-79-027, Draft, 1979.
7. Rawson, G., "Semi-Empirical Set of Equations Relating Ground Motion and Earth Properties to Estimating Explosion Produced Cavity Size," DELTA Work in Progress.
8. Rawson, G., "Estimating an Upper Bound for Block Motion Magnitude as a Function of Yield Depth of Burst, and Geologic Setting," RDA Work in Progress.
9. Desert Research Inst., "Geologic, Geophysical, and Hydrological Investigations of the Sand Springs Range, Fairview Valley and Four Mile Flat, Churchill Co., Nev., "Nev. Bu. Mines, Reno, Nevada, 1962.
10. Houser, F. N. and F. G. Poole, "Preliminary Geologic Map of the Climax Stock and Vicinity, Nye Co., Nev.," Map 1-328, Misc. Geol. Inv. USGS, 1960.
11. Obert, Leonard, "Static Stress Determinations -- Operation NOUGAT, Shot HARDHAT, U.S. Bu. Mines, College Park, Maryland, POR-1804, 1963.
12. Emerick, W.L., et al., "Summary of Post-Shot Geologic Effects in the 1500 Tunnel, Area 15, NTS, Nye Co., Nev.," U.S.G.S. Tech. Letter Area 15-3.

13. Barosh, P. J., "Geologic Effects from an Underground Test at the PILEDRIVER Site, Area 15, NTS," U.S.G.S. Tech. Letter NTS-197, 1967.
14. Aki, K., "A Note on Surface Waves from the HARDHAT Nuclear Explosion," J. Geophys. Res., 69, no. 6, March 1964.
15. Rabb, David, Ariz. Bu. Mines, formerly LLL, involved in PILEDRIVER post-shot exploration -- personal oral communication.
16. Carr, W. J., "Summary of Tectonic and Structural Evidence for Stress Orientation at the Nevada Test Site," U.S.G.S. open file report 74-176, 1974.
17. Hoffman, H. U. and F. M. Sauer, "Free Field and Surface Motions -- Operation Flintlock -- Shot PILEDRIVER," SRI-POR-4000, 1969.
18. Faure, Jean, "Research on Geologic Effects of Underground Nuclear Explosions in a Sahara Granite Massif," Vols. 1 & 2 Dissertation for Ph.D. Univ. of Nancy, 1970 -- LLL had translated.
19. Derlich, Sarge, "Underground Nuclear Explosions -- Study of the Zones of Fracturing," translated from the French Atomic Energy Commissariat Report No. CEA-R-3941, 2970, for LLL.
20. Hamilton, R.M., et al., "Earthquakes Caused by Underground Nuclear Explosions on Pahute Mesa, Nevada Test Site," BSSA, 62, no. 5, pp. 1319-1341, 1972.
21. LaComb, Joe, oral communication, 1977.
22. Hasbrouck, W. P. and J. H. Allen, "Quasi-Static Magnetic Field Changes Associated with the CANNIKAN Nuclear Explosion," BSSA, 62, no. 6, pp. 1479-1487, 1972.
23. Perret, W. R., "Close-In Ground Motion from the MILROW and CANNIKAN Events", BSSA Vol. 62, no. 6, 1972.

APPENDIX E

EXPLOSION ENERGY PARTITIONING
THAT MAY REFLECT MATERIALS PROPERTIES VARIATIONS
AND VARIATIONS IN GROUND MOTION DATA

DELTA-PR-79-040

EXPLOSION ENERGY PARTITIONING
THAT MAY REFLECT MATERIALS PROPERTIES VARIATIONS
AND VARIATIONS IN GROUND MOTION DATA

PROGRESS SUMMARY

by

Glen Rawson
Consultant to

Del Mar Technical Associates
P. O. Box 1083, Del Mar, California 92014

December 1979

Sponsored by
Advanced Research Projects Agency (DOD)
ARPA Order No. 3368-4

Monitored by AFOSR Under Contract # F49620-79-C0230

In February, 1978, a draft working paper (DELTA-TR-78-0016) was submitted in which a tentative set of semi-empirical equations were proposed to relate explosion produced cavity volume history to free-field radial displacement history.⁽¹⁾ Cavity history and free-surface interactions were also postulated for many contained nuclear explosion events, which apparently failed the overburden to form a "shear zone plug". This cone of overburden failure is thought to significantly influence the subsequent cavity collapse and chimney development. By considering the regions of rock failure associated with the "shear zone plug" and the probable response of pre-stressed material to the reduced confinement temporarily induced by spall, it was further proposed that there was a substantially larger cross-sectional area available for the release of tectonic stress and/or surface wave generation than generally recognized. The stress waves and cavity history interactions with the ground free-surface to produce both a spalled region and early overburden failure of the chimney region have been more completely evaluated in the accompanying draft reports (DELTA-TR-79-027 and DELTA-TR-79-038).^(2,3)

The equations in the early 1978 draft are overly simplified and reflect errors. This progress summary is intended to provide an update relating cavity volume history to ground motion history. There are two primary goals associated with this investigation:

- To determine if the complex partitioning in wave mechanics theory, of near-field and far-field terms, can be more simply approximated and related to near source ground motion measurements.
- To determine if the maximum (dynamic) cavity size can be approximated from the ground motion records so that more accurate empirical relations can be developed to describe cavity dynamics, rock properties, and ground motion history interactions.

Ground motion data from the SALMON event are still considered the most instructive in that the records are minimally polluted with indeterminant variables and heterogeneous complexities. Because of the salt's plasticity, the confining stress field was essentially hydrostatic and probably about equal to the overburden weight. Thus, the four important rock properties variables thought to dominate cavity size are well known:

- Compaction — can be assumed negligible.
- Water Content — can be assumed negligible
- Heterogeneities — can be assumed minimal.
- Confining Stress — the three principle stresses can be assumed effectively equal and equivalent to the overburden weight.

In addition, the salt vapor does not rapidly condense and the plastically responding salt does not allow appreciably early gas leakage. The cavity pressure history, then, can be expected to reflect the induced stress history for at least the first few seconds.

In order to minimize instrumentation errors, free surface effects and integration uncertainties, only gauges directly installed to give radial motions lateral to the detonation were considered. Of these, only displacements determined from radial velocity gauges were used to represent the late time history. Therefore, of the approximately 55 subsurface ground motion records obtained at SALMON and located in Figure 1, only the four shot level gauges oriented horizontally (radially) are used.⁽⁴⁾ Displacement histories from these four records are in Table 1 and shown in Figure 2. Notice that the close-in gauge (at 165.8 meters range) showed failure at about 1.2 seconds and the record after 0.4 seconds is questionable. The other three records are assumed then to provide accurate measurements of the displacement histories at those ranges (318.2 m, 621.8 m, and 744 m). Tabulated are the initial peaks (δ_1) the second peak (δ_2) and the residual displacement (δ_3). Also tabulated is the differential displacement δ^* which is defined as the difference in peak height between δ_1 and δ_2 . The time interval between the first shock wave arrival (TOA) before δ_1 and the δ_2 peak is approximately constant at 0.26 ± 0.05 seconds.

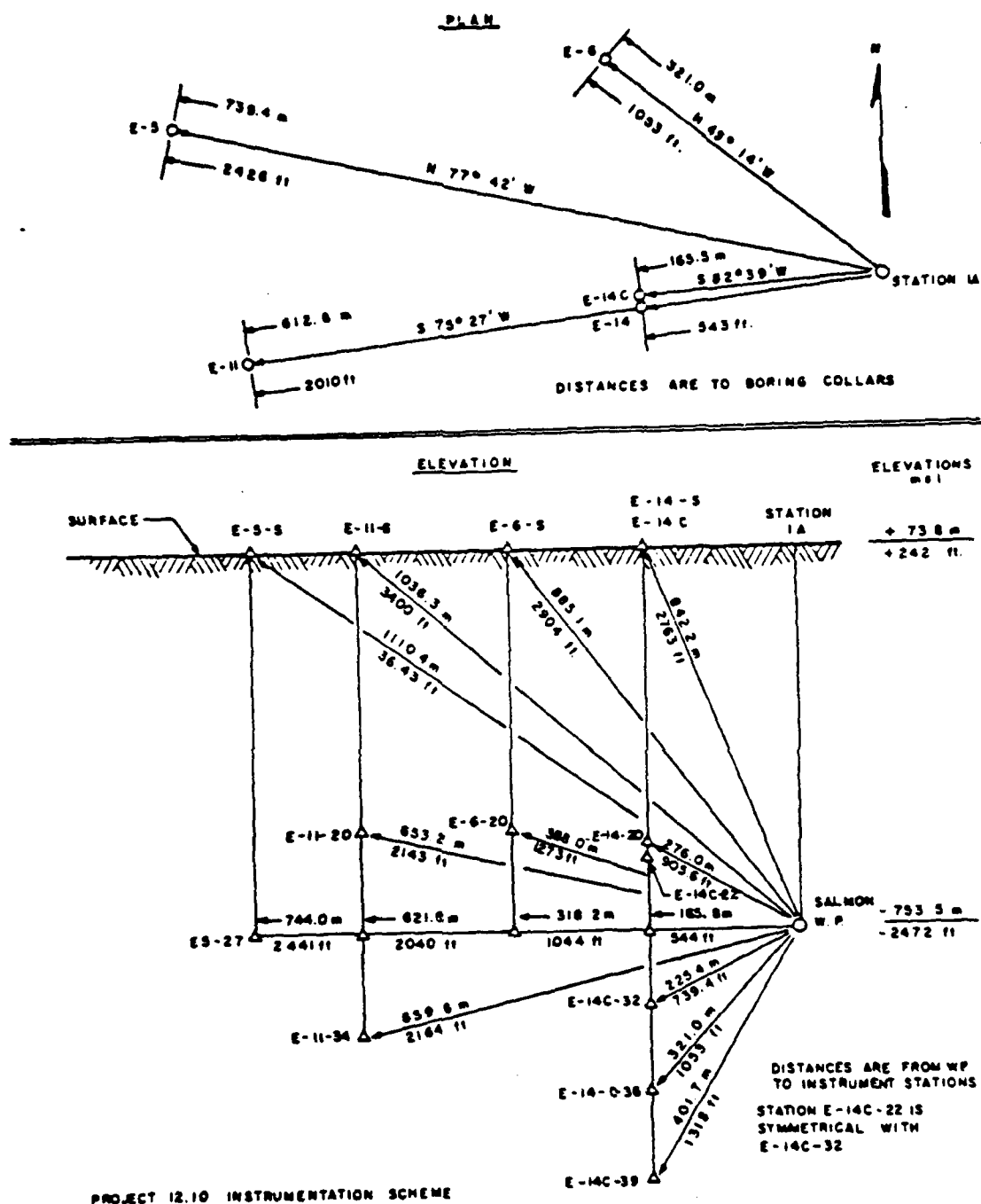
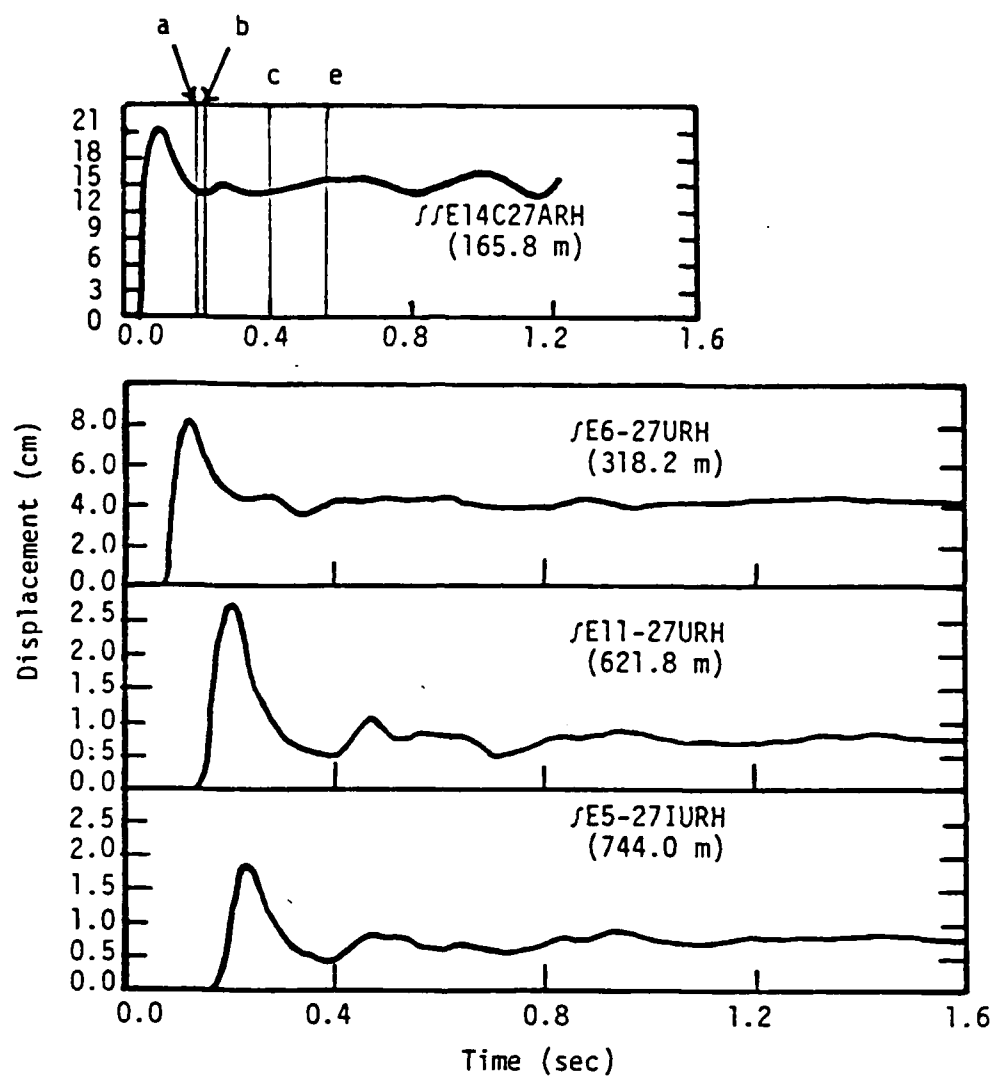


Figure 1. Distribution of ground motion gauges associated with Sandia Laboratories Project 12.10 SALMON event instrumentation program.

TABLE 1
SALMON Horizontal (Radial) Displacement Peaks

Record Number	Slant Range Equals Horizontal Range (m)	Displacements (cm)			†Estimated Dynamic Cavity Radii at	
		Initial δ_1	2nd δ_2	Δ Residual	+ 0.25 sec After 1st TOA	+ 1.6 sec After Shot
SE14C-27ARH	165.8	21.8	15.4	6.4 --	23.33	--
SE6-27URH	318.2	8.2	4.7	3.5 4.3	24.26	23.55
SE11-27URH	621.8	2.7	1.1	1.6 0.8	23.37	21.01
SE5-27-1UKH	744	1.9	0.85	1.05 0.8	24.17	23.68

$$^{\dagger}R_x = [3 R_{SL}^2 \delta_y]^{1/3}$$



Reflectors	Distance	V_p km/sec	Reflection Return
a. Salt Top	~ .450 km	4.67	0.19 sec
b. Salt Near Side	~ 0.4 km	4.67	0.17 sec
c. Salt Far Side	~ 1.0 km	4.67	0.4 sec
d. Salt Base	7.24 km	4.67	3.1 sec
e. Salt Free Surface	.83 km	3	0.55 sec

Figure 2. Radial displacement histories at shot level associated with the SALMON event along with estimated arrivals from major reflectors.

Interpretation of these records is represented schematically by Figure 3. This shows the first displacement pulse being complex with the remaining wave train essentially showing damped oscillations of the explosion produced cavity. Actual records (Figure 2) probably are complicated by reflected waves from the surface and salt boundaries. The maximum cavity size \bar{R}_m cannot be directly discerned from the records because of the complex nature of the first pulse. It is assumed to be accurately reflected, however, in the second displacement peak δ_2 even though some damping probably occurs. The second cavity size peak is probably a little smaller than that thought to be buried in the initial displacement peak.

The assumption of negligible compaction of the rock surrounding the cavity can be represented as follows:

$$R_x = \left[3 R_{SL}^2 \delta_y \right]^{1/3} \quad (1)$$

where R_x is the implied cavity size (m) associated with displacement δ_y (m) at range R_{SL} (m). Thus \bar{R}_m or the maximum cavity size under dynamic conditions is equal to or greater than the R_m that is calculated from δ_2 . The residual cavity size R_r is calculated from δ_3 and the final cavity size (traditionally R_c) is the late time apparent size determined by post shot exploration — a time that may follow considerable induced stress adjustment. Dynamic cavity radii associated with δ_2 and δ_3 are shown in Table 1. The indicated R_m is equal to or greater than about 23.8 m or essentially 24 m. This size apparently decreases slightly to about 23 meters by 1.6 seconds after the detonation and then slowly creeps to a final size of 17.4 meters at the time of post shot exploration four months after the detonation.⁽⁵⁾ At the time of post shot exploration the explosion induced stresses thought to have existed in the rock surrounding the cavity had apparently crept and relaxed — opening or dilating slightly along explosion induced rock failure surfaces. For example, at a lateral distance of 15 meters from the cavity, the rock porosity had changed from nearly 0% pre-shot to about 3%. The compressional and shear wave velocities had decreased 20%

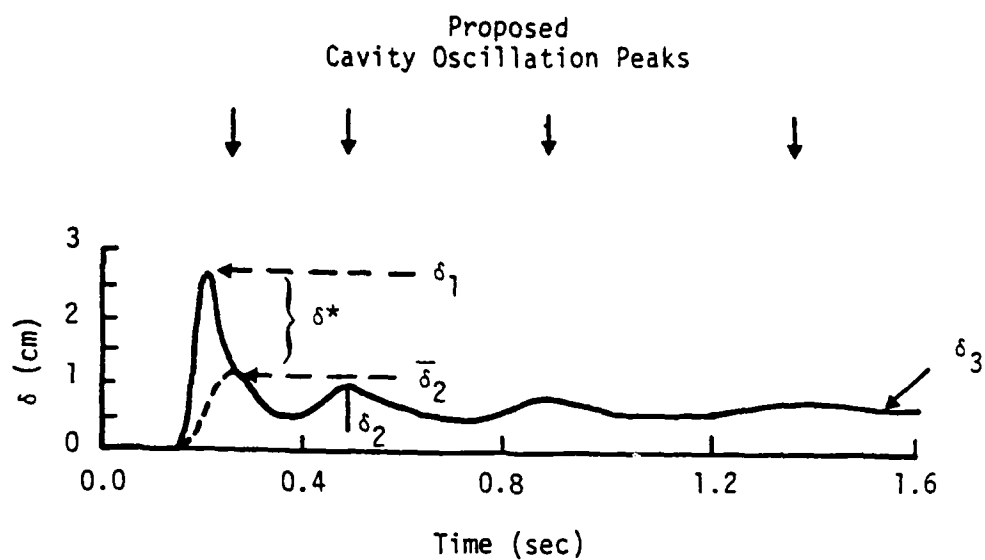


Figure 3. Idealized displacement time record modified after gauge record JEl1-27URH.

and 11% from pre-shot values.⁽⁵⁾ The only evidence of explosion induced residual stress was below the cavity and this was probably the result of creep at elevated temperature due to the close proximity of the solidified "puddle". Clearly for SALMON the cavity size at early times must have been larger than 17.4 m. The earlier analysis by Perret similarly interpreted the early residual cavity size at 1.6 seconds as 22.3 meters using more data than this analysis and having a range of 16.3 to 26.9 m. He used the same relationship as Equation (1) for his interpretation. Prior to the explosion, Rogers calculated the expected maximum cavity size at 22 m.⁽⁶⁾

Assuming that the displacement peak δ_2 is a reasonable approximation of the maximum cavity size, it is proposed that the initial peak δ_1 shown in Figure 3 can be partitioned into roughly two categories of apparent displacement:

- δ^* representing predominantly the far field displacement component, which is the difference between δ_1 and $\bar{\delta}_2$.
- $\bar{\delta}_2$ which is equal to or slightly greater than δ_2 and represents predominantly the near field displacement component.

The proposition (corrected from that made earlier in 1978) is that the initial displacement peak δ_1 is approximately partitionable as follows:

$$\delta_1(R_{SL}) = \frac{K}{R_{SL}^{1.58}} \approx \frac{K_{NF}}{R_{SL}^2} + \frac{K_{FF}}{R_{SL}} \quad (2)$$

and where

$$\delta^* \approx \frac{K_{FF}}{R_{SL}} \approx \text{far field term}$$

$$\delta_2 \approx \frac{K_{NF}}{R_{SL}^2} \approx \text{near field term}$$

The attenuation of δ_1 for SALMON was determined by Perret to be:⁽⁵⁾

$$\delta_1 = 7.03 \times 10^4 R_{SL}^{-1.58} \quad (3)$$

A check on the possible validity of Equation (2) is shown in Figure 4 — plotting the attenuation with distance of δ_1 , δ_2 and δ^* versus R_{SL} — using the values determined in Table 1. Note that the selected values of δ_1 reflect $R_{SL}^{-1.58}$ in Equation (3). The displacement component δ_2 attenuates approximately as R_{SL}^{-2} and δ^* attenuates approximately as R_{SL}^{-1} as anticipated by Equation (2). Considerably more effort is needed to determine if it is in fact feasible to approximate near and far field motion terms in the near field ground motion data from a variety of detonations. If this is achievable, it may then be possible to more directly relate the near field ground motion data to far field teleseismic data and better assess the source (explosion/earth) interactions as they may relate to teleseismic data.

The indication that the first cavity oscillation maximum is responsible for the second displacement peak, or at least may be discernable from selected records, is encouraging. These results indicate that an earlier reported equation for predicting cavity size can be improved to give the cavity size at the time of maximum cavity growth by assuming equilibrium with the effective confining stress (overburden as well as possible tectonic stress). Equation (4) is that introduced by Higgins and Butkovich in 1967 where R_c is the final cavity radius determined by the exploration and B is the "medium independent constant" or universal constant of 100:⁽⁷⁾

$$R_c = B \left[\frac{(\bar{\gamma}-1) p_v^{(1/\bar{\gamma})} - 1}{(\rho h)^{1/\bar{\gamma}}} W \right]^{1/3} \quad (4)$$

where W is yield, ρ is overburden density, h is the depth of burst, and values of the chemical properties related to a water content correction $\bar{\gamma}$, $\bar{\gamma}^+$ and P_v are determined by their study.

Work in progress is to determine a similar relationship for R_m , substituting a confining stress term L_s for ρh ; and to determine a corresponding earth constant E_k in place of B . Because of the change in size from R_c to R_m , a B of 100 appears from preliminary work to generally correspond to an E_k of about 70

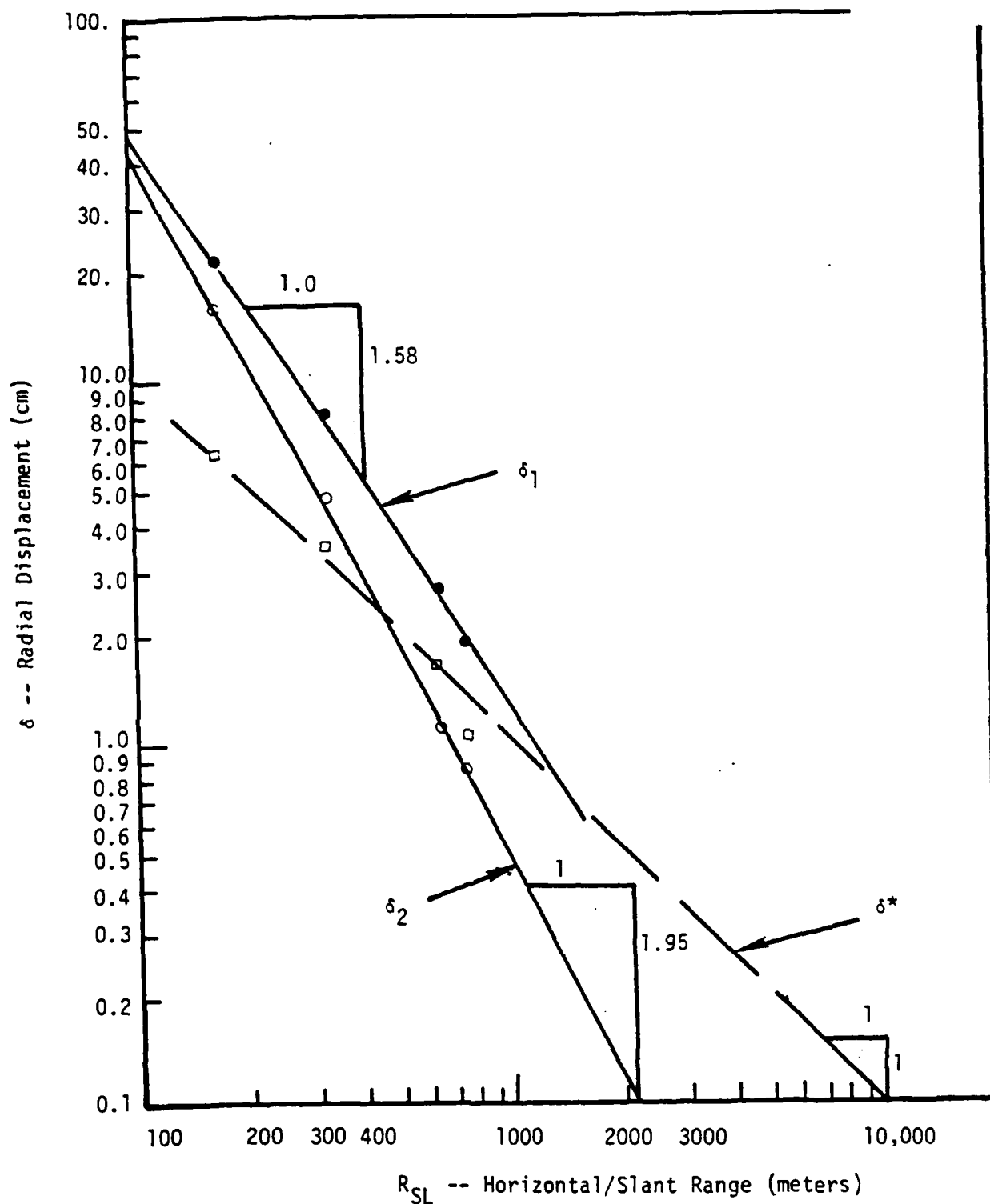


Figure 4. SALMON radial displacement peak possibly reflecting near and far field energy partitioning.

with no compaction or water corrections. If E_k can be confirmed as truly a material independent constant then the following equation could become a powerful tool in evaluating the phenomena of in-situ stress and compaction variables upon cavity dynamics and associated ground motions and seismic waves.

$$R_m = E_k \left[\frac{(\bar{\gamma}-1) P_v^{(1/\gamma)^+} W}{\ell_s^{(1/3\gamma)^+}} \right]^{1/3} \quad (5)$$

Continued work in this area is planned for the near future. Analysis of French records to compare with the U.S. data would be helpful in refining the investigation. It would also help to resolve the importance of pre-stress and other rock properties differences between U.S. and French experience. The initial displacement peaks (δ_1) for the data from the two countries are similar. The French data in fact display less data scatter and thus may have less difference between maximum and minimum horizontal stress. The magnitude of in-situ stress is clearly higher for the French and the water content may be significantly less. The final cavity radii are much smaller. This study anticipates that if δ_2 can be resolved or approximated from later oscillations, it will be considerably less for comparable yields and depths of burst than U.S. experience.

Continued work with the appropriate ground motion data from detonations in alluvium and tuff might be expected to enable using ground motion data to better model the compaction history and residual stress history associated with detonations in these type materials.

REFERENCES

1. Rawson, Glen, "A Semi-Empirical Equation Relating Ground Motions to Explosion Dynamics and Variations in Earth Properties," Draft Topical Report DELTA-TR-78-0016, February 1978.
2. Rawson, Glen, "Spall from Contained Explosions Related to Yields, Depths of Burst, and Material Properties," Draft Technical Report DELTA-TR-79-027, March 1979.
3. Rawson, Glen, "An Interpretive Analysis of Those Nuclear Explosion Tests Where Surface Wave Analyses Have Been Reported," Draft Preliminary Report DELTA-IR-79-0038, October 1979.
4. Perret, W. R., "Free-Field Particle Motion from a Nuclear Explosion in Salt, Part I: SALMON Event, VUF-3012, 1964.
5. Rawson, D.E., et al., "Review of the SALMON Experiment — A Nuclear Explosion in Salt," Die Naturwissenschaften, Heft 20, S 525-531, 1967.
6. Rogers, L. A., J. Geophysical Research, Vol. 171, 1964.
7. Higgins and Butkovich, "Effect of Water Content, Yield, Medium and Depth of Burst on Cavity Radii," Lawrence Livermore Laboratory, TID-4500, UC-35, UCRL-50203, 1967.

APPENDIX F
FINITE ELEMENT MODELING OF
TOP SURFACE SPALL

DELTA-TR-77-0

FINITE ELEMENT MODELING OF
TOP SURFACE SPALL

Technical Report

Joel Sweet

Del Mar Technical Associates
P. O. Box 1083, Del Mar, CA 92014

Sponsored by
Advanced Research Projects Agency (DOD)
ARPA Order No. 3368
Monitored by AFOSR Under Contract No. F49620-77-C-0079

I. INTRODUCTION

Proper interpretation of teleseismic data emanating from underground explosions first requires an evaluation of the near source effects. The present study considers the modeling of one of these near source phenomena, i.e., top surface spall. The importance of this near source manifestation is suggested by field data from several underground explosions.⁽¹⁻³⁾ Acceleration records from surface locations directly above the buried explosion exhibit multiple spikes which can be explained by a spall layer forming and then impacting the earth due to gravitational and elastic forces.

The model investigated in this study is a pre-existing plane of weakness parallel to the ground surface. Failure occurs when the explosion compression wave reflects from the top surface as a tensile wave causing failure along the plane of weakness.

A numerical simulation utilizing the SWIS finite element code^(4,5) was chosen for this study. The fracture model applied for modeling the top surface spall is similar to the technique previously used in finite difference⁽⁶⁾ and finite element⁽⁷⁾ codes. Briefly, the finite element mesh containing the explosion cavity is first prestressed with the gravitational load using the static mode of the SWIS code. A dynamic pressure history is applied to the cavity interior resulting in a simulated explosion environment. The fracture model allows the spall layer to rise, due to the trapped vertical momentum, and then impact the earth.

The particular problem configuration utilized in this study was chosen for demonstration purposes only and is not meant to represent an actual explosion. Succeeding studies will investigate realistic explosion environments and their teleseismic behavior.

II. FRACTURE MODEL

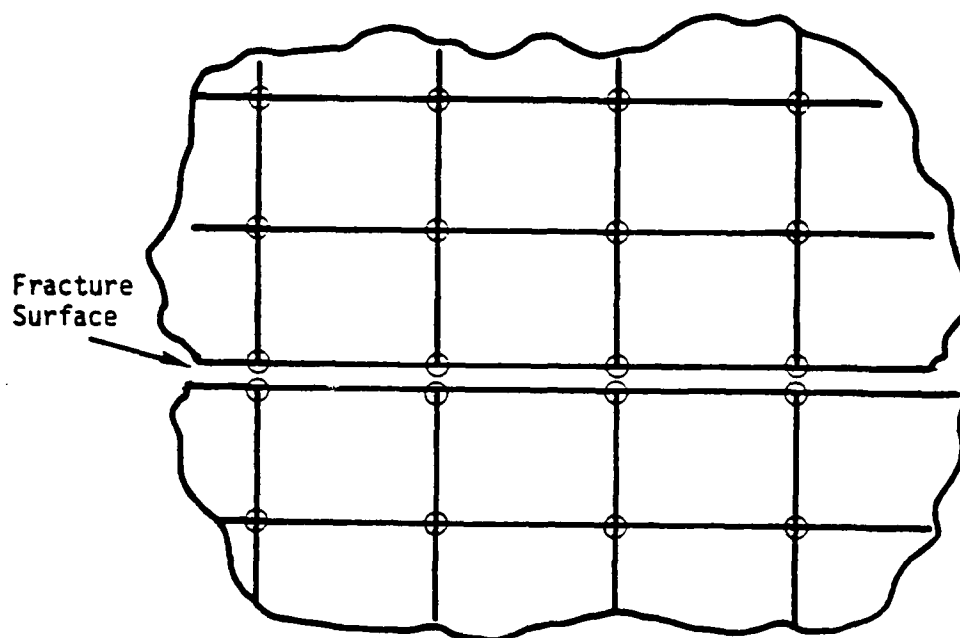
The basic philosophy in modeling fracture surfaces in the SWIS code is to represent the surface with a double node configuration. When the material is in an unfractured state the two nodes adjacent to the fracture surface are assumed to be pinned together. When tensile or shear failure occurs the adjacent nodes move apart or slide relative to each other, respectively. An example of a finite element representation of a fracture surface can be seen in Figure 1.

The behavior at a point along the fracture surface is determined by the behavior of the adjacent nodes. External nodal forces f_t and f_n are assumed to act at these nodes, and their values are chosen to correspond to the appropriate state of the fracture; i.e., pinned, free or sliding. The equilibrium equations describing the behavior of the mass particles a and b of Figure 1 are given by

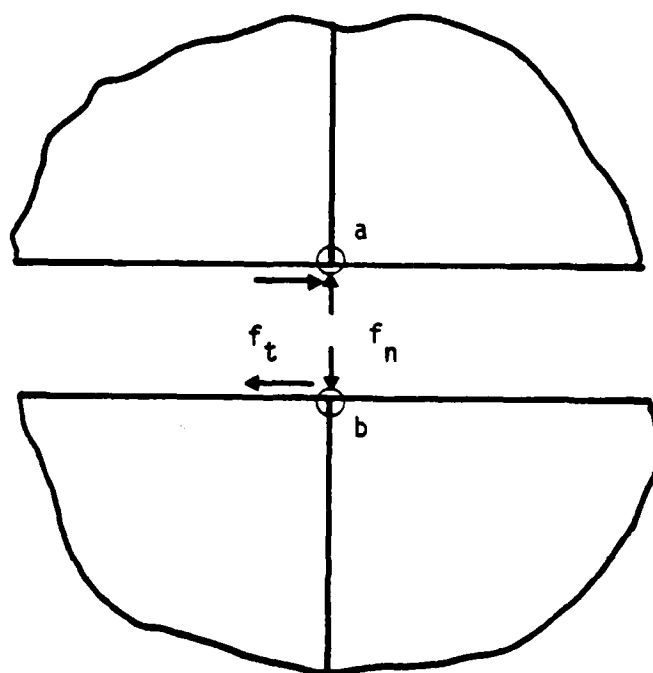
$$\left. \begin{aligned} m_a \ddot{u}_a &= -R_{ua} + f_t \\ m_a \ddot{v}_a &= -R_{va} + f_n - m_a g \\ m_b \ddot{u}_b &= -R_{ub} - f_t \\ m_b \ddot{v}_b &= -R_{vb} - f_n - m_b g \end{aligned} \right\} \quad (1)$$

where u and v are horizontal and vertical displacements, respectively, m_i is the mass of point i , g is the gravitational acceleration and R_{ij} are the restoring forces due to adjacent element stresses acting in direction i and at node j .

The determination of the nodal forces f_t and f_n for the three fracture states is described below.



(a) Finite element representation of fracture surface utilizing two adjacent nodes at a point.



(b) Detail of two adjacent nodes.

Figure 1. Fracture surface simulation.

- (1) FREE SURFACE: In this case the adjacent surfaces have moved apart ($v_a > v_b$).

$$f_t = 0 \quad (2)$$

$$f_n = 0$$

- (2) INTACT SURFACE: Before fracture occurs the adjacent nodes are pinned and

$$\ddot{u}_a = \ddot{u}_b$$

$$\ddot{v}_a = \ddot{v}_b$$

Therefore, using Eq. (1), f_t and f_n become

$$f_t = \frac{m_b R_{ua} - m_a R_{ub}}{m_a + m_b} \quad (3)$$

$$f_n = \frac{m_b R_{va} - m_a R_{vb}}{m_a + m_b}$$

- (3) SLIDING SURFACE: Shear fracture occurs when the tangential force exceeds its limiting value. This state is characterized by normal displacement continuity ($\ddot{v}_a = \ddot{v}_b$) and the following friction law

$$f_t = \pm K f_n \quad (4a)$$

where K is the friction coefficient and the sign of f_t is chosen to be opposite that of the relative tangential velocity ($\dot{u}_a - \dot{u}_b$). Normal displacement continuity again yields

$$f_n = \frac{m_b R_{va} - m_a R_{vb}}{m_a + m_b} \quad (4b)$$

In a typical calculation the nodes along the fracture surface are first assumed to be pinned together and the nodal forces f_t and f_n are calculated using Eq. (3). If σ_t is the material tensile strength, tensile failure occurs when

$$\frac{f_n}{A} < -\sigma_t$$

where A is the area associated with the nodal location in question. Similarly, shear failure occurs when

$$\frac{|f_t|}{A} > \tau$$

where τ is the material shear strength. As time passes during the calculation the free surfaces may come together again or sliding may cease.

III. EXAMPLE CALCULATION

The fracture modeling approach of Section II was utilized for the simulation of the configuration of Figure 2. The first step in the calculation is the application of gravitational loads to the continuum containing the spherical cavity. This was accomplished using the static capability of the SWIS code. The deformed mesh after this step can be seen in Figure 3.

After the application of gravitational "in situ" stress, a dynamic pressure was applied to the cavity boundary. For this test calculation a step pressure of 10 kbars was utilized. The spall layer thickness of 102 meters represents a deep spall configuration. Results of this (explicit dynamic) phase of the calculation can be seen in Figure 4. As can be seen the spall behavior is completed by 0.25 sec (one way travel time from the cavity to the free surface is 0.18 sec). The initial fracture noted in Figure 4(b) actually results from the "tensile tail" of the outgoing explosion wave. (For this calculation only tensile failure was considered and after the spall layer impacted the continuum the shear stress along the fractured surface was assumed to be zero.)

This calculation was also performed with no spall fracture by prescribing the tensile strength to be high enough to prevent failure. Results for the two calculations are seen in Figure 5 where motion of the free surface at the axis of symmetry are compared. The more complicated nature of the acceleration record for the spall configuration should be noted.

The calculation discussed in this section was performed in order to test the spall modeling approach of Section II. Future studies will consider more realistic explosion and material behaviors as well as teleseismic manifestations.

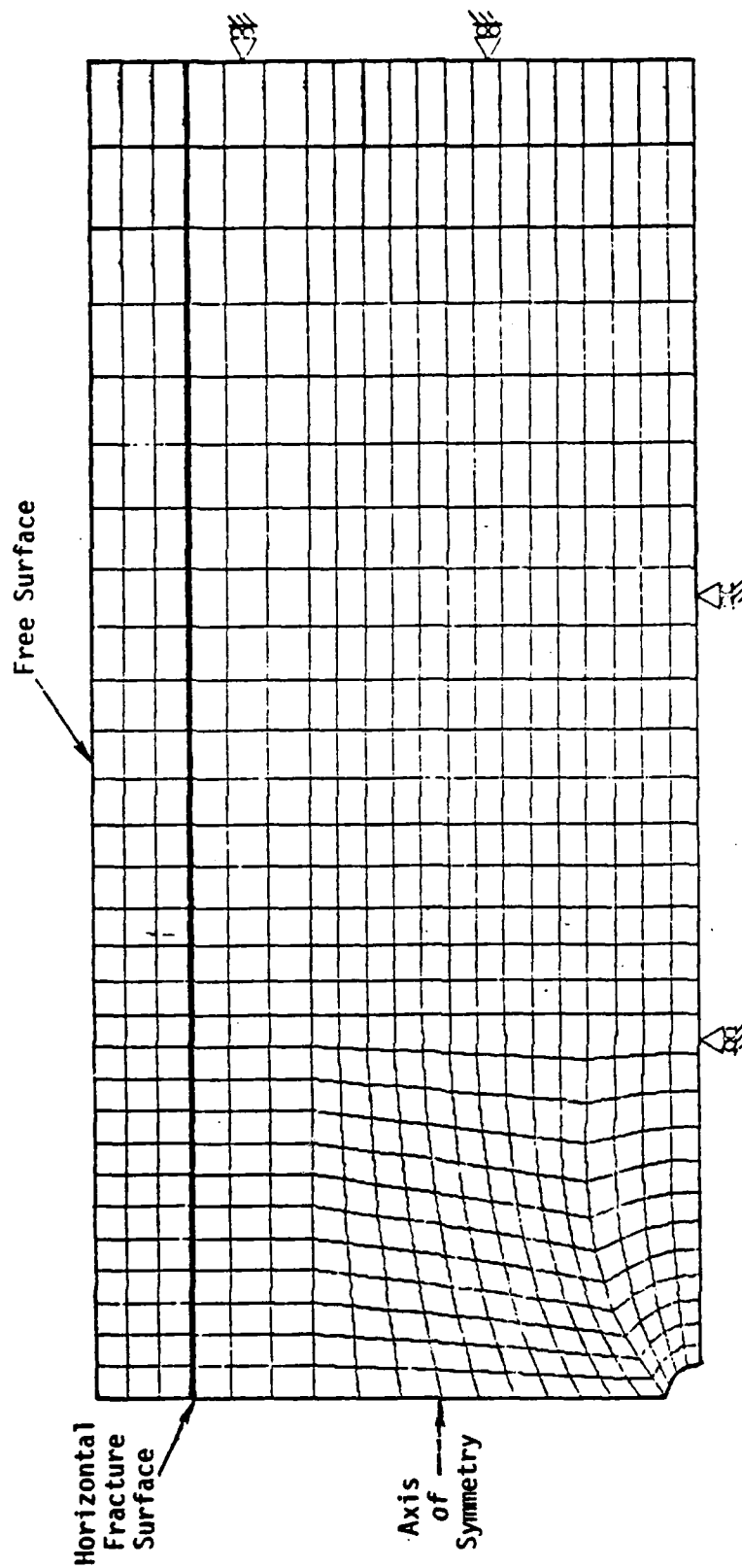


Figure 2. Finite element mesh representation of spall test calculation. The depth of burial, cavity radius and spall layer thickness are 625, 34.3, and 102 meters respectively. For test purposes, a step pressure of magnitude 10 kbars was applied at the cavity boundary. The density of the material is 2 gm/cm^3 and the P and S wave velocities are 3.5 km/sec and 2 km/sec respectively.

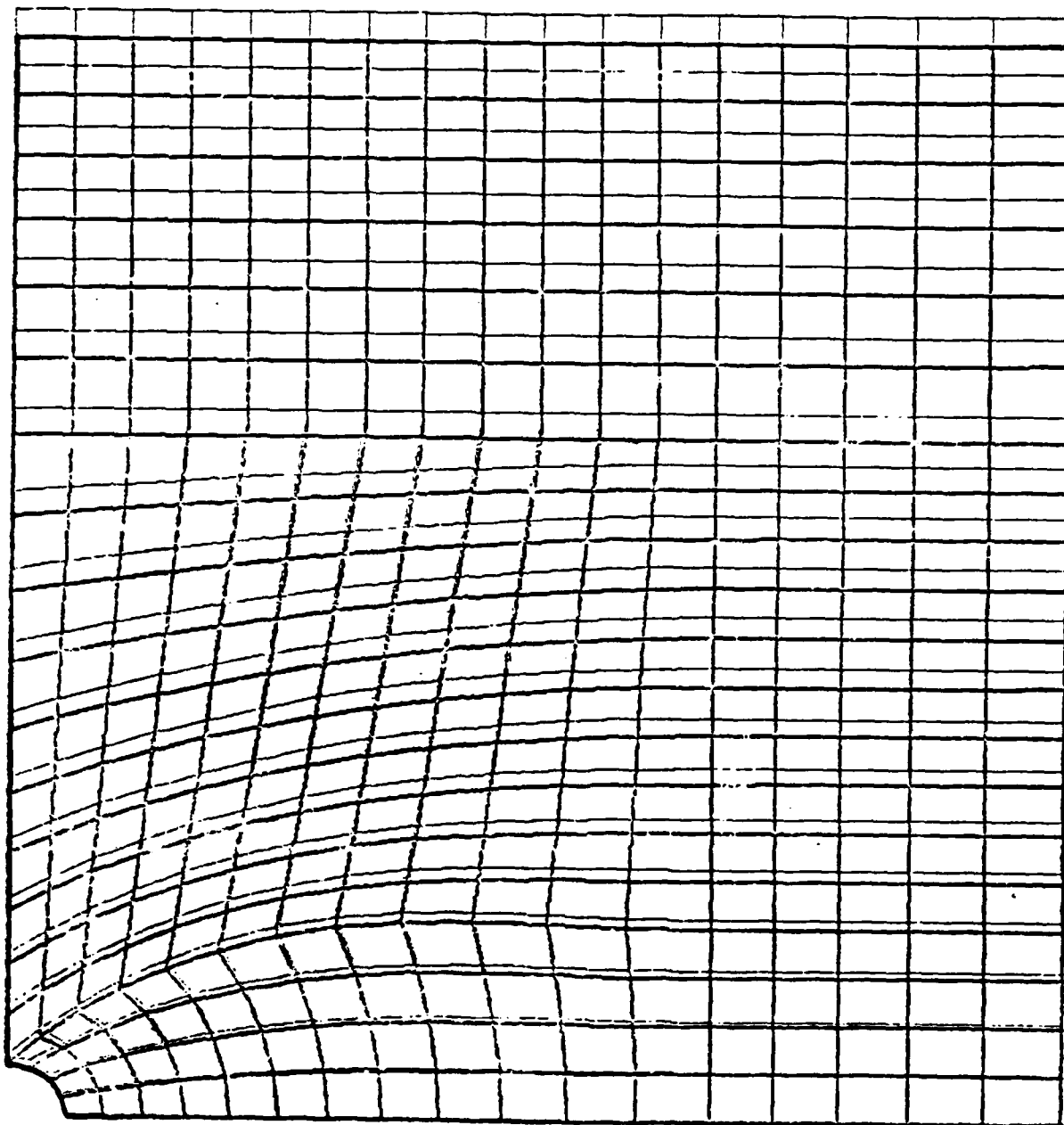
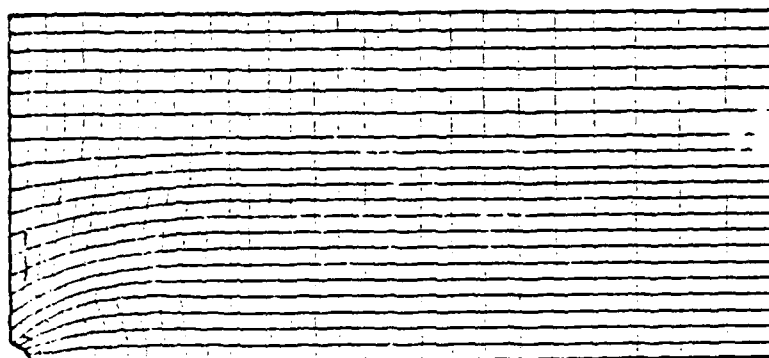
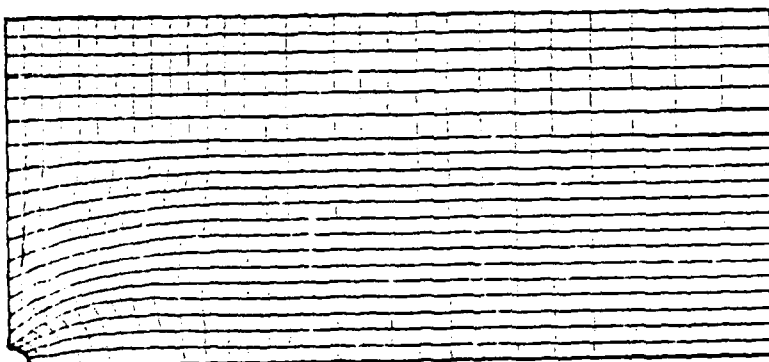


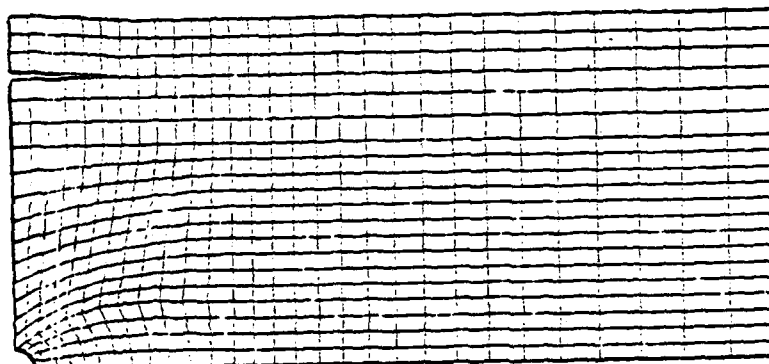
Figure 3. Detail of finite element mesh after the application of static gravitational loads. Deformed mesh (dark lines) has its displacements magnified by 100 for clarity.



(a) $t = 0.169$ sec

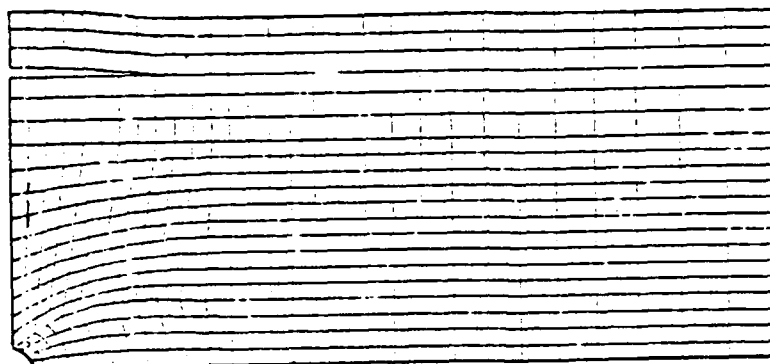


(b) $t = 0.179$ sec

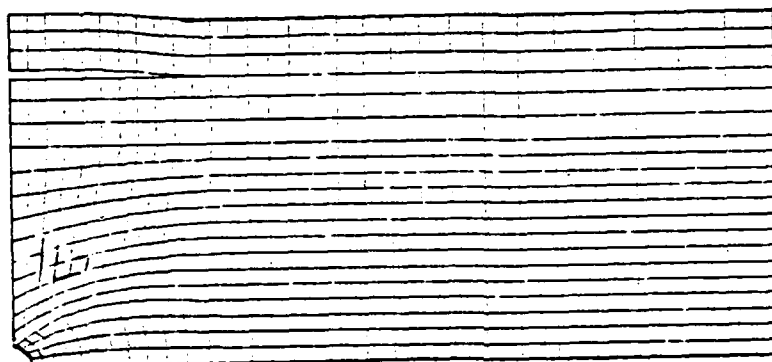


(c) $t = 0.188$ sec

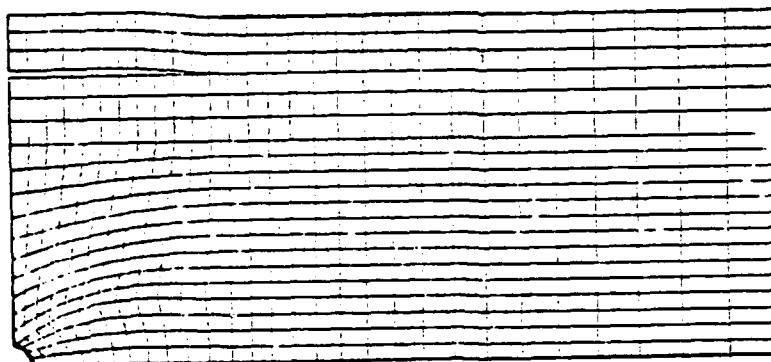
Figure 4. Configuration of mesh at specific times during the dynamic spall calculation. A tensile strength (σ_t) of the spall fracture surface of 1.0 bar was utilized.



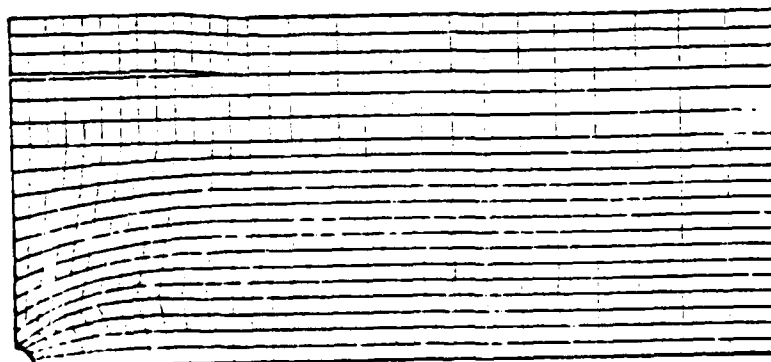
(d) $t = 0.198 \text{ sec}$



(e) $t = 0.207 \text{ sec}$

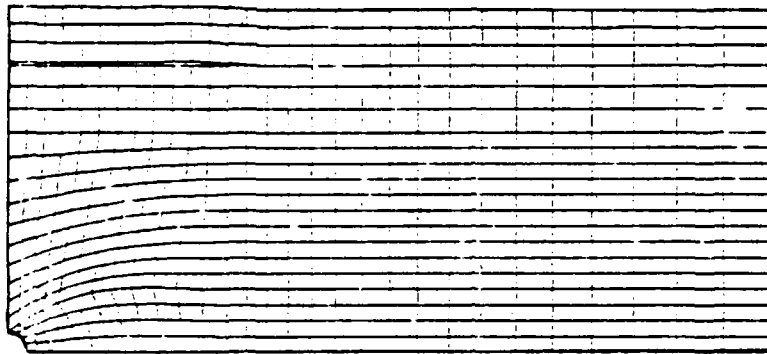


(f) $t = 0.217 \text{ sec}$

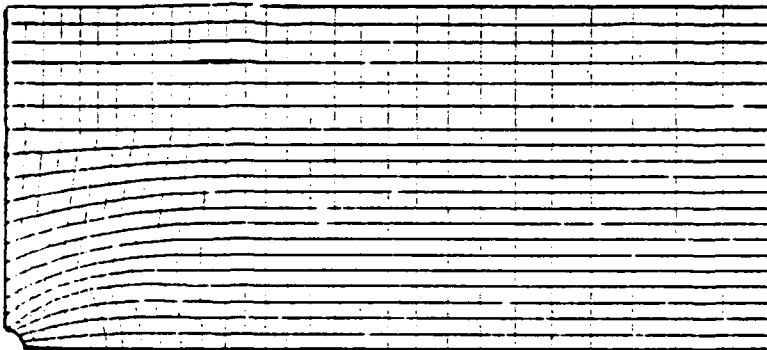


(g) $t = 0.226 \text{ sec}$

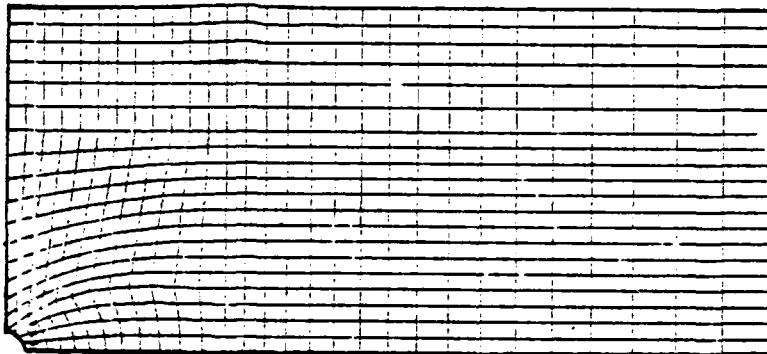
Figure 4 (continued)



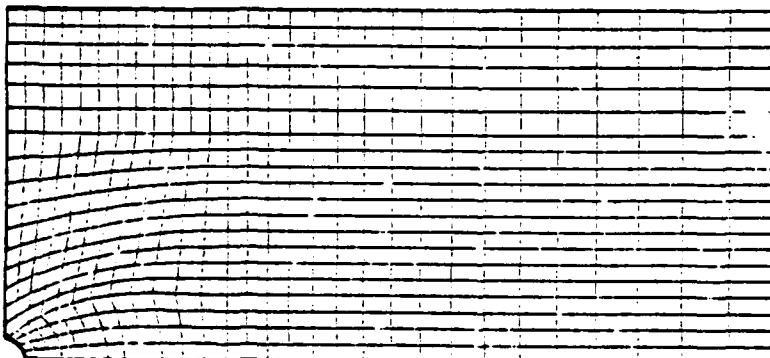
(h) $t = 0.236 \text{ sec}$



(i) $t = 0.245 \text{ sec}$



(j) $t = 0.247 \text{ sec}$



(k) $t = 0.254 \text{ sec}$

Figure 4 (continued)

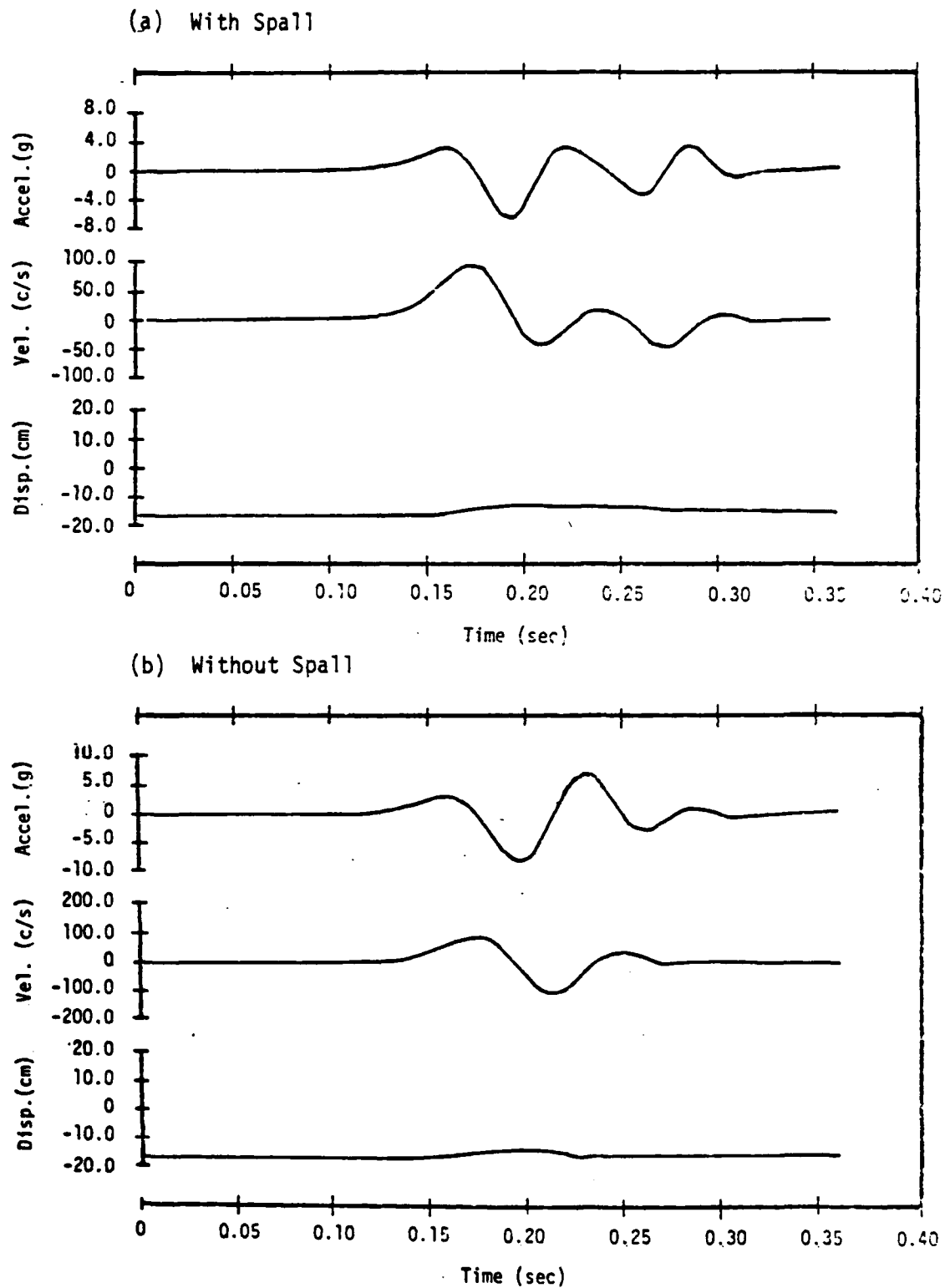


Figure 5. Comparison of the motion of the free surface at the axis of symmetry for the configurations with and without spallation.

IV. REFERENCES

1. Gvozdez, A. A. and V. V. Kuznetsov, "Spall Observed in the Ground During Seismic Prospecting," *Izv. Acad. Sc. USSR Phys. Solid Earth*, 5, pp. 280-283 (1967).
2. Springer, D. C., "Secondary Sources of Seismic Waves from Underground Explosions," *B. Seis. Soc. Am.*, 64, 581-594 (1974).
3. Tolman, Sisenore and Terhune, "The Rio Blanco Experiment: Subsurface and Surface Effects Measurements," UCRL-51504 (1973).
4. Frazier, G. A., and C. M. Petersen, "3-D Stress Wave Code for the ILLIAC IV," Systems, Science and Software Report No. SSS-R-74-2103 (1974).
5. Sweet, Joel, "SWIS Finite Element Computer Code — Nonlinear Version," Del Mar Technical Associates Report DELTA-TR-77-005, May 1977.
6. Sweet, Joel, "Slip Line Calculation Techniques," Generation of Shear Waves from Underground Explosions, Systems, Science and Software Report SSS-R-73-1918, October 1973.
7. Sweet, Joel, "Incorporation of Slip Surfaces in a Finite Element Computer Code," U. C. San Diego Report No. AMES-NSF TR-75-1 (1974).